VSB TECHNICAL UNIVERSITY OF OSTRAVA

FACULTY OF MATERIALS SCIENCE AND TECHNOLOGY

2023

PhD STUDENTS´ DAY FMST 2023

PhD students´ day FMST 2023

Faculty of Materials Science and Technology

VSB – Technical University of Ostrava

15. 6. 2023

Issued by: VSB – Technical University of Ostrava
17. listopadu 15/2172, 708 00 Ostrava-Poruba, Czech Republic, EU

Editors: Dalibor Novák, Klára Drobíková, Kateřina Skotnicová,
Marcela Ščepková

Dear readers,

you are now reading the proceedings of a conference featuring contributions by PhD students at the VŠB Technical University of Ostrava's Faculty of Materials Science and Technology. The authors gave oral presentations of their work online as part of a Doctoral Students' Day held on 15 June 2023, and they reflect the challenging work done by the students and their supervisors in the fields of metallurgy, materials engineering and management. There are 82 contributions in total, covering a range of areas – metallurgical technology, thermal engineering and fuels in industry, chemical metallurgy, nanotechnology, materials science and engineering, and industrial systems management. This represents a cross-section of the diverse topics investigated by doctoral students at the faculty, and it will provide a guide for Master's graduates in these or similar disciplines who are interested in pursuing their scientific careers further, whether they are from the faculty here in Ostrava or engineering faculties elsewhere in the Czech Republic. The quality of the contributions varies: some are of average quality, but many reach a standard comparable with research articles published in established journals focusing on disciplines of materials technology. The diversity of topics, and in some cases the excellence of the contributions, with logical structure and clearly formulated conclusions, reflect the high standard of the doctoral programme at the faculty.

At first glance, it may appear that in today's world, saturated with information technologies, disciplines such as metallurgy and materials engineering are Cinderellas, largely neglected by industry. However, in reality the opposite is true: the evolution of new technologies is placing higher and higher demands on graduates in technology disciplines, and an excellent awareness of the latest developments and their practical application is an essential requirement when recruiting graduates. Effective design of materials and technologies will remain a necessity in the future. Doctoral studies at the Faculty of Materials Science and Technology thus represent an excellent preparation for a successful career in industry. However, it is also important to present research findings in an appropriate way, and our Doctoral Students' Day plays an irreplaceable role in that regard. I am confident that these contributions will also point the way forward for the future development of the faculty, helping to formulate new interdisciplinary research topics, expanding the range of these topics and boosting their flexibility.

We can already look forward to the next Doctoral Students' Day at the faculty, which will take place from 9 to 13 September 2024 as part of the 10th Czech-Japanese Workshop. Everybody who takes part will be able to gain feedback on their work from teachers and researchers based abroad, offering a unique opportunity to test themselves and push their limits forward.

I look forward to meeting you next year.

Prof. Ing. Bohumír Strnadel, DrSc.

Vice-dean for Science and Research

Contents

Metallurgical Technology

KEY FACTORS INFLUENCING THE DILATATION OF SILICA SANDS

Author(s): Martina BAŠISTOVÁ

Supervisor: doc. Ing. Petr LICHÝ, Ph.D.

Department: Department of Metallurgical Technologies, Faculty of Materials Science and Technology, VSB – Technical University of Ostrava

Abstract

The dilatation of silica sands depends on many factors and their combinations. In this study, three silica sands with different grain sizes were evaluated: a 3D printing sand and two samples for conventional technology. The SEM, XRFS and sieve analysis results were correlated with the resulting dilatation. The findings proved the SiO_2 content and sorting degree as factors affecting the dilatation, with the highest dilatation for 3D printing sand of 34.1 %.

Key words:

Linear thermal expansion, Chemical composition, Sieve analysis, 3D sand print, Moulding mixtures.

1. INTRODUCTION

For the production of high-quality castings cast into foundry disposable molds, silica sand of high chemical purity is commonly used [1]. These sands are used for both conventional molding technologies and modern 3D printing technologies for sand molds and cores [2]. The main disadvantage of silica sands is their high dilatation with a nonlinear behavior, which is characteristic of pure quartz. Besides the expansion due to cristobalite, the phase change of β SiO_2 to α SiO_2 with a volume change of up to 3.9 % occurring around 573 °C is equally important from a foundry perspective [3]. This change results in the dilatation of the entire mixture, which, if not relaxed, for example, by the burning of added expanded perlite [4], leads to the development of restrained stress and the formation of surface defects on castings [5, 6]. It has been confirmed that besides grain size, shape, sorting degree [7], and compaction of the mold, the dilatation size also depends on the chemical composition of the silica sand, particularly the SiO_2 content [8]. This issue is significant not only for conventional methods but also for 3D printing of molds, where fine-grained, highly sorted silica sand of high chemical purity is used. In the case of this technology, the resulting surface quality of the casting is influenced by the properties of the sand, which is still a subject under investigation. Therefore, the aim of this experiment is to compare the influence of the sand's chemical composition and particle size distribution on the resulting dilatation, both for sands used in conventional methods and for 3D printing.

2. MATERIALS AND METHODS

For the purposes of the experiment, silica sand used for sand 3D printing technology was selected, characterized by high fineness and homogeneity. As comparative samples, two samples of silica sand from one locality of origin (Biala Gora, Poland) with different mean grain size used for conventional molding were chosen: finer sand (labeled BG 21) and coarser sand (labeled BG 27). All these sands have a high SiO_2 content.

The chemical composition was determined using X-ray fluorescence spectroscopy (XRFS) on an analyzer Rigaku Supermini 200. All sand samples were transformed into tablets containing 4 g of finely ground sand. Individual samples were also evaluated using a scanning electron microscope (SEM) Fei Quanta-Feg450. Images were captured at a magnification of 120x and chemical analysis was performed using EDX.

The samples were evaluated using sieve analysis on a laboratory sieve shaker with sieves ranging from 0.710 to 0.063 mm. This analysis included determining the soluble fractions and constructing a grain size distribution curve for precise determination of the mean grain size (d_{50}).

Dilatation measurements were performed on a Netzsch DIL402/C dilatometer with a corundum container for bulk materials. The samples were poured into the container and homogenized with strikes to a sample height of 10 ± 0.1 mm. The measurements were conducted in an inert atmosphere (argon)

with a flow 100 ml/min at a temperature between 25 - 1130 °C. The temperature was increased at a rate of 15°C/min.

Measurements were performed on at least 3 samples each time. The results were subsequently averaged. The used results did not deviate by more than max. 5%.

3. RESULTS AND DISCUSSION

SEM measurements demonstrated a noticeable higher presence of non-silica white grains in sample BG 21 (Figure 1). These white particles, confirmed by EDX analysis, exhibited a high content of Ti and TiO_2 (Figure 1a). In the BG 27 samples, these particles were not present (Figure 1b). Thus, the presence of other minerals and elements was confirmed only in the form of impurities adhered to the surface of the grains. No foreign particles were detected. In the case of sand for 3D printing molds, white foreign particles were also present, similar to the BG 21 sample. However, these particles contained not only SiO_2 but also a high amount of Zr (Figure 1c). The occurrence of foreign particles was lower than in the case of BG 21 and larger in size.

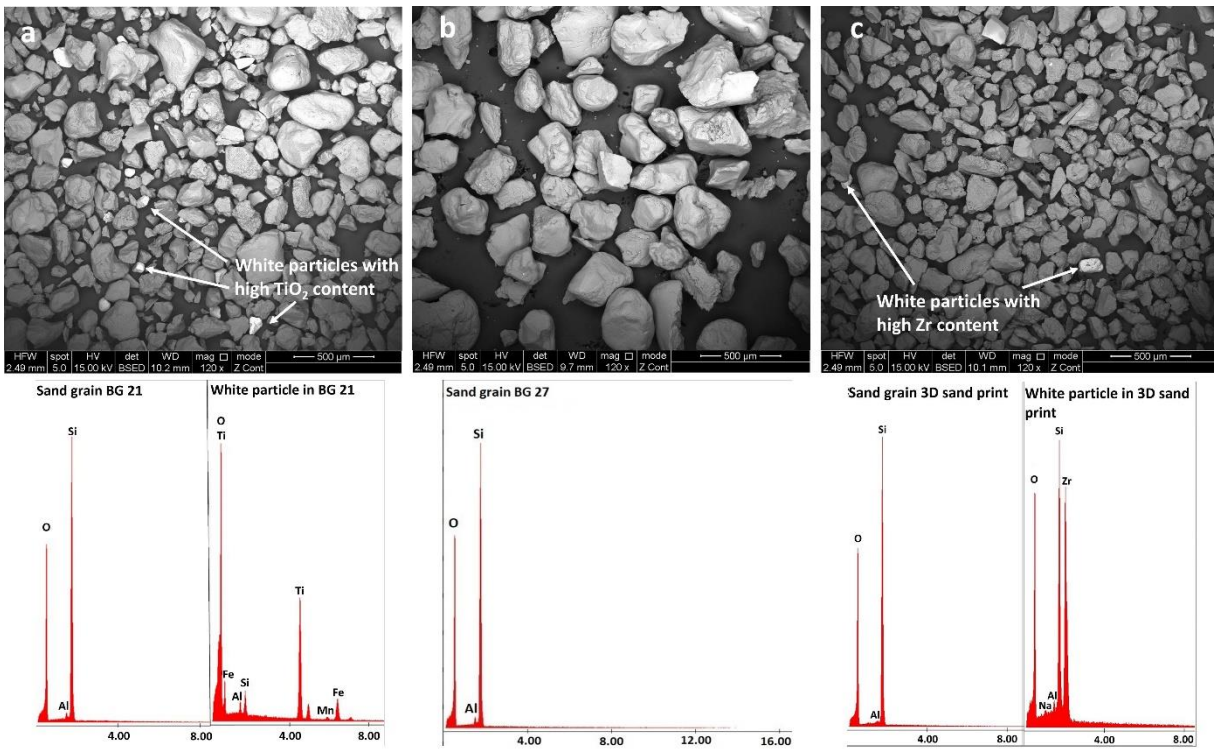

Figure 1 SEM images and EDX analysis of the samples: a) BG 21, b) BG 27, c) 3D print sand.
Source: (own)

Chemical analysis using XRFS in Table 1 subsequently confirmed the aforementioned distinct chemical composition of all three silica sand samples. Silica sands BG 21 and BG 27 exhibited different compositions despite being samples of the same origin. Generally, silica sands are sorted by the manufacturer based on the desired mean grain size (d_{50}). This size-based sorting demonstrated a significant influence on the chemical composition, with the coarser sand BG 27 exhibiting a 1.3 % higher SiO_2 content than finer BG 21. Specifically, 99.127 % SiO_2 for BG 27 and 97.8 % SiO_2 for BG 21. Silica sand for 3D printing contained 98.035 % SiO_2, which was 0.24 % higher compared to the finer BG 21 sand. Interestingly, the 3D sand had a higher content of Al_2O_3 compared to the BG 21 and BG 27 sands, as well as a higher content of K_2O, indicating a higher presence of feldspar remnants. In the case of sands used for conventional molding, BG 21 sand exhibited higher concentrations of Al_2O_3, K_2O, TiO_2, and Fe_2O_3, compared to BG 27 sand, due to its lower chemical purity.

Table 1 The chemical composition of individual sand samples (XRFS). Source: (own)

Sample	SiO_2 (wt.%)	Al_2O_3 (wt.%)	SO_3 (wt.%)	K_2O (wt.%)	CaO (wt.%)	TiO_2 (wt.%)	Fe_2O_3 (wt.%)	ZrO_2 (wt.%)
BG 21	97.800	0.778	0.020	0.083	0.036	0.829	0.234	0.151
BG 27	99.127	0.459	0.028	0.052	0.052	0.107	0.145	0.030
3D sand	98.035	1.032	0.025	0.108	0.024	0.462	0.185	0.085

From the sieve analysis, the different grain sizes of the sand samples were evident (Figure 2a). While sand BG 21 had the majority of grains in the fractions of 0.180 mm and 0.125 mm, in the case of BG 27, the highest representation was in the fractions of 0.250 mm and 0.180 mm, and for 3D sand in the fractions of 0.125 mm and 0.090 mm. The mean grain size (d_{50}) therefore corresponded to 0.19 mm for sand BG 21, 0.23 mm for BG 27, and 0.14 mm for 3D sand. Thus, the coarser grading of BG 27 and the finest grain size of the 3D sand were confirmed. Sands BG 21 and BG 27 exhibited a polyfractional character with a more uniform representation of all grain fractions (log W 61 and 64), whereas the 3D sand showed more monofractional grading, with 90 % of all grains represented in only 2 fractions (log W 41). This is also reflected in the steepness of the curves in Figure 2a, where a steeper curve indicates monofractional grading.

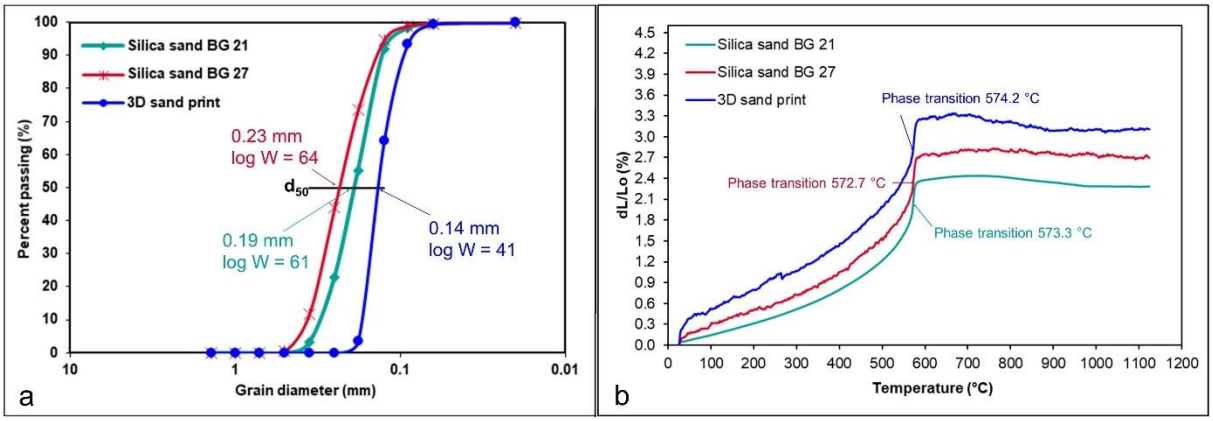

Figure 2 Granularity (a) and dilatation (b) curves for all samples. Source: (own)

The assumption of grain size-dependent dilatation yielded the lowest dilatation for 3D sand (finest), and the highest for BG 27 (coarsest), according to the rule that larger grains exhibit greater dilatation. However, the highest dilatation was observed in the sample of 3D sand (Figure 2b), measuring 3.34 %. The thermal dilatation of the coarse-grained BG 27 reached a value of 2.90 %, which was 13.2 % lower. Silica sand BG 21 exhibited a dilatation of 2.49 %, which was 14.1 % less than BG 27 and 25.5 % less than 3D sand. The grain size rule only manifested in the case of sands for conventional technologies, where grain size, i.e., grading, significantly influences the chemical composition and subsequently, the dilatation.

The non-linear curve of thermal dilatation for silica sands is evident in Figure 2a, caused by the transformation of β SiO_2 to α SiO_2. During the dilatation evaluation, a difference in phase transition temperatures was observed for individual samples. In the case of chemically purer coarse-grained sand BG 27, the transformation occurred at a temperature of 572.7 °C, while for fine-grained BG 21 with lower chemical purity, it occurred at 573.3 °C. Therefore, the phase change in BG 27 occurred at a temperature 0.6 °C lower. It can be inferred that a higher SiO_2 content lowers the temperature of the phase transition process.

For 3D sand, the phase transition occurred at a temperature of 574.2 °C, the highest temperature among all examined samples. Chemically, the 3D sand was positioned between the two samples for conventional technologies, closer to BG 21. Based on the purely chemical composition, could be expected a dilatation result, including the transition temperature, somewhere between the examined samples of BG 21 and BG 27. However, the 3D sand achieved higher dilatations than BG 27 and a shift of phase transition to higher temperatures than BG 21. The reason for this outcome lies in the grading and the character of the 3D sand, which was highly graded and nearly monofractional. Monofractional sands exhibit the smallest number of free pores between individual grains, which hinders effective relaxation of sand dilatation. For this reason, highly graded monofractional sands demonstrate

high dilatation, which is even more pronounced in the case of highly chemically pure sands. This was also true for the examined 3D sand sample with a SiO_2 content of 98.127 %.

4. CONCLUSION

This study observed key factors influencing the dilatation of silica sands, including grain size, SiO_2 content, and grading for three samples: fine-grained sand for 3D printing and two reference samples with the same origin but different mean grain sizes (d_{50}) for conventional technologies. The results revealed:

- The sand with larger grains, BG 27, contained 1.3 % more SiO_2 and exhibited a dilatation 16.5 % higher than the fine-grained BG 21. Thus, the influence of grain size grading on the chemical purity and resulting dilatation of the sand was demonstrated.
- Sands with smaller grain sizes contained higher levels of impurities and additives.
- The fine-grained 3D sand achieved the highest values of thermal dilatation, surpassing BG 21 by as much as 34.1 %, despite its lower chemical purity compared to the purest coarse-grained BG 27. The higher impact of the monofractional nature of the sand on the resulting dilatation was demonstrated on 3D sand, despite its lower chemical purity.
- The combination of chemical purity, monofractionality, and high dilatation makes the 3D printing sand the most susceptible to the occurrence of defects from restrained stress, such as veining or increased surface roughness.

ACKNOWLEDGEMENT

This research was funded by the project of MEYS (grant number CZ.02.1.01/0.0/0.0/17_049/0008399). This research was carried out with the support of projects of student grant competition (project number SP2023/022).

REFERENCES

[1] BŘUSKA, M., J. BEŇO, M. CAGALA, V. JASINKOVÁ. Dilatometric characterization of foundry sands. *Archives of Foundry Engineering*. 2012, **12**, 9–14. DOI: 10.2478/v10266-012-0027-8.

[2] SIVARUPAN, Tharmalingam, Nagasivamuni BALASUBRAMANI, Prateek SAXENA, Devarajan NAGARAJAN, Mohamed El MANSORI, Konstantinos SALONITIS, Mark JOLLY, Matthew S. DARGUSCH. A review on the progress and challenges of binder jet 3D printing of sand moulds for advanced casting. *Additive Manufacturing*. 2021, **40**, 101889. DOI: 10.1016/j.addma.2021.101889

[3] THIEL, J., M. ZIEGLER, P. DZIENKONSKI, S. JOYCE. Investigation into the technical limitations of silica sand due to thermal expansion. *Transactions of the American Foundry Society*. 2007, **115**, 383-400.

[4] BOBROWSKI, A., D. DROŻYŃSKI, J. JAKUBSKI, M. SZUMERA, K. KACZMARSKA, B. GRABOWSKA. Thermal Deformation of Moulding and Core Sands with an Inorganic Binder Containing a Relaxation Additive. *Archives of Foundry Engineering*. 2018, **18**-4, 93-98. DOI: 10.24425/afe.2018.125175.

[5] HRUBOVČÁKOVÁ, M., I. VASKOVÁ, M. BENKOVÁ, M. CONEV. Opening Material as the Possibility of Elimination Veining in Foundries. *Archives of Foundry Engineering*. 2016, **16**, 157-161. DOI: 10.1515/afe-2016-0070.

[6] JANUŠEVIĆ, Z., Z. GULIŠIJA, S. RADOSAVLJEVIĆ, Z. AĆIMOVIĆ. A contribution to study of processes on the steel cast–sand mould contact surface during casting. *Materials Letters*. 2000, **45**.5, 235-240.

[7] RADKOVSKÝ, Filip, Martina GAWRONOVÁ, Václav MERTA, Petr LICHÝ, Ivana KROUPOVÁ, Isabel NGUYENOVÁ, Šimon KIELAR, Martin FOLTA, Josef BRADÁČ, Radim Kocich. Effect of the Composition of Hybrid Sands on the Change in Thermal Expansion. *Materials*. 2022, ***15***(17), 6180. DOI: 10.3390/ma15176180

[8] SVIDRÓ, Josef, József Tamás SVIDRÓ, Attila DIÓSZEGI. The role of purity level in foundry silica sand on its thermal properties. *Journal of Physics: Conference Series*. 2020, **1527**(1), 012039. DOI: 10.1088/1742-6596/1527/1/012039.

EFFECT OF A DEFORMATION TEMPERATURE AND APPLIED STRAIN RATE LEVEL ON THE DEFORMATION BEHAVIOR OF THE 3D PRINTED INCONEL 718 SUPERALLOY

Author(s): Marek BENČ

Supervisor: prof. Ing. Radim KOCICH, Ph.D.

Department: Department of Metallurgy and Technologies, Faculty of Materials Science and Technology, VSB – Technical University of Ostrava

Abstract

The Inconel 718 is high-strength, corrosion-resistant nickel-based superalloy. It is known for its excellent mechanical properties and resistance to high temperature. Determining of the deformation behaviour of materials is crucial for the appropriate use of the material for specific applications. This work investigates the effect of deformation behaviour of 3D printed Inconel 718 alloy, which has been tested over a wide range of temperatures and strain rates. Based on the experimental data obtained, it was possible to determine the peak stress levels as well as the onset of dynamic softening extra with an emphasis on the corresponding mathematical description. The experimental data revealed a minimal and maximal flow stress level of 98 MPa and 683 MPa as for the combination of 1473 K – 0.1 s^{-1} and 1173 K – 10 s^{-1}, respectively. The experimental data of the course of the peak strain did not support the assumed trend and onset of dynamic recrystallization as in the calculated data.

Key words:

*Inconel 718, 3D metal printing, hot compression test, peak stress***.**

1. INTRODUCTION

3D metal printing is the process of creating three-dimensional objects by successively joining and adding layers of metal material. The Selective Laser Melting (SLM) method is one of the additive manufacturing techniques that falls into the category of powder bed fusion. During the SLM process, a thin layer of metal powder is gradually fused in the powder bed layer by layer through a powerful laser. The advantages of SLM technology are cost efficiency, accuracy and rapid of production. Nonetheless, these printed powder materials also have disadvantages such as limited dimensions, surface roughness, internal porosity or residual stress. One alternative to avoid these disadvantages and improve material properties is to combine additive technology with plastic deformation mechanisms. For example, in a study by DA, Lesyk et al. investigating the porosity characterization of 3D printed 718 Inconel treated with HIP technology, it was found that the HIP process reduced the residual porosity from 99.862% to 99.997% and the average pore size value from approximately 6.5 μm to 1.25 μm. [1,2,3]

Inconel 718 is a superalloy, one of the important nickel and nickel-based alloys. This alloy has found its place in many industries due to its unique properties such as high oxidation resistance, corrosion resistance even at very high temperatures and also retains high mechanical strength under these conditions. Is widely used as components in aircraft engines, chemical processing, pressure vessels, steam turbine power plants, aerospace vehicles, medical, marine. [4,5]

The main objective of this research is to reveal the effect of deformation temperature and applied strain rate on the deformation behaviour of 3D printed Inconel 718 alloy with a more detailed focus on the maximum stress levels achieved and onset of dynamic recrystallization.

2. SLM SUPERALLOY AND HOT COMPRESSION TEST

The samples for the experiment (see Figure 1) had cylindrical shape with a diameter of 10 mm and a height of 15 mm. The parts were printed in the vertical direction of the stripe strategy by selective laser melting on a Renishaw AM 400 3D printer. The original powder with a particle size of 15-45 μm was melted in 60 μm thick layers using a powerful of 200 W laser in an inert argon atmosphere. Series utilizing a hot compression tests were performed range of thermomechanical conditions, specifically the temperature levels of 1173 K, 1273 K, 1373 K, 1423 K with combination strain rate levels of 0.1 s^{-1}, 1 s^{-1}, 10 s^{-1} and 12 flow curves in total. Testing was carried out in a test chamber under vacuum, the

sample-anvils interface separated by tantalum foils and a nickel-based grease, direct electrical resistance heating, a temperature control via thermocouple wires, sample heating directly up to a deformation temperature, dwell-time of 300 s. Analysis of the obtained flow curves provided the coordinates of the peak point (peak strain and peak stress) corresponding to each tested combination of temperature and strain rate

Figure 1 Experiment samples before and after hot compression test. Source: (own)

3. RELATIONSHIP BETWEEN COORDINATES OF PEAK POINTS

The experimental peak coordinates were processed using regression analysis to determine the functional relationships between the predictors (i.e., deformation temperature, T (K) and strain rate, $\dot{\varepsilon}$ (s^{-1})) and corresponding outcomes (i.e., peak strain, ε_p (-) and peak stress, σ_p (MPa)). These relations are given by equations (1) – (3). Corresponding material constants were firstly estimated via the methodism enabling to obtain rough estimate [6, 7]. This estimate was then refined via a nonlinear least square algorithm. The differences between the initial and refined estimates are documented in Figure 2. This figure imply that the refined estimate offers slightly better regression fit.

$$\varepsilon_p = 0.06352 \cdot Z^{0.021} \tag{1}$$

$$\sigma_p = \frac{1}{0.0035} \cdot \operatorname{arcsinh} \sqrt[5.2679]{\frac{Z}{1.18E{+}19}} \tag{2}$$

$$Z = \dot{\varepsilon} \cdot \exp\left(\frac{494{,}87}{R \cdot T}\right) \tag{3}$$

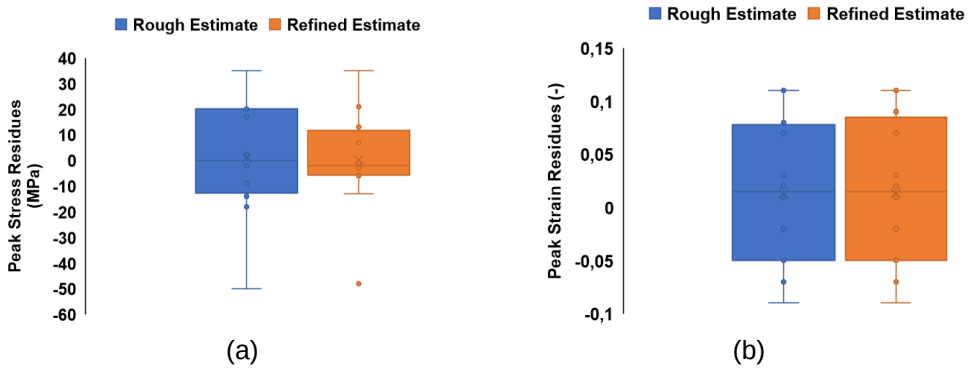

Figure 2 Differences between the initial and refined materials constants a) peak stress residues b) peak strain residues. Source: (own)

4. RESULTS AND DISCUSION

The experimentally obtained and calculated coordinates of the peak points are presented graphically in Figure 3. Experimental and model data show the same trend of peak stress levels, the higher the strain temperature, the lower the stress. The effect of strain rate is then reversed. The observed peak stress data then show minimum and maximum stress levels approximately 98 MPa and 683 MPa for the combinations of 1473 K- 0.1 s^{-1} and 1173 K - 10 s^{-1}, respectively. With respect to the peak strain course, the experimental data are out of the assumed trend and the description via equation

(1) is thus unable to reflect this experimental course. The position of the peak strain coordinate relates with the onset of dynamic recrystallization. Generally, higher temperatures and lower strain rates accelerate this softening mechanism, which is manifested by the offset of peak strain coordinate toward lower values. However, the experimentally acquired trends entirely disturb this theory. This can be probably attributed to the porosity structure of the 3D printed material since the porosity can negatively influence the nucleation of new grains – specifically the number of suitable germinal sites.

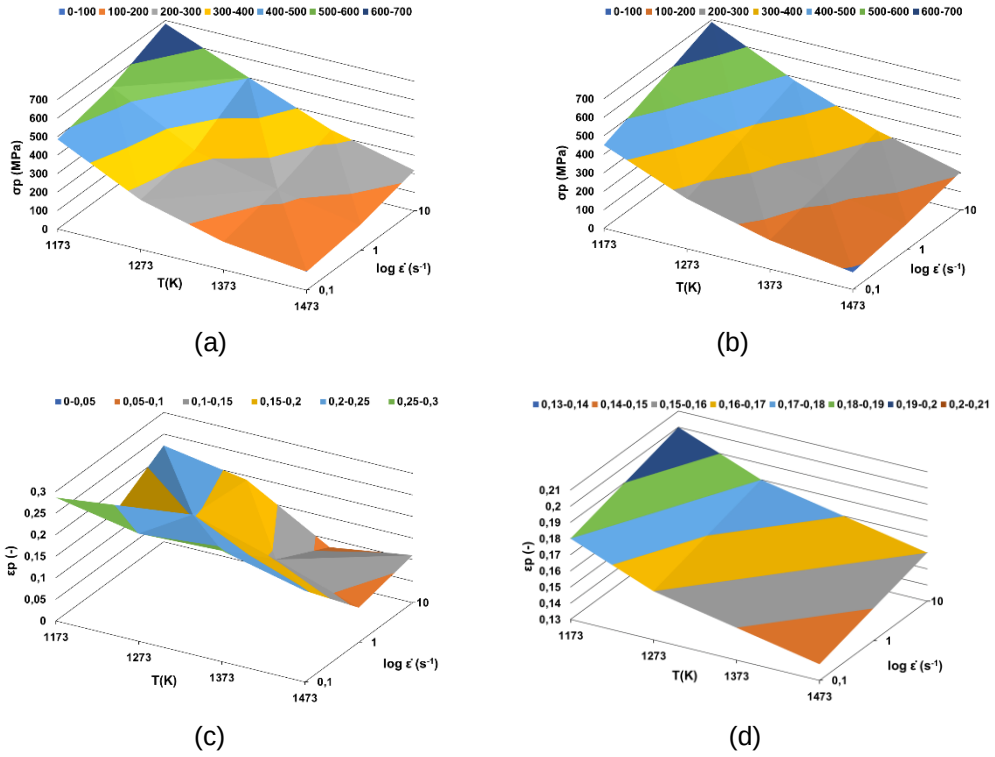

Figure 3 Experimentally and calculated peak point coordinates a) σ_p-experiment b) σ_p-calculed c) ε_p-experiment d) ε_p-calculed. Source: (own)

5. CONCLUSION

This work investigated the effect of deformation temperature and level of applied strain rate on the deformation behaviour of 3D printed Inconel 718 alloy and also focus the onset of dynamic recrystallization. The flow curves obtained from the compression test results were used to obtain a global peak corresponding to each tested. combination of temperature and strain rate. The rough estimates of the corresponding material constants were calculated via a linear least square methodism and subsequently refined by a nonlinear regression analysis. The experimentally obtained and calculated coordinates of the peaks are expressed graphically as a function of the corresponding predictors.

For both experimental and calculed data, the higher the deformation temperature, the lower the peak coordinates. The effect of strain rate is opposite. The experimental data revealed a minimal and maximal flow stress level of 98 MPa and 683 MPa as for the combination of 1473 K – 0.1 s−1 and 1173 K – 10 s−1, respectively. The experimental and calculated deformation coordinates has different course. The measured experimental strain values have a decrease in certain regions at strain temperatures of 1173 K and 1373 and strain rates of 1 s^{-1} and 10 s^{-1}. The experimental data of the course of peak strain described by the equation (1) are outside the predicted trend. The experimentally obtained peak strain coordinates did not support the onset of dynamic recrystallization, as this softening manifest itself at higher temperatures and lower strain rates by shifting the maximum strain coordinates towards lower values. The reason for this finding can probably be the porosity of the 3D printed *material*.

ACKNOWLEDGEMENT

This work was made with the financial support of the "Student Grant Competition" projects „Development of alternate ways for preparation of progressive materials and their processing" SP2023/022

REFERENCES

[1] Zhang, Dongyun, Pudan Zhang, Zhen Liu, Zhe Feng, Chengjie Wang, Yanwu Guo, Thermofluid field of molten pool and its effects during selective laser melting (SLM) of Inconel 718 alloy. *Additive Manufacturing*. 2018, **21**, 567-578.

[2] KUNČICKÁ, L, Radim, KOCICH, Gergely, NÉMETH, Karel, DVOŘÁK, Marek, PAGÁČ. Effect of post process shear straining on structure and mechanical properties of 316 L stainless steel manufactured via powder bed fusion. Additive Manufacturing, 2022, **59**, 103128.

[3] DYMYTRY, L, S, Martinez, O, Pedash, V, Dzhemelinskyi, Aitzol Lamikiz. Porosity and surface defects characterization of hot isostatically pressed Inconel 718 alloy turbine blades printed by 3D laser metal fusion technology. *MRS Advances* 2022, **7**, 197–201.

[4] Hosseini, Ehsan, V. Popovich. A review of mechanical properties of additively manufactured Inconel 718, Additive Manufacturing, 2019,**30**,100877.

[5] Huang Jiankang, Li, Fuqian Yang, YU, Xiaoquan, Ni, YU, Fan, Ding.Effects of electric current on δ phase evolution and tensile behavior of Inconel 718, Materials Science and Engineering: 2022, **855**,2022,143886.

[6] OPĚLA, P, Petr, KAWULOK, Ivo, SCHINDLER, Rostislav, KAWULOK, Stanislav, RUSZ, Horymír, NAVRÁTIL. On the Zener–Hollomon Parameter, Multi-Layer Perceptron and Multivariate Polynomials in the Struggle for the Peak and Steady-State Description. Metals. 2020, **11**, 1413.

[7] SCHINDLER, I, Petr, KAWULOK, Rostislav, KAWULOK, Eugeniusz, HADASIK, Dariusz, KUC. Influence of Calculation Method on Value of Activation Energy in Hot Forming. High Temp. Mater. Processes 2013, **32**, 1.

PHYSICAL MODELLING OF THE INFLUENCE OF LADLE SHROUD DEFLECTION IN THE FIVE-STRAND TUNDISH

Author(s): Jiří CUPEK, Josef WALEK

Supervisor: prof. Ing. Markéta TKADLEČKOVÁ, Ph.D.

Department: Department of Metallurgical Technologies, Faculty of Materials Science and Technology, VSB – Technical University of Ostrava

Abstract

The paper presents with the study of steel flow in the tundish using the method of physical modelling. Experimental device was a physical model of an asymmetric five-strand tundish. The aim of the paper is to compare the influence of the critical deflection of the ladle shroud, the shape of the impact pad and the casting speed on the character of the flow.

Key words:

Continuous casting of steel, tundish, ladle shroud, casting speed, physical modelling.

1. INTRODUCTION

Continuous casting has become the dominant method of steel casting over the past 50 years, as more than 95% of all steel produced is currently cast this way. Continuous casting of steel is a technological process in which liquid steel is processed into billets, which are of the desired shape with an almost unlimited length and are most often intended for further processing [1].

The tundish is one of the most important technological parts of the casting machine. It primarily provides supplying steel during ladle change and steel distribution between casting strands. The tundish is the last reactor in which it is possible to influence the final quality and purity of the cast steel, for this reason it is necessary to optimize the flow of steel in the tundish [1, 2].

Optimum steel flow in the tundish is essential for continuous casting equipment. Impact pads, baffles, dams and weirs can be used to optimize the flow. The so-called retention time is related to the nature of the flow. It is the time for which a certain element of melt remains in the tundish. Under physical modelling conditions, the residence time is determined by injecting a dye, acid or salt, the concentration of which is recorded on the tundish submerge entry nozzles. Concentration curves are compiled from the result of modelling [3, 4].

The flow in the tundish can be divided into active and passive. Active flow is referred to as the active volume of the tundish, being divided into a well-mixed volume and a plug flow volume. In the case of a well-mixed volume, it is a turbulent flow that occurs mainly in the vicinity of the ladle shroud. It follows the area of the tundish with a predominantly plug flow volume, which is characterized by a slow, orderly flow. Passive volume is referred to as dead volume. There is almost no flow in this area, which reduces the effective space of the tundish. The dead volume is characterized by achieving almost twice the residence time compared to the so-called theoretical residence time, which is defined as the ratio of the volume of the tundish and the volume flow of steel into the tundish. It is important to increase the active volume (especially the plug flow volume) as much as possible and to eliminate the passive (dead) volume [3, 4, 5, 6].

2. EXPERIMENTAL CONDITIONS OF PHYSICAL MODELLING

Physical modelling is a method in which the real system is replaced by a model whose behaviour is as close as possible to the behaviour of a real operating system. The principle of physical modelling consists in the targeted use of similarities between the real device and its model. The fluid flow in the technological process is modelled again by the fluid flow in the model, but in a certain scale of lengths, volume flow rates, viscosities, etc. The condition for transferring results from the model to the prototype is the similarity of the processes taking place in the model and the prototype [3, 5, 6, 7].

One of the advantages of physical modelling is the possibility of visualizing processes that contribute to the understanding of the processes taking place in real operating systems. From the results

achieved on the model, it is possible to predict the behaviour of the real operating system during various process changes. For physical modelling, a plexiglass model on a scale of 1:4 (see Figure 1) is used for the operating tundish. Part of the physical model are two ladles, ladle shroud, stopper rods, SEN and moulds. The character of the steel flow in the tundish is simulated at physical modelling by the model liquid (water) [1, 6, 7].

Figure 1 The Physical model of five-strand tundish. Source: (own)

Water is most often used as a medium for physical modelling of metallurgical processes. Water is characterized by low costs and its high availability. The important physical properties is the kinematic viscosity, which is similar to water at 20 °C as to steel at 1520 °C. A comparison of the basic physical properties of water and steel is shown in table 1 [1, 3].

Table 1 Comparison of the basic physical properties of water and steel. Source: [1]

Physical properties	Symbol	Unit	Steel	Water
Temperature	t	[°C]	1520	20
Density	ρ	[kg·m^{-3}]	7000	998
Dynamic viscosity	η	[kg·m^{-1}·s^{-1}]	5,0·10^{-3}	1,0·10^{-3}
Kinematic viscosity	ν	[m^{2}·s^{-1}]	0,913·10^{-6}	1,02·10^{-6}
Surface tension	σ	[kg·s^{-2}]	1,69	0,09

For physical modelling there were used three types of impact pads (IP1 – basic square configuration, IP2 - rectangular configuration, IP3 – same as IP2 with convex bottom) (see Figure 2). Using these impact pads, two positions of the ladle shroud were observed: the ladle shroud is located vertically above the centre of the relevant impact pad; deflection of the ladle shroud by 8°. Physical modelling was performed for volumetric flow rates of 12.4 and 14.2 l·min^{-1}.

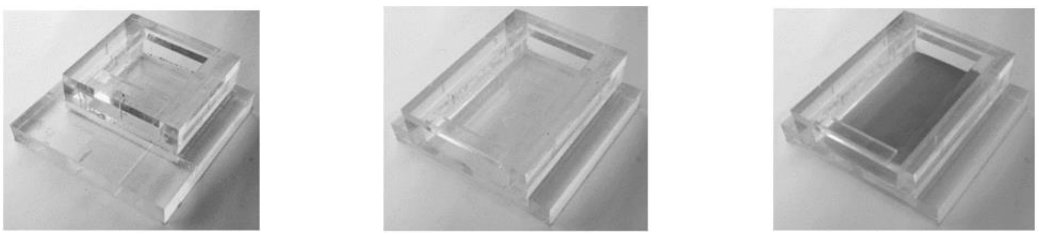

a) b) c)

Figure 2 Impact pads used for physical modelling: a) IP1; b) IP2; c) IP3. Source: (own)

3. RESULTS AND DISCUSION

Table 2 shows the minimum retention times that were determined using the Dirac impulse method. The method consists of injecting KCl into the ladle shroud and monitoring its response at all nozzles (Casting Strands - CS). The minimum retention time indicates the time from injection to the first detection on the nozzle. It is important to obtain the highest possible minimum residence time with the lowest possible variability, which is set by the coefficient of variation (CV) [3].

Table 2 Minimal residence times for all experimental configurations. Source (own)

Impact pad	Flow rate ($l \cdot min^{-1}$)	Ladle shroud (-)	τ_{min}						
			CS1 (s)	CS2 (s)	CS3 (s)	CS4 (s)	CS5 (s)	CV (%)	Ø (s)
IP1	12	Vertical	73	42	16	20	46	58	39
	14	Vertical	88	51	22	22	53	59	47
	12	Deflected	77	37	23	23	53	54	42
	14	Deflected	65	39	23	19	43	49	38
IP2	12	Vertical	101	47	27	21	39	68	47
	14	Vertical	65	36	21	21	39	50	36
	12	Deflected	77	44	23	24	36	54	41
	14	Deflected	65	35	19	20	28	56	34
IP3	12	Vertical	84	42	21	23	48	59	44
	14	Vertical	67	33	19	19	38	55	35
	12	Deflected	85	38	26	23	37	60	42
	14	Deflected	66	34	20	21	32	54	34

Based on residence times, the representation of characteristic volumes in the tundish was determined. Flow in the tundish can be divided into active and passive. The active flow is referred to as the active volume of the tundish, and is divided into the mixed and the plug flow volume. In the case of a mixed volume, it is a turbulent flow that occurs especially near the ladle shroud. This is followed by a plug flow volume region characterized by slow, orderly flow. Passive volume is referred to as dead volume. There is almost no flow in this area, which reducing the effective space in the tundish. The ratio between plug flow volume and dead volume (V_p/V_d) was compared for all configurations (see Figure 3). The IP3_D_14 variant with a Vp/Vd ratio of 2,44 performed best. Another indicator was the occurrence of dead volume only (see Figure 4). Here, the IP3_D_14 configuration performed best. Variants with impact pad IP1 always performed the worst.

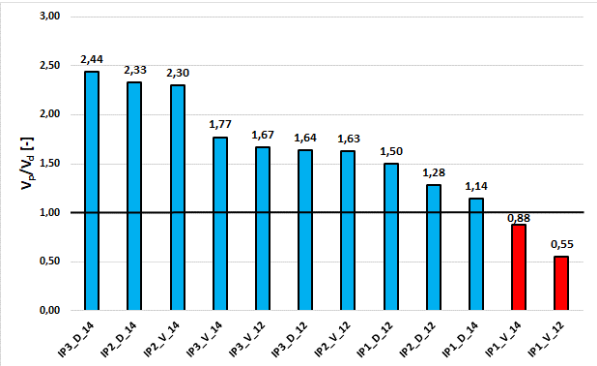

Figure 3 The ratio between plug flow volume and dead volume (all configurations). Source: (own)

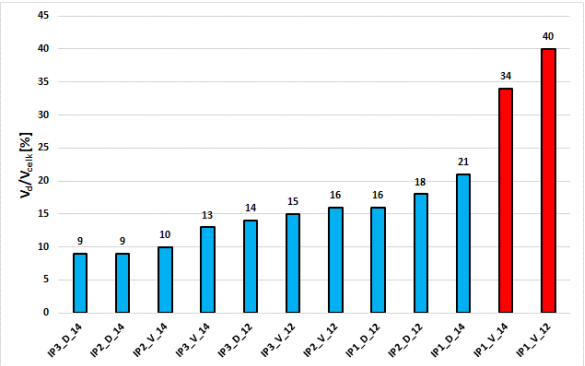

Figure 4 Dead volume occurrence (for all configurations). Source: (own)

Flow visualizations were performed as part of the research. An aqueous solution of potassium permanganate was used for flow visualization. Figure 5 shows flow visualizations after 100 seconds of solution injection. It can be seen that the IP3_D_14 configuration performed best. It can be seen that the IP3_D_14 configuration performed best, as the smallest dead volume area was obtained (see Figure 5d).

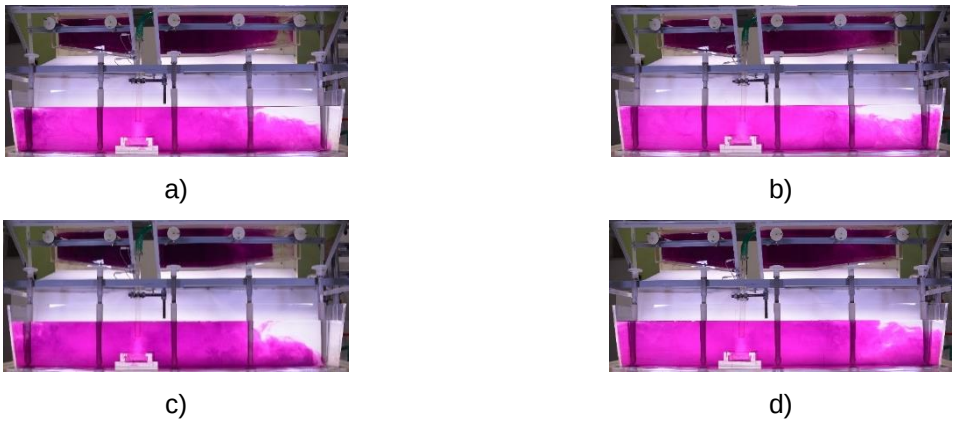

a) b)

c) d)

Figure 5 Visualization after 100 seconds: a) IP3_V_12; b) IP3_D_12; c) IP3_V_14; d) IP3_D_14.
Source: (own)

4. CONCLUSION

As part of the research, 12 different variants were evaluated. Different types of impact pads, different casting rates were used and deflection of ladle shroud was also evaluated. Evaluation based on the ratio of plug flow volume to dead volume revealed that the IP3_D_14 variant performed best, achieving the highest value of this ratio of 2.44. On the contrary, variants IP1_V_12 and IP1_V_14 performed the worst, reaching values of 0.55 and 0.88. By comparing the total dead volumes of all variants, it was found that variants IP3_D_14 and IP2_D_14 performed best, achieving the smallest dead volume area of 9%. On the other hand, variants IP1_V_12 and IP1_V_14 fared the worst, which achieved very high values (34% and 40%).

ACKNOWLEDGEMENT

The article was created thanks to the project No. CZ.02.1.01/0.0/0.0/17_049/0008399 from the EU and CR financial funds provided by the Operational Programme Research, Development and Education, Call 02_17_049 Long-Term Intersectoral Cooperation for ITI, Managing Authority: Czech Republic—Ministry of Education. The article was created within the solution of the Student Grant Competition of number SP2023/022.This paper also has been elaborated in the framework of the grant programme „Support for Science and Research in the Moravia-Silesia Region 2022" (RRC/12/2022), financed from the budget of the Moravian-Silesian Region.

REFERENCES

[1] MICHALEK, Karel. *Využití fyzikálního a numerického modelování pro optimalizaci metalurgických procesů*. Ostrava: VŠB-TU Ostrava, 2001, ISBN 80-7078-861-5.

[2] LOUHENKILPI, Seppo. Continuous Casting of steel. *Treatise on Process Metallurgy*. 2014, **3**, 373-434. ISBN 978-0-08-096988-6.

[3] ZHANG, J., YANG, S., LI, J., TANG, H. JIANG, Z. The Effect of a Dissipative Ladle Shroud on Mixing in Tundish: Mathematical and Experimental Modelling. *High Temperature Materials and Processes* [online]. 2018, **37**(1), 25-32. Avalible from (DOI):http://doi.org/10.1515/htmp-2016-0093.

[4] SUJATA, D., RAJEEV, K. S., AMITAVA, P. Role of Tundish Argon Diffuser in Steelmaking Tundish to Improve Inclusion Flotation with CFD and Water Modelling Studies. *International Journal of Engineering Research and Technology* [online]. 2015, **4**(8), 213-218. Avalible from (DOI):http://doi.org/10.17577/IJERTV4IS080223. ISSN 2278-0181.

[5] HARNSIHACACHA, Anawat, PIYAPANEEKOON, Adisorn, WATTANAPORN, Chanon. Flow prediction in the multi-strand continuous casting tundish of Millcon Steel PLC. *Materials Today: Proceedings.* 2018, **5**(3), 9229-9237. ISSN 2214-7853.

[6] CUPEK, Jiří, PIEPRZYCA, Jacek, WALEK, Josef, SATERNUS, Mariola, TKADLEČKOVÁ, Markéta, MERDER Tomasz. Optimization of the Steel Flow in the Two-Strand Tundish Using Different Geometry of Impact Pad. *Journal Metalurgija*. 2023, **62**(2). ISSN 0543-5846.

[7] ZHANG, Hua, FANG, Qing, LIU, Chao. Effect of flow control devices on grade change process in a five-strand Tundish. *Metallurgical research and Technology* [online]. 2022, 119(3). Avalible from (DOI): https://doi.org/10.1051/metal/2022039

EFFECT OF AUSTENITIZATION TEMPERATURE ON DCCT DIAGRAM OF MN-CR-MO PIPE STEEL

Author(s): Svatopluk ČECH

Supervisor: prof. Ing. Ivo SCHINDLER, CSc.

Department: Department of Metallurgical Technologies, Faculty of Materials Science and Technology, VSB – Technical University of Ostrava

Abstract

The steel with 0.3% C – 1.2% Mn – 0.8% Cr – 0.2% Mo is intended for the production of seamless pipes in the Mannesmann method. The heating and finishing temperatures are relatively high and it is therefore necessary to know the continuous cooling transformation (CCT) diagrams in a wider range of temperature conditions. At a heating rate of 0.167 °C/s, the temperature Ac_3 = 824 °C was determined dilatometrically for the investigated steel. Subsequently, two different austenitization temperatures were chosen for dilatometric tests. Continuous cooling transformation diagrams with previous deformation (DCCT) were constructed after the compressive true strain of 0.35 with the strain rate of 1 s^{-1}, carried out at the appropriate austenitization temperature of 860 °C and/or 1000 °C. Dilatometric curves were obtained after cooling at constant rates in the range of 0.1 – 35 °C/s. Their mathematical processing was combined with metallographic analysis and hardness measurement of selected samples. After cooling at rates lower than about 0.8°C/s, the structure consisted of ferrite, bainite and pearlite in varying proportions. Higher cooling rates led to an increasing share of martensite. In the high-temperature DCCT diagram, bainite plays a more significant role, and both the Ferrite-start and Pearlite-start curves are shifted towards longer times. This can be explained by the coarser initial austenitic grains after heating the samples to a temperature of 1000 °C.

Keywords:

Low-aloy steel, dilatometry, DCCT diagram, microstructure.

1. INTRODUCTION

One of the key objectives of the steel industry is the increasing efficiency associated with cost savings for the production and processing of material. This can be achieved, among other things, by the technology of controlled rolling with the following controlled cooling from the finish-rolling temperature, which leads to the formation of the required fine-grained microstructure of the material and to the acquisition of the corresponding mechanical properties [1,2]. Knowledge of Continuous Cooling Transformation (CCT) diagrams plays a key role in this. The type and kinetics of individual phase transformations are mainly influenced by the chemical composition of the steel and the cooling rate [3-5]. However, the initial structure, which is the result of the previous thermo-mechanical processing, also plays an important role [6-10]. The aim of the work was to study the effect of austenitization temperature on DCCT diagrams (i.e. with the effect of previous deformation) of low-alloy steel with 0.29 % C – 1.20 % Mn – 0.27 % Si – 0.78 % Cr – 0.21 % Mo – 0.030 % Al – 0.0097 % N.

2. EXPERIMENTAL PROCEDURES

The work was based on dilatometric tests, performed using a non-contact optical scanning system on a hot deformation simulator Gleeble 3800-GTC. The starting material was cuttings from thick-walled pierced semi-products. From them, samples with a diameter of 6 mm and a length of 86 mm were taken parallel to the longitudinal axis of the rolled blanks and at an identical depth below the surface, and turned. First, the phase transformation temperatures Ac_1 = 747 °C and Ac_3 = 824 °C were determined by analyzing the dilatation curve during slow heating at a rate of 0.167 °C/s (i.e. 10 °C/min). Based on these findings and considering the specific technological conditions when using the Mannesmann method of the seamless pipes' production, two different austenitization temperatures were chosen for the construction of DCCT diagrams: 860 °C and 1000 °C. The individual samples were resistively heated in the measured zone at a rate of 10 °C/s to the selected austenitization temperature and, after holding for 600 s, deformed by uniaxial compression at a strain rate of 1 s^{-1} to a true strain of 0.35. Immediately afterwards, they were cooled at selected constant rates (i.e. nominally 0.1 – 35 °C/s) almost to room temperature. The registered dilatometric curves were analyzed using special CCT

software (DSI) and the mathematical program Origin (OriginLab). **Figure 1** shows examples of the dilatation curve and its additional analysis using numerical derivation.

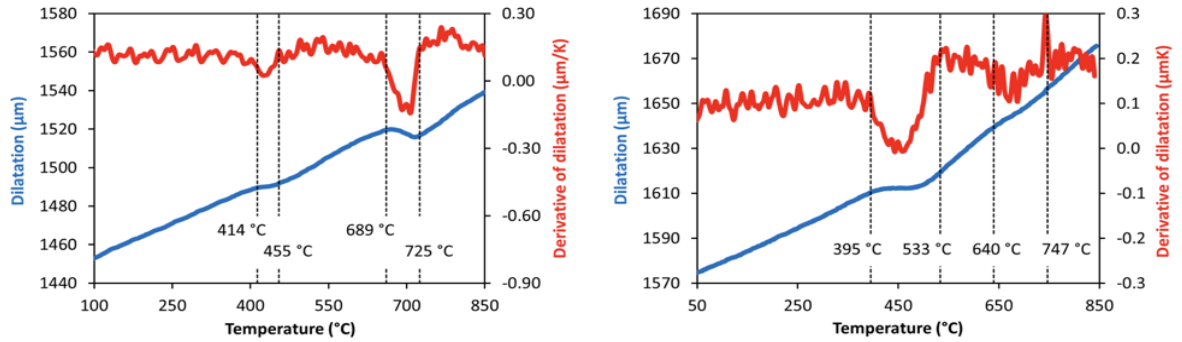

a) 0.2 °C/s b) 1.0 °C/s

Figure 1 Analysis of dilatation curves after cooling from a temperature of 860 °C at different rates. Source: (own)

The temperatures and types of phase transformations determined in this way were verified in selected cases by metallographic analysis using light microscopy, or by measuring the hardness of HV 30 on the cross-section of the samples (always in half the length of the packed part). Micrographs in **Figure 2** document the effect of cooling rate on the resulting structure. **Table 1** shows the average values of measured hardness and phase composition (F = ferrite, P = pearlite, B = bainite, M = martenzite).

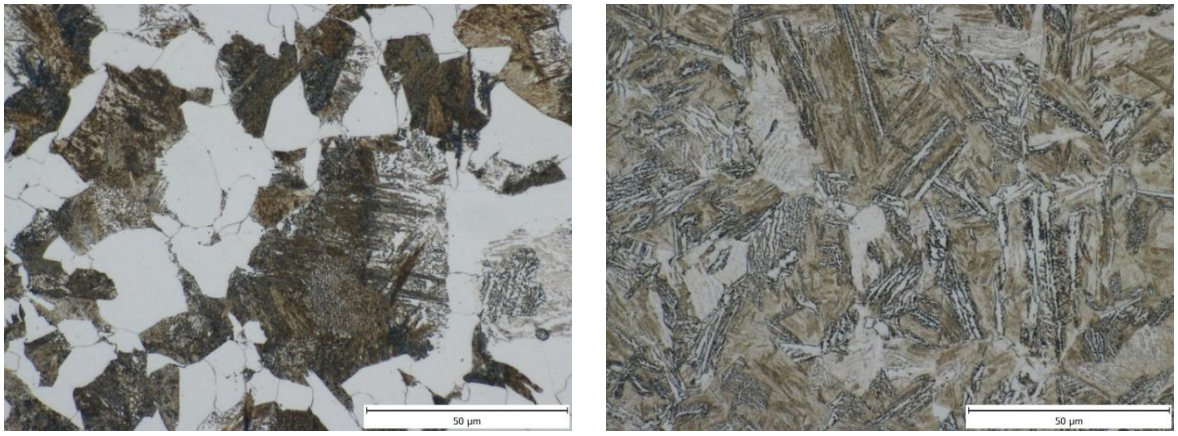

a) 0.2 °C/s b) 7.0 °C/s

Figure 2 Effect of cooling rate on the microstructure after cooling from a temperature of 1000 °C. Source: (own)

3. COMPARISON OF DCCT DIAGRAMS

On the basis of these three types of results, mostly closely correlated with each other, it was possible to set a low-temperature and a high-temperature DCCT diagram of the investigated steel – see **Figure 3**. The horizontal lines correspond to the experimentally determined temperature Ac_3 = 824 °C and specific austenitization temperature (860 °C or 1000 °C). Metallographic analysis proved to be necessary especially for samples with a minor occurrence of some phase components in the structure, because these are practically not detectable by dilatometric tests in the case of a volume fraction below approx. 5%.

Table 1 Effect of cooling rate on phase composition and hardness. Source: (own)

Cooling rate (°C/s)	Austenitization temperature			
	860 °C		1000 °C	
	Phase components	Hardness HV 30	Phase components	Hardness HV 30
0.1	F+P+B	228	–	–
0.2	–	–	B+F+P	263
0.4	F+B+P	272	B+F+(P)	271
0.6	–	–	B+F+(P)	289
1.0	F+B+M+(P)	313	B+F	298
1.5	B+M+F	352	B+(M)+(F)	309
2.0	–	–	B+M	333
3.0	M+B+(F)	401	–	–
4.0	–	–	B+M	383
5.0	–	–	B+M	414
6.0	M+B+(F)	466	–	–
7.0	–	–	M+(B)	483
10	M+(B)	519	–	–
35	M	569	M	570

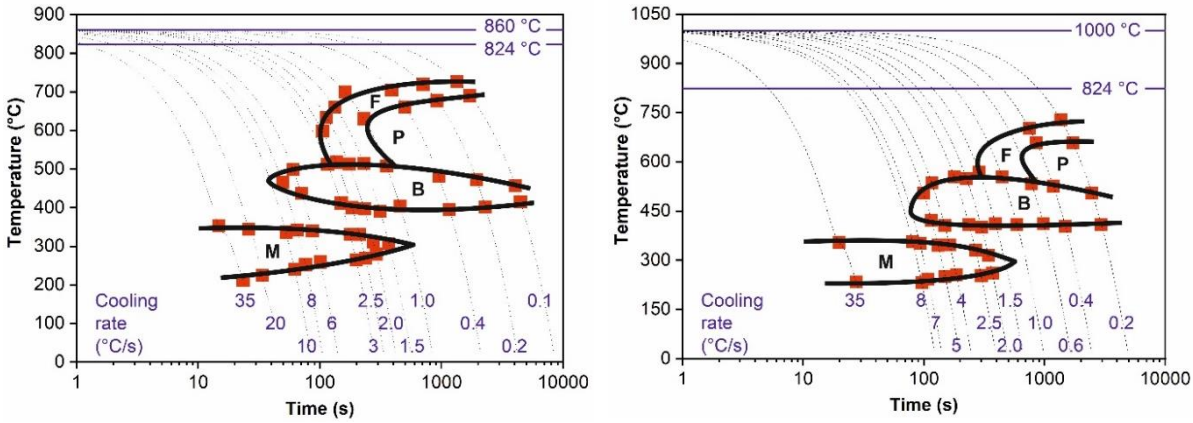

a) low-temperature diagram b) high-temperature diagram

Figure 3 DCCT diagrams of the tested steel. Source: (own)

After cooling at low rates, the structure is composed of ferrite, bainite, and pearlite in varying proportions. Conversely, high cooling rates are associated with the existence of a mixture of bainite and martensite, or only martensite. The temperatures of start of the individual phase transformations do not differ fundamentally when comparing the two diagrams. In the high-temperature diagram, however, a shift of the ferritic and pearlitic regions towards longer times (or lower cooling rates) is evident. To explain this phenomenon, an additional analysis was carried out, consisting of the etching of the prior austenitic grain boundaries in samples cooled at a rate of 35 °C/s (i.e. with a structure fully formed by martensite). The austenitic grains were fully recrystallized but showed a significantly different size as determined by the software QuickPHOTO INDUSTRIAL (PROMICRA). After austenitization and deformation at a temperature of 860 °C, the mean grain size was 9.7 ± 0.9 μm, but after deformation at a temperature of 1000 °C it was roughly twice (21.7 ± 2.0 μm; the data scatter was characterized by the confidence interval with a 95% confidence level). The reason is the formation of a smaller amount of suitable nucleation sites.

The HV 30 hardness grows steadily with the increasing proportion of the product phases in quenching until the moment when the structure consists exclusively of martensite. The influence of austenitization temperature is relatively small; the respective differences in hardness are the result of slightly different phase composition and grain size.

4. CONCLUSIONS

DCCT diagrams of pipe steel low-alloyed with Mn, Cr and Mo were constructed and compared for very different austenitization/deformation temperatures of 860 °C and 1000 °C. Even a relatively very low cooling rate of 0.1 °C/s did not prevent the appearance of bainite in the resulting microstructure. Higher cooling rates led to an increasing share of martensite. In the high-temperature DCCT diagram, bainite plays a more significant role, and both the Ferrite-start and Pearlite-start curves are shifted towards the lower cooling rates. This is associated with the coarser initial austenitic grains after heating on temperature of 1000 °C, as well as after high-temperature deformation followed by a long-lasting static recrystallization or even coarsening of the new grains.

ACKNOWLEDGEMENTS

This article was created with the contribution of the Student grant competition project SP2023/049 "The influence of production parameters and operating conditions on the microstructure and utility properties of metallic materials" (VSB-TUO).

REFERENCES

[1] MCQUEEN, H. J. Historical aspects of thermomechanical processing for steels. *Materials Science Forum*. 2007, vol. 539-543, pp. 4397-4404.
[2] VERLINDEN, B., DRIVER, J., SAMAJDAR, I., DOHERTY, R.D. *Thermo-Mechanical Processing of Metallic Materials.* Great Britain: Elsevier, 2007.
[3] LIU, S.K., YANG, L., ZHU, D.G., ZHANG, J. The influence of the alloying elements upon the transformation kinetics and morphologies of ferrite plates in alloy steels. *Metallurgical and Materials Transactions A*. 1994, vol. 25, pp. 1991-2000.
[4] XIE, H.J., WU, X.C., MIN, Y.A. Influence of Chemical Composition on Phase Transformation Temperature and Thermal Expansion Coefficient of Hot Work Die Steel. *Journal of Iron and Steel Research International*. 2008, vol. 15, pp. 56–61.
[5] CALVO, J., JUNG, I.H., ELWAZRI, A.M., BAI, D., YUE, S. Influence of the chemical composition on transformation behaviour of low carbon microalloyed steels. *Materials Science and Engineering: A*. 2009, vol. 520, pp. 90–96.
[6] KHLESTOV, V.M., KONOPLEVA, E.V., MCQUEEN, H.J. Effects of deformation and heating temperature on the austenite transformation to pearlite in high alloy tool steels. *Journal of Materials Science and Technology*. 2002, vol. 18, pp. 54–60.
[7] TIMOSHENKOV, A., WARCZOK, P., ALBU, M., KLARNER, J., KOZESCHNIK, E., GRUBER, G., SOMMITSCH, C. Influence of deformation on phase transformation and precipitation of steels for oil country tubular goods. *Steel Research International*. 2014, vol. 85, pp. 954–967.
[8] HAN, J., SILVA, A.K., PONGE, D., RAABE, D., LEE, S.M., LEE, Y.K., HWANG, B. The effects of prior austenite grain boundaries and microstructural morphology on the impact toughness of intercritically annealed medium Mn steel. *Acta Materialia*. 2017, vol. 122, pp. 199–206.
[9] ZHAO, H., WYNNE, B.P., PALMIERE, E.J. Effect of austenite grain size on the bainitic ferrite morphology and grain refinement of a pipeline steel after continuous cooling. *Materials Characterization*. 2017, vol. 123, pp. 128–136.
[10] KAWULOK, R., SCHINDLER, I., MIZERA, J., KAWULOK, P., RUSZ, S., OPĚLA, P., PODOLINSKÝ, P., ČMIEL, K.M. Transformation diagrams of selected steel grades with consideration of deformation effect. *Archives of Metallurgy and Materials*. 2018, vol. 63, pp. 55–60.

PROCESSING OF HIGH GRADES OF STEEL USING VACUUM METALLURGY WITH USING OF NUMERICAL MODEL TO CONTROL HYDROGEN CONTENT

Author(s): Miroslav DOSTÁL

Supervisor: prof. Ing. Markéta TKADLEČKOVÁ, Ph.D.

Department: Department of metallurgical technologies, Faculty of Materials Science and Technology, VSB – Technical University of Ostrava

Abstract

The main topic discussed in this work is the reduction of hydrogen content in high grades of steel for the production of seamless pipes using processes of secondary metallurgy and vacuum degassing. The aim of this paper is the statistical analysis of operational data with a follow-up to the preparation of a statistical model for calculating the final hydrogen content in steel after processing in a vacuum. The preparation of the model consisted in the analysis of operating conditions from available production data, statistical evaluation of individual input parameters and their mutual dependence and impact on melt processing. From the results of the analytical part, the necessary inputs for the preparation of a prediction model were obtained, which enables the simulation of the resulting values of the final hydrogen content in the melting on the key´s input parameters defined by the analysis. The result of the predictive statistical model is the approximate expected final hydrogen content, including the values of the other variables that enter into the process.

Key words:

Secondary metallurgy, vacuum degassing, statistical model.

1. INTRODUCTION

At Liberty Ostrava, a.s. (formerly ArcelorMittal Ostrava, a.s.) a vacuum station (VD) was built in 2013 as part of the modernization of the continuous steel casting equipment (Continous caster No. 1), which is part of the secondary metallurgy of the steel plant. The equipment enables the removal of non-metallic inclusions, modification of the chemical composition of steel, thermal and chemical homogenization. With its parameters, the device will ensure a reliable possibility of producing microalloyed and special steels with strict requirements for chemical composition, including steel degassing and precise alloying in the required time and with minimal heat loss. Part of the overall reconstruction of the facility was also the construction of a new continuous steel casting technology enabling the increased production of cast formats depending on the customer's requirements, thereby increasing competitiveness on the market. The main goal was to analyse the start-up of the new vacuum station and subsequently define the key parameters for the processing of steel in a vacuum, both from the point of view of current theoretical knowledge and operational experience. Target was to develop on the basis of the analyses carried out from the tracked operational key input parameters of the steel processing process in a vacuum a statistical model for calculating the final hydrogen content. Statistical model works with the possibility of variation of individual input parameters for possible simulation and prediction itself.

2. PRINCIPLE OF REMOVAL OF HYDROGEN FROM MOLTEN STEEL

The removal of hydrogen from steel melts during out-of-furnace refining takes place in a ladle in a caisson-type device through bubbles of blown inert gas and a free surface exposed to the effect of reduced pressure, or by means of so-called vacuuming [1]. If a carbon reaction is also caused by the reduced pressure above the steel level in the ladle, then the resulting CO bubbles also ensure the release of hydrogen from the melt [2]. The basic thermodynamic condition for steel degassing is therefore a lower partial pressure of hydrogen in the gas phase (in the atmosphere above the bath or gas bubble in the metal bath) than the equilibrium pressure of these gases corresponding to their content in the steel [2]:

$$P_{H2} < P_{H2}, \quad (1)$$

The beneficial effects of steel vacuuming consist mainly not only in reducing the content of gases dissolved in steel, but also in influencing the course of the carbon reaction, the product of which is gas phase – carbon monoxide [3].

3. EXPERIMENTAL PART

The aim of the experimental part was to create a statistical model of hydrogen reduction (melt degassing) by vacuum technology in highly demanding grades of steel intended for the production of seamless pipes. On the basis of theoretical knowledge, a partial goal was to verify process observations in industrial plant and to define key parameters as important inputs for second part of experimental part. Furthermore, the goal was to use these data for statistical evaluations and to create a simple statistical model of the final hydrogen content in the melt from the obtained dependencies. The primary goal was to create a statistical model that is based on the key parameters of the process, i.e. those that are verified by statistical evaluation within the variables [4].

3.1 Regression analysis

The results of measuring the hydrogen content were processed for the period 7/2014 to 6/2015. In total, the file for the above period contained data for 199 meltings. As part of data file preparation, data that do not correspond to the actual process state (e.g. measurement error, system malfunctions) were removed. The partial correlation output shows the significance of other process parameters on the final hydrogen content after VD [4]. According to the result of the processed data, the processing time in a deep vacuum, the maximum achieved negative pressure, the amount of blown argon and the total processing time at VD were identified as key parameters.

3.2 Results of regression statistics of hydrogen content and importante parameters

An important result of the regression curve is primarily the correlation coefficient R , which can take on the values (0;1>; the closer it is to one, the more the dependence can be considered linear). The coefficient of determination R2 expresses the percentage of cases affected by a given addiction, hence the reliability of this addiction. A certain degree of linear dependence can be considered from the value of the correlation coefficient R of 0.2. The p-value is the probability that the test statistic takes on values that are "worse" (more against the hypothesis being tested) than the observed value of the statistic. For a variable to be included in the regression equation, the P value should be within 0.1, preferably within 0.05. The α value indicates the angle that the regression line makes with the x-axis. The closer the absolute value of this quantity is to the angle α = 45°, the more intensively the regressor affects the hydrogen content. The values of individual parameters are shown in **Table 1**, which are the results of regression statistics [4].

Table 1 Results of regression statistics of hydrogen content and important parameters. Source: [4]

Content of [H]	R	P	α
Duration of total treatment time	0,0574	0,05	-3,5°
Duration of vacuum treatment	**0,5490**	0,071	-9,8°
Maximum value of the vacuum pressure	**0,3439**	0, 063	-8,3°
Amount of blowed Ar	**0,2555**	0,120	9,2°

3.3 Evaluation of the influence of key process parameters on the final hydrogen content

Figure 1 shows an example of the resulting linear regression with a significant dependence of the final hydrogen content on the maximum value of the negative pressure achieved at the vacuum station [4].

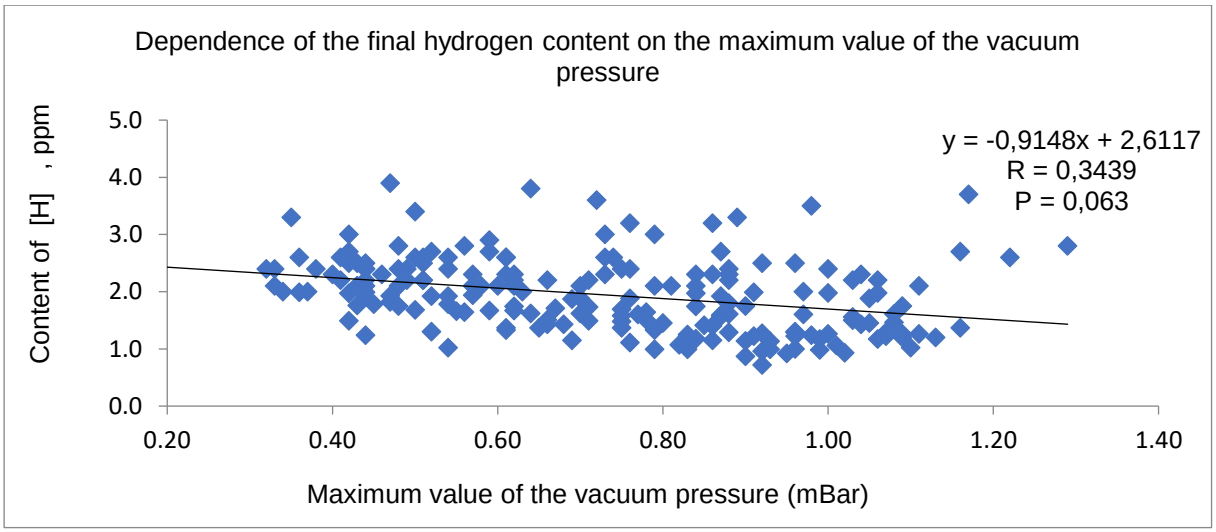

Figure 1 Dependence of the final hydrogen content on the maximum value of the vacuum achieved. Source: [4]

The maximum value of vacuum achieved is a key parameter together with the vacuuming time for the effective removal of hydrogen in steel. It is known from practice that the maximum depth of vacuum should be achievable below 1mBar in the tank, with a duration of processing in deep vacuum of at least 15 minutes. In this process mode, the input hydrogen content is not decisive, as its decrease is very significant at the beginning of the vacuum processing [4].

3.4 Preparation a statistical model for calculating the final hydrogen content

The results of the previous analyses were subsequently used to create a prediction of individual operating conditions with the aim of calculating the final theoretical value of hydrogen at the end of the vacuum treatment for a given combination of key parameters. The input value of hydrogen is defined by a constant of 8 ppm for easier entry of the mathematical calculation. The effectiveness of the degassing process at VD in our conditions is greatly influenced by the time of vacuuming, together with the maximum value of vacuum pressure achieved and the amount of blown argon. The model simulation reflects the evolution of the resulting hydrogen in the melt according to the default setting of the input parameters. While always one of the parameters serves as a constant quantity for generating the range for graphic display [4]. The individual steps of calculating the statistical model can be seen in **Figure 2.** For the purposes of implementing the mathematical model, the option of the open MS VBA environment (as a licensed Microsoft Office product) was used. As part of the implementation, the algorithm described above can be divided into parts: Initialization after opening the model, Calculation for the current settings, Elements of the graphic environment, Dataset for integration into external applications (PowerBI dashboards, PowerToolkit) and Dynamic matrix generation for displaying the resulting curve [4]. Furthermore, software graphic elements were used to create a user-friendly interface for calculating the final hydrogen content under operating conditions. In a simplified way, we can describe entering model input data in connection with the images below. In **Figure 3**, we can see the basic interface of the model, where it is important to mention two parts, including entering input values for a specific example of model calculation. In the first part, it is necessary to choose a variable parameter, that is, a parameter that we want to influence and define input value [4]. An example of a model calculation was chosen with a defined constant parameter "argon consumption (12 845 Nm/l)". The combination of values entered by us for the maximum value of the negative pressure (0,61 mbar) and the time of the deep vacuum (12 min) also participates in the calculation, when we arrive at the calculated final hydrogen value of 2,18 ppm using the numerical model [4].

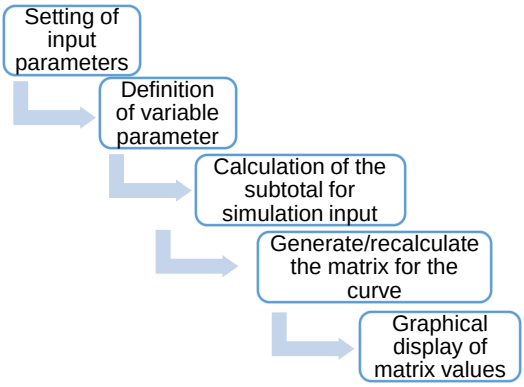

Figure 2 Process steps of statistical model calculation [4]

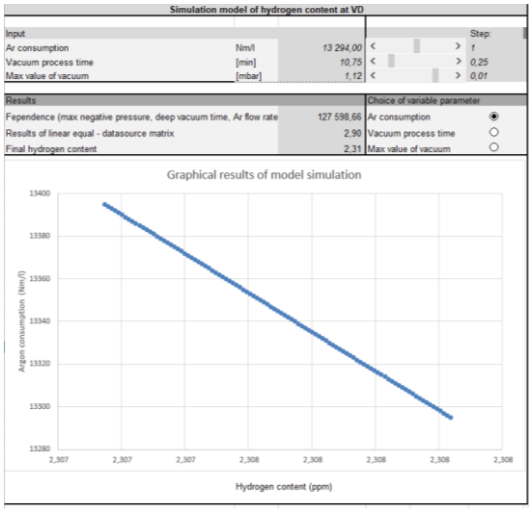

Figure 3 Model calculation of the dependence of the final hydrogen content [4]

4. CONCLUSION

This article was focused on using vacuum metallurgy with the aim of controlling the hydrogen content with using of numerical model. On the basis of these analyses and model examples, it is possible to see the significance of the inert gas blowing intensity in combination with a shorter processing time in a deep vacuum, a maximum value of the vacuum achieved, when the individual values of the calculated final hydrogen contents are not very different. Still according to the expected specifications for the quality of steel produced. The implementation and understanding of the statistical model itself is very simple for any user. At the same time, it gives a very good opportunity to define a combination of limit conditions for these key input parameters. You can immediately see where the course of the process can move us. In the case of expansion of the data set, we can very easily add additional input parameters from new operational results, thus the model can be functionally expanded and statistically refined. It is in no way a substitute for numerical models for the purposes of automatic regulation, which can react online to operating conditions without human intervention. The model gives the opportunity for real-time and past-time data verification with regard to possible theoretical optimization of the process. The actual calculation of the final result is based on the source file, which compares all the collected data with each other for an optimal estimate of the resulting value. In our case, it is the final hydrogen content at the end of the vacuum treatment. By the fact that it is a closed data file without random generation of additional input variables, it is always guaranteed that the progress is based on the combination of our key values prepared in the data file. Therefore, it is not possible to get outside the defined limits of the data file.

REFERENCES

[1] KASZPERYDES A. *Parametry ovlivňující odplynění oceli v podmínkách vakuovací stanice RH*, Bakalářská práce, FMMI, VŠB-TU Ostrava, 2012

[2] KEPKA, M. *Rafinace oceli*, 1.vyd., Praha, SNTL, 211 s.,1989

[3] ADOLF Z., DOSTÁL M., ŠÁŇA Z. *Steel refining in a vacuum unit with chemical boosting,* Materials and technology vol.43, pp. 219- 222, ISSN 1580 – 2949,2009

[4] DOSTÁL M., *Zpracování náročných jakostí oceli pomocí vakuové metalurgie s cílem řízení obsahu vodíku výpočtovým modelem*, Disertační práce, FMT,VŠB - TU Ostrava, 2023

USING COMPUTHERM SOFTWARE TO DETERMINE THE AUSTENITE DECOMPOSITION TEMPERATURES OF 20MNCR5 STEEL

Author: Lucie CHUDOBOVÁ

Supervisor: prof. Ing. Markéta TKADLEČKOVÁ, Ph.D.

Department: Department of Metallurgical Technologies FMST, VŠB – Technical University of Ostrava

Abstract

The paper presents analysis of phase transformation temperatures of 20MnCr5 steel. For calculations of required temperatures, ie. temperature of the start of austenite decomposition (Ac3) temperature of the finish of austenite decomposition (Ac1) was used CompuTherm thermodynamic database. The aim of this paper is to use calculated temperatures to design regression equations for calculating transformation temperatures.

Key words:

Phase transformation, austenite, temperature, CompuTherm.

1. INTRODUCTION

Knowledge of the temperatures of the phase transformations of steel is very important either in its production or heat treatment. These temperatures allow us to understand the basic properties of steel, to determine the correct casting temperature or to optimize the settings of metallurgical processes.

Steel changes its phase at different temperatures. Temperatures at which the state of steel is changed are called phase transformation temperatures. The most important temperatures of phase transformations of steels include the liquidus temperature (melting temperature) and the solidus temperature (solidification temperature). The temperature range between the liquidus and solidus temperature determines the so-called two-phase zone, where the liquid phase changes to solid. Knowledge of the range allows prediction of steel tendency to internal defects, determination of steel liquidus temperature allows correct setting of steel casting temperature. Knowledge of the phase transformation temperatures of austenite is important for subsequent heat treatment of steel [1,2].

The temperature of phase transformations is affected by the chemical composition of the steel melt. Most elements reduce these temperatures.

Methods of thermal analysis, dilatometry or computational methods (using empirically determined equations or software) can be used to determine phase transformation temperatures. The results obtained after the computational determination of temperatures should be also verified by experimental methods [1,2].

2. CHARACTERISTICS OF STEEL QUALITY 20MNCR5

20MnCr5 steel grade is a case-hardening steel with the addition of manganese and chromium, sometimes it is additionally modified by a certain addition of boron. It is well hardenable and after hardening it achieves good wear resistance due to high surface hardness. It is used for various applications in gears in rotary machines. Typical applications are valve bodies, pumps and fittings, screws, gears, machine tool components, shafts and other mechanical controls [3]. The chemical composition of the steel used for the calculations is given in Table 1.

Table 1 Chemical composition of 20MnCr5 steel used for calculations. Source: (Own)

	Chemical composition of steel 20MnCr5 [wt.%]						
	C	Si	Mn	P	S	Cr	Cu
Range	0,17 – 0,22	≤ 0,40	1,10 – 1,40	≤ 0,035	≤ 0,035	1,00 – 1,30	≤ 0,40
Min.	0,17	0,00	1,10	0,000	0,000	1,00	0,00
Avg.	0,20	0,20	1,25	0,018	0,018	1,15	0,20
Max.	0,22	0,22	1,40	0,035	0,035	1,30	0,40

3. CHARACTERISTICS OF AUSTENITE

Austenite (γ) is one of the iron-carbon interstitial solutions. It has a face-centered cubic lattice and its structure is made up of regular grains. It occurs in steel at higher temperatures and is formed by the so-called austenitization (transformation of the ferritic-cement structure) [4].

During its cooling, different phases or structural components can be formed. Depending on the cooling rate of the steel, it can form: pearlite (low cooling rate), bainite (medium rate) or martensite (high cooling rate). The basis of the ongoing transformations is the change of the cubic surface-centered lattice of iron γ to the space-centered lattice of iron α. Furthermore, there is also a decrease in the carbon content and the formation of cementite [4, 5].

The breakdown of austenite takes place in the case of hypoeuctoid steels (with a carbon content of 0.02 – 0.765 wt.%, which also includes 20MnCr5 steel), in the interval of two temperatures, namely between: the temperature of the beginning of the decomposition of austenite (Ac3) and the temperature of the end of the decomposition of austenite (Ac1) [5].

Temperatures Ac3 and Ac1 can be affected by the presence of individual elements in the steel. The elements Ni, Mn or C are austenite-forming, so they expand the austenite area and thus lower the temperatures of the beginning and end of the austenite breakdown. On the contrary, elements such as Si, S, P or Cu belong to ferrite-forming elements, they narrow the austenite region and thus increase the temperature of the beginning and end of decomposition. Cr also belongs to the ferrite-forming elements, but it increases the temperature of the end of austenite breakdown and, on the contrary, lowers the temperature of the beginning of austenite breakdown [4].

4. CALCULATION OF PHASE TRANSFORMATION TEMPERATURES USING COMPUTHERM

4.1 CompuTherm software characteristics

The CompuTherm thermodynamic database (version 14.5), which is part of the ProCAST software (version 2019.0) available at the Department of Metallurgical Technologies, was used to calculate the required phase transformation temperatures of 20MnCr5 steel.

This program allows you to calculate the thermophysical properties of steel after entering the chemical composition of steel and, if necessary, monitor changes in the required properties after adjusting the chemical composition. Calculable parameters include liquidus temperature, solidus, austenite decomposition temperatures, density, enthalpy, viscosity or thermal conductivity as a function of temperature. The calculation can be performed for metallic materials based on Al, Fe, Ni, Ti, Mg or Cu. For the calculation of steel is used the calculation based on Fe, where it is possible to further define the content of these elements: Al, B, C, Co, Cr, Cu, Mg, Mn, Mo, N, Nb, Ni, P, S, Si, Ti, V, W [6,7].

The resulting phase transformation temperatures are determined from the graph. Figure 1 shows an example of an austenite breakdown graph showing the temperatures Ac3 and Ac1 for one of the variants of the chemical composition of 20MnCr5 steel, calculated using the CompuTherm thermodynamic database.

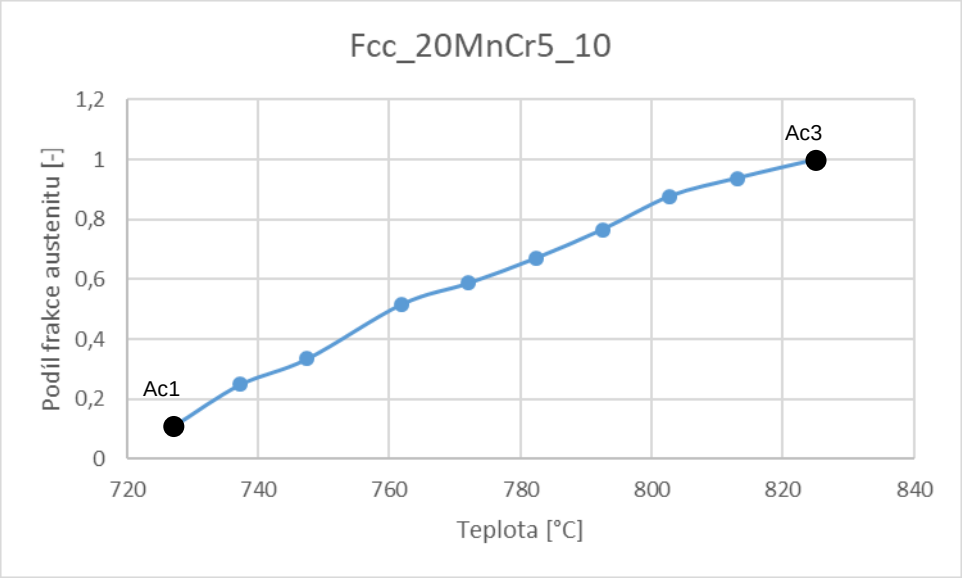

Figure 1 Example of austenite decomposition (Ac3) and end (Ac1) temperatures obtained by calculation in CompuTherm thermodynamic database. Source: (Own)

4.2 Calculation of Ac3 and Ac1 temperatures

Calculations in the CompuTherm database were used to determine the regression equations, when 66 different variants of the chemical composition were created for the 20MnCr5 steel. This is the minimum number of combinations to include all possibilities of the minimum, average and maximum content of individual elements in steel and for the subsequent correct execution of the regression analysis. The Lever microsegregation model was used for the calculation.

The temperatures calculated for the minimum, average and maximum chemical compositions calculated by the CompuTherm software are shown in Table 2.

Table 2 Calculated temperatures [°C]. Source: (Own)

	Ac3	**Ac1**
Min.	781	697
Avg.	825	728
Max.	806	714

5. CONSTRUCTION OF REGRESSION EQUATIONS

When calculating the regression, we consider the standard level of significance α = 0.05, i.e. 5% unreliability of results (or 95% confidence). From the result that this program provides, we evaluate the statistical significance of the regression model as a whole, using Fisher's F-test (Significance F). The Reliability value R parameter is also important here. Furthermore, the statistical significance of individual regression coefficients is evaluated using the results of the Student's t-test (t-Stat), where the significance level of the t-test (P value) is an important parameter [8].

5.1 Regression equation for temperature Ac3

The chemical composition has a statistically significant effect on the temperature of the onset of austenite breakdown (Ac3) of 20MnCr5 steel from 94% and from 6% other influences affect the temperature of Ac3. The regression coefficients of the elements C, Mn, Cu, and Cr acquire lower values in the significance level of the t-test (P value) than the chosen significance level α. Therefore, they have a statistically significant influence on the Ac3 temperature. The coefficients of elements S, P and Si do not meet this condition, and therefore their influence on the temperature of Ac3 will not be significant. The resulting equation for Ac3 has this form:

Ac3 = 894.3 – 257.5 · (% C) – 27.8 · (% Mn) – 19.4 · (% Cu) – 9.3 · (% Cr) + 25.7 · (% S) + 164.3 · (% P) + 34.9 · (% Si) (1)

5.2 Regression equation for temperature Ac1

The chemical composition has a statistically significant effect on the temperature of the end of austenite breakdown (Ac1) of 20MnCr5 steel from 90.9% and from 9.1% other influences affect the temperature of Ac1. The regression coefficients of the elements Mn, Cu, and C acquire lower values in the significance level of the t-test (P value) than the chosen significance level α. Therefore, they have a statistically significant influence on the Ac1 temperature. This condition is not met by the coefficients of the elements P, S, Si, and Cr, and therefore their influence on the temperature Ac1 will not be significant. The obtained relation for Ac1 has this form:

Ac1 = 728.6 – 34.6 · (% Mn) – 10.7 · (% Cu) – 56 · (% C) + 6.4 · (% P) + 89.4 · (% S) + 11.7 · (% Si) + 32.8 · (% Cr) (2)

6. CONCLUSION

The paper presents the calculated austenite decomposition temperatures for the quality of steel 20MnCr5. These temperatures are determined using the CompuTherm thermodynamic database. From the above results it is clear, that in the calculation of individual temperatures, the chemical composition has a significant effect on changes in the values of given temperatures.

For the given steel, the average temperatures are 806 °C for Ac3 and 714 °C for Ac1. The calculated temperatures vary depending on the chemical composition by up to 44 °C (in the case of the Ac3 temperature).

Furthermore, the resulting regression equations (1 - 2) are determined in the work, determined by regression analysis of 66 possible variants of chemical composition of steel 20MnCr5 phase transformation temperatures determined for defined chemical compositions by thermodynamic database CompuTherm. These equations can be used in operational practice for calculations of phase transformations in the limit values of the used chemical composition of a given steel grade. When using a different range of chemical composition, these equations can be used, but without guaranteed results.

ACKNOWLEDGEMENT

The work was created with the support of the project "Support for Science and Research in the Moravian-Silesian Region 2021 - RRC/10/2021" and with the financial support of project "Student Grant Competitions" number SP2023/022.

REFERENCES

[1] MARTINÍK, O.; SMETANA, B.; DOBROVSKÁ, J. et al. Prediction and measurement of selected phase transformation temperatures of steels. *Journal of Mining and Metallurgy. Section B: Metallurgy* [online]. 2017, vol. 53, no. 3 [viewed: 2023-5-27], p. 391-398. Avalible from (DOI): <https://doi.org/10.2298/JMMB170711030M>. ISSN 1450-5339.

[2] MIETTINEN, J.; HOWE, A. A. Estimation of liquidus temperatures for steels using thermodynamic approach. *Ironmaking & Steelmaking* [online]. 2000, vol. 27, no. 3 [viewed: 2023-05-27], p. 212-227. Avalible from (DOI): <https://doi.org/10.1179/030192300677516>. ISSN 1743-2812.

[3] Ovako product catalog. *Ovako*. [online] [viewed: 2023-05-27]. Avalible form: <https://www.ovako.com/globalassets/global-blocks/ovako-product-catalog.pdf>.

[4] SOJKA, J.: *Nauka o materiálu I*. (Studijní opora) Ostrava: VŠB – TU Ostrava, Fakulta metalurgie a materiálového inženýrství, 2008, 195 s.

[5] JONŠTA, Z.: *Nauka o kovech II*, 2. vyd. Ostrava: VŠB – TU Ostrava, 2000. 116 s. ISBN 80-7078-958-1.

[6] TKADLEČKOVÁ, Markéta; MICHALEK, Karel. et al. *Studijní opora: Základy 3D modelování metalurgických procesů*. 1. vyd. VŠB - TU Ostrava, Fakulta metalurgie a materiálového inženýrství, 2013, 100 s. ISBN 978-80-248-3350-7.

[7] ProCAST 2019, User´s manual. ESI Group.

[8] Úvod do regresní analýzy. *StatSoft.cz* [online] [viewed: 2023-05-27]. Avalible from: <http://www.statsoft.cz/file1/PDF/newsletter/2014_26_03_StatSoft_Uvod_do_regresni_analyzy.pdf>.

THE EFFECT OF DIFFERENT MIXING PRINCIPLES ON THE PROPERTIES OF GREEN SAND MIXTURE

Author(s): Šimon KIELAR

Supervisor: doc. Ing. Petr LICHÝ, Ph.D.

Department: Department of of Metallurgical Technologies, Faculty of Materials Science and Technology, VSB – Technical University of Ostrava

Abstract

Green sand mixtures are widespread all over the world and still maintain their popularity, which will be even greater in the future. Due to the increasing requirements for emission reduction in the industry, these mixtures are among the options to meet these conditions. An important factor is that these mixtures meet the high quality requirements of the castings. Currently, the emphasis is on the quality of the raw material at the expense of mixing, which is often neglected. The aim of this work is to describe the differences in the evolution of mixture properties during mixing on two types of mixers.

Key words:

Bentonite, Green sand mixture, Wheel mixer, Eddy mixer, Green compressive strength.

1. INTRODUCTION

Green sand mould making is one of the oldest mould making technologies. Despite its "obsolescence", this technology is still widespread, mainly due to the considerable advantages it offers. These are mainly its economic availability combined with good technological properties such as ease of production, reusability, good strength and disintegration after casting [1]. These properties, together with the other properties of these mixtures, may not always be sufficient to produce castings that have to meet ever higher quality requirements together with environmental standards. For these reasons, these mixtures are the subject of a number of studies aimed at improving these properties or finding new alternative sources of input materials for these mixtures [2].

Green sand mixtures can be defined as a mixture of silica sand, bentonite clay, water and other additives [3]. The quality of these raw materials along with the mixing process has a major influence on the final properties of these mixtures. Mixing can be simply described as the process during which the mixture achieves the desired properties, but in reality the process is far more complicated. First of all, it is necessary to ensure the most perfect homogeneity of all the individual components. Next, a water and bentonite plastic dough must be created, which is then used to coat the sand particles. [4] Properly set mixing parameters are required to create a quality homogeneous mix with a well incorporated clay dough. This means sufficient mixing time to allow all the sub-stages of mixing to take place and correctly set mixer parameters [5]. Different types of mixers are used to mix green sand mixtures. The most commonly used types are wheel mixers along with eddy mixers. Mixing in a wheel mixer is carried out by means of two impellers which move in a circular motion by means of a rotor at a speed of 20-40 rpm. The mixture is kneaded under the impellers and the bottom of the bowl by rolling motion. The mixing time for these wheel mixers is reported to be around five minutes. In the case of the eddy mixer, the principle is based on the counter-current movement of the mixture inside the mixer, where the mixture is set in motion by a rotor equipped with blades and the counter-rotation of the bowl. The individual layers of the mixture rub intensely against each other and a sliding motion occurs. The mixing of the mixture can therefore be said to take place throughout the entire volume of the mixture. From this point of view, it can be seen that the mixture is mixed much more intensively than in the case of wheel mixers. This fact is also apparent from the mixing time, which is around 90 seconds [6].

Although this mould making technology has been the subject of much research, the effect of the mixing process itself on the quality of the green sand mixture has been neglected. The quality of the input raw material alone cannot ensure the desired properties of the mixture, but the effect of the mixing process must also be taken into account. The parameters of a mixture mixed on two different mixers will not be the same. For this reason, it is necessary to understand the aspects of each mixer and the behaviour of the mixture during mixing.

2. MATERIALS AND METHODS

The aim of the experiment was to compare the properties of mixtures with the same input parameters in individual minutes of mixing on two types of laboratory mixers. In this way to compare the effect of these mixers on the properties of the mixtures.

The results of mixtures mixed on a wheel mixer were taken from previous research that looked at the effect of the order of input materials on the properties of mixtures [5]. The results of mixtures mixed on an eddy mixer were measured, processed, and further compared with data from previous research as part of the experiment.

Materials

For the preparation of the mixture, Silica sand from Biala Gora BG 27 with d_{50} 0.27 mm was used. Soda-activated bentonite Sabenil from Keramost a.s. was used as binder. Water for the preparation of the mixture was used from the water supply network. As in the previous experiment [5], neither the water content of the bentonite nor the moisture content of the sand was taken into account. The measured mixtures were exclusively blended from new raw materials and their parameters are given in Table 1.

Table 1 Composition of used green sand mixture: Source: (own)

	Sand	Binder	Water
Weight ratio (%)	100	8	2.5
Mass (g)	6000	480	150

The LM-2e wheel mixer and the LM-3e eddy mixer were used for the experiment. A laboratory semi-automatic tamping machine LUA-2e/Z was used to prepare cylindrical test specimens with dimensions Ø 50 mm x 50 mm. A universal strength measuring device LRu-2e was used to measure the strength of the green sand mixture. All these devices were supplied by Multiserw-Morek.

Experiment

For the purpose of the experiment, the mixture with the addition of water in the second order was selected from the previous research. This order was also applied when mixing the mixtures in the eddy mixer, where sand was first added to the mixer followed by water. The water-sand mixture was then mixed for 20 seconds at a rotor speed of 1400 rpm and a mixer speed of 40 rpm. Bentonite was then added to the mixture and the mixture was further mixed at a rotor speed of 2600 rpm and a bowl speed of 60 rpm. This moment was considered as the beginning of the mixing of the mixture (time 0 min). The mixture was mixed for 5 min and at each minute of mixing, a portion of the mixture was removed and tested. In this way, 3 mixes were mixed and the moisture content, Apparent density, green compressive strength, green split tensile strength and green shear strength were measured. From these results, the toughness of the mix was further derived as a ratio of the green split tensile strength to the compressive strength.

3. RESULTS AND DISCUSSION

These measured data were processed and, together with the data from the previous experiment, were converted into graphical form (Figure 1-6), where the average property values for a given mixing minute are plotted along with the trend line and standard deviations for a given mixer.

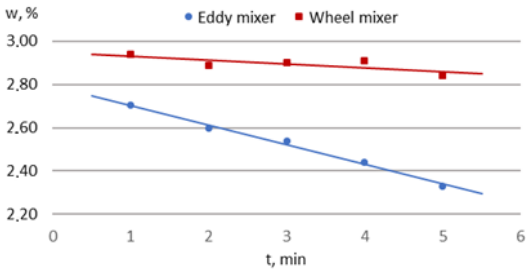

Figure 1 Moisture contents, w (%). Source: (own)

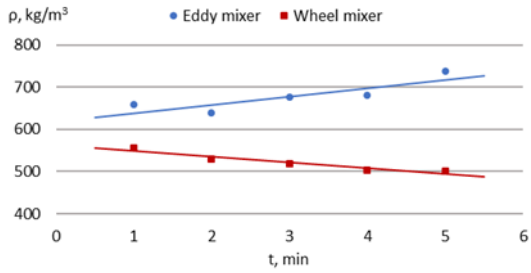

Figure 2 Apparent density, ρ (kg/m³). Source: (own)

In the graph (Figure 1) of the moisture contents evolution, we can notice the different moisture drop of the mixtures. When mixing the mixtures, friction occurs, which causes the mixture to heat up. Increasing the temperature of the mixture leads to more intense evaporation of water and loss of moisture, as is the case with a mixture mixed on the eddy mixer. In the case of the wheel mixer, the moisture loss over the mixing time is not as significant. The total moisture loss for the wheel mixer was 0.1 %, which translates into a decrease of 3.4 % compared to the initial moisture content of the mixture. In the case of the eddy mixer, there was a decrease of 0.37 % (13.7 % calculated). It can therefore be said that the moisture loss in the case of the eddy mixer is approximately 10 % higher than in the case of the wheel mixer.

In the evolution of the Apparent density (Figure 2) of the eddy mixer, we can see an increasing trend line, where the Apparent density increases with decreasing moisture content of the mixture. This overall increase corresponds to an increase of 12 % compared to the Apparent density of the first minute of mixing. In the case of the mixture mixed on the wheel mixer, the trend is reversed and the decrease in Apparent density corresponds to 10 % compared to the mixture measured after one minute of mixing. This slight decrease in Apparent density can be attributed to the better incorporation of bentonite in the mixtures, where these mixtures also have a visually denser character.

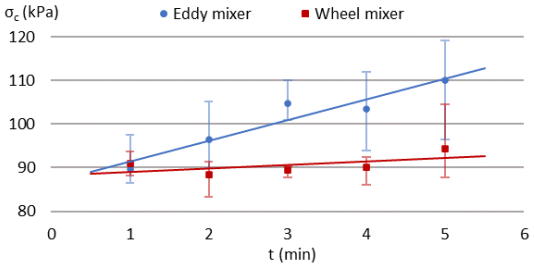

Figure 3 Green compresive strength, σ_c (kPa). Source: (own)

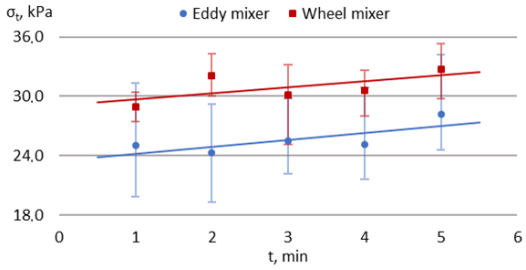

Figure 4 Green split tensile strength, σ_t (kPa). Source: (own)

In the green compressive strength graph (Figure 3), we can see the different strength increase for the two mixers. The different development is due to the decreasing moisture content of the mixtures but also to the mixing intensity. As the moisture content of the mixture decreases, the strength increases, as can be seen in the green compressive strength trend line for the eddy mixer. Over the course of mixing, the strength of the mixtures for this mixer increased by 20.3 kPa. This increase corresponds to 22.6 % compared to the mixtures after the first minute of mixing. For mixtures mixed on the wheel mixer this increase was on average lower.

In the case of green split tensile strength (Figure 4), we can see a different development than for Compressive Strength. On average, mixtures mixed on the eddy mixer achieve lower strengths than mixtures mixed on a wheel mixer. The trend lines for the mixtures blended on these two mixers are similar in nature (the percentage increase in strength is approximately 13 % for both mixtures), but the mixtures blended on the wheel mixer show higher green split tensile strength in the range 3.9-7.7 kPa depending on the mixing time. This strength of the moulding mix is closely related to the binding capacity of the bentonite. As the strength increases, a greater amount of incorporated bentonite is present in the mixture, which actively contributes to the bonding capacity of the mixtures. It can therefore be concluded that the bentonite in the mixtures mixed on the wheel mixer is much better incorporated and therefore contributes more to the binding capacity of the mixture, as can be seen in this graph.

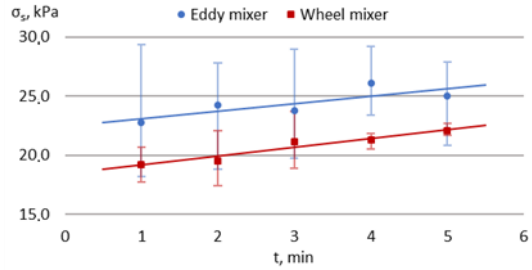

Figure 5 Green shear strength, σ_s (kPa). Source: (own)

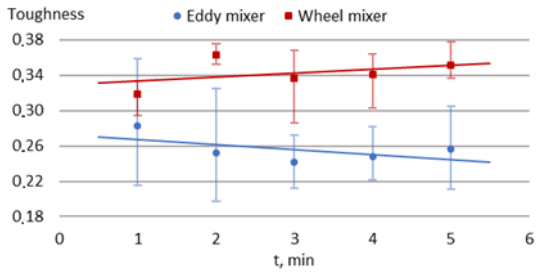

Figure 6 Toughness (-). Source: (own)

The evolution of the shear strength (Figure 5) of the mixtures blended on these two mixers is similar in nature. The overall increase in strength is 12.8 % for the eddy mixer and 15.1 % for the wheel mixer. The mixtures mixed on the wheel mixer show a slightly higher percentage increase (2.3 %) but the strength level does not reach the values of the mixtures mixed on the eddy mixer. The difference in strength ranges from 2.7 kPa to 4.8 kPa depending on the specific mixing time. Mixtures mixed on the eddy mixer achieve higher strengths due to lower moisture content.

In this graph (Figure 6) we can see the evolution of the toughness of the mixture. Mixtures mixed on the wheel mixer have on average a higher toughness than mixtures mixed on the eddy mixer. This is mainly due to the higher moisture content of the mixes and the better incorporation of bentonite into the mix. The trend line showing the toughness of the mixtures mixed on the wheel mixer has a slightly increasing tendency during the mixing process. In the case of mixtures mixed on the eddy mixer, the trend line is decreasing. This is due to decreasing moisture content and increasing green compressive strength, respectively, since the toughness of the mixture is determined by the ratio of the green split tensile strength to the green compressive strength. For the eddy mixer, the decrease in toughness is 0.02, while for the wheel mixer the toughness increases by 0.03. Although the toughness of the mixtures mixed on the wheel mixer decreases and its average lowest value is 0.24 (3 min), we can still classify this mixture as satisfactory. The toughness value of these bentonite mixtures should be higher than 0.22.

4. CONCLUSION

In this experiment, identical mixtures blended on two different mixers were compared to compare the two mixers using mixture properties. The mixture parameters and properties of the mixtures mixed on the wheel mixer were taken from the previous experiment. These mixture parameters were further applied to mixing the mixture on the eddy mixer for which the mixture properties were determined at each minute of mixing. A summary of the results can be summarized as follows:

- It was found that the eddy mixer mixes the mixture much more intensively than the wheel mixer, which causes higher heating of the mixture and the associated higher loss of moisture content during mixing.
- This decrease in moisture content is further reflected in the average increase in green compressive strength, which is 15.7 kPa higher at 5 minutes of mixing than that of the mixture mixed on the wheel mixer.
- The wheel mixer develops the bonding properties of bentonite much better, which can be seen in the slightly increasing Apparent density (by 10 %) but also in the green split tensile strength (13 % increase) and toughness.
- The toughness of the mixtures mixed on the eddy mixer is lower than that of the mixtures mixed on the wheel mixer and tends to decrease. This is due to the higher green compressive strength. In spite of the low toughness of the mixtures mixed on the eddy current mixer, these mixtures can still be considered suitable for moulding.
- It can be concluded that mixtures mixed on the eddy mixer achieve higher green compressive strengths in a shorter period of time at the expense of lower activation of the bonding properties of the bentonite in the mixture.

ACKNOWLEDGEMENT

This research was funded by the project of MEYS (grant number CZ.02.1.01/0.0/0.0/17_049/0008399). This research was carried out with the support of projects of student grant competition (project number SP2023/022).

REFERENCES

[1] SADARANG, Jain; Ramesh Kumar, NAYAK; Ishim, PANIGRAHI. Challenges and future prospective of alternative materials to silica sand for green sand mould casting: A review. Transactions of the Indian Institute of Metals, 2021, 74.12: 2939-2952.

[2] SADARANG, Jain; Ramesh Kumar, NAYAK; Ishim, PANIGRAHI. Effect of binder and moisture content on compactibility and shear strength of river bed green sand mould. Materials Today: Proceedings, 2021, 46: 5286-5290.

[3] JELÍNEK, Petr. Binder systems of foundry moulding mixtures – chemistry of foundry binders. (1st ed.). Ostrava. ISBN: 80-239-2188-6. (in Czech)

[4] TROY, E. C.; FERENCY, D. L. A Mulling Index Applied to Sand-water-bentonite. AFS Transactions, 1971, 79: 213-224.

[5] GAWRONOVÁ, Martina; Šimon, KIELAR; Petr, LICHÝ. Mulling and its Effect on the Properties of Sand-Water-Bentonite Moulding Mixture. Archives of Foundry Engineering, 2022, 22.

[6] CHRÁST, Jaroslav. Slévárenská zařízení. Brno: Akademické nakladatelství CERM, 2006. ISBN 80-7204-456-7.

OPTIMIZATION OF THE NECKING SEAMLESS STEEL CYLINDERS WITH DIAMETER 204

Author(s): Tomáš MERVA

Supervisor: prof. Ing. Radim KOCICH, Ph.D.

Department: Department of Metallurgical Technologies, Faculty of Materials Science and Technology, VSB – Technical University of Ostrava

Abstract

This study introduce about necking of hot-formed semi-finished products on special single-purpose equipment with one shaped roller like a tool and spindle with chuck unit and unloading system for automatic operation. This machine can be used for the production of seamless steel cylinders for technical, medical and inert gases with diameter from 140 to 235 mm. The production necking ends obtain turbulent conditions during forming which include issues with folding material in phase forming neck or also end closing. We focus on based principle for no-scrap forming with well-adjusted steps during end-closing or necking. Material of semi-finished tubes is 34CrMo4. Chemical composition of material 34CrMo4 define the ISO standard 9809. The experiment was performer on a blank with a diameter of 204 mm and a nominal wall thickness of 4.4 mm. The resulting necked tube is use for the M25x2 neck.

Key words:

Hot forming, necking, seamless steel cylinders, 34CrMo4.

1. INTRODUCTION

The technology of end closing and necking is mainly used in the sector of gas storage and transport, in the form of pressure vessels and pressure cylinders. The input semi-finished product can be from pipe or from product of the backward extrusion. The quality of the input semi-finished product has a main infuence on the forming process. Inaccuracies caused by eccentricity, ovality, hemisphericity or bad alignment can result in an internal or external defect that cannot be removed during finishing machining [1, 2]. The development of the necking proces sis focused on a possible waste free technology by new purpose of steps during closing. It also focuses on the influence of the trajectory of the tool movement in particular steps and different speed of rotation [3]. In addition, a way is sought to ideally use the finite element method for the most reliable prediction of the proposed necking or closing process. Axisymmetri, shell and 3D models of FEM are compared [4-8].

2. EXPERIMENTAL PROCEDURES

The input blank for the necking operation is a back-extruded semi-finished product. Production takes place from the material 34CrMo4. The chemical composition of the material is shown in **Table 1**. The correctness of the chemical composition, compliance with the micro-purity and prescribed mechanical properties of the 34CrMo4 steel is checked by taking samples and takes place before the start of serial production from the input semi-finished product.

Table 1 Chemical composition of the material 34CrMo4, in wt %. Source: [2]

C	Si	Mn	P	S	Cr	Mo
0,30 – 0,37	max. 0,40	0,60 – 0,90	max. 0,035	max. 0,035	0,90 – 1,20	0,15 – 0,30

Defects in the neck part are caught in the neck machining workplace during the production process of pressure cylinders. Verification of the quality of the necks is carried out by means of the check with caliber. Possible defects are identified by a magnetic test. One of the mismatched cylinders was selected, on which a detailed examination of the inside defect. For the possibility of internal examination, a transverse cut was made on a band saw in the place of the cylindrical part. After cutting and cleaning, it can be seen that the defect inside the neck can be characterized as a fold maked during

forming. The fold before machining extends to the center of the closed end. After machining the neck, the measured length of the remaining part of the fold is 9 to 12 mm, see **Figure 1**.

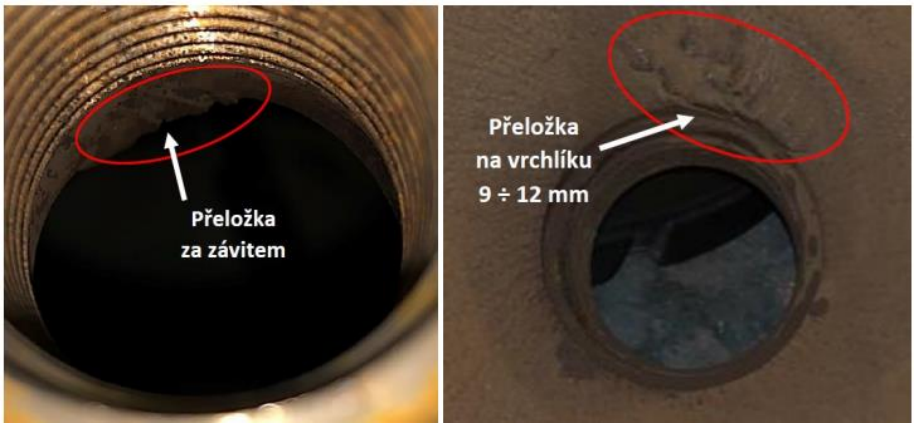

Figure 1: Defects causing cracks on the threads, folds from the inside of the bottle. Source: [2]

The production of these necks is carried out with a method using a rotary forming cylinder on a line with an Autospin 1060 CC forming machine. The line consists of a grate with a dispenser that feeds the semi-finished products onto rolls before induction heating. Subsequently, the piston will move and push the blank into the induction heating unit. The heating of the semi-finished products in the furnace is controlled through power and time. After heating, a series of manipulation steps and transport of the heated blank to the spindle unit will take place. After reaching a safe distance between the manipulator and the loading conveyor, the forming subprogram will be called. The spindle spins to the nominal rotation set in the CNC program, the tool moves to the working position, the burners and tool cooling are started. In the case of the product 204 x 4.4 – M25x2, there are a total of 10 forming steps. Below are pictures of the forming steps taken during the closing and operational tests. From the pictures, we can very well see the forming of the fold during the fourth step. When closed, the fold remains in the central area. We can see the closure and the formation of the fold in **Figure 2**. The formation of the neck with the fold for change in **Figure 3**.

Figure 2: The creating of a fold during closing. Source: [2]

Figure 3: **Forming the neck in the last step with a fold on the outer diameter of the neck.** Source [2]

Based on the creation of the fold, the size of forming steps was adjusted. The modification consisted in reducing the deformation in the fourth step. The modification of the size of deformation is shown in **Figure 4**. Equations are given below figure (1), (2). The forming after the optimization of the forming steps can be seen in **Figure 5**. We can see that there is no folding on the finished product during the forming of the neck.

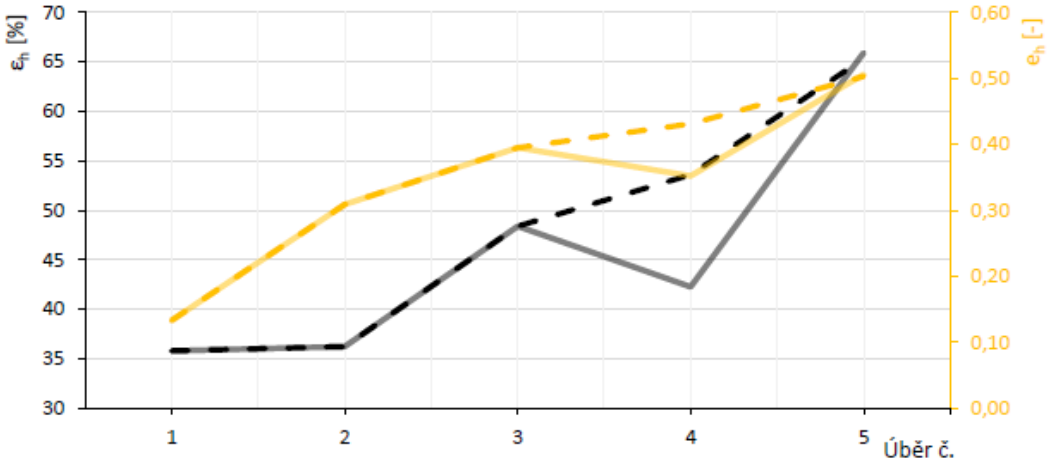

Figure 4: **Deformation during closing before (dashed line) and after change (full line).** Source: [2]

Equations for necking and end closing:

$$\varepsilon_h = 1 - \frac{(D_0{}^2 - d_0{}^2)}{(D_1{}^2 - d_1{}^2)} \quad (1)$$

$$e_h = ln\frac{(D_0{}^2 - d_0{}^2)}{(D_1{}^2 - d_1{}^2)} \quad (2)$$

D_0 – outside diameter of tube befor deformation (mm)
D_1 – outside diameter of tube after deformation (mm)
d_0 – inside diameter of tube befor deformation (mm)
d_1 – inside diameter of tube after deformation (mm)

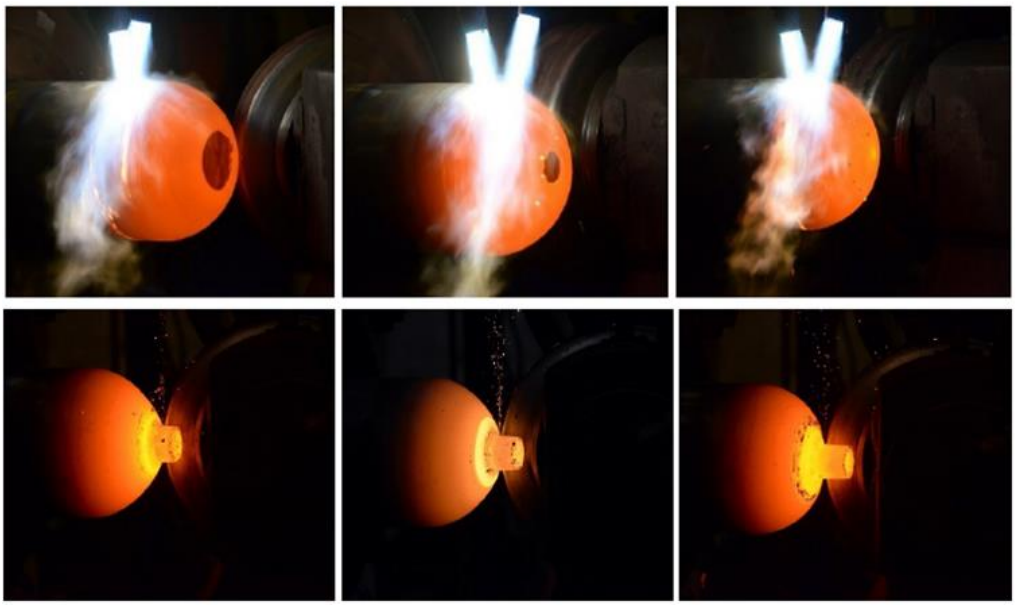

Figure 5: End closing and necking after optimization of the forming steps. Source: [2]

3. CONCLUSION

The experiment concerned the necking of semi-finished products with diameter 204 mm and nominal wall thickness 4,4 mm. These necked semi-finished products with thread M25x2 in neck are use like seamless steel cylinders for technical gases. The neck is forming on an Autospin 1060 CC forming machine. The aim of the optimization was to reduce the total number of non-conforming products below the specified quality limit. The creation of folding is described and documented in detail. On the basis of the performer analysis, modify of forming steps is proposed. Through to this adjustment, it was possible to eliminate the occurrence of folds during the necking.

REFERENCES

[1] MERVA, T. Optimization of the back extrusion process of seamless steel cylinder blanks. Ostrava, 2020. Bachelor thesis. VSB – Technical University of Ostrava.
[2] MERVA, T. Optimization of the hot forming necking and end closing process of seamless steel cylinders and pressure vessels. Ostrava, 2022. Diploma thesis. VSB – Technical University of Ostrava.
[3] ROY, B., YANNIS, P., ARAI, Y., ARAKI, W., JIJIMA, T., KOUYAMA, J. A study of forming of thin-walled hemispheres by mandrel-free spinning of commercially pure aluminum tubes. Journal of Manufacturing Processes. Elsevier, 2020.
[4] WANG, L., LONG H. A study of effects of roller path profiles on tool forces and part wall thickness variation in conventional metal spinning. J Mater Process Technol 2011.
[5] WANG, L, LONG H. Investigation of materiál deformation in multi-pass conventional metal spinning. Mater Des 2011.
[6] ZOGHI H., AREZOODAR F., SAYEAFTABI M. Effect of feed and roller contact start point on strain and residual stress distribution in dome forming of steel tube by spinning at an elevated temperature. Proc IMechE Part B J Eng Manuf 2013; 226 (11):1880-90.
[7] ZOGHI H., AREZOODAR F., SAYEAFTABI M. Enhanced finite element analysis of material deformation and strain distribution in spinning of 42CrMo4 steel tubes at elevated temperature. Mater Des 2013; 47:234-42.
[8] ROY, B., YANNIS, P., ARAI, Y., ARAKI, W., JIJIMA, T., KOUYAMA, J. Experimental and numerical investigation of deformation charecteristics during tube spinning. Int J Adv Manuf Technol 2020, 110:1851-67.

3D HOT DUCTILITY MAP OF CHN35VT STEEL

Author(s): Josef NĚMEC

Supervisor: prof. Ing. Ivo SCHINDLER, CSc.

Department: Department of Metallurgical Technologies, Faculty of Materials Science and Technology, VSB – Technical University of Ostrava

Abstract

In this study, ductility tests were performed on Chn35VT steel to investigate its mechanical behavior under various test parameters. The tests were conducted at different temperatures ranging from 850-1310°C and stroke rates of 0.1-1000 mm/s. The results were used to create ductility maps, which provide a comprehensive understanding of the material's deformation characteristics. The findings will aid in the optimization of the manufacturing process and design of components made from Chn35VT steel.

Key words:

Ductility map, ChN35VT, Gleeble 3800.

1. INTRODUCTION

ChN35VT steel, also known as 17335 according to the Czech norm, is a type of alloy steel which is due to its excellent mechanical properties commonly used in various industries such as cryogenic engineering, thermal and nuclear power. Ductility is one of the most critical mechanical properties of steel, as it measures the material's ability to deform under tensile stress without breaking or cracking. Understanding the ductility of ChN35VT steel under different test parameters is essential for optimizing the manufacturing process and designing components made from this material [1, 2, 3, 4, 5].

In this study, we performed ductility tests on ChN35VT steel at various temperatures and stroke rates to investigate its deformation characteristics. The data collected from these tests were used to create ductility map, which provide a visual representation of the material's ductility under different testing conditions. The maps allow us to better understand the material's mechanical behavior and can be used to optimize the manufacturing process and design components made from Chn35VT steel.

The use of ductility map in materials science has been gaining popularity due to their ability to provide comprehensive insights into the mechanical behavior of materials. By plotting the results of ductility tests under different test parameters, ductility maps can reveal patterns and trends in the material's deformation behavior, which can be used to optimize the material's performance in various applications.

The ductility map created in this study will provide a useful tool for engineers and researchers working with ChN35VT steel. By using these maps, they can better understand how the material behaves under different conditions. Additionally, the results of this study can provide a basis for further research into the mechanical properties of ChN35VT steel and other similar materials.

2. EXPERIMENT

In this experiment, ductility tests were conducted on ChN35VT steel (see Table 1) samples to investigate their deformation behavior under different test parameters.

Table 1 Comparison of chemical composition of both steels. Source: (own)

Element	C (%)	Mn (%)	Si (%)	P (%)	S (%)	Cr (%)	Ni (%)	Ti (%)	W (%)
CHN35VT	0.09	1.55	0.44	0.018	0.009	14,9	35.10	1.29	2.99

The samples were prepared by rolling them from a diameter of 55 mm to a diameter of 12.3 mm, followed by turning them on a lathe to a diameter of 10 mm and a length of 86 mm with 15,25 mm long M10 x1,50-g threads on both sides of specimen. Technical drawing of the specimen is shown in figure 1.

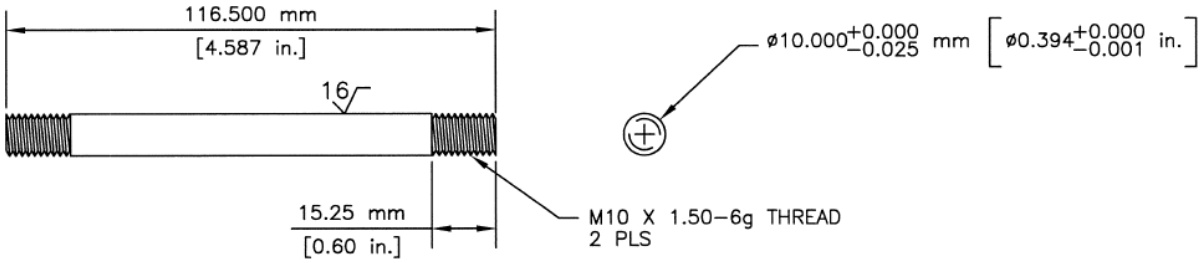

Figure 7 Drawing of specimen used for tensile tests. Source: (own)

The tests were performed using a Gleeble 3800 device, which is a highly advanced and versatile thermo-mechanical simulator. The device allowed for precise control of the test parameters and real-time monitoring of the sample's behavior during testing [6]. The samples were heated to temperatures ranging from 850-1310 °C at a heating rate of 5 °C/s, followed by a 300-second hold to ensure uniform temperature throughout the sample's volume as is it shown in Figure 2. To avoid oxidation of sample during the tests, testing chamber had been vacuumed before heating. Value of vacuum during the tests was around 26,7 Pa.

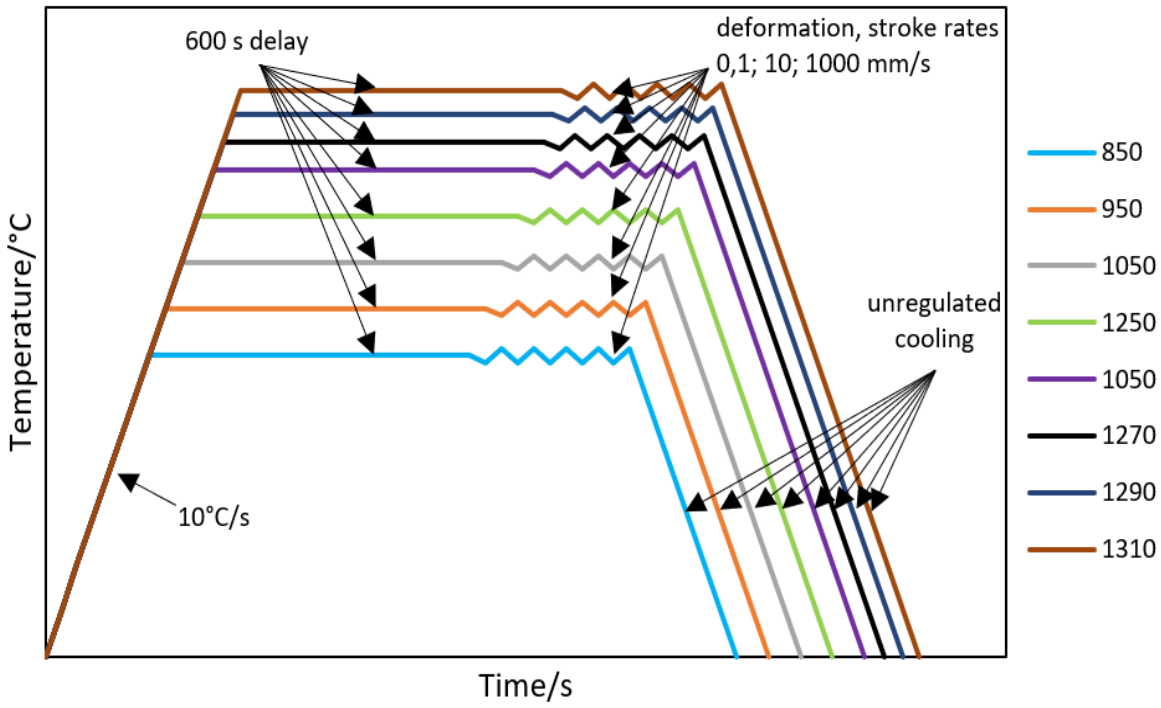

Figure 2 Schematical temperature evolution of conducted tests. Source: own

After the hold, the samples were subjected to ductility tests at different stroke rates of 0.1, 10 and 1000 mm/s. The specimens were loaded in tension until failure, followed by uncontrolled cooling in air with heat transfer through the machine jaw. The resulting stress-strain data were collected and analyzed.

The collected data were used to create ductility map, which shows the material's ductility under different testing conditions. The map was created by plotting the ductility values obtained from the stress-strain data as a function of temperature and stroke rate. This allowed for the visualization of the materials deformation behavior under different conditions, enabling the identification of any trends or patterns. Formula (1) was used to calculate the ductility from the tensile test data [7].

$$\varepsilon = (l_1 - l_0)/l_0 \quad (1)$$

where:
l_1 – final gage length (mm),
l_0 – initial gage length (mm),

Overall, the experiment provided valuable insights into the deformation behavior of ChN35VT steel under various test parameters. The use of the Gleeble 3800 device allowed for precise control of the test conditions.

3. RESULTS AND DISCUSSION

Figure 3 shows results of ductile tests and ductility map for temperatures 850, 950, 1050, 1150, 1250 and 1270 °C and stroke rates 0.1, 10 and 1000 mm/s.

For mentioned stroke rates, higher temperature always meant lower force required for deformation. The effect of stroke rate is the opposite according to the measured results. Tensile strength increases with increasing stroke rate. The biggest decrease of tensile strength was observed between temperatures 850 and 950 °C for stroke rate 10 mm/s. The highest tensile strength was measured for the combination of temperature 850 and stroke rate 1000 mm/s and its nominal value is cca. 31 kN.

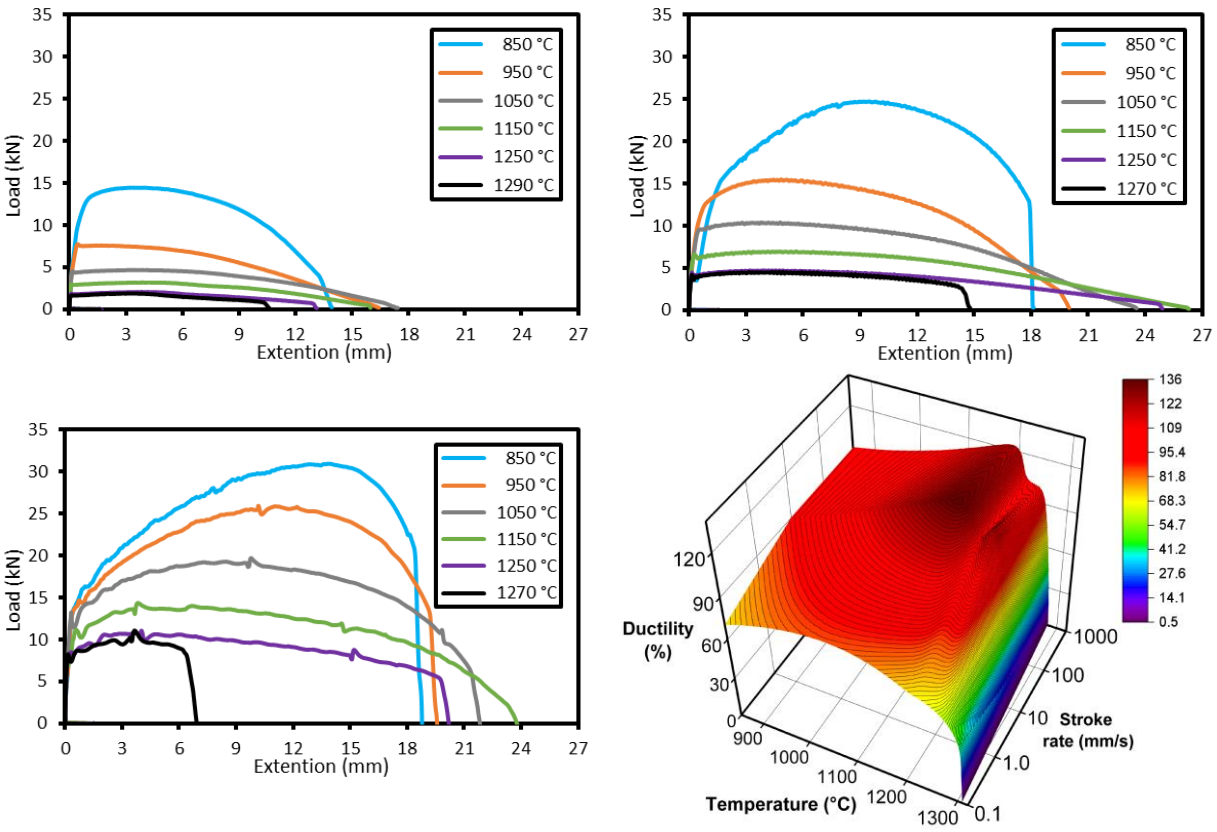

Figure 3 Tensile diagrams of ChN35VT at different stroke rates: (a) 0.1 mm/s; (b) 10 mm/s; (c) 1000 mm/s; and ductility map (d). Source: (own)

It was observed that the ductility decreased with increasing stroke rate. At higher temperatures, the steel showed greater ductility with lower susceptibility to cracking. This applies only up to a certain temperature, when the steel overheats and then the ductility drops sharply with increasing temperature. This means that the ductility increases with increasing temperature up to temperatures of 1150 °C for stroke rates of 10 and 1000 mm/s, after which the ductility decreases. For this decrease in ductility, a convex curve shape is first observed which becomes concave. At the lowest stroke rate, the highest ductility is reached at 1050 °C after which the ductility drops and the curve is concave throughout.

4. CONCLUSION

In this study, the ductility and tensile strength of steel were examined using a tensile test. Based on the performed tests and measured values here are some observations:

(1) The tensile strength for all tests performed always decreased with increasing temperature and lower stroke rate.

(2) As the stroke rate increases, the ductility at the highest temperatures decreases significantly.

(3) At higher stroke rates (10 and 1000 mm/s), there was observed a significant decrease in ductility with the following convex part of the curve after reaching the maximum ductility. To clarify this phenomenon, further study of the samples is necessary.

ACKNOWLEDGEMENT

I would like to take this opportunity to express my heartfelt appreciation to Prof. Schindler for his unwavering support, guidance, and encouragement. I would also like to extend my thanks to ZDAS and Mr. Ruzicka for providing the material for testing and for sharing the chemical composition of the material. Their contributions have been vital in shaping the final outcome of this article, and I am deeply grateful for their support.

REFERENCES

[1] Ocel ChN35VT [online]. ŽĎAS, a. s. – Technický list oceli ChN35VT [cit. 10.5.2023]. Avaliable from: https://www.zdas.com/files/uploads/2021/06/ChN35VT_CZ.pdf

[2] HAJ, Mehdi, Hojjatollah MANSOURI, Reza VAFAEI, et al. Hot compression deformation behavior of AISI 321 austenitic stainless steel. *Materials Science and Engineering: A*. 2011, **528** (6-7), 2797-2805.

[3] RADIONOVA, Liudmila V., Danil V. PEREVOZCHIKOVMAKOVECKII, Aleksandr N. EREMIN, et al. Study on the Hot Deformation Behavior of Stainless Steel AISI 321. *Materials Science Forum*. 2019, **945**, 199-204.

[4] ČÍHAL, Vladimír. *Korozivzdorné oceli a slitiny*. Praha: Academia, 1999. ISBN 80-200-0671-0.

[5] BANABIC, Dorel, et al. Formability of metallic materials: Plastic Anisotropy, Formability Testing, Forming Limits. Springer, 2000, 327 s. ISBN 3-540-67906-5.

[6] *Gleeble® 3800 System* [online]. GLEEBLE® [cit. 10.5.2023]. Avaliable from: https://gleeble.com/products/gleeble-3800.html

[7] SILBERNAGEL, Arnošt, Miroslav GREGER, Vojtěch HRUBÝ, et al. aj. *Struktura, vlastnosti, zkoušení a použití kovů*. Ostrava: Kovosil Ostrava, 2011. ISBN 978-80-903694-6-7

NUMERICAL MODELING OF ADVANCED ALUMINUM ALLOY WITH HIGH CONTENT OF RECYCLED MATERIAL USED IN LPDC TECHNOLOGY

Author(s): Jakub RUŠAJ

Supervisor: doc. Ing. Petr LICHÝ, Ph.D.

Department: Department of Metallurgical technologies, Faculty of Materials Science and Technology, VSB – Technical University of Ostrava

Abstract

The aim is determinate and validate virtual alloy with high content of recycled (secondary) material for casting simulation in the software MAGMA 5 and in the following steps optimize a technology of low pressure die casting (LPDC) for this new alloy. Validation of current and new virtual material will be realized by comparison of real and simulated thermal analyze curves.

Key words:

Simulation, CO_2 footprint, Secondary material, Thermal analyze, LPDC.

1. INTRODUCTION

The aim of this research is CO_2 footprint reduction of aluminum wheels for light vehicle passenger's cars and the researcher itself is only one step on a way to CO_2 neutral serial production in automotive industry.

Current melting mix used in standard serial production of aluminum wheels is 50% primary and 50% secondary aluminum alloy and the primary one has a taken key role in CO_2 footprint of each produced wheel. New melting mix will contain at least 70% of secondary (scrap) aluminum alloy. This change brings new concerns about internal metal quality, amount of inclusion, inoculation agents, the grain size, solidification range, etc. Modification of metal refining process will be necessary as an optimization of low pressure die casting (LPDC) process.

For those reasons has been choose numerical simulation as an effective tool to find an optimal chemical composition for new alloy and optimize LPDC technology. Key role in successfully casting simulation play a perfect conformity between real/virtual alloy, the metallurgical point of view and real/virtual LPDC process, the technological point of view. In this research is presented feasibility study, the base line for current alloy (50/50 – secondary/primary), the comparison between real/virtual alloy and the conformity between real/virtual LPDC process.

2. FEASIBILITY STUDY

Before start of the project has been made the feasibility study, what part of vehicle has the biggest potential to reduce CO_2 footprint in vehicle production process and later will be used the study as a base line for project evaluation.

The comparison of inherent emissions per produced vehicle, in total 7 tCO_2, shown 25% emission are caused by aluminum parts see Fig. 1, and then has been made the selection of aluminum components in vehicle, to see what component the biggest impact has. From analyze in table 1 is clearly visible, that aluminum wheels play main role in total weight of aluminum components used in the vehicle. Aluminum is with key role for decarbonization of car production, with 25% of production emissions 8% from wheels.

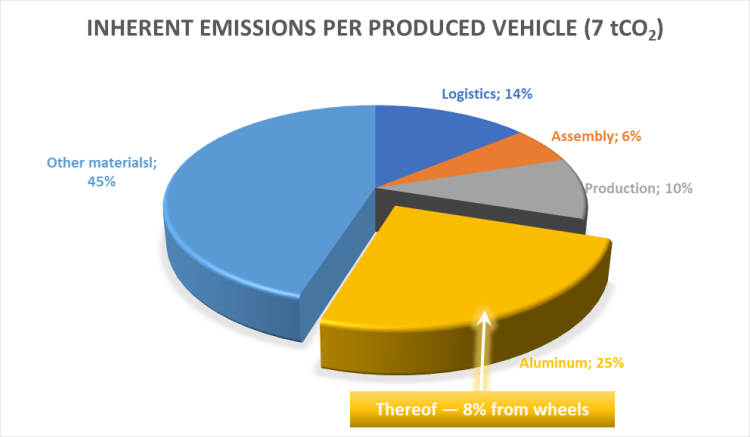

Figure 1 Inherent emissions per produced vehicle (7 tCO_2). Source: (own)

Table 2 Weight of vehicle's components and percentage of aluminum. Source: (own)

Component	Weight (kg)	Alu share
Engine	126	38 %
Body & Structural	568	1 %
Electronics & Electric	55	0 %
Transmission	97	24 %
Interior	129	0 %
Axels & Driveshafts	123	4 %
Climate Control & cooling	41	18 %
Suspension	19	0 %
Braking	65	2 %
Steering	21	43 %
Fuel System	18	0 %
Passenger Restraints	14	0 %
Audio & Telematics	7	0 %
Exhaust	31	8 %
Wheel & Tires	**105**	**47 %**
Body Glass	49	0 %
Total (Kg)	**1468**	**152**

3. LPDC TECHNOLOGY FOR WHEEL PRODUCING

Filling of the mold cavity is realized by increasing the pressure above the surface of the metal in the holding furnace, forcing the metal from the furnace through a rising tube up into the mold, see Fig 2. The filling speed is regulated by increasing the pressure in the holding furnace it provide smooth filling with minimum turbulences and reoxidation of liquid aluminum in the mold cavity. The quality of castings produced by LPDC technology is extremely high. Castings have a minimum inclusions and gas defects [1 - 3] therefore, those castings are characterized by excellent tightness. This procedure is suitable and, in some cases, even the only possible if we require a high internal quality of a casting. It is the dominant technology to produce aluminum wheels for light vehicle passenger's cars on a global scale. The LPDC technology is shown in Fig. 2 [4].

4. NUMERICAL MODELING OF ALUMINUM ALLOY

One of the most critical factors for precise casting simulation is correct setup of virtual alloy. The alloy itself is determined by chemical composition, fraction solid, thermal conductivity, and heat capacity. In this research has been optimized the alloy AlSi7Mg (A356) used in commercial wheel producer in Czech Republic. The default alloy for casting simulation has been used standard AlSi7Mg from library of casting simulation software see Fig. 4 and compared with the Real alloy used in serial production. The composition of the real alloy is 50% scrap aluminum (secondary Al) and 50% brand new aluminum from smelter (primary Al), the ratio is 50/50 primary / secondary Al. For the real alloy has been determined chemical composition and thermal curve by thermal analysis equipment TA110, see Fig. 3.

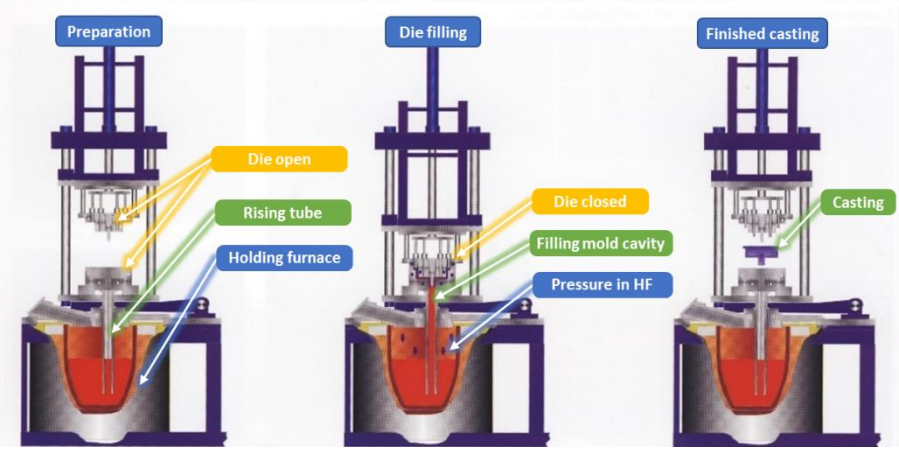

Figure 2 LPDC Technology – Casting cycle. Source: (own)

Figure 3 left is transport ladle (800Kg) during degassing and refining process, right is thermal analyze of treated alloy A356. Source: (own)

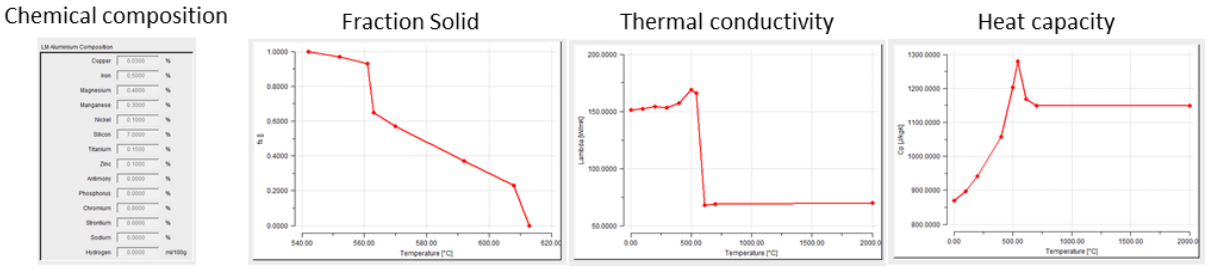

Figure 4 standard virtual AlSi7Mg alloy from library of simulation software. Source: (own)

After that has been generated in the software JMatPro new optimized virtual alloy based on measured chemical composition and furthermore optimized in casting simulation sw. for perfect conformity with the real 50/50 alloy, in Fig. 5, is visible the differences in thermal curves, between virtual default, virtual optimized_3 and Real alloy.

Next, has been validated the prediction of casting defects (microporosity) of the new virtual optimized_3 alloy in casting simulation sw. see Fig 6. Is visible significant improvement of predicted defects, the positions 1, 3, 4 are in perfect match with real casting defects and position 2 and 5 not so far from reality. Default virtual alloy predicting in some cases wrong position for defect and to high intensity of the defect (microporosity). The level of simulation's accuracy with optimized virtual alloy is convenient for further steps.

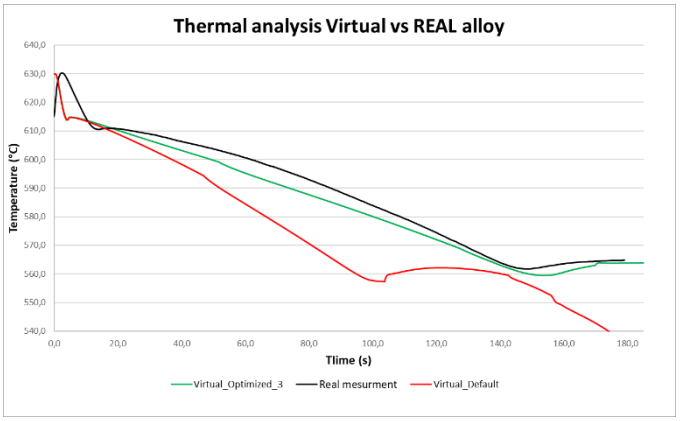

Figure 5 Thermal curves comparison – Real 50/50, Virtual Default and Virtual optimized_3 alloy. Source: (own)

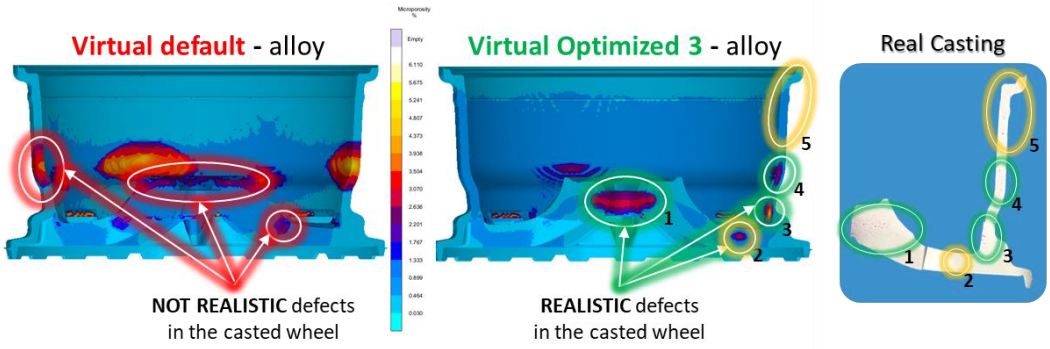

Figure 6 Defect position in the simulation: Virtual (Default, Optimized3) vs Real 50/50 alloy. Source: (own)

5. CONCLUSION

The feasibility study shown the aluminum component of the vehicle to be focused on, if the CO_2 footprint reduction during vehicle production, is needed. Analyze of LPDC process prove the concept of increasing the ratio of secondary (scraped) aluminum in the alloy AlSi7Mg, from 50/50% (secondary/primary Al) to 70/30%.

Entire process will be optimized in casting simulation; therefore, the calibration of virtual alloy is needed. Has been carefully determined properties of the real alloy and according to measured date optimized the virtual alloy. After that has been proceeded the validation and approved for further seps. In further research will be optimize new virtual alloy with ration of secondary/primary aluminum 70/30.

ACKNOWLEDGEMENT

This research was funded by the project of MEYS (grant number CZ.02.1.01/0.0/0.0/17_049/0008399). This research was carried out with the support of projects of student grant competition (project number SP2023/022).

REFERENCES

[1] OU Jun, Chunying WEI, Savanna LOGUE, Steve COCKCROFT, Daan MAIJER, Yacong ZHANG, Zhi CHEN. A study of an industrial counter pressure casting process for automotive parts. *Journal of Materials Research and Technology.* 2021, **15**, 7111-7124. ISSN 2238-7854.

[2] ZHANG Yacong, Daan MAIJER, Steve COCKCROFT. Development of a 3-D thermal model of the low-pressure die-cast (LPDC) process of A356 aluminum alloy wheels. *Materials Science and Engineering*. 2007, **464**, 295-305. ISSN 0921-5093.

[3] WEI Chunying, Jun OU, Farzaneh Farhang MEHR, Daan MAIJER, Steve COCKCROFT, Xu WANG, Zhi CHEN, Zhihua ZHU. A thermal-stress modelling methodology in ABAQUS for fundamentally describing the die/casting interface behaviour in a cyclic permanent die casting process. *Journal of Materials Research and Technology*. 2021, **15**, 5252-5264. ISSN 2238-7854.

[4] MERLIN Mattia, Giulio TIMELLI, Franco BONOLLO, Gian Luca GARAGNANI. Impact behaviour of A356 alloy for low-pressure die casting automotive wheels. *Journal of Materials Processing Technology*. 2009, **209** (2), 1060-1073. ISSN 0924-0136

COMPARISON OF SINGLE-STEP WITH MULTI-STEP DEFORMATION OF A RADIALLY FORGED OF 34MNB5 STEEL

Author: Jan SMOLKA

Supervisor: prof. Ing. Radim KOCICH, Ph.D.

Department: Department of Metallurgical Technologies, Faculty of Materials Science and Technology, VSB – Technical University of Ostrava

Abstract

The radial forging process plays a critical role in the manufacturing industry, providing a method for shaping metals into desired components. Among the various radial forging techniques, one-step forging and two-step forging are commonly employed, and each has its advantages and applications. This is presented as a comparison via analysis of these two forging methods, mainly focusing on the mechanical properties of the resulting workpiece.

Key words:

Radial forging, reduction, steel forming.

1. INTRODUCTION

In steel manufacturing and forming world are many approaches how you can achieve required result. During the history there were many ways how to form a steel. From hammering and bending on early beginning development of rolling mill in the 17th century but it is not stopped to evolving. During in the 20th century, steel forming continued to evolve with significant improvement. The new techniques came as extrusion, casting and forging [1].

In radial forging, round bar/billet is formed between two or four dies and it is shaped to desired parameters. The dies exert pressure on the material, causing it to flow radially outward and conform to the shape of the dies. The process can be repeated multiple times until the desired shape and size are achieved **Chyba! Nenalezen zdroj odkazů.**.

The radial forging can be also used for forming of exotic metals or alloys for example ZK60 magnesium alloy. The study aimed to investigate the effect of radial forging on the microstructure and mechanical properties of ZK60 magnesium alloy. The results showed that radial forging significantly improved the microstructure and mechanical properties of the magnesium alloy. The process led to a refinement of the grain size, an increase in the hardness, and an improvement in the ultimate tensile strength and elongation of the alloy [3].

On field of simulations, the radial forging takes interest of many researchers. It was found the forging load is decreasing with decreasing forging spring stiffness. Also was simulated during the multi pass forging was reached dynamic recrystallization that caused uniform grain and strain gradually penetrated the core of the billet [4].

The important condition for the radial forging is design of the tools. The design of the tools has big impact several aspects of the forging process, such as the deformation behavior of the material, the shape and dimensions of the final product, and the surface finish of the forged part. The tool design must account for the high pressures and temperatures involved in the forging process, as well as the wear and tear that the tools will experience over time. The tools must be designed to withstand these conditions and maintain their shape and accuracy over repeated cycles of use [5].

2. USED MATERIAL AND METHODS

For this experiment was used 34MnB5 low-alloy steel with diameter 36 mm. This steel alloy contains high amount of manganese and boron (see table.1 and for mechanical properties see table. 2). This steel is commonly used in the automotive industry, most importantly for producing crankshafts, axle shafts and gears [6].

Table 1: Chemical composition (wt. %) of 34MnB5. Source [6]

	C	Mn	P	S	Si	Al	Cr	Ti	B
	min. - max.	min. - max.	max.	max.	min. - max.	min. - max.	min. - max.	min. - max.	min. - max.
34MnB5	0.33 - 0.37	1.20 - 1.40	0.015	0.010	0.20 - 0.25	0.020 - 0.060	0.100 - 0.180	0.020 - 0.035	0.0020 - 0.0035

Table 2: Mechanical properties of 34MnB5. Source [6]

Grade	Test Direction	Yield strength R_p (MPa)	Tensile strength R_m (MPa)	Elongation[1] A_5 (%)
34MnB5 Typical	L	400	650	23

The used method was used cold radial forging in (it was done under room temperature). Samples was manufactured by one-step forging and two-step forging. One-step forging is done directly from 36 to 22 and on the other hand two step forging is done from 36 mm to 28 and from 28 to 22 mm. For both samples was used mandrel with diameter 11 mm. The used machine was SKK06 by GFM company.

3. RESULTS AND DISCUSION

In one-step forging, the entire process is completed in a single operation, resulting in rapid and intense deformation. This leads to increased hardness, which is slightly higher compared to two-step forging. In two-step forging, the process is divided into two smaller deformations, resulting in an increase in hardness, but not as high as in one-step forging. This can be seen on figure 3 where is hardness HV5 measured on multiple spots (in Fig it is defined as length). This also confirms test on 32CDV 13 steel, which was cold radially forged. The hardness of 32CDV 13 steel increased with deformation with higher reduction. Reduction for this sample was 38 % [7].

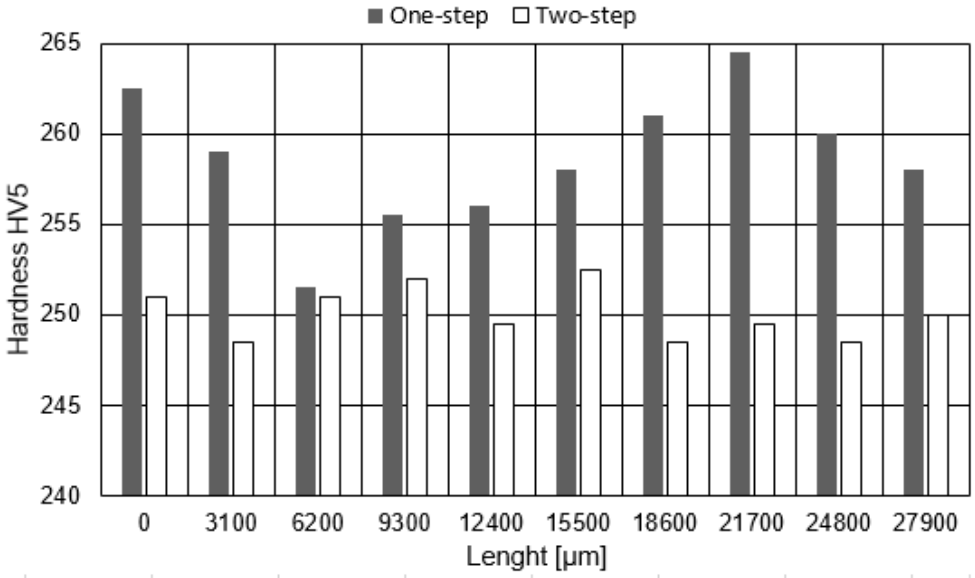

Figure 3: Comparison of hardness for both samples – one step and two step. Source: (own)

However, one-step forging, due to its larger deformation, can cause cracks on the inner side of the material originating from the mandrel. These cracks are clearly visible in the figure 3, showing single and parallel scratches. This investigation was conducted on two-step forged material, where no such scratches were found (see figure 4).

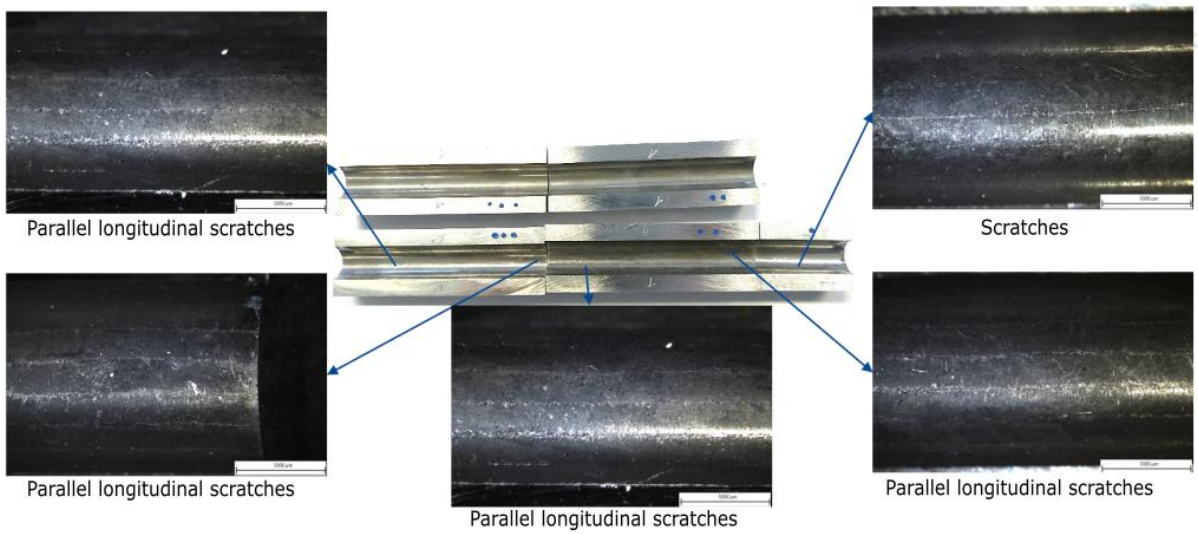

Figure 3: Macroscopic investigation of inner surface of the one-step sample. Source: (own)

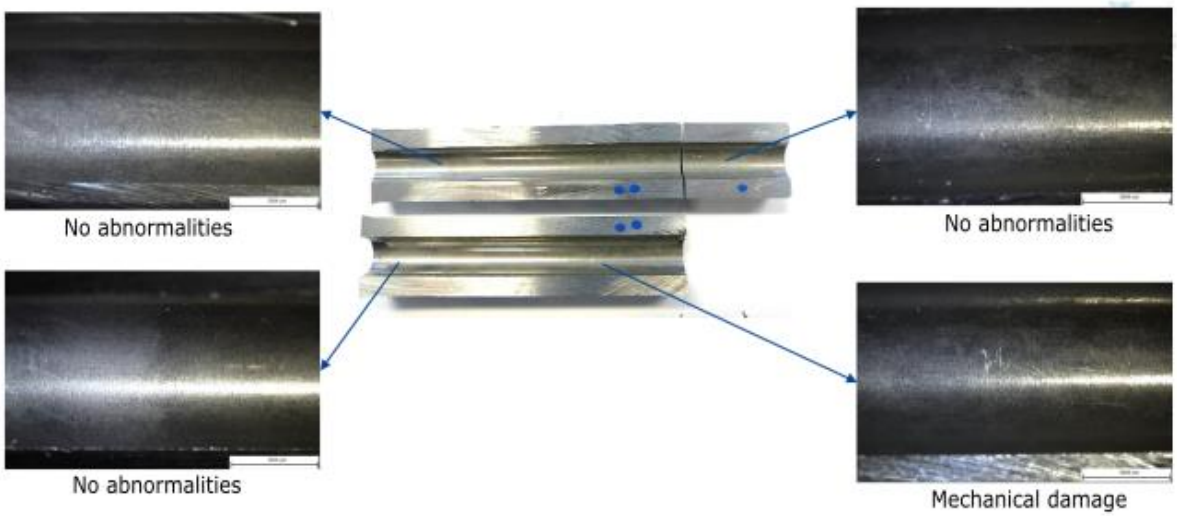

Figure 4: Macroscopic investigation of inner surface of the one-step sample. Source: (own)

Further investigation of the inner surface of the one-step forged material revealed numerous cracks with a maximum depth of 280 µm (see figure 5). On the other hand, the inner surface of the two-step forged material exhibited smaller cracks to a depth of approximately 27 µm (see figure 6). The cracks are common defects [8].

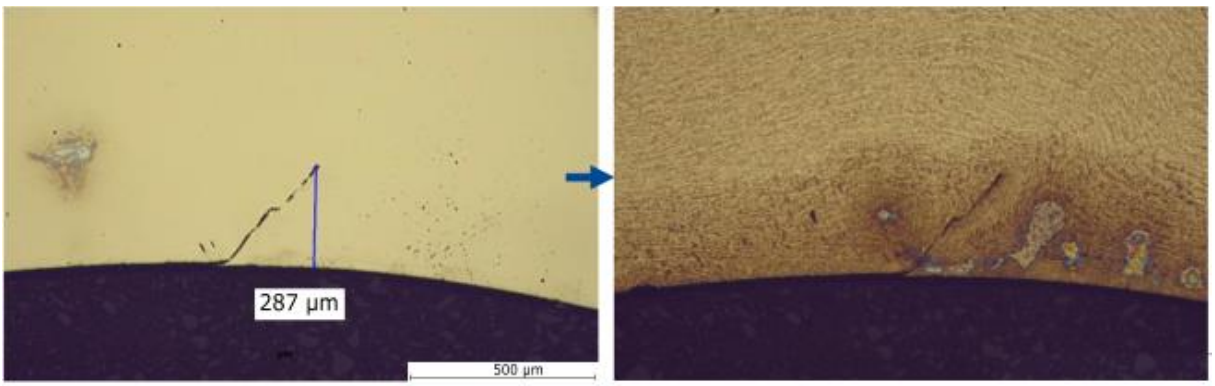

Figure 5: Example of the crack with depth of 280 µm on inner surface of one-step surface. Source: (own)

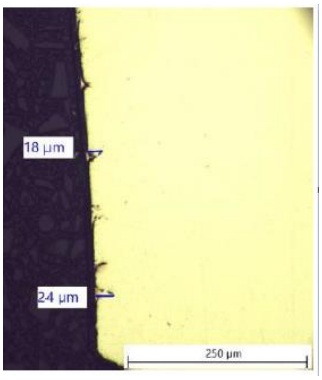

Figure 6: Example of the cracks with depth of 18, 24 µm on inner surface of one-step surface.
Source: (own)

4. CONCLUSION

This paper compares one-step and two-step radial forged 34MnB5 steel, revealing distinct characteristics and trade-offs. The one-step process yields higher hardness, indicating enhanced material strength. However, it is accompanied by the presence of cracks, which can compromise the structural integrity and performance of the forged steel. On the other hand, the two-step radial forging process results in much smaller cracks in the final product, ensuring a structure that is much closer to being defect-free compared to the one-step process. Although the hardness achieved in the two-step process is not as high as in the one-step process, it still represents a notable increase compared to the unformed material.

When considering the application and requirements of the final product, both processes have advantages and disadvantages. If high hardness is the primary focus, the one-step radial forging is preferred despite the presence of cracks. However, in applications where a low amount of deep cracks is needed, the two-step radial forging process is a much better choice than the one-step radial forging.

ACKNOWLEDGEMENT

I would like to thank my supervisor, prof. Ing. KOCICH RADIM, Ph.D., for the patient guidance, and advices he has provided me.

REFERENCES

[1] Swank, James M.,History of the Manufacturers of Iron in All Ages, Published by Burt Franklin 1892, p.91
[2] Cold and Hot Forging: Fundamentals and Applications. 1. United States of America: ASM International, 2005, 337 s. ISBN 0-87170-805-1. Dostupné také z: http://ressources.unit.eu/cours/MediaMef3/module-forgeage-materiaux/res/Cold_and_Hot_Forging_Fundamentals_and_Applications.pdf
[3] ZOU, Jingfeng, Lifeng MA, Weitao JIA, Qichi LE, Gaowu QIN a Yuan. Microstructural and mechanical response of ZK60 magnesium alloy subjected to radial forging. Journal of Materials Science & Technology [online]. 2021, (83) [cit. 2023-04-26]. ISSN 1005-0302. Available from: doi:https://doi.org/10.1016/j.jmst.2020.11.080
[4] HUANG, Jianglin, Carl D. SLATER, Anup MANDRAL a Paul BLACKWELL. A Dynamic Model for Simulation of Hot Radial Forging Process. Procedia Engineering [online]. 2017, 207, 478-483 [cit. 2023-04-27]. ISSN 18777058. Available from: doi:10.1016/j.proeng.2017.10.808
[5] AHOTI, G.D., L. LIUZZI a T. ALTAN. Design of dies for radial forging of rods and tubes. Journal of Mechanical Working Technology [online]. 1977, 1(1), 99-109 [cit. 2023-05-01]. ISSN 03783804. Available from: doi:10.1016/0378-3804(77)90016-X
[6] 34MnB5: Consistent formability combined with excellent strength after heat treatment [online]. In: . [cit. 2023-04-25]. Available from: https://www.tatasteeleurope.com/sites/default/files/tata-steel-engineering-34MnB5-hr-manganese-boron-wear-resistant-precision-tubes-datasheet-en.pdf
[7] ARREOLA-HERRERA, Rodolfo, Alejandro CRUZ-RAMÍREZ, Miguel Ángel SUÁREZ-ROSALES a Ricardo Gerardo SÁNCHEZ-ÁLVARADO. The effect of cold forming on structure and properties of 32 CDV 13 steel by radial forging process. Materials Research [online]. 2014, 17(2), 445-450 [cit. 2023-06-07]. ISSN 1980-5373. Available from: doi:10.1590/S1516-14392014005000041
[8] PARMAR Keyur. (2015). A Review on Unfilling Defect Found in Forging Process. International Journal for Scientific Research & Development. 3. 541-543.

USE FACTSAGE SOFTWARE TO OPTIMIZE METALLURGICAL PROCESSES

Author: Michal SNIEGOŇ

Supervisor: prof. Ing. Markéta TKADLEČKOVÁ, Ph.D.

Department: Department of Metallurgical Technologies, Faculty of Materials Science and Technology, VSB – Technical University of Ostrava

Abstract

The submitted contribution deals with the possibilities of using the FactSage simulation software, which has applications in the simulation of metallurgical processes in the areas of secondary metallurgy. Optimizing production processes in operational conditions is difficult, therefore, in laboratory conditions, it is advantageous to use simulation software, which makes it possible to effectively simulate a specific solved problem associated with steel production. Among the most used simulation software is FactSage, which serves to optimize metallurgical processes, especially to determine the properties of steel or slag during their processing. The aim of the present paper is to present the use of SW FactSage in the optimization of the desulfurization process, the formation of a ternary slag system and the determination of phase transformation temperatures.

Key words:

Secondary metallurgy, refinery slag, desulfurization, FactSage.

1. INTRODUCTION

Equipment from the field of secondary metallurgy is an integral part of modern steel plants, which were introduced depending on the increasing demands of the customer on the quality of steel. If undesirable elements are present in steel, the physical and mechanical properties of steel products may be reduced. For example, oxygen and sulfur contribute to the formation of non-metallic inclusions that negatively affect the properties of steel. Thanks to the optimization of metallurgical processes, the time needed to perform experimental smelting is reduced and the financial costs for performing the experiment in operating conditions are reduced [1, 2, 3].

One of the auxiliary software that can be used in the evaluation of the course of metallurgical processes is FactSage [4]. SW is a thermodynamic/thermochemical software that, based on thermodynamic calculations of energy functions from empirically obtained values of thermophysical properties of materials (heat capacity, enthalpy, phase transformation temperatures, etc.), steel and slag, determines e.g. phase or chemical transformations during metallurgical processes. Thermodynamic calculations of the equilibrium phase composition of n-dimensional systems (binary, ternary, quaternary to multicomponent systems) are usually based on the criterion of thermodynamic equilibrium and consist in finding the minimum total Gibbs energy at constant temperature, pressure and chemical composition [4, 5]. The results can be processed into informative ternary or multicomponent diagrams and the behavior of the molten steel or slag during processing can also be predicted. The software is widely used in metallurgy, where it is used to determine the formation of solid and liquid phases in steel and slag, simulation of deoxidation and desulfurization of steel, production of ferronickel steel, simulation of reoxidation and inclusions and their modification, or calculation of the material balance in the oxygen converter. Following the factors mentioned above, this article will deal with the application of FactSage software for the optimization of metallurgical processes.

2. BASIC PRESENTATION OF SW FACT SAGE

Currently, FactSage is installed in more than 100 universities worldwide, where it is used as a research tool and educational aid. Also, around 100 industrial users switched from the old ones and more complex computing software on FactSage due to ease of use, flexible access to different databases and powerful computing modules [4-5].

Structure of the FactSage program

Knowledge of chemical thermodynamics is necessary to operate the software. However, with regular use of the program, a practical understanding of the principles of thermochemistry, especially

when it comes to complex phase equilibria, can be gained relatively quickly. The software interface is shown in **Fig.1**

Fig.1 Main menu SW FactSage 8.1. Source: (own)

SW FactSage Steel Database

FactSage software has a wide scope that includes many databases. For the modeling of metallurgical reactions, it uses two basic databases FSstel and FT oxide - Slag.

Fsstel is a database that is intended for the simulation of reactions taking place in metal. The steel database contains data on 115 fully evaluated binary alloy systems that contain the elements: Al, B, Bi, C, Ca, Ce, Co, Cr, Cu, Fe, La, Mg, Mn, Mo, N, O, Nb, Ni, P, Pb, S, Sb, Si, Sn, Ti, V, W, Zr. It is intended to provide a reliable basis for calculations covering a wide range of steelmaking processes, e.g. oxygen reduction prior to desulfurization of steel at secondary metallurgy facilities. It also contains a wide range of steels, including austenitic, ferritic and duplex stainless steels, including the formation of carbides and nitrides; conditions for heat treatment operations in order to create the required conditions for scrap remelting to maintain the smallest possible concentrations of undesirable elements, interaction with refractory material, etc. [4-5].

The FT oxide – Slag database is used in metallurgy for process simulation and control of slag composition. Nowadays, he can work with the simulation of these slag systems, for example: molten slag intended for steel refining, fluxes for casting, control of non-metallic inclusions, refractory materials.

3. APLICATION SW FACTSAGE IN PROCESSING METALLURGY

This section describes the use of the software in metallurgy. An example of the SW FactSage implementation in secondary metallurgy is the simulation of desulphurization in a refinery using a given desulphurization medium.

Desulfurization of steel

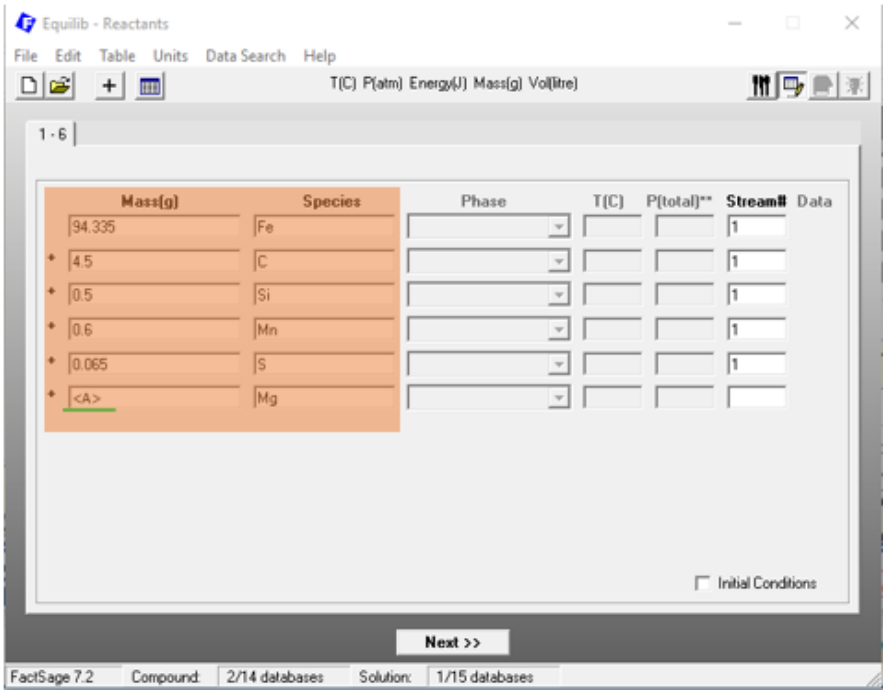

Fig. 2 Selected chemical composition. Source: (own)

In **Fig.2** we can see the interface of the Equilib function, where we simulate the desulphurization of pig iron before it is put into the oxygen converter.

Pig iron desulfurization simulation consists of several parts, the first part is selecting the chemical composition of pig iron, the second part is choosing the desired desulfurization medium, the third part is the correct selection of the database, and the fourth part is setting the basic unit. The equilib function can be used to optimize metallurgical processes during pig iron desulfurization, specifically choosing the right desulfurization medium [6-8].

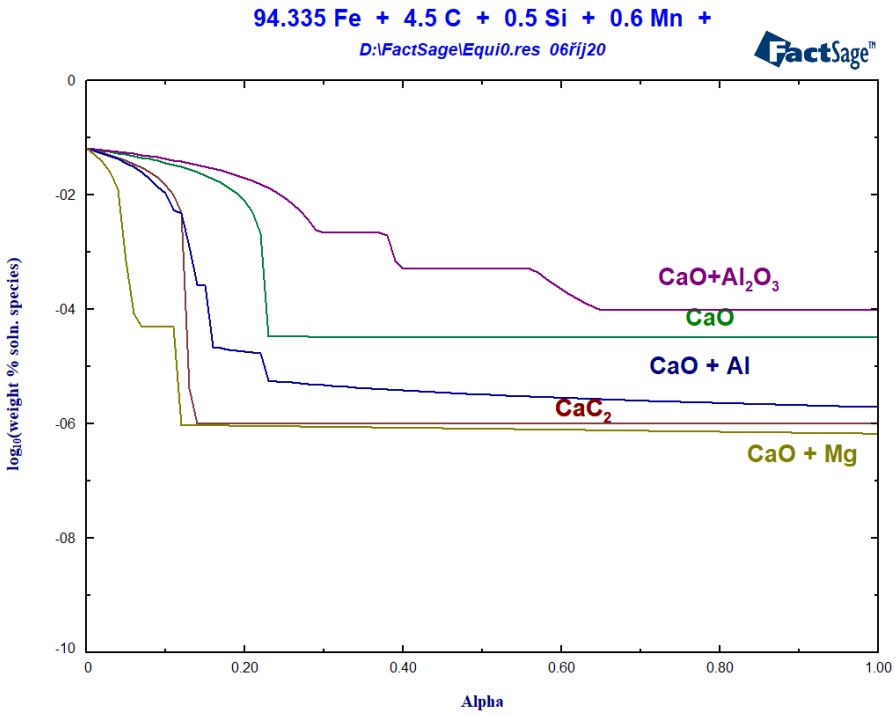

Fig. 3 pig iron desulfurization simulation results. Source: (own)

Using the pig iron desulfurization simulation shown in **Fig. 3**, we can determine the appropriate desulfurization element, oxide for the given metallurgical operation. According to the graph in Fig. 3, the combination of a mixture of CaO + Mg and CaC_2 is the best variant of the desulphurization alloy. We proceed from the displayed graph (Fig. 3), where the other combinations of the mixture did not show a high desulfurization ability.

4. CONCLUSION

The aim of the presented contribution was to get acquainted with the possibilities of using sw FactSage in metallurgy. The simulation of metallurgical processes makes it possible to optimize the production process and thus reduce the financial costs of conducting experimental smelting in practical conditions. The software can be used to determine the liquidus temperature of the slag, it can predict the phases that occur during steel refining. Furthermore, the software is used to determine the optimal desulfurization medium. Nowadays, a technologist cannot do without simulation software.

ACKNOWLEDGEMENT

The work was supported by "Support for Science and Research in the Moravian-Silesian Region 2021-RRC / 10/2021"and the work was also supported by the project Student grant competitions number SP2023/022

REFERENCES

[1] ADOLF, Z. Teorie procesů při výrobě železa a oceli Část II – Teorie ocelářských pochodů. first edition. VSB – Technical University of Ostrava, 2013, 94 s. ISBN 978-80-248-3349-1.

[2] KEPKA, M. Rafinace oceli. first edition. Praha: SNTL, 1989, 200 s. ISBN 80-03-00079-31989.

[3] MICHALEK, K.; SOCHA, L.; ADOLF, Z.; BAŽAN, J. Rafinace a odlévání oceli: didactic text. VSB – Technical University of Ostrava, 2013, 89 s. ISBN 978-80-248-3551-4.

[4] BALE, C., BÉLISLE, E., CHARTRAND, P., DEGTEROV, S. A.; ERIKSSON, G., HACK, K., JUNG, I. Ho., KANG, Y. B., MELANÇON, J., PELTON, A, D., ROBELIN, CH., PETERSEN, S. FactSage Thermochemical Software and Databases – Recent Developments. Part of special issue: Tools for Computational Thermodynamics [online]. Amsterdam: Elsevier. 2009, vol. 33, no. 2, [23.5.25] p. 295-311. Available from (DOI): <10.1016/j.calphad.2008.09.009>. ISSN 0364-5916

[5] BALE, C., CHARTRAND, P., DEGTEROV, S. A.; ERIKSSON, G., HACK, K., BEN MAHFOUND, R., MELANCON, J., PELTON, A, D., PETERSEN, S. FactSage thermochemical software and databases. CALPHAD-COMPUTER COUPLING OF PHASE DIAGRAMS AND THERMOCHEMISTRY [online] Amsterdam: Elsevier. 2002. vol. 26, no. 2, [23.5.25], pp. 189-228. Available from (DOI): <10.1016/S0364-5916(02)00035-4>. ISSN 0364-5916

[6] BULKO, B., KIJAC, J., BOROVSKY, T. The influence of chemical composition of steel on steel desulphurization. Archives of metallurgy and materials [online]. Kraków: Commitee on Metallurgy of Polish Academy of Sciences 2011, vol. 56, no. 3, [23.5.25], p. 605-609. Available from (DOI): <10.2478/v10172-011-0065-1>. ISSN 1733-3490

[7] ANDERSSON, M., HALLBERG, M., JONSSON, L., JONSSON, P. Slag-metal reactions during ladle treatment with focus on desulphurization. IRONMAKING & STEELMAKING [online]. London: Taylor & Francis. 2002, vol. 29, no. 3, [23.5.25], p. 224-232. Available from (DOI): <https://doi.org/10.1179/030192302225004106>. ISSN 0301-9233

[8] PIVA, SPT., KUMAR, D., PISTORIUS, PC., Modeling Manganese Silicate Inclusion Composition Changes during Ladle Treatment Using FactSage Macros. *METALLURGICAL AND MATERIALS TRANSACTIONS B-PROCESS METALLURGY AND MATERIALS PROCESSING SCIENCE* [online]. New York: Springer. 2017. vol. 48, no. 1, [23.5.25, pp. 37-45. Available from (DOI): <10.1007/s11663-016-0764-0>. ISSN 1073-5615

EXPERIMENTAL AND THEORETICAL STUDY OF SPECIFIC HEATS OF Fe-C-Ni ALLOYS IN THE MELTING RANGE USING THERMAL ANALYSIS

Author: Svetlana SOROKINA

Supervisor: prof. Ing. Bedřich SMETANA, Ph.D.

Department: Department of Chemistry and Physico-Chemical Processes, Faculty of Materials Science and Technology, VSB – Technical University of Ostrava

Abstract

Thermal analysis has been widely used in various scientific fields for a long time, it can also be used for a studying of thermodynamic properties, such as specific heats of metallic materials based on iron, carbon and nickel. This paper is devoted to the study of specific heats of three alloys based on Fe-C-Ni in the melting range. Studied alloys contained carbon in a range of 0.338 – 0.382 wt. % and nickel 1.084 – 4.478 wt. % and were made by induction melting using furnace Leybold Heraus in the laboratory. Experimental data of specific heats, depending on the composition, were obtained using thermal analysis method, such as differential scanning calorimetry (DSC) in continuous mode, Setaram MHTC 96 Line with a 3D DSC sensor. Theoretical data were calculated using SW Thermo-Calc and SW JMatPro. The aims of the paper were obtaining of new experimental data and discussing and comparing obtained data with theoretical.

Key words:

Fe-C-Ni alloys, specific heats, DSC method, SW Thermo-Calc, SW JMatPro.

1. INTRODUCTION

Steels are commonly used metallic materials, that's why many authors investigate various grades of steels [1-2]. Thermodynamical properties (specific heats, phase transformations temperatures, enthalpy, entropy, Gibbs energy and other properties) are one of the most important quantities of materials, which are needed for understanding of behavior of materials under defined conditions. Specific heats were obtained using thermal analysis method, such as differential scanning calorimetry (DSC) in continuous mode.

Performed study presents experimental data of specific heats of the laboratory prepared Fe-C-Ni alloys. These data were compared and discussed with theoretical data calculated using SW Thermo-Calc and SW JMatPro. Study of Fe-C-Ni systems is still a relevant topic, because there are no enough of accurate experimental data, which can be used for a simulation of metallurgical processes and for technological purpose.

2. THEORETICAL BACKGROUND

2.1 Thermal analysis

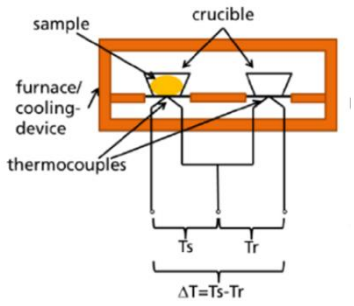

Figure 1 Arrangement of DSC method.
Source: (own)

The method of thermal analysis, such as DSC method, was used for achieving of the aim.

Thermal analysis is a group of techniques in which a property of the sample is monitored against time or temperature while the temperature of the sample, in a specified atmosphere, is programmed [3].

DSC method (differential scanning calorimetry) is a thermoanalytical technique in which the difference in the amount of heat required to increase the temperature of a sample and reference is measured as a function of temperature [4]. Arrangement of DSC method is presented in the Figure 1.

2.2 Continuous method

DSC method in continuous mode is used for a determining of specific heats depending on the temperature and other factors.

The continuous method consists three measurements (Figure 2). The first is called "blank" with an empty measuring and comparison crucible. The second measurement is performed with a standard of known mass and known heat capacity, which is stored in the measuring crucible while the reference crucible is empty. The third measurement is performed using sample of known mass, which is placed in a measuring crucible and the reference crucible is again empty

The measurement consists of an isothermal endurance at the initial temperature, followed by heating at a constant heating rate to the final temperature, at which the system is again maintained for some time [5].

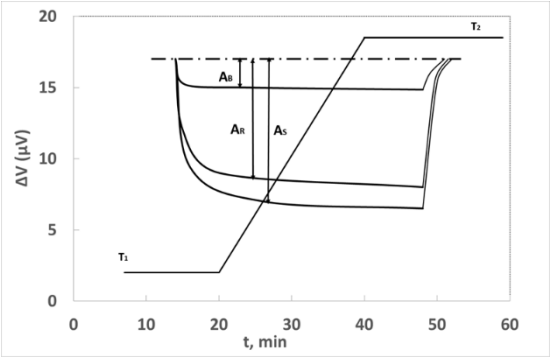

Figure 2 Arrangement of DSC method. Source: (own)

3. EXPERIMENT

3.1 Sample characterization

The studied alloys contained carbon in a range of 0.338 – 0.382 wt. % and nickel 1.084 – 4.478 wt. % and other minor elements presented in the Table 1. Studied samples were made by induction melting in the laboratory and then were analyzed using DSC. For DSC analysis the samples had the shape of a cylinder with a diameter 5 mm, height 8 mm and sample weight was 1250 ± 10 mg. The samples were polished and cleaned in acetone using ultrasound.

Table 1 Chemical composition of alloys /wt. %. Source: own

Alloy	C	Ni	Cr	Al	Cu	Co	W
A	**0.382**	**1.084**	**0.010**	**0.010**	**0.014**	**0.001**	**0.001**
B	**0.375**	**2.990**	**0.012**	**0.011**	**0.009**	**0.001**	**0.001**
C	**0.338**	**4.478**	**0.010**	**0.011**	**0.012**	**0.001**	**0.001**

3.2 Differential scanning calorimetry and experimental conditions

Figure 3 Setaram MHTC 96 Line. Source: (own)

Experimental data of specific heats were obtained by DSC method with continuous method (with calibration Pt) for a studied alloys A, B and C using Setaram MHTC 96 Line with a 3D DSC sensor (Figure 3), which is used due to better capture of the thermal effect, which is transferred to the sample or removed from the sample. The measurements were carried out in the atmosphere of helium with purity at least 6 N to protect the samples against oxidation. Temperature calibration was done using Pd for all samples. The heating rate was 5 °C/min. Evacuation around the sample was performed 3 times. All measurements were performed in the melting range using corundum sleeve in Pt crucible.

4. RESULTS AND DISCUSSION

The specific heats of alloys A, B and C were studied in the melting range. Theoretical values of the heat capacities were obtained by SW Thermo-Calc and SW JMatPro and compared with measured experimental values. Obtained experimental and theoretical values of the specific heats are presented in the Figures 4 – 7.

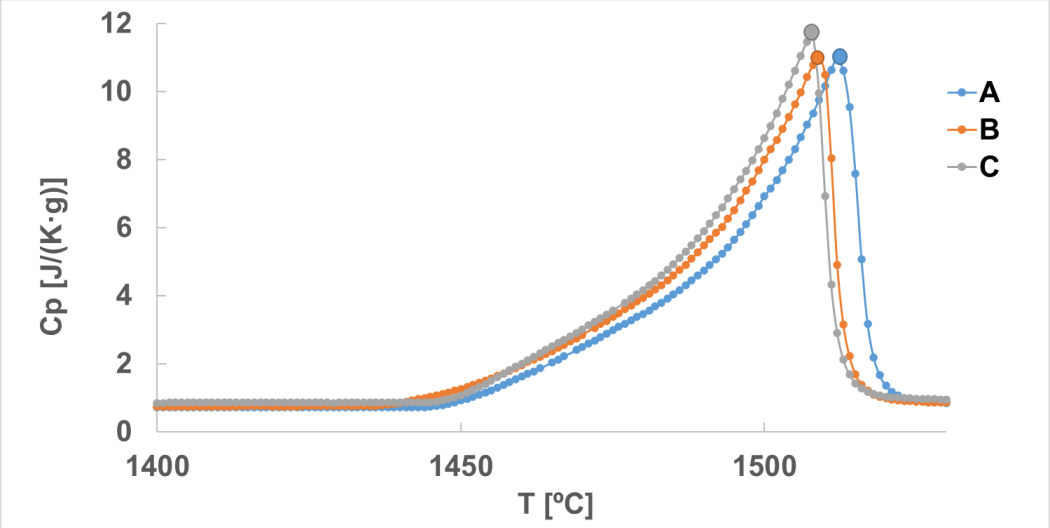

Figure 4 Experimental data of specific heats of studied alloys A, B and C in the temperature range 1400 – 1520 °C. Source: (own)

From Figure 4 it is evident, that obtained experimental data of alloys have the same trend. With increasing of content of nickel in studied alloys the maximum values of specific heats in the temperature of liquidus increase as well. The highest experimental value of the specific heat is 11.61 J/K·g (alloy C).

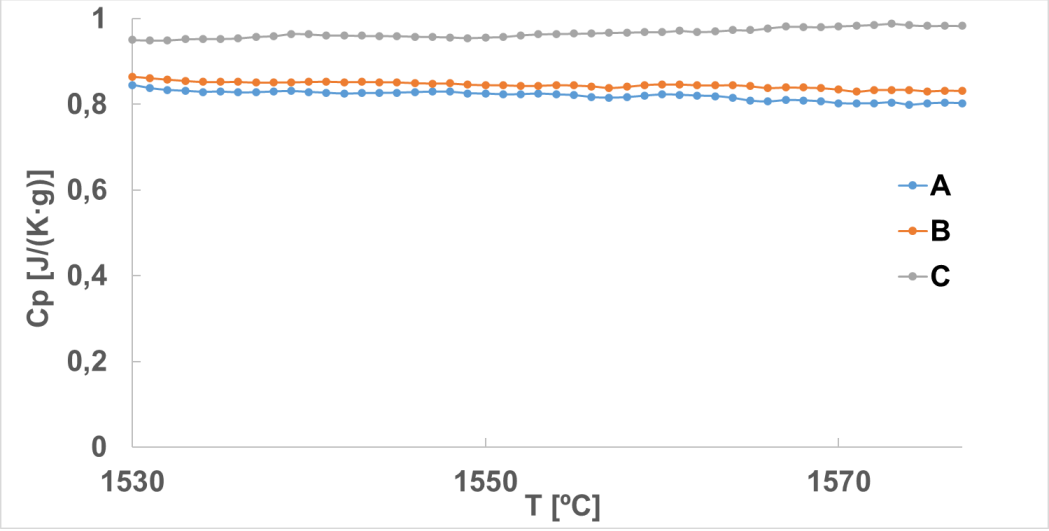

Figure 5 Experimental data of specific heats of studied alloys A, B and C in the melting range 1530 – 1580 °C. Source: (own)

From the dependence of specific heats on temperature (Figure 5) we can see, that with increasing of content of nickel in studied alloys values of specific heats also increase in the melting range 1530 – 1580 °C. Experimental values of specific heats of alloy A are 0.80 – 0.85 J/ K·g, of alloy B are 0.83 – 0.87 J/ K·g and of alloy C are 0.95 – 0.99 J/ K·g. The highest experimental value of the specific heat is 0.99 J/K·g (alloy C).

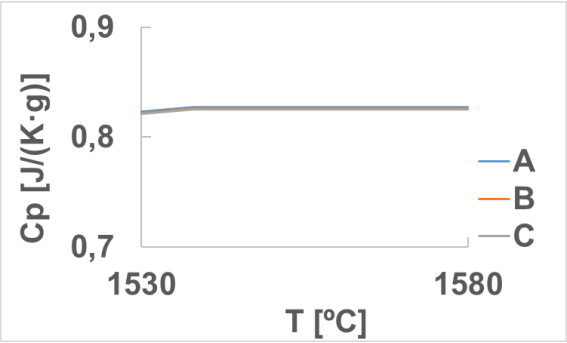

Figure 6 Theoretical data of specific heats of studied alloys A, B and C obtained using SW JMatPro in the melting range 1530 – 1580 °C. Source: (own)

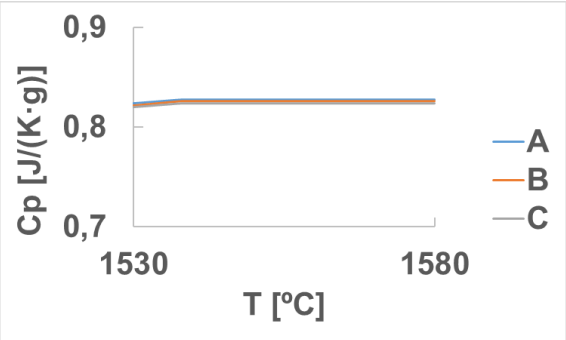

Figure 7 Theoretical data of specific heats of studied alloys A, B and C obtained using SW TC in the melting range. 1530 – 1580 °C
Source: (own)

From the dependences of specific heats on temperature (Figures 6 – 7) it is visible, that calculated theoretical data have the same trend in the melting range. Values of specific heats are 0.82 – 0.83 J/ K·g in all temperature range.

CONCLUSION

In the presented work specific heats of three alloys based on iron, nickel and carbon were studied. Experimental values of specific heats were detected by DSC (experimental curves) and compared with theoretical values calculated by use SW Thermo-Calc and SW JMatPro. With increasing of content of nickel in studied alloys values of specific heats increase as well. As for calculated theoretical data, data have the same trend in the melting range. New original experimental data were obtained for studies alloys, which can be used for a simulation of metallurgical processes and for technological purpose.

ACKNOWLEDGEMENT

This paper was supported in the frame of solution of project No. CZ.02.1.01/0.0/0.0/17_049/0008399 Call 02_17_049 Long-Term Intersectoral Cooperation for ITI, Managing Authority: Czech Republic - Ministry of Education, Youth and Sports, students projects SP2023/034 a SP2022/39, Podpora vědy a výzkumu v Moravskoslezském kraji 2020 (08078/2020/RRC) and Podpora talentovaných studentů doktorského studia na VŠB-TUO 2020

REFERENCES

[1] DROZDOVÁ, Ľubomira, Bedřich SMETANA, Mario MACHŮ, et al. Study of the influence of experimental conditions on the temperatures of the phase transformations in high-temperature area for Fe-C-Cr and Fe-C-Ni based systems. In Metal *2019*: *28rd International Conference on Metallurgy and Materials*. *Ostrava: Tanger, 2019*, 78–83.

[2] KALUP, Aleš, Simona ZLÁ, Monika KAWULOKOWÁ, Jana DOBROVSKÁ, Bedřich SMETANA. Comparison of measured and calculated thermophysical properties of nickel super-alloys. *Metalurgija.* 2016, **55** (3), 345–348.

[3] GALLAGHER, Paul. *Handbook of Thermal Analysis and Calorimetry: Principles and Practice*. New York: Elsevier, 1998. ISBN 0-444-82086-8.

[4] ŠESTÁK, Jaroslav. *Heat, Thermal Analysis and Society*. Hradec Králové: Nucleus HK, 2004. ISBN 80-86225-54-2.

[5] ŽALUDOVÁ, Monika, Bedřich SMETANA, Simona ZLÁ, et al. Study of heat capacity of real steel grade. In Metal *2014: 23rd International Conference on Metallurgy and Materials*. *Ostrava: Tanger, 2014*, 559–563.

STUDY OF THE CASTABILITY OF BRONZE CASTINGS GRAVITY CAST INTO GYPSUM MOULDS

Author(s): František ZLÁMAL

Supervisor: doc. Ing. Petr LICHÝ, Ph.D.

Department: Department of Metallurgical Technologies, Faculty of Materials Science and Technology, VSB – Technical University of Ostrava

Abstract

This work deals with the development of a suitable technological test for the determination of castability in the casting of copper alloys into gypsum moulds at different mould and casting temperatures. The experiment deals with the production of the gypsum moulds and the casting of a copper alloy. At the end of the experiment, the chemical composition and metalography is evaluated.

Key words:

Castability, copper alloy, metalography, casting.

1. INTRODUCTION

Metal casting castability is a critical property of molten metal that determines its ability to flow into the mould cavity without any disruptions or defects. It is one of the most crucial factors that affect the casting process's quality, integrity, and final product's overall performance. Castability is defined as the ability of molten metal to fill the entire mould cavity completely before it solidifies. [1] The castability property of molten metal depends upon several factors, including temperature, alloy composition, casting speed, and mould design, however, the most significant influencing factor is temperature. [2,3] As the temperature of molten metal increases, its viscosity decreases, and it becomes more fluidic. Conversely, if the temperature decreases, viscosity increases, and castability decreases. Rapid casting speeds result in smoother and more complete fillings of the mould cavity, while slow casting speeds may cause shrinkage defects in the casting. Moreover, rapid cooling due to high casting speeds can also improve the mechanical properties of the final product.

Poor castability can result in several defects in casting. For example, incomplete filling might lead to porosity or voids in castings that can significantly reduce their mechanical properties. [3] Moreover, inadequate castability can cause mould filling defects such as misruns or cold shuts, resulting in scrap or rework. Proper control and optimization of the factors that affect castability are essential for improving the casting process's quality and integrity. [4] Proper understanding and optimization of the factors affecting castability can significantly improve the final product's mechanical properties, surface finish, and reduce scrap or rework. Further research and development of advanced techniques can offer new ways to improve castability, leading to more efficient and economical casting processes.

2. METHODS AND MATERIALS

For the needs of the Department of Metallurgical Technologies of VŠB-TUO, a castability test was created, which was adapted to the available technologies and materials used there. 3D modelling in the Autodesk Fusion 360 software interface and subsequent 3D printing on Prusa MK3S+ FDM printers were used to create the castability test. The resulting pattern was composed of round profiles set vertically on the runner. The profiles were 2, 2.5, 3, 3.5, 4, 5, 6, 7, 8 and 10 mm in diameter and 165 mm long. The runner was 100 mm in diameter and 8 mm in height. The sprue post was 15 mm in diameter. These dimensions were chosen because of the maximum size of the cuvettes used, which was 120 mm in diameter and 230 mm in height. To create the pattern, wax injection moulds had to be created. These moulds were created using steel rods of the required diameter and 3D printed parts - a runner, a sprue post and an auxiliary ring (which was used when creating the gypsum moulds to keep the profiles vertical and evenly spaced). A silicone mould with sprue system adapted for wax injection was then created on the steel rod and 3D printed parts. Once all the necessary silicone moulds were created, the models were removed and the silicone moulds were used for wax injection

The wax was injected into silicone moulds using a manual pump injection device. The pressure used to inject the wax ranged between 0.4 and 0.6 bar depending on the mould requirements whereas the wax temperature was set at 70 °C according to the manufacturer's recommendations. After injection, the wax models had to be removed from the silicone moulds and any overflow or other defects removed/repaired. Once all parts of the pattern were prepared, the pattern was soldered together using a hand soldering iron, or a burner and spatula of the appropriate shape. Once the pattern was assembled, the model was weighed, placed in the cap and inserted into the cuvette. The pattern, seated in the cuvette, was then covered with mixed jewellery gypsum and left to cure. Once sufficient curing had been achieved (approximately 30 minutes after the gypsum had been poured), the hat and auxiliary ring were removed from the cuvette. The cleaned cuvette without the cap was then placed in the dryer to remove the wax, creating the necessary cavity in the same shape as the wax model. The mould prepared like this was then annealed according to the recommendations of the manufacturer of the jewellery gypsum used, in order to remove all moisture from the mould (see Figure 1).

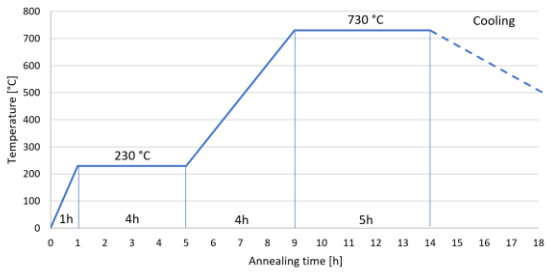

Figure 1 Annealing cycle of the moulds.
Source: (own)

Table 1 Numerical identification of castings.
Source: (own)

cast\mould	200 °C	400 °C	25 °C
1100 °C	1	2	3
1150 °C	4	5	6
1200 °C	7	8	9

The annealed moulds were divided into 3 groups of 3 moulds each. The first group of moulds was left at room temperature, the second group was subsequently heated to 200 °C and the third group of moulds was heated to 400 °C. After the moulds were prepared like this, the casting process could begin, whereby one mould was selected from each group of moulds and cast at one of the 3 specified temperatures. The casting temperatures were set at 1100 °C, 1150 °C and 1200 °C. Casting was carried out directly from the tilting furnace into the prepared moulds. Each time a group of moulds was cast, the mass of metal remaining in the crucible was estimated and phosphor copper was added to deoxidise the melt, as well as the temperature has been increased. As a result, 9 moulds were cast with 3 different mould temperatures and 3 different casting temperatures (see Table 1). The cast moulds were discharged after cooling, the used gypsum was discarded and the resulting casts were blasted in a sand blasting machine. The length of the measured castability from the runner to the end of the cast profile was measured on the sand blasted castings (see Table 2).

3. RESULTS AND DISCUSSION

A total of 9 models, gypsum moulds and casts were created. All 9 moulds were successfully cast, but some of them with casting errors. As can be seen in Table 2, there is a noticeable deviation from the expected value for casting number 5. This was due to the fact that the casting was not continuous but was intermittent. For test casting number 3, there was an overflow of melt over the top of the mould, resulting in an apparent higher castability for the 10-6 mm diameter profiles. The casting of these 9 test castings achieved the expected trend that a higher mould temperature contributes to higher alloy castability. At the same time, temperature had a large effect on the castability, where higher temperature also resulted in higher values of castability. Casting speed was also a big factor, which was difficult to maintain to the same extent for all moulds, due to the casting from the tilting furnace directly into the gypsum mould. Thus, the different casting speeds partially distort the results of this measurement. For example, as can be seen in Table 2 for the set of castings 4-6, the castability at room temperature of the mould was noticeably higher than the castability for the moulds heated to 200 °C and 400 °C. This result is due to the fact that the casting speed of casting number 6, the room temperature mould, was noticeably higher than that of moulds 4 and 5. At the same time, the casting of casting number 5, the mould heated to 400 °C, was interrupted (for approximately less than 1 second), resulting

in a significant deterioration in measured castability. If this castability test is to be repeated, care must therefore be taken to keep the casting speed as constant as possible.

Table 2 Measured lenghts of the castability test casts. Source: (own)

	10 [mm]	8 [mm]	7 [mm]	6 [mm]	5 [mm]	4 [mm]	3.5 [mm]	3 [mm]	2.5 [mm]	2 [mm]
1	80.92	72.24	33.04	48.08	24.06	16.36	11.95	10.31	11.36	8.51
2	114.90	111.87	66.00	40.43	37.49	32.32	42.83	22.52	12.65	9.24
3	126.78	107.55	98.84	44.69	13.69	12.56	8.93	8.26	9.11	6.94
4	113.88	82.51	55.92	50.77	44.13	29.50	22.35	16.33	21.68	9.91
5	62.32	45.79	37.66	33.16	23.88	22.29	18.90	17.48	13.99	10.69
6	122.59	111.36	135.34	98.44	68.08	62.37	36.54	32.21	23.07	7.82
7	165.00	62.01	47.19	43.26	36.88	38.82	33.25	22.08	22.04	11.69
8	165.00	161.11	133.61	113.14	99.32	63.94	53.68	33.77	23.93	14.64
9	165.00	156.41	155.21	72.86	34.00	25.69	18.21	20.06	9.23	9.22

Once all the profiles‘ castability was measured, a portion of the inlet on castings 3 and 8 (representing extremes in casting temperature and the temperature of the mould) was cut off and used as a sample to determine the chemical composition of the castings and to obtain metallographic examination. The chemical composition of the melts was determined mainly in terms of the phosphorus content of the casting. The standard EN 1982 CC480K, CuSn10-C was used. Phosphorus copper was always added to the melt after casting, as already mentioned. It was assumed that the phosphorus would cease to have an effect as the temperature was raised to the next casting temperature (approximately 30 min). The residual phosphorus content of the castings was determined. The phosphorus in the castings was increased from a value of 0.022 wt% after the first addition of phosphor copper to a value of 0.063 wt% after the second addition of phosphor copper to a value of 0.099 wt% after the last addition of phosphor copper. The increasing phosphorus content in the melt may also have an effect on the final castability anticipating higher values of castability the higher the phosphorus content. In further experiments, it would be ideal to investigate this finding and test the effect of phosphorus on the final castability of the castings.

Two samples were taken from the inlets of castings 3 and 8 to observe the microstructure of the alloy. The samples were ground, polished, and etched to allow for the observation of their microstructure. The prepared samples were then observed under a light microscope and images of the microstructure of castings 3 and 8 were captured at 50x magnification. These samples were chosen because of their very different casting conditions. Casting number 3 was cast at a casting temperature of approximately 1100 °C in a room temperature mould, the lowest temperature of all the castings examined, indicating that it had the highest cooling rate of all the castings. Casting 8, on the other hand, had the lowest cooling rate as it was cast at a casting temperature of approximately 1200 °C into a 400 °C mould. In Figure 2 a typical dendritic structure can be observed.

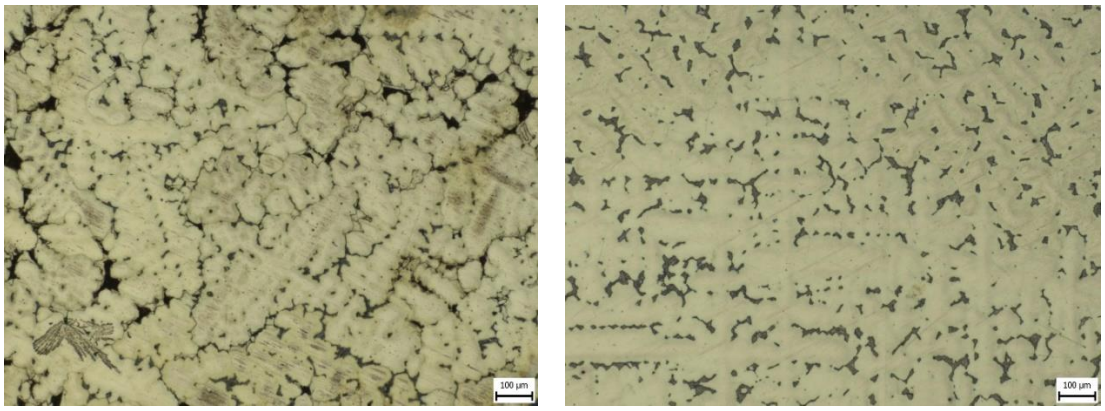

Figure 2 Microstructures of castings number 3 and 8 (on the left side casting number 3, on the right side casting number 8). Source: (own)

4. CONCLUSION

The work was focused on the production of a technological test of castability for the purpose of casting into gypsum moulds at the Department of Metallurgical Technologies. Specifically, this work investigates the castability of CuSn10 copper alloy, but in the future the same model will be used for other non-ferrous alloys. Nine moulds were cast at 3 different casting temperatures and 3 different gypsum mould heating temperatures. We can conclude that higher casting temperature and higher mould temperature increases the castability of the melt of CuSn10 as expected. However, the casting speed is undoubtedly also a major factor in the casting process, which in the case of these test castings was not machine controlled and was affected by the human factor in the casting process. It should therefore be ensured in future technological tests that the casting is carried out under as constant conditions as possible. Another aspect has been observed – the chemical composition and microstructures of the cast test castings were evaluated. Increasing phosphorus content was found, which may also have an effect on the final castability anticipating higher values of castability the higher the phosphorus content. In further experiments, it would be ideal to investigate this finding and test the effect of phosphorus on the final castability of the castings. The microstructure of the samples taken can be seen in Chapter 3. To obtain more accurate results, further research will be needed and additional sets of test castings will need to be processed. Thanks to the silicone moulds created for the wax patterns, further research will not be as time consuming and can be carried out on a large number of alloys.

ACKNOWLEDGEMENT

This research was funded by the project of MEYS (grant number CZ.02.1.01/0.0/0.0/17_049/0008399). This research was carried out with the support of projects of student grant competition (project number SP2023/022).

REFERENCES

[1] SIN, S. Lun a D. DUBÉ. Influence of process parameters on fluidity of investment-cast AZ91D magnesium alloy. *Materials Science and Engineering: A-Strucutral Materials Properties Microstructure and Procesing* [online]. 2004, **386**(1-2), 34-42. ISSN 09215093.

[2] KIM, Myoung-Gyun, Si-Young SUNG a Young-Jig KIM. Microstructure, Metal-Mold Reaction and Fluidity of Investment Cast-TiAl Alloys. *MATERIALS TRANSACTIONS* [online]. 2004, **45**(2), 536-541. ISSN 1345-9678

[3] DI SABATINO, M., L. ARNBERG a D. APELIAN. Progress on the Understanding of Fluidity of Aluminium Foundry Alloys. *International Journal of Metalcasting* [online]. 2008, **2**(3), 17-27. ISSN 1939-5981

[4] SLAMET, Sugeng, Suyitno . a Indraswari KUSUMANINGTYAS. Effect of composition and pouring temperature of Cu(20-24)wt.%Sn by sand casting on fluidity and mechanical properties. *Journal of Mechanical Engineering and Sciences* [online]. 2019, **13**(4), 6022-6035. ISSN 2231-8380

Thermal engineering and fuels in industry

ELECTRICITY STORAGE IN HIGH POTENTIAL THERMAL ENERGY FORM

Author(s): Radek NIKEL

Supervisor: prof. Ing. Jozef VLČEK, Ph.D.

Department: Department of Thermal Engineering, Faculty of Materials Science and Technology, VSB – Technical University of Ostrava

Abstract

The article, based on data of massive renewable energy recourses development and behavior of these recourses, analyze possibility of electricity storage which is transformed into high potential heat. As heat storage materials are there expected solid materials on metallic oxidic base in devices called heat batteries. In addition, the article give notice to potential of such a way of energy storage and some technical problems are mentioned there too.

Key words:

Electricity storage in high potential thermal energy form.

1. INTRODUCTION

Today's high rating development of electricity production based on renewable energy resources (OZE), especially Photovoltaic power stations (FVE) and wind power stations (VTE) – see table No. 1 – lead to unexpected surplus of electrical energy in the electricity supply system.

Table 1 - Installed capacity in the Czech Republic rated in MW. The value for years 2030 and 2040 are conservative progress scenario of MAF CZ 2022 CEPS. Source: [1 & 2]

	2015	**2016**	**2017**	**2018**	**2019**	**2020**	**2021**	**2022**	**2023**	**2030***	**2040***
VTE (MW)	267,7	276,6	280,5	290	290	331	401	381	437	742	1141
FVE (MW)	2066,7	2043,5	2045,5	2097	2097	2117	2131,5	2260	2679	8133	10005

The power of FVE and VTE has an unpredictable character not only during a year but also during individual days. Such a characteristic is demonstrating by observation done on FVE of small installed power 6.56 kWp south oriented placed in CR – see the following power chart No. 1.

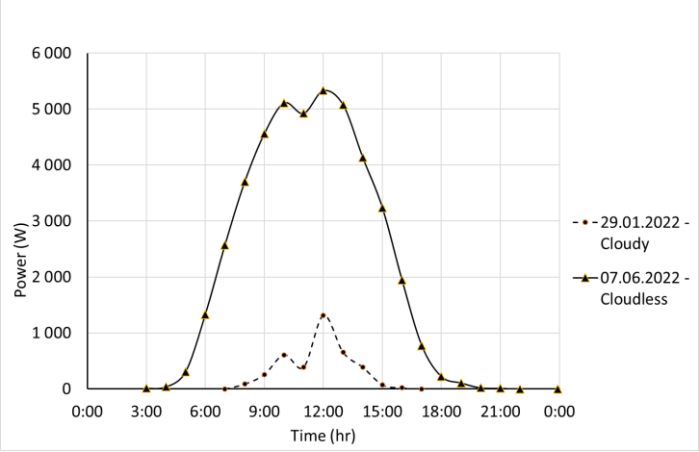

Figure 1 – FVE- daily power

The dependence on external conditions is one of the essential imperfections of FVE and VTE types of OZE. The FVE cannot generate full power while not insolated, their power fluctuates with cloud shading and depends on the photovoltaic cell temperature too. The temperature fluctuates with period summer / winter not only. VTE on the other hand badly depend on wind power used to their run. These facts lead electric grids operator (CEPS in CR) in case of extreme production to take radical steps as the disconnection of electricity producers from the grid. Such a situation occurred first time in CR during Ester holidays 2023 (10.4.2023) when the mixture of sunny weather and lack of electricity consumption, because of bank holiday, led to the termination of 400 MWp of power from FVE in CR [3]. The excess of electricity on the market led to negative value of minimal prices of electricity at that time. This is evident form spot market results obtained from Czech electricity market operator OTE from 10.4.2023 - see chart below.

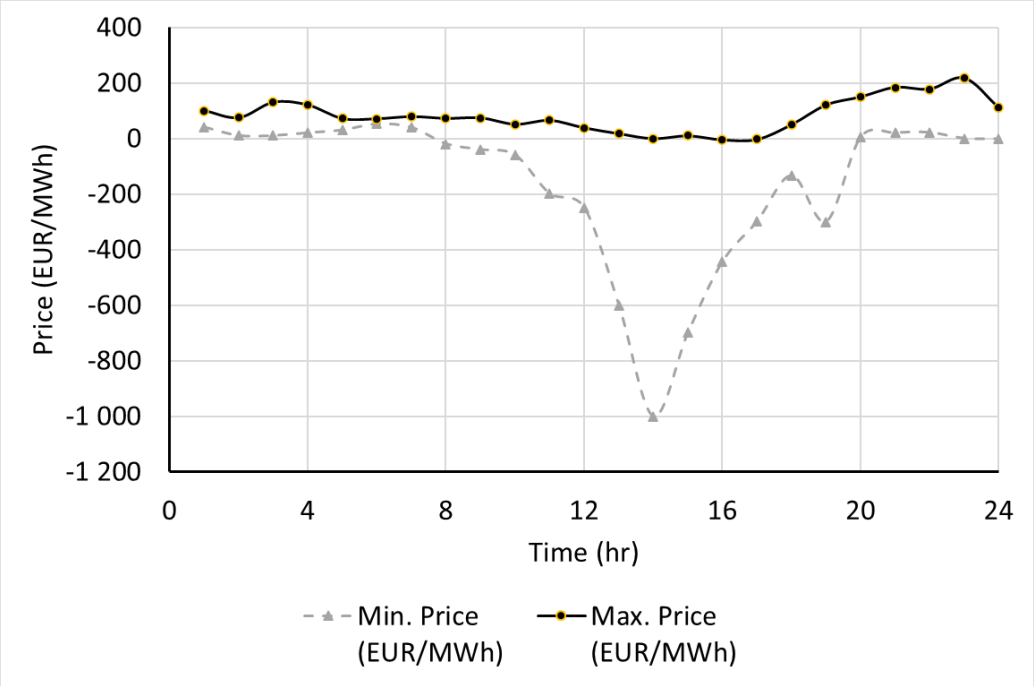

Figure 2 – Electricity price volatility on 10.4.2023 at OTE, a.s. Source: [4]

The above mentioned facts say that in some circumstances the electricity which is one of the most important secondary energy can be turned to unwanted waste. This is a reason why finding solution for storage or accumulation of electricity in the period of its over balance is important so it can be later used.

There are a lot of ways to accumulate electricity, for example as a transformation into chemical energy, electrochemical energy, mechanical energy or cryogenic energy. But there is even possibility to transform electricity to a thermal energy by using the material enthalpy change.

The accumulation of thermal energy in its enthalpy is not a new idea. It was and still is being used in many technological devices as a furnace or regenerators. However, the idea to use regenerator for heat accumulation produced from surplus of electricity after than turn the heat back to electricity when needed, seems to be new.

The sum of accumulated heat (enthalpy change) can be calculated acc to following formula [5]:

$$dQ = m \cdot c_p \cdot dT \quad \text{(J)} \qquad (1)$$

Where: dQ – Enthalpy change (J)
m – Material weight (kg)
c_p – Specific heat capacity (J kg^{-1} K^{-1})
dT – Temperature change (K)

In case we assume a specific heat capacity as a constant the formula (1) expresses linear dependence between enthalpy and temperature change. But the Specific heat capacity depends on

temperature and thus brings the nonlinearity into enthalpy calculation. The temperature dependence of the Specific heat capacity is illustrated in figure No 3. For a very approximate calculation it is possible to use the average value in specified small temperature interval.

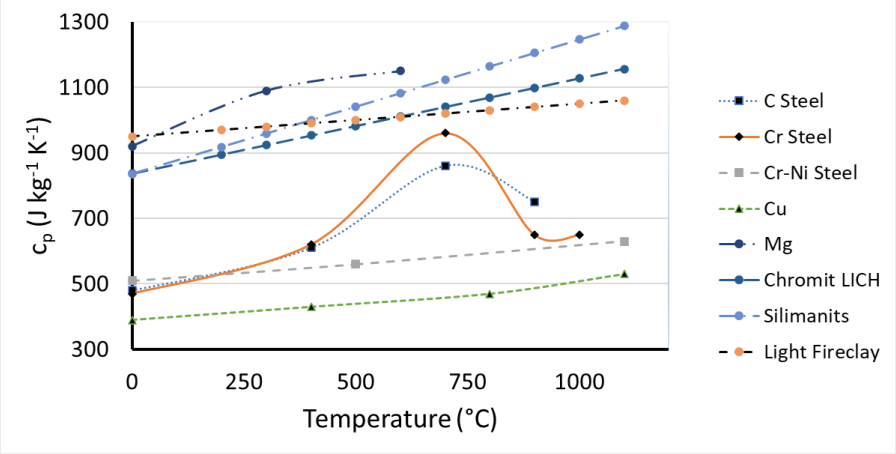

Figure 3 Specific heat capacity - temperature dependence Source: [6]

Analysis of equation (1) says that amount of accumulated heat can be driven by the selection of proper material (c_p), by the weight of heated material (m) or by the temperature difference between charged and discharged status of thermal battery (dT). The article further describes (analyses) the possibility of a creation high-potential - meaning high temperature – heat battery. The term high temperature battery means a battery operating at minimum temperature 800 °C (1073,15 K). The ceramic materials based on oxides especially MgO, CaO, SiO_2, Al_2O_3 or their suitable mixtures, appears as usable materials.

The fundamental thing for the proper and long function of heat accumulator is the selection of the material for accumulation. The material must withstand thigh temperature, high mechanical load at high temperatures, frequent temperature changes (charging / discharging). From thermomechanical point of view the material will be requested to have the highest possible specific heat capacity (c_p), high temperature conductivity giving good dynamic characteristic of charging and discharging, and low thermal expansion coefficient for maximal thermal stability of accumulator structure during the temperature changes. The price and availability of the ceramic material is important criteria because of the expected high battery volume, meaning weight for max storage capacity.

The following table 2 represents a possible theoretical battery capacity of different available ceramic materials heated from 20 °C to 1300 °C outspreaded to volume 1m^3 with presumption of 0% porosity.

Table 2 – Calculation of 1m^3 storage capacity in kWh. Source [6 & own]

	Silica DII	Chromite LICH	Cromium magnezite LIII	Carbides C48185	Corundum products	Sillimanites	Fireclay SII
ρ (kg m^{-3})	2400	2700	2950	2100	3200	2300	1900
C_{p1300}(kJ kg^{-1} K^{-1})	1,199	1,214	0,949	1,149	1,341	1,369	0,984
Q (kWh m^{-3})	1023	1165	995	859	1526	1120	665

For comparison the 1m^3 of water at pump storage plant Dlouhe Straně which has an altitude difference between upper and lower lake of 510 m has a capacity of **1,4 kWh**.

The construction of high potential thermal batteries seems to be much more effective for energy storage than building a new pump storage plant for which the suitable conditions for their construction in CR are almost exhausted.

However, there are many unresolved questions in the technical design of high-potential thermal batteries. Even if we can be inspired by common industrial regenerators the difference in the use and in the way of heating brings some modifications which have radical influence on the design itself. The way of discharging (heat extraction) and its conversion to electricity can also have an influence on the design and lay-out of heat battery. In addition, it is necessary to point out that the article mentions not only high

temperature battery but also high storage capacity which leads to installations of devices with huge volume (weight) size of industrial buildings. For such equipment with high investment costs, it is necessary to take care of all even small details from the very beginning of the projects it means in the basic design phase.

Among the basic questions, that need to be resolved, besides determining the battery capacity and the suitable heat absorbing material, are the determination of the shape of the device with respect to heat loss, the internal structure of the accumulating material with respect to minimizing thermal stresses in the building and the dilatation caused by thermal expansion of the material, the determination of the heat transfer from the source to the whole battery for its swift charging and discharging. Furthermore, the suitable placing of heat sources in regards to battery dimensions and determination of the way of heat mining and the best position of discharging equipment to minimize safety risks and finally the battery insulation question that must be solved too. An indispensable part of design is MaR (field instrumentation and automation) of this equipment which must ensure safety, fluent and effective thermal battery operation in the most economic conditions.

The above-mentioned technical problems are only connected with the thermal battery itself. However, the solution of the problem discussed in the beginning of the article bonded with accumulation of electricity surpluses that lead to battery extension for following equipment which can turn the stored heat to electricity. There are available either commonly used steam turbo generators or Stirling engines for generator powering. Here, it is necessary to design a system which is capable of transporting the heat from the battery to the generator. These problems are out of limits of this article.

2. CONCLUSION

In conclusion, it is evident that the storage of electricity in the high potential heat form seems to be a perspective field, in which we can expect a huge development soon due to the rapid increase of renewable energy recourses especially FVE and VTE. There are first commercial attempts of heat storage in solid materials as concrete or sand. For now, these systems are working on temperature level up to 500°C so they are low potential. The low potential systems are not entirely suitable for further transformation of heat to electricity. The temperature level of mentioned low-potential systems is influenced mostly by the materials used for battery peripheries or the battery parts. The High potential heat batteries are facing this problem as well and it must also be dealt with.

Because of the higher capital expenditure for building an experimental high-potential heat battery, the further research of the high-potential heat storage is necessary (requested). It is necessary to collect huge volume of data and basic design calculations which can simulate conditions inside of the equipment, especially the nonstationary processes during repeated battery charging and discharging. These theoretical works should verify in advance the applicability of high potential thermal battery for inserting it into electricity production chain. The above mentioned theoretical works and calculations should be used as a base for go/no-go decision about possible erection of experimental equipment.

ACKNOWLEDGEMENT

This work was supported by project SP2023/034 Research and development of composite multifunctional materials for sustainable progress.

REFERENCES

[1] *Hodnocení zdrojové přiměřenosti ES ČR do roku 2040 (MAF CZ 2022)* [online]. OTE, a.s. 2018. [cit.10.4.2023]. Dostupné z: https://www.mpo.cz/assets/cz/energetika/jaderna-energetika-a-nove-jaderne-zdroje/zapojeni-ceskeho-prumyslu/2023/3/87772_ceps-maf-2022.pdf

[2] *Roční příprava provozu 2014, 2015, 2016,2017, 2018, 2019, 2020* [online]. ČEPS, a.s. [online]. Dostupné z: https://www.ceps.cz/cs/priprava-provozu/

[3] KUBÁTOVÁ, Zuzana. *O svátcích odpojil ČEPS stovky zelených elektráren* [online]. Seznam Zprávy, a.s, 2023 [cit. 12.4.2023]. Available from: https://www.seznamzpravy.cz/clanek/ekonomika-firmy-velikonocni-stopka-o-svatcich-odpojil-ceps-stovky-zelenych-elektraren-229281?

[4] *Krátkodobé trhy, vnitrodenní trh 2023* [online]. OTE, a.s. 2018. [cit.10.4.2023]. Dostupné z: https://www.ote-cr.cz/cs/kratkodobe-trhy/elektrina/vnitrodenni-trh?date=2023-04-10

[5] ATKINS, P. W. a Julio DE PAULA. *Fyzikální chemie*. Přeložil Lidmila BARTOVSKÁ. Praha: Vysoká škola chemicko-technologická v Praze, 2013. ISBN 978-80-7080-830-6

[6] BLAHOŽ, Vladimír a Vladimír LAPČÍK. *Návody do cvičení z termomechaniky*. Ostrava: Vysoká škola báňská, 1989.

CASTING VELOCITY INFLUENCE ON HEAT TRANSFER IN MOULD

Author(s): Luboš POLCAR

Supervisor: doc. Ing. Marek VELIČKA, Ph.D.

Department: Department of Thermal Engineering, Faculty of Materials Science and Technology, VSB – Technical University of Ostrava

Abstract

Presented paper evaluates correlation of casting velocity on heat transfer via primary cooling zone. Studied primary cooling zone is a copper mould insert with inner dimension of 150 x 150 mm. Wall temperature of mould insert was measured and obtained data was further analysed. As a result, a strong positive correlation was found between heat transfer and casting velocity as well as in increase of vertical temperature in all walls of mould insert. Increase in casting velocity also decreases vertical temperature gradient in mould as measured vertical temperature differences decrease.

Key words:

Casting, velocity, temperature, primary, cooling.

1. INTRODUCTION

Continuous casting of steel represents a highly economical, modern and efficient manufacturing process. During manufacturing process, it is important to extract enough heat from solidifying steel as it goes through primary, secondary and tertiary cooling zones. Heat removal must secure, that the entire cross-section is solidified before steel leaves casting machine so it can undergo cutting operation [1].

Heat from steel is transferred via wall of casting mould insert into cooling water. Local heat flux can reach over 2 MW/m^2 [2]. Heat removal that takes place in mould must lead to growth of solid shell at circumference of the molten steel. Mould undergoes intense heat stress as inner working surface can exceed 400 °C at the very top where molten steel starts to solidify. This heavily stressed area exhibits most intensive deformation of the mould insert [3] while stress is mostly accumulated in the corners of the mould [4]. Temperature of the mould also increases with increase in casting velocity [5, 6]. As a prevention to excess abrasive wear there is a casting powder dispersed around the inner circumference of mould insert. Powder decreases friction between mould and therefore also improves surface quality of final product. Powder however undergoes cycles of melting and solidifying that are dependent of current thermal conditions. As it changes phases it also alters heat transfer via mould. Heat removal is very dependent on physical contact between steel shell and mould insert as heat transfer via gap is greatly reduced.

In order to support heat removal mould inserts are shaped to stay in direct contact with shrinking solidifying steel. Shrinkage is most significant in corners at the inner cross section of the mould [7] and heat transfer can differ over 50 % at the level of meniscus [8]. A proper condition for heat removal is also dependent on proper spatial setting of mould insert and submerged entry nozzle [9]. Uniformity of heat transfer is greatly enhanced if mould is properly centred which is obtained by its physical setting. Even so, solidifying steel changes its ideal centred position based on current parameters of casting.

This paper presents correlation of mould insert wall temperature and casting velocity. Calculation of presented data was based on measurements that were conducted in real manufacturing conditions during steel production.

2. COLLECTING OF DATA

For conducted measurements a radial billet casting machine of the 150 x 150 mm format was chosen. Mould insert wall thickness was 13 mm and length was 1 m. Flow of cooling water was directed from the top of the mould to the bottom. Top level of molten steel was steadily kept at the distance of 179 mm below the top of mould insert. Temperature in the mould insert wall was measured by twenty thermocouples, that were positioned vertically in the middle of each wall. Thermocouples were inserted in drilled holes to be in distance of 2 mm from the mould inner surface. They were placed at levels of

250 mm, 400 mm, 550 mm, 700 mm and 850 mm from the top of the mould. Measured data was logged periodically once per second for 85 minutes.

Presented temperatures were obtained during casting of steel with chemical composition that can be seen in Table 1. Other parameters such as temperature of molten steel and flow of cooling water were measured as stable.

Table 1 Casted steel chemical composition. Source: (own)

Element	C	Mn	Si	P	S	Cu	Cr	Ni	Mo
wt. %	0.176	0.66	0.095	0.017	0.032	0.01	0.05	0.03	0.008

3. EVALUATION OF DATA

Measured data needed to be filtered and further processed. Processing measured time in period of 512 s delivered arithmetic values of: measured temperature for each thermocouple, cooling water flow and its temperature at the mould inlet and outlet, casting velocity. Measured temperatures can be seen in Figure 2.

Based on evaluation of acquired data it can be concluded that overall heat transfer via mould insert from solidifying steel into cooling water has positive strong and statistically significant correlation to casting velocity as correlation coefficient is 0,96 see Figure 1.

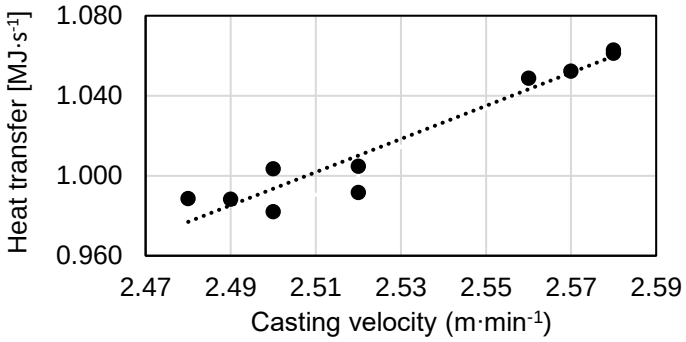

Figure 1 Change in heat transfer with increase in casting velocity. Source: (own)

Temperature in the mould wall exhibits also very strong positive and statistically significant correlation to increase in casting velocity as can be seen in Table 2 and graphically demonstrated in Figure 2. However, correlation coefficients in levels of 250 mm and 400 mm are significantly lower than coefficients at lower levels. It can be therefore concluded, that change in temperature as the response to change in casting velocity can be very well observed especially at lower levels of mould insert.

Table 2 Correlation values for casting velocity and level temperatures. Source: (own)

Correlation to casting velocity	**Heat transfer**	**Level (mm)**					
	MJ·s^{-1}	**250**	**400**	**550**	**700**	**850**	**Total**
coefficient	0.96	0.74	0.77	0.95	0.96	0.97	0.93
p-value	1.0E-05	1.4E-02	9.2E-03	3.6E-05	1.4E-05	5.4E-06	9.2E-05

There is also interesting observation in Figures 2 and 3 as temperature at 550 mm increases with casting velocity significantly above temperature at 400 mm. The rate of temperature increase at levels of 250 and 400 mm is lower compared to temperatures at lower levels. It can be concluded, that increase in casting velocity decreases vertical temperature gradient in wall of mould insert as measured temperature exhibit trend to equalize.

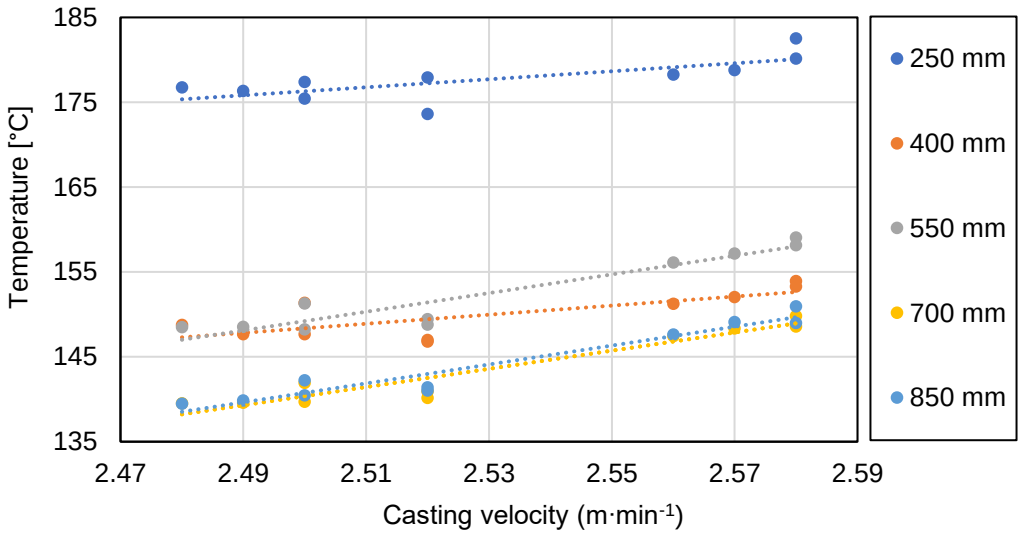

Figure 2 Change in temperature at measured levels. Source: (own)

In order to describe change in temperature gradient in mould insert, a percentage difference in temperatures was studied. For that purpose, a temperature at 250 mm was set as referential. Percentage difference was obtained as a ratio of measured temperature to referential temperature. Obtained percentage differences of lower temperature to referential temperature can be seen in Figure 3.

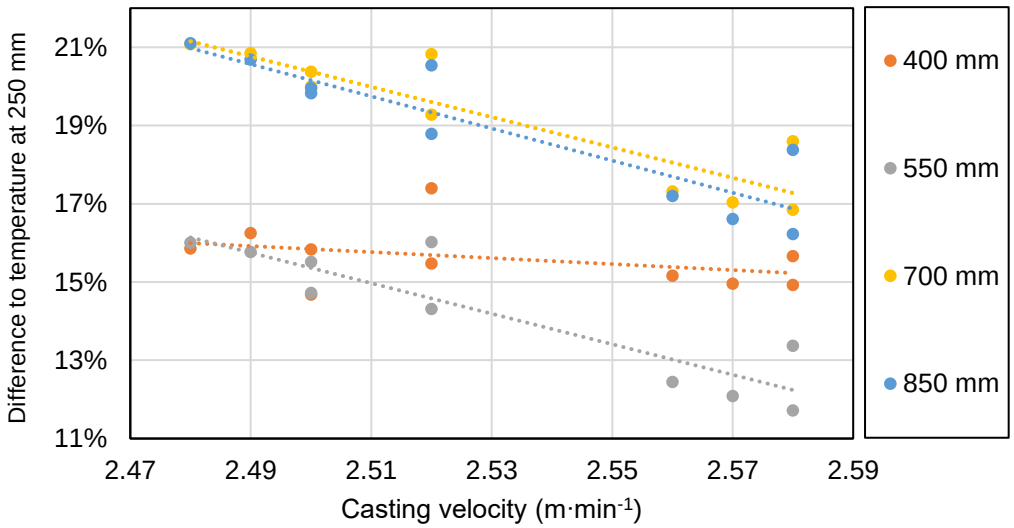

Figure 3 Change in temperature at measured levels. Source: (own)

Correlation of percentage difference values to casting velocity was studied. Correlation coefficient values are presented in Table 3. For levels below 550 mm there is a statistically significant negative correlation of percentage difference to casting velocity. The rate of decrease in percentage difference is similar for temperatures below 500 mm. Rate of decrease at level of 400 mm is significantly lower compared to other three levels.

Table 3 Correlation coefficient and p-values for casting velocity and percentage difference of temperature at each level compared to 250 mm level. Source: (own)

Correlation to casting velocity	Level (mm)				
	400	550	700	850	Total
coefficient	-0.37	-0.90	-0.90	-0.90	-0.87
p-value	2.9E-01	3.6E-04	3.4E-04	3.7E-04	1.1E-03

4. CONCLUSION

Presented paper investigated influence of casting velocity on heat removal from continuous casting mould insert as well as impact on vertical temperature of mould. Investigation was conducted on the radial billet casting machine of the 150 x 150 mm format.

It was discovered, that casting velocity directly influences heat transfer through mould. The dependency of heat transfer exhibits positive linear dependence with increase in casting velocity. Correlation is statistically significant, coefficient of obtained dependency is positive and very strong with coefficient 0,96 that indicates close to function dependency.

Correlation of casting velocity and vertical temperatures in the centreline of mould wall is significantly dependent on distance from mould top. Although all measured temperatures exhibit significant positive correlation to increase in casting velocity, increase of temperature at lower levels was higher and exhibited stronger correlation in comparison to higher levels. It can also be concluded, that increase in casting velocity leads to vertical equalization of temperature in walls of mould insert.

ACKNOWLEDGEMENT

The work was supported by the specific university research of the Ministry of Education, Youth and Sports of the Czech Republic No. SP2023/034 - Research and development of composite multifunctional materials for sustainable progress.

REFERENCES

[1] ŠTĚTINA, Josef, František KAVIČKA, Jaroslav KATOLICKÝ, Tomáš MAUDER, Lubomír KLIMEŠ. Importance of the experimental investigation of a concasting technology. In *The Application of Experimental and Numerical Methods in Fluid Mechanics and Energy 2018*. MATEC Web of Conferences, 2018, 1-6.

[2] UDAYRAJ, Saurav CHAKRABORTY, Suvankar GANGULY, E.Z. CHACKO, S.K. AJMANI, Prabal TALUKDAR. Estimation of surface heat flux in continuous casting mould with limited measurement of temperature. *International Journal of Thermal Sciences*. 2017, 118, 435-447. 1290-0729.

[3] PARK, Kil Joong, Indira V. SAMARASEKERA, Brian G. THOMAS, Sok U YOON. Analysis of thermal and mechanical behavior of copper mould during thin slab casting. In *83rd Steelmaking Conference Proceeding*. Pittsburgh (PA): Iron and Steel Society, 2000, 9-21.

[4] DU, Feng-mi, Xu-dong WANG, Yu LIU, Tian-yi LI, Man YAO. Analysis of Non-uniform Mechanical Behavior for a Continuous Casting Mold Based on Heat Flux from Inverse Problem. *Journal of Iron and Steel Research, International*. 2016, 23 (2), 83-91. 1006-706X.

[5] ZHANG, Xingzhong, Zhengyi JIANG, Qiang ZHANG, Chunxia DOU. Investigation of Thermal Performance of Mold Copper Plate in Slab Continuous Casting. *The Open Mechanical Engineering Journal*. 2011, 14 (5), 39-42. 1874-155X.

[6] JEONG, Heetae, Jong-Yeon HWANG, Jung-Wook CHO. In-depth study of mold heat transfer for the high speed continuous casting process. *Metals and Materials International*. 2016, 22 (2), 295-304.

[7] YU, Sheng, Mujun LONG, Mengyuan ZHANG, Dengfu CHEN, Pei XU, Huamei DUAN, Jie YANG. Effect of mold corner structures on the fluid flow, heat transfer and inclusion motion in slab continuous casting molds. *Journal of Manufacturing Processes*. 2021, 68, 1784-1802. 1526-6125.

[8] VAKA, Ananda S., Suvankar GANGULY, Prabal TALUKDAR. Novel inverse heat transfer methodology for estimation of unknown interfacial heat flux of a continuous casting mould: A complete three-dimensional thermal analysis of an industrial slab mould. *International Journal of Thermal Sciences*. 2021, 160, 1290-0729.

[9] ZHANG, Weiven, Jixiang GAO, Pradeep K. ROHATGI, Haidong ZHAO, Yuanyuan LI. Effect of the depth of the submerged entry nozzle in the mold on heat, flow and solution transport in double-stream-pouring continuous casting. *Journal of Materials Processing Technology*. 2009, 209 (15-16), 5536-5544. 0924-0136.

DEVELOPMENT OF ADVANCED MATERIAL FOR PRECAST FLOW CONTROL ACCESSORIES FOR THE TUNDISH

Author(s): Ivan PRIESOL

Supervisor: prof. Ing. Jozef VLČEK, Ph.D.

Department: Department of Thermal Engineering, Faculty of Materials Science and Technology, VSB – Technical University of Ostrava

Abstract:

The paper describes experience with the development, production and application of advanced ceramic materials for long-term exposure in steel melt. The basic feature of this type of advanced materials is their innovative sol-gel binding system, which replaces calcium alumina cement (CAC) binder in refractory concrete mixtures. This substitution brings advantages in the form of lower energy intensity of the production of such mixtures and also their significantly lower energy requirements for drying and heat preparation of products from such refractory mixtures. All this is done while fully preserving the physical and mechanical properties of the products, in comparison with products made of classic castable mixes.

Finally, examples are given from the experimental application of this type of product under real operating conditions.

.

Key words

Advanced ceramic materials, sol-gel, refractory concrete, CA cement.

1. INTRODUCTION

The current requirements for the high purity of produced steels place particular demands on ceramic materials used in steel production, especially for ceramic accessories for tundish, which are the last equipment in which steel is still in a liquid state and where it is still possible to rid or contaminated steel of non-metallic inclusions. These inclusions mostly have the character of metal oxides and are found in a solid state. These inclusions are divided into endogenous – i.e. those that are a by-result of technological operations in steel production, and exogenous – those where their source is the external environment, especially refractory ceramics. Classic cement-bound refractory castables also contribute to the occurrence of exogenous inclusions. This fact leads to the realization that for the production of ceramic products applied in the tundish and having direct contact with liquid steel, a new advanced material will be needed that will meet these demanding criteria. These criteria have been set in accordance with the requirements imposed by the current state of steel production in Europe, current European legislation and which bring trends related to the Industry 4.0 agenda.

Basic objectives of materials research:

1.Long-term exposure in dynamic liquid steel, especially those used in the area of steel inflow into the tundish. The material must have such properties as ensure the shape stability of precast parts used to ensure flow control steel in the tundish.

2.Preparation of the mixture for the production of precast parts and the production of precast parts with the lowest possible energy consumption and lowest carbon footprint.

In order to achieve these objectives, the idea of producing precast parts based on LCC and ULCC concrete was abandoned, due to their obvious disadvantages related mainly to point 2. Research has focused on the preparation of cement-free mixtures using a binder prepared on the basis of the sol-gel method. The mixtures prepared in this way showed good resistance to corrosion phenomena caused by cast steel and particularly by the slag.

2. RESULTS AND DISCUSSION

In connection with the development of its own binder system prepared by the sol-gel method, a silicate-aluminate colloidal solution (1) prepared in cooperation with IPC Refractories a.s., Košice, SK

and VŠB-TUO, CZ was tested, which is unique not only for its composition, but also for its properties, which directly supports the set goal[1].

The reason why sol-gel binders were used was an effort to reduce the shortcomings of classical ceramic materials such as high-temperature preparation of binder materials or their structural instability of raw materials for their production. The use of binders prepared by the sol-gel method makes it possible to eliminate a whole range of these shortcomings. This method allows to control the purity of starting materials for the formation of binders, the stability of their composition, influence the properties of binders such as microporosity, binding lattice density or the resulting form of binding xerogel.

The advantage of using the sol-gel process in ceramic production is the formation of new products based on oxides at relatively low temperatures. This is due to the fact that reactants are solvent-dispersed at the molecular level, with very short diffusion distances of the reactive components, causing a rapid reaction under relatively very mild conditions compared to conventional ceramic materials (3).

The result of this effort was the preparation of a mixture that uses a silicate-aluminate binder prepared by the sol-gel method and which after its application in concrete material, in addition to standard physical properties comparable to LCC/ULCC concrete of an adequate grade (bauxite aggregates), exhibits these properties in the formation of final ceramic phases such as mullite, α-corundum or cristobalite.

This binder was tested as a thermal processed xerogel at various annealing temperatures (110 °C, 500 °C, 800 °C, 1000 °C, 1200 °C and 1400 °C) and subsequently the samples were subjected to XRD analysis.

Up to 800 °C, the gel remained amorphous. At a temperature of 1000 °C (Fig. 1) (2), mullite has already been recorded in xerogel, and at a temperature of 1200 °C (Fig. 2) (2), α-corundum also appears. Closer monitoring later recorded the beginning of mullite formation at temperatures around 950 °C, and the first signs of α-corundum formation began at temperatures slightly above 1100 °C.

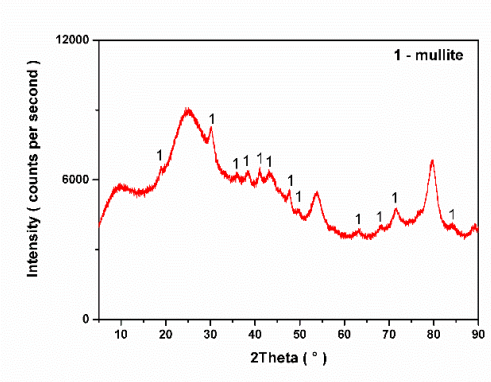

Fig. 1 XRD xerogel 1000°C, source: [2]

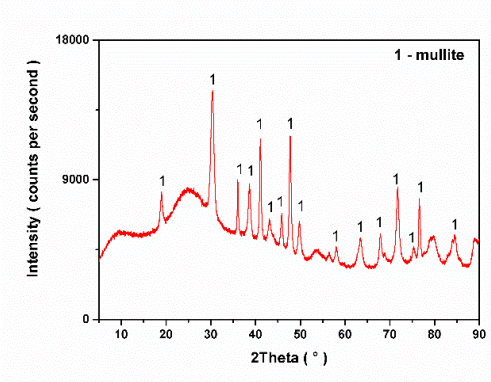

Fig. 2 XRD xerogel 1200 °C, source [2]

In both cases, the beginning of the formation of the final ceramic luminate phases, mullite and α-corundum, is shifted down by almost 100 °C, which significantly contributes to reducing energy consumption during the final phase transition. This fact has a significant impact on reducing the carbon footprint of both the concrete itself using the sol-gel binder and the products prepared from it.

After a series of experiments with the composition of the final castable mixture, for thixotropic processing, industrial tests of impact plates with spherical surfaces were carried out. The composition of the castable is presented in table number 1 (5), and the physical properties of such castable are presented in table number 2 (5). (Legend to table 2: CCS – cold compressive strength, PLC – Permanent linear change)

The behavior of the developed silicate-aluminate sol, used as a binder in the above-described mixture of designed refractory castable (table 1), is also extremely interesting. Test bodies made of this material were subjected to corrosion tests by steel melt and these bodies were subsequently subjected to optical analysis on the Keyence VHX microscope. This analysis is focused on the study of corrosion, the study of discovered microcracks, and the behavior of the material towards penetrated metal particles in the matrix of concrete.

Table 1 Compositon of castable. Source: [5]

Developed castable	
Material	%
Bauxite 0-6 mm	66
Tabular alumina	15
reactive alumina	14
Si-Al sol-gel binder	5

Table 2 Physical value of developed castable. Source: [5]

Castable for flow control precast parts	
Properties	Value
Bulk density 110 °C/2h g.cm^{-3}	2,9
Bulk density 1200 °C/5h g.cm^{-3}	2,89
PLC 110 °C ins.500 °C %	-0,19
PLC 110 °C fir.1200 °C %	-0,11
CCS 110 °C/2h MPa	28
CCS 1200 °C/5h MPa	122

Figure 3 shows the condition of the test body after a corrosion test of resistance of developed castable against steel attack that lasted 5 hours at 1500°C. A very weak interaction between liquid metal and castable can be seen. In Figure 4, we can see the behavior of the matrix, including the binder, in the resulting microcrack and the behavior on contact with the metal inclusion. It can be concluded that part of the binder based on the developed silicate-aluminate sol probably retains an amorphous character. This stage has the ability to gradually close, respectively, significantly reduce the diameter of such a crack (4).

Such behavior of the matrix of designed concrete is the reason for its convenient resistance to thermal shocks and, accordingly, crack formation. From the behavior of the matrix on contact with liquid steel, we can also infer the exceptionally good resistance of the designed refractory concrete to metal corrosion.

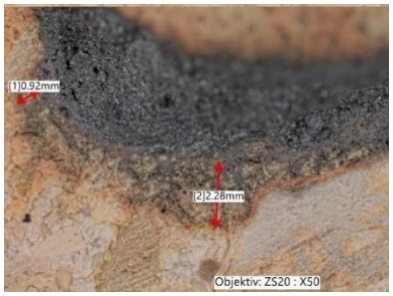

Fig. 3 Corrosion test, source: [4]

Fig. 4 Inclusion in matrix, source: [4]

After completion of laboratory testing of the designed refractory concrete, the intended shape product for the flow control of steel in the tundish – spherical impact plate – was proceeded. Special requirements are placed on this product, both for mechanical properties and for corrosion resistance.

Designed castable products with sol-gel binder have demonstrated excellent performance in operational tests. The products have been tested on long series. In figure number 5 (5) we see the incorporation of the product – the impact plate to the point of impact of steel in the tundish. In Figure 6 (5), this built-in impact plate is after casting is complete. On the presented impact plate, 32 smelts, each with a volume of 180 tons, were cast, so a total of 5760 tons of steel were cast.

As can be seen, the proposed material confirmed the expectations placed on it, including the reduced energy intensity in the production of the product, as well as the reduced carbon footprint of the designed concrete. At the same time, for a given product, it qualitatively surpasses conventional concrete bound by CA cements.

Fig. 5 Impact pad Installation. source: [5]

Fig. 6 Condition of the impact plate after after casting 32 heats. source: [5]

3. CONCLUSIONS

Based on the operational tests carried out, it can be concluded that the developed material meets both set development goals. The processing of the designed concrete is fully applicable in operating conditions. The thermal preparation of cast parts, impact plates, was extremely short compared to classic CAC concrete. The energy consumption for the preparation of these parts was more than 4 times lower.

The designed material showed exceptional properties in its ability to withstand the dynamic liquid steel environment that prevails during tundish casting. The ability to withstand erosion phenomena without deforming the shape of specially shaped precast products is essential to maintain the same dynamic steel flow conditions throughout the continuous steel casting process.

The developed material is fully suitable for industrial application.

REFERENCES

[1] VLČEK Jozef, Miroslava KLÁROVÁ, Michaela TOPINKOVÁ, Výskumná zpráva, část A: Vývoj sol-gel pojivového systému, *Smlouva o dílo HS7501527*, Ostrava, 2016, VŠB-TU Ústav průmyslové keramiky

[2] KLÁROVÁ Miroslava, Jozef VLČEK, Michaela TOPINKOVÁ, Jiří BURDA, Alexandr MARTAUS, Ivan PRIESOL, Jacek SZCZERBA, Cement Substitution In High-Temperature Concrete, *Minerals*, 2021, 11, 1161, https://www.mdpi.com/2075-163X/11/11/1161?type=check_update&version=1

[3] VLČEK Jozef, Miroslava KLÁROVÁ, Ivan PRIESOL, Vývoj bezcementových pojivových systémů, In *X Žiaromateriály pece a tepelné* izolácie, Jasná – Demänovská Dolina SK, 2018, Lumakon, 82 - 86

[4] PRIESOL Ivan, Nikola PRIESOLOVÁ, Štefan SLOSIAR, Jozef VLČEK, Miroslava KLÁROVÁ, Porovnanie vlastností vybraných žiarobetónov využívajúcich bezcementové nanospojivo, In *XI Žiaromaterály, pece a tepelné izolácie*, Košice SK, Lumakon, 2021, 14 - 28

[5] BUĽKO Branislav, Ivan PRIESOL, Peter DEMETER, Peter GAŠPAROVIČ, Geometric Modification Of The Tundish Impact Point And The Advanced Material For This Application, In *ALAFAR Congress*, Foz do Iguaçu BR, ALAFAR, 2022 http://www.alafar.org/papers/2022/03-Bulko.pdf

DETERMINATION OF THE OVERALL VALUE OF THE HEAT TRANSFER COEFFICIENT ON THE OUTSIDE OF THE CYLINDRICAL WALL

Author(s): David RIGO

Supervisor: doc. Ing. Marek VELIČKA, Ph.D.

Department: Department of Thermal Engineering, Faculty of Materials Science and Technology, VSB – Technical University of Ostrava

Abstract

The subject of the present paper is to determine the total value of the heat transfer coefficient on the outside of an uninsulated heat pipe passing through a room by means of mathematical and physical analysis. The calculation is performed for two variants of the piping. The calculations performed can be used in the next stage to determine the total heat loss or the amount of heat transferred to the surroundings from the pipe casing surface and subsequently to design the optimum pipe insulation thickness. Based on the design of the optimal pipe insulation thickness, it is also possible to further evaluate the investment and operating costs of both new and existing hot water piping systems.

Keywords

Heat transfer coefficient, Nusselt criterion, characteristic dimension.

1. INTRODUCTION

In the current energy policy of the EU and the Czech Republic, buildings are now seen as energy consumers and this implies requirements for energy management in buildings. The energy performance of buildings can be reduced not only by reducing heat leakage through the building envelope, but also by reducing the heat loss of building technical equipment (HVAC), or piping systems and systems [1]. Optimal design of the insulation thickness of piping systems and systems is one of the requirements for reducing the energy consumption of building operation. HVAC insulation is carried out in all types of buildings. Effective insulation is essential to maintain, for example, the correct operating temperature of HVAC systems. As these devices and systems consume large amounts of energy, it is imperative that energy consumption is kept as low as possible and their operation is highly efficient. Basic physical laws of heat transfer and fluid flow are used to calculate the heat loss of piping systems. Heat loss can be defined as the fraction of the thermal energy of a fluid (water, air, refrigerant) flowing in a pipe that is dissipated through the pipe wall to the surroundings. The thickness of the pipe insulation can be determined from the surface temperature of the pipe or the heat flux density. In addition, the following boundary conditions need to be determined for the calculation: The temperature of the flow medium in the pipe, the ambient temperature, the diameter of the pipe, the thermal conductivity coefficient of the insulation material at the mean temperature, the total heat transfer coefficient on the outside. Of the boundary conditions defined above, the value of the total heat transfer coefficient on the outside is the most challenging to determine.

2. MATHEMATICAL AND PHYSICAL ANALYSIS

The mathematical and physical analysis determines the total heat transfer coefficient on the outside α ($W \cdot m^{-2} \cdot K^{-1}$) of an uninsulated heat pipe with an outer diameter D = 0.05 m and length L = 3.00 m passing through a large room. The calculation is performed for two variants. In the first variant, the pipe is routed horizontally under the ceiling of the room, in the second variant the calculation assumes that the pipe is routed vertically against the wall of the room. The input values of the calculation model are given in Table 1 below.

Table 1 Input values of the calculation model. Source: (own)

Variant		t_p (°C)	$t_{p\text{-step}}$ (°C)	t_{air} (°C)	L_{ch} (m)		ε (1)	S (m^2)
A	**B**	80	5	20	**0.05**	**3.00**	0.65	0.47

A/ Determination of characteristic temperature and characteristic dimension

The characteristic temperature t_{ch} (°C) and the characteristic dimension L_{ch} (m) are entered into the calculation model. The characteristic temperature is defined as the arithmetic mean of the average pipe wall surface temperature t_p (°C) and the average ambient air temperature t_{air} (°C). The characteristic dimension is the outer diameter D (m) for horizontal pipelines and the height H (m) for vertical pipelines, see Figure 1.

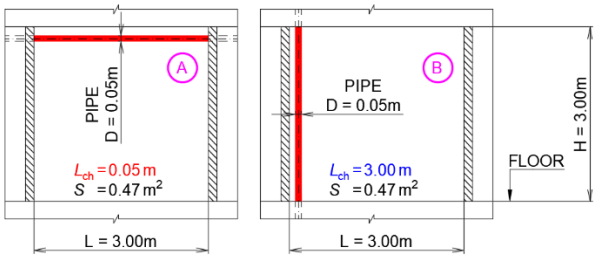

Figure 1 Pipeline diagram. Source: (own)

B/ Determination of physical parameters

Using regression analysis, the functional dependencies needed to calculate the similarity criteria (*Pr*, *Gr*, *Nu*) were determined from the tabulated values of the physical parameters (c_p, λ, ν, ρ,) for air. The dependencies of the physical parameters on air temperature were expressed by a polynomial of degree 3, see Table 2. The characteristic temperature is substituted for the air temperature in the obtained dependencies.

Table 2 Functional dependence of physical parameters for air. Source: (own)

Applies to temperature range t = 0 až 100 °C; pressure p = 101 325 Pa c_p, λ, ν, ρ, = f (t); where $t = t_{ch}$
$c_p = 9.2593 \cdot 10^{-7} \cdot t^3 - 2.0139 \cdot 10^{-4} \cdot t^2 + 2.6890 \cdot 10^{-1} \cdot t + 9.8420 \cdot 10^2$
$\lambda = 3.4722 \cdot 10^{-11} \cdot t^3 - 4.2262 \cdot 10^{-8} \cdot t^2 + 7.5081 \cdot 10^{-5} \cdot t + 2.3629 \cdot 10^{-2}$
$\nu = -6.0375 \cdot 10^{-14} \cdot t^3 + 1.1093 \cdot 10^{-10} \cdot t^2 + 8.8224 \cdot 10^{-8} \cdot t + 1.3295 \cdot 10^{-5}$
$\rho = -3.3414 \cdot 10^{-8} \cdot t^3 + 1.5757 \cdot 10^{-5} \cdot t^2 - 4.7067 \cdot 10^{-3} \cdot t + 1.2930$

C/ Calculation of the Prandtl number

The Prandtl number *Pr* characterizes the physical properties of a fluid in convective and diffusive heat transfer. These are phenomena related to energy transfer in the boundary layer. *Pr* expresses the degree of similarity between the velocity and temperature fields and is given by equation (1). Where: ν – kinematic viscosity of air ($m^2 \cdot s^{-1}$) , a – coefficient of thermal diffusivity of air ($m^2 \cdot s^{-1}$), ρ – density of air ($kg \cdot m^{-3}$), η – dynamic viscosity of air (Pa·s), c_p – specific heat capacity of air ($J \cdot kg^{-1} \cdot K^{-1}$) [2].

$$Pr = \frac{\nu}{a} = \frac{\nu \cdot \rho \cdot c_p}{\lambda} = \frac{\eta \cdot c_p}{\lambda} \tag{1}$$

In the computational model, the *Pr* number values for air ranged from 0.7170 to 0.7182. In engineering calculations, a value of $Pr_{air} = 0.7$ is commonly considered.

D/ Calculation of the Grashof number

The Grashof number *Gr* characterizes the natural convection of a fluid induced by a density difference, due to a temperature gradient in the fluid and is determined by relation (2). Where: β – thermal volume expansion coefficient of air (K^{-1}), g – gravitational acceleration (9.81 $m \cdot s^{-2}$), t_p, t_{air} – surface temperature, air temperature (°C), L_{ch} – characteristic dimension (m), ν – kinematic viscosity of air ($m^2 \cdot s^{-1}$) [2].

$$Gr = \frac{\beta \cdot g \cdot (t_p - t_{air}) \cdot L_{ch}^3}{\nu^2} \tag{2}$$

In the computational model, the *Gr* number values ranged from $8.9 \cdot 10^4$ to $1.5 \cdot 10^{11}$.

E/ Calculation of the Nusselt number

The Nusselt number *Nu* characterizes the similarity between heat transfer by convection and conduction in a fluid boundary layer. The *Nu* number can be determined from relation (3), the so-called number equation for natural convection [2].

$$Nu = \mathrm{C} \cdot (Gr \cdot Pr)^{\mathrm{n}} \tag{3}$$

The constants C and n in the number equation are chosen based on the value of the product *Gr·Pr*. The constants C, n = *f* (*Gr·Pr*). If the product of *Gr·Pr* is in the range of $1 \cdot 10^{-3}$ to $5 \cdot 10^{2}$; the constants C = 1.180 and n = 0.125 are chosen (the constants C and n characterize the laminar fluid flow in the boundary layer). If *Gr·Pr* is between $5 \cdot 10^{2}$ and $2 \cdot 10^{7}$; then C = 0.540 and n = 0.250 (intense laminar flow and turbulent eddy flow in the boundary layer). If *Gr·Pr* comes out in the range of $2 \cdot 10^{7}$ to $1 \cdot 10^{13}$; then C = 0.135, n = 0.333 (turbulent flow in the boundary layer) [2]. In the computational model, the values of the product of *Gr·Pr* for the L_{ch} = 0.05 m variant ranged from $6.3 \cdot 10^{4}$ to $5.1 \cdot 10^{5}$. For the L_{ch} = 3.00 m variant, the values ranged from $1.4 \cdot 10^{10}$ to $1.1 \cdot 10^{11}$. The values of the *Nu* criterion can be read from Figure 2 below. Due to the high values of the product *Gr·Pr* on the x-axis, the power function of the *Nu* number equation for the two variants considered was transformed and expressed as a logarithmic relationship. The *Nu* number expresses the dimensionless heat transfer value. In the computational model, it is applied to determine the convective heat transfer coefficient α_c (W·m^{-2}·K^{-1}).

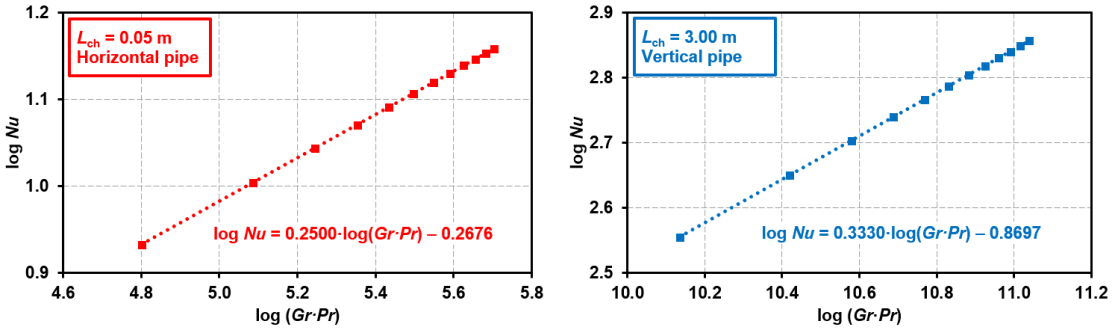

Figure 2 Heat transfer with natural air flow. Source: (own)

F/ Calculation of convection heat transfer coefficient

The convective heat transfer coefficient α_c (W·m^{-2}·K^{-1}) expresses the amount of heat transferred per unit time between a fluid (air) and a unit surface area of a body, where there must be a unit temperature gradient between the body and the fluid. The coefficient α_c can be determined according to relation (4). Where: *Nu* – Nusselt number (1), λ – coefficient of thermal conductivity of air (W·m^{-1}·K^{-1}), L_{ch} – characteristic dimension (m) [2]. The usual values of the coefficient α_c are in the following ranges: For gases under natural convection from 5 to 100. For water at natural convection from 100 to 1000. In the calculation model, the values of the convection heat transfer coefficient for the L_{ch} = 0.05 m (horizontal pipe) variant range from 4.3 to 7.9 W·m^{-2}·K^{-1}, for the L_{ch} = 3.00 m (vertical pipe) variant range from 2.7 to 5.8 ·m^{-2}·K^{-1}.

$$\alpha_c = \frac{Nu \cdot \lambda}{L_{ch}} \quad (\mathrm{W \cdot m^{-2} \cdot K^{-1}}) \tag{4}$$

G/ Calculation of the radiation heat transfer coefficient

The heat transfer coefficient of radiation α_r (W·m^{-2}·K^{-1}) is determined according to relation (5). Where: ε – emissivity of the pipe surface (1), σ_0 – Stefan-Boltzmann constant ($5.67 \cdot 10^{-8}$ W·m^{-2}·K^{-4}), T_p, T_{air} – thermodynamic temperature of the surface, thermodynamic air temperature (K), t_p, t_{air} – temperature of the surface, air temperature (°C) [2].

$$\alpha_r = \frac{\varepsilon \cdot \sigma_0 \cdot \left[(T_p)^4 - (T_{air})^4 \right]}{t_p - t_{air}} \quad (\mathrm{W \cdot m^{-2} \cdot K^{-1}}) \tag{5}$$

In the calculation model, the values of the α_r coefficient for the two variants ranged from 3.8 to 5.0 W·m^{-2}·K^{-1}. In both variants, ε = 0.65 was considered. It is therefore valid that $\alpha_r = f(\varepsilon)$.

H/ Calculation of the overall heat transfer coefficient

The overall value of the heat transfer coefficient α (W·m^{-2}·K^{-1}) is obtained by summing the convection and radiation heat transfer coefficients, see relation (6).

$$\alpha = \alpha_c + \alpha_r \quad (\mathrm{W \cdot m^{-2} \cdot K^{-1}}) \tag{6}$$

The contribution of the individual coefficients (%) to the total value of the heat transfer coefficient can be read from Figure 3 below. The overall value of the coefficient α (W·m^{-2}·K^{-1}) can also be read from the figure. It is clear from the graphical representation that the more intense heat transfer occurs in the horizontal pipe and the dominant coefficient for both variants is the convection heat transfer coefficient α_c. The above is mathematically related to relations (2), (3), (4) and the value of the characteristic dimension L_{ch} (m). From a physical point of view, in a horizontal hot water pipeline, natural convection causes air circulation in a perpendicular section to the pipe axis and it does not matter whether the medium (water) in the pipe flows from left to right or vice versa. In vertical pipe, the effect of natural convection is determined by the direction of flow of the medium in the pipe and whether the medium (water) in the pipe is heated or cooled. In the calculation model, the direction of flow of water and air is the same in the vertical pipe, and the water is cooling in the pipe. The natural convective transfer in both variants is due to the temperature difference in the fluid volume, i.e. due to heat sharing. The determining criterion for natural convection is the Grashof number.

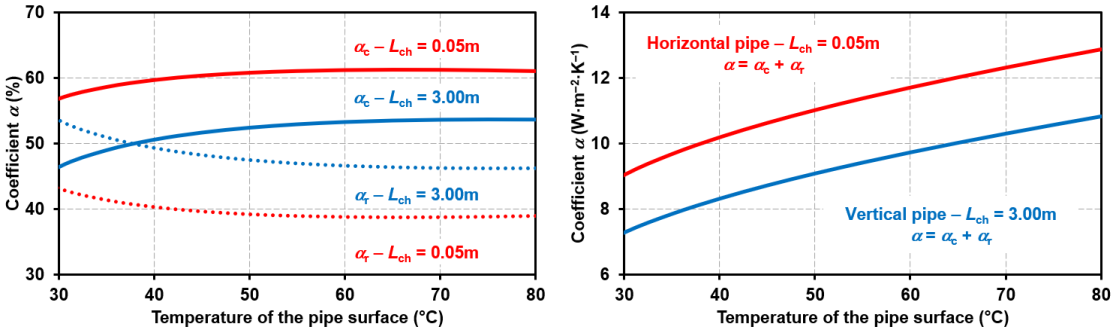

Figure 3 Heat transfer coefficient. Source: (own)

3. CONCLUSION

The paper shows an engineering approach for determining the overall value of the heat transfer coefficient on the outside of an uninsulated heat pipe, i.e. a cylindrical wall passing through a room in the horizontal and vertical direction. The calculation model shows that the heat transfer is more intense in the horizontal pipework and the dominant coefficient for both variants is the convection heat transfer coefficient. From the overall value of the heat transfer coefficient, the temperature difference between the pipe surface and the ambient air temperature and the pipe area, the total heat flux lost (W) can be determined. Based on the calculation of the heat loss of the pipe, the optimum thickness of the thermal insulation can then be designed. The heat loss of hot water piping systems cannot be completely eliminated, but it can be reduced by economically viable measures based on mathematical and physical analyses and thus contribute significantly to the energy optimization of building operation.

ACKNOWLEDGEMENT

The work was supported by the specific university research of the Ministry of Education, Youth and Sports of the Czech Republic No. SP2023/034 - Research and development of composite multifunctional materials for sustainable progress.

REFERENCES

[1] RIGO, David. Modelling of heat loss and annual energy demand for heating the building. In: *PhD students´ day FMST 2022*. Ostrava: Vysoká škola báňská – Technická univerzita Ostrava, 2022. ISBN 978-80-248-4653-8.

[2] VDI-Wärmeatlas. 10., bearb. und erw. Aufl. Berlin: Springer, c2006. ISBN 3-540-25504-4.

ANALYSIS OF BLOOMERY SLAG FROM ARCHAEOMETALLURGICAL EXPERIMENTS

Author(s): Jan RŮŽIČKA

Supervisor: doc. Ing. Marek VELIČKA, Ph.D.

Department: Department of Thermal Engineering, Faculty of Materials Science and Technology, VSB – Technical University of Ostrava

Abstract

The chemical analysis of the slag is presented in this work. Three slag samples were selected for it. These were taken from the hearth part of the furnace. The slag samples were identified optically based on experience from previous smelting and experiments. Furthermore, a diffraction analysis of the slag was performed to determine the homogeneity of the samples taken. Finally, the samples were analyzed using fluorescence analysis and were compared to a set of historical findings.

Key words

Archaeometallurgy, slag, iron making, furnace.

1. INTRODUCTION

Archaeometallurgy is a field focused on the early and primary period of metal processing. From the point of view of the focus of this work, iron is the most interesting one. Since its discovery, iron has been the most important metal known to mankind. Nowadays it is taken for granted. In addition, the discovery and use of iron led mankind to many important milestones that changed the course of history. Iron is the most widely used metal material today.

An important aspect is the monitoring of the products of the melting itself. Our ancestors were able to estimate the quality of the iron and the success of the process by the behavior of the slag. Slag is an integral part in the production of sponge iron. It has a major influence on its quality Slag fulfills an important role as chemical and mechanical protection. It covers the iron bloom in the hearth and thus protects it from reverse oxidation. With a small amount of slag iron bloom is oxidized and its degradation occurs. A high amount of slag then causes flooding of the nozzle and reduces the amount of air blown into the furnace space and consequently the temperature [1].

The chemical analysis of the slag is presented in this work. Three slag samples were selected for it. These were taken from the hearth part of the furnace after the end of the reduction process and after the complete cooling of the entire furnace. The slag samples were identified optically based on experience from previous smelting and experiments. Small fragments of the bloomery iron remain in the ashes in the furnace, which are similar to slag. Slag often has the character of a previously solidified liquid substance, so-called solid lava, so it could be easily identifiable. If not, the weight of the fragment is a good indicator. When a higher weight indicates the presence of pure iron, and therefore the iron fungus itself. The samples are than analyzed by diffraction and fluorescence analysis. After the chemical composition is known its confronted with some historical findings [2].

2. SLAG DIFFRACTION ANALYSIS

The chemical composition of the slag was measured using X-ray diffraction analysis. Three slag samples were selected, photographed and ground into a very fine fraction. X-ray diffraction analysis was performed on a Rigaku MiniFlex. On this device, the sample is irradiated with X-rays. The wavelength of the rays is comparable to the dimensions of the crystal lattice when the radiation is refracted. This refraction can then be accurately captured and evaluated. In this case, the device can monitor up to eight samples with great accuracy. In this case three samples were tested.

Slag diffraction diagram is presented in the next **figure 1** lower. It contains three separate curves that symbolize three different samples of slag. These slag samples are named “struka_1”, “struska_2” and “struska_3”.

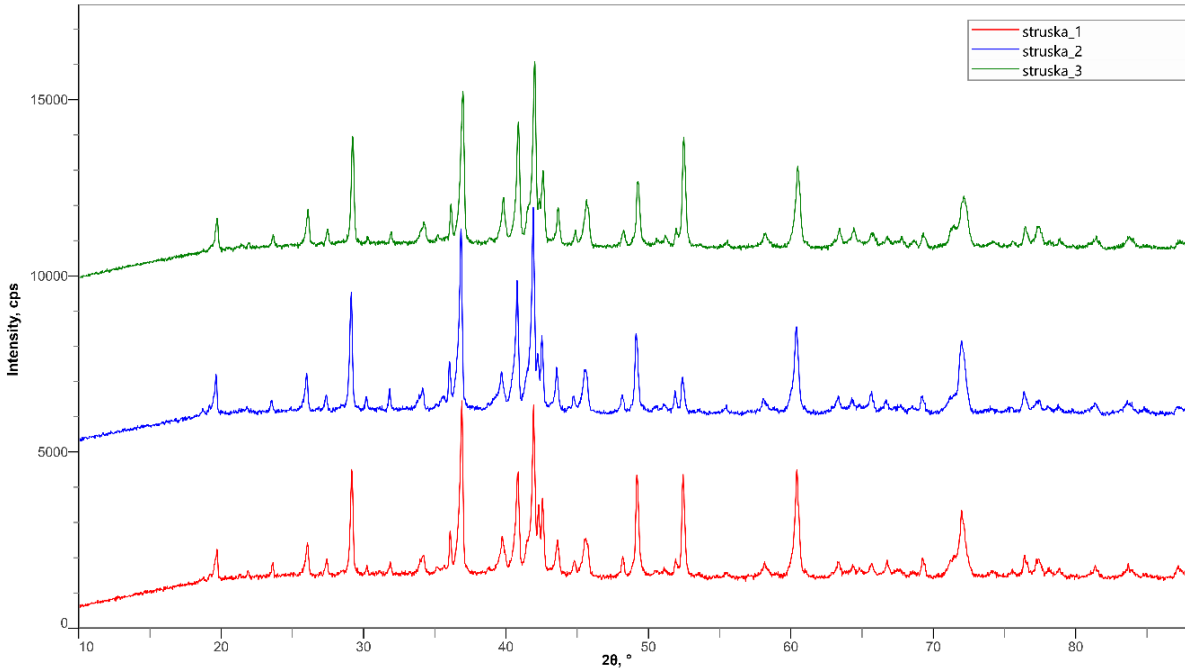

Figure 1 Slag diffraction diagram of three slag samples. Source (own)

Even after a quick evaluation, it is clearly visible that all samples show a very similar chemical spectrum. All peaks are at identical angular values. And their intensities also differ only slightly.

The contents of the hearth of the furnace were mixed very vigorously by removing the bloomery iron mass. The fact that the samples showed such a similar chemical composition shows a very homogeneous slag. This statement subsequently supports the reasoning that the reduction was successful.

3. SLAG FLUORESCENCE ANALYSIS

From the same three slag samples, X-ray fluorescence analysis of the chemical composition was performed on a Rigaku Supermini200 instrument. The mentioned device can perform complex analyzes of matrix materials.

The wide spectrum of the device can determine both light and heavy metals. The distinguishing and analytical advantages are very high even for difficult samples. The instrument is equipped with three positions for the light crystals of the spectrometer. Two of the three positions are occupied by LiF (200) and PET and this is the standard. A Ge or RX25 crystal can be inserted into the third position. The RX25 crystal provides high resolution for peak values of elements from oxygen to magnesium. With the Rigaku Supermini200, it is possible to study up to 12 samples each fixed in one position of the rotating matrix.

The samples must be prepared before inserting them into the positions in the device. First by fine grinding and then by mixing with a binder. The binder exhibits a similar viscosity to glucose. Subsequently, the mixture is inserted into an aluminum mold and pressed. Pressing is done at a pressure of 120 MPa and for 30 seconds. The sample prepared in this way can be inserted into the ring of the analyzer controller.

The actual chemical composition is shown in the next **table 1**. Table shows high concentration of elements typical for common iron production. The main difference is in the concentration of Fe_2O_3 which is astronomically high in comparison to modern type of iron making process.

Table 1 Chemical composition of bloomery slag. Source (own)

	MgO	Al_2O_3	SiO_2	P_2O_5	SO_3	Cl	K_2O	CaO
n	w(%)	w(%)	w(%)	w(%)	w(%)	w(%)	w(%)	w(%)
1	0,5915	4,8294	15,7513	0,2728	0,2119	0,0059	1,1971	3,8011
2	0,4511	4,9858	15,4416	0,281	0,0854	0,002	1,2224	4,1881
3	0,4129	3,8817	12,8078	0,2752	0,0791	0,0024	0,9313	3,5865
Average	**0,4852**	**4,5656**	**14,6669**	**0,2763**	**0,1255**	**0,0034**	**1,1169**	**3,8586**

	TiO_2	Cr_2O_3	MnO	Fe_2O_3	Co_2O_3	SrO	ZrO_2	LOI
n	w(%)	w(%)	w(%)	w(%)	w(%)	w(%)	w(%)	w(%)
1	0,2133	0,0355	0,1053	63,6825	<0.001	0,0143	0,0081	9,28
2	0,2525	0,0303	0,1253	65,072	<0.001	0,0217	0,0108	7,83
3	0,1733	0,0299	0,1045	67,1599	0,0605	0,0161	0,0088	10,47
Average	**0,2130**	**0,0319**	**0,1117**	**65,3048**	**0,0605**	**0,0174**	**0,0092**	**9,1933**

The second most dominant component is silicon dioxide. Silica sands are added to the clay clay mixture and are an integral part of the process. During reduction in the furnace, they also serve as additional slag-forming media that adjust the basicity of the slag. Furthermore, the content of aluminum oxide is visible, which was also introduced into the slag from the clay mass. Charcoal-derived fluxes are also present in the slag, which simplify the reduction process. Namely, it is potassium oxide and calcium oxide.

High iron oxide contents can be read from the table. That means that a large amount of unprocessed potential pure iron is ignored by reduction. This fact indicates the inefficiency of the production process in La Tene furnaces. Iron oxides, especially FeO, are abundantly found in iron slag found all over the world.

In the **table 2** below are shown chemical compositions of some found historical bloomer slags. Two types of iron oxides are present in these finds. But in **table 1** only Fe_2O_3 can be seen.

Table 2 Chemical composition of some historical bloomery slag. Source [3]

Place, country, and date of origin.	Chemical composition (%)							
	FeO	Fe_2O_3	SiO_2	CaO	MnO	Al_2O_3	MgO	P_2O_5
Maiden Castle, UK (24. – 25. AD.)	53	22,87	15,95	2,75		1,47	0,45	0,4
Sirzi, Tur. (7. cen. BC.)	55,65	13,96	8,6	5,16	7,18	1,89	4,87	1,95
Noreia, Aus. (7. -6. cen. BC.)	48,26	24,29	14,78	2,13	1,29	3,65	0,9	0,2
Noreia, Aus. (4. cen. AD.)	55,39	12,62	24,48	1,99	2,35	2,54	1,43	0,15
Noreia, Aus. (La Tene)	55,72	10,33	20,72	3,85	2,38	1,96	1,85	0,4
Mšecké Žehrovice, CZ (La Tene)	51,63	20,08	18,37	1,73	0,46	0,6		1,83

The table above lists the different values and ratios of iron oxides. However, in general, the values of latent and unprocessed iron are very similar. Which shows that the experiment was very close to real facts. However, it must be noted that the contents of the chemical components of the slag will vary significantly depending on the ore used. Which is probably one of the reasons why there was no FeO in the experimental slag, but only Fe_2O_3.

4. CONCLUSION

The results of the analyzes show a similar chemical composition as in the case of the historical findings. A significant difference in the slag samples that were selected for this chemical investigation is the absence of FeO. This fact was probably caused by the ore used In the reduction process.

Comparing the measured slags and slags from the finds, it is possible to assume that the processes used in experiment for iron reduction are very close to those that were used historically. The exact values vary, but the nature of the slag is very similar. These slags contain a fairly high amount of unreduced iron oxide. This is a typical sign of the reduction process taking place in the La Tene period furnaces. Furthermore, the presence of CaO and K2O is evident, which are again two compounds typical for the smelting process. Especially K2O, which is present in charcoal and acts as a flux.

These slags can be broadly described as; heavy, dark gray, brown or black heterogeneous silicon complexes. These complexes arise from the tailings part of the iron ore, which is largely mixed with unreduced iron oxides. The oxides are not reduced due to the imperfect direct reduction process.

The temperature which is lower than temperature in the blast furnace is main issue for historical reduction process. Temperature is the main reason that reduction only occurs, but the iron ore is not melted into a liquid. These fluxes form charcoal are main reason why is this type of reduction even possible. Or at least is possible by some measurable degree.

REFERENCES

[1] HLAVA, Miloš, David VÍCH. Laténské osídlení Boskovická. *Pravěk, Supplementum*. 2007, **17** (1), 11-86.
[2] CONSTANTINESCU, Dan, Beatrice Adriana CÂRLAN. A short history of the iron and steel industry in central europe during the roman iron age. *Metal 2016*. 2010, **1**(1), 72-77. ISSN 2694-9296.
[3] TYLECOTE, Ronald, Frank, Brian GILMOUR. *The metallography of early ferrous edge tools and edged weapons.* Oxford, 1986. ISBN 0 86054 401 X.

CONCEPT DESIGN OF A DEVICE FOR H_2S REMOVAL FROM THE SYNTHESIS GAS

Author(s): René SOMMR

Supervisor: prof. Ing. Jozef VLČEK, Ph.D.

Department: Department of Thermal Engineering, Faculty of Materials Science and Technology, VSB – Technical University of Ostrava

Abstract

Purification of raw synthesis gas attracts attention these days. This is due to the expected increase of energetic use of renewable sources and wastes with procedures under reduction conditions, i.e. with the pyrolysis process by plasma treatment. The option to use the available synthesis gas for green energy production features considerable economic and ecological benefits. This design presents two-level adsorption method for effective separation of hydrogen sulfide from the raw synthetic gas or other energy gases. Dry method of cleaning with solid sorbents is described. The cleaning process is made in two temperature phases and with two different sorbents. Carrier gas N_2 serves to transfer the hydrogen sulfide on sorbents under constant flow in reduction atmosphere. The text describes the concept design of presented structural equipment.

Key words:

Synthesis gas, hydrogen sulfide.

1. INTRODUCTION

The term “synthesis gas” (syngas) designates a mixed gas containing dominant components CO, H_2, CO_2, CH_4. The mentioned gas is obtained by various processes from carbonaceous materials. Natural gas, distillation residues from oil and coal processing are today especially used in the industry. Intensive development of technologies for synthesis gas obtaining from renewable sources or wastes is underway with regard to the future expected subsequent decrease of fossil sources use. As synthesis gases, as their title indicates, are an intermediate product for future synthesis of other compounds, their subsequent use determines requirements for the gas composition and purity [1].

Depending on initial carbonaceous material and production process the raw synthesis gas has various composition and contains other additional substances (impurities), in addition to macro components, often even in trace amounts, that shall be often separated before the further use of the gas, as stated by authors Trejbal and Krátký, table 1. The gas purity is important for the use of such gas for energetic purposes from the point of view of the lifetime of the final technology for its processing. Emission limits also often define gas purity requirements that shall be met by the synthesis gas.

Table 1 Composition of raw synthesis gas depending on the raw material and production process. Source: [1]

Raw material	Coal		Distillation residue		Natural gas		Wood		
Process	Koppers Totzek	Lurgi	Shell	Texaco	Lurgi	Lurgi	Li et al	Pfeifer et al	Harris Inc.
Pressure, bar	1	29	54	85	22	21	1	1	9
	output from gasifier	output from gasifier	output from scrubber	output from CO converter	input in CO converter	output from CO converter	air	vapour	vapour+O_2 behind reformer
Composition, % vol.									
H_2	28,7	43,2	45,9	63	76,1	78,3	4,5	43,9	37,5
CO	57	11,6	48,5	1,8	10,6	0,4	13,8	27,2	31,5
CH_4	0,1	10,7	0,5	0,3	3,3	3	2,7	8,3	2
N_2	1,4	0,3	0,2	0,1			62,8		4,5
CO_2	12,6	32,9	4	34,2	10	18,3	16,2	18,8	21,5
H2S	0,2	0,3	0,8	0,6					0,01

Gas, hydrogen sulfide H_2S, is one of acid impurities of synthesis gas that shall be removed. The concept presented here deals with the process of this synthesis gas component removal.

There are various technologies reducing H_2S content in energy gases, as for ex. biogas, landfill gas, synthesis gas etc. H_2S gas is highly poisonous and colorless, heavier than air, well soluble in liquids including water and is hazardous to human health. At low concentrations this gas has an irritating to suffocating effect, smelling like rotten eggs, at high concentrations it rapidly paralyses the

olfactory cells, loses its smell and suffocation occurs. Hydrogen sulfide formed under reducing conditions can reach very high concentrations in the units of tens of $g \cdot m^{-3}$. This concentration is not only hazardous to organisms, but it also affects the machinery and technological equipment and its lifetime (cogeneration units). Individual technologies of H_2S separation differ in their separation principle, process selectivity and robustness in terms of process reliability and resistance to changes in technological and raw material conditions.

For the H_2S separation and reduction of H_2S concentration, the most widespread technologies can be used, including:

- **adsorption** – capturing technology using solid adsorbents,
- **adsorption** - chemical and physical washing by acid that dissolves well the hydrogen sulfide,
- **membrane separation** – penetration through porous materials,
- **biological separation** – chemical separation in biological reactors using appropriate bacteria.

When studying and assessing the appropriate method of H_2S separation it was found that there is no universal method of separation. Each method is specific and suitable for a particular synthesis gas application.

The solution presented here is a "dry" adsorption separation method combining two solid sorbents in two temperature zones. The advantage of this method lies in the availability, stability and regeneration of the sorbent used with low technical complexity and maintenance of the technological equipment. At the same time, it is necessary to evaluate the energy consumption of the technology, where the high-temperature adsorption does not require the costly purified energy gas to cool. The nature of the sorbent used in terms of its environmental impact is another factor. All these factors result into an economic consideration of the suitability of the chosen H_2S separation technology.

2. DESIGN OF APPARATUS FOR H_2S REMOVAL

An apparatus for H_2S removal enabling testing of chosen sorbents (CaO and Fe_2O_3) and measuring of all necessary data of this process was designed based on long-term experience in the area of flue gas cleaning for hazardous waste incineration in practice.

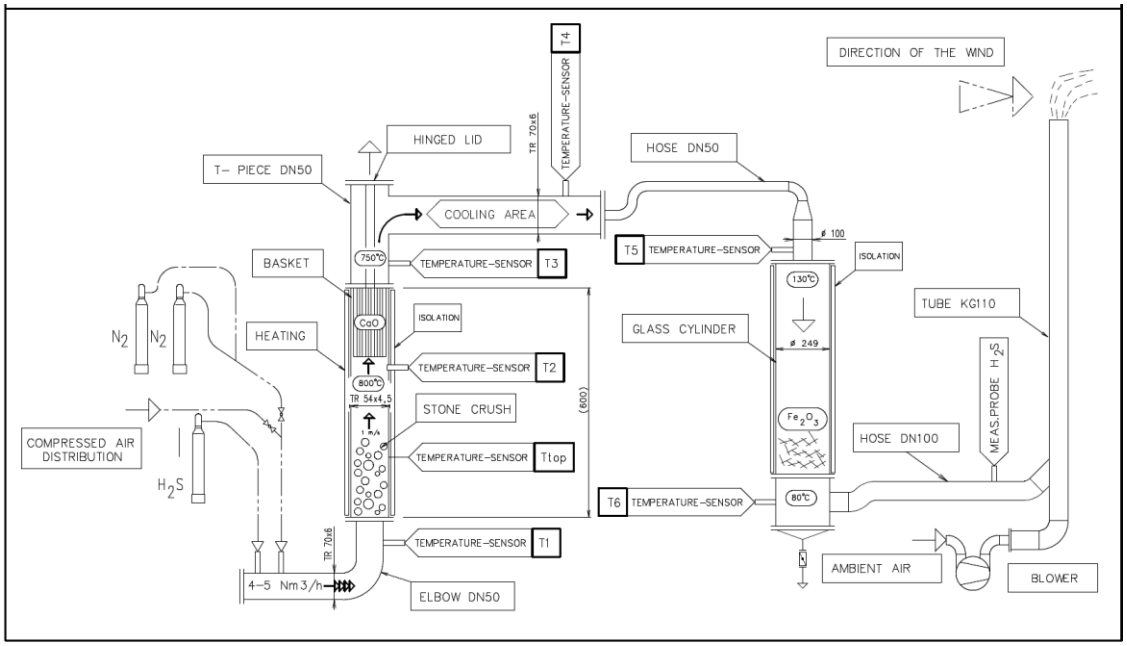

Figure 1 Scheme of testing apparatus

The figure 1 shows the hermetically closed testing apparatus designed by the author which is made of two vertical reactors for the input of sorbents, at the inlet there is a supply of N_2carrier gas and

at the outlet there is a blower that will carry and dilute the mixed gas from the apparatus into the surroundings. It must be emphasized that this is a testing apparatus, in real conditions the gas from the outlet of the cleaning apparatus will be taken for further processing.

The first reactor is designed from the steel TR 54x4,5 with AISI 309 quality and covered with an insulation with resistance wire for the apparatus heating controlled manually with an autotransformer. Half of the reactor is filled with aggregate in order to accumulate the thermal energy; the carrier gas will pass through this aggregate and be heated to the desired temperature. Under the hinged lid at the top of the reactor, a stainless steel sieve basket will be placed designed for insertion of the sorbent to be tested.

The second reactor is a glass cylinder with an inner diameter of 249 mm in which a perforated stainless steel plate bed will be used to situate the second tested sorbent. Both reactors will be connected with a flexible hose with a section for gas cooling with small after-cooling gas-air exchanger. The carrier gas and hydrogen sulfide flows through the apparatus will be measured with a float flowmeter. The whole apparatus will be equipped with temperature sensors for continuous temperature measurement in individual temperatures zones as the gas passes through the apparatus.

The apparatus is designed for the gas flow approx. 4 to 5 $Nm^{3}\cdot hr^{-1}$ with the least possible pressure loss in terms of the layout and performance.

The apparatus shall be situated on two transport euro pallets with regard to its mobile handling and simple transfer to the suitable testing point, as stated in the figure 2.

Figure 2 Testing apparatus

The synthesis gas purification process in the designed apparatus can be divided in two phases as described below.

I-phase means testing of CaO saturation in the basket of specific grain size and mass in the reactor at the temperature 700 to 900°C. At this high-temperature H_2S reduction using the calcium oxide the following reaction occurs (1):

$$CaO + H_2S \rightarrow CaS + H_2O \quad (1)$$

The temperature and water vapor content in purified gas considerably affect the reaction of (1) CaO and H_2S. Authors Solich a kol. have described the equilibrium concentration of H_2S for the reaction with CaO for various temperatures and water content.[2]

The speed of CaO and H_2S reaction at the high-temperature reduction is affected with further factors.
Properties of CaO itself, grain size, porosity and external surface are the fundamental factors. In addition, they include also the composition of purified gas. The concentration of individual components, namely of H_2S itself and the effect of H_2O have been mentioned. The final factors affecting the course of the reaction are temperature, pressure and flow rate through the adsorbent layer itself. [3]

The used sorbent is not regenerated but landfilled. The calcium sulphide formed during the reaction described above is unstable and unsuitable substance for landfilling and must therefore be stabilized by an oxidation reaction (2):

$$CaS + 2O_2 \rightarrow CaSO_4 \quad (2)$$

The resulting product - calcium sulphate, is solid, poorly soluble and chemically nearly inert and suitable for landfilling. [3]

II-phase means the saturation of iron oxides on the metal bed Fe_2O_3 (layer of corroded cuts) at given grain size and mass in the reactor at temperatures 100 to 200°C. It can pass through various transformations for Fe_3O_4, FeO to Fe in the reduction atmosphere of Fe_2O_3. Here, Fe_3O_4 is the most stable oxide form. [4] The following reaction occurs (3):

$$Fe_3O_4 + H_2S \leftrightarrow FeS + Fe_2O_3 + H_2O \quad (3)$$

The chemical affinity of iron and iron oxides for sulphur is considerable. Sorbents based on Fe_2O_3 for H_2S removal from the energy gas are known for may years but in processes at low temperatures.

Fe_2O_3 has many benefits, it is available in iron ores or as a waste product, it is relatively inexpensive, requiring no chemical treatment. After its use the sorbent can be regenerated with air or a mixture of water vapor and air, the regenerated sorbent is used repeatedly and when the regeneration can no longer be carried out then it can be landfilled.

During the test, according to the previously approved work schedule, the test apparatus will be heated first, the flow rate of the carrier gas N_2 will be changed, the input concentration of H_2S will be changed and the reaction time for saturation of the sorbents in the individual reactors will be changed.

3. CONCLUSION

Further texts are to describe in detail the evaluation of H_2S removal from the synthesis gas, using weighing tested samples and measuring the input and output H_2S concentration from the apparatus using an emission analyzer.

The H_2S removal method suitability will be also assessed based on the regeneration of used sorbents and evaluation of their impact on the environment when their lifetime expires.

ACKNOWLEDGEMENT

This work was supported by project SP2023/034 Research and development of composite multifunctional materials for sustainable progress.

REFERENCES

[1] TREJBAL, Jiří, Lukáš KRÁTKÝ. Výroba, úprava a použití syntézních plynů z různých surovin. *Chemické listy*. 2020, **114**, 737-745.
[2] SOLICH, M., S. SKOBLJA, B. KOUTSKÝ, J. MALECHA. Možnosti vysokoteplotního odstraňování sulfanu při zplyňování biomasy a alternativních paliv. *Energie z biomasy*. Brno, 2004, **III**.
[3] HARTMAN, Miloslav, Karel SVOBODA, Otakar TRNKA, Václav VESELÝ. Reakce vápenatých a hořečnatých materiálů při vysokoteplotním odsiřování spalin a energetického plynu. *Chemické listy*. 2002, **96**, 777-783.
[4] HARTMAN, Miloslav, Karel SVOBODA, Otakar TRNKA, Václav VESELÝ. Odsiřování horkého generátorového plynu tuhými sorbenty. *Chemické listy*. 1999, **93**, 99-106.

PREDICTION OF EMISSION LOAD FROM COMBUSTION PROCESSES OF FUELS PREPARED FROM WASTE

Author(s): Radim SZKANDERA

Supervisor: prof. Ing. Jozef VLČEK, Ph.D.

Department: Department of Thermal Engineering, Faculty of Materials Science and Technology, VSB – Technical University of Ostrava

Abstract

This study investigates the combustion process of RDF in waste incinerators, specifically the transformation of fuel elements into emissions. The research offers valuable insights for combustion and flue gas treatment technology selection and operation optimization. The study also introduces a calculation tool that provides a comprehensive analysis of combustion processes from fuel elements composition to emission generation, and mitigation techniques, facilitating decision-making in selection and facility design of incineration technology, and regulatory compliance.

Key words:

Best Available Techniques, Refuse Derived Fuel, Emission Assessment, waste combustion.

1. INTRODUCTION

The escalating global demand for energy, coupled with growing climate change concerns and the need for sustainable waste management, has led to a surge of interest in Waste-to-Energy (WtE) technologies. One of the most common WtE methods is the direct combustion of fuels derived from waste, such as Municipal Solid Waste (MSW) converted into Refuse Derived Fuel (RDF). The combustion process involves the thermal conversion of waste in a boiler into valuable energy. A comprehensive understanding of the combustion processes, emission generation, and their mitigation at the source is important for efficient and environmentally friendly operation of waste incineration plants. This work aims to investigate the transformation of elemental constituents in the fuel into emissions during combustion, devise strategies to reduce emissions below given emission limits, and utilize knowledge of emission limits from the Best Available Techniques (BAT) reference document [1] for plants with a fuel capacity below and above 3 tons per hour (tph). By evaluating expected differences in emission limits, this study seeks to provide insights for selecting appropriate technologies considering the size of the facilities and flue gas cleaning systems for waste incinerators using RDF as fuel.

For effective operation of waste incinerators, thorough knowledge of combustion processes, emission generation factors, and available emission mitigation technologies is essential [2]. Such understanding allows optimization of plant performance and ensures efficient energy recovery while minimizing environmental impacts and optimizing cost for flue gas treatment. By comparing the emission limits for BAT in facilities with fuel capacities below and above 3 tph [1] , this work contributes valuable insights for selecting appropriate technologies and plant size concept for various waste combustion scenarios.

The development of a calculation tool is essential for the procedure of project development in the waste-to-energy sector. This tool will enable stakeholders and its employee to predict emission loads accurately and efficiently, providing an asset for anticipating and evaluating the costs associated with emission control. By understanding the behavior of the combustion process and flue gas treatment, the tool will assist in selecting the most suitable technology for a given projects. The selection of the right technology is a crucial step in the investment decision-making process, directly impacting operational costs and environmental performance. Furthermore, the tool will make the project development process faster, facilitating quicker iterations and providing a solid foundation for informed decision-makers.

The result of this work is a comprehensive analysis of combustion processes, emission generation, and emission mitigation techniques in the form of a computational calculator or described computational algorithm from fuel to emissions. By examining differences in BAT emission limits in facilities with varying fuel capacity, the work aims to provide information for decision-making processes in designing facilities, selecting technologies, and complying with legal regulations.

2. Emission calculation tool

The Emissions Calculator is a versatile calculation tool that allows users to enter fuel analysis data for various solid fuel types. By incorporating empirical conversion ratios between fuel elements and emissions produced by selected combustion processes, such as grate or fluidized bed systems, the calculator can evaluate the combustion process and predict the raw gas emissions produced, prior to flue gas cleaning.

The emission calculator also takes into account the knowledge and limitations of the different flue gas cleaning mechanisms. Users can thus determine the efficiency, consumption of various sorbents and clean gas concentration resulting from the implementation of emission control technologies such as deNOx systems, acid gas concentration reduction and activated carbon injection. By comparing the calculated emission concentrations with the established emission limits, users can ensure compliance with regulatory requirements or evaluate the margin for safe long-term operation or possible fuel switching.

The emissions calculator serves as a valuable decision-making tool for optimizing operating costs, a critical aspect of any investment decision. As shown in the process flow diagram in figure 1 providing a comprehensive analysis of the emissions produced and the effectiveness of various emission control technologies, the calculator allows users to identify areas for improvement and cost optimization.

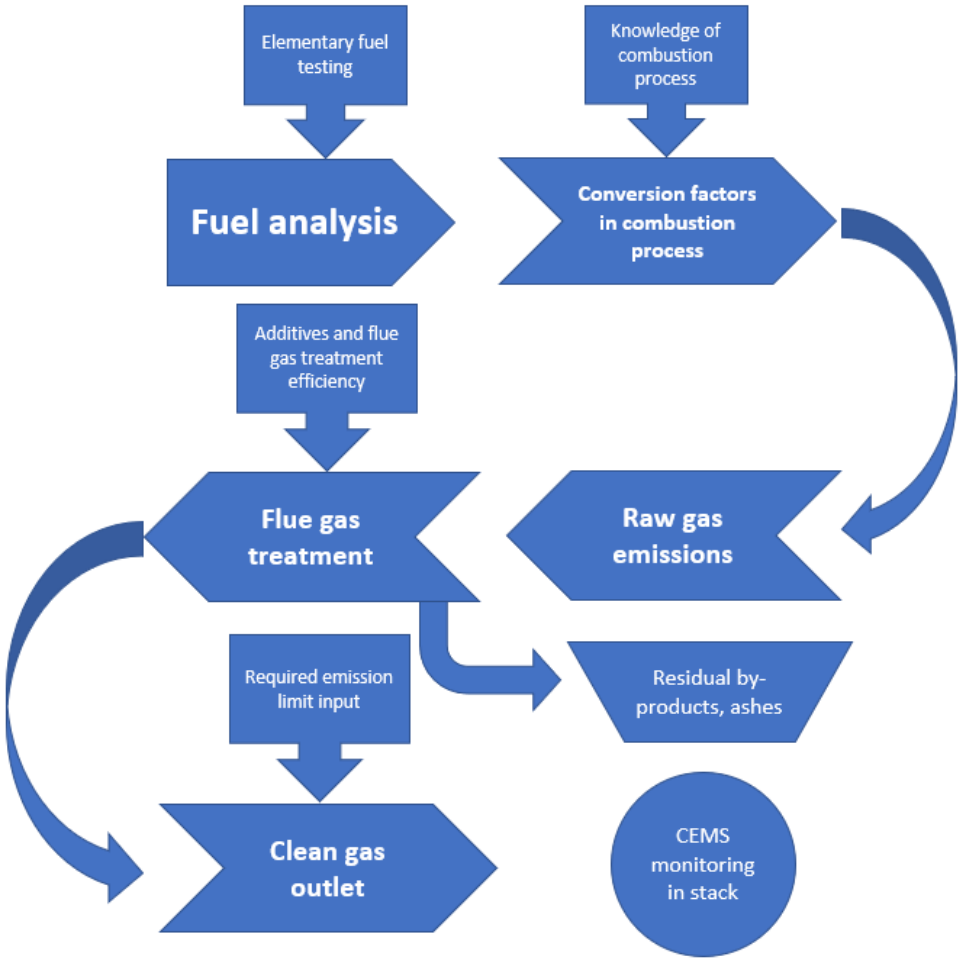

Figure 1 Algorithm of process from fuel to emissions. Source: (own)

At glance, we need to understand fuel elementary analysis of fuel which goes into combustion system. In the combustion system, there is mechanism of conversion of fuel elements into emissions, which is valid for ashes, fuel nitrogen to NOx emissions, and so on. These conversions are applied for all fuel elements and emissions are made within certain conversion factors. Raw gas concentration is then important parameter for flue gas treatment technology selection and its consumable consumption,

which are going to be evaluated with widely used methods for different emission decrease technologies. We can easily demonstrate the concept in deNOx with following paragraph.

One significant element that this calculator can handle is Nitrogen Oxides (NOx) emissions. NOx is often produced from the nitrogen in the fuel used, and it's a major pollutant with harmful effects on both human health and the environment. The calculator can determine the amount of NOx created from fuel nitrogen and combustion air and evaluate the effectiveness of various deNOx technologies [3]. These technologies include Selective Catalytic Reduction (SCR), Selective Non-Catalytic Reduction (SNCR), and other emerging technologies [4]. SCR uses a catalyst and a reducing agent of ammonia water to convert NOx into nitrogen and water. SNCR, on the other hand, uses a reducing agent of urea mixture with water but no catalyst, which has implications for its efficiency and operating temperature range. As shown in Figure 2 below, it can also compute the amount of additives required for these technologies and the potential impact on the final emissions.

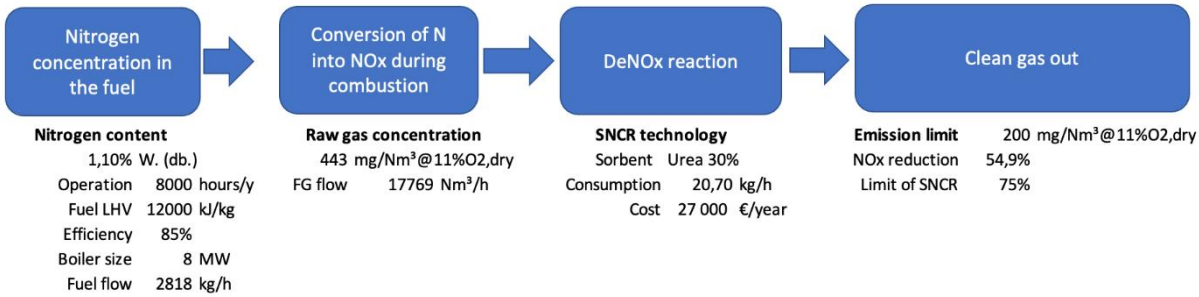

Figure 2 Process of DeNOx for model case. Source: (own)

As an example, we can use provided fuel analysis with nitrogen content of 1.1. % weight in dry base sample for a modeling this scenario. For 8 MWt boiler, we need 2818 $kg \cdot h^{-1}$ of fuel to generate enough power. From fuel analysis of the sample, we have concentration of nitrogen, which is in this case resulting into 443 mg/Nm^3 of NOx concentration with fluegas flow of 17 769 Nm^3/hour. To decrease into the emission limit here set to 200 mg/Nm^3, we need to feed 20.7 kg/h of sorbent Urea 30 % into SNCR system. This setup will result into overall cost of 27 000 € per year of continuous 8 000 hours yearly operation. According to this model, we can similarly evaluate different fuel concentrations, methods of deNOx nor sorbent reagent selection. We also can evaluate risk associated with this method, As we see quite a big margin between NOx reduction and technology potential at level up to 75 % [3], we can clearly mention, that technology can withstand stricter emission limits or higher concentration in the fuel, taking in mind fuel range variation possibility.

By incorporating a deNOx technology selection feature, the emissions calculator could evaluate the fuel analysis data, calculate the potential NOx emissions, and then suggest the most suitable deNOx technology for that specific scenario. It could take into account various factors like the expected NOx concentration, the operating conditions, the cost of implementation, and the efficiency of the technology.

In conclusion, such an emissions calculator would be a comprehensive tool that not only provides valuable insights into raw gas emissions but also assists in choosing the best flue gas cleaning technology. It's a one-stop solution for emission calculation and control, thereby making it an invaluable resource for all stakeholders in waste-to-energy projects and RDF combustion processes.

3. CONCLUSION

To address this problem of predicting the emissions burden, a calculator could be developed to determine the operating costs associated with different technologies and abatement strategies in waste incinerators [5]. The calculator would take into account various parameters such as

- Plant performance
- Fuel composition
- Boiler size and design
- DeNOx abatement technology, acid gas decrease, AC injection
- Reagents consumptions
- Bottom ash, fly ash and other by-products management
- Required emission limits
- Energy consumption and service costs

- Cost of consumables such as chemicals and filter media.

Once the relevant data are entered, the calculator would provide emissions and OPEX predictions for various scenarios when fuel, power, etc. are changed, allowing operators and plant developers to compare and evaluate their options in advance of actual construction. This would help them determine the most cost-effective and environmentally responsible solution for an incinerator or other solid fuel thermal processing facility. The development of an OPEX calculator can be complex because it requires a thorough understanding of the factors affecting the operating costs of incinerators as well as expertise in abatement technologies. The final output visualization can then be graphed into one overview of complex technology with a lot of possible data from financial or operational perspective.

ACKNOWLEDGEMENT

This work was supported by project SP2023/034 Research and development of composite multifunctional materials for sustainable progress.

REFERENCES

[1] European Commission. (2019). Best Available Techniques (BAT) Reference Document for Waste Incineration. Joint Research Centre. Available at: https://eippcb.jrc.ec.europa.eu/sites/default/files/2020-01/JRC118637_WI_Bref_2019_published_0.pdf [Accessed: 2023-05-11].

[2] GAŁKO, Grzegorz, Izabela MAZUR, Michał REJDAK, Barbara JAGUSTYN, Joanna HRABAK, Miloud OUADI, Hessam JAHANGIRI and Marcin SAJDAK. Evaluation of alternative refuse-derived fuel use as a valuable resource in various valorised applications. Energy [online]. 2023, 263. ISSN 03605442. Available at: https://doi.org/10.1016/j.energy.2022.125920 [Accessed: 2023-05-11]

[3] ZHAO, Shilin, Junlin PENG, Runqi GE, Siyu WU, Kehui ZENG, Huajun HUANG, Kaibo YANG a Zhiqiang SUN. Research progress on selective catalytic reduction (SCR) catalysts for NO removal from coal-fired flue gas. Fuel Processing Technology [online]. 2022, 236. ISSN 03783820. Available at: https://doi.org/10.1016/j.fuproc.2022.107432 [Accessed 2023-05-11]

[4] ZHOU, Zhijian, Jian CHANG a Xin WANG. Large eddy simulation of hydrodynamics and deNOx process in a coal-fired power plant SCR system. Journal of Environmental Management [online]. 2022, 320. ISSN 03014797. Available at: https://doi.org/10.1016/j.jenvman.2022.115800 [Accessed 2023-05-11]

[5] MARGALLO, M., A. DOMINGUEZ-RAMOS, R. ALDACO, A. BALA, P. FULLANA a A. IRABIEN. Environmental sustainability assessment in the process industry: A case study of waste-to-energy plants in Spain. Resources, Conservation and Recycling [online]. 2014, 93, 144-155. ISSN 09213449. Available at: https://doi.org/10.1016/j.resconrec.2014.09.014 [Accessed 2023-05-11]

Chemical Metallurgy

METHODS OF THERMAL ANALYSIS AND THEIR USE IN THE DETERMINATION OF THERMODYNAMIC PROPERTIES OF MATERIALS

Author(s): Petr DOSTÁL

Supervisor: prof. Ing. Bedřich SMETANA, Ph.D.

Department: Department of Chemistry and Physico-chemical Processes, Faculty of Materials Science and Technology, VSB – Technical University of Ostrava

Abstract

Thermal analysis methods are one of the ways to determine the thermodynamic properties of materials such as heat capacities and their dependence on temperature, phase transition temperatures and "latent" heat of phase transformations. Of the whole group, differential thermal analysis (DTA), differential scanning calorimetry (DSC), thermogravimetry (TG) and calorimetry are of great importance.

Key words:

Thermal analysis, heat capacity, phase change temperature.

1. INTRODUCTION

Steel is still one of the most widely used technical materials. With this material, more and more demands are placed on its properties. Despite the fact that many authors deal with this area, there is still a lack of original experimental data on these systems. Therefore, it is very important to constantly supplement and refine this data.

The content of Fe and alloying elements and additives, such as carbon, nitrogen, oxygen and others, significantly affects the properties of ferrous alloys. The most important mentioned alloying element is carbon. Any changes in the concentration of this element in the alloy have a great influence on the resulting properties of steels. For this reason, the Fe-C binary system was chosen as the basic system for studying the behavior of steels. Several types of binary diagrams were created for it, compiled by authors e.g. [1] based on thermodynamic calculations. Another possibility, which was discussed by a group of authors e.g. [2, 3, 4], was to compare experimentally obtained data with theoretical thermodynamic calculations. These comparisons revealed very significant differences between the measured and experimental data.

2. THERMAL ANALYSIS

Thermal Analysis is a group of methods that monitor the change in the state of the examined material by measuring its certain properties as a function of temperature or time [5]. The monitored properties include, for example, thermodynamic properties (temperature, heat, enthalpy, mass, volume). Various physical or chemical processes occurring during a change in temperature or also depending on time cause changes in the monitored property of the investigated substance. Methods of thermal analysis are important sources of information on the properties of not only solids. These are dynamic methods that obtain information about the course of changes in the state of the sample, which is most often obtained by constant (linear) heating of the sample. Changes in the state of the sample are determined directly by measuring the selected physical property or indirectly by measuring the property of the environment surrounding the sample [6, 5, 7].

Classification of thermal analysis methods [23]:

a) Methods associated with the change of thermal properties of samples – these methods include, for example, direct thermal analysis (Heating/Cooling Curve determination), Differential Thermal Analysis (DTA), Heat-flux Differential Scanning Caloriemtry (DCC), differential scanning calorimetry (DSC)
b) (b) Methods involving changes in the mass of components contained in the sample — such methods include Thermogravimetry (TG), Evolved Gas Analysis (EGA), Differential Pressure Analysis
c) Methods associated with the change of other properties of the sample – these methods include, for example, Thermodilatometry, TMA (Thermomechanical Analysis), Emanation Thermal Analysis, and others

3. METHODS OF OBTAINING HEAT CAPACITIES

a. "Continuous" method

It is the most commonly used method, which consists of three DSC measurements. The first measurement, the blank, takes place with an empty measuring and reference crucible. The second measurement is carried out with a standard of known weight and known heat capacity in the measuring crucible and with an empty reference crucible. The last measurement is made with the sample to be examined. All measurements are carried out according to the same temperature program – isothermal endurance at the initial temperature Ti, heating at constant speed and isothermal endurance at temperature Tf. The measurement process is graphically shown in Fig. 1 (the segments Ab, AC and AS are evaluated).

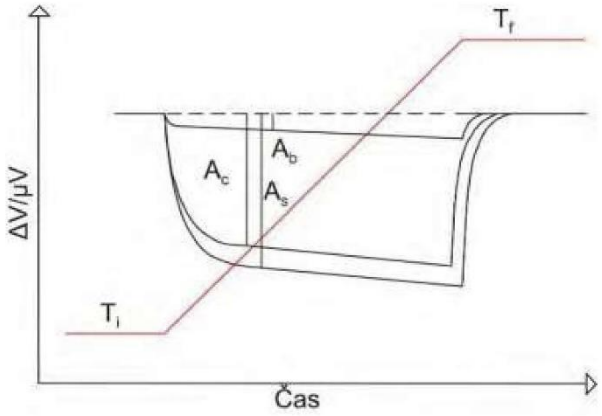

Fig. 1 Graphically illustrated course of heat capacity measurement by the "continuous" method. Source: [8]

The heat capacity of the sample can then be calculated using formula (1):

$$C_p = C_{pc} \cdot \frac{m_c(A_S - A_b)}{m_s(A_c - A_b)} \quad (1)$$

where:
C_p – heat capacity of the measured sample [J/K.g]
C_{pc} – heat capacity of reference sample [J/K.g]
m_C – weight of measured sample [g]
m_s – weight of reference sample [g]
A_b – blank amplitude [μV]
A_c – amplitude of measured sample [μV]

A_s – amplitude of reference sample [μV]

b. Stepwise" method

Also with this method, three measurements are carried out – empty-crucible, standard and sample. The temperature regime here represents the alternation of isothermal endurance with linear heating speed. The measurement process is graphically shown in Fig. 2 (the area is evaluated)

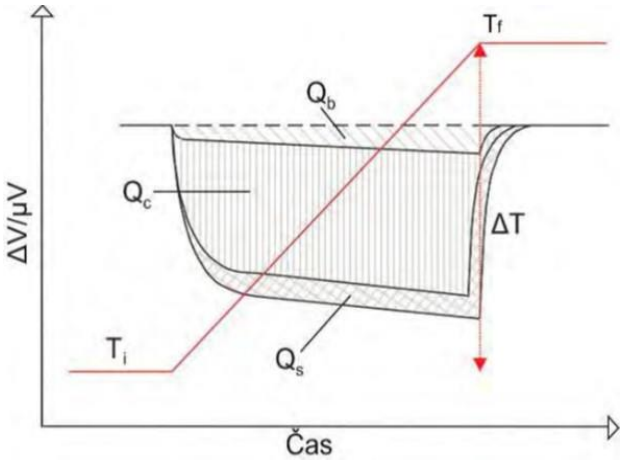

Fig. 2 Graphically illustrated course of heat capacity measurement by the "stepwise" method. Source: [8]

Using the above method, we obtain the mean value of the heat capacity, which can be calculated using the formula (2) [8].

$$\overline{C}_p = \overline{C}_{pc} \cdot \frac{m_c \cdot (Q_s - Q_b)}{m_s \cdot (Q_c - Q_b)} \quad \textbf{(2)}$$

where:
C_p – mean value of heat capacity of the measured sample [J/K.g]
C_{pc} – mean heat capacity of the reference sample [J/K.g]
m_c – weight of the measured sample [g]
m_s – weight of standard (reference) sample [g]
Q_b – area proportional to the heat received by the system when measuring blank [μV.s]
Q_c – area proportional to the heat received by the measured sample [μV.s]
Q_s – area proportional to the heat received by the standard [μV.s]

4. EXPERIMENTAL PART

The experimental part of the thesis will deal with the study of heat capacities (their temperature dependencies) and other thermodynamic functions of real polycomponent systems and selected model systems based on Fe by thermal analysis methods. New original experimental data will be obtained for solid phase and melt in the temperature range of 100-1580 °C.

Samples of real steel grades and model steel will be used for the study. Model steels (based on Fe-C-X; X=Cr,Ni) will be prepared with graduated contents of selected elements (especially Cr, Ni). The planned composition of steels can be characterized by the maximum content of elements in alloys: carbon content max. 2 wt. %, content Mn up to 2 wt. %, content of Cr and Ni up to 5 wt. %.

Three types of instruments will be used to study the selected thermodynamic properties - Setaram SETSYS 18TM, Setaram MHTC 96 and Netzsch STA 449 F3 Jupiter.

5. CONCLUSION

The aim of the work will be to obtain original experimental data and knowledge about the behavior of Fe-based alloys, based on the study of heat capacities in solid phase and melt, based on the study of latent heats of phase transformations and other thermodynamic functions in a wide temperature range (100-1580 °C). The partial goal is to obtain temperatures of phase transformations. The connection of chemical and phase composition and structure with the obtained data will be assessed. The conformity or non-conformity of the experimental data obtained will be assessed. The influence of chemical composition on the agreement of experimental data with the results of the calculation of empirical relationships and software will be verified.

The obtained data will be used as input parameters of mathematical models simulating casting and subsequent solidification of these materials. The data that will be obtained for the high-temperature area (above 1200°C) can be used in the foundry industry to set optimal casting conditions and solidification conditions of the produced steels. The data obtained for the low-temperature range (below 1200 °C) can be further used in the field of subsequent thermal and mechanical treatment of steel alloys.

ACKNOWLEDGEMENT

The work was supported by the specific university research of the Ministry of Education, Youth and Sports of the Czech Republic SP2023/034 and project DMS CZ.02.1.01/0.0/0.0/17_049/0008399.

REFERENCES

[1] GUSTAVSON, P., A Thermodynamic Evaluation of the Fe-C System. *Scandinavian Journal of Metallurggy. 1985*, **50** (3), 101-106.
[2] BENZ, M.G., ELLIOTT, J.F. The Austenite Solidus and Revised Iron-Carbon Diagram. *Transactional of the metallurgical society of AIMEI*. 1961, **221**, 323-330.
[3] CHICCO, B., THORPE, W. R. A Further Determination of the Austenite Solidus of the Fe-C System. *Metallurgical Transactions.* 1983, **14** (2), 312-314.
[4] HASEBE, M., OHTANI, H., NISHIZAWA, T. Effect of Magnetic Transition on Solubility of Carbon in bcc Fe and fcc Co-Ni Alloys. *Metallurgical Transactions*. 1985, 16 (5), 913-921.
[5] ROSICKÝ, J. *Termická analýza,* Dočasná vysokoškolská učebnice, Praha 1989
[6] ŽALUDOVÁ M. Studium fázových transformací vybraných kovových systémů na bázi Fe a Fe – C, *Teze disertační práce*, VŠB-TU Ostrava, 2012
[7] DOČEKALOVÁ, *Teze disertační práce*, Katedra fyzikální chemie a teorie technologických pochodů, VŠB – TU Ostrava, Ostrava 2007
[8] SETARAM Instrumentation. Brožura k zařízení MHTC 96. Francie. 2009. 121 s.

EFFECT OF BORON OXIDE ON THE RHEOLOGICAL PROPERTIES OF GLASS-BASED OXIDE SYSTEM $CaO-MgO-SiO_2-Al_2O_3-B_2O_3$

Author: Barbora ENGL

Supervisor: doc. Ing. Lenka ŘEHÁČKOVÁ, Ph.D.

Department: Department of Chemistry and Physico-Chemical Processes, Faculty of Materials Science and Technology, VSB – Technical University of Ostrava

Abstract

To ensure a smooth production process in the glass industry, data on a wide range of glass properties is required. Knowledge of the liquidus temperature, crystallization temperature and viscosity of the system is essential in manufacturing. This work investigates the effect of B_2O_3 on the above properties of the glass oxide system $CaO-MgO-SiO_2-Al_2O_3-B_2O_3$. The flow properties and the dependence of the dynamic viscosity of the system on temperature and change in chemical composition were investigated. An Anton Paar FRS 1600 high-temperature viscometer was used for the measurements. At 1 550 °C, the samples exhibited Newtonian behaviour, and the viscosity decreased exponentially with increasing temperature and with the addition of B_2O_3.

Key words:

Oxide system, liquidus temperature, viscosity, borosilicate glass, boron oxide.

1. INTRODUCTION

Borosilicate glasses show favourable properties such as mechanical and thermal resistance; therefore, they are widely used (laboratory glass, heat-resistant pharmaceutical glass, sealing glass, etc.). Studies [1,2] dealt with a new type of borosilicate glass with excellent chemical stability and high ultraviolet transmittance to develop optical materials with better performance and higher transparency in the ultraviolet band. Most colourless optical glass has high transmittance in the visible light band and varying degrees of absorption in the ultraviolet light band. Quartz glass is the most common UV-transparent material but has demanding production conditions and high production costs. The research addresses the effect of Al_2O_3 and B_2O_3 on the oxide system of glass. It was found that increasing the amount of Al_2O_3 decreases the chemical stability and UV transmittance, and the addition of B_2O_3 showed the opposite trend. Another study [3,4] dealt with sealing glass in fuel cells, where silicate glass with the addition of B_2O_3 was used. Boron oxide has favourable properties - it reduces viscosity and tends to crystallise. It was found that adding boron oxide improved the chemical stability of the system, the glass surface was strengthened (mechanical strength), and the glass core retained its elastic state. Publication [5] deals with the wettability of glass putty on metal samples based on the SiO_2/B_2O_3 ratio. Studies [6,7] addressed the effect of alkalinity (CaO/SiO_2 mass ratio) and B_2O_3 on the viscosity and structure of the oxide system. The results show that increasing the alkalinity decreased the viscosity of the melt SiO_2-B_2O_3-Al_2O_3-MgO. The addition of B_2O_3 also reduced the system's viscosity and break temperature. B_2O_3 forms trihedral and tetrahedral structural units in the oxidic system. A study [8,9] dealing with fire-resistant borosilicate glass states that the content of silica in this type of glass is very high, and the alkali content is very low - due to this, it has good optical performance, electrical performance, coefficient of thermal expansion, high hardness, and durability. The problem is high melting temperatures, long clarification times, and high viscosity. It was found that the optimal composition of the glass sample, which has excellent thermal properties and is suitable for production, is composed of 82.7 mol% SiO_2, 12.2 mol% B_2O_3, 4 mol% Na_2O and 1.1 mol% CaO. In another study [10,11,12], they dealt with the influence of B_2O_3 and the Cao/SiO_2 ratio on the viscosity and structure of the oxide glass system. In general, it was concluded that adding B_2O_3 reduced the viscosity, fracture temperatures, and activation energy for viscous flow if the crystallisation phases were the same in the solid-liquid coexisting region. With a higher CaO/SiO_2 ratio, the viscosity decreased, and the fracture temperature with activation energy affected the crystallisation behaviour. Based on the information obtained from the mentioned publications, which describe the difficulty of the production process and the increase of production costs due to higher melting temperatures and viscosity values of the oxide glass system, this work investigates

the effect of different addition of B_2O_3 (0 to 30 wt%) on the softening temperature, liquidus temperature, flow behaviour, viscosity of the SiO_2-CaO-MgO-Al_2O_3-B_2O_3 oxide glass system.

2. EXPERIMENTAL

2.1 Sample preparation

An oxide system based on CaO-MgO-SiO_2-Al_2O_3-B_2O_3 glass with the addition of 0, 5, 15 and 30 wt% boron oxide (samples 1 - 4) was subjected to an experimental study of rheological properties. The experiment aimed to investigate the effect of different amounts of boron oxide on the oxide system, specifically on the system's viscosity, the start and end softening temperature and the liquidus temperature.

Oxide systems were prepared from pure chemicals in powder form of analytical purity with a minimum content of 96.5% of the given substance. The system's total weight was 56 g; based on the predetermined composition in wt%, the loadings of individual substances were determined (Table 1). The mixture of pure oxides was mixed after weighing, ground in parts in a laboratory mill and remixed to ensure homogenization of the system.

2.2 Experimental method

An Anton Paar FRS 1600 high-temperature rotational viscometer was used to measure the rheological properties of the glass-based system. This device comprises two main parts, the laboratory furnace and the DSR 301 measuring head. The other parts of the device are the upper and lower corundum shaft, graphite spindle, and graphite cup filled with the given substance. During the measurement, the cup with the sample fixed on the lower shaft is inserted into the furnace. A spindle that rotates at a frequency of 150 rpm is inserted into the crucible with the sample. The measuring head of the device measures the spindle torque with a resolution of 0.1 nNm. Other parameters recorded are the normal force acting on the sample's surface (resolution 0.5 mN) and the position of the spindle with a resolution of 1 μm. The measurement occurred in an inert gas flow atmosphere, namely nitrogen (purity 4N), with a flow rate of 150 $dm^3 \cdot h^{-1}$.

During heating to the maximum temperature, the position of the spindle and the normal force applied perpendicular to the sample surface were monitored. Softening start, softening end, and liquidus temperatures were subsequently determined from the given dependencies. The maximum temperature of glass-based oxide systems was 1 550 °C. At this temperature, the flow behaviour of the systems was investigated. Subsequently, the temperature dependence of the dynamic viscosity was measured during cooling at a rate of 3 $°C \cdot min^{-1}$ from a temperature of 1 550 °C to a temperature at which the given system showed a viscosity of 120 Pa·s.

Table 1 Examined samples, composition of individual components in wt%. Source:(own)

Sample	SiO_2	CaO	MgO	Al_2O_3	B_2O_3
1	64.6	15.9	10.0	9.5	0.0
2	61.1	14.4	10.0	9.5	5.0
3	53.9	11.6	10.0	9.5	15.0
4	43.2	7.3	10.0	9.5	30.0

3. RESULTS AND DISCUSSION

3.1 Softening and liquidus temperatures

Softening start temperature, softening end temperature and liquidus temperature were evaluated from the temperature dependencies of the spindle position and normal force. These temperatures for all samples are listed in Table 2, and an illustration of the dependencies for sample 2 is shown in Figure 1. The initial softening temperature was assessed based on a 1% drop in the spindle position, and the final softening temperature was a 40% drop in the spindle position. The liquidus temperature was defined as the temperature at which the spindle reached the measuring position and the zero value of the normal force.

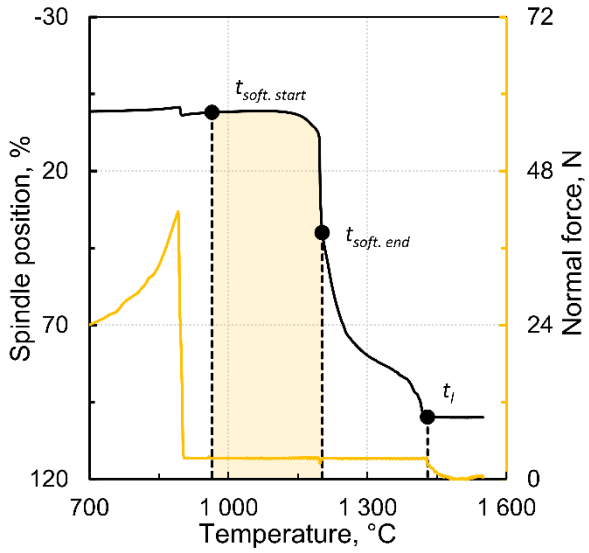

Figure 1 Temperature dependencies of spindle position and normal force. Source (own)

Table 2 Liquidus temperature, softening start and softening end temperatures of the samples analysed. Source: (own)

Sample	$t_{soft.\ start}$ [°C]	$t_{soft.\ end}$ [°C]	$t_{liquidus}$ [°C]
1	1 291	1 313	1 510
2	1 160	1 203	1 430
3	1 010	1 075	1 425
4	896	1 046	1 332

3.2 Flow curve

At the maximum temperature of 1 550 °C, the dependence of the dynamic viscosity on the shear rate and the dependence of the shear stress on the shear rate were monitored. Based on Figure 2 (for sample 2), we can see that the shear stress increases linearly with the shear rate, and the dynamic viscosity is constant. Therefore, one can conclude that the system exhibits Newtonian behaviour.

The flow curves and viscosity curves of the other samples of glass-based oxide systems had a similar character.

3.3 Dependencies of viscosity on temperature and chemical composition

Figure 3 shows the temperature dependencies of viscosity, where we can see the exponential growth of viscosity with decreasing temperature and a noticeable change in dynamic viscosity with a change in chemical composition. Besides, dynamic viscosity decreases with increasing B_2O_3 content.

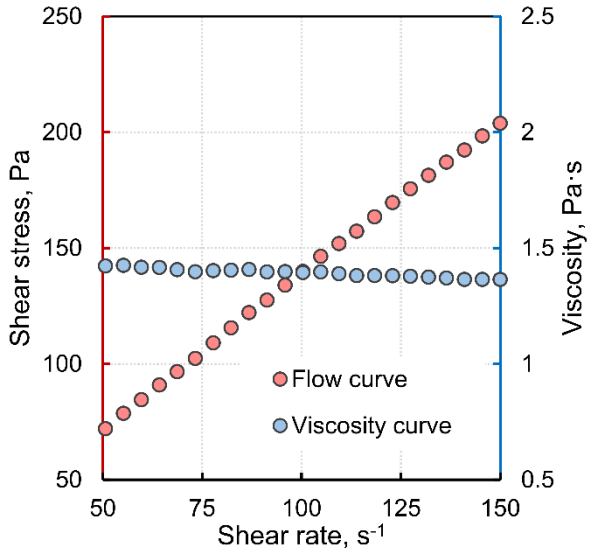

Figure 2 Flow curve and viscosity curve of sample 2. Source: (own)

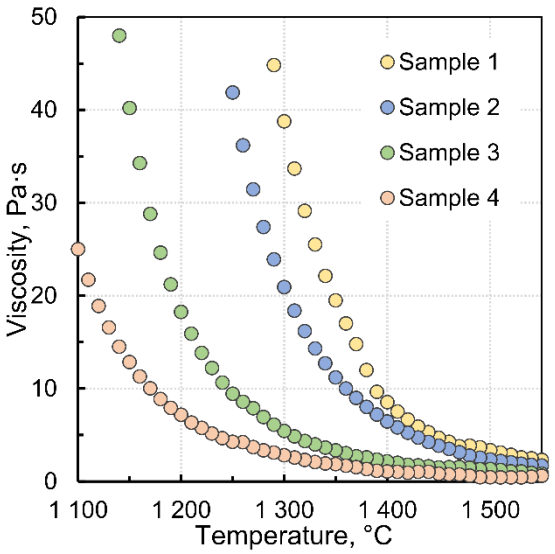

Figure 3 Temperature dependencies of the viscosity of individual samples. Source: (own)

4. CONCLUSION

This work investigated the influence of the addition of B_2O_3 (0 – 30 wt%) on the glass-based oxide system's properties.

The results of this research can be summarized as follows:

- Softening start and softening end temperature decreased with increasing B_2O_3 content,
- liquidus temperature with the addition of B_2O_3 decreased,
- at a maximum temperature of 1 550 °C, the investigated glass-based oxide systems exhibit Newtonian behaviour,
- the dynamic viscosity of the systems decreases exponentially with increasing temperature and with the addition of B_2O_3.

In conclusion, the dynamic viscosity varies with temperature and chemical composition and is also dependent on the internal structure of the oxide system, which will be further investigated.

ACKNOWLEDGEMENT

This work was supported by the project no. CZ.02.1.01/0.0/0.0/17_049/0008399 (EU and CR financial funds—provided by the Operational Programme Research, Development and Education, Call 02_17_049 Long-Term Intersectoral Cooperation for ITI, Managing Authority: Czech Republic-Ministry of Education, Youth and Sports) and student project SP2023/034.

REFERENCES

[1] SHOU, Peng, Ke ZHENKUN. A novel type of borosilicate glass with excellent chemical stability and high ultraviolet transmission. *Journal of Non-Crystalline Solids.* 2020, 528.
[2] ZHUFENG, Shao, Jia Yanan. Analysis of influence of high temperature homogenizing on UV transmittance of quartz glass, *Key Engineering Materials.* 2016, 285-288.
[3] YAN, Jiajia, Yukun WU. Structural transformation-induced surface strengthening of borosilicate sealing glass for solid oxide fuel cells. *Ceramics International.* 2019, 15629-15635.
[4] PARTYKA, Janusz, Magdalena LEŚNIAK. Raman and infrared spectroscopy study on structure and microstructure of glass-ceramic materials from SiO_2-Al_2O_3-Na_2O-K_2O-CaO system modified by variable molar ratio of SiO_2/Al_2O_3. *Spectrochimica Acta Part A: Molecular and Biomolecular Spectroscopy.* 2016, 82-91.
[5] JOSHI, Rakesh, Rahul CHHIBBER. Effect of SiO_2/B_2O_3 ratio on the thermophysical and wetting properties of borosilicate glass sealent for glass-metal joint. *Journal of Materials Processing Tech.* 2018, 186-194.
[6] HUANG, Sanxi, Sheng LI. Effect of B_2O_3 on structure and properties of CaO-MgO-B_2O_3-Al_2O_3-SiO_2 glasses. *Journal of Inorganic and Organometallic Polymers and Materials.* 2015, 816-822.
[7] LUO, Wei, Zhenhong BAO. Effect of B_2O_3 on the crystallization, structure and properties of MgO-Al_2O_3-SiO_2 glass-ceramics. *Ceramics International.* 2019, 24750-24756.
[8] KE, Zhenkun, Xin CAO. The effect of alkali metal oxide on the properties of borosilicate fireproof glass: Structure, thermal properties, viscosity, chemical stability. *Ceramics International.* 2021, 19605-19613.
[9] JABRAOUI, H., E.M. ACHHAL. Molecular dynamics simulation of thermodynamic and structural properties of silicate glass: Effect of the alkali oxide modifiers. *Journal of Non-Crystalline Solids.* 2016, 16-26.
[10] KIM, Gi Hyun, SOHN. Effect of CaF_2, B_2O_3 and CaO/SiO_2 mass ratio on the viscosity and structure of B_2O_3-containing calcium-silicate-based melts. *Journal of the American Ceramic Society.* 2019, 6575-6590.
[11] WANG, Lin, Yaru CUI. Melting properties and viscosity of SiO_2-CaO-Al_2O_3-B_2O_3 system. *Steel Research International.* 2015, 670-677.
[12] CALAHOO, Courtney, Lothar WONDRACZEK. Ionic glasses: Structure, properties and classification. *Journal of Non-Crystalline Solids.* 2020, 100054.

EFFECT OF SUBSTRATE MATERIAL ON WETTING BY CaO-MgO-SiO_2-Al_2O_3-B_2O_3 OXIDE SYSTEM USING SESSILE DROP METHOD

Author(s): Dalibor NOVÁK

Supervisor: doc. Ing. Lenka ŘEHÁČKOVÁ, Ph.D.

Department: Department of Chemistry and Physico-Chemical Processes, Faculty of Materials Science and Technology, VSB – Technical University of Ostrava

Abstract

Oxide systems are of great application importance in steel production, as part of slag, and in other areas, particularly in ceramic processing, glass production, and construction. When considering their application at high temperatures, their rheological and surface characteristics play an essential role. This work deals with the wettability of poly-component oxide systems on two types of substrates, i.e., platinum substrate and polished graphite substrate. The tested systems were subjected to a high-temperature wetting test in the temperature range from liquidus temperature to 1 550 °C by sessile drop method. Four oxide systems were tested with graded boron oxide content, namely 0, 5, 15 and 30 wt%. The experiments were conducted in a CLASIC high-temperature resistance observation furnace and an inert atmosphere of high-purity argon. During the experiments, reactive and non-reactive wetting occurred depending on the type of substrate. Time and temperature dependencies of the average wetting angles and images of droplet silhouettes during thermal load were evaluated.

Key words:

Glass-based oxide system, boron oxide, high-temperature wetting, sessile drop method.

1. INTRODUCTION

Aluminoborosilicate glasses and melts find applications as substrates for flat panel displays, fibre glasses, radioactive waste containments and other materials [1,2]. The CaO-MgO-Al_2O_3-SiO_2-B_2O_3 system is commonly used to produce E-glass. There are many references on the structure and properties of these glasses [3,4]. However, there is a lack of scientific papers dealing with rheological and surface properties, where it is commonly considered that non-wetting behaviour is expressed by a contact angle greater than 90 degrees, while a contact angle close to 90 degrees corresponds to the transition from non-wetting to wetting, and an angle less than 90 degrees refers to wetting behaviour [5]. It is also worth noting that spreading a melt on a substrate without reaction/absorption by the substrate material is called non-reactive or inert wetting, while a wetting process affected by a reaction between the spreading liquid and the substrate material is termed reactive wetting [6]. Although platinum and carbon are used as measuring systems, they can react with the sample. Carbon tends to reduce oxides. Platinum can alloy with some metals such as iron, lead, zinc, tin and antimony, and the uptake of contaminating metals lowers the alloy's melting point. Non-metallic elements can also react under reduction conditions, particularly arsenic, phosphorus, boron, bismuth, silicon, and sulphur.

This work investigates the effect of boron oxide on wetting two substrates, platinum, and polished graphite, by a poly-component oxide system where reactive wetting can be assumed.

2. EXPERIMENTAL

2.1 Preparation of tested oxide samples

The tested oxide system consisted of boron, silica, calcium, aluminium, and magnesium oxides, while the content of B_2O_3 varied at the expense of SiO_2 and CaO, whose relative ratio was preserved. The oxide systems were prepared from chemicals of analytical purity. After weighing the appropriate amounts of oxides (see Table 1), the mixture with a total weight of 10 g was homogenized for 30 min in a mortar. Approximately 0.7 g was then weighed to pellet a 1 cm diameter tablet.

Table 1 Composition of the tested oxide systems in weight percent. Source:(own)

Sample	B_2O_3	SiO_2	CaO	Al_2O_3	MgO
1	0.0	64.6	15.9	9.5	10.0
2	5.0	61.1	14.4	9.5	10.0
3	15.0	53.9	11.6	9.5	10.0
4	30.0	43.2	7.3	9.5	10.0

2.2 High-temperature tests

The experimental determination of the wetting angles was carried out using the sessile-drop method in a CLASIC high-temperature observation resistance furnace (see Figure 1). The temperature range was determined from the liquidus temperature, obtained by measuring the normal force on an ANTON PAAR FRS 1600 viscometer, up to 1 550 °C. The tablets were placed on a polished graphite or platinum substrate in the furnace. The furnace was then hermetically sealed, evacuated to approximately 1 Pa and flushed with high-purity Argon (6N). The heating rate was adjusted to 5 °C/min, which, given the furnace arrangement and sample size, is a good rate to ensure sample heating. During the temperature loading, the temperature was measured with a Pt - 13% Rh/Pt thermocouple located close to the sample. The experiments were conducted in an inert argon atmosphere, and a CANON EOS550D high-resolution camera captured the droplet silhouettes.

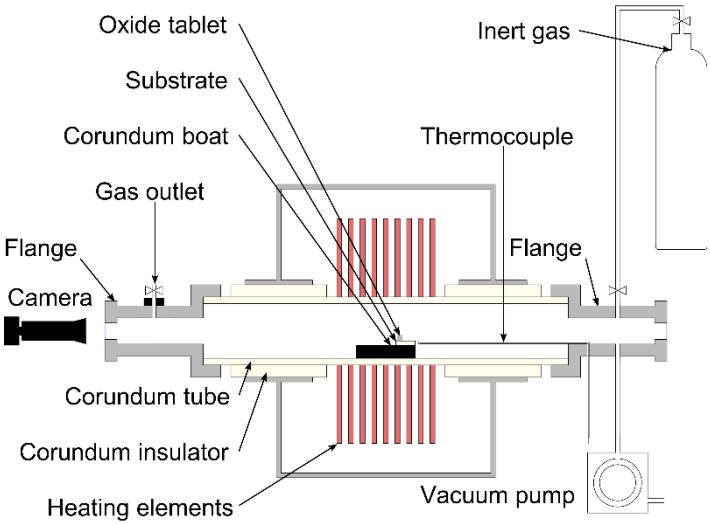

Figure 1 Schematic of a CLASIC high-temperature resistance observation furnace. Source: (own)

3. RESULTS AND DISCUSSION

One series of model oxide systems was prepared to assess the effect of boron oxide content, which ranged from 5 to 30 wt%, on the wettability of platinum and graphite substrates. Figures 2 and 3 show the temperature dependence of the average wetting angle and wetting kinetics. Figure 2 shows that for the oxide system/graphite substrate couple, there was a monotonic decrease in contact angle with the temperature only for the sample containing 5 wt% boron oxide. Nonreactive wetting likely occurred since the wetting angle was greater than 90 deg. However, in the case of the samples containing 15 and 30 wt% B_2O_3, there was a significant decrease in the contact angle and a transition from non-reactive to reactive wetting at 1 534 °C and 1 490 °C, respectively [7]. It can be assumed that the interaction was accompanied by both the dissolution of the substrate and the formation of new interfacial compounds. However, this suggestion needs to be supported by microstructural analysis.

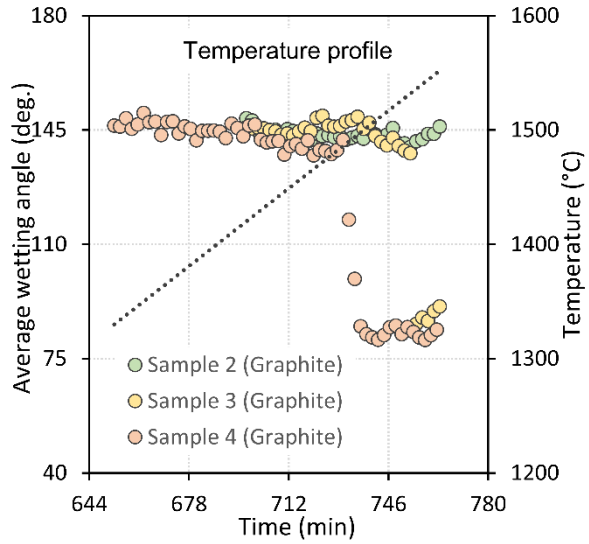

Figure 2 Wetting kinetics of the metal oxide/graphite substrate couple. Source: (own)

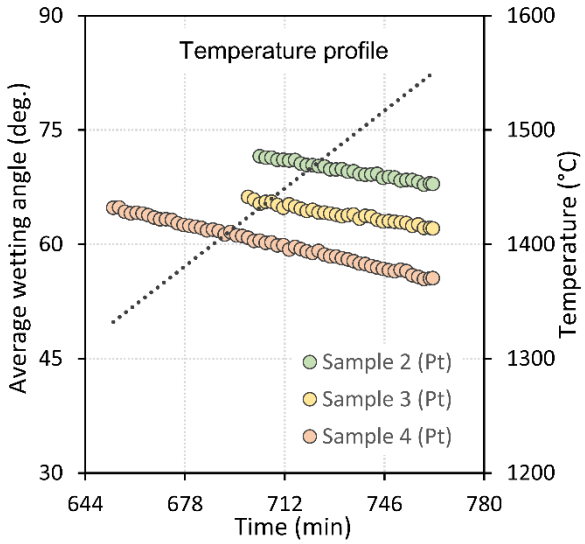

Figure 3 Wetting test of the metal oxide/platinum substrate couple. Source: (own)

In the case of the platinum substrate, the temperature dependence of the average wetting angles was monotonic for all the oxide specimens. Since the wetting angles were less than 90 deg, reactive wetting occurred. The wetting angles varied both with temperature, when they decreased, and with the boron oxide content. The higher the boron oxide content, the smaller the contact angle and the higher the interaction between the sample and the substrate.

Figure 4 presents the silhouettes of the molten droplets of all oxide samples at liquidus temperature and a maximum temperature of 1 550 °C. The shape changes correspond to the temperature and time dependencies shown in Figures 2 and 3. The liquidus temperatures evaluated by normal force measurements decreased with increasing boron oxide content in the samples.

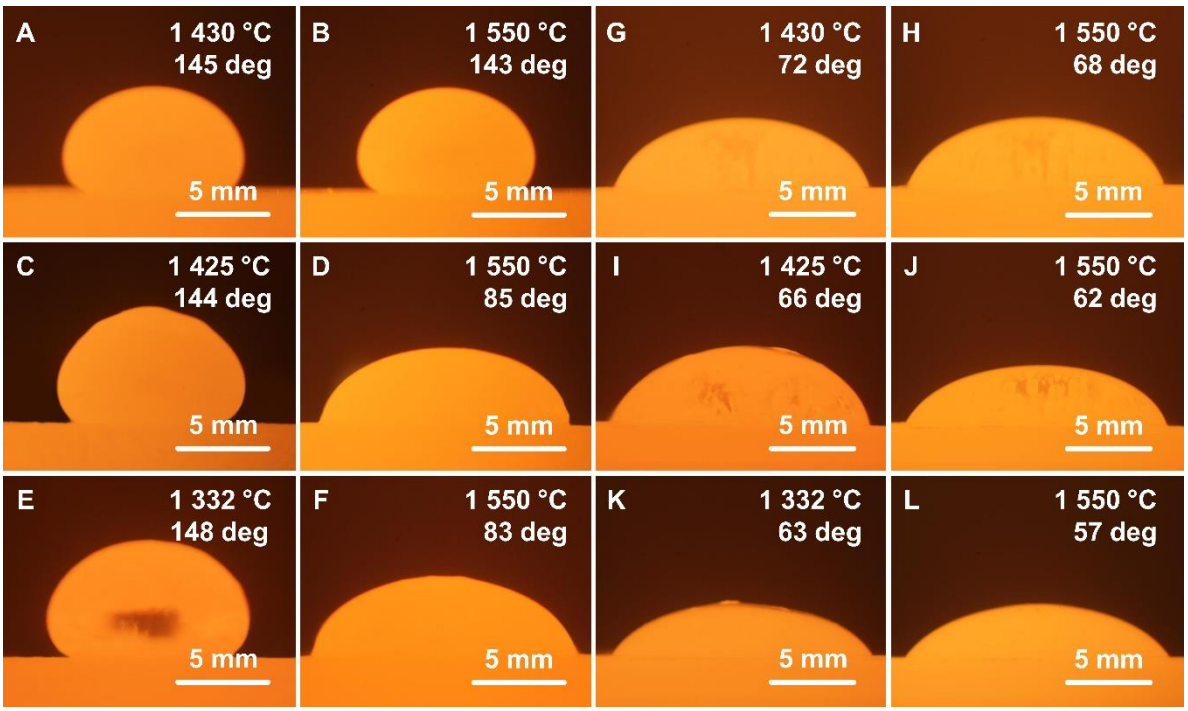

Figure 4 Silhouettes of molten oxide systems on graphite (A, B sample 2, C, D sample 3 and E, F sample 4) and platinum (G, H sample 2, I, J sample 3 and K, L sample 4) substrates at liquidus temperature and a maximum temperature of 1 550 °C. Source: (own)

4. CONCLUSION

This work addressed wetting two different substrates, platinum, and graphite, by an oxide system with graded amounts of boron oxide ranging from 5 to 30 wt%. The results can be summarized as follows:

- The boron oxide content influenced wetting; with increasing amounts, the contact angles decreased when wetting the platinum substrate. For the graphite substrate, the differences were negligible.
- In the case of wetting of platinum substrate, the wettability increased with increasing B_2O_3 content.
- For all samples, the magnitude of contact angles decreased with increasing temperature.
- Non-reactive wetting occurred only in the case of the sample containing 5 wt% B_2O_3 and the graphite substrate. For the other cases, wetting was reactive, with sharp transitions for the sample 3 and sample 4/graphite substrate couples at temperatures of 1 534 and 1 490 °C, respectively.
- The wettability determined by the lying drop method for the oxide system is influenced by substrate selection.

The interaction at the phase interface was not investigated and will be the subject of further research.

PODĚKOVÁNÍ – ACKNOWLEDGEMENT

This work was supported by the project no. CZ.02.1.01/0.0/0.0/17_049/0008399 (EU and CR financial funds – provided by the Operational Programme Research, Development and Education, Call 02_17_049 Long-Term Intersectoral Cooperation for ITI, Managing Authority: Czech Republic-Ministry of Education, Youth and Sports) and student project SP2023/034.

REFERENCES

[1] WU, Jingshi, STEBBINS, Jonathan F. Quench rate and temperature effects on boron coordination in aluminoborosilicate melts. *Journal of Non-Crystalline Solids*. 2010, **356** (41-42), 2097-2108.

[2] WU, Jingshi, STEBBINS, Jonathan F. Temperature and modifier cation field strength effects on aluminoborosilicate glass network structure. *Journal of Non-Crystalline Solids*. 2013, **362** (1), 73-81.

[3] HUANG, Sanxi, LI, Sheng, WU, Fengnian, YUE, Yunlong. Effect of B_2O_3 on Structure and Properties of CaO–MgO–B_2O_3–Al_2O_3–SiO_2 Glasses. Journal of Inorganic and Organometallic *Polymers and Materials*. 2015 **25** (4), 816–822.

[4] WU, Jingshi, GROSS, Timothy M., HUANG, Liping, JACCANI, Siva Priya, YOUNGMAN, Randall E., RZOSKA, Sylwester J., BOCKOWSKI, Michal, BISTA, Saurav, STEBBINS, Jonathan F, Smedskjaer, Morten M. Composition and pressure effects on the structure, elastic properties and hardness of aluminoborosilicate glass. *Journal of Non-Crystalline Solids*. 2020, **530**, 119797.

[5] POLKOWSKI, Wojciech, SOBCZAK, Natalia, POLKOWSKA, Adelajda, NOWAK, Rafał, KUDYBA, Artur, BRUZDA, Grzegorz, GIURANNO, Donatella, GENEROSI, Amanda, PACI, Barbara, TRUCCHI, Daniele M. Ultra-High Temperature Interaction Between h-BN-Based Composite and Molten Silicon. *Metallurgical and Materials Transactions A: Physical Metallurgy and Materials Science*. 2019, **50** (2), 997–1008.

[6] KUMAR, Girish, PRABHU, K.Narayan. Review of non-reactive and reactive wetting of liquids on surfaces. *Advances in Colloid and Interface Science*. 2007, **133** (2), 61–89.

[7] EUSTATHOPOULOS, Nicolas. Progress in understanding and modeling reactive wetting of metals on ceramics. *Current Opinion in Solid State and Materials Science*. 2005, **9** (4-5), 152-160.

Process Engineering

DISTRIBUTION OF HEAVY METALS WITHIN MAGNETIC AND NON-MAGNETIC FRACTIONS OF COAL COMBUSTION BOTTOM ASH

Authors: Filip KOVÁR, Lucie BARTOŇOVÁ

Supervisor: doc. Mgr. Lucie BARTOŇOVÁ, Ph.D.

Department: Department of Chemistry and Physico-Chemical Processes FMST, VSB – Technical University of Ostrava

Abstract

The paper evaluates distribution of Fe_2O_3 and heavy metals during dry magnetic separation of particle-size fractions of bottom ash originating from fluidized-bed combustion. The aim of the research was to evaluate the enrichment factors of heavy metals in magnetic and non-magnetic concentrates, which could facilitate further technological utilization.

Key words:

Magnetic separation, heavy metals, Fe_2O_3, coal combustion, bottom ash.

1. INTRODUCTION

Throughout the world, coal combustion residues (ashes or slags) are produced in vast quantities; for example, in India and China the produced amount is approximately 112 Tg/ y and 100 Tg/y, in USA and Germany it is estimated to be 75 Tg/y and 40 Tg/y, in UK and Poland it is around 15 Tg/y and 4 Tg/y, respectively [1,2]. On the one hand, heavy metals present in coal combustion residues (Co, Cr, Cu, Mn, Ni, Pb, Zn etc.) are potentially toxic and pose a hazard to public health and a surrounding environment [3-5]. From this perspective, distribution of toxic elements (e.g., heavy metals) in coal combustion residues is a key information for safe handling, storage, or for possible utilization. On the other hand, at the end of February 2022, the U.S. Geological Survey has released a new list of 50 mineral commodities critical to economy and national security including (among others) Cr, Co, Mn, Ni, and Zn [6]. Therefore, it is not surprising that coal combustion residues are intensively studied also as a possible source of valuable components [7-9].

Magnetic separation paired with particle size fractionation is a simple and effective ash treatment technology [10]. Therefore, application of particle-size separation in combination with magnetic separation could be used either for increasing the levels of valuable elements or decreasing the concentrations of the undesirable ones.

The aim of this study is to evaluate the concentrations of heavy metals in the magnetic and non-magnetic fractions of bottom ash after magnetic separation applied on particle-size fractions. Another goal is to evaluate the enrichment factors of the target elements (heavy metals) in the magnetic or non-magnetic fractions.

2. MATERIALS AND METHODS

Bottom ash (BA) samples were collected during coal combustion at atmospheric circulating fluidised-bed power plant at 850°C where dry desulphurization additive was added to fluidised bed for the retention of gaseous emissions of sulphur. After collecting the composite ash samples at regular time intervals (during the whole combustion test), 3-5 kg samples were quartered and stored aside for laboratory research. Particle-size fractions of a bulk ash sample were produced on sieves (when dry). To minimize leaching of the elements investigated, magnetic fractions were manually separated using a hand-held magnet and dry sample. The target element concentrations were measured using a wavelength-dispersive X-ray fluorescence spectrometer ARL PERFORM' X 4200 (Switzerland).

3. RESULTS

After dry magnetic separation with a hand magnet, the fractions (dry samples) were subjected to determination of the target metals – elements evaluated in this study were Fe, V, Cr, Mn, Co, Ni, Cu,

Zn, and Pb. For an easier evaluation, the concentrations of the studied elements were plotted in a graph (Figure 1) to compare their levels in the magnetic (MAG) or non-magnetic (NON) fraction in a given particle size.

Fe_2O_3 is generally more or less enriched in magnetic concentrates depending on the separation procedure and the nature of the sample, which might not be the case of other elements. For easier examination of the overall distribution patterns of the target components, an enrichment factor (EF) was calculated. The EF (of the i-th element) in magnetic fraction in relation to corresponding non-magnetic one was calculated using the formula:

$$EF_{(i)} = \frac{w_i(\text{magnetic fraction})}{w_i(\text{non-magnetic fraction})} \quad (1)$$

where, w_i values are weight fractions of the *i*-th element (or its oxide) in magnetic or non-magnetic ash fraction.

EF values (calculated according to Eq. 1) are listed in Table 1. For easier evaluation, the enrichment in magnetic fraction (value above 1) was highlighted in thick italics, while the depletion (value below 1) was listed in the table without highlighting.

Table 1. Enrichment factors (EF) of Fe_2O_3 and heavy metals in magnetic (vs. non-magnetic) fractions of BA. Source: (own)

Particle size (mm)	<0.4	0.4-0.5	0.5-0.6	0.6-1	>1
Fe_2O_3	***6.7***	***8.7***	***9.0***	***9.1***	***8.0***
V	0.4	0.3	0.3	0.2	0.2
Cr	0.4	0.3	0.2	0.1	0.2
Mn	***6.4***	***8.3***	***8.8***	***8.7***	***7.8***
Co	***3.9***	***6.4***	***6.2***	***6.7***	***6.2***
Ni	0.8	0.6	0.4	0.5	0.5
Cu	0.9	0.7	0.8	0.6	0.4
Zn	0.8	0.7	0.8	0.8	0.6
Pb	0.2	0.3	0.2	0.1	0.3

As expected, Fe_2O_3 was enriched in magnetic concentrates by approximately 7-fold in the size fraction below 0.4 mm and 8-9 -fold in all other particle sizes (above 0.4 mm).

EFs of Mn showed rather similar trend as in case of Fe_2O_3 - it was also highly (6-9 -fold) enriched in magnetic concentrates which agrees with other studies [11,12]. Another element showing enrichment in magnetic concentrates in literature is Co [13,14] which is consistent with the observed ca. 4-7 -fold higher concentration of this metal in the magnetic concentrate (Table 1). In addition to strong magnetic properties of both these metals, it is interesting to note that there is a general consensus in literature that ferrite phases abundant in magnetic concentrates are not pure but highly substituted. Quite common is magnesioferrite [15,16] but substitution of other elements has also been described in literature. For example, as indicated in the formula published by Gomes et al. [16] – from all heavy metals, only Mn is included there:

$$[Fe^{3+}_{0.92}\, Ca^{2+}_{0.06}\, Si^{4+}_{0.02}]^{tetra}\, [Fe^{3+}\, Fe^{2+}_{0.16}\, Mg^{2+}_{0.73}\, Mn^{2+}_{0.11}]^{octa}\, O_4$$

As shown in Table 1, other metals (V, Cr, Ni, Cu, Zn, and Pb) were depleted in all magnetic fractions and their EF values were below 1.

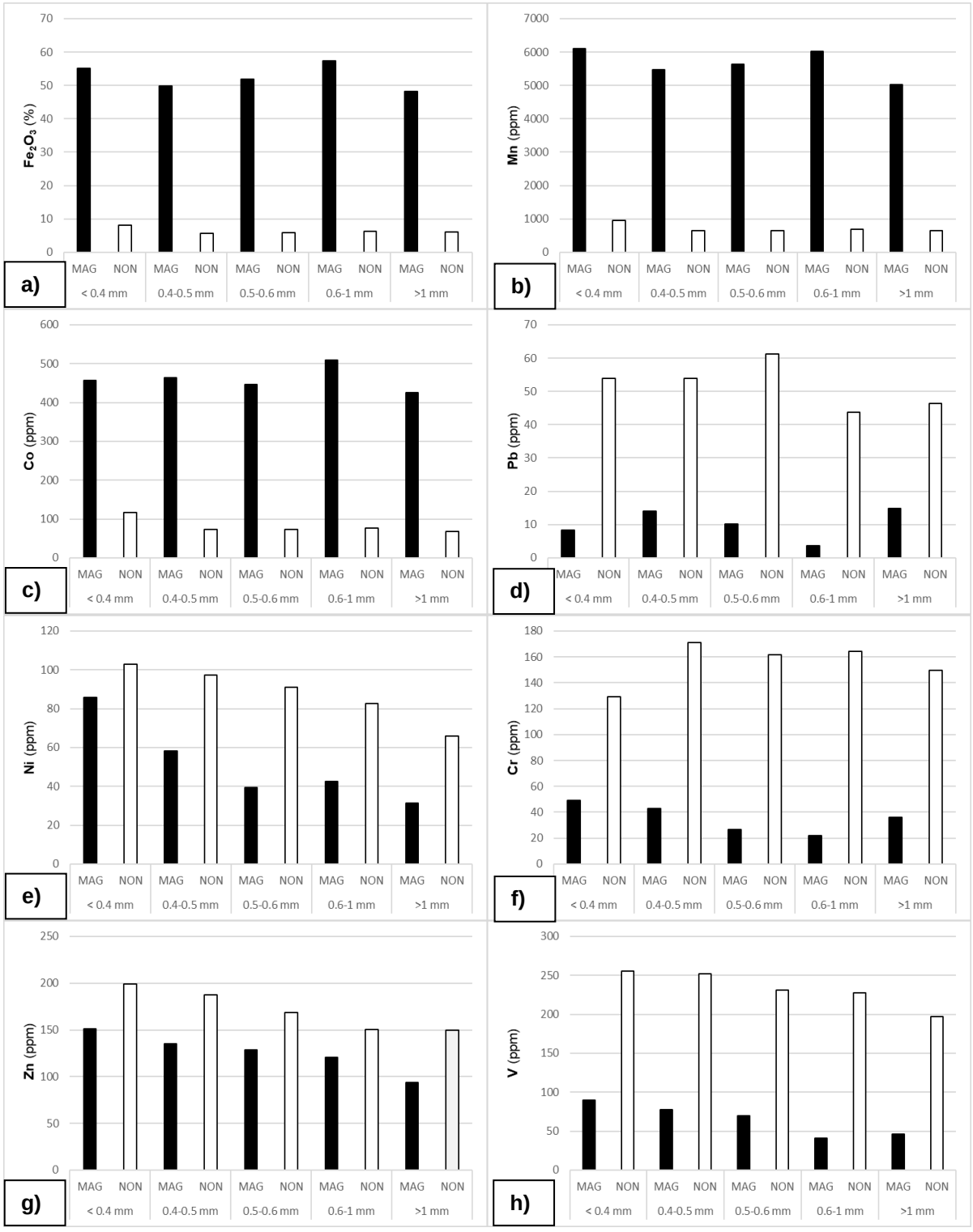

Figure 2 Distribution of a) Fe_2O_3 (wt.%), b) Mn (ppm), c) Co (ppm), d) Pb (ppm), e) Ni (ppm), f) Cr (ppm), g) Zn (ppm) and h) V (ppm) in magnetic (MAG) and non-magnetic (NON) particle-size fractions of BA. Source: (own)

4. CONCLUSION

Magnetic separation is a commonly used method for separating coal ash into two fundamental components: magnetic and nonmagnetic fractions facilitating their independent handling and utilization. Nonmagnetic fractions frequently include increased CaO levels due to desulphurization additives applied to coal during fluidized bed combustion, while magnetic concentrates are rich in Fe_2O_3. Both

fractions have the ability to bind certain elements during combustion, which is an important parameter in terms of further utilization of these fractions.

When using dry magnetic separation with a hand magnet, the magnetic concentrates contained 48.11% - 55.06% Fe_2O_3, which was enriched there 6.7-9.1 -fold. Nearly the same enrichment results were shown by Mn and quite similar ones were obtained also for Co; both these metals exhibited elevated levels in all evaluated magnetic fractions. The enrichment factors (calculated for individual particle size fractions) for Co were from 3.9 to 6.7 and for Mn these values ranged from 6.4 to 8.8, respectively. The other evaluated metals (Zn, V, Cr, Ni, Cu, and Pb) were enriched in all non-magnetic fractions, which corresponds with the values of EFs being always below 1.

Magnetic separation of ashes is often conducted to facilitate utilization of magnetic and nonmagnetic fractions when used separately. This means that magnetic fractions depleted in toxic elements such as chromium and lead (which are mainly concentrated in non-magnetic fractions) could have the potential for further technological use, for example in the production of heavy suspensions or the production of catalysts.

ACKNOWLEDGEMENT

The authors gratefully acknowledge the support by project SP 2023/034 "Research and development of composite multifunctional materials for sustainable development" and by project SP2022/68 "Specific Research in Metallurgical, Materials and Process Engineering".

REFERENCES

[1] ŚWIETLIK Ryszard, Marzena TROJANOWSKA, Malgorzata A. JÓŹWIAK. Evaluation of the distribution of heavy metals and their chemical forms in ESP-fractions of fly ash. *Fuel Processing Technology*. 2012, **95**, 109-118.

[2] ZHAO Shilin, Yufeng DUAN, Jincheng LU, Rejender GUPTA, Deepak PUDASAINEE, Shuai LIU, Jianhong Lu. Chemical speciation and leaching characteristics of hazardous trace elements in coal and fly ash from coal-fired power plants. *Fuel*. 2018, **232**, 463-469.

[3] HE Ana, Xiaoping LI, Yuwei AI, Xiaolong LI, Xiaoyun LI, Yucho ZHANG, Yu GAO, Bin LIU, Hongtao YU. Potentially toxic metals and the risk to children's health in a coal mining city: An investigation of soil and dust levels, bioaccessibility and blood lead levels. *Environment International*. 2020, **141**, 105788.

[4] BARTOŇOVÁ Lucie, Helena RACLAVSKÁ. Behavior of Cr during coal combustion: An overview. *Fuel*. 2022, **322**, 124210.

[5] PATRA, Selina, Shin Teen WHAUNG, Wei Lek KWAN. Analysis of heavy metals in Incineration Bottom Ash in Singapore and potential impact of pre-sorting on ash quality. *Energy Procedia*. 2017, **143**, 454-459.

[6] BURTON, Jason. *U.S. Geological Survey Releases 2022 List of Critical Minerals* [online]. 2022 [cit. 25.5.2023]. Available from: https://www.usgs.gov/news/national-news-release/us-geological-survey-releases-2022-list-critical-minerals

[7] BARTOŇOVÁ Lucie, Helena RACLAVSKÁ, Jan NAJSER. Vanadium – Valuable and toxic element in coal combustion ash: An overview. *Process Safety and Environmental Protection*. 2023, **172**, 923-940.

[8] DAI Shifeng, Ian T. GRAHAM, Colin R. WARD. A review of anomalous rare earth elements and yttrium in coal. International *Journal of Coal Geology*. 2016, **159**, 82-95.

[9] HOWER C. James, David J. ROBERTSON. Chemistry and petrology of fly ash derived from the co-combustion of western United States coal and tire-derived fuel. *Fuel Processing Technology*. 2004, **85(5)**, 359-377.

[10] VALEEV Dmitry, Irina KUNILOVA, Alexander ALPATOV, Alika VARNAVSKAYA, Dianchun JU. Magnetite and Carbon Extraction from Coal Fly Ash Using Magnetic Separation and Flotation Methods. Minerals. 2019, 9(5), 320.

[11] HOWER C. James, Robert F. RATHBONE, J.David ROBERTSON, Gilman PETERSON, Alan S. Trimble. Petrology, mineralogy, and chemistry of magnetically-separated sized fly ash. *Fuel*. 1999, **78(2)**, 197-203.

[12] MYAZIN V. P., L. V. SHUMILOVA, K. K. RAZMAKHNIN, S. A. BOGIDAEV. Integrated Processing of Ash and Slag from Thermal Power Plants in Eastern Transbaikalia. *Journal of Mining Science*. 2018, **54(5)**, 845-857.

[13] VASSILEV V. Stanislav, Christina G. VASSILEVA, Ali I. KARAYIGIT, Yilmaz BULUT, Andres ALASTUEY, Xavier QUEROL. Phase-mineral and chemical composition of fractions separated from composite fly ashes at the Soma power station, Turkey. *International Journal of Coal Geology*. 2005, **61(1)**, 65-85.

[14] DAI Shifeng, Lei ZHAO, Suping PENG, Chen-Lin CHOU, Xibo WANG, Young ZHANG, Dan LI, Yingying SUN. Abundances and distribution of minerals and elements in high-alumina coal fly ash from the Jungar Power Plant, Inner Mongolia, China. *International Journal of Coal Geology*. 2010, **81(4)**, 320-332.

[15] KOVÁR Filip, Lucie BARTOŇOVÁ. Distribution of As within Magnetic and Non-Magnetic Fractions of Fluidized-Bed Coal Combustion Ash. *Minerals*. 2021, **11(12)**, 1411.

[16] GOMES S., M. FRANCOIS, M. ABDELMOULA, Ph. REFAIT, C. PELLISSIER, O. EVRARD. Characterization of magnetite in silico-aluminous fly ash by SEM, TEM, XRD, magnetic susceptibility, and Mössbauer spectroscopy. *Cement and Concrete Research*. 1999, **29(11)**, 1705-1711.

ASSESING THE FEASIBILITY OF ANAEROBIC DIGESTION FOR WASTE MATERIALS PRODUCED BY *ZOPHOBAS MORIO* BREEDING

Author: Petra WOJNAROVÁ

Supervisor: prof. Ing. Lucie OBALOVÁ, Ph.D.

Department: Institute of Environmental Technology, Faculty of Materials Science and Technology, VSB – Technical University of Ostrava

Abstract

Insect farming is a growing industry worldwide, resulting in the generation of biowaste from breeding practices. This waste is a mixture of insect excreta, feed residues, and insect parts. Typically, this waste is only utilized as a fertilizer for plants. This paper aims to evaluate the potential of using insect waste in anaerobic digestion processes within biogas plants. The waste produced from rearing Zophobas morio larvae was selected as the model substrate for the biochemical methane potential test. The average CH_4 content was greater than 61 vol% in biogas produced at a rate of 0.720 $m^3 kg_{VS}^{-1}$.

Key words:

Anaerobic digestion, insect breeding, waste, Zophobas morio.

1. INTRODUCTION

At present, insects are an essential dietary component for over 2 billion people worldwide, with more than 2,100 edible species found across all continents. Their nutritional value, including high levels of fat, protein, vitamins, minerals, and fiber, has made them increasingly popular in the food industry [1,2,3]. For example, the amount of unsaturated omega-3 and six fatty acids in larvae Tenebrio molitor is equivalent to the amount in fish and even higher than in cattle or pigs. Furthermore, these larvae' protein, vitamin, and mineral content are similar to fish and meat [3,4]. Most insects are high in micronutrients such as K, Ca, Fe, Mg, and Se, with higher levels of Ca and Fe than beef, pork, and chicken meat [5]. For example, consuming 100g of caterpillars can provide 335% of the minimum recommended daily intake of Fe, 76% of the recommended daily intake of protein, and nearly 100% of the daily intake of vitamins for the human body [6]. Another important thing is that insects have a high food conversion rate, e.g., crickets need six time less feed than cattle, four times less than sheep and twice less than pigs and chickens to produce the same amount of protein. Additionally, insect farming produces fewer greenhouse gases and ammonia than traditional livestock. Lastly, insects can be reared on organic waste, an additional advantage for sustainability [4,7].

Due to their composition, insects are used not only for the food industry but also for isolating individual valuable elements. One of then is chitin for application in medicine, cosmetic, or textile industry [1,8,9]. Nguyen et al. used direct transesterification of insect *Hermetia illucens* kept on wheat bran to produce biodiesel [10]. Another possibility of biofuel production is anaerobic digestion of insects and insect waste.

As the production and usage of insects continue to grow, it is anticipated that there will also be a rise in the amount of waste produced during their breeding process. Hence, it's essential to discover the optimal application of this kind of waste. The research hypothesis assumes that the waste generated after insect breeding (consisting of a mixture of insect excreta, feed residues, and insect parts) has the potential to serve as an appropriate substrate for producing biogas via anaerobic digestion. This paper's aim is to assess the possibility of utilizing this waste from one of the most bred insects *Zophobas morio.*

2. MATERIALS AND METHODS

Substrate: The larvae of *Zophobas morio* and the solid waste resulting from the breeding of *Zophobas morio* were analyzed in this study (see Figure 1). Both substrate samples were obtained from Papek s.r.o., the largest insect farm in Central Europe and the Czech Republic.

The waste material consisted of insect excrement, leftover feed (i.e., food waste), and insect remains. Table 1 presents the fundamental physical and chemical parameters.

Figure 1 (a) Larvae of *Zophobas morio*
(b) *Zophobas morio´* s waste from breeding. Source: own

Inoculum: The inoculum used in this study was a liquid fermenting suspension (digestate) obtained from the first-stage anaerobic fermentor at the Pustějov II agricultural biogas plant located in the Moravia-Silesian Region of the Czech Republic and operated by Zemspol Studénka a.s. The pH value of the inoculum fell within the optimal range for methanogens, which is between 6.7 and 7.5, as reported in references [11]. All parameters analyzed in this study are listed in Table 1.

Table 1 Analytical parameters of *Zophobas morio* and *Zophobas morio´s* waste.
Source: (own)

Parameter		*Zophobas morio*	*Zophobas morio´s waste*	Inoculum
pH-H_2O	pH	7.68	7.88	7.68
Total solids (105°C)	TS (wt. %)	95.98	88.81	6.77
Volatile solids (550 °C)	VS_{TS} (wt. %)	96.51	92.26	77.21
Density	ρ (kg/m^3)	-	1407	1619
Carbon	C (wt. $\%_{TS}^{*}$)	58.30	44.80	41.29
Hydrogen	H (wt. $\%_{TS}$)	8.46	5.95	4.85
Nitrogen	N (wt. $\%_{TS}$)	8.13	4.53	3.69
Oxygen	O (wt. $\%_{TS}$)	8.16	36.57	27.22
Sulfur	S (wt. $\%_{TS}$)	0.33	0.28	0.57

*TS total solid

Biochemical methane potential test (BMP): The VDI 4630 norm was used to conduct a batch test to determine the biochemical methane potential [12]. The test apparatus consisted of a 1-liter reaction bottle, a 1.2-liter gas burette, and a 2-liter expansion bottle containing a saturated water-salt solution. The test was performed in a 1-liter bioreactor tank containing 800 g of inoculum. The initial substrate (insect waste) dosage was 6.5, 6.7, and 7.0 g, with two reactors used for each loading, as well as for endogenous biogas production from the inoculum. The reaction bottles were placed in a thermostatic water bath with a temperature setting of 40 ± 0.2 °C. The gas burette was located in a laboratory fume hood at a temperature of 20 ± 2 °C. Measurements of the ambient temperature (i.e., the temperature of the biogas), barometric pressure, and biogas volume increase were recorded every working day at 8 am for 30 days. The biogas volume was recalculated to standard conditions of 0 °C and 101,325 kPa. A portable GEOTECH Biogas5000 UK analyzer was used to measure the biogas

composition. During weekends, no measurements were taken, and missing data on biogas volume and composition were interpolated linearly.

3. RESULTS AND DISCUSSION

The waste generated by breeding *Zophobas morio* is defined by a substantial amount of total solids (88.81%), primarily consisting of organic compounds (92.26%). The diagrams in Figure 2 display the composition of the raw biogas. The most significant amount of methane (65-66 vol%) was observed for weights measuring 6.7 and 7.0 grams. Based on the data representation of the graph, there seems to be a slight increase in methane concentration during the following days. Especially interesting is the unusually high concentration of hydrogen in the first three days of the test. The graph shows that on the first day of the test, the hydrogen concentration reached 5000 ppm for the lowest weight. Conversely, the lowest H_2 concentration was measured for 7.0 and 7.2 g. High concentrations could have caused partial inhibition of methanogenesis since the maximum concentration is approximately 100-200 ppm [13]. However, by the third day of the test, the concentration had decreased to below 300 ppm in all cases. Higher hydrogen sulphide concentrations could also cause partial inhibition of the methanogenic phase. The concentrations exceeded the maximum recommended concentration of 400-500 ppm of H_2S [14]. The lowest H_2S content was observed for the weight of 7.0 grams, which showed the highest biogas production with the highest CH_4 content throughout the test.

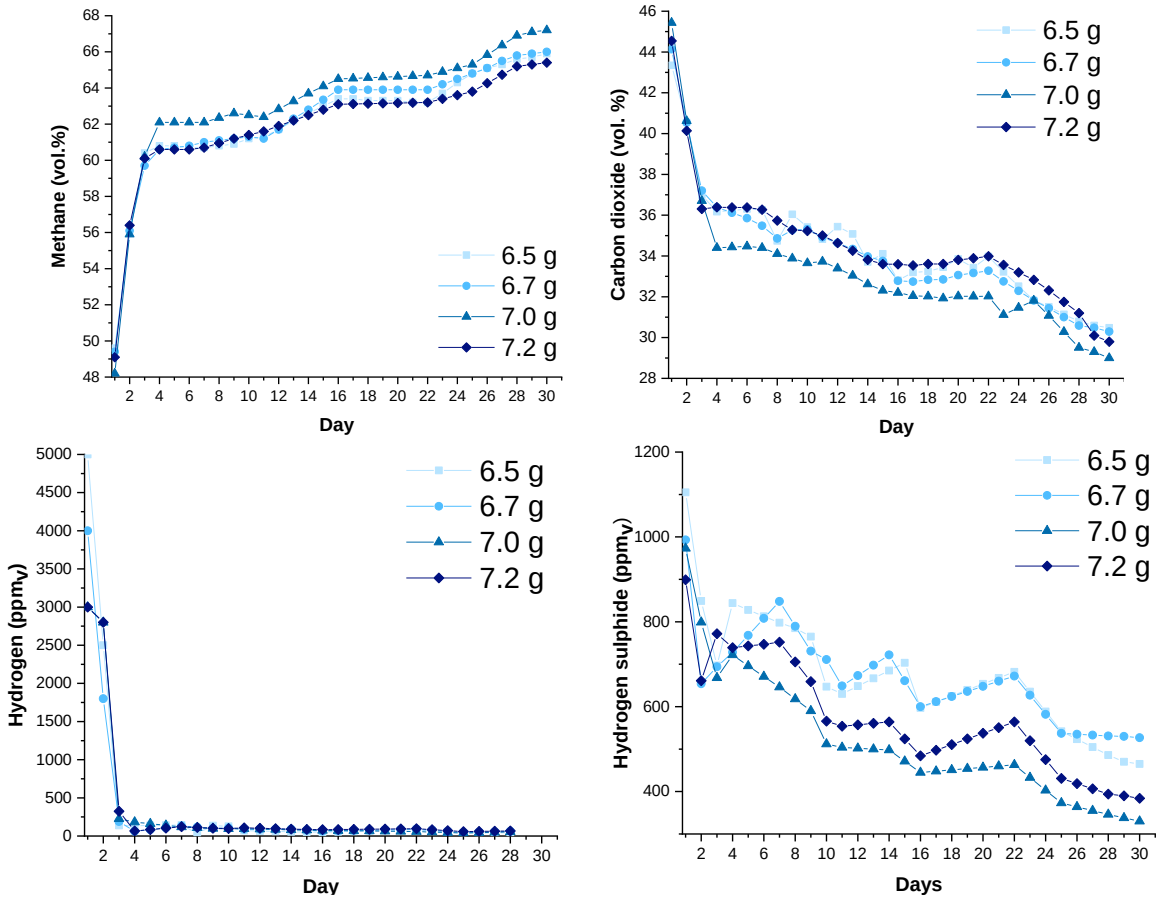

Figure 2 Composition of biogas from the anaerobic digestion of *Zophobas morio´s* breeding waste**.** Source: (own)

The biogas production of *Zophobas morio´s* breeding residue was 0.720 $m^3kg_{VS}^{-1}$ representing a relatively high value compared to other more common in anaerobic digestion substrates.

4. CONCLUSION

The thirty-day test biochemical methane potential test from *Zophobas morio´s* breeding waste confirmed the possibility of using this substrate for anaerobic digestion. The substrate appeared to provide very good quality.

ACKNOWLEDGEMENT

Experimental results were accomplished by using Large Research Infrastructure ENREGAT supported by the Ministry of Education, Youth and Sports of the Czech Republic under project No. LM2023056.

REFERENCES

[1] ZŁOTKO, Katarzyna, Adam WAŚKO, KAMIŃSKI Daniel M., BUDZIAK-WIENCZOREK Iwona, BULAK Piotr, BIEGANOWSKI Andrzej. Isolation of Chitin from Black Soldier Fly (*Hermetia illucens*) and Its Usage to Metal Sorption, *Polymers*. 2021,**13**(5), https://doi.org/10.3390/polym13050818.

[2] WOJNAROVÁ, Petra, Jiří RUSÍN. Tenebrio molitor as substrate for anaerobic digestion, *Waste Forum*. 2020, **3**, 121-130. ISSN 18040195

[3] HUIS van Arnold, ITTERBEECK van Joost, KLUNDER Harmke, MERTENS Esther, HALLORAN Afton, MUIR Giulia, VANTOMME Paul. *Edible Insects: Future Prospects for Food and Feed Security*, 1st ed., Food and Agriculture Organization of the United Nations: Rome, Italy, 2013. ISBN 978-92-5-107595-1.

[4] RUMPOLD, Birgit A., SCHLŰTER Oliver K. Nutritional composition and safety aspects of edible insects, *Mol. Nutr. Food Res*. 2013, **57**, 802-823. https://doi.org/10.1002/mnfr.201200735.

[5] PAN, Jiayin, XU Haining, CHENG Yu, MINTAH Benjamin K., DABBOUR Mokhtar, YANG Fan, CHEN Wen, ZHANG Zhaoli, DAI Chunhua, HE Ronghai, MA Haile. Recent Insight on Edible Insect Protein: Extraction, Functional Properties, Allergenicity, Bioactivity, and Applications, *Foods,* 2022, **11**, 2931. https://doi.org/10.3390/foods11192931

[6] AGBIDYE, F.S. OFUYA T.I, AKINDELE S.O. Some edible insect species consumed by the people of Benue State, Nigeria. *Pakistan Journal of Nutrition*. 2009, **8**, 946-950. https://doi:10.3923/PJN.2009.946.950

[7] SYNOWIECKI, Józef, AL-KHATEEB Nadia. Production, Properties, and Some New Applications of Chitin and Its Derivatives. *Critical Reviews in Food Science and Nutrition*. 2010, **43**(2) 145-171. https://doi.org/10.1080/10408690390826473

[8] NGUYEN, Hoang Chinh, LIANG Shih-Hsiang, DOAN Thien Thanh, SU Chia-Hung, YANG Pei-Cheng. Lipase-catalyzed synthesis of biodiesel from black soldier fly (Hermetica illucens): Optimization by using response surface methodology, *Energy Convers. Manag*. 2017, **145**, 335-342. https://doi.org/10.1016/j.enconman.2017.05.010

[9] NGUYEN, Hoang Chinh, NGUYEN My Linh, LIANG, Shih-Hsiang., SU Chia-Hung, WANG Fu-Ming. Switchable Solvent-Catalyzed Direct Transesterification of Insect Biomass for Biodiesel Production. *BioEnergy Research*. 2020, **13**. https://link.springer.com/content/pdf/10.1007/s12155-019-10085-8.pdf.

[11] BULAK, P., PROC, K., PAWLOVSKA, M., KASPRZYKA, A., BERUS, W., & BIEGANOWSKIi, A. Biogas generation from insects breeding post production wastes. Journal of Cleaner Production. 2019, 244. https://doi.org/10.1016/J.JCLEPRO.2019.118777.

[12] VDI 4630, 2006. Fermentation of organic materials. Characterisation of the substrates, sampling collection of material data, fermentation tests. Verein Deutscher Ingenieure (Ed.), VDI-Handbuch Energietechnik.

[13] SPEECE R.E. 1983. Anaerobic biotechnology for industrial wastewater treatment. *Environmental Science Technology*. 17(9). https://dio.org/10.1021/es00115a725.

[14] PARKIN G., LYNCH N., et al. 2020. Interaction between Sulfate Reducers and Methanogens Fed Acetate and Propionate. *Research Journal of the Water Pollution Control Federation*, 62(6), pp. 780-788. www.jstor.org/stable/2504391.

Chemical and Environmental Engineering

ADVANCED OXIDATION PROCESSES FOR THE TREATMENT OF TOLUENE CONTAINING WASTE AIR IN THE PILOT PLANT UNIT

Author(s): Alena KULIŠTÁKOVÁ

Supervisor: prof. Ing. Kamila KOČÍ, Ph.D.

Department: Institute of Environmental Technology (IET), Centre for Energy and Environmental Technologies (CEET), FMST, VSB – Technical University of Ostrava

Abstract

This paper describes the usage of advanced oxidation processes for the treatment of toluene-containing waste air in the two-step pilot plant unit. The unit consists of a photolytic/photooxidation reactor (dry-VUV_{185}/UV_{254}) and a photochemical scrubber (aqueous-UV_{254}/H_2O_2 reactor). The inlet toluene concentration was set to 50 ppmv and the waste air flow rate was 100 m^3/h. The average toluene conversion after passing the first step and after passing both steps achieved 19.6 % and 42.5 %, respectively. The addition of a photocatalytic step (ceramic foam boards covered by TiO_2 film) to the dry reactor was also tested. In this case, toluene conversion in the first step was increased almost by one third. However, the presence of a photocatalyst had no effect on total toluene conversion after both steps.

Key words:

Advanced oxidation processes, hydroxyl radical, photocatalysis, toluene.

1. INTRODUCTION

Air contamination by volatile organic compounds (VOCs) still remain a big environmental issue. Production of VOCs by traffic is well characterized, quantified, and limited against the other big source of VOCs, which is solvent emission. The European Solvents Industry Group (ESIG) estimates the total solvent emissions in EU27 at 3.9 kg/per capita/per year in 2013 [1]. However, based on the ESIG solvent VOC emission inventories finalized in 2019, the emissions of solvent VOCs in whole European Union stabilized since 2008 and stays around 2 000 ktons [2]. General emission reduction commitments for EU members were published in 2016. The Czech Republic, as member of EU, is obligated to reduce non-methane VOC annual emissions by 18 % from 2020 and by 50 % from 2030 (compared to 2005 level) [3]. The VOC emission levels in the Czech Republic was 441, 176 and 139 ktons per annum in 1990, 2005 and 2018, respectively [4]. It is clear the Czech Republic is already fulfilling the 2020 limits, however, in order to decrease the VOC emissions by 50 % (compared to 2005 level) significant effort needs to be done. The existing technologies used for the decreasing emissions of VOC are based on accumulation of contaminants in condensate separators [5], on adsorbents [6], filters [7], membranes [8], sludge, etc. These technologies are already reaching to their maximum capacity in removing VOC and since the VOC are not being decomposed, only accumulated, these filters and adsorbents need to be treated after saturation. It is clear a new efficient technology has to be developed in order to fulfill the above-mentioned commitment of the Czech Republic.

Advanced oxidation processes (AOPs) seem to be an important promising technology used for the removal of VOC from waste air and water. These processes were first studied and described by the American scientist W.H. Glaze in the 80's of the 20th century [9]. AOPs use the production of highly reactive radicals (especially hydroxyl radicals), which attack pollutant molecules and oxidatively decompose them into simple inorganic compounds (mineralization). Since the AOPs directly oxidize the organic molecules no post-treatment of filters and adsorbents is required which is a huge benefit compared to the non-destructive above-mentioned technologies. AOPs can be used e.g. as the last decontamination step in many applications, where conventional methods of waste air and water purification are not sufficient or disadvantageous.

The usage of continuous-flow photochemical pilot plant unit for the treatment of toluene containing waste air was tested in this study. The unit consists of a photolytic/photooxidation reactor (dry-VUV_{185}/UV_{254}) and a photochemical scrubber (aqueous-UV_{254}/H_2O_2 reactor). The addition of photocatalytic step to the dry reactor was also tested.

2. MATERIALS AND METHODS

The experiments were performed in two step pilot plant unit (Fig. 1). The first step (R1) was a photolytic reactor made from stainless steel utilizing strong UV irradiation provided by 16 UV lamps (185/254 nm). The irradiated volume in this reactor was 2.45 · 10^{-1} m^3. The second step (R2) was a continuous flow photochemical wet scrubber (UV/H_2O_2) with 26 UV lamps (254 nm). There was a storage tank (300·dm^3) at the bottom of the wet scrubber with a water solution of hydrogen peroxide (0.1 mol·dm^{-3}).

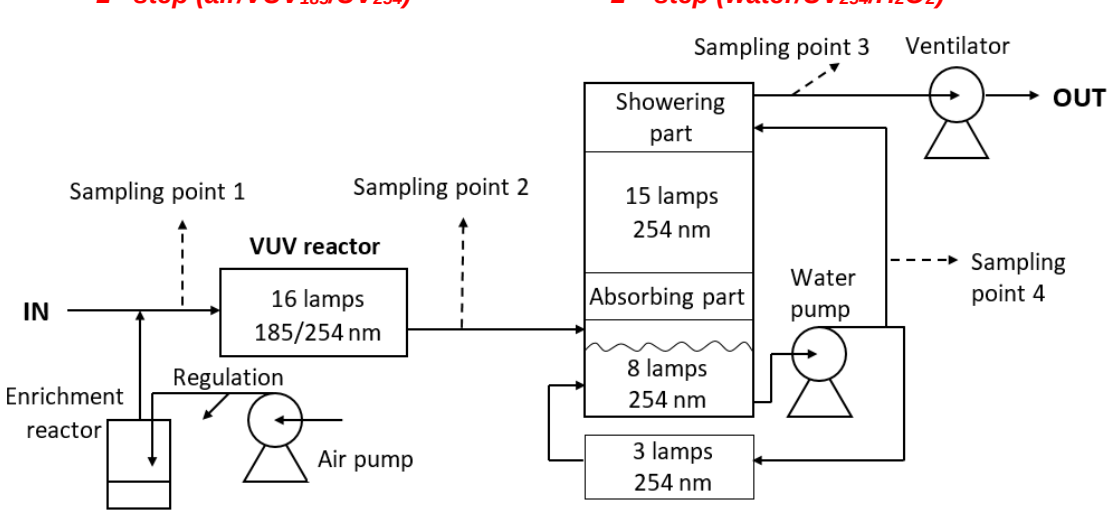

Figure 1 Two steps pilot plant unit.

The effect of photocatalysis was also studied. 6 ceramic foam boards (420x170x32 mm) covered by TiO_2 film were inserted into the VUV reactor to extend the degradation efficiency by photocatalysis in the final experiments.

The airstream was enriched by the toluene vapors by driving small amount of air through a specially designed gas enrichment glass reactor. The solvent vapors concentration was measured online by a portable total hydrocarbon analyzer (FID 2010T, Testa GmbH). The air samples were taken from sampling points (behind the first and behind the second step) with a gas-tight syringe and were analyzed on a gas chromatograph with a flame ionization detector (8890 GC System, Agilent Technologies Inc.). Water samples were regularly taken from the scrubber and analyzed on the total carbon analyzer (Formacs^{HT-I}, Skalar Ltd.). The pH of the water samples was measured using a pH-meter (Multi 3420, WTW) with pH-probe (SenTix 940-3, Xylem Inc.). Intermediates and products of the degradation were determined in selected water samples with gas chromatograph with quadrupole mass selective detector (GC 7890 + MSD 5975, Agilent) and ion chromatograph (Eco IC, Metrohm). The airflow rate was monitored by flow meter Testo 435-4.

Conversion of xylene/styrene was chosen as a determining value for the effectiveness of the solvent vapors' degradation according to the Eqs. (1) and (2):

$$X = \frac{n_{0,k} - n_k}{n_{0,k}} \tag{1}$$

$$X = \frac{c_{0,k} - c_k}{c_{0,k}} \qquad V = const. \tag{2}$$

where X is the degree of conversion (-), $n_{0,k}$ is the initial substance amount of solvent vapors (mol), n is the solvent vapors substance amount (mol), c_0 is the initial concentration of solvent vapors (ppmv) and c is the solvent vapors concentration at the set time (ppmv).

3. RESULTS AND DISCUSSION

The lamps in the **first step of the unit** - photolytic/photooxidation reactor (dry-VUV_{185}/UV_{254}) produce strong UV irradiation, which decomposes oxygen molecules in the air into oxygen atoms. Ozone is then formed from the oxygen atom and oxygen molecule [10]. Ozone is able to oxidize present pollutants and also is photolytically decomposed to produce an electronically excited singlet oxygen atom that reacts with a water molecule to yield two hydroxyl radicals [11]. Another important source of •OH is water (humidity) photolysis under 190 nm. The hydrogen atom (or hydroperoxyl radical $•HO_2$, which also occurs in water photolysis in the presence of O_2) is then able to react with ozone to form more •OH [12]. When the photocatalyst is added (foams coated with TiO_2) to the first step, the system is extended to the next source of hydroxyl radicals. When a semiconductor photocatalyst particle absorbs the photon with an energy equal to or greater than the semiconductor band gap energy, an electron (e^-) from the valence band is excited into the conduction band, leaving behind a positively charged hole (h^+) in the valence band (ionization). In a few nanoseconds, electrons and holes are recombined back in the valence band, generating heat; or they can migrate to the surface of the photocatalyst to react with donors (D), or acceptors (A) of electrons adsorbed on the surface of the particle. Thereby, redox reactions, leading to the desired degradation of organic substances, are initiated. Valence band holes as oxidants can directly oxidize electron donors D – any compound with a redox potential more negative than the flat band potential of the valence band. Conduction band electrons as reductants can reduce electron acceptors A – any compound with the redox potential more positive than the flat band potential of the conduction band. From the toluene degradation point of view, the most important reaction is the oxidation of surface water or hydroxide ions to form the next hydroxyl radicals.

Thus, in the first step, toluene can undergo direct photolytic degradation by UV irradiation, but the rate of these reactions is much lower than the rate of oxidation by photo-induced radicals [13]. The reaction of toluene and ozone (generated by VUV lamps) is also much slower than the reaction with radicals formed from atmospheric oxygen and water vapor after VUV irradiation, especially by hydroxyl radicals [14].

After passing through the first step, part of the toluene vapor is already mineralized, part is oxidized into degradation intermediates and part stays unchanged. Then, **in the second step of the unit** (*aqueous-UV_{254}/H_2O_2*), the residual contaminants are absorbed into the aqueous phase and primarily oxidized by radicals formed from H_2O_2 after UV_{254} irradiation [15] or further oxidized in the gas phase through the UV_{254} irradiation in the scrubber. Photolytic degradation intermediates are often much more soluble in water than toluene themselves, so they should be more easily absorbed into the water and mineralized in the second step. Furthermore, ozone formed in the first step, which would not be consumed for solvent degradation, would be absorbed into the H_2O_2 solution in the second step, where it would be partly utilized for the next solvent oxidation and also partly removed.

UV irradiation (λ = 254 nm) produced by the lamps in the photochemical reactor (wet scrubber) decomposes H_2O_2 yielding 2 •OH radicals. Homolytic cleavage is the most commonly accepted mechanism of H_2O_2 photolysis [16].

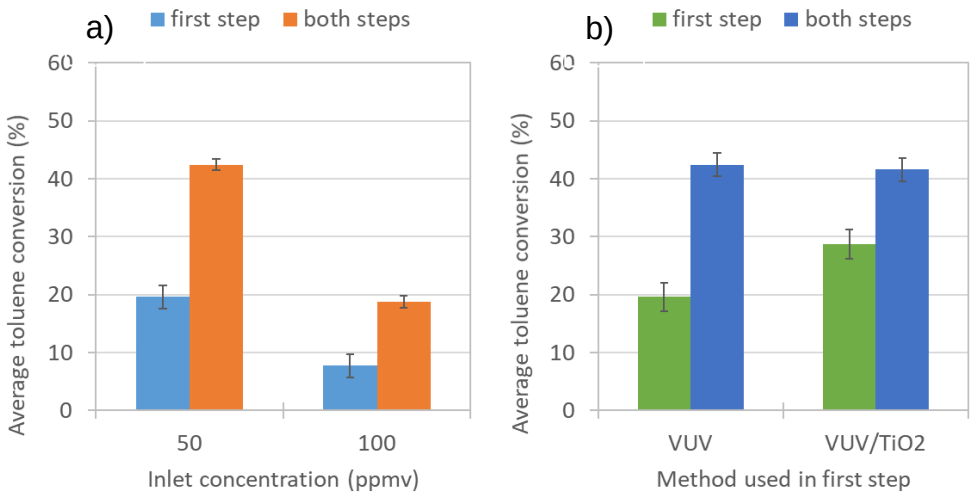

Figure 2 The average toluene conversion:
a) in experiments with inlet toluene concentration 50/100 ppmv

b) in experiment with added photocatalyst (inlet toluene concentration 50 ppmv)

Figure 2 represents the average toluene conversion in experiments using the gas flow rate of 100 m^3/h. Figure 2 a) shows the average achieved toluene conversion in experiments when two different inlet toluene concentrations were used (50 and 100 ppmv). After passing the first step, and both steps, 19.6 %, and 42.5 % of toluene, respectively, were completely removed, while the used inlet toluene concentration was 50 ppmv. Is clearly visible, that the average conversion is rapidly decreasing with increasing toluene content. Figure 2 b) shows the comparison of the average achieved toluene conversion in experiments with the inlet toluene concentration 50 ppmv when the ceramic foams with TiO_2 photocatalyst were added to the first step (method VUV/TiO_2). The toluene degradation efficiency of the first step has increased almost by one third (28.7 %) thanks to photocatalysis. However, when both steps were utilized, the average toluene conversion was almost the same, when only VUV was used.

4. CONCLUSION

The two-step continuous-flow photochemical pilot plant unit was tested for the treatment of toluene-containing waste air. The inlet toluene concentration was set to 50 ppmv and the waste air flow rate was 100 m^3/h. The average toluene conversion after passing the first step (dry-VUV_{185}/UV_{254} photoreactor) and after passing both steps after adding the second step (aqueous-UV_{254}/H_2O_2 photoreactor) achieved 19.6 % and 42.5 %, respectively. The first photocatalytic experiments with interesting results were also conducted. The average toluene conversion was increased by almost a third when the ceramic foams boarders covered by TiO_2 film were inserted into the first step.

ACKNOWLEDGEMENT

EU structural funding in Operational Programme Research, Development and Education, project No. CZ.02.1.01./0.0/0.0/17_049/0008419 „COOPERATION“.

REFERENCES

[1] PEARSON, J.K. European solvent VOC emission inventories based on industry-wide information. *Atmospheric Environment*, 2019. **204**: p. 118-124.
[2] *Solvent VOC Emission Inventories 2019*. [cited 2021-11-09]; Available from: www.esig.org.
[3] *Directive (EU) 2016/2284 of the European Parliament and of the Council of 14 December 2016 on the reduction of national emissions of certain atmospheric pollutants, amending Directive 2003/35/EC and repealing Directive 2001/81/EC (Text with EEA relevance)*, in *OJ L 344*. 2016. p. p. 1–31.
[4] *State of the Environment Reports*. [cited 2021-11-09]; Available from: https://www.mzp.cz/en/state_of_the_environment_reports_documents.
[5] WANG, H., et al. Thermodynamic analysis of a petroleum volatile organic compounds (VOCs) condensation recovery system combined with mixed-refrigerant refrigeration. *International Journal of Refrigeration*, 2020. **116**: p. 23-35.
[6] ZHU, L., et al. A critical review on VOCs adsorption by different porous materials: Species, mechanisms and modification methods. *Journal of Hazardous Materials*, 2020. **389**: p. 122102.
[7] WU, H., et al. Recent progress and perspectives in biotrickling filters for VOCs and odorous gases treatment. *Journal of Environmental Management*, 2018. **222**: p. 409-419.
[8] ALTALYAN, H.N., et al. Removal of volatile organic compounds (VOCs) from groundwater by reverse osmosis and nanofiltration. *Journal of Water Process Engineering*, 2016. **9**: p. 9-21.
[9] LITTER, M.I.. *Introduction to Photochemical Advanced Oxidation Processes for Water Treatment, in Environmental Photochemistry Part II*, 2005, Springer Berlin Heidelberg: Berlin, Heidelberg. p. 325-366.
[10] DOHAN, J.M. et al. The Photochemical Generation of Ozone : Present State–of–the–Art. *Ozone: Science & Engineering*, 1987. **9**(4): p. 315-334.
[11] BUCKLEY, P.T. and BIRKS, J.W. Evaluation of visible-light photolysis of ozone-water cluster molecules as a source of atmospheric hydroxyl radical and hydrogen peroxide. *Atmospheric Environment,* 1995. **29**(18): p. 2409-2415.
[12] BAULCH, D.L., et al. Evaluated Kinetic and Photochemical Data for Atmospheric Chemistry: Supplement II. CODATA Task Group on Gas Phase Chemical Kinetics. J*ournal of Physical and Chemical Reference Data,* 1984. **13**(4): p. 1259-1380.
[13] WANG, J.H. and RAY, M.B. Application of ultraviolet photooxidation to remove organic pollutants in the gas phase. *Separation and Purification Technology*, 2000. **19**(1): p. 11-20.
[14] RAY, M.B. Photodegradation of the Volatile Organic Compounds in the Gas Phase: A Review. *Developments in Chemical Engineering and Mineral Processing*, 2000. **8**(5-6): p. 405-439.
[15] LIU, G., et al. *UV/H_2O_2:* An efficient aqueous advanced oxidation process for VOCs removal. *Chemical Engineering Journal*, 2017. **324**: p. 44-50.
[16] LEGRINI, O., et al. Photochemical processes for water treatment. *Chemical Reviews,* 1993. **93**(2): p. 671-698.

MONITORING OF PESTICIDES IN SURFACE WATERS

Author(s): Tereza MOTÚZOVÁ

Supervisor: prof. Ing. Kamila KOČÍ, Ph.D.

Department: Institute of Environmental Technology, Faculty of Materials Science and Technology, VSB – Technical University of Ostrava

Abstract

The research was focused on the introduction of a chromatographic method for the detection of pesticides and the subsequent monitoring of pesticides in surface waters, namely in the surroundings of Ostrava and Potštát. Solid phase extraction (SPE) using EnvirElut Pesticides extraction columns was used for sample preparation. Subsequent analysis was performed by liquid chromatography with tandem mass spectrometry (LC-MS/MS) using a Synergi Fusion RP column and 5 mM ammonium formate in methanol (MF A) and 5 mM ammonium formate in water (MF B).

Key words:

Monitoring, pesticides, SPE, surface water, LC-MS/MS.

1. INTRODUCTION

Pesticides are chemicals that are used primarily in the agricultural industry to protect plants from plant and animal pests. With the growing consumption of pesticides in agriculture, the contamination of water sources with these substances is increasing. The original forms of pesticides, as well as their degradation products, can subsequently enter surface and underground waters due to rain, irrigation or soil erosion. They can remain in the environment for several years, which can also have a negative impact on drinking water. Through drinking water, these substances can enter the food chain. For that reason, monitoring these substances in the environment is an important step. In waters, they can also have a negative effect on non-target organisms. [1-3].

2. EXPERIMENTAL

In this research, pesticides were monitored in surface waters. Sampling was carried out at regular monthly intervals. Figure 1 and Table 1 show individual sampling points in the surroundings of Ostrava and Potštát.

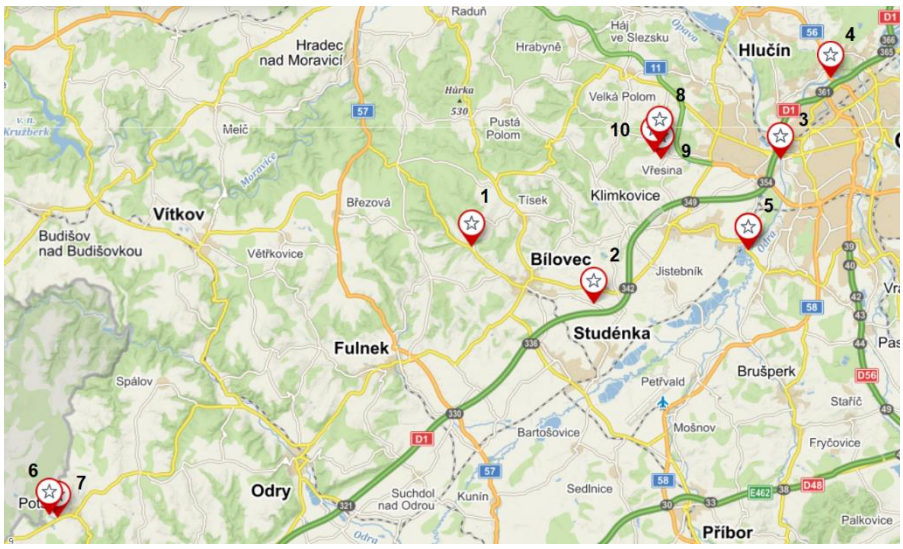

Figure 8 Sampling points. Source: (own)

Table 1 Marking of the sampling points. Source: (own)

Number	Sampling point
1	Stará Ves
2	Velké Albrechtice
3	Ostrava Nová Ves
4	Ostrava Přívoz
5	Polanka nad Odrou
6	Potštát Harta (end)
7	Potštát Harta (beginning)
8	Vřesina, Porubka u Hřiště
9	Vřesina, potok Mokřad
10	Vřesina, Rybník u Oší

Water samples were collected in screw-on glass containers. They were kept in a refrigerator at a temperature of 4 °C until analysis. The water samples were freed of unwanted impurities using a vacuum filtration apparatus with microfilters of 47 mm size, for a particle size of 1.2 μm. Subsequently, solid phase extraction was performed using EnvirElut Pesticides extraction columns, which were placed in a manifold with an attached vacuum pump.

Solid-phase extraction is a powerful technique for the targeted isolation of an analyte from a sample and its subsequent concentration, with a small sample volume being sufficient for analysis. Extraction columns are formed by a sorbent on which the given analyte is captured due to its physical and chemical properties. Sorbents are chosen according to the properties of the analyte. [4]

The extraction was carried out in several steps. Firstly, conditioning was performed with 2 mL methanol (MeOH) and 2 mL H_2O. Then, 100 ml of water sample was applied to the column with the addition of 25 μl of an internal standard of c = 1 μg/ml. A flow rate of approximately 5 drops per minute was used to ensure a sufficiently long sample residence time. Subsequently, a 10-minute vacuum was applied to dry the column. In the last step, elution was carried out using 2 ml of MeOH in plastic disposable tubes.

The solution was evaporated to dryness using a stream of nitrogen in a sample concentrator. The residue was dissolved in 100 μl H_2O and subsequently measured on LC-MS/MS.

The monitored pesticides are listed in Table 2. The pesticides were selected from the list of the most used pesticides, issued by the Central Institute for Supervising and Testing in Agriculture in 2019.

Table 2 Monitored pesticides including retention times and MRM transitions

Pesticide	Retention time	MRM transition
Alachlor	5,36	270,081 / 238,0
Chlormequat	0,61	122,007 / 93,9
Chlorotoluron	2,67	213,022 / 139,8
Chlorpyrifos	4,20	349,865 / 197,8
Metamitron	1,11	203,025 / 174,6
Metazachlor	2,79	296,091 / 130,9
Metolachlor	5,39	284,070 / 252,0
Pendimethalin	4,26	282,157 / 212,0
Pethoxamid	3,52	296,091 / 130,9
Prochloraz	3,80	375,967 / 307,9
Spiroxamine	2,12	342,996 / 150,9
Tebuconazole	3,83	298,218 / 144,0
Terbuthylazine	3,64	308,086 / 124,8
Thiophanate-methyl	3,22	230,071 / 173,9

The Synergi Fusion RP column was finally chosen for the analysis, which contains a C18 hydrocarbon chain and a hydrocarbon residue with a water group, making the column suitable for the analysis of polar substances. The column guarantees sufficient sharpness of chromatographic peaks and sufficient intensity. 5 mM ammonium formate in MeOH (MF A) and 5 mM ammonium formate in H_2O (MF B) were chosen as mobile phases. The MF B gradient was set up for the analysis, see Figure 2. Retention times and MRM (multiple reaction monitoring) transitions of individual pesticides on the Synergi Fusion column are shown in Table 2.

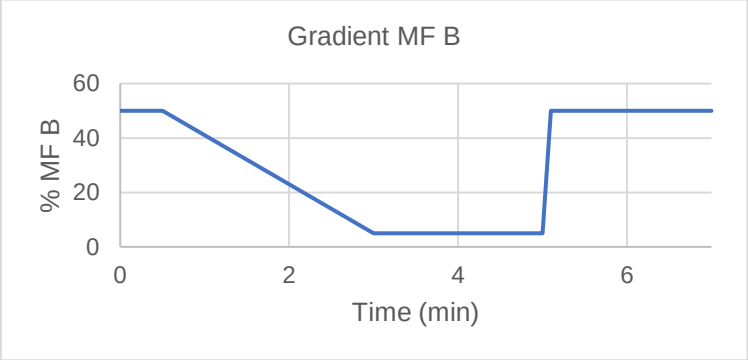

Figure 9 Gradient MF B

Table 3 lists the detected pesticides in individual sampling locations. Figure 3 then shows the seasonal detection of pesticides at the sampling site Potštát-Harta (beginning).

Table 3 Pesticides detected at individual sampling points (the number corresponds to the marking of the sampling point – see Table 1)

Pesticide	1	2	3	4	5	6	7	8	9	10
Alachlor			✓	✓			✓	✓	✓	
Chlormequat	✓		✓	✓	✓	✓	✓	✓	✓	
Chlorpyrifos			✓						✓	✓
Chlortoluron	✓	✓	✓	✓	✓	✓	✓	✓	✓	✓
Metamitron	✓				✓	✓		✓	✓	✓
Metazachlor	✓	✓	✓	✓	✓	✓	✓	✓	✓	✓
Metolachlor	✓	✓	✓	✓	✓	✓	✓	✓	✓	✓
Pendimethalin	✓		✓	✓	✓	✓	✓	✓	✓	✓
Pethoxamid	✓	✓	✓	✓	✓	✓	✓	✓	✓	✓
Prochloraz										
Spiroxamine	✓		✓				✓	✓		✓
Tebukonazole	✓	✓	✓	✓	✓	✓	✓	✓	✓	✓
Terbuthylazine	✓	✓	✓	✓	✓	✓	✓		✓	✓
Thiophanate-methyl										

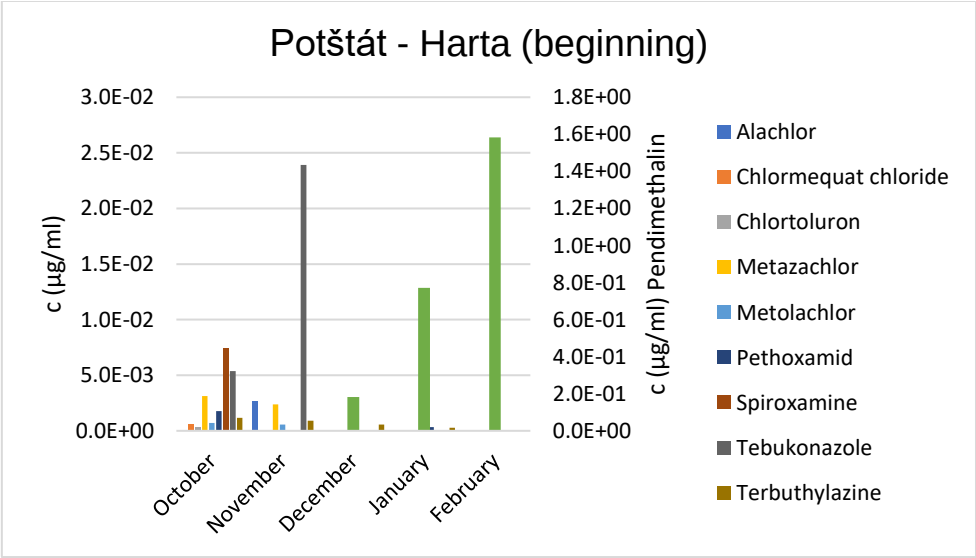

Figure 10 Seasonal detection of pesticides in the sampling point Potštát – Harta (beginning)

3. CONCLUSION

The most frequently pesticides detected in surface water were pendimethalin, metazachlor, metolachlor and tebuconazole. Pendimethalin is used for cereals, metazachlor for oil crops, metolachlor for maize and tebuconazole for cereals. Some samples also contain alachlor, the use of which is prohibited in the EU. It was mainly used for oilseed rape, corn and sunflower. The reason for the ban was its increased persistence in water with a negative impact on humans. [5] Seasonal monitoring at the sampling site Potštát-Harta (beginning) revealed an increasing concentration of pendimethalin in individual months, see Figure 3. This finding was in accordance with the ongoing agricultural season, as pendimethalin is applied before germination.

ACKNOWLEDGEMENT

„This work was supported by EU structural funding in Operational Programme Research, Development and Education, project No. CZ.02.1.01./0.0/0.0/17_049/0008419 „COOPERATION“.
„Experimental results were accomplished by using Large Research Infrastructure ENREGAT supported by the Ministry of Education, Youth ang Sports of the Czech Republic under project No. LM2018098.“
„Experimental results were accomplished by using Large Research Infrastructure ENREGAT supported by the Ministry of Education, Youth and Sports of the Czech Republic under project No. LM2023056.“

REFERENCES

[1] QUAGLIA, Gisela, Ingeborg JORIS, Steven BROEKX, Nele DESMET, Kim KOOPMANS, Karel VANDAELE a Piet SEUNTJENS. A spatial approach to identify priority areas for pesticide pollution mitigation. *Journal of Environmental Management* [online]. 2019, **246**, 583-593 [cit. 2023-05-03]. ISSN 03014797. Dostupné z: doi:10.1016/j.jenvman.2019.04.120
[2] ZHOU, Bin a Xin LI. The monitoring of chemical pesticides pollution on ecological environment by GIS. *Environmental Technology & Innovation* [online]. 2021, **23** [cit. 2023-05-03]. ISSN 23521864. Dostupné z: doi:10.1016/j.eti.2021.101506
[3] NIKONOROW, Maksym. Pesticídy a toxicita prostredia. 1983.
[4] RICHARD CREMLYN; PŘELOŽIL REINER SEIFERT. Pesticidy. 1985.
[5] PEREIRA, Susana P., Sandra M.A. SANTOS, Maria A.S. FERNANDES, et al. Improving pollutants environmental risk assessment using a multi model toxicity determination with in vitro, bacterial, animal and plant model systems: The case of the herbicide alachlor. Environmental Pollution [online]. 2021, 286 [cit. 2023-05-03]. ISSN 02697491. Dostupné z: doi:10.1016/j.envpol.2021.117239

EFFECT OF TiO_2 SYNTHESIS TECHNIQUE ON THE PHOTOCATALYTIC REDUCTION OF CO_2

Author: Rudolf RICKA

Supervisor: prof. Ing. Kamila KOČÍ, Ph.D.

Department: Institute of Environmental Technology, CEET, Faculty of Material Science and Technology, VSB – Technical University of Ostrava

Abstract

This research was based on the evaluation and comparison of the photocatalytic activity for CO_2 reduction over two types of differently synthesized TiO_2 photocatalysts. Specifically, TiO_2 photocatalyst samples were prepared by sol-gel (TiSG) and hydrothermal methods (TiHT). The physical-chemical properties of the photocatalytically TiO_2-based nanomaterials obtained were comprehensively characterized by many analytical techniques (X-ray diffraction (XRD), field emission scanning electron microscopy (FE-SEM), N_2 adsorption, UV-Vis diffuse reflectance spectroscopy (UV-Vis DRS), X-ray photoelectron spectroscopy (XPS) and photoelectrochemical measurements (photocurrent)). Based on the results, it was proved that the synthesized TiO_2-based photocatalysts showed enhanced selectivity to CO and CH_4 during the photocatalytic reduction of CO_2 compared to the most widely used photocatalyst in photocatalysis TiO_2 Evonik P25. After further investigation, the significant influences of a portion of hydroxyl oxygen species and a portion of various surface oxygen species on photocatalytic activity and thus the efficiency of the photocatalytic CO_2 reduction process were studied. This work also highlighted the relation between pH during the CO_2 reduction process and photocatalytic activity for CO_2 reduction, which is reflected in the yields of hydrogen (H_2), carbon monoxide (CO), and methane (CH_4). The results obtained from the realized CO_2 photocatalytic reduction experiments clarified the higher formation of H_2 and CO in the acidic environment. While CH_4 is mainly formed in the basic environment.

Key words:

Photocatalytic CO_2 reduction, effect of pH, TiO_2, sol-gel method, hydrothermal method.

1. INTRODUCTION

As a result of the massive depletion of fossil fuel resources and the steadily increasing concentration of CO_2 emissions in the atmosphere, it is predicted that humanity will face a serious energy and environmental crisis in the coming decades. With these facts in mind, many researchers are interested in finding new ways to solve these issues [1].

Fortunately, the photocatalytic CO_2 reduction process appears to be one of the most promising alternative ways to reduce the concentration of gaseous carbon dioxide and form solar fuels at the same time. The mechanism of the process is based on the conversion of CO_2 molecules into the form of other valuable compounds such as methane or carbon monoxide. The process takes place in the presence of the photocatalytically active material, which is activated by the use of suitable light irradiation. Nevertheless, the commercial application of this reduction process is very limited due to the low conversion of CO_2. Based on these facts, it is therefore very important to design and synthesize new photocatalysts, which will enhance the conversion of CO_2 and thus the whole photocatalytic CO_2 reduction process [2].

The most investigated material in photocatalysis is titanium dioxide (TiO_2). This material is not only cheap, but also readily available, chemically stable and exhibits high activity under UV light. Although this nanomaterial is very useful for photocatalytic reactions, some of its disadvantages are known to negatively affect the resulting photocatalytic activity. Specifically, these include the slow reaction rate, which is due to the high recombination of photoinduced pairs and the wide band gap of the material (3.2 eV). To overcome these drawbacks and enhance the photocatalytic activity, the TiO_2 photocatalyst is most often doped with metals (Ag, Au, Cu, etc.) and non-metals (S, N) or forms heterostructures with other compounds (g-C_3N_4/TiO_2, CeO_2/TiO_2, CuO/TiO_2, etc.) [3, 4].

2. EXPERIMENTAL SECTION

2.1 Synthesis of TiSG photocatalyst

The TiSG sample was synthesized by the sol-gel technique from titanium isopropoxide in isopropanol. First, the aqueous titanium(IV)hydroxide sols were prepared by hydrolysis and peptization of titanium(IV)isopropoxide with distilled water in IPA (isopropanol). Subsequently, a 20 vol.% $Ti(OCH(CH_3)_2)_4$ solution was hydrolyzed by dropwise addition of water (H_2O:$Ti(OCH(CH_3)_2)_4$ = 5:1) and used as a 20 vol.% solution in IPA. Further, nitric acid was added to the IPA-water solution to peptize the sol. The resulting solution was added dropwise to the $Ti(OCH(CH_3)_2)_4$ solution at room temperature with stirring. Finally, the precipitated mixture was evaporated on a rotary evaporator [5].

2.2 Synthesis of TiHT photocatalyst

TiHT photocatalyst was prepared by hydrothermal method from titanium oxysulphate ($TiOSO_4$) and NH_4OH. $TiOSO_4$ represented the source of Ti. TiHT was synthesized in the following steps: First, 15 wt.% titanium oxysulphate was magnetically stirred at room temperature until complete dissolution. Then NH_4OH was diluted to 10% and added to the $TiOSO_4$ solution with vigorous stirring until a pH of 8 was reached. By mixing these solutions, a vigorous white gel was formed. Subsequently, the gel was filtered and rinsed with distilled water. This step was carried out several times to ensure sufficient removal of sulphate and ammonium ions. The absence of sulphate was verified by adding $BaCl_2$ to the filtrate after the third rinse. The amount of water was adjusted so that the TiO_2 content was 5 wt.%. The gel was then dispersed by stirring in aqueous medium at 4500 rpm for 30 minutes. Nitric acid was used as a peptizing agent and added to the dispersed gel. The molar ratio between TiO_2 and HNO_3 was set to 1:1. Teflon-lined stain-less steel autoclave (volume of autoclave = 50 ml) was loaded with 30 g of the prepared gel and a small amount of IPA to adjust the crystal phase content. The autoclave was sealed and placed in a preheated oven at 200 °C for 18 hours. Finally, the products were removed from the oven, cooled to room temperature, rinsed and dried [6].

2.3 Photocatalytic CO_2 reduction experiments

Photocatalytic CO_2 reduction tests were performed at different pH (pH = 7.0/12.9) in a batch photoreactor (volume 357 ml, Figure 1). Photocatalytic experiments were carried out in the presence of a reaction mixture containing 100 ml of 0.2 M NaOH with 0.1 g of a photocatalyst. The photoreactor was thoroughly closed, and the mixture was saturated by CO_2 (pH = 7.0) or He (pH = 12.9) to purge the air from the reactor. An UV-C 254 nm 8 W pen-ray lamp (Ultra-Violet Products Inc.) was used as the irradiation source. The lamp was placed on a quartz glass window at the top of the photoreactor. Before the start of the reaction, the photoreactor was tightly closed and a sample of the gaseous phase was taken through the septum by syringe. Subsequently, the gaseous samples were analyzed using a gas chromatograph (GC, Shimadzu Nexis GC-2030) equipped with a BID detector (dielectric barrier discharge ionization detector). The reaction mixture was irradiated for 8 hours and samples of the gaseous phase were taken at 2, 4, 6 and 8 hours for analysis on a GC-BID device. All experiments were repeated to ensure reproducible results. H_2, CO, and CH_4 were detected as the main products of the experiments. The stability of the photocatalysts was verified by repeated use of the same batch with reproducible results.

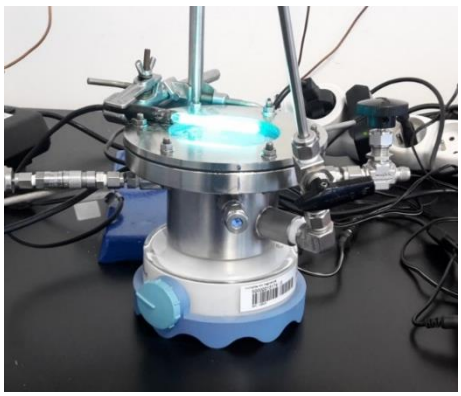

Figure 1 Image of a batch photoreactor. Source: (M. F. Edelmannová)

3. RESULTS AND DISCUSSION

3.1 Results of photocatalytic CO_2 reduction

Based on the results of photocatalytic CO_2 reduction experiments shown in Figure 2, it is evident that both synthesized TiO_2 photocatalysts (TiSG, TiHT) have significantly higher photocatalytic activity compared to the commercial TiO_2 P25, regardless of the pH of the environment during the process. The concentration of dissolved CO_2 at pH = 7.0 was found to be considerably higher than that at pH = 12.9 (Table 1), but this fact cannot be considered as essential for the formation of products during the photocatalytic reduction of CO_2 process. Furthermore, it was observed that while the H_2 and CO yields were higher at pH = 7.0, the formation of CH_4 was higher for the experiments carried out at pH = 12.9. Fortunately, this phenomenon can be explained by the pH of the solution. It has been confirmed that the excess of OH^- in the basic environment (pH = 12.9) can act as a hole scavenger, resulting in the decrease of the recombination rate of generated photoinduced pairs and the utilization of more electrons for the reduction of CO_2 molecules. On the other hand, the lower pH (pH = 7.0 in this case) during the photocatalytic CO_2 reduction is accompanied by a higher concentration of H^+ ions, which is related to the consumption of the generated electrons and the subsequent participation of H^+ ions in the competitive reaction that promotes the formation of hydrogen.

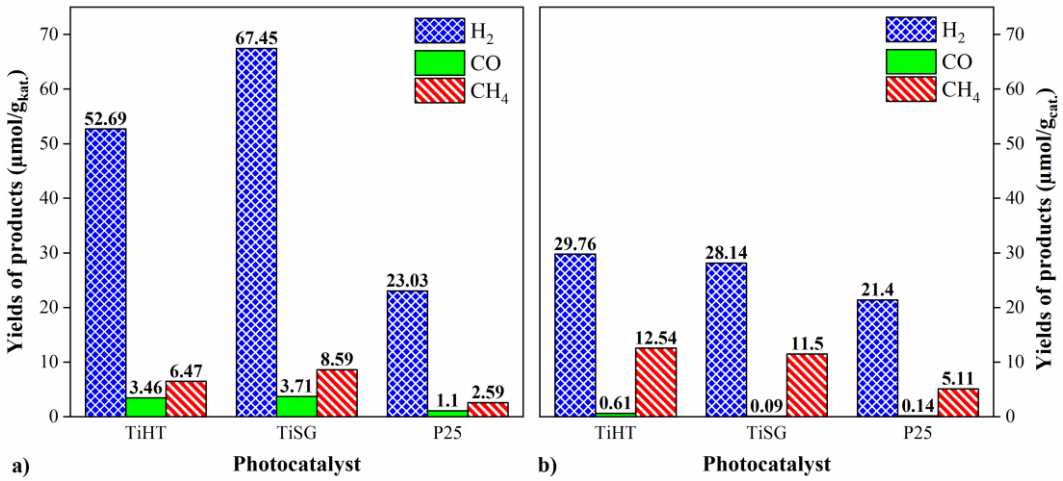

Figure 2 Yields of products after 8 hours of 254 nm irradiation during photocatalytic CO_2 reduction at a) pH = 7.0 and b) pH = 12.9 over synthesized TiO_2 photocatalysts and commercial TiO_2 P25. Source: (own)

Table 1 Measured values of pH and contents of dissolved inorganic carbon and CO_2 in different solutions. Source: [6]

Solution	Content of dissolved inorganic carbon (mg/dm^3)	Content of dissolved CO_2 (mg/dm^3)	pH
0.2M NaOH	23	84	12.9
0.2M NaOH + CO_2	2675	9744	7.0

Further analysis also revealed that the investigated samples of photocatalysts have different proportions of lattice oxygen and oxygen comprised in surface hydroxyl (OH^-) groups. Specific data of portions of hydroxyl oxygen species and various surface oxygen species were determined by XPS measurement (Table 2). The results obtained show that CO and CH_4 yields increase with decreasing amounts of OH^- species. The formation of hydroxyl radicals is due to the reaction between the photogenerated holes and the surface OH^- groups. These radicals are considered to be very strong oxidizing agents that promote the separation of charge carriers, thereby enhancing the selectivity of the photocatalytic CO_2 reduction process.

Table 2 O-containing species on the surface of investigated samples of photocatalysts. Source: [6]

Sample	Oxygen						
	Bulk O^{2-}		OH^-		O (C) *1 s*		Portion of OH^- to total oxygen
	E_b (eV)	(at.%)	E_b (eV)	(at.%)	E_b (eV)	(at.%)	
TiHT	529.1	**54.2**	530.6	**20.2**	532.2	**3.5**	**25.9**
TiSG	529.2	**50.5**	530.6	**15.8**	532.1	**3.1**	**22.8**
P25	529.1	**40.7**	530.3	**23.5**	532.1	**4.3**	**34.0**

4. CONCLUSION

The photocatalytic properties of the investigated samples of photocatalysts were evaluated by the photocatalytic CO_2 reduction process performed at two different pH (7.0, 12.9). Based on the results obtained, it is possible to summarize that the different synthesis ways of the tested materials caused deviations in surface properties. A significant increase in the photocatalytic activity of the synthesized samples of TiO_2-based photocatalysts (TiSG, TiHT) compared to commercial TiO_2 P25 was observed. This increase in the photocatalytic activity for CO_2 reduction of the investigated photocatalysts is related to the portions of OH^- oxygen species to the total oxygen, which were lower for the prepared TiO_2-based nanomaterials than for P25. In addition, the influence of pH on the photocatalytic CO_2 reduction process was also studied. It was confirmed that the basic environment during the mentioned photocatalytic process promotes higher CH_4 formation and, in contrast, an acidic environment promotes CO formation. This fact can be attributed to the participation of electrons in the competitive reaction, which promotes the production of hydrogen.

ACKNOWLEDGEMENT

The work was financially supported by ERDF "Institute of Environmental Technology – Excellent Research" (No. CZ.02.1.01/0.0/0.0/16_019/0000853), Large Research Infrastructure ENREGAT (project No. LM 2023056, GA CR 20-09914 S, and Specific university research (MSMT No 21-SVV/2021). The authors also thank the financial support provided by the Slovenian Research Agency (Grant Nos. N2-0188, P2-0273, P1-0134).

REFERENCES

[1] LINGAMPALLI, S.R., M.M. AYYUB, C.N.R. Rao. Recent progress in the Photocatalytic Reduction of Carbon Dioxide, *ACS Omega.* 2017, **2** (6), 2740-2748.

[2] LI, Q., S. WANG, Z. SUN, Q. TANG, Y. LIU, L. WANG, H. WANG, Z. WU. Enhanced CH_4 selectivity in CO_2 photocatalytic reduction over carbon quantum dots decorated and oxygen doping g-C_3N_4. *Nano Research*. 2019, **12** (11), 2749-2759.

[3] BARROCAS, B.T., N. AMBROŽOVÁ, K. KOČÍ. Photocatalytic Reduction of Carbon Dioxide on TiO_2 Heterojunction Photocatalysts - Review. *Materials*. 2022, **15** (3), 1-33.

[4] SHTYKA, O., R. CIESIELSKI, A. KEDZIORA, W. MANIUKIEWICZ, S. DUBKOV, D. GROMOV, T. MANIECKI. Photocatalytic Reduction of CO_2 Over Me (Pt, Pd, Ni, Cu)/TiO_2 Catalysts. *Topics in Catalysis*. 2020, **63**, 113-120.

[5] TOBALDI, D.M., N. ROZMAN, M. LEONI, M.P. SEABRA, A.S. ŠKAPIN, R.C. PULLAR, J.A. LABRINCHA. Cu-TiO_2 Hybrid Nanoparticles Exhibiting Tunable Photochromic Behavior. *The Journal of Physical Chemistry C*. 2015, **119** (41), 23658-23668.

[6] EDELMANNOVÁ M.F., M. RELI, P. NADRAH, N. ROZMAN, R. RICKA, A.S. ŠKAPIN, M. NOSAN, U.L. ŠTANGAR, K. KOČÍ. A comparative study of TiO_2 preparation method on their photocatalytic activity for CO_2 reduction. *Catalysis Today*. 2023, **413-415**, 113944.

DICHLOROMETHANE OXIDATION OVER Pt/TiO_2-CeO_2 PREPARED USING TITANYL SULPHATE AS TiO_2 PRECURSOR

Author(s): Adéla ŠLACHTOVÁ, Lenka MATĚJOVÁ

Supervisor: Ing. Lenka MATĚJOVÁ, Ph.D.

Department: Institute of Environmental Technology (IET), Centre of Energy and Environmental Technologies (CEET), VSB – Technical University of Ostrava

Abstract

A set of Pt/TiO_2-CeO_2 catalysts in different molar Ti:Ce compositions and parent Pt/TiO_2 and Pt/CeO_2 catalysts were prepared by co-precipitation and impregnation, using titanyl sulfate as a precursor of TiO_2. Prepared catalysts were investigated in oxidation of 500 ppm of dichloromethane in moist conditions (1.5 vol.% of H_2O) in the temperature range of 100-500 °C at WHSV of 71 $m^3/kg_{cat}^{-1} \cdot h^{-1}$ via light-off tests. Pt/TiO_2 catalyst showed the highest catalytic activity, achieving 100% dichloromethane conversion, as well as HCl yield. Concerning unwanted by-products, while CH_2O and CO were detected over all Pt/TiO_2-CeO_2 and Pt/TiO_2 catalysts, over Pt/CeO_2 traces of CO and $CHCl_3$ were identified.

Key words:

Titania-Ceria, Platinum, Titanyl sulphate, Catalytic oxidation, Chlorinated volatile organic compounds.

1. INTRODUCTION

Due to their volatility VOCs (volatile organic compounds) and CVOCs (chlorinated volatile organic compounds) are among the most common air pollutants that damage human health, as they are easily inhaled at room temperature [1, 2].

Catalytic oxidation appears to be a promising technology for reducing CVOC emissions and is attracting increasing interest due to escalating environmental pollution [3, 4]. For this reason, great emphasis is currently focused on the preparation of suitable catalysts to reduce VOCs and CVOCs by catalytic oxidation [5, 6]. In general, the oxidation mechanism of dichloromethane (DCM) is based on its adsorption and disproportionation of C-Cl and H bonds on the acidic sites of the catalyst. Subsequently, the oxidation of intermediates to CO_2, HCl and Cl_2 takes place [6, 7].

Transition metal oxides-based catalysts are used for CVOC degradation mainly because of their low cost and high resistance to chlorine poisoning [8]. Other widely studied catalysts for the catalytic oxidation of CVOCs include catalysts formed from noble metals due to their high activity at low temperature [9, 10]. An important factor in the catalytic oxidation of DCM is the acidity of the catalyst. TiO_2 belongs to acidic catalysts (contains dominantly Lewis acid sites) and its acidity can be enhanced by using *e.g.* titanyl sulphate [5, 6, 11].

The aim of this study was to prepare Pt impregnated TiO_2, CeO_2 and TiO_2-CeO_2 catalysts with different Ti:Ce molar ratios from titanyl sulphate and investigate their catalytic activity and selectivity in total oxidation of dichloromethane under moist conditions. Those catalysts should show higher acidity then the TiO_2 and CeO_2-based catalysts prepared from other Ti precursors. The main goal was to find out the most active and selective Pt supported catalyst in DCM oxidation.

2. EXPERIMENTAL PART

2.1 Catalysts preparation

Parent Pt/TiO_2, Pt/CeO_2 and Pt/TiO_2-CeO_2 catalysts with molar ratio of Ti:Ce = 0.9:0.1, 0.7:0.3, 0.5:0.5 and 0.3:0.7 were prepared by combining the co-precipitation and impregnation method. Titanyl sulphate solution (100g TiO_2/1 dm^3 of titanyl sulphate solution), cerium (III) nitrate hexahydrate and hexachloroplatinic acid (8 wt.%) were used as Ti, Ce and Pt precursors. Firstly, the TiO_2, CeO_2 and TiO_2-CeO_2 in various molar mixtures were co-precipitated using ammonium hydroxide solution, washed with water, dried in the oven and calcined at 550 °C for 4 h with the temperature ramp of 3°C/min. After

calcination the oxides/mixed oxides powder supports were sieved to 0.160–0.315 mm particle-size fraction. After that, ~1 wt.% of Pt was impregnated from the aqueous solution of hexachloroplatinic acid on the oxides/mixed oxides powder supports using impregnation method, this lasted ~45-60 min at 80°C. After impregnation, all Pt-impregnated catalysts were again calcined at 550 °C for 4 h with the temperature ramp of 3°C/min and sieved to 0.160–0.315 mm particle-size fraction. Such prepared Pt catalysts were used for all physicochemical characterizations and catalytic tests.

2.2 Catalysts testing in dichloromethane oxidation

DCM oxidation was carried out in a quartz fixed-bed tubular reactor at atmospheric pressure in the temperature range of 100-500 °C with the heating rate of 5 °C/min. The inlet concentration of DCM in air flow of 1.05 dm^3/min was adjusted to 500 volume ppm. 1.5 vol.% of H_2O was added during all catalytic experiments to ensure sufficient amount of hydrogen and thus improve the selectivity towards desired HCl. Before the start of each catalytic test the catalyst was pre-treated by heating up in the air stream from 25 °C to 500 °C and cooling down to 100 °C. All catalysts were tested in initial light-off tests at the space velocity of 71 $m^3/kg_{cat}^{-1} \cdot h^{-1}$. The gas phase analysis was performed on the GASMET DX-4000N FTIR analyzer which was calibrated to detected following chlorinated hydrocarbons C_2Cl_4, C_2HCl_3, CH_3Cl, CH_2Cl_2, $CHCl_3$, $COCl_2$, HCl, and following oxyderivates of hydrocarbons: CO_2, CO, CH_2O, CH_3OH, CH_4 and C_2H_4. The measured spectra were analyzed with Calcmet analysis software for Windows. The T_{50} and T_{95} temperatures, at which 50 % and 95 % conversions of DCM was observed, were chosen as a measure of catalytic activity. The HCl yield was also evaluated and this was taken as a measure of catalyst selectivity.

3. RESULTS AND DISCUSSION

In Figure 1a DCM light-off curves of investigated catalysts are shown. In Figure 1b the HCl yields of investigated catalysts are displayed. Catalytic activity and selectivity results are summarized in Table 1 and Table 2, respectively. According to DCM light-off curves, the activity of catalysts decreases in the following order: Pt/TiO_2 > Pt/Ti_3Ce_7 > Pt/Ti_7Ce_3 > Pt/Ti_5Ce_5 > Pt/Ti_9Ce_1 > Pt/CeO_2 (Table 1, Figure 1a). Reached DCM conversion over catalysts moved in the range 98-100 %. The most active Pt/TiO_2 catalyst shows also the highest HCl yield, but some unwanted oxidation by-products as 38 ppm of CH_2O and 9 ppm of CO were detected. Over the least active Pt/CeO_2 catalyst the least unwanted oxidation by-products as 4 ppm of CO and 3 ppm of $CHCl_3$ were detected. Detected concentrations of all by-products for all investigated catalysts can be seen in Table 2. In Figure 1b the HCl yields differ for individual catalysts and moves in the range 81-98 %.

Table 1 Catalytic activity of investigated catalysts. Source: own results

Catalyst	T_{50} [°C]	T_{95} [°C]	C_{max} [%]	$Y_{HCl, 50}$ [%]	$Y_{HCl, 95}$ [%]	$Y_{HCl, max}$ [%]
1 wt. % Pt/CeO_2	381	469	98	38	81	95 (472 °C)
1 wt. % Pt/TiO_2	279	318	100	34	86	96 (349 °C)
1 wt. % Pt/Ti_3Ce_7	318	433	100	37	84	89 (399 °C)
1 wt. % Pt/Ti_5Ce_5	337	414	99	44	86	87 (414 °C)
1 wt. % Pt/Ti_7Ce_3	324	393	100	38	86	89 (403 °C)
1 wt. % Pt/Ti_9Ce_1	348	438	99	40	84	86 (435 °C)

Where:
T_{50} (°C) – temperature of 50 % dichloromethane conversion
T_{95} (°C) – temperature of 95 % dichloromethane conversion
C_{max} (%) – maximum achieved dichloromethane conversion
$Y_{HCl, 50}$ (%) – yield of HCl at 50 % dichloromethane conversion
$Y_{HCl, 95}$ (%) – yield of HCl at 95 % dichloromethane conversion
$Y_{HCl, max}$ (%) – yield of HCl at maximum dichloromethane conversion

Table 2 Selectivity results and detected maximum concnetrations of unwanted oxidation by-products. Source: own results

Catalyst	Main products [%]		By-products [ppm]		
	HCl	CO_2	CH_2O	CO	$CHCl_3$
1 wt. % Pt/CeO_2	88	99	n.d.	4	3
1 wt. % Pt/TiO_2	98	86	38	9	n.d.
1 wt. % Pt/Ti_3Ce_7	89	93	63	16	n.d.
1 wt. % Pt/Ti_5Ce_5	81	96	51	21	n.d.
1 wt. % Pt/Ti_7Ce_3	82	98	62	16	n.d.
1 wt. % Pt/Ti_9Ce_1	84	93	55	13	n.d.

n.d. – not detected

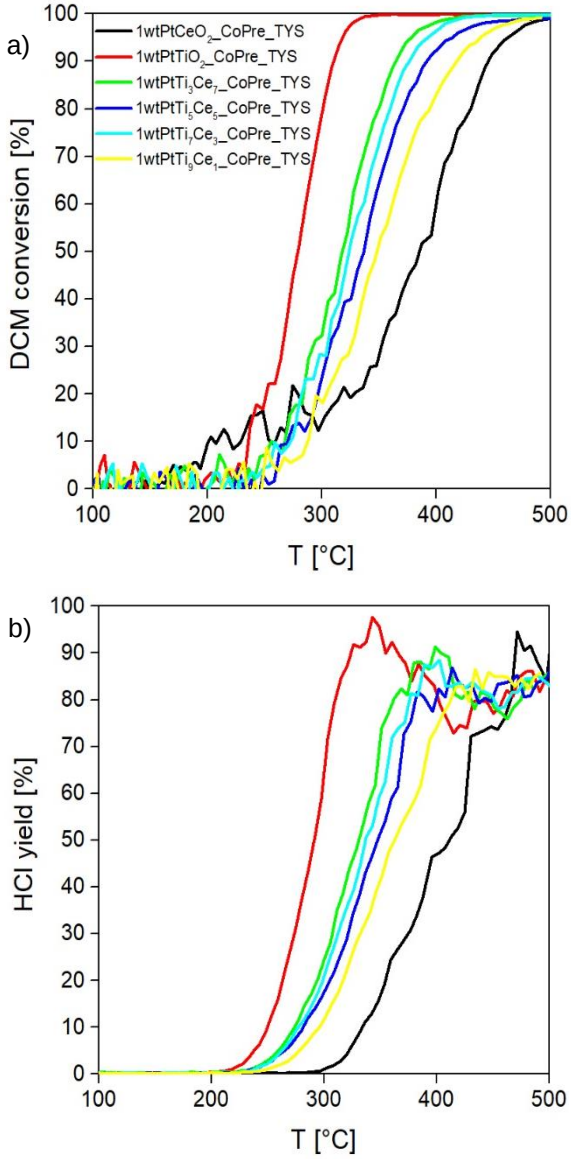

Figure 1 a) Light-off curves of dichloromethane and b) HCl yields in dichloromethane oxidation over investigated catalysts. Source: own results

4. CONCLUSIONS

Prepared Pt/TiO_2-CeO_2 catalysts in different Ti:Ce molar compositions and parent Pt/TiO_2 and Pt/CeO_2 were investigated in dichloromethane oxidation. Pt/TiO_2 showed the highest catalytic activity, reaching 100% DCM conversion at ~340°C, as well as the highest HCl selectivity. A future step of this research will be focused on physicochemical characterization of fresh and used catalysts by using *e.g.* N_2 physisorption, XRD, XRF, AAS, SEM, ICP-MS, NH_3-TPD and H_2-TPR techniques to reveal the cause/s of such catalysts efficiency, including the dichloromethane oxidation mechanism and possible deactivation of the catalysts with chlorine.

ACKNOWLEDGEMENT

„Experimental results were accomplished by using Larhe Research Infrastructure ENREGAT supported by the Ministry of Education, Youth and Sports of the Czech Republic under project No. LM2018098 and No. LM2023056.“

REFERENCES

[1] XU, S., et al., Catalytic oxidation of dichloromethane over CrFeO mixed oxides: Improved activity and stability by sulfuric acid treatment. Applied Catalysis a-General, 2022. **636**.
[2] WANG, L., et al., Promoting effect of Pd modification on the M/TiO_2 (M = V, Ce, Mn) catalyst for catalytic oxidation of dichloromethane (DCM). Chemical Engineering Science, 2021. **234**.
[3] HUANG, H.B., et al., Low temperature catalytic oxidation of volatile organic compounds: a review. Catalysis Science & Technology, 2015. **5**(5): p. 2649-2669.
[4] PITKAAHO, S., et al., Catalytic Oxidation of Dichloromethane and Perchloroethylene: Laboratory and Industrial Scale Studies. Topics in Catalysis, 2011. **54**(16-18): p. 1257-1265.
[5] RAN, L., Z.Y. Wang, and X.Y. Wang, The effect of Ce on catalytic decomposition of chlorinated methane over RuO_x catalysts. Applied Catalysis a-General, 2014. **470**: p. 442-450.
[6] CAO, S., et al., Catalyst performance and mechanism of catalytic combustion of dichloromethane (CH_2Cl_2) over Ce doped TiO_2. Journal of Colloid and Interface Science, 2016. **463**: p. 233-241.
[7] CAO, S., et al., A two-stage Ce/TiO_2-Cu/CeO_2 catalyst with separated catalytic functions for deep catalytic combustion of CH_2Cl_2. Chemical Engineering Journal, 2016. **290**: p. 147-153.
[8] YANG, P., et al., Accelerating effect of ZrO_2 doping on catalytic performance and thermal stability of CeO_2-CrOx mixed oxide for 1,2-dichloroethane elimination. Chemical Engineering Journal, 2016. **285**: p. 544-553.
[9] MAUPIN, I., et al., Bifunctional mechanism of dichloromethane oxidation over Pt/Al_2O_3: CH_2Cl_2 disproportionation over alumina and oxidation over platinum. Journal of Catalysis, 2012. **291**: p. 104-109.
[10] TIDAHY, H.L., et al., New Pd/hierarchical macro-mesoporous ZrO_2, TiO_2 and ZrO_2-TiO_2 catalysts for VOCs total oxidation. Applied Catalysis a-General, 2006. **310**: p. 61-69.
[11] RAN, L., et al., Catalytic decomposition of CH_2Cl_2 over supported Ru catalysts. Catalysis Communications, 2013. **37**: p. 5-8.

ABATEMENT OF MERCURY EMISSIONS FROM INCINERATION OF MUNICIPAL WASTE

Author: Pavel VESELÝ

Supervisor: prof. Ing. Lucie OBALOVÁ, Ph.D.

Department: Institute of Environmental Technology, Faculty of Materials Science and Technology, VSB – Technical University of Ostrava

Abstract

Waste incinerators are among the main anthropogenic sources of mercury emissions. The principle of capturing mercury in waste incinerators was described. Adsorption was chosen as suitable technology where it is worth considering further reduction of mercury in the flue gas in ZEVO Chotíkov waste incineration plant. There are several options: (i) change in the amount of adsorbent to be dosed, (ii) changing the ratio of activated carbon and calcium oxide, (iii) dosing of another adsorbent.

Key words:

Emission, waste combustion, heavy metals, mercury, adsorption, carbon.

1. INTRODUCTION

Mercury emissions from combustion of municipal waste has posed great threat to the environment and human beings due to Hg volatility, mobility, toxicity, and bioaccumulation in ecosystems and food chains.

Generally, mercury can occur as Hg^0, Hg^{1+} (Hg_2Cl_2) and Hg^{2+} ($HgCl_2$, HgO, HgS, $Hg(ONC)_2$, $Hg(CH_3)_2$).[2]

Sources of mercury include small electrical cells in e.g. cameras, toys, small portable radio receivers, calculators, measuring instruments, smoke detectors, radio microphones, in hearing aids, etc. These also include mercury-containing lamps (fluorescent lamps, mercury lamps, etc.), which is used for indoor and outdoor lighting, in projectors and reflectors, in healthcare and laboratories, in photography, etc. Mercury fills the capillaries of old types of thermometers and tonometers. Mercury and its compounds are used as pigments in paints, preservatives, in electric relays, in mercury vacuum pumps. It is often included as an antibacterial and fungicidal additive in paint materials and in lubricating oils. [2] [3]

The aim of this contribution is the description of mercury removal from flue gas from municipal waste incineration and proposal of increasing mercury capture. Improving the efficiency of mercury capture must be effective and at the same time economically advantageous (minimum modifications of the given technology). That's why it is very important to understand the principle and methods of mercury capturing.

2. FLUE GAS TREATMENT IN WASTE INCINERATION PLANT

The work will be carried out at the municipal waste incinerator ZEVO Plzeň (Figure 1). The flue gas treatment (FGT) for the waste incineration plant is conceived in such a way that the contractual requirements and the conditions of environmental legislation can be fulfilled safely.

The flue gas treatment system comprises of the following main parts:

- Spray dryer.
- Dry flue gas cleaning, including baghouse filter and policy filter with ash transportation and adsorbent handling.
- Wet flue gas cleaning, including scrubber 1 and 2, recycling water, refeeding water and neutralization system.
- Catalytic flue gas cleaning.

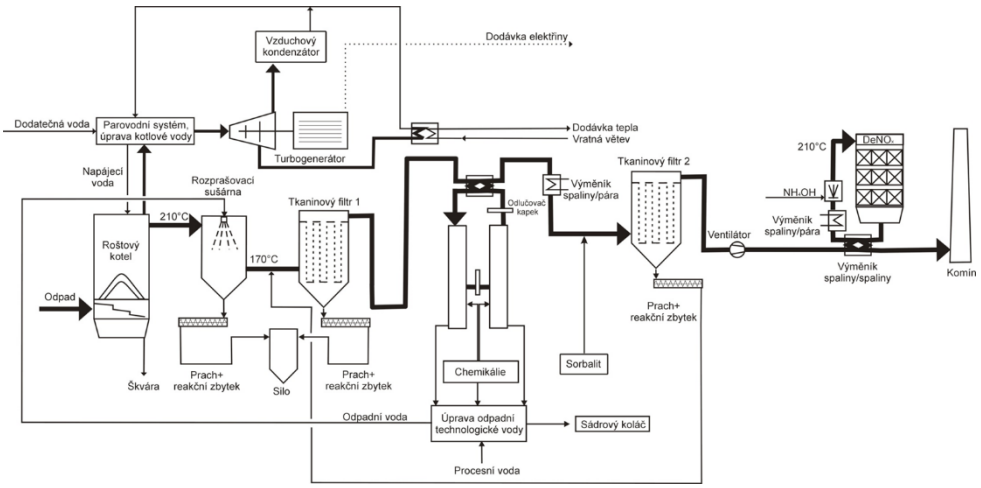

Figure 1 Schema of municipal waste incinerator ZEVO Plzeň. Source: [1]

3. REMOVAL OF MERCURY AND ITS COMPOUNDS FROM FLUE GAS

The most important factors affecting the capture of mercury in waste incinerators are the temperature and volume of the flue gas, the chlorine content in the flue gas, the concentration of mercury in the flue gas and the form of mercury. [3] The ratio of the representation of individual forms of mercury (Hg^0, Hg^{1+} and Hg^{2+}) greatly influences the approach and choice of technology used to capture mercury emissions.

The best available techniques for capturing mercury and its compounds from flue gas are described in the document: "Best Available Techniques (BAT) Reference Document for Waste Incineration, Industrial Emissions Directive 2010/75/EU, Integrated Pollution Prevention and Control, 2019" [3]. In the abbreviated version in the Czech translation in the document: "COMMISSION IMPLEMENTING DECISION (EU) 2019/2010 of 12 November 2019 establishing conclusions on the best available techniques (BAT) for the incineration of waste pursuant to Directive 2010/75/ of the European Parliament and of the Council EU" [5]. It is discussed in particular in section BAT 31 and monitoring in section BAT 4.

The primary technique for reducing mercury emissions is of course the sorting of waste and the separation of potential sources of mercury - especially battery cells, accumulators, or dental amalgams [4]. This technique is very difficult to implement for ZEVO Chotíkov, as it burns unsorted mixed municipal waste.

Secondary techniques for reducing mercury emissions are mercury capture in the flue gas cleaning system. It mainly concerns the transformation of metallic mercury into ionic form and capture in a wet scrubber, with subsequent transformation into a stable form, e.g. HgS.

Another variant is the use of a sorbent in the form of activated carbon (preferably doped with bromine or sulfur) for mercury adsorption from flue gas. By combining these techniques, very low emissions of mercury into the environment can be achieved [4].

3.1 Hg absorption in wet scrubbing

In order to satisfy the deposit requirements set, it is on the one hand necessary to take into account the different mercury compounds and on the other hand the deposit behavior thereof in wet scrubbers, and also their possible reactions to one another. Compounds that can be absorbed in wet scrubbers are $HgCl_2$, Hg_2Cl_2 (disproportionate to $HgCl_2$ and Hg^0); metallic mercury (Hg^0) however can neither be absorbed, nor condensed, in water (high vapour pressure). The distribution of the Hg compounds depends strongly on the firing temperature and the Cl content in the flue gas, whereby from a chamber temperature of approximately 900 °C, more than 95% is present as $HgCl_2$ in the raw gas. The reduction and subsequent disproportionation of already absorbed $HgCl_2$ is tried to be prevented by the low pH value as one cause of reduction is the reaction with SO_2 (Eq. 1). Reaction equation on the disproportionation of $HgCl_2$ in the scrubber is:

$$SO_2 + 2\ HgCl_2 + H_2O \leftrightarrow SO_3 + Hg_2Cl_2 + 2\ HCl \leftrightarrow Hg° + HgCl_2 \quad (1)$$

Material balance of mercury in ZEVO Chotíkov waste incinerator showed that only 5.5 wt.% from input Hg weight flow is contained in the gypsum coming out of the wet flue gas cleaning [6].

3.2 Hg adsorption in fabric filter

Before the flue gas passes the baghouse filter, partly loaded adsorbent (80 wt.% CaO and 20 wt.% activated carbon doped with bromine + dust) is added. The addition of the adsorbent enables the extraction of heavy metals, dioxins and furans. Solid flue gas components are separated from the flue gas by deep bed filtration in the baghouse filter (Figure 2). The flue gas cleaned in this manner exits the baghouse filter via the clean gas chamber in the direction of the gas-gas heat exchanger of the wet flue gas cleaning.

The separated dust particles are removed from the filter bags by blasts of compressed air and fall into the hoppers of the baghouse filter. From there the solid residues are removed from the baghouse filter hoppers by screw conveyors. After the wet flue gas treatment, the flue gas is heated up again by the gas-gas heat exchanger and the steam-gas heat exchanger before it flows through the policy filter, where the remaining dust is separated to the regulatory limits. Compared to the baghouse filter, fresh adsorbent (calcium oxide + activated carbon) is added in front of the policy filter (Figure 3). Again, the separated dust particles are removed from the filter bags by blasts of compressed air and fall into the hoppers of the policy filter. From there the solid residues are removed from the policy filter hoppers by screw conveyors.

Material balance of mercury in ZEVO Chotíkov waste incinerator showed that 81.4 wt.% from input Hg weight flow is contained in ashes from all captures of solid pollutants and sorbent from flue gas cleaning [6].

Adsorption using various sorbents is considered one of the most promising techniques for controlling mercury emissions due to simple equipment, convenient operation and high removal efficiency. Many type of adsorbents can be found in scientific literature.

Absorbent with active carbon (e.g. Fe_2O_3 and CeO_2 modified activated coke[7], carbon co-impregnate with sulfur and chloride[8], activated carbons impregnated with Na_2S [9]),

They have been appearing in the last five years carbon materials such as biochars, graphene and graphene oxides, carbon nanotubes and nanofibers, carbonspheres, carbon aerogels, metal-organic frameworks and graphitic carbon nitrides.

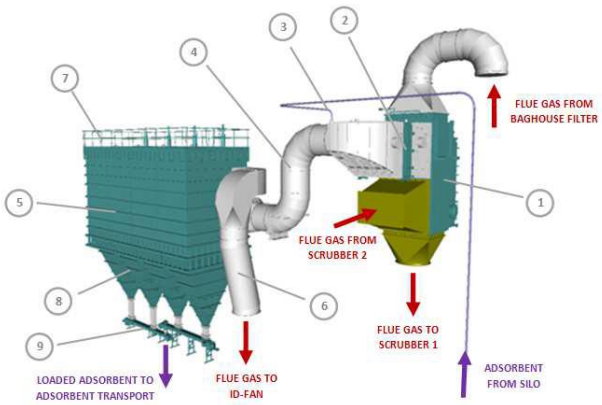

Figure 2 Baghouse filter. Source: (own)

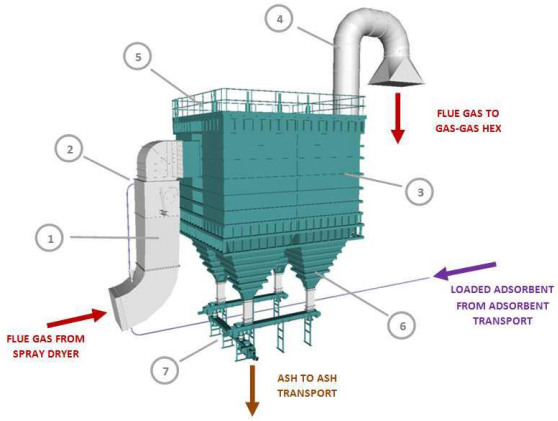

Figure 3 Police filter. Source: (own)

4. CONCLUSION

Evaluation of the operation of ZEVO Chotíkov waste incinerator in terms of influence on the emission of mercury was performed. Adsorption was chosen as suitable technology where it is worth considering further reduction of mercury in the flue gas at a reasonable economic cost. Today, an absorbent is used to reduce the Hg content in the flue gas. It is a mixture of 80 wt.% CaO and 20 wt.% activated carbon doped with bromine. Activated carbon doped with bromine can oxidize elemental mercury into an ionic form, which should then be captured on the surface of the activated carbon. If this coal is still doped with sulfur, irreversible chemisorption of mercury occurs. In the case of ZEVO Chotíkov, 0.57 kg of sorbent/t waste is dosed [6]. It is technologically very easy and at the same time economically advantageous to capture mercury using sorbents.

There are several options.

- Change in the amount of adsorbent to be dosed
- Changing the ratio of activated carbon
- Dosing of another adsorbent

REFERENCES

[1] ZEVO Chotíkov, webové stránky, Odkaz: https://www.zevoplzen.cz/schema
[2] VÁVROVÁ, Zuzana. Disertační práce: Snižování emisí rtuti ze spalování fosilních paliv. Katedra energetiky, Fakulta strojní, VŠB-TU Ostrava 2020.
[3] Látka: Rtuť a sloučeniny (jako Hg), Integrovaný registr znečišťování, https://www.irz.cz/latky/rtut_a_sl, 31.8.2021.
[4] Best Available Techniques (BAT) Reference Document for Waste Incineration, Industrial Emissions Directive 2010/75/EU, Integrated Pollution Prevention and Control, 2019, Odkaz: https://eippcb.jrc.ec.europa.eu/sites/default/files/2020-01/JRC118637_WI_Bref_2019_published_0.pdf.
[5] PROVÁDĚCÍ ROZHODNUTÍ KOMISE (EU) 2019/2010, ze dne 12. listopadu 2019, kterým se stanoví závěry o nejlepších dostupných technikách (BAT) pro spalování odpadu podle směrnice Evropského parlamentu a Rady 2010/75/EU, (oznámeno pod číslem C(2019) 7987). odkaz: https://eur-lex.europa.eu/legal-content/CS/TXT/?uri=CELEX:32019D2010.
[6] LEŠTINSKÝ Pavel, Výzkumná zpráva: Bilance rtuti v ZEVO Chotíkov. Institut environmentálních technologií, VŠB – TU Ostrava, 2021.
[7] Y. Wang, C. Li, L. Zhao, Y. Xie, X. Zhang, G. Zeng, H. Wu, J. Zhang, Study on the removal of elemental mercury from simulated flue gas by Fe2O3-CeO2/AC at low temperature, Environ. Sci. Pollut. Res. 23 (2016) 5099–5110.
[8] A. Sano, M. Takaoka, K. Shiota, Vapor-phase elemental mercury adsorption by activated carbon co-impregnated with sulfur and chlorine, Chem. Eng. J. 315 (2017) 598–607
[9] I. Ie, C. Hung, Y. Jen, C. Yuan, W. Chen, Adsorption of vapor-phase elemental mercury (Hg0) and mercury chloride (HgCl2) with innovative composite activated carbons impregnated with Na2S and S0 in different sequences, Chem. Eng. J. 229 (2013) 469–476.

Nanotechnology

TOXICITY OF SILVER NANOPARTICLES IN PLANTS

Author(s): Petr BĚČÁK[1,2]

Supervisor: prof. Ing. Jana SEIDLEROVÁ, CSc.[1,2]

Department: [1]The Department of Chemistry and Physico-Chemical Processes, Faculty of Materials Science and Technology, VSB − Technical University of Ostrava

[2]Nanotechnology centre CEET, VSB – Technical University of Ostrava

Abstract

Nanotechnology is a field of science with the potential to revolutionize today's technological advances including industrial applications, leading to an inevitable release of nanomaterials into the environment and ecosystem. Silver nanoparticles are one of the most used nanomaterials in various fields, even in the agricultural sector. Plants are the basic component of the ecosystem and the most important source of food for mankind; therefore, understanding the impacts of silver nanoparticles on plant growth and development is crucial for the evaluation of potential environmental risks on food safety animals and human health imposed by silver nanoparticles. This review briefly summarizes uptake, translocation, and accumulation of silver nanoparticles in plants, and exemplifies the phytotoxicity of silver nanoparticles on plants at morphological, physiological, cellular, and molecular levels.

Key words:

Plants, Nanoparticles, Silver, Phytotoxicity.

1. INTRODUCTION

Nanomaterials due to their size (between 1 and 100 nm) and unique chemical and physical characteristics, recently has proved to be an important tool in many industrial agricultural applications [5]. Their use is also penetrating agriculture, for example such as raising productivity of many crops. In addition to studying their benefits, it is necessary to monitor the impact of their use on the environment.

Among various types of MNPs, silver nanoparticles are the most applied nanomaterial. It is reported that nearly 25% of all nanotechnology consumer products involve silver nanoparticles (AgNPs) [28]. Silver nanoparticles are fetching more attention because of their application or requirement in daily life [3,4] Because of their well-known antibacterial and antifungal properties, they can be used in household products, food packaging, textiles, silver coated medical devices, such as nanogels, nano-fusions, antiseptics in healthcare delivery, and personal healthcare [6,12,18,22,24,25]. In order to search for better solutions to the problems related to food security and occurrence of diseases, nanosilver is gaining priority as one of the leading solutions with more stability and surface area as compared to other nano-solutions [5,11]. Apart from this, AgNPs have wide range of applications as electronic devices and in solar energy because of their good electrical conductivity and photochemical properties [2,29]. Moreover, some authors present them as suitable in wastewater treatment process [25,32].

Despite its beneficial applications, numerous harmful effects of AgNPs have also been reported in plants, animals and water organisms [17,27].

Therefore, the release of AgNPs into ecosystems raises great concerns about their safety and environmental toxicity. As plants are a vital part of ecosystem and the primary trophic level in ecosystems, representing the base of the food chain [13,15] a good understanding of the impacts of AgNPs on plants is of utmost importance for assessing their toxicity and potential to cause bacterial resistance to drugs [7].

This study briefly describes the uptake and translocation of AgNPs and gives an information of the impacts of AgNPs on, plants. The phytotoxicity mechanisms via which AgNPs cause impacts on plants and the tolerance mechanisms through which plants alleviate the detrimental effects of AgNPs are discussed for a better understanding of interactions between plants and AgNPs. Numbers of defense strategies are found in the organisms through which they avoid or lessen the possible impact of AgNPs. These defense mechanisms are important to understand as it may provide

an exact understanding toward the amelioration of the problems arising due to the nanoparticle pollution and its impact on environment. However, the effect as well as the tolerance may vary across the organisms.

2. Interaction of AgNPs with plants

With an exposure of AgNPs to plants trough soil, artificial soil i.e., perlite or aquaponics systems, nanoparticles may penetrate the cell wall and cell membrane of root epidermis. After entering the plant, they penetrate the cell wall and plasma membranes of epidermal layer of roots, and then enter inside the vascular tissues. AgNPs can reach stele of vascular plant by two possible ways, either by symplastic transport trough cells or passively through the apoplast of the endodermis. Once their reached plant vascular bundle (xylem) the AgNPs can be further translocated to plants leaves illustrated in Figure 1 [9,14,27]. Further translocation of AgNPs is aided by endocytosis [19] which include the creation of vesicle that enfold the material and finally transport AgNPs from plasma membrane to the cells.

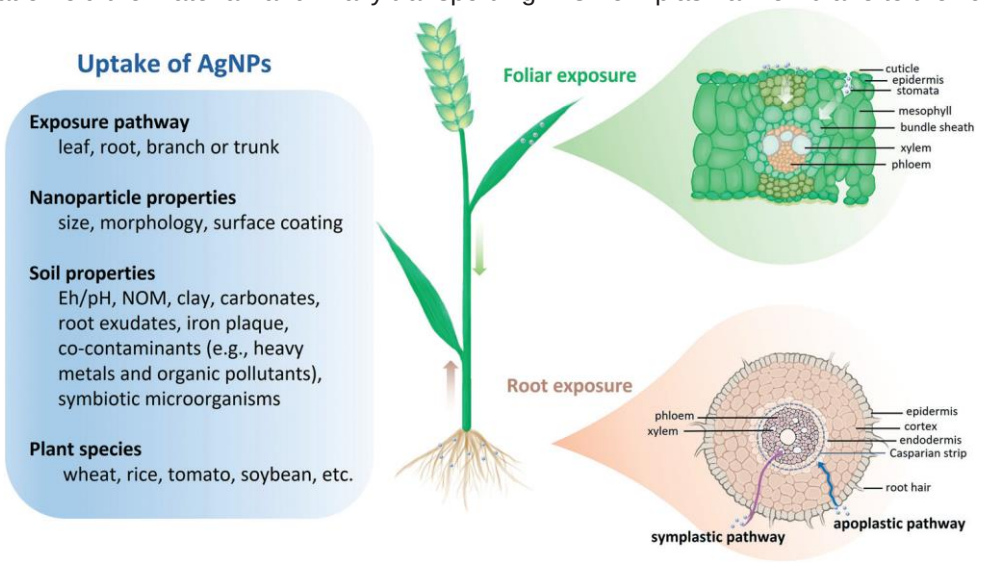

Figure 1 Schematic diagram of the uptake of AgNPs in plants and the influencing factors. Source: [9]

After the exposure to AgNPs, significant changes in the morphology of plants were observed. Growth potential, seed germination, biomass, and leaf surface area are the commonly used parameters for assessing the phytotoxicity of AgNPs in plants [1,30]. Studies have revealed that AgNPs show toxic behavior against mitochondria and generate reactive oxygen species (ROS) [8]. These ROS damage the cell membrane, disrupt adenosine triphosphate (ATP) production pathway and DNA replication and alter gene expression [16]. ROS procreation is frequently followed by a generation of oxidative stress these factors are further signs of AgNPs phytotoxicity [31]. AgNPs have negative impact on the root growth of germinating seedlings and reduces the fresh biomass of the plant through reduction in root elongation and weight [27].

The process of phytotoxicity of AgNPs to plants at the physiological level is often accompanied by a reduction of chlorophyll, carotenoids and nutrient uptake, decline of transpiration rate, and alteration of hormone levels [30]. AgNPs can disrupt the synthesis of chlorophyll in leaves and, thus, affect the photosynthetic system of the plants AgNPs modify the expression of several proteins of primary metabolism and cell defense system [14].

3. Mechanism of toxicity of AgNPs

During AgNPs uptake and translocation, Ag^+ is released from AgNPs, resulting in oxidative stress through the generation of ROS and disturbing cell function, causing phytotoxicity by binding to cell components and modifying their activities [26,30]. Manufactured AgNPs are typically stabilized and capped against aggregation through surface coating, using organic or inorganic compounds to coat the surface of AgNPs to obtain electrostatic, steric, or electrostatic repulsive forces between particles. Therefore, surface coating may change AgNP properties such as optical properties, dispersion, and shape [20,23] therefore influencing the toxicity of AgNPs to plants.

4. Mechanisms of tolerance

Phytotoxicity of AgNPs is accompanied with oxidative stress, which is caused by the production of ROS after AgNPs exposure. To avoid the harmful effects of ROS, a set of antioxidant defense mechanisms are activated in plant cells. The defense mechanism involves the activities of enzymatic antioxidants such as superoxide dismutase (SOD), catalase (CAT), ascorbate peroxidase (APX), glutathione peroxidase (GPX), dehydroascorbate reductase (DHAR), and glutathione reductase (GR) [10,21,27]. As different types of ROS have different modes of action and exhibit different effects on cellular organelles of plant cells, they can be balanced or removed by specific antioxidant enzymes [13]. For example, there are three types of SOD in plant cells, including Fe-SOD, Mn-SOD, and Cu-Zn-SOD, and they can rapidly convert highly toxic ROS ($O_2^{\bullet-}$) to less toxic species (H_2O_2). CAT can convert H_2O_2 to H_2O and O_2. APX is able to convert H_2O_2 to H_2O via ascorbate oxidation into monodehydroascorbate (MDA) and dehydroascorbate (DHA), both of which can be recycled to produce more ascorbate via the catalysis of MDA reductase (MADR) and DHAR [13]. Upon exposure to AgNPs, activities of these enzymatic antioxidants are elevated in plant cells to protect the cells from oxidative stress.

5. CONCLUSION

Silver nanoparticles are beneficial in fields of industry in healthcare, electronic, agriculture/food and energy. Despite its beneficial applications AgNPs may also be dangerous to humans, animals, and plants. This study shortly summarizes the uptake, phytotoxicity and tolerance mechanisms of the AgNPs on the plants. Toxic mechanisms of AgNPs are caused by production of ROS which is accompanied by the overproduction of ROS scavengers i.e., SOD, CAT, APX as a tolerance mechanism of the plants. However, AgNPs toxicity also depends on the shape, size, encapsulation and the tolerance mechanism of the plant, stage of growth and type of the plant.

ACKNOWLEDGEMENT

We thank for the financial support to SGS No. SP2023/095.

REFERENCES

[1] ASLANI, Farzad, Samira BAGHERI, Nurhidayatullaili MUHD JULKAPLI, Abdul Shukor JURAIMI, Farahnaz Sadat Golestan HASHEMI a Ali BAGHDADI, 2014. Effects of engineered nanomaterials on plants growth: An overview. *Scientific World Journal* [online]. **2014**. ISSN 1537744X.

[2] ASLFATTAHI, Navid, R. SAIDUR, A. ARIFUTZZAMAN, A. S. ABDELRAZIK, L. SAMYLINGAM, Mohd Faizul Mohd SABRI a Nor Azwadi Che SIDIK, 2022. Improved thermo-physical properties and energy efficiency of hybrid PCM/graphene-silver nanocomposite in a hybrid CPV/thermal solar system. *Journal of Thermal Analysis and Calorimetry* [online]. **147**(2), 1125–1142. ISSN 15882926.

[3] CHALOUPKA, Karla, Yogeshkumar MALAM a Alexander M. SEIFALIAN, 2010. Nanosilver as a new generation of nanoproduct in biomedical applications. *Trends in Biotechnology* [online]. **28**(11), 580–588. ISSN 01677799.

[4] CHEN, X. a H. J. SCHLUESENER, 2008. Nanosilver: A nanoproduct in medical application. *Toxicology Letters* [online]. **176**(1), 1–12. ISSN 03784274.

[5] DONALDSON, Ken a Craig A. POLAND, 2013. Nanotoxicity: Challenging the myth of nano-specific toxicity. *Current Opinion in Biotechnology* [online]. **24**(4), 724–734. ISSN 09581669.

[6] DURÁN, Nelson, Priscyla D MARCATO, Gabriel I H De SOUZA, Oswaldo L ALVES a Elisa ESPOSITO, 2007. Antibacterial Effect of Silver Nanoparticles Produced by Fungal Process on Textile Fabrics and Their Effluent Treatment [online]. **3**(2).

[7] GARDEA-TORRESDEY, Jorge L., Cyren M. RICO a Jason C. WHITE, 2014. Trophic transfer, transformation, and impact of engineered nanomaterials in terrestrial environments. *Environmental Science and Technology* [online]. **48**(5), 2526–2540. ISSN 15205851.

[8] HSIN, Yi Hong, Chun Feng CHEN, Shing HUANG, Tung Sheng SHIH, Ping Shan LAI a Pin Ju CHUEH, 2008. The apoptotic effect of nanosilver is mediated by a ROS- and JNK-dependent mechanism involving the mitochondrial pathway in NIH3T3 cells. *Toxicology Letters* [online]. **179**(3), 130–139. ISSN 03784274.

[9] HUANG, Danyu, Fei DANG, Yingnan HUANG, Ning CHEN a Dongmei ZHOU, 2022. Uptake, translocation, and transformation of silver nanoparticles in plants. *Environmental Science: Nano* [online]. **9**(1), 12–39. ISSN 20518161.

[10] KE, Mingjing, Yan LI, Qian QU, Yizhi YE, W. J.G.M. PEIJNENBURG, Zhenyan ZHANG, Nuohan XU, Tao LU, Liwei SUN a Haifeng QIAN, 2020. Offspring toxicity of silver nanoparticles to Arabidopsis thaliana flowering and floral development. *Journal of Hazardous Materials* [online]. **386**(October 2019), 121975. ISSN 18733336.

[11] KHANNA, Vinod Kumar, 2016. Nanomaterials and Their Properties [online]. 25–41.

[12] KUMARA, A Muthu, C KARTHIKEYAN, M RAJASIMMAN a M G DINESH, 2015. Ecotoxicology and Environmental Safety Synthesis of silver nanoparticle and its application. *Ecotoxicology and Environmental Safety* [online]. **121**(42), 211–217. ISSN 0147-6513.
[13] MA, Chuanxin, Jason C. WHITE, Om Parkash DHANKHER a Baoshan XING, 2015. Metal-Based Nanotoxicity and Detoxification Pathways in Higher Plants. *Environmental Science and Technology* [online]. **49**(12), 7109–7122. ISSN 15205851.
[14] MA, Xingmao, Jane GEISER-LEE, Yang DENG a Andrei KOLMAKOV, 2010a. Interactions between engineered nanoparticles (ENPs) and plants: Phytotoxicity, uptake and accumulation. *Science of the Total Environment* [online]. **408**(16), 3053–3061. ISSN 00489697.
[15] MAURER-JONES, Melissa A., Ian L. GUNSOLUS, Catherine J. MURPHY a Christy L. HAYNES, 2013. Toxicity of engineered nanoparticles in the environment. *Analytical Chemistry* [online]. **85**(6), 3036–3049. ISSN 00032700.
[16] MORENO-GARRIDO, Ignacio, Sara PÉREZ a Julián BLASCO, 2015. Toxicity of silver and gold nanoparticles on marine microalgae. *Marine Environmental Research* [online]. **111**, 60–73. ISSN 18790291.
[17] NAVARRO, Enrique, Anders BAUN, Renata BEHRA, Nanna B. HARTMANN, Juliane FILSER, Ai Jun MIAO, Antonietta QUIGG, Peter H. SANTSCHI a Laura SIGG, 2008. Environmental behavior and ecotoxicity of engineered nanoparticles to algae, plants, and fungi. *Ecotoxicology* [online]. **17**(5), 372–386. ISSN 09639292.
[18] OSONGA, Francis J, Ali AKGUL, Idris YAZGAN, Ayfer AKGUL, Gaddi B ESHUN, Laura SAKHAEE a Omowunmi A SADIK, [b.r.]. Size and Shape-Dependent Antimicrobial Activities of Silver and Gold Nanoparticles : A Model Study as Potential Fungicides.
[19] OVEČKA, M., I. LANG, F. BALUŠKA, A. ISMAIL, P. ILLEŠ a I. K. LICHTSCHEIDL, 2005. Endocytosis and vesicle trafficking during tip growth of root hairs. *Protoplasma* [online]. **226**(1–2), 39–54. ISSN 0033183X.
[20] PEREIRA, Susana P.P., Fátima JESUS, Sara AGUIAR, Rhaul DE OLIVEIRA, Marco FERNANDES, James RANVILLE a António J.A. NOGUEIRA, 2018. Phytotoxicity of silver nanoparticles to Lemna minor: Surface coating and exposure period-related effects. *Science of the Total Environment* [online]. **618**, 1389–1399. ISSN 18791026.
[21] QIAN, Haifeng, Xiaofeng PENG, Xiao HAN, Jie REN, Liwei SUN a Zhengwei FU, 2013. Comparison of the toxicity of silver nanoparticles and silver ions on the growth of terrestrial plant model Arabidopsis thaliana. *Journal of Environmental Sciences (China)* [online]. **25**(9), 1947–1956. ISSN 10010742.
[22] RAI, Mahendra, Alka YADAV a Aniket GADE, 2009. Silver nanoparticles as a new generation of antimicrobials. *Biotechnology Advances* [online]. **27**(1), 76–83. ISSN 0734-9750.
[23] RAVINDRAN, Aswathy, T. C. PRATHNA, Vinod Kumar VERMA, N. CHANDRASEKARAN a Amitava MUKHERJEE, 2012. Bovine serum albumin mediated decrease in silver nanoparticle phytotoxicity: Root elongation and seed germination assay. *Toxicological and Environmental Chemistry* [online]. **94**(1), 91–98. ISSN 02772248.
[24] THUY, Ngoc, Trang LE, Dai Hai NGUYEN, Ngoc Hoi NGUYEN a Yern Chee CHING, 2020. applied sciences Silver Nanoparticles Ecofriendly Synthesized by Achyranthes aspera and Scoparia dulcis Leaf Broth as an E ff ective Fungicide. 1–14.
[25] TRAN, Quang Huy, Van Quy NGUYEN a Anh-tuan LE, 2013. Corrigendum : Silver nanoparticles : synthesis , properties , toxicology ,.
[26] TRIPATHI, Ashutosh, Shiliang LIU, Prashant Kumar SINGH, Niraj KUMAR, Avinash Chandra PANDEY, Durgesh Kumar TRIPATHI, Devendra Kumar CHAUHAN a Shivendra SAHI, 2017a. Differential phytotoxic responses of silver nitrate (AgNO3) and silver nanoparticle (AgNps) in Cucumis sativus L. *Plant Gene* [online]. **11**(February), 255–264. ISSN 23524073.
[27] TRIPATHI, Durgesh Kumar, SHWETA, Shweta SINGH, Swati SINGH, Rishikesh PANDEY, Vijay Pratap SINGH, Nilesh C. SHARMA, Sheo Mohan PRASAD, Nawal Kishore DUBEY a Devendra Kumar CHAUHAN, 2017c. An overview on manufactured nanoparticles in plants: Uptake, translocation, accumulation and phytotoxicity. *Plant Physiology and Biochemistry* [online]. **110**, 2–12. ISSN 09819428.
[28] VANCE, Marina E., Todd KUIKEN, Eric P. VEJERANO, Sean P. MCGINNIS, Michael F. HOCHELLA a David Rejeski HULL, 2015. Nanotechnology in the real world: Redeveloping the nanomaterial consumer products inventory. *Beilstein Journal of Nanotechnology* [online]. **6**(1), 1769–1780. ISSN 21904286.
[29] WALSHE, J., George AMARANDEI, Hind AHMED, S. MCCORMACK a John DORAN, 2019. Development of poly-vinyl alcohol stabilized silver nanofluids for solar thermal applications. *Solar Energy Materials and Solar Cells* [online]. **201**(July), 110085. ISSN 09270248.
[30] YAN, An a Zhong CHEN, 2019. Impacts of silver nanoparticles on plants: A focus on the phytotoxicity and underlying mechanism. *International Journal of Molecular Sciences* [online]. **20**(5), 23–25. ISSN 14220067.
[31] YIN, Liyan, Benjamin P. COLMAN, Bonnie M. MCGILL, Justin P. WRIGHT a Emily S. BERNHARDT, 2012. Effects of Silver Nanoparticle Exposure on Germination and Early Growth of Eleven Wetland Plants. *PLoS ONE* [online]. **7**(10). ISSN 19326203.
[32] ZHANG, Chiqian, Zhiqiang HU, Ping LI a Shashikanth GAJARAJ, 2016. Science of the Total Environment Governing factors affecting the impacts of silver nanoparticles on wastewater treatment. *Science of the Total Environment, The* [online]. **572**, 852–873. ISSN 0048-9697.

TOWARDS METAL FREE (PHOTO)CATALYSTS - g-C_3N_4-INSPIRED COFs - RETROSYNTHESIS AND INITIAL RESULTS

Author: Daniel CVEJN

Supervisor: prof. Ing. Petr PRAUS, Ph. D.

Department: ENET Centre, CEET, VSB – Technical University of Ostrava

Abstract

Presented proceeding summarizes the motivation, structural design, retrosynthesis and initial results of covalent organic frameworks designed to mimic and modify the structure of triazine structural isomer of graphitic carbon nitride (g-C_3N_4). The structural design is carried out with the aim of enhancing the properties of g-C3N4 and creating a new material more suitable for targeted synthetic photocatalysis.

Keywords:

Catalysis, covalent organic frameworks (COFs), retrosynthethic analysis, novel materials.

1. MOTIVATION AND BACKGROUND

Depending on the statistics and/or method of calculation, the chemical industry is estimated to consume between 25 % and 40 % of the energy used by manufacturing industry as a whole. Since manufacturing accounts for 30 % of humanity's energy consumption, this activity accounts for the lion's share of our total energy consumption. As such, the chemical industry is indeed one of the biggest challenges in pursuing a more energy-efficient society, hence lowering the carbon consumption. The most straightforward way to materialize these goals is to both increase the yield of key chemical steps, and to reduce the number of chemical steps needed to obtain the target compound. The search for new catalysts and/or novel catalytic pathways appears to be the optimal strategy to tackle this challenge.

2. INTRODUCTION

Graphitic carbon nitride g-C_3N_4 is a covalent organic framework (COF) that forms spontaneously upon heating a nitrogen-rich organic compound (e. g. melamine [1], cyanoguanidine [2], cyanamide [3], urea [4]) over 500 °C. It is a compound occurring in two isomers. Triazine-based g-C_3N_4 (*t*-g-C_3N_4) and heptazine-based g-C_3N_4 (*h*-g-C_3N_4). While *t*-g-C_3N_4 is produced by co-melting the precursors with inorganic salts, *h*-g-C_3N_4 is usually a product of direct heating of the precursors in the furnace. Both *t*-g-C_3N_4 and *h*-g-C_3N_4 are materials active in photocatalysis. In particular, non-selective decays of dyes, pharmaceuticals and pollutants are carried out routinely, reproducibly and successfully by various research groups. Attempts to use these compounds in targeted (photo)catalysed reactions often suffer from significant shortcomings. As optimal as it may seem to take advantage of a metal-free (therefore “green” and cheap) catalyst, the reaction protocols selective enough to be thus made use of do not seem to materialize. Both *h*-g-C_3N_4 and *t*-g-C_3N_4 seem to be either too active photocatalysts allowing a variety of side-reactions and suffering from low selectivity, or too inactive compromising the yield of certain reactions.

The way to overcome these challenges is to selectively modify their structure. Since the *t*-g-C_3N_4 and the *h*-g-C_3N_4 are considered COFs, an obvious way to tailor those materials is via synthesis of similarly looking COFs inspired by their structure. This work documents the design of such materials, namely COFs inspired by *t*-g-C_3N_4. Their design is informed by both anticipated properties of the target compounds deduced from the precedents in references, and their possible synthetic availability and accessibility.

3. DESIGN AND RETROSYNTHETIC ANALYSES

DESIGN OF THE TARGET COFs

COFs **1**, **2a** – **2e**, **3a** – **3d** (**Scheme 1**) were selected as target derivatives taking into account probability of their successful preparation as well as their expected properties. The trivalent CH-bridged triazine COF **1** is in fact a hydrogenated derivative of half-metallic g-C_4N_3 (hm-C_4N_3), relatively novel material predicted by computational chemistry and several times successfully synthesized in various textures including nanosheets or nanotubes. Hm-C_4N_3 is known for its remarkable conductive, catalytic and gas-adsorbing properties, which were demonstrated in the real materials. Yet, the material is more often observed as an admixture and/or composite with other carbon nitrides and/or contaminated by another material [5]. Therefore, COF **1** could be a good starting point to obtain high-quality g-C_4N_3 sample, if proper oxidation pattern is found. Furthermore, due to its natural hydrogenation character, COF **1** is highly expected to have an activity in catalytic cycles such as oxygen reduction reaction and hydrogen evolution.

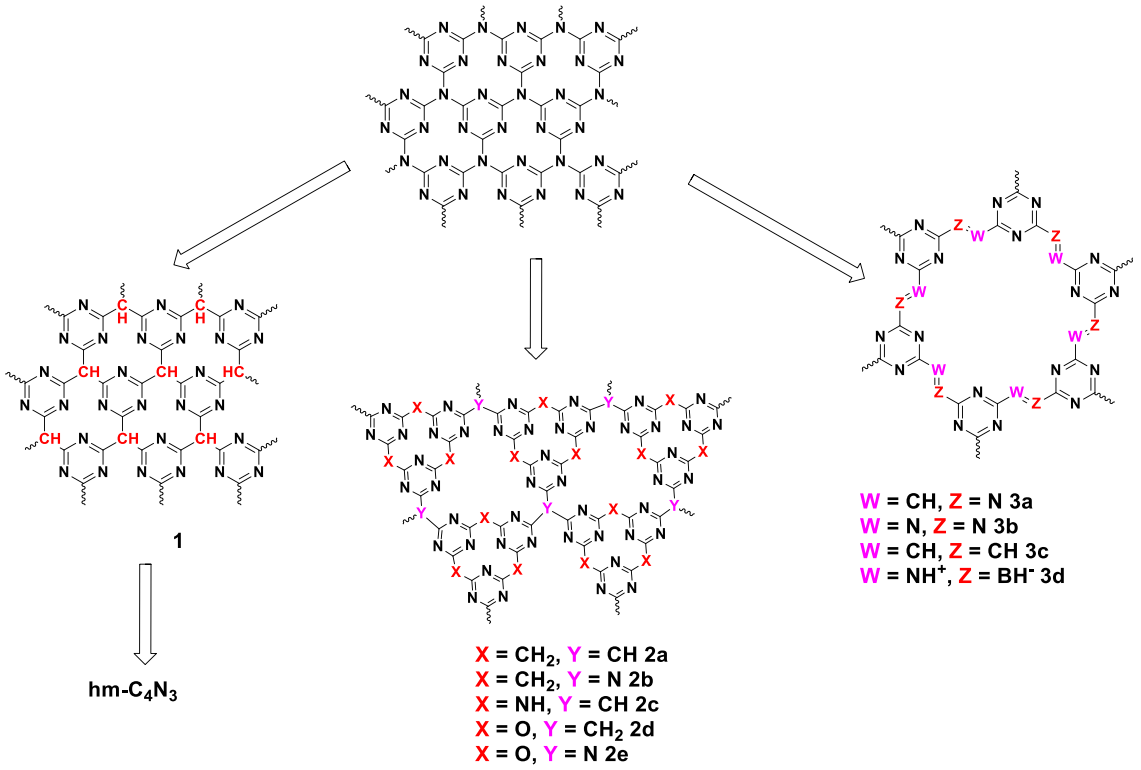

Scheme 1 Designed materials. Source: (own)

The family of COFs **2** on the other hand, resemble the structure of *h*-g-C_3N_4 where heptazine-core is replaced with a bridged tris-triazine motive. This allows for a hierarchical structure with two types of bridging moieties, the inner bridge X and the outer bridge Y (**Scheme 1**; centre). Such a material design allows the structure to be tailored by varying particular inner and outer bridges. For example, the X-bridges made of electron donors (oxygen, nitrogen, eventually sulphur) may lead to semiconducting materials with low bandgaps. On the other hand, all-carbon bridged derivatives, such as **2a** may function as surrogates for more oxidized carbon-nitride allotropes and derivatives.

The family of COFs **3** replaces the trivalent N bridges with divalent π-bridges. This results in a more porous structure, which in itself is an advantage for catalysis. Four types of π-bridges are proposed. The traditional Schiff-base –CH=N– bridge is relatively easy to construct and shown multiple times to be advantageous in construction of various COFs. The diazo –N=N– bridge offers an interesting variant to the Schiff-base and the possibility of carbon nitride material with the formal formula C_3N_6. The vinylidene –CH=CH– bridge, on the other, has been multiply demonstrated to have benefits in terms of π-electron transfer as the vinylidene-carbons are less electronegative. Finally, borazene bridge –B^-

H=N⁺H– is definitely worth attempting as it is both isoelectric to vinylidene and offers unique orbital contribution from both boron and nitrogen [6].

RETROSYNTHESIS OF SELECTED TARGETS

COF **1** not only appears to be of utmost importance from a material design point of view, but also to have the most straightforward retrosynthetic pathway (**Scheme 2**). A quick analysis of the structure reveals a possible double disconnection at the carbon-triazine bond. This leads to nucleophilic attack of carbanion to susceptible triazine-halogen bond. Two pathways are worth exploring. The first one is base-catalyzed self-polymerization of 2,4-dichloro-6-methyl-1,3,5-triazine (2CMT). In this variety the selection of base is the key to success. Nucleophilic bases such as hydroxides, alcoholates or amines are unlikely to catalyse such a reaction as the nucleophilic attack to triazine-chlorine bond will be preferred to the deprotonation of acid CH_3-moiety. The same problem can be expected in the case of butyl-lithium and other organometallics, where transmetallation, oxidative-addition and/or nuclephilic attack will either be favoured, or variety of side reactions will occur. Sterically hindered non-nuclephilic bases such as Hünig's base (DIPEA), lithium hexamethyldisilazane (LiHMDS), or 2,6-lutidine are the most likely to promote this reaction. As double deprotonation is required, an excess of base is needed and the reaction should be carried out at elevated pressure and temperature, which can be challenging as gaseous hydrogen chloride is one of the expected products. An alternative synthesis is via similar reaction where the donor of the methyl-moiety is 2,4,6-trimethyltriazine (TMT) and the other reactant is cyanuric chloride. Here, the carbanion can be generated in advance, increasing the likelihood of the reaction.

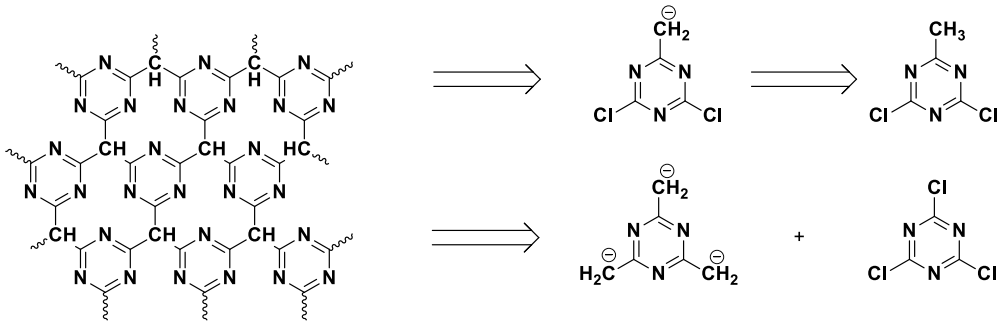

Scheme 2 Retrosynthesis of COF 1. Source: (own)

The Schiff-base product COF **3a** is another one with relatively straightforward retrosynthesis (**Scheme 3**) ending with melamine and 1,3,5-triazine-2,4,6-tricarbaldehyde (TTC). While melamine is a commercial and readily available compound the TTC is, despite its uncomplicated structure and presumed stability, an elusive building-block. Noteworthy, several commercial companies offer TTC in their portfolios, yet mostly as an intermittent or on-demand item, so the The best way to obtain it appears to be via nitrosation of TMT. Yet the references are often scarce and dated. Another possible pathway of TTC preparation is via trimerization of 2-cyano-1,3-dioxolane, which has to be prepared in at least three steps.

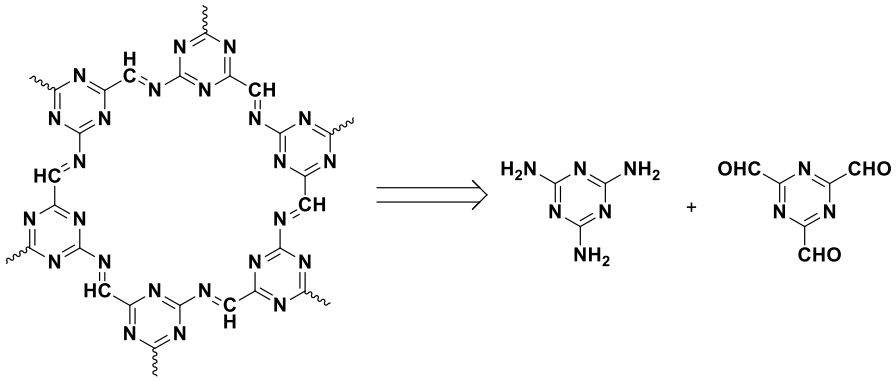

Scheme 3 Retrosynthesis of COF 3a. Source: (own)

4. INITIAL RESULTS

Syntheses of key building blocks 2CMT, TMT, TTC were attempted following the literature precedents [7]. 2CMT is readily prepared by the reaction of in-situ generated Grignard reagent with cyanuric chloride. In our conditions reaction provides mediocre 60% yield which is suboptimal according to the reported 90%+ yields and the procedure needs to be properly brushed to be reliable under the conditions of our lab [7]. TMT on the other hand, was prepared in 70% yield by cyclotrimerization of acetonitrile, which is consistent with the precedent [8]. The elusive character of TTC remains so far the attempts of repeating several literature procedures ended up with only the traces of desired product.

5. CONCLUSIONS AND OUTLOOKS

A series of target compounds **1, 2a** – **2e** and **3a** – **3d** was designed as target materials with prospective selective photocatalytic properties. For the most straightforward proposed target retrosynthetic analysis was made and with the synthetically relevant comments were made. The key building blocks 2CMT, TMT and TTC were identified as necessary to pursue the project, two of them were synthesized according to literature procedures.

The next steps in the project are clear. With the 2CMT in hand, synthesis of the COF **1** will be attempted shortly, with available targets from the COF **3** family to follow as soon as the building blocks are available. In the meantime, a synthetic strategy for the COF **2** family of materials will be found, and based on this, their synthesis will also be attempted.

ACKNOWLEDGEMENT

Experimental results were accomplished by using Large Research Infrastructure ENREGAT supported by the Ministry of Education, Youth and Sports of the Czech Republic under project No. LM2018098.

REFERENCES

[1] PRAUS, Petr, Aneta SMÝKALOVÁ, Daniel CVEJN, Sandra LOSERTOVÁ, Martin KOŠTEJN, Vlastmil NOVÁK Post-synthetic modification of graphitic carbon nitride with PCl3 and POCl3 for enhanced photocatalytic degradation of organic compounds. *Diamond and Related Materials*. 2022. Vol. 130, 109439.

[2] SMÝKALOVÁ, Aneta, Kryštof FONIOK, Daniel CVEJN, Kamil Maciej GÓRECKI, Petr PRAUS. The role of guanidine hydrochloride in graphitic carbon nitride synthesis. *Scientific Reports*. 2021. Vol. 11, no. 1, s. 1–18.

[3] YU, Quingbo, Shuai GUO, Xiahua LI, Mingxu ZHANG. One-step fabrication and high photocatalytic activity of porous graphitic carbon nitride/graphene oxide hybrid by direct polymerization of cyanamide without templates. In *Russian Journal of Physical Chemistry A* . 2014. Vol. 88, no. 10, s. 1643–1649. .

[4] Qinghua LIANG, Zhi LI, Xiaoliang YU, Zheng-Hong HUANG, Feiyu KANG, Quan-Hong YANG. Macroscopic 3D Porous Graphitic Carbon Nitride Monolith for Enhanced Photocatalytic Hydrogen Evolution. *Advanced Materials* [online]. 2015. Vol. 27, no. 31, s. 4634–4639.

[5] [WU, Jiajia, Lijun XIONG, Yingjie HU, Yong YANG, Xiaoyue ZHANG, Tianyu WANG, Zheng TANG, Aiwu SUN, Yong ZHOU, Jinyou SHEN, Zhigang ZOU. Organic half-metal derived erythroid-like BiVO4/hm-C4N3 Z-Scheme photocatalyst: Reduction sites upgrading and rate-determining step modulation for overall CO2 and H2O conversion. *Applied Catalysis B: Environmental*. 2021. Vol. 295, 120277.

[6] [YUSRAN, Yusran, Hui LI, Xinyu GUAN, Quianrong FANG. Covalent Organic Frameworks for Catalysis. *EnergyChem*. 2020. Vol. 2, no. 3, 100035..

[7] DING, Yili, Hua BAI, Xuan YANG, Jian CHAI, Quingyan YAN, Kenneth SMITH, Xianguy HUANG, Yanghui GUO. Patent - internationa. No. WO2012159557.

[8] HERRERA, Antonio, Roberto MARTÍNEZ-ALVAREZ, Pedro RAMIRO, Murad CHIOUA, Rachid CHIOUA. A practical and easy synthesis of 2,4,6-trisubstituted-s-triazines. *Synthesis* . 2004. no. 4, 503–505.

FLOWER-LIKE CARBON COATING ON CARBON SPHERES BY CHEMICAL VAPOR DEPOSITION WITH OVERPRESSURE

Author(s): Pavel CZERNEK

Supervisor: prof. Ing. Daniela PLACHÁ, Ph.D.

Department: Nanotechnology Centre, Faculty of Materials Science and Technology, VSB – Technical University of Ostrava

Abstract

Herein we refer to unique flower-like carbon coating on carbon spheres synthesized by chemical vapor deposition with overpressure. The morphology of the material was examined in detail by scanning electron microscope. The resultant carbon spheres have around 1-2 μm and are linked by accretion/coalescence phenomenon to necklace-like structures.

Key words:

Chemical vapor deposition, chemical vapor deposition with overpressure, carbon spheres, carbon coating.

1. INTRODUCTION

Since the first hypothetical explanation of carbon sphere formation [1], the research has had a long journey. The carbon spheres were synthesized through many routes, from chemical vapor deposition and its gas phase synthesis [2] to hydrothermal synthesis with polymerization of monosaccharides following the nucleation of carbon spheres under pressure, temperature, and prolonged time [3].

Chemical vapor deposition synthesis route can be done with a catalyst substrate as cages [4], or without catalyst [1]. The established routes of chemical vapor deposition synthesis of free carbon spheres can be different from low-pressure chemical vapor deposition (LPCVD) to atmospheric pressure chemical pressure deposition (APCVD) [5] and to high-pressure chemical vapor deposition (HPCVD) [6]. Herein, a reference is made to a chemical vapor deposition with overpressure that has already been used to synthesize pyrolytic carbon. [7].

Sun et al. [8] and Alazemi et al. [9] measured the mechanical properties of carbon spheres by the nanoindentation method and calculated their elastic modulus and hardness. There is an assumption that carbon spheres could be used as secondary composite filler because of their mechanical properties. Also, Yang et al. [10] performed a compression test of single porous amorphous carbon spheres with good results of elastic modulus along to calculated low density ~0,25 g/cm^3 of porous spheres.

The main objective of this article is to improve the hardness of the carbon spheres by pyrolytic carbon coating from the chemical vapor deposition method, thereby extending their application to the mechanical applications of composites as secondary fillers.

2. EXPERIMENTAL

The setup and process of the chemical vapor deposition with overpressure are described in the previous article [7]. Briefly, ethylene (C_2H_4 3.0; SIAD) as a precursor has flowed into the quartz reactor to overpressure 3-4 atm. The synthesis took place at a temperature of 1100 °C from dozens of minutes to a few hours. The scheme of chemical vapor deposition with overpressure can be seen in Figure 1.

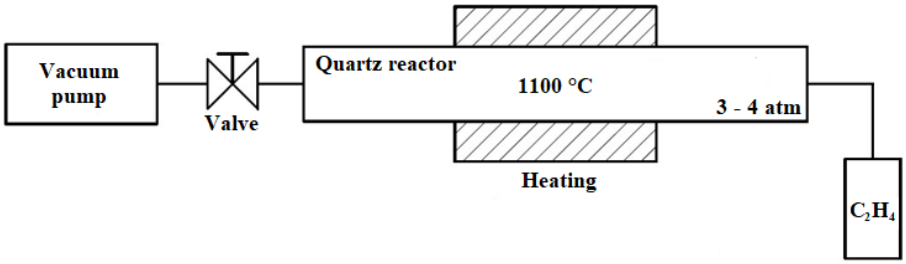

Figure 1: Scheme of chemical vapor deposition with overpressure. Edited from Czernek et al. Source: [7]

To determine the detailed morphology of prepared materials, a JEOL scanning electron microscope (SEM) with an auto-emission source was used, which enables the information available from the surfaces of the materials to be determined. The samples were scanned at an accelerating voltage of 20-25 kV using secondary electron detection. Before scanning, the samples were sputtered with a 20 nm layer of platinum using a sputtering device. Surface scanning was performed under a high vacuum.

3. RESULTS AND DISCUSSION

From the SEM images (Figure 2), the gradual nature of the formation of carbon coating on carbon spheres can be seen, depending on the time of synthesis. Firstly the carbon spheres are created then the carbon coating synthesis proceeds. In the first 30 minutes of synthesis, the nucleation of carbon coating is initiated and continues to grow saturated after 3 hours of synthesis. By morphology, there is no difference between 3 and 5 hours of synthesis. Also, a temperature of 1100 °C is necessary for growth because lower temperatures are inefficient for the nucleation of carbon coating.

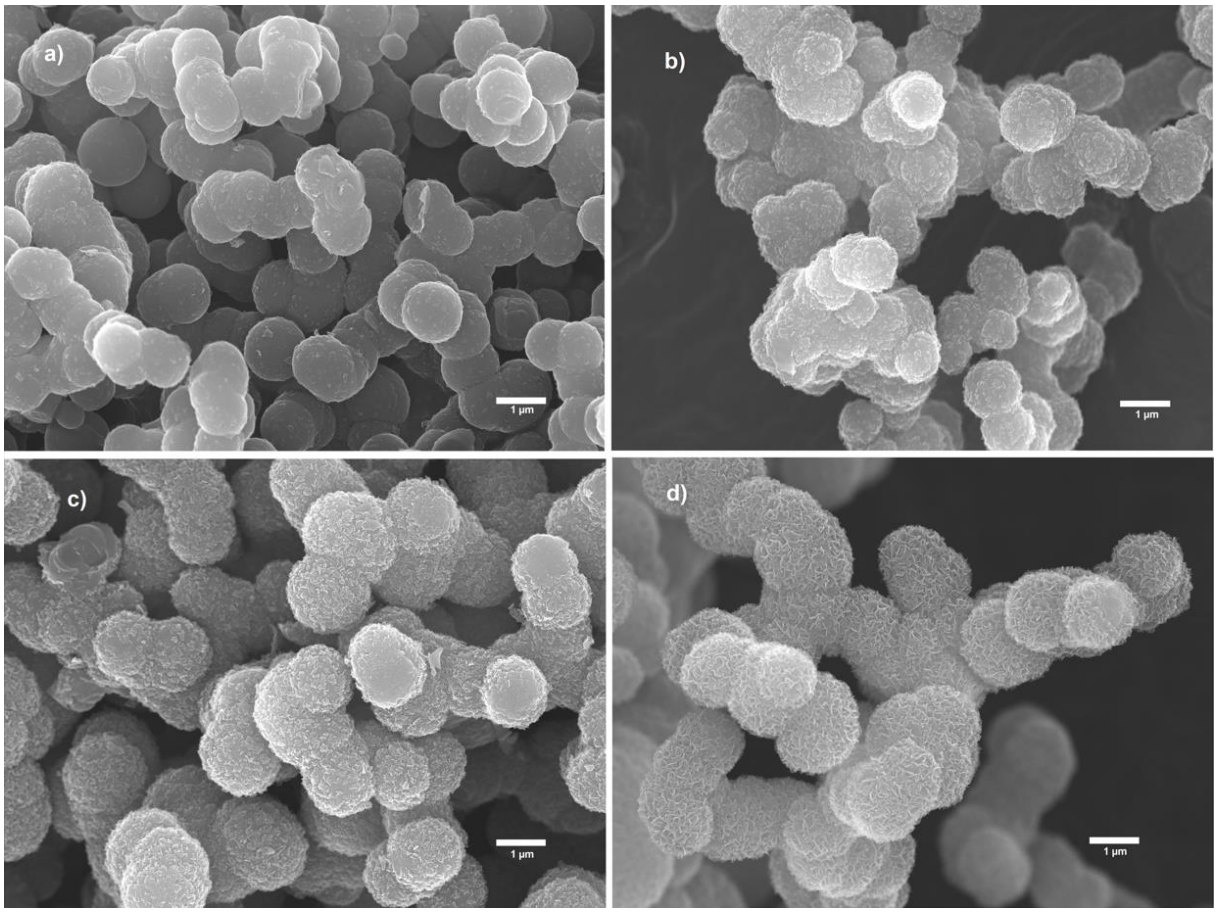

Figure 2: SEM images with 10 000x magnification (a) after 30 minutes of synthesis, (b) after 1 hours, (c) after 2 hours, and (d) carbon coating after 3 hours of synthesis. Source: (own)

As is known, the occurrence of accretion or coalescence phenomenon [11] in the synthesized carbon spheres is common in gas-phase synthesized carbon spheres. The carbon spheres are linked altogether into necklace-like structures as can be seen in Figure 2.

From a detailed SEM image (Figure 3) of carbon coating on an exposed carbon sphere is evident, that the carbon coating is around 100 nm in height. The structure of the coating seems to be porous but is more like the roughness of the carbon sphere. The specific surface area of the carbon spheres was measured as 5,7 m^2/g. Similar morphology structures were reported in SnO_2/C spheres [12], NiS_2/C spheres [13], carbon nanoflowers derived from covalent organic framework [14], and C/MnO_2 core-shell particles [15].

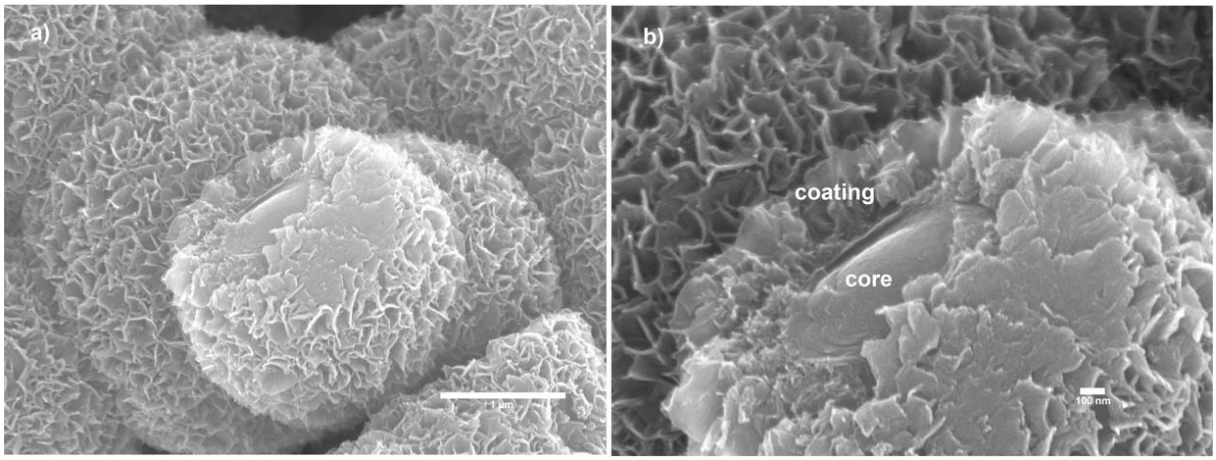

Figure 3: SEM images of carbon spheres with carbon coating after 5 hours of synthesis with (a) 25 000x, and (b) 50 000x magnification. Source: (own)

The potential application of the carbon spheres with carbon coating could be in composites after their functionalization for good interaction with polymer resins. Xingmei et al. functionalized carbon spheres in a mixture of HNO_3/H_2SO_4 for better dispersion in the polymer matrix [16]. Wang et al. dispersed carbon spheres from hydrothermal synthesis into an epoxy resin matrix and improved the mechanical and thermal properties of the resultant composite material [17].

4. CONCLUSION

In the current work, the carbon coating on carbon spheres was presented as a potential candidate for improvement of the applicability of carbon spheres for composite materials. From SEM images was seen the gradual nucleation of carbon coating. In future work, performing structural characterization of the material as well as the mechanical properties of improvement of carbon coating as hardness or compressive strength is necessary.

ACKNOWLEDGEMENT

I would like to thank Ing. Roman Gabor, Ph.D. for scanning electron microscopy images.
This work was supported by the student project SP2023/095 of VSB-Technical University of Ostrava.

REFERENCES

[1] KROTO H., K. MCKAY. The formation of quasi-icosahedral spiral shell carbon particles. *Nature. 1988.* **331**: 328–331. https://doi.org/10.1038/331328a0

[2] JIN Y. Z., *et al*. Large-scale synthesis and characterization of carbon spheres prepared by direct pyrolysis of hydrocarbons. *Carbon*. 2005. **43**(9): 1944–1953. https://doi.org/10.1016/j.carbon.2005.03.002

[3] SUN X., Y. LI. Colloidal Carbon Spheres and Their Core/Shell Structures with Noble-Metal Nanoparticles. *Angewandte Chemie International Edition*. 2004. **43**: 597–601. https://doi.org/10.1002/anie.200352386

[4] MA Y., *et al.* A practical route to the production of carbon nanocages. *Carbon*. 2005. **43**(8): 1667–1672. https://doi.org/10.1016/j.carbon.2005.02.004

[5] GUTIÉRREZ-GARCÍA C. J., *et al*. Synthesis of carbon spheres by atmospheric pressure chemical vapor deposition from a serial of aromatic hydrocarbon precursors. *Physica E: Low-dimensional Systems and Nanostructures*. 2019. **112**: 78-85. https://doi.org/10.1016/j.physe.2019.04.007

[6] KOPINAROV N., M. KONSTANTINOVA. Preparation of carbon spheres by low temperature pyrolysis of cyclic hydrocarbons. *Journal of Materials Science*. 2011. **46**: 1494-1501. https://doi.org/10.1007/s10853-010-4951-0
[7] CZERNEK P., D. PLACHÁ. Synthesis of pyrolytic carbon by chemical vapor deposition with increased pressure and its formation into scrolled carbon microtubes. *PhD students´ day FMST 2022*. VŠB – Technická univerzita Ostrava, 2022, 92-95.
[8] SUN Y. *et al*. Nanoindentation of carbon microspheres. *International Journal of Material Research*. 2016. **107**(8): 685-691. https://doi.org/10.3139/146.111366
[9] ALAZEMI A. A., A. D. DYSART, V. G. POL. Experimental Investigation of the Mechanical and Surface Properties of Sub-Micron Carbon Spheres. *Lubricants.* 2020. 8(7): 77. https://doi.org/10.3390/lubricants8070077
[10] YANG, W. et al. Large-deformation and high-strength amorphous porous carbon nanospheres. *Scientific Reports.* 2016. **6**: 24187. https://doi.org/10.1038/srep24187
[11] DESHMUKH A. A., et al. Carbon spheres. Materials Science and Engineering: R: Reports. 2010. **70**(1-2): 1-28. https://doi.org/10.1016/j.mser.2010.06.017
[12] LIU Q. *et al.* Carbon-Coated Hierarchical SnO2 Hollow Spheres for Lithium Ion Batteries. *Chemistry A European Journal.* 2016. **22**(17): 5853-5857. https://doi.org/10.1002/chem.201505122
[13] YANG Li *et al.* Hierarchical NiS_2 Modified with Bifunctional Carbon for Enhanced Potassium-Ion Storage. *Advanced Functional Materials.* 2019. 29(50): 1903454. https://doi.org/10.1002/adfm.201903454
[14] ZHENG Y. *et al.* Ultrasound-Triggered Assembly of Covalent Triazine Framework for Synthesizing Heteroatom-Doped Carbon Nanoflowers Boosting Metal-Free Bifunctional Electrocatalysis. ACS Appl. Mater. Interfaces. 2021. 13(11): 13328–13337. https://doi.org/10.1021/acsami.1c01348
[15] LEE T-T. et al. Synthesis of Petal-Like Carbon Nanocapsule@MnO2 Core-Shell Particles and Their Application in Supercapacitors. *Journal of The Electrochemical Society.* 2014. **161**(10): H598-H605. https://doi.org/10.1149/2.0061410jes
[16] XINGMEI G. *et al.* Carbon spheres surface modification and dispersion in polymer matrix. Applied Surface Science. 2012. **261**(15): 159-165. https://doi.org/10.1016/j.apsusc.2012.07.133
[17] WANG X. *et al.* The influence of carbon spheres on thermal and mechanical properties of epoxy composites. *Journal of Polymer Research.* 2018. 25(223). https://doi.org/10.1007/s10965-018-1623-2

POLARIZATION CONTROL OF SEMICONDUCTOR MICROLASERS USING NON-HERMITIAN EFFECTS

Author(s): Mariusz DRONG

Supervisor: doc. Dr. Mgr. Kamil POSTAVA

Department: IT4Innovations, National Supercomputing Center and Faculty of Materials Science and Technology, VSB – Technical University of Ostrava

Abstract

This work introduces the concept of anisotropic-cavity surface-emitting lasers (ACSELs). ACSELs are semiconductor microlasers with nanofabricated components, such as metasurfaces, designed on purpose to be effectively anisotropic. It is shown, that non-trivial combination of anisotropy in microlaser induces the existence of exceptional points (EPs) typical for non-Hermitian physical systems, which lead in this case to polarization switching. We derive the general criterion to find EPs in two-mode ACSEL.

Key words:

Microlasers, anisotropy, polarization, exceptional points.

1. INTRODUCTION

During the last decade, the research in photonics has been devoted mainly to two areas. Namely, to topological photonics and non-Hermitian photonics. In the case of topological photonics, it is the strikingly effective topological protection of photonics modes, which provides many new functionalities [1]. As for non-Hermitian photonics, it is the existence of so-called exceptional points (EPs) [2]. EPs are degeneracies of non-Hermitian systems [3]. More precisely, they are the points in parameter space, in which the eigenvalues and eigenstates of the system coalesce. It is possible due to openness of non-Hermitian systems, meaning that they contain losses (or alternatively gain). From the point of view of fundamental physics, the PT - symmetry breaking occurs at EPs [4]. Lasers are perfect example of non-Hermitian system, as they contain both losses (due to imperfect cavity) and gain (due to gain medium) [5]. In the context of lasers, the presence of EPs has led to demonstration of exotic phenomena, such as the mode switching or counter-intuitive increase of emitted intensity by increasing the losses [6]. Furthermore, the concept of EPs has been used to demonstrate the fact, that laser modes are hybrid modes of cavity and gain medium [7].

This work is concerned on the possibility of using non-Hermitian effects to control the polarization of surface-emitting microcavity lasers. The idea is based on our previous work on spin-injected vertical-cavity surface-emitting lasers (shortly spin-VCSELs), in which the non-trivial combination of anisotropy in gain medium and laser cavity theoretically induces the EPs and additionally Fermi-arc, connecting the EPs in parameter space. It was shown, that crossing of Fermi-arc leads to polarization switching, paving a way towards practical spin-VCSEL devices [8]. Here, we extend this concept to general anisotropic-cavity surface-emitting lasers (ACSELs), which in theory provide new directions in polarization control. We use our previously developed formalism to find mathematical criteria for EPs which may serve as a guide to design such devices [9]. In Sec. 2 we show our approach to anisotropy-engineering in surface-emitting lasers. Then, in Sec. 3 it is shown mathematically, how to find EPs in parameter space for two-mode ACSEL.

2. ANISOTROPIC-CAVITY SURFACE-EMITTING LASERS (ACSELs)

Recent advances in nanofabrication allow to prepare nanostructures with unprecedent precision. We propose to use this to design surface-emitting laser with fine-tuned affective anisotropy. Such proposal is depicted in Fig. 1, consisting of nanostructure fabricated on the top of device, allowing to induce the desired effective anisotropy and consequently non-Hermitian dynamics of laser modes. Note, that similar devices have already been designed and fabricated [10] [11]. However, the authors completely neglected the possibility of non-Hermitian polarization control. The key idea is to tune the

ACSEL to the state near EP, or Fermi-arc and use the external mechanisms, such as the control of cavity losses or birefringence control to cross Fermi-arc or encircle EPs to switch between the polarizations. Compared to our previous work on spin-VCSELs, this idea offers a way to switch between arbitrary pairs of polarizations, in principle.

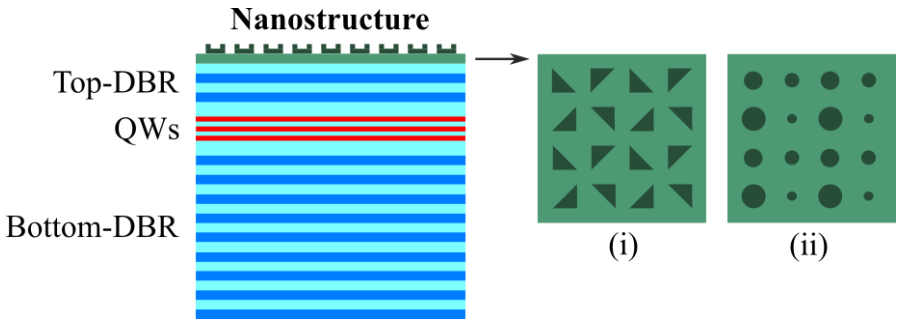

Figure 1 A scheme of ACSEL implementation consisting of quantum wells (QWs) as a gain medium enclosed within two distributed Bragg reflectors (DBRs) with anisotropic nanostructure on top. The possible geometries of the top nanostructure are labeled by (i) and (ii). Source: own

3. ANISOTROPY-INDUCED EXCEPTIONAL POINTS

It is possible to describe two-mode device shown in Fig. 1 using the following set of coupled-mode equations [12]:

$$\frac{d}{dt}A_x = \kappa(1 - i\alpha)(g_x n - 1)A_x - \gamma_{xx}A_x - \gamma_{xy}A_y, \tag{3}$$

$$\frac{d}{dt}A_y = \kappa(1 - i\alpha)(g_y n - 1)A_y - \gamma_{yx}A_x - \gamma_{yy}A_y, \tag{4}$$

where $A_{x,y}$ are the amplitudes of electric field components polarized along x and y-axis, respectively. κ is the average mode decay rate, α is the Henry's factor, crucial to describe semiconductor gain media. The possible gain anisotropy due to strain or symmetry reduction is included in $g_{x,y}$. The carrier concentration is denoted n. Note, that we do not consider equation of motion for carrier concentration, because the position of EPs can be found using near-threshold calculation [13]. Any cavity anisotropies, such as those originating from nanofabricated grating or metasurface, are described by so-called anisotropy rates γ_{ij}, where $i, j = x, y$.

After separation into real and imaginary parts, we introduce notation for polarization-resolved gain-loss ratio G_{ij} and frequency-like quantity Ω_{ij}, which leads to:

$$\frac{d}{dt}A_x = (G_{xx} - i\Omega_{xx})A_x + (G_{xy} - i\Omega_{xy})A_y, \tag{5}$$

$$\frac{d}{dt}A_y = (G_{yx} - i\Omega_{yx})A_x + (G_{yy} - i\Omega_{yy})A_y. \tag{6}$$

This set of coupled-mode equations is used to determine necessary conditions for EPs. From the condition of eigenstates coalescence, one derives:

$$\left(\frac{G_{xx} - G_{yy}}{2}\right)^2 + G_{xy}G_{yx} = \left(\frac{\Omega_{xx} - \Omega_{yy}}{2}\right)^2 + \Omega_{xy}\Omega_{yx}, \tag{7}$$

$$\frac{1}{2}(G_{xx} - G_{yy})(\Omega_{yy} - \Omega_{xx}) = G_{xy}\Omega_{yx} + G_{yx}\Omega_{xy}, \tag{8}$$

which must be satisfied simultaneously at EP. It should be noted, that above-derived condition is generally valid even for the cases with gain cross-coupling ($g_{xy,yx} \neq 0$).

We apply Eqs. *(5)* and *(6)* to specific case of ACSEL characterized by linear gain anisotropy $\Delta g = g_x - g_y$, and cavity anisotropy given by linear birefingence rate $\Delta\gamma_l$ and circular birefringence rate $\Delta\gamma_c$. The condition for EP for different magnitudes of gain anisotropy is shown in Fig. 2. One can see, that for $\Delta g = 0$ there is no EP. The peak in the center of reference frame corresponds to trivial degeneracy known as diabolic point (DP). As the gain anisotropy is being increased, pair of EPs appears. Thus, we have shown, that EPs can be found also in surface-emitting device without spin-injection.

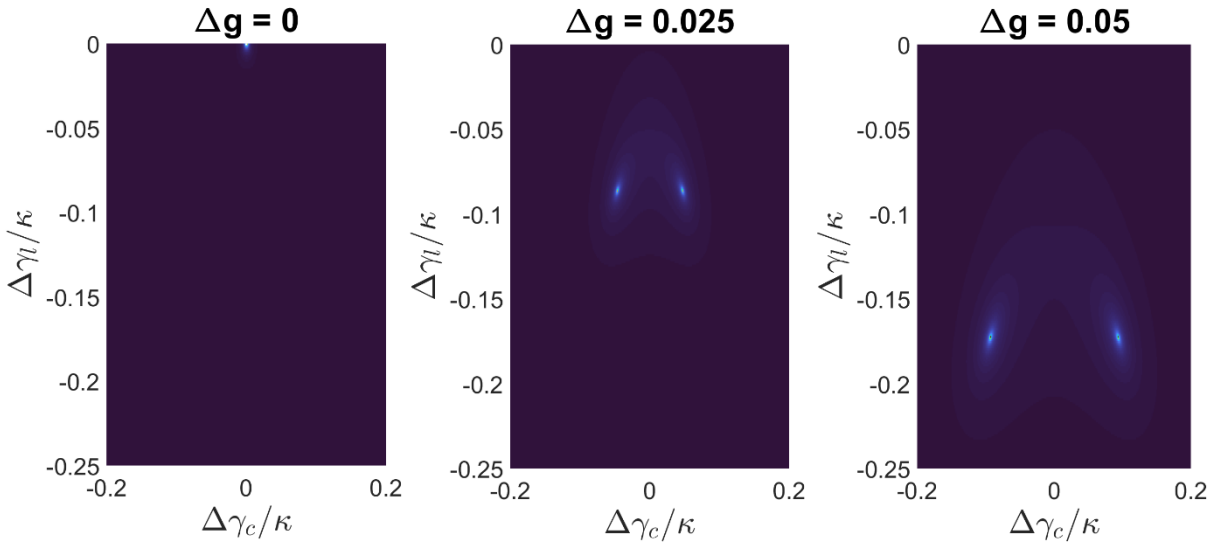

Figure 2 The appearance of EPs as the gain anisotropy Δg is being increased. Source: (own)

4. CONCLUSION

To conclude, we have introduced a concept of anisotropy-engineered surface-emitting lasers: ACSELs. Moreover, we have derived a general criteria for the occurence of EPs in a dual-mode ACSEL. Such devices can be, in principle, designed to exploit non-Hermitian effects to control the switching between arbitrary polarization states. This topic is worth of further exploration because ACSELs could be used in optical data transfer with much lower power consumption compared to intensity modulated VCSELs and possibly with larger data rates. The information would be encoded, however, in polarization state of light, similarly as in the case of spin-VCSELs.

ACKNOWLEDGEMENT

The work was supported by the by the Ministry of Education, Youth and Sports of the Czech Republic through the e-INFRA CZ (ID:90254) and Operational Programme Enterprise and Innovations for Competitiveness (OPEIC), project number CZ.01.1.02/0.0/0.0/20_321/0024953.

REFERENCES

[1] E. J. Bergholtz, J. C. Budich and F. K. Kunst, "Exceptional topology of non-Hermitian systems," *Rev. Mod. Phys.,* vol. 93, no. 1, p. 015005, February 2021.

[2] M. Parto, Y. G. N. Liu, B. Bahari, M. Khajavikhan and D. N. Christodoulides, "Non-Hermitian and topological photonics: optics at an exceptional point," *Nanophotonics,* vol. 10, p. 403–423, 2021.

[3] M.-A. Miri and A. Alù, "Exceptional points in optics and photonics," *Science,* vol. 363, p. eaar7709, 2019.

[4] C. M. Bender and S. Boettcher, "Real Spectra in Non-Hermitian Hamiltonians Having Symmetry," *Phys. Rev. Lett.,* vol. 80, no. 24, p. 5243–5246, June 1998.

[5] A. E. Siegman, Lasers, University Science Books, 1986 .

[6] B. Peng, Ş. K. Özdemir, S. Rotter, H. Yilmaz, M. Liertzer, F. Monifi, C. M. Bender, F. Nori and L. Yang, "Loss-induced suppression and revival of lasing," *Science,* vol. 346, pp. 328-332, 2014.

[7] A. A. Zyablovsky, I. V. Doronin, E. S. Andrianov, A. A. Pukhov, Y. E. Lozovik, A. P. Vinogradov and A. A. Lisyansky, "Exceptional Points as Lasing Prethresholds," *Laser & Photonics Reviews,* vol. 15, p. 2000450, 2021.

[8] M. Drong, J. Peřina, T. Fördös, H. Y. Jaffrès, K. Postava and H.-J. Drouhin, "Spin vertical-cavity surface-emitting lasers with linear gain anisotropy: Prediction of exceptional points and nontrivial dynamical regimes," *Phys. Rev. A,* vol. 107, no. 3, p. 033509, March 2023.

[9] M. Drong, M. Dems, J. Peřina, T. Fördös, H. Y. Jaffrès, K. Postava and H.-J. Drouhin, "Time-dependent laser cavity perturbation theory: exploring future nano-structured photonic devices in semi-analytic way," *Journal of Lightwave Technology,* vol. 40, pp. 4735-4745, 2022.

[10] M. Dems, I.-S. Chung, P. Nyakas, S. Bischoff and K. Panajotov, "Numerical Methods for modeling Photonic-Crystal VCSELs," *Opt. Express,* vol. 18, p. 16042–16054, July 2010.

[11] A. A. Maksimov, E. V. Filatov, I. I. Tartakovskii, V. D. Kulakovskii, S. G. Tikhodeev, C. Schneider and S. Höfling, "Circularly Polarized Laser Emission from an Electrically Pumped Chiral Microcavity," *Phys. Rev. Applied,* vol. 17, no. 2, February 2022.

[12] M. Drong, T. Fördös, H. Y. Jaffrès, J. Peřina, K. Postava, P. Ciompa, J. Pištora and H.-J. Drouhin, "Spin-VCSELs with Local Optical Anisotropies: Toward Terahertz Polarization Modulation," *Phys. Rev. Applied,* vol. 15, no. 1, p. 014041, January 2021.

[13] H. Wang, S. Assawaworrarit and S. Fan, "Dynamics for encircling an exceptional point in a nonlinear non-Hermitian system," *Opt. Lett.,* vol. 44, p. 638–641, February 2019.

[14] A. U. Hassan, B. Zhen, M. Soljačić, M. Khajavikhan and D. N. Christodoulides, "Dynamically Encircling Exceptional Points: Exact Evolution and Polarization State Conversion," *Phys. Rev. Lett.,* vol. 118, no. 9, p. 093002, March 2017.

INTRODUCTION TO SECURITY HOLOGRAPHY WITH DIRECT LASER LITHOGRAPHY

Author(s): Tomáš KOHUT

Supervisor: doc. Dr. Mgr. Kamil POSTAVA

Department: IT4Innovations National Supercomputing Center, Faculty of Materials Science and Technology, VSB – Technical University of Ostrava

Abstract

Various types of nano- and micro-structures, such as security holograms and diffractive optical elements, can be prepared directly into a photoresist using direct-write optical lithography. Precise knowledge of photoresist properties, parameters of exposure, and photoresist development time is essential to achieve the required structures. In this paper, we will describe the basic design and steps of fabricating security holograms for industrial applications.

Key words:

Laser lithography, security holography, positive photoresist, diffractive gratings, developer, colour mixing.

1. INTRODUCTION

Direct-write optical lithography (DWL), also called maskless lithography, is used to fabricate microstructures and nanostructures down to feature sizes of hundreds of nanometres. Exposure is performed by direct illumination of a photoresist with a laser diode with a typical wavelength of 405 nm in the form of a focused Gaussian beam. Using lithographic processes such as wet/dry etching or lift-off, the photomask can be prepared for mass production [1,2]. In our laboratory, we focus on the application of security holography and the development of a new way to protect holograms against counterfeiting and fabrication of masters for industrial mass production.

The security hologram consists of a binary structure in the form of a diffraction grating or a grayscale structure in the form of a blazed grating [3]. For this reason, we use a binary-sensitive positive photoresist that enables removing the exposed area of the photoresist during development. A binary-sensitive photoresist is inherently designed for binary structures but can still be exposed linearly to form grayscale structures. A linearly exposed photoresistor, however, does not produce an ideal linear blazed structure and therefore there is a need to optimise the exposure process, how we do it was explained in our SPIE proceeding [4].

In this paper, we show a basic introduction to the fabrication of security holograms, from substrate preparation, and photoresist coating to lithography exposure with our system. And next, we will briefly show how to design diffractive colour mixing and the results of our advanced holographic elements.

2. PHOTORESIST AND LITHOGRAPHY EXPOSURE

a. Photoresist and substrate preparation

The positive photoresist ma-P 1200 series from Microresist Technology company is used in this research, more specifically the ma-P 1275. This photoresist can be also diluted by the thinner ma-T 1050. The change in photoresist thickness as a function of coating speed and solvent concentration is shown in our SPIE proceedings [4].

As a substrate, we use window float glass, cut to a square shape of 54×54 mm with a thickness of 2 mm. The substrate needs to be cleaned before use. It is done by acetone bath in a beaker on a hot plate heated at 100°C. After 15 minutes the substrate is dried by blowing with compressed dry air and put into an isopropyl alcohol (IPA) bath also on the heated hotplate. After another 15 minutes, the substrate is removed from IPA and dried by dried air. After the substrate is cleaned, it is necessary to heat the substrate to remove condensate water on the hot plate heated up to 140°C for 10-20 minutes.

After that, the substrate needs to be cooled down to room temperature before applying photoresist via spin coating.

The spin-coater POLOS SPIN 150i/NPP capable to spin up to 12 000 RPM was included. The photoresist is applied on the substrate in the form of a large droplet and spun at 3000 RPM for 20 seconds with an acceleration of 1000 RPM/s, then the speed is reduced to 500 RPM/s for 10 seconds. After spin coating, the substrate must be soft-baked (post-bake) to evaporate a solvent for 10 minutes on the hot plate heated to 100°. According to this recipe, we achieve a 10 micrometres thick photoresist on the float glass substrate.

b. Lithography and resist developer

Our DWL system is PicoMaster PM100 from RAITH Nanofabrication. The optical module of our system is equipped with a GaN diode with a wavelength of 405 nm. The system has 3 different exposure resolutions, the High Resolution (HR) with a spot size of 300 nm, the Medium Resolution (MR) 550 nm, and the Low Resolution (HR) 850 nm. The spot size mean diameter of the focused beam on the surface of the substrate. The substrate moves in the path of exposition and when the line of exposition is complete, the optical module is moved by adjustable step and continuous in position direction. The step size should be at least half the spot size, so the intensity profile is overlapped. The exposure dose is in mJ/cm^2 and the typical value for clear binary grating holograms is 50 mJ/cm^2 and for grayscale structures 300 mJ/cm^2.

After exposure, the substrate is placed in a bath of mr-D 331 (NaOH-based) or ma-D 526/S (TMAH-based) developers for 2 min. (for dose 50 mJ/cm^2) or 5 min. (for dose 300 mJ/cm^2) to dissolve the exposed areas. The development process is stopped by putting the substrate in a beaker with deionized water. Differences between different-based developers are evident in Figure 1. TMAH-based developers are suitable for preparing grayscale structures and NaOH-based for more binary structures.

The last step in the processing of the developed photoresist before the measurement or metallization is the bleaching process, in which the substrate is illuminated with daylight or UV light to expose the unexposed area of the photoresist. Substrates with are not bleached before metallisation, can damage sputtered metal layer with nitrogen bubbles erased from the post-exposure process by daylight.

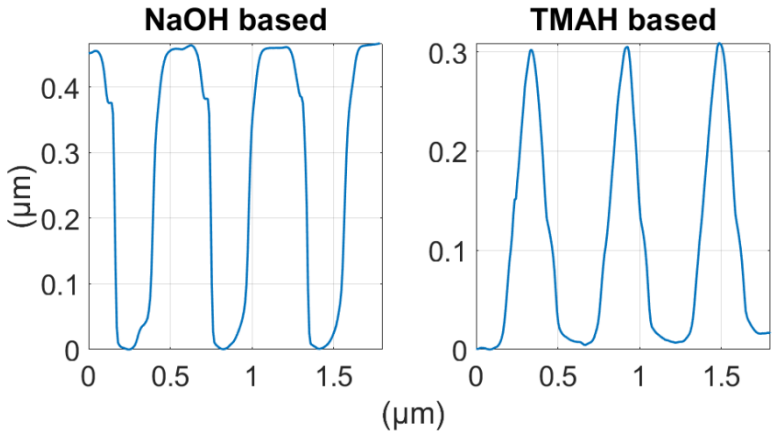

Figure 1 Different profile shapes of diffractive grating with 600 nm period affected by different based developer mr-D 331 and ma-D 526-S respective. Measured by AFM NTEGRA. Source: (own)

3. HOLOGRAPHIC SECURITY ELEMENTS

Security diffractive holographic elements are used to protect ID cards, passports, banknotes, goods, and papers. Lithographic fabricated “master” of hologram in the photoresist is metalized and by galvanic plating, the nickel cope is grown. These nickel copes are then used for mass production as a stamp to make a copy by pressing them into plastic foil on a printing machine [5]. Images of security holograms before and after metallisation are in Figure 2. Metallization is also required for studying the hologram because the metal has a much higher refractive index than photoresist, so the metallised hologram has more refractive contrast for observation, to see if they are any defects or if the design is

correct. For galvanic growth, the top metal must not be chromium or aluminium due to passivation. The recommended coating is silver, vanadium and nickel sputtered vie DC magnetron sputtering.

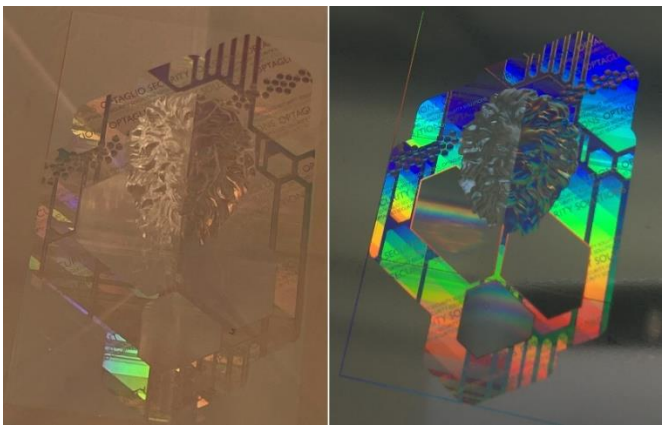

Figure 2 Left hologram after photoresist development, right hologram after metallisation. Source: (own)

The main carrying element of the security hologram is diffraction gratings, which are responsible for the "rainbow" colour of the hologram. The observable wavelength of grating with period *d* is given by equation (1) [6,7].

Diffraction grating equation:

$$\lambda = \frac{d\cdot(\sin\theta_i - \sin\theta_m)}{m} \tag{1}$$

where:
λ – wavelength,
d – grating period,
θ_i – angle of incident,
θ_m – angle of maxima.
m – diffraction order.

We are choosing the wavelength range of visible spectral range, from 400 nm to 700 nm. To design demanded colour we chose a standard observable situation, where the hologram is illuminated perpendicularly, angle of incident 0 degrees and observed under an angle of 45 degrees. After choosing a graphical and colour design, the motive area is filled with a grating of the selected period and fill factor. By azimuth rotation of grating orientation, we can achieve colour switching and by combining grating with different periods, we can achieve colour mixing. Combining red, green, and blue colours together with different diffraction orders we can achieve a white or pastel colour effect, see Figure 3.

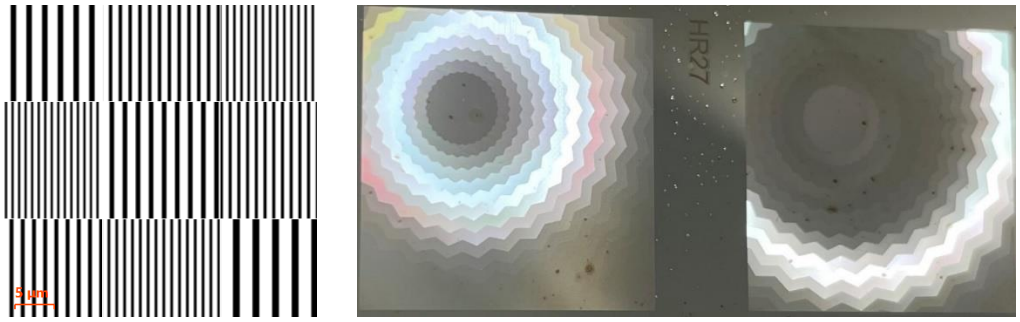

Figure 3 Left image shows different grating patterns forming white to pastel colour effects observable in the right image. Source: (own)

Figure 4 shows images of our designed and fabricated advanced holographic elements for security applications. The most remarkable achievement is the middle image, the Czech lion with a

hidden secure element. The whole hologram under normal conditions is fully visible (daylight observation). But under linearly polarized light or observable with a linearly polarizing filter, the hologram shows only the image of the lion for horizontal polarization or the outline of the emblem for vertical polarization. The right image of the horse is the demonstration of our NanogravureTM technique and the left image of the balls is the combination of NanogravureTM with colour grating, where the stereoscopic design is used for different images for the left and right eye to make 3D perception stronger [3].

Figure 4 Example of our designed advanced diffractive holographic element. Left: Hologram with colour 3D effect. Middle: hologram switched by linearly polarized light. Middle lion observable under normal conditions, without polarization. Right: Hologram with Nanogravure™ technique. Source: (own)

.

4. CONCLUSION

In this very limited contribution, we introduce the basics of designing and fabricating security diffractive holographic elements. We describe the basic steps of choosing the colour effects of the hologram by changing the period of diffraction gratings. And we show that we can prepare holographic masters at the industrial level for mass production. Thanks to this we have industrial cooperation with the Czech company Optaglio s.r.o. and Australian CCL Secure in the field of researching new ways of protecting before counterfeiting.

ACKNOWLEDGEMENT

The work was supported by the Ministry of Industry and Trade of the Czech Republic No CZ.01.1.02/0.0/0.0/20_321/0024953, No. CZ.01.1.02/0.0/0.0/20_321/0024348, and the e-INFRA CZ (ID:90140); Student Grant System SP2023/026.

REFERENCES

[1] KOCH Christian, Titus J. RINKE, *PHOTOLITHOGRPAHY Basics of Microstructuring*. Second Edition. Friedrichshafen: Siegl Druck & Medien GmbH & Co.KG, 2020.

[2] LEVINSON Harry J., *Principles of Lithography*, Fourth edition. Bellingham: SPIE, 2019. ISBN: 9781510627604

[3] GONCHARSKY Alexander, Anton GONCHARSKY, Svyatoslav DURLEVICH, “Diffractive optical element for creating visual 3D images,” *Optics Express*. 2016, **24**(9), 9140.

[4] KOHUT, Tomáš, Jakub TOBĚRNÝ, Kamil POSTAVA. Optimization of exposure parameters for direct laser writing in optical lithography. In *22nd Polish-Slovak-Czech Optical Conference on Wave and Quantum Aspects of Contemporary Optics*. Bellingham: SPIE, 2022, 125020M1-125020M5

[5] HART, Tony. *Electroforming with Nickel* [online]. Eugen G. Leuze Verlag, 2018 [cit. 29.5.2023]. Available from: https://cets-eu.be/wp-content/uploads/2019/01/Hart.pdf

[6] HARVEY, James E., Richard N. PFISTERER. Understanding diffraction grating behavior: including conical diffraction and Rayleigh anomalies from transmission gratings. *Optical Engineering*. 2019, **58**(08). ISSN 0091-3286.

[7] VOISIAT, Bogdan, Wei WANG, Max HOLZHEY a Andrés Fabián LASAGNI. Improving the homogeneity of diffraction based colours by fabricating periodic patterns with gradient spatial period using Direct Laser Interference Patterning. Scientific Reports. 2019, 9(1) [cit. 2023-06-01]. ISSN 2045-2322.

ASPECTS OF THE PREPARATION OF SELF-STANDING MODIFIED GRAPHENE OXIDE FILMS

Author(s): Vít KUBÁŇ

Supervisor: prof. Ing. Gražyna SIMHA MARTYNKOVÁ, Ph.D.

Department: Nanotechnology Centre, Faculty of Materials Science and Technology, VSB – Technical University of Ostrava

Abstract

In this short work, a description of the technology process of thin composite layers is given, together with the parameters of the synthesis of the individual components of the composite. The modified preparation process of graphene oxide nanoparticles and the sustainable preparation of silver nanoparticles by phytosynthesis are the two main technological steps that are key to the desired GO-nAg blend. It was found that the casting method of the thin film is dependent on the density of the suspension, the casting conditions and the environmental conditions at the time of drying. The properties of the prepared films on both sides were monitored in terms of their morphological character and the properties of the films were tested for wettability.

Key words:

Graphene oxide, nanosilver, exfoliation.

1. INTRODUCTION

The graphene and graphene oxide (GO) play significant role in recent nanotechnology research and development. Owing to interesting properties of graphene/graphene oxide reported so far [1], such as Young's modulus (>1060 GPa/200 GPa), electron conductivity (6000 S/cm/ low), thermal conductivity (~3000 W/mK / 1-1000 W/mK), lightness and inexpensivity, it is widely used in many applications, like sensors, biomedicines, mechanic resonators, ultra-capacitors, etc. By down-sizing graphite from micro to nano-scale, namely graphene, the applications would further widen to polymer composites, anode materials for Li-ion batteries, supercapacitors, hydrogen storage materials, adsorbers and catalysts [2]. Mass production of monolayer graphene or few layer graphene (FLG) is being hindered by the expensive cost and environmental threat of its conventional synthesis. For example, disadvantages of chemical vapor deposition are high cost and limitation of area. Chemical routes, so called Hummers' methods, suffered from usage of strong acid and oxidants during oxidation processes. A vast amount of waste acids resulted in environmental pollution and problems. Based on these issues, many researchers focus on green process to synthesize graphene or FLG, such as electrochemical exfoliation, ultrasonication process and so on.

In this work the modification method and technique for film casting is discussed. Since the process brings a few aspects for replicable and stable technology of uniform film preparation, the work will focus on parameters of preparation and testing of the surface characteristics.

2. PREPARATION OF MATERIALS AND RESULTS

To prepare the aimed thin self-standing graphene oxide film, that is modified with silver nanoparticles, we consider two preparations of components of composite film. The films consist mainly of two components. First one is graphene oxide (GO) prepared via modified Hummer's method[3]. The other component is phytosynthetically prepared silver nanoparticles. Both components are prepared in suspension state.

Firstly, the mixture of inorganic acids is prepared using sulfuric and phosphoric acid in ratio 9:1, then the mixture is placed on heater with magnetic stirrer and during whole preparation solution is thoroughly mixed (100rpm). [3] Powdered graphite is added and whole blend is put into ice bath. Potassium permanganate is added slowly because the reaction is exothermal. Weight ratio of potassium permanganate to graphite is 7:1. Everything is then put back on heater and heated at 90°C for 24h. Next step is adding hydrogen peroxide. Once the mixture is stabilized distilled water is added to dilute very

acidic solution (lower than pH 0). Next step is decantation and dilution until reaching pH 3, which is hastened by using centrifugation. Final product is suspension (Figure 1).

Figure 1 Real sample of graphene oxide suspension as prepared in lab. Source: (own)

Second component of the composite is bio-prepared nanosilver. Dried nettle is immersed in 80°C warm distilled water and let extract for 10 min. Then mixing nettle extract with 100mM silver nitrate solution in ratio 1:1 and leave to react until reaching orange colour with no dark turbidity. Nanosilver needs to be kept in unchanged chemical state, so final product must be covered in aluminum foil and put in the fridge. Last step is centrifugation of silver colloid to obtain higher concentration. (Figure 2). [4]

Figure 2 Real sample of nanosilver suspension as prepared in laboratory. Source: (own)

Final step of film preparation is combining GO and nanosilver together, where 8 ml of GO suspension are mixed with 40 mg of centrifuged AgNPs. Mixture is then ultrasonicated for 5 min at 75% power and 21°C temperature.

Suspension is then casted [5] on PTFE substrate (Fig.3) and for square 5x5 cm, 8 ml of mixture is used. Film is dried covered by glass where humidity and temperature changes are evaluated using laboratory thermometer and humidity meter.

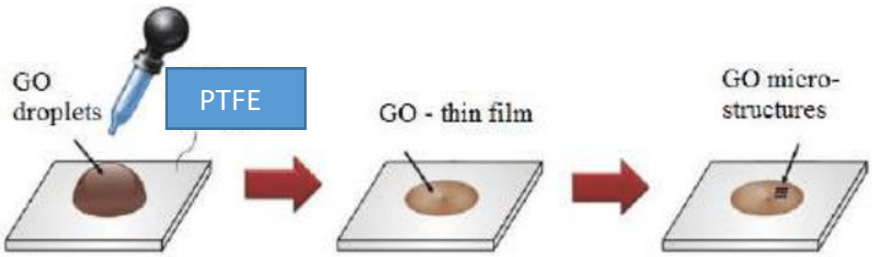

Figure 3 Schema of casting technology of thin GO film. Source: [6]

Since the aim of the preparation is to obtain self-standing film, the adhesion to the surface of the support should be low. The PTFE substrate is suitable for two reasons, one is the smooth non-adhesive surface, and second the flexibility of the polymer, therefore the removing process is relatively straightforward. During preparation it is important to work out some factors, like humidity, temperature, ratio liquid: solid. Ratio liquid: solid concerning GOAg is included in Table 1.

Table 1: Ratio of liquid: solid for GOAg and average values. Source: (own)

GOAg	Dry solid mass (mg)	Suspension volume (ml)
Sample 1	4.8	1
Sample 2	5.6	
Sample 3	5.1	
Sample 4	5.9	
Sample 5	5	
Average	5.28	

Final films were characterized for morphology, structure and surface properties. One of the chosen was scanning electron microscopy (SEM) analysis using JEOL JSM-7610F for the surface morphology analysis. Pure GO film and GOAg film are shown in Figure 4 where differences regarding their morphology can be seen. This method was chosen because it is important to see what was prepared and how the morphology of the films looks like.

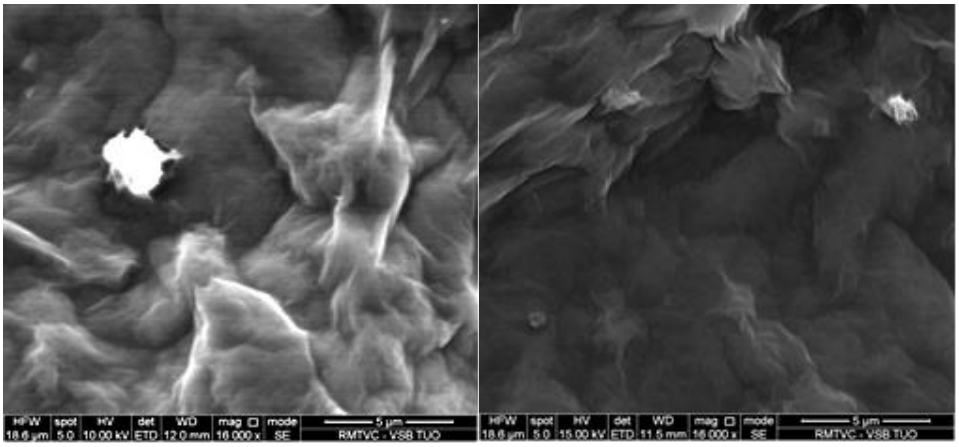

a) b)

Figure 4 SEM images of a) GO film, b) GOAg film. Source: (own)

Comparison of behaviour of both prepared films with polar and non-polar solvent were observed by measuring contact angle with water and monopropylene glycol (organic). It is important parameter for potential application as separator or coating of conventional separator in batteries. Graphic representation of resulting contact angles is in Figure 5.

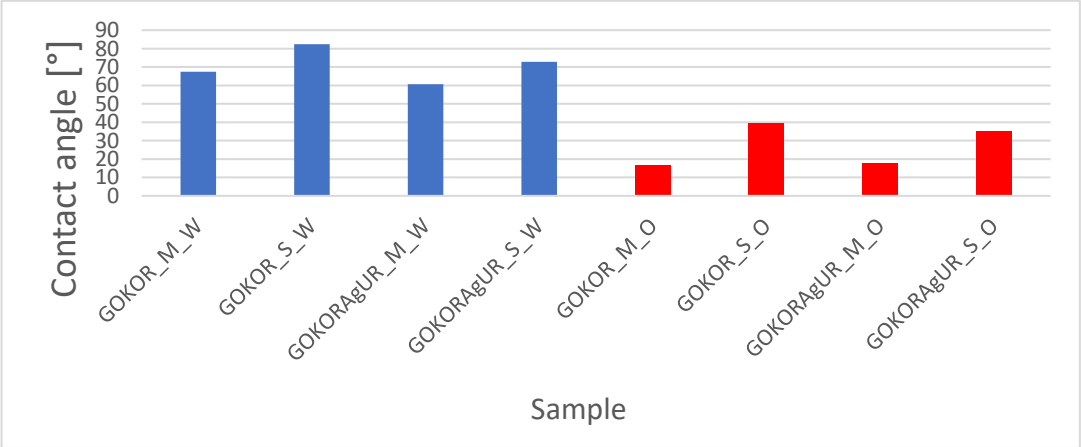

Figure 5 Contact angle values with water and organic solvent. Source: (own)

3. DISSCUSION AND CONCLUSION

Comparing the prepared film regarding the preparation technique, several specific features were observed.

To control the parameters, such as purity, particle size distribution, uniformity of particles, solid-liquid ratio for centrifugation for the phytosynthetical reduction of nano silver particles, following strategies and techniques can be implemented:

1. Purity (total Ag reduction and impurities): Use of high-quality starting materials to minimize impurities; optimization of the reaction conditions, such as temperature, pH, and reaction time, to maximize the conversion of impurities into desired products; employment of appropriate purification techniques like filtration, precipitation, or solvent extraction to remove impurities.

2. Particle Size Distribution: Adjust the reaction parameters, including temperature, reaction time and reactant concentrations, to control nucleation and growth rates.

The key control factor for final film preparation is necessary to be formulated. To achieve uniform distribution of dispersion, the ratio of solid to liquid for centrifugated material should be defined, and low adhesion to the substrate in the casting process is given. Uniform distribution of dispersion can be achieved by properly mixing the components of the dispersion to ensure a homogeneous mixture before casting along with utilization of suitable mixing techniques such as mechanical stirring, ultrasonication, or magnetic stirring to disperse the solid particles uniformly in the liquid medium.

Differences between GO and GOAg surfaces can be seen using scanning electron microscopy. One of the differences is smoother morphology in GO film whereas in GOAg the surface is rougher, and more particles and graphene sheets are sticking out.

Another important analysis/test is contact angle measurement which shows philicity/phobicity to polar and non-polar solvents. With potential application as separator or coating of separators it is important that films are organophilic and hydrophobic, which both GO and GOAg films fulfill. Contact angle with thermal stability, which was also confirmed using DSC analysis, and mechanical stability are important parameters for separators. GO and GOAg are fulfilling these requirements so their potential use will be tested further.

ACKNOWLEDGEMENT

The work was supported from the project MEYS SP 2023/026, „Support for Science and Research in the Moravia-Silesia Region 2022" (RRC/12/2022) and Technology Agency of the Czech Republic as part of the National Center of Competence Program, project National Center for Energy II (TN02000025)".

REFERENCES

[1] ZHU Y, S. MURALI, W. CAI, X. LI, J. W. SUK, J. R. POTTS, R. S. RUOFF. *Graphene and graphene oxide: synthesis, properties, and applications.* Advanced materials. 2010, **22**(35), 3906-3924. 1521-4095.

[2] CHEN, J., B. YAO, C. LI, G. SHI. *An improved Hummers method for eco-friendly synthesis of graphene oxide.* Carbon. 2013, **64**, 225-229. 1873-3891.

[3] ZAABA, N. I., K. L. FOO et al. Synthesis of Graphene Oxide using Modified Hummers Method: Solvent Influence. Procedia Engineering. 2017, **184** (15), 469-477. 1877-7058.

[4] KONVIČKOVÁ Z., K. ČECH BARABASZOVÁ, V. HOLIŠOVÁ, G. KRATOŠOVÁ. *Phytosynthesis of Ag, ZnO and ZrO 2 Nanoparticles Using Linden: Changes in Their Physical-Chemical Nature Over Time*. Journal of Nanoscience and Nanotechnology. 2019, **19**(12), 7926-7933. 1533-4880.

[5] ZHAO C, L. XING, J. XIANG, L. CUI, J. JIAO, H. SAI, Z. LI, F. LI. *Formation of uniform reduced graphene oxide films on modified PET substrates using drop-casting method.* Particuology. 2014, **17**, 66-73. 2210-4291

[6] NIKOLAOU Ioannis. *Properties of graphene by chemical recognition on Surface Acoustic Wave (SAW) sensors : Application to the detection of chemical compounds in the gaseous state.* Electronics. Université de Bordeaux, 2019. English. NNT: 2019BORD0379ff. tel-02930977 Available from: https://theses.hal.science/tel-02930977.

TERAHERTZ OPTICAL ACTIVITY MODELLING AND MEASUREMENT IN CRYSTALS

Author(s): Jiaming LIU

Supervisor: doc. Dr. Mgr. Kamil POSTAVA

Department: IT4Innovations National Supercomputing Center, Faculty of Materials Science and Technology, VSB-TUO

Abstract

Chirality exists in large amount of natural materials. As an asymmetric geometric property, chirality identifies that an object cannot be superimposed with itself after mirroring transformation. In pharmacy, the enantiomers of one kind of biomedicine, even if they have the same chemical composition, show individual stereoselectivity due to chirality. Hence, the isomers exhibit obviously disparities in toxicity and treatment efficacy. In addition, the chiral molecules exhibit optical activity – different complex refractive indices for the left and right circular polarization. Thus, optical activity measurement has already become an attractive method in chiral material measurements. Techniques of circular dichroism and optical rotatory dispersion in infrared, visible and ultraviolet range have matured for the measurements of vibration and rotation modes in low weight molecules. In biomolecules, such as amino acids and protein, vibration modes of these crystalized molecular complexes belong to THz frequencies. In this paper, the THz polarization response in quartz is observed, which shows strongly support for the future measurements of amino acids, proteins and other biomedical samples. Jones matrices describes the whole measurement procedure mathematically. The optimized plasmonic Born-Kuhn model explains the complex THz optical activity spectra. In experiment, THz time-domain ellipsometric spectroscopy identifies the different THz responses of several kinds of samples. which enables the THz ellipsometry detection to become a reasonable method in the THz analysis of anisotropic natural materials.

Key words:

Chirality, Terahertz radiation, optical activity, polarization.

1. INTRODUCTION

The terahertz (THz) spectral range from electromagnetic radiation (frequency range from 0.1 to 30 THz, wavelength range from 10 micrometers to 3 mm), located between the microwave and infrared radiation in the electromagnetic spectrum, has been attracting significant attention as a consequence of its promising applications in biomedicine [1], 6th generation (6G) communication, industrial non-destructive testing, detection of hazardous substances, and security screening.

In the field of biological and medical analysis, the THz beam is a great probe in detecting the vibration modes of complex biological macromolecules, due to its suitable spectral range and non-ionizing character [2]. Also, typical biomedical molecules exhibit unique chiral symmetry, which cause different response for left- and right-circularly polarized THz radiation.

The terahertz time-domain spectrometry (THz-TDS) acts as a marvellous technique for sensing in THz range. In THz-TDS, the obtained spectra contain not only the amplitudes but also phases, which gives the complex information about sample response with high sensitivity, wide spectral precision, and temporal resolution. THz time domain spectroscopic ellipsometry (THz-TDSE) combines the THz-TDS and polarization selectivity on the propose of measuring and analysing the special form of anisotropy – Terahertz circular dichroism (TCD) and Terahertz optical rotatory dispersion (TORD). The THz complex optical activity, represented by TORD and TCD [2], is important for chirality of molecular complexes and protein with a potential impact in biomedicine and pharmacy [3]. Chirality enables the molecules to be distinguished into two types of enantiomers which exhibit the incompatible binding and interaction between a drug and its target to shape the pharmacology of a drug [4]. Chiral medicine isomers could exhibit different effects in pharmacology, toxicology [5].

Moreover, in the recent research, the THz response is still difficult to measure. Hence, how to enhance the THz response in natural chiral material is the step to achieve. Thus, we will construct theorical model, build THz-TDSE, and optimize both of them to get deeper understanding in the THz chirality of biomedicine structure. At the meanwhile, the chiral artificial metamaterials exhibit huge THz optical activity [6]. On the one hand, the artificial metamaterials can be designed as the same structure

of the simplified theoretical model to get the reasonable comparison with the real molecules. On the other hand, the model will play a role in the design of nano-structure with stronger THz response.

2. THz optical activity

The circular dichroism (CD) and optical rotatory dispersion (ORD) describe the optical activity of materials. Circular dichroism shows the different absorptions of the left- and right-circular light in the material. Optical rotatory dispersion measures the rotated azimuth angle of the polarized beam after passing through a sample. In order to analyze optical activity response, polarization spectra dependence of the optical activity have to be modelled. Molecules normally are simplified as classical driven harmonic oscillators. The crystalized chiral biomolecules could be viewed as a type of two coupled oscillator system, where the motion of each atom in the molecule is coupled to the motion of the surrounding atoms. The oscillation of each atom is influenced by the chirality of neighboring atoms, leading to a complex network of interdependent motions. As a theorical model, a system with two coupled oscillators shown in figure 1 is sufficient to represent chiral structure.

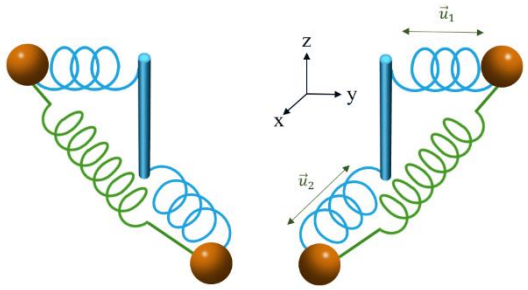

Figure 1 (a) Left hand system (b) Right hand system state. Source: (own)

The oscillator directions are shown as u1 and u2 in Figure 1. In a classical model of the oscillation system, as light is present, the electric field strength denoted by E undergoes oscillation, thereby producing a Coulomb force on the charge carriers. Consequently, an oscillating induced dipole moment emerges. The equation of motion of a single charge carrier in this model is now.

$$m\frac{\partial^2}{\partial t^2}\vec{u}_i + 2\gamma m\frac{\partial}{\partial t}\vec{u}_i + m\,\omega_0^2\vec{u}_i + m\,\zeta\vec{u}_j = -eE_0e^{-i\omega t} \quad (1)$$

where m is the oscillator mass, $\vec{u}_i$denotes the displacement of one oscillator where i = 1and 2, γ represents damping parameter, ω_0 indicates oscillation centre frequency, ζ shows the coupling strength, e is the electron charge and $E_0e^{-i\omega t}$ represent the input time dependent electric field.

From Equation (1), in the oscillation system, the current density, susceptibility tensor are obtain from the oscillator‘s displacements. The circular dichroism and the optical rotatory disperstion are related to the real and imaginary parts of nonlocality tensor Γ which is a portion susceptibility tensor.

At the meanwhile, the refractive index of the material for left and right polarized beam are shown as [2]

$$n_{R,L}^2 = \bar{n}^2 \pm \Gamma\bar{n} \quad (2)$$

In Equation (2), $n_{R,L}$ are given by the refractive index for right and left circular light, and $\bar{n}$ represents the average refractive index.

With Equation (2), the refractive index difference between the right and left circular polarized beam is equal to the nonlocality. Thus the optical activity is calculated by:

$$CD = \frac{\omega}{2c}Re\{\Gamma\} \quad (3)$$

$$ORD = 2\frac{\omega}{c}Im\{\Gamma\} \quad (4)$$

where CD is the circular dichroism, ORD represents the optical rotatory dispersion, ω denotes angle frequency, c is given as the light velocity in vacuum, and Γ indicates the nonlocality tensor of the material.

The refractive indices also act as a necessary parameter in the Jones Matrices for the description of the whole procedure:

$$\begin{bmatrix} E_x \\ E_y \end{bmatrix} = [M_{Detector}][M_{Polarizer}]\left[M_{Sample}\right]\left[E_{THz}^{input}\right] \quad (5)$$

where E_x, E_y represents the measured THz amplitude in x and y axis, M is the Jones matrix of detector, polarizer and sample and E_{THz}^{input} denotes the angle frequency.

In the modeling, the Jones matices of polarizer and detector are considered as ideal polarizers only described by azimuth angle. In addition, the Jones matices of the sample is more complex. Its parameters also contain refractive indices, sample thickness and wave vector. With the simulation and measurement data, the parameters of every component in the setup are ensured. Figure 2 shows the THz setup and the measurement results with the two polarization states of THz emitter and three polarization states of polarizer.

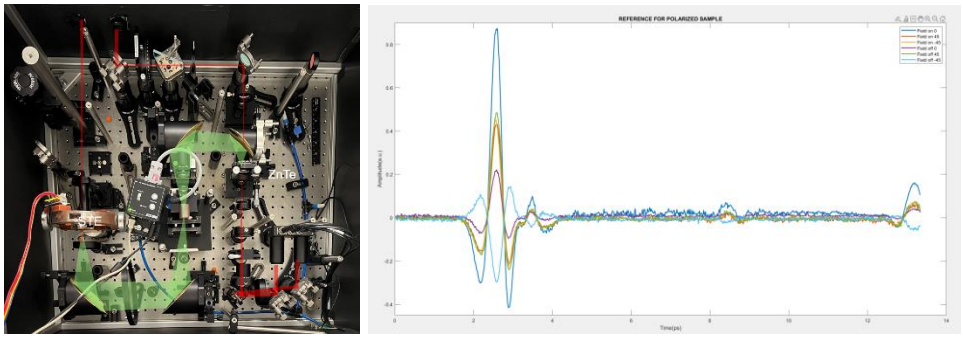

(a) **(b)**

Figure 2 (a) THz time domain polarization spectroscopy (b) Measured signal in dry air.
Source: (own)

Plotted as red in Fig.2(a), the laser pulse with the wavelength of 808 nm and 50 fs pulse duration propagates into the THz setup box from the front left corner. Then it illuminates the spintronic emitter (STE). With the illumination of the laser, the carriers in the STE generate a current. The photocurrent generates THz pulse (green), the polarization of which is controlled by the external magnetic field. Passing through two parabolic mirrors, the THz beam is focused on the sample position in front of the polarizers. The selected polarized THz ray which carries the sample information pass through the motorized polarizer. Then the THz radiation overlaps with laser beam (red) on ZnTe crystal. The laser beam with driven information from the THz pulse is split into left and right circular polarized beams and detected by the balanced detector.

Figure 2 (b) shows the THz signal in different polarizations. The STE emits vertical (0°) and near horizontal (75°) polarized THz beam. When the polarizer is also set vertical, the largest pulse is gotten. When the polarizer is at ±45°, the signals are for the analysing of the THz response in perpendicular axes.

In the measurement of THz time domain spectroscopy, amplitude and phase are both detected. Compared with infrared or visible spectroscopy, only intensity is measured. Thus in the spectrum analysing with phase is identical in THz measurement.

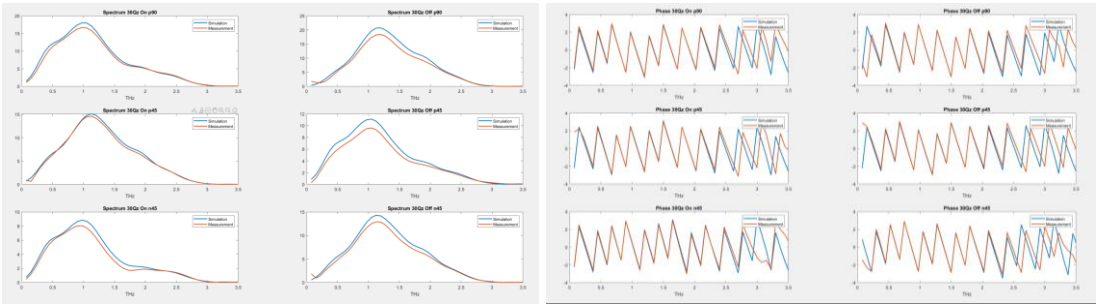

(a) (b)

Figure 3 THz measurements and simulation of quartz sample (a) Spectrum (b) phase.
Source: (own)
the two figures (a) and (b) shows the comparison of the spectrum and phase in the measurement and simulation. The red one is the experiment results and the blue one shows the simulation results.

In figure 3, The simulation results show the good dependence with experiment. The phases in experiment and simulation have the same slop which respect to refractive index. In this case, the mean square error is 0.61 and quartz refractive indices are gotten as 2.02 and 2.12, which are compared with reference. It implies that the preliminary results satisfy initial expectations.

3. CONCLUSION

In this paper, the method of THz optical activity measurement and modelling are described. Also, the measurement and fitting results of quartz sample shows good dependence mutually. Thus, the modelling and measurements give good preliminary results which support the THz optical activity measurements to go step by step. In the future, the aim is about the more complicated optical sample, such as amino acids crystal, DNA and other biomedicines.

ACKNOWLEDGEMENT

The financial support from the project S-Nebula: Novel Spin-Based Building Blocks for Advanced Terahertz Applications and Czech Science Foundation are acknowledged.

REFERENCES

[1] CHOI, Won Jin, Keiichi YANO. Chiral phonons in microcrystals and nanofibrils of biomolecules. *Nature Photonics*. 2022, **16** (5), 366-373.
[2] VALA, Daniel, Martin MICICA. Molecular chirality from the viewpoint of Mueller ellipsometry. *22nd Polish-Slovak-Czech Optical Conference on Wave and Quantum Aspects of Contemporary Optics*. Proc. SPIE 12502. 2022, 1250210-1250216.
[3] YIN, Xinghui, Martin SCHAFERLING. Interpreting Chiral Nanophotonic Spectra: The Plasmonic Born-Kuhn Model. *Nano Letters*. 2013, **13** (12),6238-6243.
[4] SILVESTRI, Ilaria Proietti, Paul J. J. COLBON. The Growing Importance of Chirality in 3D Chemical Space Exploration and Modern Drug Discovery Approaches for Hit-ID: Topical Innovations. *ACS Med. Chem. Lett*. 2021, **12** (8), 1220-1229.
[5] MCCONATHY, Jonathan, Michael J. OWENS. Stereochemistry in Drug Action. *Prim Care Companion J Clin Psychiatry*. 2023, **5** (2), 70-73.
[6] KAN, Tetsuo, Akihiro ISOZAKI. Enantiomeric switching of chiral metamaterial for terahertz polarization modulation employing vertically deformable MEMS spirals. *Nature Communications*. 2015, **6** (1), 8422.

LAMB'S LETTUCE AS A MODEL ORGANISM FOR STUDY IMPACT NANOPARTICLES TO ENVIRONMENT

Author(s): Gabriela MIKESKOVÁ

Supervisor: prof. Ing. Jana SEIDLEROVÁ, CSc.

Consultant: Mgr. Oldřich MOTYKA, Ph.D.

Department: Nanotechnology Centre, CEET, Faculty of Mining and Geology, Faculty of Materials Science and Technology, VŠB – Technical University of Ostrava

Abstract

Lamb's lettuce (Valerianella locusta L.) is often a popular food for consumption without the need for cooking. It contains many nutrients beneficial to health, its growing is good replicable and undemanding growing conditions. It also has the advantage that it can be grown both hydroponically and in soil, which extends its practicality in research. The present work deals with the possibility of its use as a model organism representative of terrestrial plants for monitoring the impact of nanoparticles on the environment. The preliminary experiments have shown that this is possible.

Key words:

Lamb's lettuce, model organism, toxikology, growing.

1. INTRODUCTION

The environmental impact assessment of materials and wastes also includes toxicity and ecotoxicity assessments. Toxicity and ecotoxicity assessments are performed on organisms of different trophic levels using bioindicators. Standardised methods with a defined bioindicator type are used for the purpose of the assessment, but these are no longer applicable to the whole ecosystem. Ecotoxicity is defined in the Czech Republic legislation in the Decree of the Ministry of the Environment No. 591/2020 Coll., on the evaluation of hazardous properties of waste under the code H14 among hazardous properties of waste. According to the Decree, a waste is evaluated as hazardous if its aqueous leachate shows LC50 (EC50, IC50) values in acute toxicity tests of less than 10 $ml.L^{-1}$ for at least one of the test organisms at the specified time of exposure to the tested waste [1, 2].

The test organisms used for ecotoxicity assessment by law are the fish *Poecilia reticulata* or *Brachydanio rerio* (96 h exposure time) [3], the pearl mussel *Daphnia magna* (48 h exposure time) [4] and the fish *Daphnia magna* (48 h exposure time) [4], the algae *Raphidocelis subcapitata* (*Selenastrum capricornutum*) or *Scenedesmus subspicatus* (exposure time 72 hours) [5] and the land plant *Sinapis alba* (exposure time 72 hours) [6, 7, 8].

Contact tests, which are becoming more popular in ecotoxicity assessment but are not yet standardised, are proving more suitable. For example, soil toxicity in land plants is most commonly detected by germination, emergence and growth of land plants *Avena sativa* and *Brassica rapa* and water quality monitoring using root length inhibition toxicity tests for *Sinapis alba* and *Lactuca sativa* [1, 2].

2. LAMB'S LETTUCE AS A MODEL ORGANISM

Lamb's lettuce (*Valerianella locusta L*.) is an annual small plant of the *Valerianaceae* family grown mainly for direct consumption in salads because of its good flavour. [9] The disadvantage is that it can only be stored for fourteen days, after which time it wilts and rot infects the leaves, rendering it useless [10, 11]. It is grown in the ground or hydroponically mostly in France. We must also not forget its nutritional values. It contains large amounts of carotenoids, vitamin C, phenolic compounds, folic acid, sterols and fatty acids [11, 12].

It is used as a model organism for research on flower shape diversification. Most of the focus is on size, bilateral symmetry, asymmetry and shape [13, 14]. It is also investigated in terms of cultivation and infection by bacteria under laboratory conditions on different parts of the plant body. For example, the bacteria *Salmonella enterica Serovar Typhimurium, or Escherichia coli O104:H4* have been used [14, 15].

Lamb's lettuce was detected as a suitable plant organism for transmission through the whole plant body when the aqueous solution was aspirated through the root system and the highest content of the substance was in the leaf part [16]. However, for the consumer, this advantage is hazardous to health. It is necessary to control the exact composition of the hydroponic solution, as nutrients are more soluble in water and excess nutrients can cause osmotic stress, ionic toxicity and nutrient imbalance. These factors lead to leaf and plant deterioration and nitrate accumulation [17].

It is also interesting to note, however, that lamb's lettuce is not susceptible to disease as it grows relatively quickly and can be harvested at any time of the year. A row about 3 metres long yields 1-3 kg of above-ground parts. The advantage is that it does not have to be cut off whole, but only part of the green leaf. For these reasons it can be a permanent bioindicator of the environment [18].

3. GROWING CONDITIONS

In the framework of doctoral thesis, the possibility of using Lamb's lettuce as a model organism to investigate the ecotoxicology of nanoparticles for both dry and wet deposition is verified. It is a representative of land plants. It grows relatively fast, with an easily sustainable temperature and does not need much care. A temperature of 20 °C is ideal. A higher temperature, 25 °C as an example, causes the plant to grow faster, but also damages the already grown leaves, which wither and turn yellow due to the temperature. In the beginning I recommend watering the plants twice a week, and the mature plants once a week to prevent rotting. It is also ideal to transplant the plants to a larger space at about 4 weeks of age, so that they can grow sideways and not crowd each other. It is also ideal to alternate a 12-hour light/dark cycle. The light should be in the visible part of the spectrum. It should also be noted that the growth cycle is complete after about a month of growth [9].

The following figures show the cultivation of Lamb's lettuce in figure 1, showing several plants at 4 weeks of age just after transplanting.

Figure 1 Lamb's lettuce, 4 weeks old after transplanting. Source: (own)

Changes in leaf chlorophyll content, growth rate etc. can be studied during dry or wet deposition. After deposition, changes in the elemental content in the above or below ground part of the plant, cell structure or DNA mutations could be determined. Initial experiments have been carried out to monitor the effect of TiO_2 nanoparticles.

4. CONCLUSION

Based on the evaluation of the pilot experiments, it can be concluded that a lamb's lettuce is an ideal choice for detecting the toxicity of individual nanoparticles. In addition, it absorbs individual particles of many sizes well, which can later be analysed by chemical analytical methods and qualitatively and qualitatively determined, and from this the environmental status of the water or air can subsequently be determined. In addition, it grows relatively quickly without the need for special conditions. The experiment with lamb's lettuce can also be repeated very easily.

ACKNOWLEDGEMENT

We thank for the financial support to SGS project number SP2023/095

REFERENCES

[1] REINKE, Emily N.; ADAMS, Valerie H. Tiered In Vitro Toxicity Testing of the Novel Energetic N-Propylnitroguanidine (PrNQ). Army Public Health Center, 2021.
[2] AHMAD, Ali, et al. Influence of metallic, metallic oxide, and organic nanoparticles on plant physiology. Chemosphere, 2022, 290: 133329.
[3] ČSN EN ISO 7346-2 Jakost vod - Stanovení akutní letální toxicity pro sladkovodní ryby [Brachydanio rerio Hamilton-Buchanan (Teleostei, Cyprinidae)] - část 2: Obnovovací metoda
[4] ČSN EN ISO 6341 Jakost vod - Zkouška inhibice pohyblivosti Daphnia magna Straus (Cladocera, Crustacea) - Zkouška akutní toxicit
[5] ČSN EN 28692 Jakost vod - Zkouška inhibice růstu sladkovodních řas Scenedesmus subspicatus a Selenastrum capricornutum (ISO 8692; 1989)
[6] MŽP (2007): Metodický pokyn ke stanovení ekotoxicity odpadů, věstník MŽP 4/2007
[7] 294/2005 Sb. – Vyhláška Ministrstva životního prostředí o podmínkách ukládání odpadů na skládky a jejich využívání na povrchu terénu
[8] ČSN EN 14735, Charakterizace odpadů – Příprava vzorků odpadu pro testy ekotoxicity (česká verze evropské normy EN 14735:2005 včetně opravy EN 14735:2005/AC:2006-06)
[9] GARCÍA-VALCÁRCEL, Ana I., Iñigo LOUREIRO, Concepción ESCORIAL, Encarnación MOLERO a José L. TADEO. Uptake of azoles by lamb's lettuce (Valerianella locusta L.) grown in hydroponic conditions. Ecotoxicology and Environmental Safety [online]. 2016, **124**, 138-146 [cit. 2023-05-08]. ISSN 01476513. Dostupné z: doi:10.1016/j.ecoenv.2015.10.021
[10] DECOMBEL, A., B.A.J.G. JACOBS, J. VAN LOMMEL, I. VANDEVELDE, B.E. VERLINDEN a P. BLEYAERT. Impact of cooling temperature and wrapping on storage quality of lamb's lettuce (Valerianella locusta L.). Acta Horticulturae [online]. 2019, (1242), 153-156 [cit. 2023-05-03]. ISSN 0567-7572. Dostupné z: doi:10.17660/ActaHortic.2019.1242.21
[11] SKRYPNIK, Liubov, Tatiana STYRAN, Tamara SAVINA a Nadezhda GOLUBKINA. Effect of Selenium Application and Growth Stage at Harvest on Hydrophilic and Lipophilic Antioxidants in Lamb's Lettuce (Valerianella locusta L. Laterr.). Plants [online]. 2021, **10**(12) [cit. 2023-01-27]. ISSN 2223-7747. Dostupné z: doi:10.3390/plants10122733
[12] SCHMITZER, Valentina, Mateja SENICA, Ana SLATNAR, Franci STAMPAR a Jerneja JAKOPIC. Changes in Metabolite Patterns During Refrigerated Storage of Lamb's lettuce (Valerianella locusta L. Betcke). Frontiers in Nutrition [online]. 2021, **8** [cit. 2023-01-27]. ISSN 2296-861X. Dostupné z: doi:10.3389/fnut.2021.731869
[13] BERGER, Brent A., Barbara A. AMBROSE, Jingjing TONG a Dianella G. HOWARTH. Flower development in Fedia graciliflora and Valerianella locusta (Valerianaceae). Flora [online]. 2021, **275** [cit. 2023-01-27]. ISSN 03672530. Dostupné z: doi:10.1016/j.flora.2020.151754
[14] ELPERS, Laura, Juliane KRETZSCHMAR, Sean-Paul NUCCIO, Andreas J. BÄUMLER, Michael HENSEL a Christopher A. ELKINS. Factors Required for Adhesion of Salmonella enterica Serovar Typhimurium to Corn Salad (Valerianella locusta). Applied and Environmental Microbiology [online]. 2020, **86**(8), 02757-19 [cit. 2023-01-27]. ISSN 0099-2240. Dostupné z: doi:10.1128/AEM.02757-19
[15] EISSENBERGER, Kristina, David DRISSNER, Fiona WALSH, Agnes WEISS a Herbert SCHMIDT. Plant variety and soil type influence Escherichia coli O104: H4 strain C227/11ϕcu adherence to and internalization

into the roots of lettuce plants. Food Microbiology [online]. 2020, **86** [cit. 2023-01-27]. ISSN 07400020. Dostupné z: doi:10.1016/j.fm.2019.103316

[16] AHMED, S. A. T., ELMWAFIE, S. M., ET ISMAIL, S. S. Assessment of nurses' performance regarding decubitus ulcer prevention for hospitalized children. Current Pediatric Research [online]. 2023, **27**(1) [cit. 2023-03-27]. DOI: 10.35841/0971-9032.27.01.1770-1779.

[17] MANZOCCO, Lara, Martina FOSCHIA, Nicola TOMASI, Michela MAIFRENI, Luisa DALLA COSTA, Marilena MARINO, Giovanni CORTELLA a Stefano CESCO. Influence of hydroponic and soil cultivation on quality and shelf life of ready-to-eat lamb's lettuce (Valerianella locusta L. Laterr). Journal of the Science of Food and Agriculture [online]. 2011, **91**(8), 1373-1380 [cit. 2023-05-08]. ISSN 00225142. Dostupné z: doi:10.1002/jsfa.4313

[18] FABEK, S., N. TOTH, B. BENKO, J. BOROŠIĆ, I. ZUTIĆ a B. NOVAK. LAMB'S LETTUCE GROWING CYCLE AND YIELD AS AFFECTED BY ABIOTIC FACTORS. Acta Horticulturae [online]. 2011, (893), 887-894 [cit. 2023-05-24]. ISSN 0567-7572. Dostupné z: doi:10.17660/ActaHortic.2011.893.98

APPLICATION OF PVDF IN FORM OF MEMBRANE FOR HYDROGEN PURIFICATION

Author: Lukáš PLESNÍK

Supervisor: prof. Ing. Gražyna SIMHA MARTYNKOVÁ, Ph.D.

Department: Nanotechnology Centre, CEET, Faculty of Materials Science and Technology, VSB – Technical University of Ostrava

Abstract

This paper experimental work is based on the theoretical knowledges on PVDF polymer materials used for energy application, especially for hydrogen purification. PVDF is used in this application in form of polymeric membrane, because of its relevant properties, such as mechanical, chemical and thermal stability. PVDF membrane material was prepared by nonsolvent-induced phase separation process (NIPS) and characterised using optical microscopy.

Key words:

PVDF nanocomposites, membrane separator, hydrogen purification.

1. INTRODUCTION

With the growing demand for clean energy sources, there is an increasing need to explore alternatives to the predominantly used fossil fuels. Hydrogen presents itself as a potential solution that could replace fossil fuels in certain areas in the future (Figure 1). However, it is important to note that even hydrogen may not always be carbon neutral. Depending on the production process, hydrogen can be categorised into several variants, each described with a different colour. The most common variant is grey hydrogen, which is derived from natural gas or methane through steam reformation without capturing greenhouse gases. Another variant is blue hydrogen, which involves capturing and storing greenhouse gases that are by-products of the production process. In the future, the greatest demand for green hydrogen is expected, obtained by electrolysis of water using energy from solar and wind power plants [1].

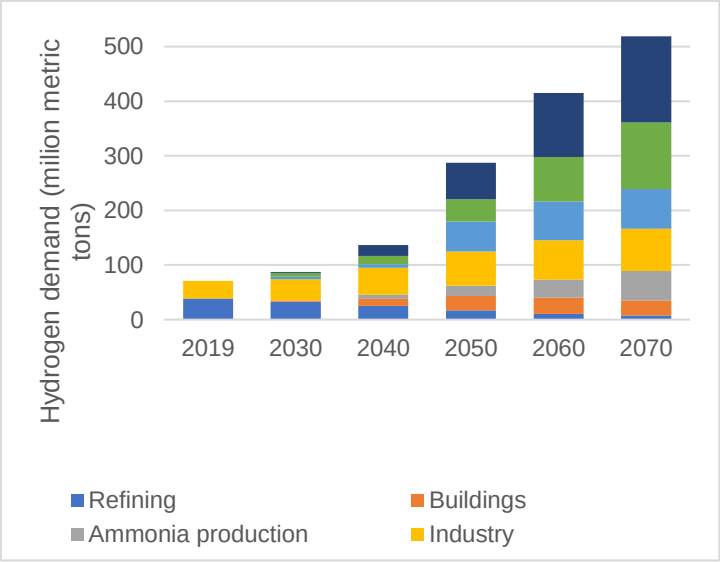

Figure 1 Graph of hydrogen quantity demand forecast devoted for different use. Source: [2]

However, the process of electrolysis is known to be energy intensive, and utilising renewable energy sources such as solar and wind power can present additional challenges. Consequently, it is advisable to explore efficient alternatives for generating high-purity hydrogen. The extraction or

purification of hydrogen from gas mixtures emerges as an alternative approach to satisfy the growing demand [3].

The membrane gas separation process stands out as a highly appealing and alternative technology compared to other methods such as cryogenic distillation or pressure swing adsorption (PSA). PSA is based on the ability of the adsorbent to adsorb impurities under high pressures, which is not feasible for H_2. On the other hand, cryogenic distillation is known to be economically inefficient and energy intensive, with complications arising from the deposition of frozen CO_2 and H_2O. In contrast, membrane technology offers advantages such as lower energy consumption, great adaptability potential, and reduced investment costs in comparison to conventional separation methods. Its installation and operation are easy to maintain, suitable for both small- and large-scale applications [3].

PVDF is commonly used in the fabrication of microfiltration and ultrafiltration membranes because of its desirable properties, such as excellent thermal stability, high mechanical strength, rigidity, and resistance to acids, bases, and chemical solvents. These properties remain effective even in challenging environments such as ultraviolet and nuclear settings. However, the inherent hydrophobicity of PVDF often leads to the adsorption and deposition of nonspecific biological and organic pollutants on the membrane surface. This phenomenon, known as membrane fouling, occurs frequently during practical filtration processes, resulting in decreased flux and separation efficiency [4, 5].

Several types of membrane are used for H_2 purification, for example, organic (polymer) and inorganic (silica, zeolite, carbon, ceramic). Membranes are further divided according to porosity into dense and porous polymeric membranes, generally porous polymeric membranes are prepared by the waist inversion technique. In this method, the polymer state is converted from a liquid state to a solid state, and the membrane is synthesised. Both porous and nonporous membranes can be prepared by this technique. Mechanism of transport on the molecular sieving axis of the porous membrane, whereas diffusion of solution is found in the case of dense polymer membranes [6].

Membrane performance is determined by two key factors: selectivity and membrane permeability. For microporous membranes, the flux is directly proportional to the pressure, whereas for inorganic membranes, the flux is proportional to the square root of the pressure. Microporous membranes are capable of operating at high pressures and temperatures, with their permeability significantly increasing as the temperature rises. In terms of permeability and selectivity, inorganic membranes and hybrid membranes exhibit excellent performance. However, their higher cost and challenges related to modularization have led many researchers to focus on modifying polymer materials to create cost-effective membranes capable of withstanding elevated temperatures while maintaining good performance. Today, polymers are utilised for large-scale membrane production because of their high mechanical resistance in comparison to that of inorganic membranes. Additionally, grafting of various polymeric materials onto membranes is carried out to improve their perforation properties [7].

PVDF is extensively utilised in membrane manufacturing because of its favourable processability and solubility in various organic solvents, including N,N-dimethylformamide (DMF). The membrane derives its thermal stability and flexibility from a combination of its crystalline and amorphous phases. Additionally, PVDF exhibits a highly hydrophobic nature and excellent chemical resistance to corrosive substances such as acids, bases, oxidants, and halogens. The selectivity and permeability of hydrogen through the membrane are found to be influenced by factors such as membrane material, additives, membrane porosity, and membrane morphology [7, 8].

2. MATERIAL PREPARATION AND RESULTS

The PVDF granules (from Sigma Aldrich) were used for the preparation of PVDF nanocomposites. The granules were dissolved in the presence of DMF and acetone as a solvent. This mixture was processed with constant mixing at temperature 80 ° C. After complete dissolution of PVDF, the mixture was transferred to the glass substrate. The polymer was spread with a blade coater obtaining uniform thickness, and after that the mixture was immersed in a nonsolvent solution which was in this case a water bath. The concentration of the substance in which PVDF is soluble (DMF) changes with respect to the nonsolvent environment (H_2O). The DMF is diluted and its concentration in the prepared mixture is reduced until the PVDF precipitates in the nonsolvent H_2O environment. The mixture was immersed into a H_2O bath for 1, 60 and 1200 minutes. After this treatment, PVDF samples were dried at 25 °C for 48 hours (Figure 2).

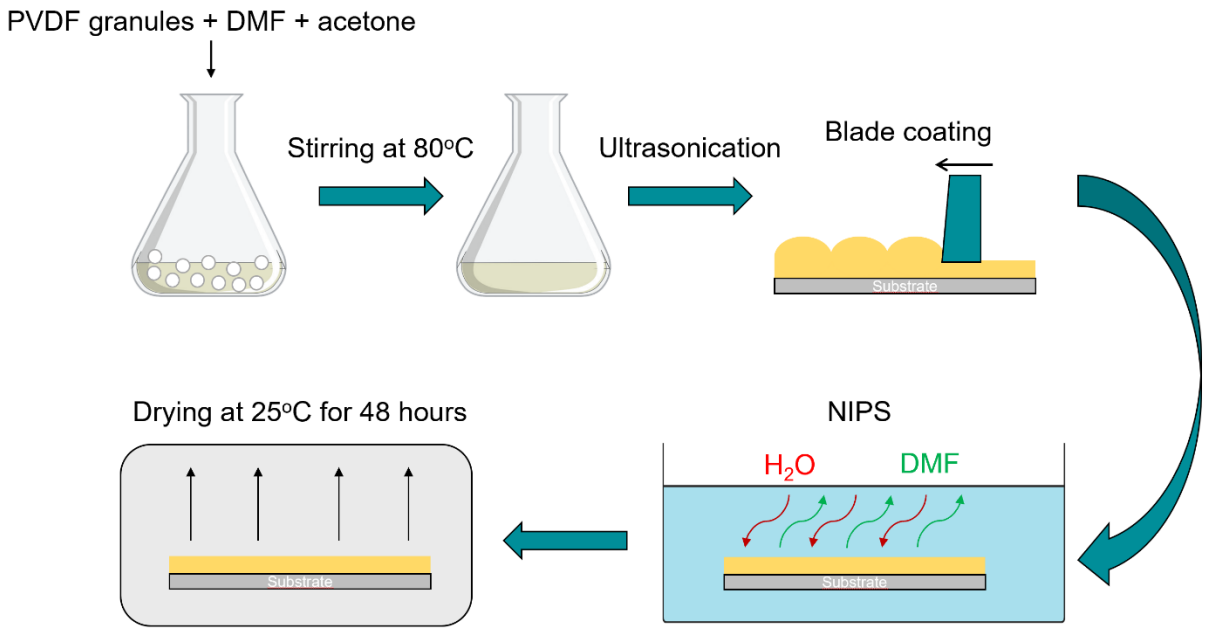

Figure 2 Scheme of PVDF membrane samples preparation. Source: (own)

Primary characterisation was performed using an OLYMPUS BX51 optical microscope (OM) and Stream Essentials software. Images were taken at a magnification of four times with a resolution of 2080x1544 pixels. The SEM images of the PVDF membrane samples are shown in Figure 3. The prepared samples were non-homogeneous and had a structure similar to a nonwoven fabric. The samples were very soft, fragile, and easy to be deformed. The sample immersed for 1 minute in a nonsolvent environment achieved fine thread-shaped elements. After 60 minutes in the water bath, the PVDF sample reached the most compact character, but still contained many fine elements. In the case of PVDF immersed for 1200 minutes, the clumps were firmly grouped in an otherwise fine structure.

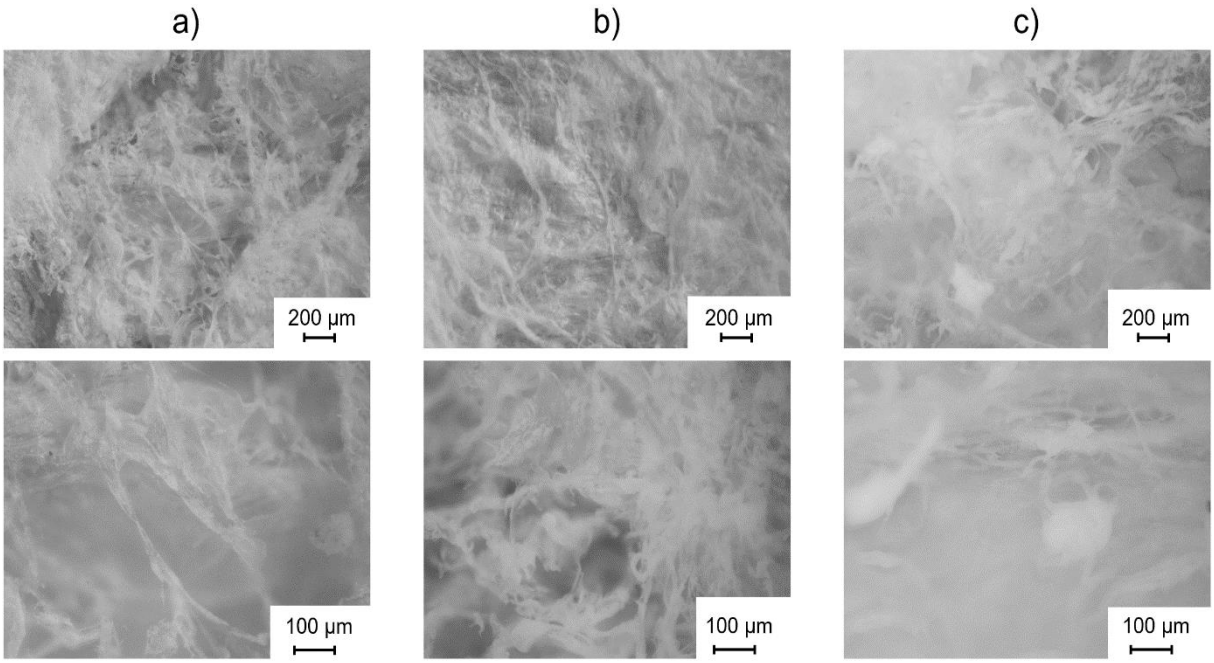

Figure 3 OM images of PVDF membrane samples: a) 1 min, b) 60 min, c) 1200 min. Source: (own)

3. CONCLUSION

The samples that were prepared in this work were at first characterised by optical microscope. The images obtained from this analysis provided an initial description of the structure of the prepared material, revealing the presence of the porous structure required for the intended application of the membrane. The membrane will be fabricated using a nanocomposite material comprised of PVDF and various nanofillers. The selection of nanofillers will consider their influence on sorption properties and selectivity enhancement, both are crucial in hydrogen purification application. In addition, the prepared samples will be subjected to further characterisation to determine their properties such as thermal stability and porosity, and the type of PVDF phase that will be obtained. Furthermore, the preparation method will be optimised to achieve a more homogeneous and solid sample.

ACKNOWLEDGEMENT

This work was supported by the project No. SP2023/026 "Smart nanomaterials for storage and savings of energy".

REFERENCES

[1] RAVI, Sai Sudharshan, Muhammad Aziz. Clean hydrogen for mobility – Quo vadis? *International Journal of Hydrogen Energy*. 2022, **47** (1), 20632-20661.

[2] AIZARANI, Jessica. *Forecast hydrogen demand worldwide in a sustainable development scenario from 2019 to 2070, by sector* [online]. Statista, 2023 [cit. 22.4.2023]. Available from: https://www.statista.com/statistics/760001/global-hydrogen-demand-by-sector-sustainable-scenario/

[3] SHEFFI, Yossi, James RICE. A Supply Chain View of the Resilient Enterprise. *MIT Sloan Management Review*. 2005, **47** (1), 8-41.

[4] PRASAD, Divya, Komal N. Patil, Chaitra C. R., Sandhya N., Jayesh T. Bhanushali, Suresh W. Gosavi, Arvind H. Jadhav, Bhari Mallanna Nagaraja. Sulfonic acid functionalized PVA/PVDF composite hollow microcapsules: Highly phenomenal & recyclable catalysts for sustainable hydrogen production. *Appl. Surf. Sci.*, 2019, **488** (1), 714-727.

[5] XIAO, Wu, Dongdong Kang, Nan Liu, Huiju Shao, Xiaolinang Dong, Shihao Qin. Microstructure manipulation in PVDF/SMA/MWCNTs ultrafiltration membranes: Effects of hydrogen bonding and crystallization during the membrane formation. *Sep. Purif. Technol.* 2022, **278** (1), 119523:1-119523:9.

[6] AYDIN, Muhammed Iberia, Ibrahim Dincer. An assessment study on various clean hydrogen production methods. *Energy*. 2022, **245** (1), 123090:1-123090:11.

[7] PAL, Priya, S.P. Chaurasia, Sushant Upadhyaya, Rajesh Kumar, S. Sridhar. Development of hydrogen selective microporous PVDF membrane. *International Journal of Hydrogen Energy*. 2020, **45** (1), 16965-16975.

[8] ČECH BARABASZOVÁ, Karla, Holešová Sylva, Plesník Lukáš, Kolská Zdeňka, Joszko Kamil, Gzik-Zroska Božena. Hybrid Nanofillers Creating the Stable PVDF Nanocomposite Films and Their Effect on the Friction and Mechanical Properties. *Polymers*. 2022, **14** (1), 3831:1-3831:15.

BROADBAND MUELLER ELLIPSOMETER AS AN UNCONVENTIONAL TOOL FOR THE OPTICAL ACTIVITY SENSING

Author(s): Daniel VALA

Supervisor: doc. Dr. Mgr. Kamil POSTAVA

Department: IT4Innovations National Supercomputing Center and Faculty of Materials Science and Technology, VSB – Technical University of Ostrava

Abstract

Spectroscopic Mueller matrix ellipsometry (MMSE) is a widespread optical characterization method, which is exceptionally sensitive to the phase shift between orthogonal modes of polarized light, including the circular, which reflects the optical activity of material. We exploit that this versatility of MMSE extends beyond classical optics into the chemical sciences to accurately reveal optical activity in molecular solutions exhibiting complex chiroptical signal.

Key words:

Mueller matrix spectroscopic ellipsometry, optical activity, excitone coupling, chiroptical spectroscopy.

1. INTRODUCTION

In recent years, cutting-edge application of Mueller matrix spectroscopic ellipsometry (MMSE) have been bursting far beyond its homeland of photonics and material sciences, bringing us probes into cancer diagnostics [1,2], ultrafast electronic processes [3,4], solar and hydrogen energy harvesting [5,6], and much more. The unique flexibility of MMSE stems from the contactless ability of light polarization to track even the subtlest material attributes. It is virtually the signature of the interplay between circular polarizations and chiral objects, supporting us with experimental observables elucidating their spatial conformation. Specifically, different travel speeds of left- and right-circular polarizations in each medium reflect its optical activity (OA). In the light of the MMSE, we directly observe a Mueller matrix – a characteristic quantity embracing OA dispersion (optical rotation, circular birefringence, optical rotatory dispersion) and its Kramers-Kronig related absorptive counterpart – circular dichroism.

Traditional chiroptical spectroscopies include electronic circular dichroism (ECD) [7], vibrational circular dichroism (VCD) [8], Raman optical activity (ROA) [9], etc. Although these methods are highly accurate, reliable and with great application possibilities, they inherently do not allow the measurement of the complex chiroptical response; only circular dichroism. It entails principal limitations. First, it is the impossibility of measuring the chiroptical response outside the dichroic spectral region of the molecule, which typically arises due to electronic absorptions over deep UV. Second, the application of physical models can be inaccurate in more complicated cases and can lead to unphysical interpretations.

In this work, we employ a commercial MMSE (193 nm–1700 nm) for chiroptical sensing of optically active molecular solutions. As the MMSE approach essentially combines the abilities of electronic circular dichroism (ECD) and optical rotatory dispersion spectroscopies, the measured MM simultaneously accesses the circular dichroism (CD) and circular birefringence (CB/ORD) spectra. We demonstrate this by measuring the chiroptical signal in organic dyes exhibiting exciton coupling [10]. Yielding a complex chiroptical signal possesses a great potential to open a new pathway in subsequent data modelling providing better insight into the problematics and more room for development of physical phenomenological models itself. Furthermore, we attempt to demonstrate that MMSE may stand as an equivalent chiroptical technique to complement those considered traditional.

2. MUELLER MATRIX SPECTROSCOPIC ELLIPSOMETRY

MMSE measures the change in the arbitrary (generally elliptical) polarization state of light after interaction with a sample. The polarization state change records a 4×4 Mueller matrix $\mathbf{M}$, which reflects complete polarimetric response of a sample, including the effect of optical activity in chiral liquids. In this work, we will use only the approximated analytical form of the Mueller matrix representing the general

solution for optically active liquids shown elsewhere [11]. If both circular dichroism and circular birefringence is small, following form of Mueller matrix is sufficient,

$$\mathbf{M} = \begin{bmatrix} 1 & 0 & 0 & \Gamma' \\ 0 & 1 & -\Gamma & 0 \\ 0 & \Gamma & 1 & 0 \\ \Gamma' & 0 & 0 & 1 \end{bmatrix}. \quad (1)$$

Here, Γ is the circular birefringence, and Γ' is the circular dichroism, and $\Gamma, \Gamma' \ll 1$. We can put those into a single complex variable named the complex circular retardation $\tilde{\Gamma} = \Gamma + \mathrm{i}\,\Gamma'$, where the real and imaginary parts are interconnected via Kramers-Kronig relations.

In the present work, we use a commercial Mueller matrix spectroscopic ellipsometer Woollam RC2-DI, which operates in the spectral range 193–1700 nm and allows complete determination of the polarimetric response of a sample, including depolarization, in other words, all 16 Mueller matrix elements. All measurements were taken in the transmission configuration.

3. SAMPLES

(R,R)-(−)-N,N′-Bis(3,5-di-tert-butylsalicylidene)-1,2-cyclohexanediaminocobalt(II) and (S,S)-(−)-N,N′-Bis(3,5-di-tert-butylsalicylidene)-1,2-cyclohexanediaminocobalt(II) were purchased from Sigma-Aldrich and used without further purification. These samples will be referred to as R-Complex and S-Complex, respectively. The samples were dissolved in toluene (Penta, p.a.) to yield concentrations of 10 mg/ml, 5 mg/ml, 2.5 mg/ml, 1.25 mg/ml, 0.625 mg/ml, and 0.3125 mg/ml. All samples were measured in quartz cuvettes without residual stress in facets (Starna Scientific) with an optical path of 2 mm.

4. RESULTS AND DISCUSSION

In the first step, we measured the transmission Mueller matrix response of each sample at each concentration (see Section 3). The obtained signals are quite close to the accuracy limit in each element of the measured Mueller matrix, which is 0.001. To eliminate random and systematic errors due to minor temperature fluctuations or non-ideal stability of the calibration, we perform the following procedure and data treatment: first, we subtract the polarimetric response of the background, which in this case is the Mueller matrix of pure toluene in the cuvette, from the data. Next, we take the average of the MM elements, which we will refer to as dichroic (CD) elements, and we will refer to the average of the elements as birefringent (CB) elements. Figure 1 shows the CD and CB curves of R- and S-Complex at each concentration.

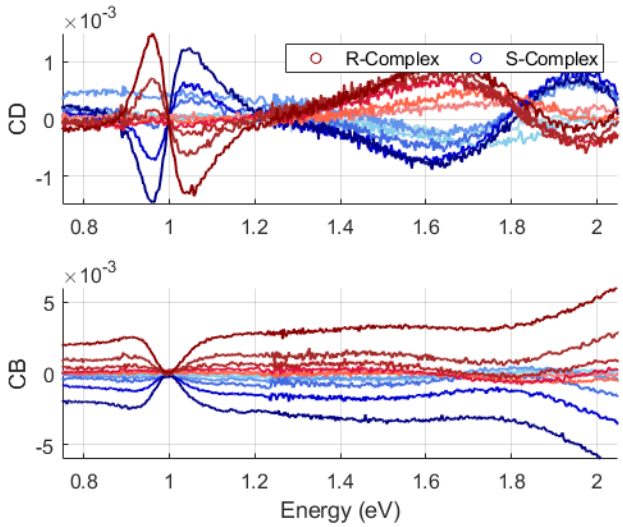

Figure 1 CD and CB spectra of R-Complex and S-Complex measured at six different concentrations (represented by the line contrast) after background correction and averaging of the dichroic and birefringence MM elements. Source: (own)

Figure 1 further shows reasonably good concentration scaling in the bisignate peak around 1 eV for measurements taken at higher concentrations but is poorly scaled for lower concentrations. The concentration scaling gets worse with increasing energy and eventually fails completely. It is due to the strong absorption of R- and S-Complexes at higher energies and the low sensitivity of applied MMSE over lower energies. Therefore, we are spectrally limited to energies below 2.1 eV in this study. To further model the data, we selected only those spectral points at each concentration where both the sensitivity of the MMSE is sufficient, and the absorption of the sample is low. We normalized the signals by concentration and cuvette path length and took their averages in the corresponding spectral regions. This data-stitching approach allows us to determine the complex chiroptical signal over broader energy range, which would otherwise remain inaccessible from single raw measurements.

We used a spectral model $\theta(E)$ based on the theory of spatial dispersion of optical activity [12,13], which assumes a coupling between the transition electric dipole moments excited within the molecule,

$$\theta(E) = \mathrm{Re}\{\theta(E)\} + i\,\mathrm{Im}\{\theta(E)\}, \tag{2a}$$

$$\mathrm{CD}(E) \propto \mathrm{Im}\{\theta(E)\} = \frac{2A\gamma\xi E\left(E_0^2 - E^2\right)}{\left[\xi^2 - \left(E_0^2 - E^2\right)^2 + \xi^2 E^2\right]^2 + 4\xi^2 E^2 \left(E_0^2 - E^2\right)^2}, \tag{2b}$$

$$\mathrm{CB}(E) \propto \mathrm{Re}\{\theta(E)\} = \frac{A\xi\left[\left(E_0^2 - E^2\right)^2 - \gamma E^2 - \xi^2\right]}{\left[\xi^2 - \left(E_0^2 - E^2\right)^2 + \xi^2 E^2\right]^2 + 4\xi^2 E^2 \left(E_0^2 - E^2\right)^2}. \tag{2c}$$

Here, A is the oscillator amplitude, E_0 is the central energy of the excitation, γ is the damping coefficient, and ξ is the coupling strength between the dipole moments, which directly reflects the optical activity of the system. Note, if $\xi(E) = 0$, then $\theta(E) = 0$, in other words, the system is not optically active.

Figure 2a shows the experimental spectra of CD and CB of the S-Complex and the R-Complex after numerical treatment discussed above. Their comparison with the spectral model is in good agreement. To fit the measured spectra, we used spectral model $\theta_{\mathrm{FIT}}(E)$ represented by the sum of three oscillators (see Eq. 2), $\theta_{\mathrm{FIT}}(E) = \sum_{i=1}^{3} \theta_{\mathrm{i}}(E)$.

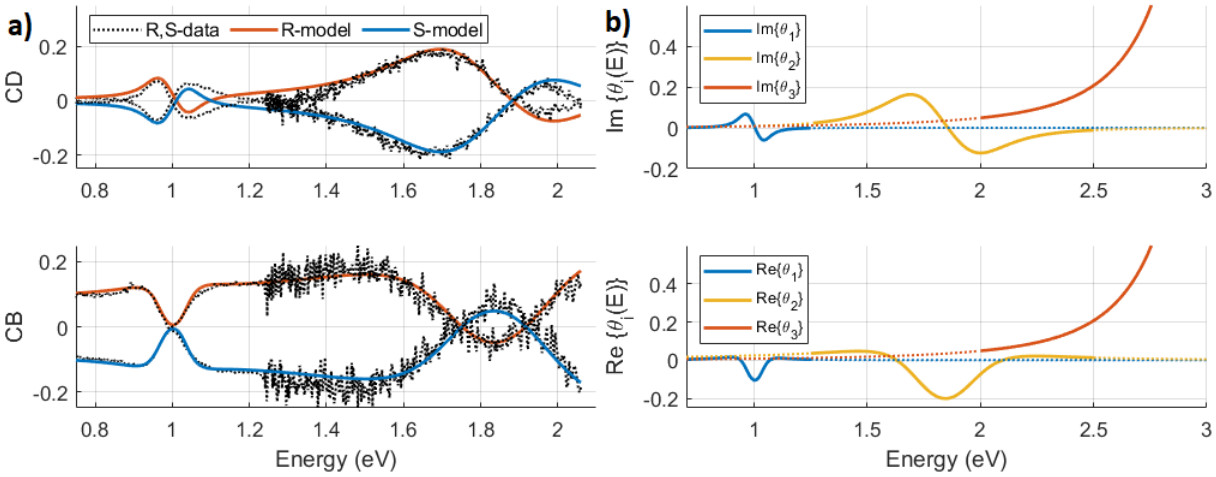

Figure 2 a) Comparison of the R- and S-Complex CD and CB experimental data with the model. b) Individual contributions of each oscillator to the spectral model. Source: (own)

We summarize the fitted parameters of each oscillator in Tab. 1. In Fig. 2b, we additionally show the contribution of each individual oscillator. The bisignate shape of spectra modelled by oscillators $\theta_{1,2}$ is due to excitone coupling, which is an electromagnetic interaction between two transition electric dipole moments, each bounded to a single π-π^* conjugated system – in this case, a couple of butylsalicylidene chromophores. Although the oscillator θ_3 phenomenologically accounts for cumulative electronic absorption mainly over the ultraviolet spectral range, it must be included in $\theta_{\mathrm{FIT}}(E)$. The contribution of θ_3 to CD is that it dampens the absorption peak at 2 eV and forms a dispersion across the measured CB spectrum.

Table 1 Fitted parameters of $\boldsymbol{\theta_{\mathrm{FIT}}(E)}$. Source: (own)

	A	E_0	γ	ξ
θ_1	0.0149	1.0037	0.0980	0.0837
θ_2	0.3713	1.8559	0.4133	0.4149
θ_3	555.42	3.1655	0.3989	0.0128

5. CONCLUSION

In this work, we have presented the MMSE as an offbeat technique for sensing optical activity. Picking the case molecules (S- and R-Complex) with circular dichroism exhibiting the excitone coupling over visible spectral range, we established the measurement and data treatment methodology to obtain the best possible experimental results ready for subsequent data modeling. Applying the physical model based on optical activity spatial dispersion, we have fitted the measured spectra with good agreement and physically interpreted the contribution of each spectral oscillator.

Concluding, the presented method could stand as a quick and reliable way to model the complex chiroptical response of a molecular system, despite the fact it cannot compete with the traditional chiroptical techniques mainly due to its low sensitivity. Nonetheless, it provides us with better insight into the problematics and offers more room for the development of physical phenomenological models itself.

ACKNOWLEDGEMENT

This work was supported by the following projects: Czech Science Foundation 22-33060S; the Ministry of Education, Youth and Sports of the Czech Republic through the e-INFRA CZ (ID:90140); Student Grant System SP2023/026.

REFERENCES

[1] He, C., H. He, J. Chang, B. Chen, H. Ma, M. J. Booth. Polarisation optics for biomedical and clinical applications: a review. *Light: Sci. Appl*., 2021, **10**, 1-20.

[2] Rodriguez-Nunez, O., P. Schucht, E. Hewer, T. Novikova, A. Pierangelo. Polarimetric visualization of healthy brain fiber tracts under adverse conditions: ex vivo studies. *Biomed. Opt. Express*, 2021, **12**, 6674–6685.

[3] Herrfurth, O., S. Richter, M. Rebarz, S. Espinoza, J. Zuniga-Perez, C. Deparis, J. Leveillee, A. Schleife, M. Grundmann, J. Andreasson, R. Schmidt-Grund. Transient birefringence and dichroism in ZnO studied with fs-time-resolved spectroscopic ellipsometry. *Phys. Rev. Res*., 2021, **3**, 013246.

[4] Richter, S., O. Herrfurth, S. Espinoza, M. Rebarz, M. Kloz, J. A. Leveillee, A. Schleife, S. Zollner, M. Grundmann, J. Andreasson, R. Schmidt-Grund. Ultrafast dynamics of hot charge carriers in an oxide semiconductor probed by femtosecond spectroscopic ellipsometry. *New J. Phys*., 2020, **22**.

[5] Halagačka, L., Z. Gelnárová, M. Al-Ghzaiwat, I. Florea, J. Horníček, K. Postava, M. Foldyna. Tin reduction from fluorine doped tin oxide for silicon nanowire-based solar energy harvesting and storage. *Opt. Express*, 2021, **29**, 31465-31477.

[6] Mrázková, Z., I. P. Sobkowicz, M. Foldyna, K. Postava, I. Florea, J. Pištora, P. R. Cabarrocas. Optical properties and performance of pyramidal texture silicon heterojunction solar cells: Key role of vertex angles. *Prog. Photovoltaics Res. Appl*., 2018, **26**, 369-376.

[7] Albano, G., G. Pescitelli, L. Di Bari. Chiroptical Properties in Thin Films of π-Conjugated Systems. *Chem. Rev*., 2020, **120**, 10145-10243.

[8] Sato, H. A new horizon for vibrational circular dichroism spectroscopy: a challenge for supramolecular chirality. *Phys. Chem. Chem. Phys*., 2020, **22**, 7671-7679.

[9] V. Parchaňský, J. Kapitán, P. Bouř. Inspecting chiral molecules by Raman optical activity spectroscopy. *RSC Adv*., 2014, **4**, 57125-57136.

[10] Pescitelli, G. ECD exciton chirality method today: a modern tool for determining absolute configurations. *Chirality*. 2022, **34**(2), 333-363.

[11] Vala, D., M. Mičica, D. Cvejn, K. Postava. Broadband Mueller ellipsometer as an all-in-one tool for spectral and temporal analysis of mutarotation kinetics. *RSC Adv*. 2023, **13**(10), 6582-6592.

[12] Franta, D., J. Vohánka. Constitutive equations describing optical activity in theory of dispersion. *JOSAB*, 2021, **38**, 553-561.

[13] Davis, M. S., W. Zhu, J. K. Lee, H. J. Lezec, A. Agrawal. Microscopic origin of the chiroptical response of optical media. *Sci. Adv*. 2019, **5**(10).

GRAPHITIC CARBON NITRIDE AS HIGHLY EFFICIENT PHOTOCATALYSTS FOR THE DEGRADATION OF RHODAMIN B

Author(s): Zuzana VILAMOVÁ

Supervisor: prof. RNDr. Richard DVORSKÝ, Ph.D.

Department: Nanotechnology Centre, CEET, Faculty of Materials Science and Technology, VSB – Technical University of Ostrava

Abstract

Over the last few decades, because of population growth and rapid industrialisation, contamination such as organic pollutants and heavy metals increased in water resources. Graphitic carbon nitride (g-C_3N_4), a promising conjugated polymer semiconductor, has been used in many photocatalytic pollutant degradations. However, the bulk form of g-C_3N_4 is characterised by many defects and its small specific surface area, leading to a decrease in photocatalytic activity.

In this work, several exfoliation methods were investigated and compared to the bulk form of g-C_3N_4. The optical and structural properties of the prepared powder samples were characterised by methods such as scanning electron microscopy, a specific surface analyser, or a UV-vis spectrometer. The photocatalytic activity of the prepared bulk and exfoliated forms for rhodamine B degradation was investigated in a batch reactor. After thermal exfoliation and high-power visible light sources, the time needed for complete degradation of rhodamine B was reduced from several hours to just a few minutes.

Keywords:

Photocatalysis, degradation kinetics, pollutant, exfoliation method.

1. INTRODUCTION

Photocatalysis seems as a promising alternative for the degradation of contaminants such as organic pollutants and heavy metals in the water resources or air. Titanium dioxide and zinc oxide photocatalysts are the most widely used and can be found as part of filters for wastewater treatment [1] or air treatment [2], but their high band gap energy and toxic properties [3] limit their use. However, g-C_3N_4 proved its antibacterial properties while maintaining its non-toxic character [4]. It is a semiconducting metal-free photocatalyst, whose easy synthesis, low band gap energy (2.7 eV), easy functionalisation, and high physicochemical stability predispose it to use in the photodegradation of organic pollutants [4, 7] and pathogenic microorganisms [4].

The bulk form of g-C_3N_4 can be prepared from several precursors by the polycondensation method, such as urea [5, 6], thiourea [6] or melamine [7]. However, the bulk form of g-C_3N_4 is characterised by many defects and its small specific surface area, leading to a decrease in photocatalytic activity. The photocatalytic activity of the g-C_3N_4 particles increased significantly after exfoliation of their lamellar structure. To enhance photocatalytic activity, methods such as thermal exfoliation [7], sonication [8], or planetary mill [9] were studied, compared, and evaluated in this work.

2. EXPERIMENTAL PART

SAMPLES PREPARATION

Bulk g-C_3N_4 was synthesised by thermal polycondensation of melamine ($C_3H_6N_6$, 99 %, Sigma Aldrich) , following previous experience [7]. Briefly, the precursor was placed in ceramic crucibles with ceramic cups and heated for 4 h in air at 525 ˚C; the heating rate was set at 3 ˚C·min^{-1}. The sample was then naturally cooled to room temperature and bulk g-C_3N_4 material (M_bulk) was milled in an agate bowl for further analysis and exfoliation process. Several methods of exfoliation were performed: thermal, ultrasound, and planetary milling.

Thermal exfoliation of the bulk precursor was carried out in a muffle furnace, for 2 h at 500 ˚C; the heating rate was set at 2 ° C min^{-1}. The sample was labelled M_thermal.

Exfoliation by high-frequency ultrasound of an aqueous dispersion (1 g M_bulk/50 ml of H_2O) in a glass flask for 1 h using a frequency of 80 kHz. The final powder form was obtained by freeze-drying followed by freeze-sublimation and was labelled M_ultrasound.

Exfoliation of the planetary milling of bulk g-C_3N_4 was carried out in an aquatic environment using balls of agate (diameters 4.5 and 9 mm) and in an ultrasound bath. Setting of milling was fixed at 1000 rpm for 16 h. The final powder sample, M_mill, was obtained by freeze-drying followed by freeze-sublimation.

MATERIALS CHARACTERISATION

The particle surface was observed under a JEOL 2200FS (Japan) high-resolution transmission electron microscope (HRTEM/STEM).

The specific surface area of the samples was determined by analysis of N_2 adsorption isotherms at 77 K using the Brunauer-Emmett-Teller (BET) method using a Quantachrome NOVA 4200e multistation apparatus.

The UV-vis diffuse reflectance spectrum (DRS) was recorded with a Shimadzu UV-2600 (IRS-2600Plus) spectrophotometer at room temperature in the range of 220-700 nm.

PHOTOCATALYTIC ACTIVITY EXPERIMENT SET UP

The photocatalytic properties of the prepared powder materials were tested by degradation of RhB ($C_{28}H_{31}ClN_2O_3$, 98+%Acros Organics B.V.B.A.,) in a batch reactor (250 mL). Reactions were performed under ultraviolet light-emitting diode (UV-LED) with an emission line peaks at 412 nm. In an experiment, the initial RhB concentration was 10 mg·L^{-1} and the catalyst load was kept at 1 g·L^{-1}. Before irradiation, 50 ml of aqueous suspension containing RhB and catalyst were placed in an ultrasound bath and sonicated for 5 s to provide good homogenisation of the dispersion. Before LEDs were turned on, the solution was stirred in the dark for 60 min to reach the equilibrium of adsorption-desorption in the whole system. 1 ml of sample was taken and then centrifugated for 10 min at 9000 rpm. The liquid phase that contained RhB above the sediment was analysed using a UV-Vis spectrophotometer (UV-1601, Shimadzu) using the calibration curve method.

3. RESULTS AND DISCUSSION

MATERIALS CHARACTERISATION

As can be seen in Figure 1, the surface analysis for the bulk form, thermal and ultrasound method showed aggregates with a non-homogeneous particle size distribution. The particles in the M_ultrasound sample, Figure 1 c), did not change their morphology compared to the bulk form. The surface of the particles prepared by the thermal exfoliation method, Figure 1 b), showed higher porosity, which was also proven by measuring the specific surface area. STEM images of the M_mill sample showed a homogeneous distribution of particle sizes with macroporous surface, Figure 1 d).

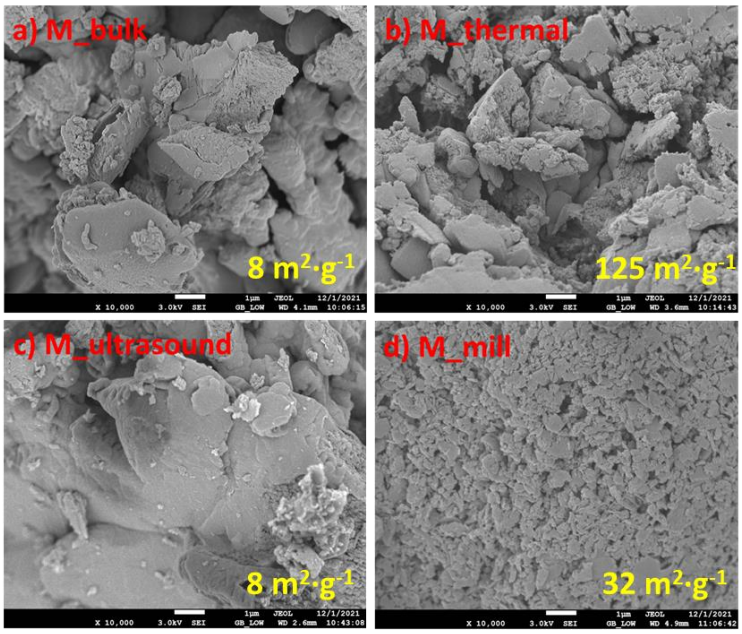

Figure 11 STEM images of powder sample s surface a) M_bulk, b) M_thermal, c) M_ultrasound and d) M_mill. Source: (own)

The results of the specific surface area measurements are written in Figure 1 for each sample. SSA is dependent on the size of the particles, as well as on the structure and porosity of the material. The high-frequency ultrasound exfoliation technique did not cause any change in SSA compared to the bulk form, both 8 $m^2 \cdot g^{-1}$. The thermal and mill technique led to an increase in SSA, which affected the resulting photocatalytic activity of the samples and will be discussed in further detail. The highest increase in SSA was observed for the thermal exfoliation method which increased from 8 $m^2 \cdot g^{-1}$ to 125 $m^2 \cdot g^{-1}$.

The optical properties of the powder samples were investigated by diffuse reflectance UV-Vis spectroscopy as can be seen in Figure 3. The band gap of the bulk form was 2.73 eV. The band gaps for M_ultrasound and M_mill were similar to bulk form. Furthermore, the band gap, obtained from M_thermal, showed two values of 2.77, which correspond to the bulk form, and 2.86 eV.

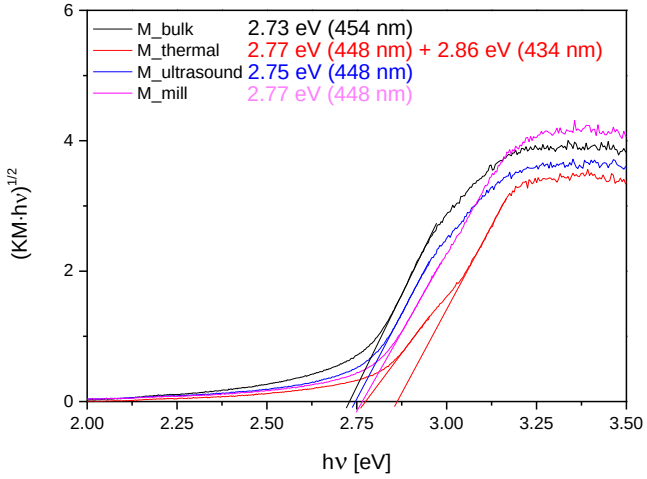

Figure 12 The optical properties of prepared powder samples: M_bulk, M_thermal, M_ultrasound and M_mill. Source: (own)

EVALUATION OF PHOTOCATALYTIC ACTIVITY

The results of photocatalytic activity are in agreement with previous morphological studies. The photocatalytic activity of the powder samples, in Figure 3, was studied according to the zero-order reaction kinetics, with measurement coefficients (R^2) as high as 0.99, indicating the appropriate use of zero-order reaction kinetics. The k-value for the bulk form was calculated 0.01066 min^{-1}. M_thermal, M_ultrasound, and M_mill were calculated to be 0.06926, 0.01053 and 0.01599 min^{-1}, respectively. For RhB photolysis, the rate constant k was set at 0.00012 min^{-1}.

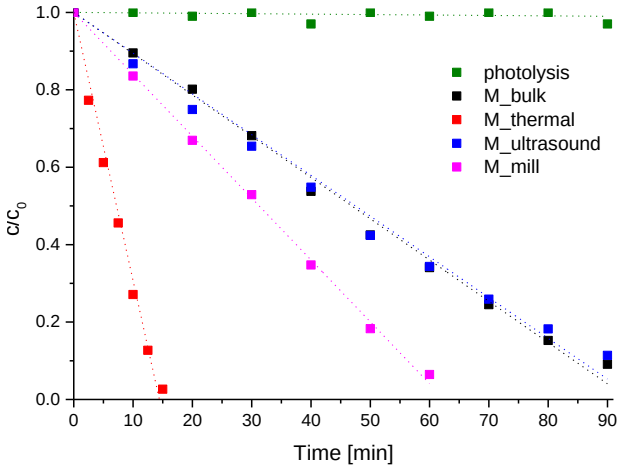

Figure 13 Degradation kinetics of RhB by prepared powder samples M_bulk, M_thermal, M_ultrasound, M_mill and photolysis of RhB. Source: (own)

In summary, thermal exfoliation leads to a significant increase in specific surface area 16 times and furthermore to the highest photocatalytic activity compared to bulk g-C_3N_4 and other powder samples prepared for this study. However, one of the important parts of the evaluation is its yield and cost-effectiveness. Although the use of thermal exfoliation leads to the highest photocatalytic activity, it is characterised by a high mass loss during the process compared to the other exfoliation methods.

4. CONCLUSION

In this work, several photocatalytic powder samples were successfully prepared, and their optical and structural properties were investigated.

The main aim of the work was photocatalytic evaluation of prepared samples by RhB degradation. The bulk form of g-C_3N_4 and the ultrasound method were evaluated with similar results. The particles prepared by the mill method showed an increase in photocatalytic activity and higher SSA. The thermal exfoliation process significantly increased SSA compared to bulk g-C_3N_4, which led to the highest photocatalytic activity compared to other samples.

Although thermal exfoliation leads to the highest photocatalytic activity, it is characterised by a high mass loss during the process compared to the other methods, which has to be considered as well.

ACKNOWLEDGEMENT

This work was supported by the student project SP2023/095 of the VSB-Technical University of Ostrava.

REFERENCES

[1] AL-MAMUN, M. R., S. KADER, M. S. ISLAM a M. Z.H. KHAN. Photocatalytic activity improvement and application of UV-TiO2 photocatalysis in textile wastewater treatment: A review. *Journal of Environmental Chemical Engineering* [online]. 2019, **7**(5). ISSN 22133437. Dostupné z: doi:10.1016/j.jece.2019.103248

[2] SHARMA, Sarika, Rohit KUMAR, Pankaj RAIZADA, Tansir AHAMAD, Saad M. ALSHEHRI, Van Huy NGUYEN, Sourbh THAKUR, Chinh Chien NGUYEN, Soo Young KIM, Quyet Van LE a Pardeep SINGH. An overview on recent progress in photocatalytic air purification: Metal-based and metal-free photocatalysis. *Environmental Research* [online]. 2022, **214**(P3), 113995. ISSN 10960953. Dostupné z: doi:10.1016/j.envres.2022.113995

[3] JIA, Xiaochuan, Shuo WANG, Lei ZHOU a Li SUN. The Potential Liver, Brain, and Embryo Toxicity of Titanium Dioxide Nanoparticles on Mice. *Nanoscale Research Letters* [online]. 2017, **12**. ISSN 1556276X. Dostupné z: doi:10.1186/s11671-017-2242-2

[4] DENG, Le, Lei JIANG, Qingwen TANG a Haixiang LI. G-C3N4 Photocatalysis Technology Application in Water Treatment. *IOP Conference Series: Materials Science and Engineering* [online]. 2018, **392**(3). ISSN 1757899X. Dostupné z: doi:10.1088/1757-899X/392/3/032043

[5] THURSTON, John H., Necia M HUNTER, Lacey J. WAYMENT a Kenneth A. CORNELL. Urea-derived graphitic carbon nitride (u-g-C3 N4) films with highly enhanced antimicrobial and sporicidal activity. *J Colloid Interface Sci.* [online]. 2017, (1), 910–918. Dostupné z: doi:10.1016/j.jcis.2017.06.089.Urea-derived

[6] HONG, Yuanzhi, Enli LIU, Junyou SHI, Xue LIN, Lizhi SHENG, Ming ZHANG, Longyan WANG a Jiahui CHEN. A direct one-step synthesis of ultrathin g-C 3 N 4 nanosheets from thiourea for boosting solar photocatalytic H 2 evolution. *International Journal of Hydrogen Energy* [online]. 2019, **44**(14), 7194–7204. ISSN 03603199. Dostupné z: doi:10.1016/j.ijhydene.2019.01.274

[7] SVOBODA, Ladislav, Petr PRAUS, Maria J. LIMA, Maria J. SAMPAIO, Dalibor MATÝSEK, Michal RITZ, Richard DVORSKÝ, Joaquim L. FARIA a Cláudia G. SILVA. Graphitic carbon nitride nanosheets as highly efficient photocatalysts for phenol degradation under high-power visible LED irradiation. *Materials Research Bulletin* [online]. 2018, **100**(January), 322–332. ISSN 00255408. Dostupné z: doi:10.1016/j.materresbull.2017.12.049

[8] YIN, Wenjie, Song BAI, Yijun ZHONG, Zhengquan LI a Yi XIE. Direct Generation of Fine Bi2WO6 Nanocrystals on g-C3N4 Nanosheets for Enhanced Photocatalytic Activity. *ChemNanoMat* [online]. 2016, **2**(7), 732–738. ISSN 2199692X. Dostupné z: doi:10.1002/cnma.201600041

[9] MA, Zixuan, Peiwen ZHOU, Linping ZHANG, Yi ZHONG, Xiaofeng SUI, Bijia WANG, Yimeng MA, Xueling FENG, Hong XU a Zhiping MAO. g-C3N4 nanosheets exfoliated by green wet ball milling process for photodegradation of organic pollutants. *Chemical Physics Letters* [online]. 2021, **766**(2999), 138335. ISSN 00092614. Dostupné z: doi:10.1016/j.cplett.2021.138335

CHANGE OF SURFACE MORPHOLOGY OF PLA AFTER SUPERCRITICAL TREATMENT

Author(s): Jakub ZÁGORA

Supervisor: prof. Ing. Daniela PLACHÁ, Ph.D.

Department: Nanotechnology Centre, Faculty of Materials Science and Technology, VSB – Technical University of Ostrava

Abstract

Bone injury and implantation operation are often accompanied by microenvironment damage of bone tissue, which seriously affects the process of osseointegration of implants, the way to overcome this is to use polymeric coatings which increase the integration. Polylactide (PLA) is a suitable polymer for this application with the disadvantage of its hydrophobicity. This issue can be solved by surface modification, by increasing the roughness of the surface and increasing the interactions with bone tissue. Supercritical fluid technology can add to increase the roughness of the surface. The surface roughness of PLA mats increased from 332.6 ± 33.4 nm to 71 ± 17 nm in the case of R_a (the distance between lines and valleys) and from 332.6 ± 80.4 nm to 248.3 ± 37.2 in the case of R_z (high of this valleys) after 1 h of treatment into SC-CO_2. The chemical composition of the samples was not changed. Supercritical treatment can be one step to the preparation of surfaces for excellent integration of bone implants.

Keywords:

Polylactide, supercritical fluids, surfaces, carbon dioxide, tissue engineering.

1. INTRODUCTION

Worldwide the second mostly grafted organ is the bone the first one is blood transfusion. Population aging will bring even more increase in types of operations (bone grafting and bone graft substitutes). Even though the bone possesses self-regeneration capacity, large fractures require the assistance of implants to restore the native bone structure. The grafting of implants, which are alien material inside the human body can cause several issues, such as infections, alterations or even loosening. The material used has to meet requirements, such as biocompatibility, biodegradability, bioactivity, and tolerance to bone stress during regeneration [1]. To eliminate the issues mentioned above, tissue engineering is the approach to do so. Creating of 3D scaffold increases the growth of bone mass or simpler modifications of bone graft materials such as titanium or polymers [2–5]. Modification of the surface can be done via a chemical reaction or by modification by atmospheric plasma or coatings [2–6]. The roughness of the surface can do done by lithographies (Langmuir-Blodgett, electron beam), microreplication, or in the case of polymers by supercritical fluid technology [7].

Polylactic acid is a rigid thermoplastic created from lactic acid. L-lactic acid is a dimer of lactic acid and its polymer PLLA shows the best mechanical properties so most nowadays research is underdone with this dimer. PLA has good biocompatibility, is biodegradable and the products from degradation can be eliminated and excreted from the human body. For successful integration of implants, fibroblast and osteoblast must meet and interact with the surface where they can adhere. Only in this case, the cell will survive, otherwise, it will undergo apoptosis. Several strategies can be used to increase the interactions of fibroblast and osteoblast with the implant surface. Such as surface modification with macromolecules containing amino, carboxyl, or hydroxyl groups or change of surface roughness (micro- or nanoroughness surfaces have higher interactions) [1, 3].

Supercritical fluid technology is becoming an increasingly popular method for the production of coatings or modification of surfaces. This technology allows the production of rough surfaces. The basic principle behind this method involves the use of supercritical fluids, which are fluids that are in a state between liquid and gas. These fluids are maintained at high pressure and temperature and can penetrate the surface of materials with ease dissolving partially the material [7]. One of the key advantages of using supercritical fluid technology for the production of rough surfaces is the even distribution of these created irregularities and the low material cost of this process. Additionally, supercritical fluid technology is a relatively eco-friendly method of production, as it does not produce hazardous waste or by-products [7-9].

2. MATERIALS AND METHODS

The following chemicals were used to prepare the samples:

Polylactide (PLA) IngeoTM 4032D was supplied by RESINEX Czech Republic s.r.o. The basic properties of the PLA used: density 1.24 g/cm3, glass transition temperature (Tg) 59 °C, melting point 160 °C. The molecular weight (Mw) of the PLA is 182,000 g/mol was used for forming the mats. Carbon dioxide (CO2) (4.8) was supplied by the company SIAD.

PLA mats were prepared with a press under conditions: temperature of 190 °C (above the melting point of the PLA), pressure of 0.1 MPa for 2 min (heating and melting), 1 MPa for 3 min (pressuring), and 1MPa for 2 min (cooling) and thickness of 0.2 mm.

Conditions for supercritical modification were obtained by experiments with solubility PLA in CO2. Conditions were 60 °C and 20 MPa, with reaction periods from 1 h to 8 h.

The samples were characterized using XRD by X-ray RIGAKU, Cu lamp (energy 8,04 keV, wavelength 15.406 nm), voltage 40 kV, current 40 mA, K-β filter, scintillation detector. The SEM JEOL JSM-7610F Plus (JEOL, Japan) with auto emission source was used for the study of the morphology of the samples. The samples were monitored at an accelerating voltage of 3 and 20 keV using secondary electron detection. For sputtering the samples used Quorum Q150V ES plus, using gold 2 nm, electricity 30 mA. For evaluation of the topography of the surface, the samples were measured by AFM on device LiteScopeTM in contact mode, the area of measuring in x and y was 20x20 μm. FTIR analysis was done on Nicolet iS50, measured on ATR diamond crystal, 62 scans in mid-infrared spectra (400 - 4000 cm-1), with ATR correction and set to baseline in program OMNIC.

3. RESULTS AND DISCUSSION

The prepared composites and their starting materials were subjected to chemical and physical characterizations using XRD, SEM, AFM, and FTIR. The characteristic high-intensity diffraction peak of 16.86° and 19.12° and low-intensity diffraction peak of 22.54° typical for PLA is occurring (Fig. 1) after supercritical treatment from initially amorphous PLA. From the data can be seen that the recrystallization is happening since the beginning of the process after 1 h are occurring the high-intensity peaks, and after 2 hours the low-intensity peak is present.

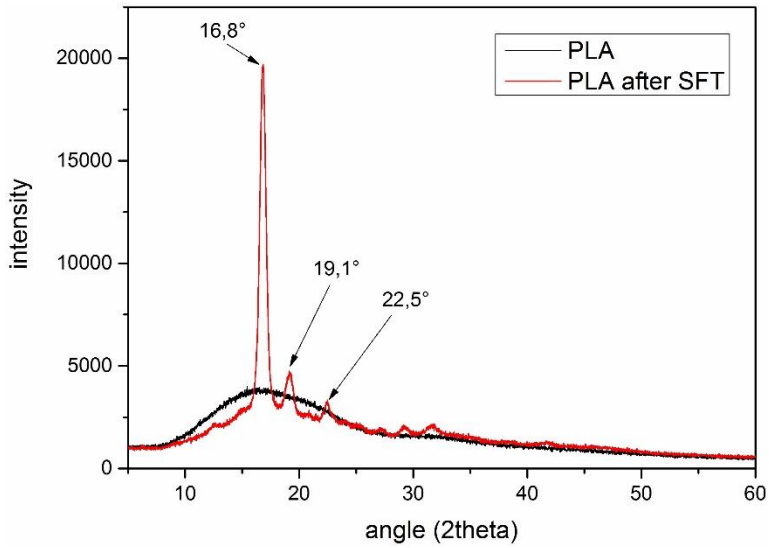

Figure 1 XRD spectra of pure PLA mats and PLA mats after supercritical treatment.
Source: (own)

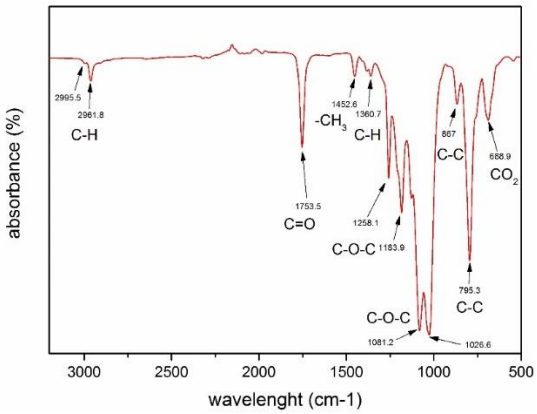

Figure 2 Infrared spectra of PLA. Source: (own)

Fig. 2 shows the ATR-FTIR spectra of pure PLA mats, the carbonyl stretching vibration (C = O) at 1745-1751 cm^{-1}, deformation of the -CH_3 bond at 1454 cm^{-1}, the -C-O-C bond at 1265-1027 cm^{-1}, and the C-C bond at 867 cm^{-1}.

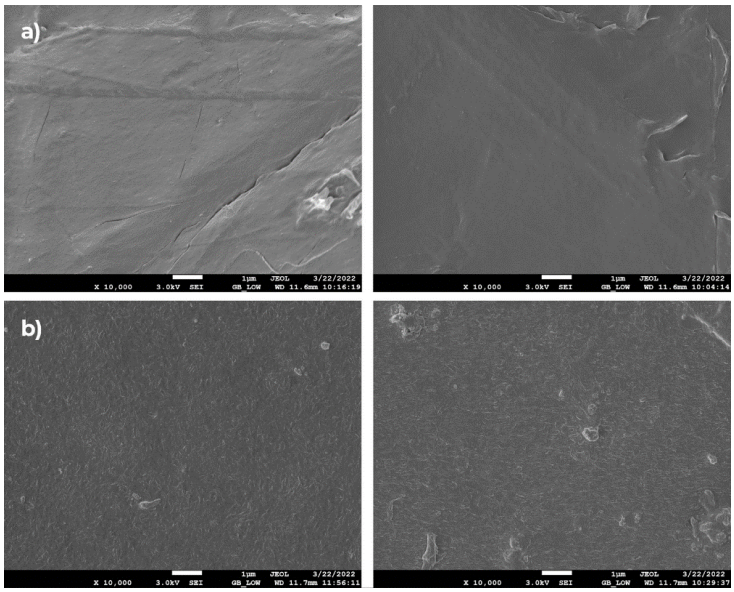

Figure 3 a) Pure PLA, b) PLA after supercritical treatment. Source: (own)

Fig. 3 shows a change in the surface morphology of PLA mats, from non-processed PLA Fig. 3a) with a smooth surface with only minor defects to processed PLA Fig. 3b) with an increase of defects of surface which occur due to recrystallization process and dissolution of PLA into SC-CO_2, this change on morphology can be seen as a predisposition for more interaction between surface and fibroblast and osteoblasts. This observation was also confirmed by AFM.

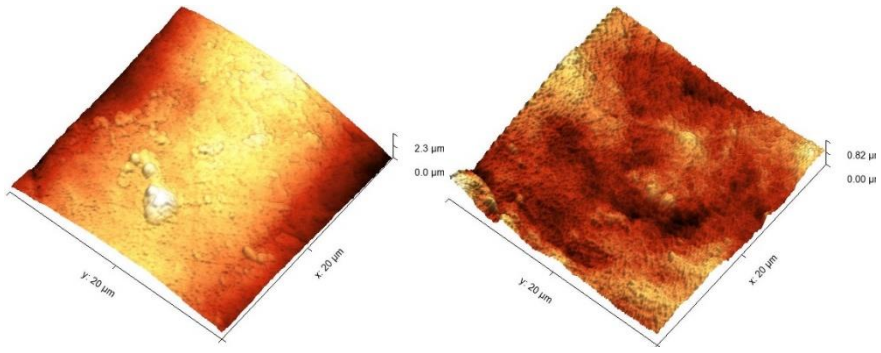

Figure 4 AFM images of PLA samples left) pure PLA mats, right) PLA mats after supercritical treatment. Source: (own)

Fig. 4 shows a change of roughness of pure PLA mats to mats that were modified by SFT. After supercritical treatment changed roughness of the surface from 332.6 ± 80.4 nm to 248.3 ± 37.2 nm in the case of R_z. and from 332.6 ± 33.4 nm to 71 ± 17 nm in R_a.

4. CONCLUSION

Surface modification of polylactide mats was done by supercritical fluid technology. SC-CO_2 in the process increased the roughness of the surface of PLA mats. The roughness was increased from 332 ± 33 nm to 71 ± 17 nm. This was caused by the dissolving of PLA from the surface and the recrystallization of PLA. Infrared spectroscopy did not show any change in the chemical composition of PLA mats. In future research will be determined the change of hydrophobicity of the surface.

ACKNOWLEDGEMENT

This work was supported by the project no. CZ.02.1.01/0.0/0.0/17_049/0008441 "Innovative Therapeutic Methods of Musculoskeletal System in Accident Surgery" within the Operational Program Research, Development of Czech Republic and by the student project SP2023/095 of VSB-Technical University of Ostrava.

REFERENCES

[1] TILKIN, Rémi G., Nicolas RÉGIBEAU, Stéphanie D. LAMBERT a Christian GRANDFILS. Correlation between Surface Properties of Polystyrene and Polylactide Materials and Fibroblast and Osteoblast Cell Line Behavior: A Critical Overview of the Literature. *Biomacromolecules* [online]. 2020, **21**(6), 1995–2013. ISSN 15264602. Dostupné z: doi:10.1021/acs.biomac.0c00214

[2] MOHAMMADALIPOUR, Mohammad, Mehrdad ASADOLAHI, Zahra MOHAMMADALIPOUR, Tayebeh BEHZAD a Saeed KARBASI. Plasma surface modification of electrospun polyhydroxybutyrate (PHB) nanofibers to investigate their performance in bone tissue engineering. *International Journal of Biological Macromolecules* [online]. 2023, **230**. ISSN 18790003. Dostupné z: doi:10.1016/j.ijbiomac.2023.123167

[3] TEIMOURI, Reihaneh, Khalil ABNOUS, Seyed Mohammad TAGHDISI, Mohammad RAMEZANI a Mona ALIBOLANDI. Surface modifications of scaffolds for bone regeneration. *Journal of Materials Research and Technology* [online]. 2023, **24**, 7938–7973. ISSN 22387854. Dostupné z: doi:10.1016/j.jmrt.2023.05.076

[4] GAUTAM, Sneh, Shiv Dutt PUROHIT, Hemant SINGH, Amit Kumar DINDA, Pravin D. POTDAR, Chhavi SHARMA, Chia Fu CHOU a Narayan Chandra MISHRA. Surface modification of PCL-gelatin-chitosan electrospun scaffold by nano-hydroxyapatite for bone tissue engineering. *Materials Today Communications* [online]. 2023, **34**. ISSN 23524928. Dostupné z: doi:10.1016/j.mtcomm.2022.105237

[5] DING, Yao, Bailong TAO, Ruichen MA, Xin ZHAO, Peng LIU a Kaiyong CAI. Surface modification of titanium implant for repairing/improving microenvironment of bone injury and promoting osseointegration. *Journal of Materials Science and Technology* [online]. 2023, **143**, 1–11. ISSN 10050302. Dostupné z: doi:10.1016/j.jmst.2022.09.044

[6] KOWALCZYK, Piotr, Paulina TRZASKOWSKA, Ilona ŁOJSZCZYK, Rafał PODGÓRSKI a Tomasz CIACH. Production of 3D printed polylactide scaffolds with surface grafted hydrogel coatings. *Colloids and Surfaces B: Biointerfaces* [online]. 2019, **179**, 136–142. ISSN 18734367. Dostupné z: doi:10.1016/j.colsurfb.2019.03.069

[7] ZIZOVIC, Irena. *Supercritical fluid applications in the design of novel antimicrobial materials* [online]. B.m.: MDPI AG. 1. červen 2020. ISSN 14203049. Dostupné z: doi:10.3390/molecules25112491

[8] PLACHÁ, Daniela, Petr STUCHLÍK, Ondřej DUTKO, Tomáš SOSNA a Marcel MIKESKA. Supercritical Fluid Extraction as a Method for Preparation of Submicron Particles of Cimetidine and Hydrochlorothiazide. *Advanced Science Letters,*. 2016, **22**(3), 670–674.

[9] LV, Cuifang, Xia LIAO, Fangfang ZOU, Wanyu TANG, Shaowei XING a Guangxian LI. Generating porous polymer microspheres with cellular surface via a gas-diffusion confined scCO2 foaming technology to endow the super-hydrophobic coating with hierarchical roughness. *Chemical Engineering Journal* [online]. 2022, **442**. ISSN 13858947. Dostupné z: doi:10.1016/j.cej.2022.136192

Material Science and Engineering

EFFECT OF ADHEREND THICKNESS ON THE MECHANICAL PROPERTIES OF BONDED JOINTS OF ALUMINIUM SHEETS EN AW 5754 WITH LASER-CLEANED SURFACE

Author(s): Marek BESEDA, Pavel KLAUS, Tomáš PAWLENKA, Martin JURÁNEK

Supervisor: doc. Ing. Kateřina SKOTNICOVÁ, Ph.D.

Department: Department of Materials and Technologies for Vehicles, Faculty of Materials Science and Technology, VSB – Technical University of Ostrava

Abstract

This paper deals with the testing of a bonded joint of aluminium alloy EN AW 5754 and the effect of adherend thickness on the mechanical properties. The laser cleaner MRJ FL C120 was used to prepare the surfaces of the bonded joints. A given uniform laser beam setting was used to achieve the desired roughness. The bonded joints were formed using a two-component high-strength epoxy adhesive. The research analyses the effect of adherend thickness on the bonded joint strength under tensile test. The adhesion of the adhesive to the surface of the bonded material is analysed. Furthermore, the tensile strength test results as a function of adherend thickness are evaluated. In the evaluation of the results, the influence of the adherend thickness of aluminium sheet material EN AW 5754 formed by laser cleaning method on the strength of the bonded joint was addressed.

Key words:

5754, laser, surface, bonding, mechanical properties.

1. INTRODUCTION

There is currently a big trend to reduce the weight of electric cars. The trend is to switch to lighter materials, as electric cars have a much higher weight than combustion engine vehicles because of the batteries. Carbon materials are ideal for weight reduction, but their cost and the technology required to process them are too expensive for conventional cars. Therefore, automakers are starting to look at aluminium materials, which are lighter in weight than steel materials, at a comparable cost. These materials need to be joined, but the heat introduced by welding changes their mechanical properties and leaves problematic heat-affected areas where the material is more brittle and damage occurs, for example, under dynamic stress. Therefore, it is advisable to apply a bonding technology where the surface of the material is not heated and, depending on the selected type of adhesive and the required strength of the bonded joint, dynamic stresses can be partially eliminated by using a higher thickness of the adhesive in the bonded joint, but this is at the expense of the strength of the bonded joint [1, 2]. For strength adhesives (e.g. methyl acrylate adhesives), which reach a strength of around 30 MPa, the thickness of the bonded joints is around 0.3 mm [3]. However, these adhesives are susceptible to dynamic stresses and peel loads due to their hardness, where they lose their high strength. Another disadvantage of generally bonded joints is their dependence of strength on temperature. Another disadvantage of bonded joints is, for example, the high sensitivity of some adhesives to UV radiation. Therefore, bonded joints must be tested to guarantee their quality and to verify their high durability [4].

2. EXPERIMENTAL

The aim of the experiment was to test how the adherend thickness affects the final shear strength of the bonded joint. The joint was chosen to be simply re-clad, as this type of joint achieves the highest strength. 3M Scotch-Weld 7260 B/A FC adhesive was used to form the bonded joint. This is a two-component structural epoxy adhesive. The base of the adhesive consists of a curable phenol formaldehyde resin and the second component is a cure accelerator (modified amine). The adhesive also contains 0.3 mm diameter glass bead spacers. The working time of the adhesive after mixing the components is a maximum of 90 min. The joints will be tensile tested to verify the shear strength. The

following values have been chosen for the length of the reflow: 12.5 mm (from EN 1465). Tested aluminium sheets EN AW 5754 with thicknesses of 1 mm, 3 mm, 5 mm and 8 mm. Adhesive thickness 0.3 mm. The required roughness was achieved by cleaning the bonded surface with a laser cleaner MRJ FJ C120C with the given laser beam parameters.

The adhesive thicknesses tested were 1; 3; 5 and 8 mm with a reflow length of 12.5 mm and an adhesive thickness of 0.3 mm. **Table 1** shows the measured results of the seven sets of samples tested. There is minimal difference in strength between the 5- and 8-mm thicknesses. For smaller adherend thicknesses of 1 and 3 mm, deformation of the adherend occurred near the bonded area. This caused an increase in the area perpendicular to the applied load, which deteriorated the resulting strength. Therefore, the 1 mm thick adherend has the lowest strength because it was deformed the most, see **Figure 1** shows the dependence of the shear stress on the adherend thickness from the measured data.

Table 1 Shear strength of measured adherent thicknesses. Source: (own)

Shear strength [MPa]										
No. of measurements	**1**	**2**	**3**	**4**	**5**	**6**	**7**	**diameter**	**standard deviation**	**relative deviation [%]**
1 mm	16.20	16.30	15.30	15.90	14.90	16.30	14.80	**15.67 MPa**	0.23	1.5
3 mm	22.78	28.60	25.73	23.54	24.79	23.10	27.40	**25.13 MPa**	0.78	3.1
5 mm	32.09	32.44	31.42	32.56	28.84	30.53	30.70	**31.23 MPa**	0.46	1.5
8 mm	30.97	32.00	30.36	31.75	31.58	30.49	32.13	**31.33 MPa**	0.29	0.9

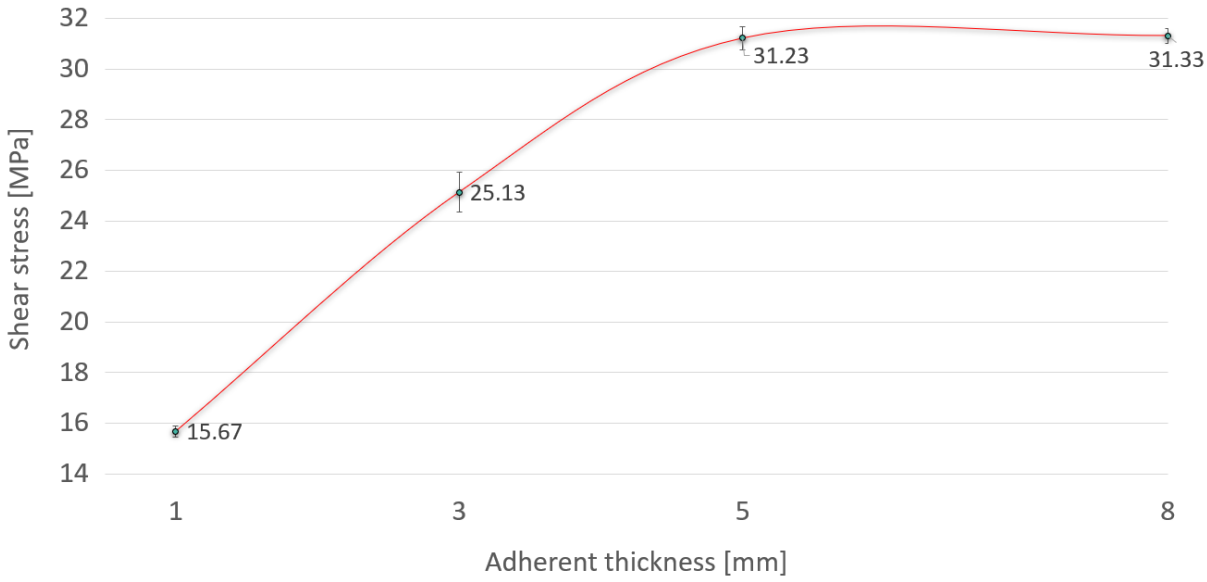

Figure 1 Dependence of shear stress on adherend thickness. Source: (own)

Comparison of the adherend thicknesses shows the low bond strength of the 1 mm adherend as seen in **Figure 2**, which deformed the most. **Figure 3** shows the progression of all adherend thicknesses. The 1 mm thick adherend has the greatest elongation due to deformation. This joint achieved elastic deformation compared to the other thicknesses, which showed a rigid joint without adherend deformation, i.e., with less elongation. The 3 mm thick adherend also showed a small deformation, which also affected the resulting strength and elongation. The highest strengths were achieved by the 5 mm and 8 mm adherends, which showed no deformation, so the resulting strength depended only on the adherend thickness. In all cases, a specific cohesive failure occurred.

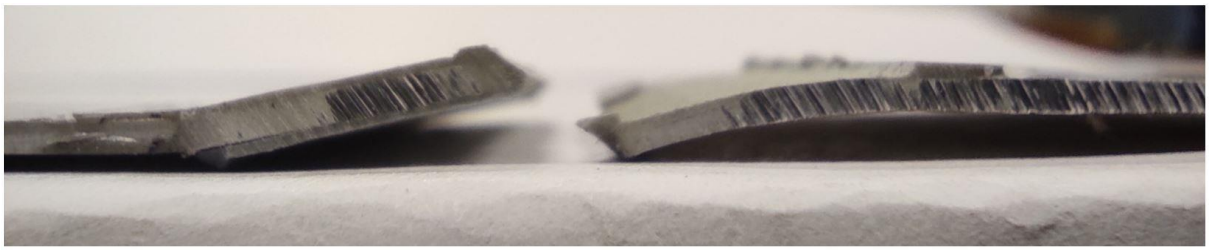

Figure 2 Detail of deformation of 1 mm thick adherent**.** Source: (own)

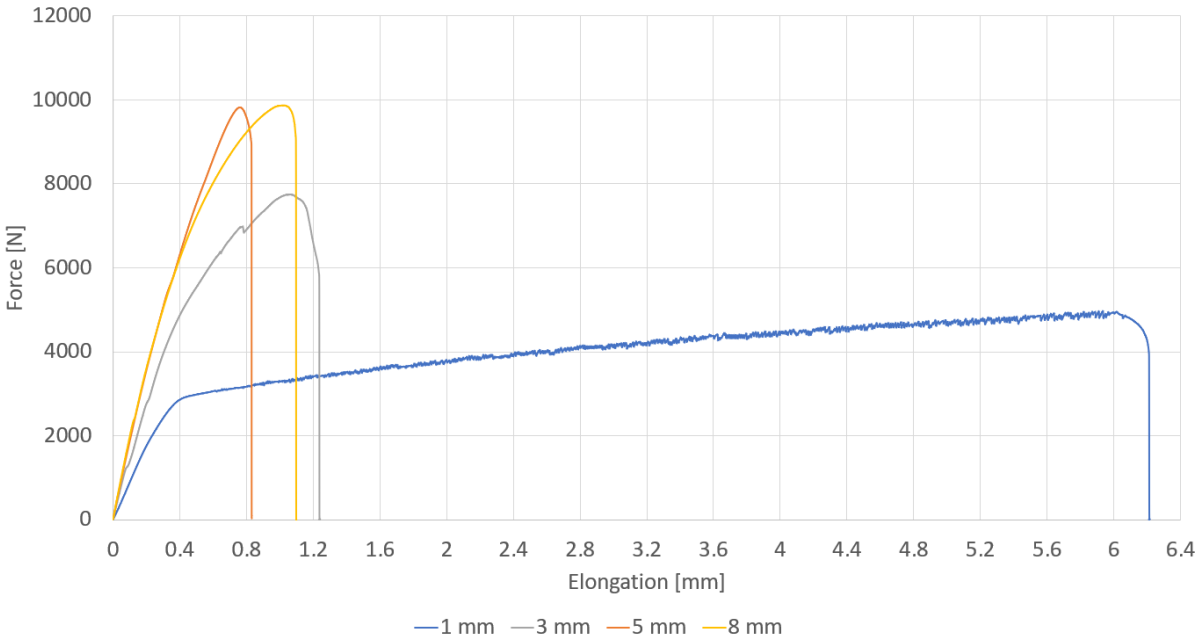

Figure 3 Comparison of adherent thicknesses. Source: (own)

3. CONCLUSION

Interesting results were obtained when testing samples of different thicknesses of the base material. As can be seen in the testing of specimen thicknesses (3 mm and 1 mm), there was a combined deformation, thus changing the stress axis due to the testing of the overlapped bonded joint. In this case, there is no uniform axis of stress and the combined tensile stress and partial debonding of the bonded joint occurs when the two independent axes of tension tend to converge into a single axis during tensile testing. For this reason, these specimens exhibited lower bond strength values, as they were partially affected by the peeling mechanism, which tends to be problematic for bonded joints achieving high strengths. This theory is supported by tensile tests on 5 mm and 8 mm thick material, which were sufficiently stiff for the proposed joint. The results obtained for these thicknesses of base material were already close to the maximum bonded joint strength for the chosen adhesive, which is derived from the adhesive manufacturer's datasheet. Thus, this observed phenomenon highlights the problem of tensile testing of thin materials, where the final strength of the bonded joint is affected, which is realistically higher for materials of higher thicknesses because it is not affected by deformations of the base material. Therefore, it would be advisable to align the axis of the bonded joint by means of a milled area at both ends of the specimens, if this is possible in the subsequent bonding application.

ACKNOWLEDGEMENT

This paper was created Results were achieved thanks to the financial by the project no. SP2023/082Single-seat electric vehicle design for micro-mobility in urban environments and university campuses.

REFERENCES

[1] PETERKA, Jindřich. Lepení konstrukčních materiálů ve strojírenství. Praha: SNTL, 1980, 792 s. DT 621.792:621.

[2] SAHIN, Resul, Salih AKPINAR, Cristina ALÍA, Xiayu LI, Xiumin ZHANG a Hongfan YANG. The effects of adherend thickness on the fatigue strength of adhesively bonded single-lap joints. International Journal of Adhesion and Adhesives. 2021, 107(3), 160-165. ISSN 01437496. Dostupné z: doi:10.1016/j.ijadhadh.2021.102845

[3] ARENAS, José M., Julián J. NARBÓN, Cristina ALÍA, Xiayu LI, Xiumin ZHANG a Hongfan YANG. Optimum adhesive thickness in structural adhesives joints using statistical techniques based on Weibull distribution. International Journal of Adhesion and Adhesives. 2010, 30(3), 160-165. ISSN 01437496. Dostupné z: doi:10.1016/j.ijadhadh.2009.12.003

[4] *adhesive-bonding-of-aluminium-manual.pdf* [online]. [vid. 2023-05-26]. Dostupné z: https://www.shapesbyhydro.com/globalassets/download-center/publications/adhesive-bonding-of-aluminium-manual.pdf

ELECTRICALLY CONDUCTING COMPOSITE FROM GLUCOSE-MONTMORILLONITE NANOCOMPOSITE

Author: Markéta DAVIDOVÁ

Supervisor: doc. Ing. Lenka KULHÁNKOVÁ, Ph.D.

Department: Department of Chemistry and Physico-Chemical processes, Faculty of Materials Science and Technology, VSB – Technical University of Ostrava

Abstract

The main objective of this study was to investigate the feasibility of preparing an electrically conductive composite containing graphite or graphene from a glucose-montmorillonite nanocomposite. Four different ratios of crystalline glucose and MMT were mixed, pressed into tablets, and then calcined at 1300 °C. The electrical conductivity of noncalcined powder samples and tablets was measured. During calcination, the tablets were damaged, so the calcined samples were ground into powder for further testing. Various analytical techniques, including XRD, infrared spectroscopy, Raman microscopy, and TEM, were employed to analyse the calcined samples.

Key words:

Montmorillonite, glucose, calcination, graphite, graphene.

1. INTRODUCTION

Researchers are interested in ways how to prepare composites that contain graphite or graphene as a conductive component. These components cause high electrical conductivity. The most common method of preparing these composites involves the use of commercially available graphite or graphene and applying them to a selected matrix. However, graphite or graphene can also be produced in situ from a suitable precursor such as SiC or phyllosilicate matrices intercalated with organic substances [1,2]. When these intercalates are calcined, graphite or graphene can be formed in the resulting composite. In this paper, clay mineral montmorillonite was used as a matrix, which has a great ability to expand and accept other molecules into its interlayers to form an intercalate. As a precursor for the preparation of electrically conductive composites, the organic D-glucose was used. D-glucose as an organic molecule is the most abundant monosaccharide, is easily available, is cheap, and because of its structural modification, it is prone to producing a new compound [3].

2. EXPERIMENT

2.1 Materials and samples preparation

Na-MONTMORILLONITE Portaclay (MMT) was purchased from Ankerpoort NV, The Netherlands. Basal spacing of the MMT is ~ 1.245 nm and the crystallochemical formula $(Al_{2,85}\ Mg_{0,71}\ Ti_{0,02}\ Fe^{3+}_{0,42})(Si_8)O_{20}(OH)_4$ with a layer charge ~ 0.7 el. per unit cell. D-glucose was purchased from mikroCHEM, Slovakia.

MMT and D-glucose were mixed in four different mass ratios – 1:4; 2:3; 3:2 and 4:1. To ensure a good mixing of the two substances, the mixtures were then rubbed in a friction bowl. From each of the mixtures, a tablet was pressed. The pressed tablets were calcined in the high-temperature tube resistance furnace (CLASIC CZ, spol. s.r.o., Czech Republic) equipped with a Pt-13% Rh/Pt thermocouple. In the tube, the inert atmosphere (>99.9999% Ar) was maintained under a constant overpressure of $1.06 \cdot 10^5$ Pa. The process included controlled heating and cooling within a temperature range of 25 to 1300 °C at a rate of 5 °C/min. The tablets were exposed to the target temperature of 1300 °C for 1 h. The Ar atmosphere was replaced four times during the process: at 900 °C, at 1100 °C, at the beginning and at the end of the 1 h interval at 1300 °C. The rate of each replacement was 5 dm^3/min, and each replacement took 5 min. The internal volume of the tube was 2.26 dm^3.

2.2. Characterization methods

XRD analysis was performed on a Miniflex600 powder diffractometer (Rigaku, JP) with a DTex/Ultra 1D detector. The samples were measured in reflex mode, ranged from 5 to 80º 2θ, with a step of 0.02º and a step time of 5º/min. During the measurement, a cuprum lamp (CuKα; λ=1.5418 nm) was used.

An XploRA^{TM} confocal Raman microscope (HORIBA Jobin Yvon) was used to obtain Raman spectra. The device is equipped with an Olympus BX41/51 optical microscope with three lenses. For the measurements a lens with magnification of 50x, which is suitable for powder samples, was used. The detector is a highly sensitive, air-cooled 1024 pixel 1" CCD chip. All operation of the instrument takes place via the LabSpec PC software. An excitation source with a wavelength of 532 nm, 10% laser intensity was used for the analysis. Each spectrum was scanned 10 times with a duration of 10 s. From each of the sample spectra were obtained from 10 different points. An average spectrum was then created from these points.

Jeol JEM-2010 transmission electron microscope (TEM) was used to observe the morphology of the samples. To conduct this analysis, the samples were dispersed in water and a LaB_6 crystal served as the source of electrons. The TEM images were obtained using acceleration voltages of 25 kV and 160 kV.

2.3. Conductivity measurements

For DC conductivity measurement, a special measuring apparatus was constructed using DC POWER SUPPLY HY 3003 D-2, programmable DC POWER SUPPLY BK PRECISION 9120, pA-meter KEITHLEY 6487. For the measurement of the DC conductivity of noncalcined tablets, flat CU electrodes were used. The DC conductivity of the noncalcined powder samples was measured on a special measuring apparatus intended to measure powder samples. Because of damaging tablets during calcination, they had to be crushed into a fine powder and their DC conductivity was measured in the same way as the noncalcined powder samples. For that reason, only the electrical conductivities of the powdered samples were compared.

3. RESULTS

3.1 Electrical conductivity

According to Table 1, the electrical conductivities of noncalcined samples are almost zero because there are not naturally electrically conductive components. Calcination of these samples resulted in significant increase in electrical conductivity. The σ_{calc} values are 6 orders of magnitude higher compared to $\sigma_{noncalc}$ values. This is caused by formation of some electrically conductive form of carbon. In order to determine the form of carbon, two samples with the highest conductivity (2M_3G, 3M_2G) were chosen to be thoroughly analysed.

Table 3 Electrical conductivities of noncalcined and calcined powdered samples. (own)

Sample	$\sigma_{noncalc}$ (S·m^{-1})	σ_{calc} (S·m^{-1})
1M_4G	$2.53 \cdot 10^{-5}$	13.87
2M_3G	$2.39 \cdot 10^{-5}$	49.63
3M_2G	$6.19 \cdot 10^{-5}$	15.81
4M_1G	$8.78 \cdot 10^{-5}$	0.05

3.2 XRD analysis

The (001) basal reflection of pure MMT and both uncalcined samples 2M_3G and 3M_2G can be seen in Figure 1. For pure MMT, the reflection is diffused, without clear maximum (~8,5° 2θ) and with basal spacing 1,182 nm. This is caused by non-orderliness of MMT particles. By adding glucose to MMT, intensity of the reflections increased, the reflection became narrower and basal spacing increased to 1,411 nm (2M_3G) and 1,413 nm (3M_2G). That means, glucose occurs in the MMT interlayer and caused the arrangement of MMT particles.

The XRD patterns of calcined samples 2M_3G and 3M_2G (Figure 2) suggests the formation of amorphous carbon (the baseline is not flat but forms a kind of “hump”). Calcination caused the dehydroxylation of the MMT structure, leading to the disappearance of the (001) line and the formation of mullite (in the picture marked as 1), cristobalite (marked as 2) and graphite (marked as 3).

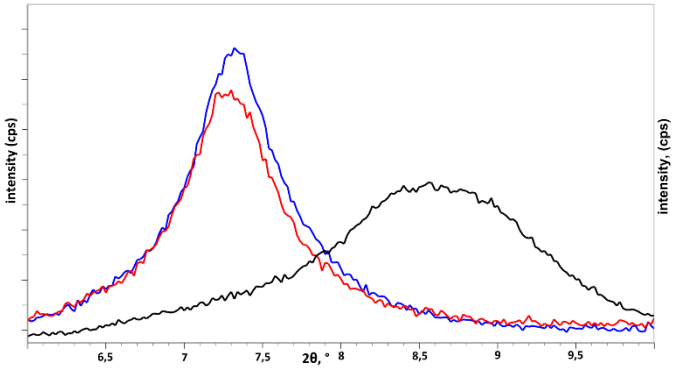

Figure 1 XRD pattern of pure MMT (black), 2M_3G (red) and 3M_2G (blue) (own)

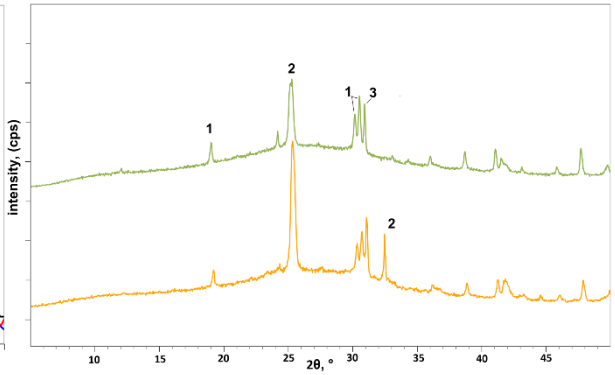

Figure 2 XRD patterns of calcined 2M_3G (yellow line) and calcined 3M_2G (green line). (own)

3.3 Raman microscopy

Two intense bands can be seen in the Raman spectra of both calcined samples (Figures 3 and 4). The first band around 1330 cm^{-1} is the disorder band of carbon suggesting presence of defects in these samples. Also, a graphitic band situated at 1562 cm^{-1} can be seen in both spectra. When the intensities of these two bands are compared, the D band is more intensive, which means that the structure has more crystals of disordered carbon than crystals of graphite [4, 5]. At 2673 cm^{-1} the overtone of 2D graphite occurs. These three intensive peaks can also be found in Raman spectra of graphene but in different ratios of intensities [6].

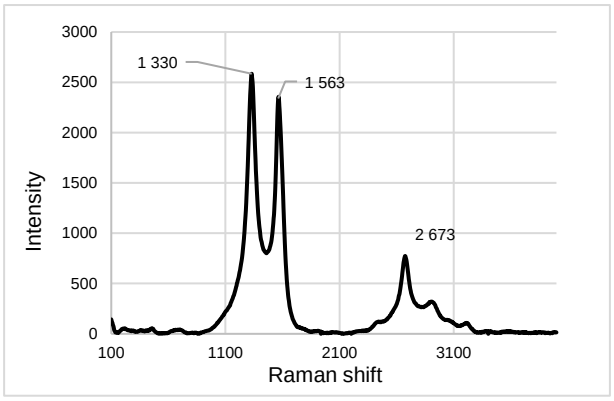

Figure 15 Raman spectra of 3M_2G (own)

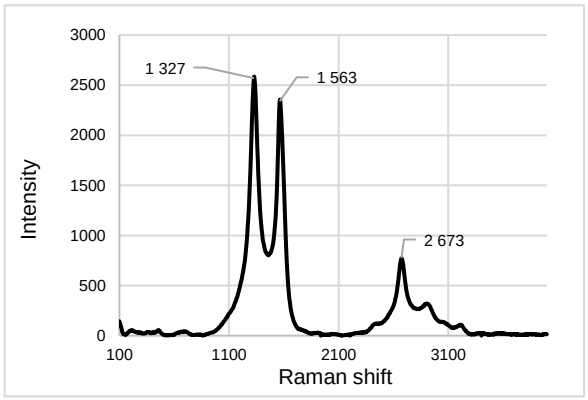

Figure 14 Raman spectra of 2M_3G (own)

3.4 TEM

In Figure 5, TEM images of the calcined samples can be seen. In both samples, the graphitic layers are clearly visible and easily countable. Areas where layers can be seen are marked in white circles. By enlarging these areas, 7 to 9 layers can be distinguished very well. As stated in [7], if the layers are up to 10, there is the possibility that it is multilayer graphene.

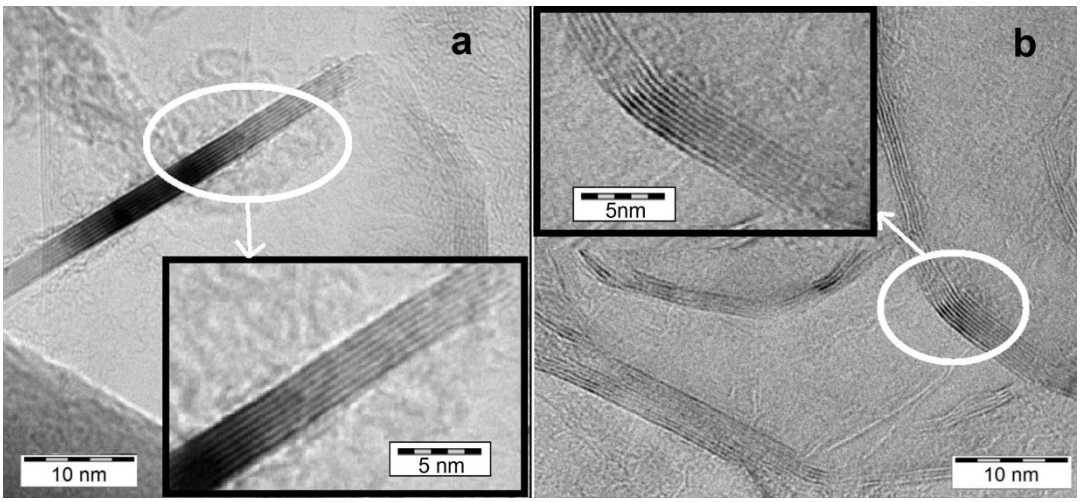

Figure 16 TEM images of calcined samples a) 2M_3G and b) 3M_2G (own)

4. CONCLUSION

This article discusses the preparation and characterisation of composite tablets made from montmorillonite and D-glucose. Calcination of these tablets significantly increased their electrical conductivity, likely due to the formation of conductive carbon material. X-ray diffraction analysis revealed an improved particle arrangement and increased diffraction peak intensity after glucose was added to MMT. Calcination resulted in the formation of amorphous carbon, cristobalite, mullite, and graphite. Raman microscopy confirmed the presence of carbon structure and TEM images revealed multilayer graphene. Further research should focus on examining composition-property relationships, optimising the calcination process, and explore what else parameters has an impact on prepare of graphite/graphene.

ACKNOWLEDGEMENT

This work was supported by the Czech Republic Ministry of Education, Youth, and Sports project (SP2023/034)

REFERENCES

[1] MIRANZO, Pilar, Cristina RAMÍREZ, Benito ROMÁN-MANSO, et al. In situ processing of electrically conducting graphene/SiC nanocomposites. *Journal of the European Ceramic Society*. 2013, **33**(10), 1665-1674. Available from: https://doi.org/10.1016/j.jeurceramsoc.2013.01.021

[2] C. Xu, G.Ning, X. Zhu, G. Wang, X. Liu, J. Gao, Q. Zhang, W. Qian, F. Wei, Synthesis of graphene from asphaltene molecules adsorbed on vermiculite layers. *Carbon* 62 (2013) 213–221. Available from: http://dx.doi.org/10.1016/j.carbon.2013.05.059

[3] SILVA, R.O., J.R. FREITAS FILHO a J.C.R. FREITAS. D-Glicose, uma Biomolécula Fascinante: História, Propriedades, Produção e Aplicação. *REVISTA VIRTUAL DE QUIMICA*. 2018, **10**(4), 875-891. Available from: doi:10.21577/1984-6835.20180064

[4] REICH, Stephanie a Christian THOMSEN. Raman spectroscopy of graphite: One contribution of 13 to a Theme 'Raman spectroscopy in carbons: from nanotubes to diamond'. *Philosophical Transactions of The Royal Society A Mathematical Physical and Engineering Sciences*. 2004, **362**(1824), 2271-2288. Available from: doi:10.1098/rsta.2004.1454

[5] FERRARI, A.C., J.C. MEYER, V. SCARDACI, et al. Raman Spectrum of Graphene and Graphene Layers. *Phys. Rev. Lett*. 2006, **97**(18). Available from: https://doi.org/10.1103/PhysRevLett.97.187401

[6] MALARD, L.M., M.A. PIMENTA, G. DRESSELHAUS a M.S. DRESSELHAUS. Raman spectroscopy in graphene. *Physics Report*. 2009, **473**(5-6), 51-87. ISSN 0370-1573. Available from: https://doi.org/10.1016/j.physrep.2009.02.003

[7] BIANCO, Alberto, Hui-Ming CHENG, Toshiaki ENOKI, et al. All in the graphene family – A recommended nomenclature for two-dimensional carbon materials. *Carbon*. 2013, **65**, 1-6. Available from: https://doi.org/10.1016/j.carbon.2013.08.038

MEASUREMENT OF THRESHOLD STRESS INTENSITY FACTOR ON CHROMIUM MOLYBDENUM PRESSURE VESSEL STEEL IN 30 MPa HYDROGEN GAS

Author(s): Marek DOBIÁŠ, Petr ČÍŽEK, Ladislav KANDER, Petr JONŠTA

Supervisor: doc. Ing. Petr JONŠTA, PhD.

Department: Department of Materials Engineering and Recycling, Faculty of Materials Science and Technology, VSB – Technical University of Ostrava

Abstract

There are many methods, which can be used for evaluation of resistance to hydrogen assisted cracking of metal pressure vessels, but almost each of them shows different results. Theirs application can depend on strength of steel and surely some of them need harmonisation. This paper contains constant displacement test done according to method C in EN ISO 11114-4 standard on modified compact tension specimens and evaluation of quasistatic fracture toughness in air and in hydrogen environment in terms of J-R curve, where monotonic rising displacement tests on multiple compact tension specimens were done. Testing was performed on chromium molybdenum steel 34CrMo4 widely used for pressure vessels in 30 MPa hydrogen gas. Both tests show dissimilar results, which are more conservative for constant displacement test in our case, that is opposite in works of other researchers. Interesting is also comparison with probably the most conservative method B of standard above specified, which is stepwise rising load test. To understand this, there must be done far more tests.

Key words:

Threshold stress intensity factor, pressure vessel, Cr-Mo steels, hydrogen gas.

1. INTRODUCTION

Chromium molybdenum steels are largely used as a material for pressure cylinders production and this paper is focused on 34CrMo4 steel. Both constant displacement test and monotonic rising displacement test in air and in high-pressure gas at 30 MPa were done to compare yielded results.

2. MATERIAL PROPERTIES

Results of chemical analysis are compared with standard values in Table 1.

Table 1 Chemical analysis and standard values in (wt%). Source: (own)

Element	C	Si	Mn	P	S	Cr	Cu	Mo
EN ISO 683-2 [1]	0.30-0.37	0.10-0.40	0.60-0.90	≤0.025	≤0.035	0.90-1.20	≤0.40	0.15-0.30
Chemical analysis [2]	0.35	0.302	0.78	0.003	<0.001	1.13	0.0114	0.203

Measured values are in agreement with standard. Tensile tests were provided on three longitudinal specimens with diameter of 10.01 mm in air environment at ambient temperature. Average values are 830 MPa for ultimate tensile strength, σ_{UTS}, and 661 MPa for 0.2 % yield strength, $\sigma_{0.2}$.

3. APPARATUS

Apparatus for high-pressure hydrogen environment consists of autoclave, plunger, hydrogen pressure vessel and vacuum pump, which are connected by pressure tubes. Autoclave can be static, where specimens are simply inserted inside, or dynamic, where one specimen is tested on servohydraulic machine. Volume of both autoclaves is 0.552 dm^3. Dynamic autoclave was developed and patented by MMV. Used hydrogen gas with purity of 5N5 was pressurized to 30 MPa with help of plunger because of lower pressure in pressure cylinder. Procedure of pressurizing was as follows:

scavenging with nitrogen gas, vacuum pumping and pressurizing with hydrogen gas to required pressure.

4. MONOTONIC RISING DISPLACEMENT TEST

Monotonic rising displacement test was conducted according to EN ISO 12135 [3] so that the result was J-R curve. Five 0.5T-C(T) specimens with dimensions showed in Figure 1 a) were fabricated, precracked at maximum stress intensity factor K_{MAX} = 28 MPa·m$^{0.5}$ and stress ratio R = 0.1 and subsequently tested. Testing rate was 5·10^{-3} mm·s^{-1}. Unloaded specimens were heat tinted and broken with aid of liquid nitrogen. Measured values of crack length were used for obtaining the equivalent of fracture toughness $K_{JC0.2}$ value of 206.47 MPa·m$^{0.5}$, which was calculated according to equation (1) from corresponding fracture resistance at 0.2 mm crack growth including blunting, $J_{0.2}$. This quantity, $K_{JC0.2}$, is comparable to threshold stress intensity factor $K_{I,H}$.

$$K_{JC0.2} = \frac{J_{0.2} \cdot E}{(1-\nu)^2} \tag{1}$$

where:
$K_{JC0.2}$ – the equivalent of fracture toughness (MPa·m$^{0.5}$),
$J_{0.2}$ – fracture resistance at 0.2 mm crack growth including blunting (kJ·m^{-2}),
E – Young's modulus (MPa),
v – Poisson's ratio (-) [3].

Another set of five 0.5T-C(T) specimens were used for monotonic rising displacement test in high-pressure hydrogen environment. Precracking was done according to conditions above mentioned and tests were conducted without extensometer for crack mouth opening displacement measurement, due to limited space in autoclave and due to its impropriety for measuring in hydrogen environment, so in this case, crack tip opening displacement δ_0 was calculated thanks to algebraic difference of notch opening displacement V before and after test, which is equivalent to plastic component V_p, measured under microscope. Testing rate was 2·10^{-4} mm·s^{-1}. The remaining steps are same as above. CTOD δ_0 was converted to fracture resistance J_0 according to approximated equation (2) [3].

$$J_0 = 2 \cdot \sigma_{0.2} \cdot \delta_0 \tag{2}$$

Resulting value of equivalent of fracture toughness $K_{JC0.2}$ is 147.68 MPa·m$^{0.5}$. Dependence of fracture resistance J_0 on crack extension Δa is in Figure 2.

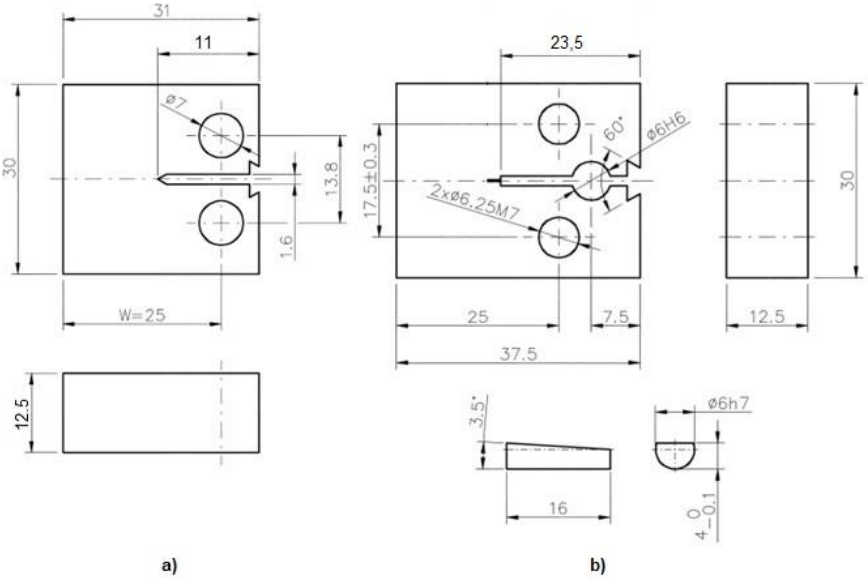

Figure 1 Specimen 0.5T-C(T) for a) monotonic rising displacement test, b) constant displacement test. Source: (own)

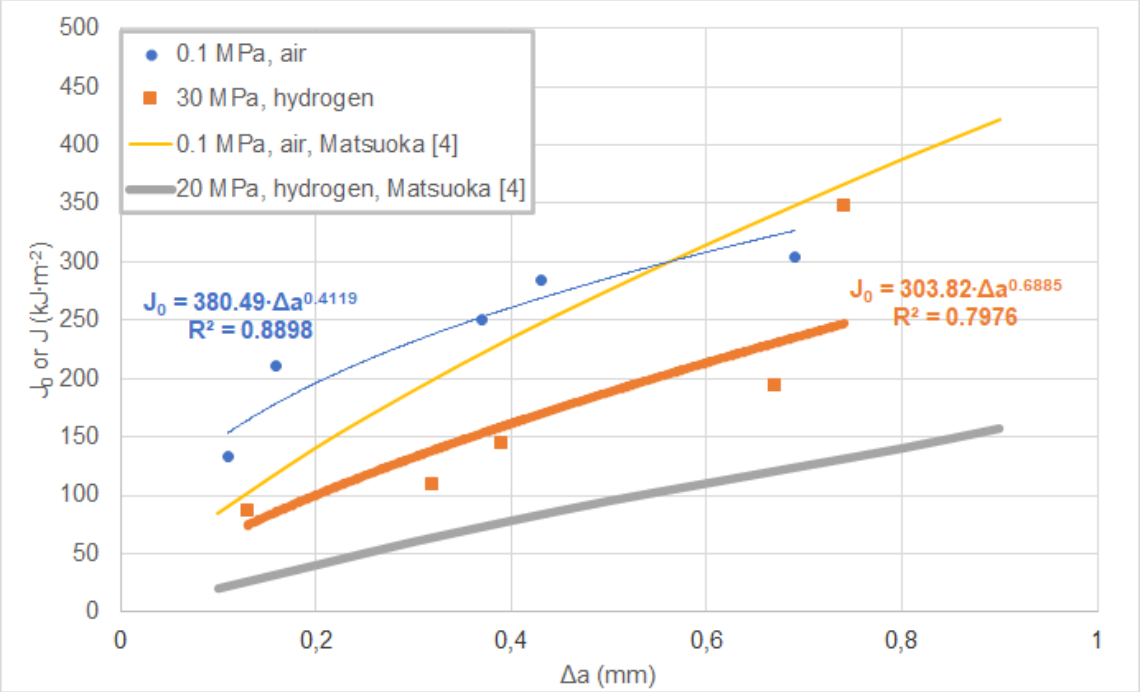

Figure 2 J_0 – Δa plot. Source: (own)

5. CONSTANT DISPLACEMENT TEST

Constant displacement test was done according to method C, mentioned in EN ISO 11114-4 [5], i.e., test method to determine the resistance to hydrogen assisted cracking of steel cylinders. Three modified 0.5T-C(T) specimens of the Y-X orientation, see Figure 1b), were machined with central hole serving for fixing static load with help of two wedges. Precracking conditions were same as above. Then specimens were loaded to constant displacement computed from applied elastic stress intensity factor K_{IAPP} = 78.61 MPa·m$^{0.5}$, which was calculated according to equation (4) [5], fixed with wedges, placed in static autoclave and tested for 1,000 hours.

$$K_{IAPP} = 1.5 \cdot 60 \cdot \frac{R_m}{950} \tag{4}$$

Specimens were broken after the test and crack extension Δa was measured as noted above. Resulting value of threshold fracture toughness was equal to K_{IAPP} due to no crack extension, except one specimen having crack extension $\Delta a \approx 15$ µm.

6. DISSCUSION

It is unusual according to trend, e.g. works of Matsumoto et al. [6] and Nibur et al. [7], that monotonic rising displacement test shows almost two times higher value of equivalent of fracture toughness $K_{JC0.2}$ than threshold stress intensity factor $K_{I,H}$ of constant displacement test.

Previous work by Čížek and Kander [8], where method B (stepwise rising load test) was carried out on 34CrMo4 steel with two different heats (σ_{UTS} = 1050 MPa and $\sigma_{0.2}$ = 972 MPa for first heat; σ_{UTS} = 1062 MPa and $\sigma_{0.2}$ = 989 MPa for second heat [9]) in 30 MPa hydrogen gas, showed results of threshold stress intensity factor $K_{I,H}$ range from 40.5 to 94.3 MPa·m$^{0.5}$. These values are lower than ours due to higher tensile strength.

Matsuoka et al. [4, 10] done several tests on JIS-SCM435 pressure cylinder steel, which is equivalent to 34CrMo4 steel, with σ_{UTS} = 824 MPa and $\sigma_{0.2}$ = 687 MPa. Value of threshold fracture toughness $K_{I,H}$ gained from elasto-plastic fracture toughness test according to ASTM E1820 [11] in 20 MPa hydrogen gas was two thirds lower than our value, see J-integral dependence on crack extension Δa in Figure 2. However, they used L-R oriented specimens with width W = 50.8 mm, which can exhibit different behaviour in hydrogen gas. Calculated value of threshold fracture toughness $K_{I,H}$ from polynomial curve for constant displacement test done according to ASME BPVC VIII-3 KD-10 [12] on was 118.6 MPa·m$^{0.5}$, which is higher than our value. They also provided fatigue crack growth rate

tests, which proved ductile crack appearance for steels with ultimate tensile strength $\sigma_{UTS} \leq 900$ MPa that is in agreement with our result of ductile fracture in specimens after monotonic rising displacement test.

Nonetheless, it must be stated, that, according to [13], European standard mentioned above is suitable only for high strength steels.

7. CONCLUSION

Monotonic rising displacement test and constant displacement test were done on specimens made of 34CrMo4 steel. First mentioned test showed decrease of equivalent to fracture toughness $K_{JC0.2}$ due to hydrogen impact. Latter test showed no crack extension except one with stable crack growth $\Delta a \approx 15$ µm. Threshold stress intensity factor is more conservative for constant displacement test than for monotonic rising displacement test. These data can be used for future testing.

ACKNOWLEDGEMENT

This paper was created in the frame of the Institutional support for long-term and conceptual development of a research organization in 2023, provided by the Ministry of Industry and Trade of the Czech Republic.

REFERENCES

[1] EN ISO 683-2. *Heat-treatable steels, alloy steels and free-cutting steels - Part 2: Alloy steels for quenching and tempering*. Geneva, Switzerland: ISO, 2016.

[2] CHARBULÁKOVÁ, Lenka. *Studium chování CrMo oceli pro výrobu ocelových bezešvých vysokotlakých lahví v prostředí vodíku*. Ostrava, 2022. Diploma thesis. VSB-TUO.

[3] EN ISO 12135. *Metallic materials - Unified method of test for the determination of quasistatic fracture toughness.* Geneva, Switzerland: ISO, 2021.

[4] MATSUOKA, et al. Effect of hydrogen-gas pressure on threshold of hydrogen-induced crack growth for carbon steel JIS-SM490B, low-alloy steel JIS-SCM435 and stainless steel JIS-SUS304. *Transactions of the JSME*. Japan: JSME, 2019. 85, 872, pp. 18-00415. ISSN: 2187-9761.

[5] EN ISO 11114-4. *Transportable gas cylinders - Compatibility of cylinder and valve materials with gas contents - Part 4: Test methods for selecting steels resistant to hydrogen embrittlement*. Geneva, Switzerland: ISO, 2017.

[6] MATSUMOTO, T. et al. Threshold stress intensity factor for hydrogen-assisted cracking of CR-MO steel used as stationary storage buffer of a hydrogen refueling station. *International Journal of Hydrogen Energy*. 2017, 42, 11, pp. 7422-7428. ISSN 03603199.

[7] NIBUR, K. A. et al. The Relationship Between Crack-Tip Strain and Subcritical Cracking Thresholds for Steels in High-Pressure Hydrogen Gas. *Metallurgical and Materials Transactions A*. 2013, 44, 1 pp. 248-269. ISSN 1073-5623.

[8] ČÍŽEK, P. and L. KANDER. FRACTURE BEHAVIOR OF 34CrMo4 STEEL IN HIGH-PRESSURE HYDROGEN ENVIRONMENT. In: *METAL 2020: 29th International Conference on Metallurgy and Materials.* Ostrava: TANGER, 2020. pp. 597-602.

[9] ČÍŽEK, P. and G. ROŽNOVSKÁ. *Výzkum a vývoj materiálových charakteristik potřebných pro hodnocení spolehlivosti a životnosti ocelí pro vodíkové hospodářství: Výzkumná zpráva za rok řešení 2019*. Ostrava, MMV, 2019.

[10] MATSUOKA, et al. Test method for threshold of hydrogen-induced crack growth $K_{I,H}$ of SCM435 in 115 MPa hydrogen gas. *Transactions of the JSME*. Japan: JSME, 2018. 84, 857, pp. 17-00385. ISSN: 2187-9761

[11] ASTM E1820. *Standard Test Method for Measurement of Fracture Toughness*. West Conshohocken, PA, USA: ASTM International, 2023.

[12] BPVC.VIII.3. *BPVC Section VIII-Rules for Construction of Pressure Vessels Division 3-Alternative Rules for Construction of High Pressure Vessels*. New York, NY, USA: ASME, 2023. ISBN: 9780791875841.

[13] SAN MARCHI, Chris et al. *Development of Standards for Evaluating Materials for Service in High-Pressure Gaseous Hydrogen* [online presentation]. USA, 2013 [cited 2023-05-31]. Available from: http://www.ichs2013.com/images/presentations/10-09/118.pdf

MICROSTRUCTURE OF SPD CP-TI AFTER HEAT TREATMENT AT 450°C

Author(s): Kryštof HRADEČNÝ

Supervisor: prof. Ing. Vlastimil VODÁREK, CSc.

Department: Department of Materials Engineering and Recycling, Faculty of Materials Science and Technology, VSB – Technical University of Ostrava

Abstract

This study focuses on the microstructural changes in SPD CP-Ti Grade 4 material in as-received state and after annealing at 450°C. After annealing, local changes in microstructure, mainly grain coarsening, were observed. The results suggest that the increase in grain size during annealing influenced the microhardness values, which showed a decrease. Despite these microstructural changes were identified areas where the original material structure was retained.

Key words:

Commercially pure titanium, TEM, light microscopy, heat treatment, thermal stability.

1. INTRODUCTION

Commercially Pure Titanium (CP-Ti) has found widespread use in various biomedical applications, particularly in the production of dental implants, due to its excellent biocompatibility and corrosion resistance [1]. However, the mechanical properties of CP-Ti, such as its strength and ductility, often need improvement to meet the demands of implants. Severe plastic deformation techniques (SPD), such as Equal Channel Angular Pressing (ECAP), have been shown to be potential method for enhancing the mechanical properties of CP-Ti [2]. The reduction in grain size has increased in yield strength and therefore CP-Ti has the required properties to produce dental implants [2,3].

Treatments such as the application of protective coating are also applied to SPD CP-Ti. These further treatments are carried out at elevated temperatures and the microstructure may become unstable due to the temperatures. The increase in temperature can cause microstructural changes and can lead to a deterioration in mechanical properties and degradation of the material [4]. Therefore, it is important to understand the behaviour of SPD CP-Ti at elevated temperatures and to find the appropriate temperature at which microstructural changes will be not significant. Microstructure of SPD CP-Ti appears to be stable at temperatures up to 450°C [5].

The aim of this work was to study the microstructural changes of SPD CP-Ti Grade 4, which was processed by SPD process, and to observe it in its original state and after heat treatment at 450°C. The microstructural analysis was performed by transmission electron microscopy and optical microscopy. The analysis also included the determination of microhardness values and grain size measurements.

2. MATERIAL AND EXPERIMENTAL TECHNIQUES

SPD CP-Ti Grade 4 material in the form of thin bars with a diameter of 4 mm was used for the experiment. The rods were annealed at 450°C for 1 hour under vacuum (2mbar) followed by cooling in air. Table 1 shows the chemical composition of the material and Table 2 summarizes its mechanical properties.

Microstructural analysis was performed using light microscopy Olympus BX51 and transmission electron microscopy JEM 2100. Samples for light microscopy were pressed into bakelite, ground on SiC papers, polished using diamond suspensions and final polishing using a 1:1 solution of colloidal suspension SiO_2 and 30% hydrogen peroxide H_2O_2. The samples were etched in a solution of 60 vol% glycerine, 20 vol% nitric acid and 20 vol% hydrofluoric acid. For TEM analysis, the samples were prepared as thin slices, which were cut using a slow-speed saw Buehler IsoMet Struers and subsequently ground on SiC papers. The aim was to prepare a thin slices with a thickness

of 0.1 mm. Next, electropolishing by Struers Tenupol 3 in Struers 3 electrolyte was required. The microstructure characteristics were investigated in the transverse directions and longitudinal directions of the rod. The microhardness determination according to Vickers was carried out with a load of 500 g on DuraScan G5. The grain size was determined according to ČSN EN ISO 643.

Table 1 The chemical composition of SPD CP-Ti Grade 4 [wt.%]. Source: (own)

Fe	Co	C	H	N	O	Trace elements	Ti
0.178	< 0.010	0.001	0.002	0.003	0.350	<0.400	The rest

Table 2 The mechanical properties of SPD CP-Ti Grade 4. Source: (own)

Yield strength [MPa]	Tensile strength [MPa]	Ductility [%]	Hardness HV	Modulus of elasticity [GPa]
814	1056	19.6	453	110

3. RESULTS

Figure 1 shows images of the microstructure of the SPD CP-Ti Grade 4 taken using a light microscope (LM). The original state of the sample, shown in Figures 1a, represents a homogeneous microstructure in transeverse section. While in the longitudinal direction, microstructure have an elongated morphology (Figure 1b). After annealing at 450°C, a difference in microstructure was observed as shown in Figures 1c and 1d. Compared to the as-received state, it is slightly noticeable that the appearance of the microstructure has changed in both directions after annealing. Grains are not distinguishable at this level of resolution.

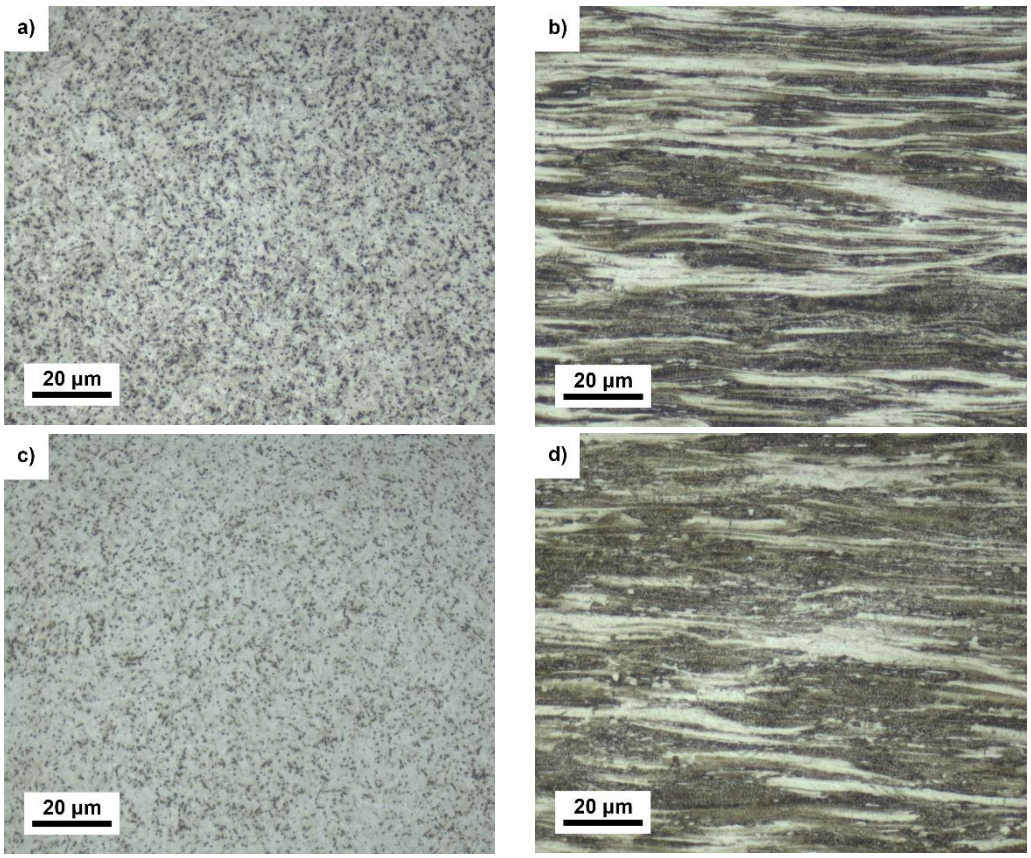

Figure 1 Microstructure of SPD CP-Ti Grade 4: a) as-received in transverse section, b) as-received in longitudinal section, c) after annealing in transverse section, d) after annealing in longitudinal section. Source: (own)

Transmission electron microscopy (TEM) was used to study the microstructure in more detail. A lighter contrast indicates that the grain is separated from its surroundings by low-angle grain boundaries and dark contrast indicates separation of the grain from the surroundings by a high-angle boundary. Figure 2 shows the microstructure of SPD CP-Ti in original state and after annealing. Figure 2a and 2b show a homogeneous microstructure with a subgrain/grain size of less than 100 nm. In some areas, grains with accumulated dislocations are observed, which is typical of the microstructure obtained by SPD process (Figure 2a). In the longitudinal section (Fig. 2b), the grains have a stretched morphology with the appearance of subgrain boundaries. Annealing caused changes in the microstructure due to elevated temperature. Local recovery and recrystallization of grains occurred, which led grain coarsening. Figure 2c shows an area with local grain coarsening in the transverse direction. In the longitudinal direction, the microstructure retained its original grain morphology. But there were also areas in which larger grains were recrystallized, as shown in Figure 2d. The original elongated grains were replaced by recrystalized equiaxed grains.

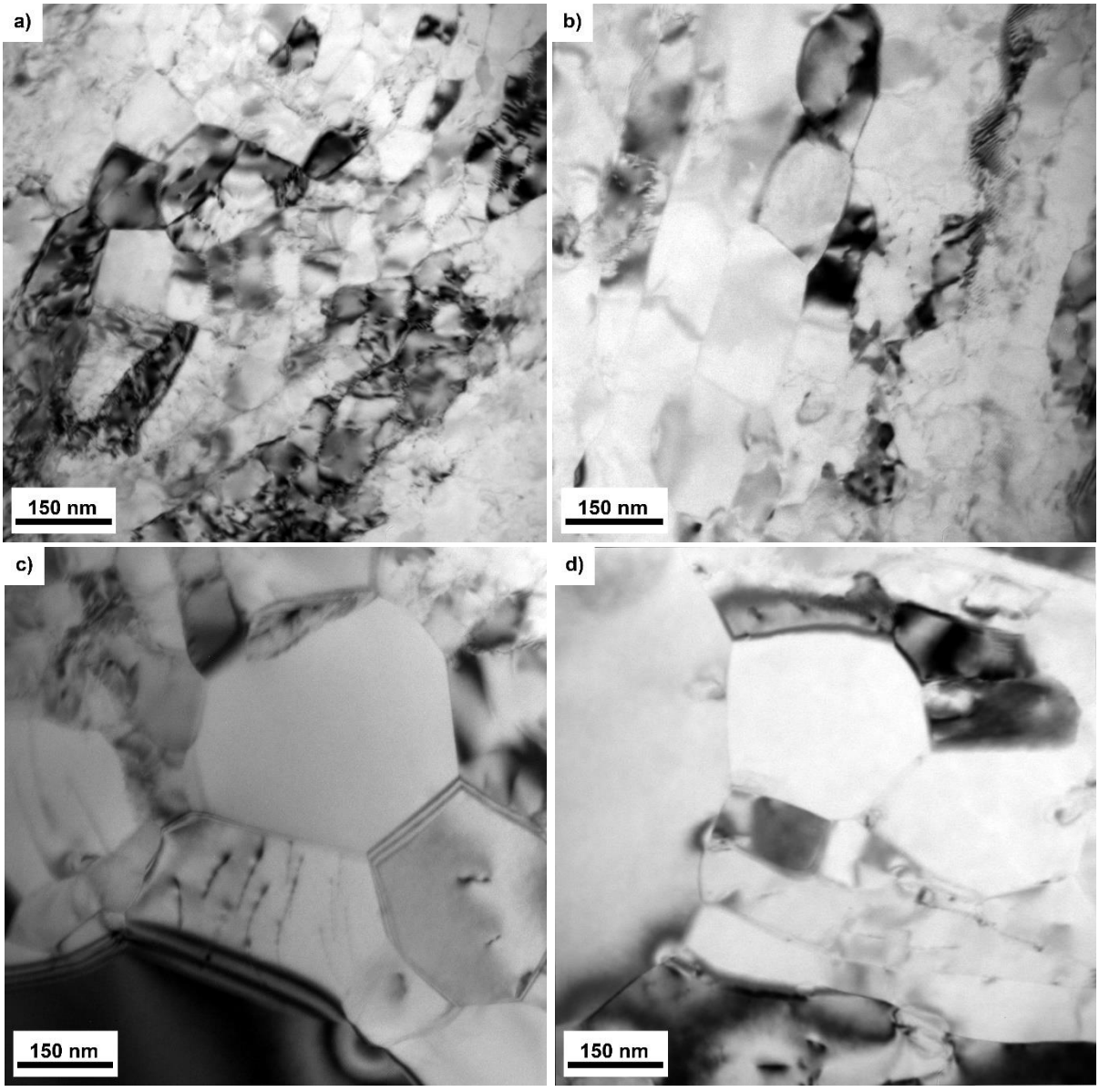

Figure 2 TEM documentation of SPD CP-Ti Grade 4: a) as-received in transverse section, b) as-received in longitudinal section, c) after annealing in transverse section, d) after annealing in longitudinal section. Source: (own)

Microhardness was measured according to the Vickers for the samples in as-received state and after annealing. The measurement results are presented in Table 3. From the results there is a slight

decrease in microhardness. This decrease can be attributed to an increase in grain size, which has a negative effect on the material's performance.

The grain size was determined in accordance with ČSN EN ISO 643. The measurement results are summarised in Table 4. From the result of the grain sizes, it can be observed that the annealing temperature caused an increase in grain size. The results show high variability in grain size. It is a need to better identify the grain boundaries because there exist high-angle grain boundaries and low-angle grain boundaries in the microstructure, which are obtained from the EBSD analysis results. Based on these results, the grain size can be better determined.

Table 3 Results of microhardness measurements $HV_{0.5}$. Source: (own)

	As-received	After annealing
Longitudinal $HV_{0.5}$	340.5 ± 8.5	326.9 ± 7.5
Transverse $HV_{0.5}$	315.5 ± 7.3	292.5 ± 6.5

Table 4 Grain size *d* measurement results. Source: (own)

Grain size	As-received	After annealing
Longitudinal d [nm]	147.6 ± 76.3	367.7 ± 227.9
Transverse d [nm]	67.2 ± 9.1	201.1 ± 132.2

4. CONCLUSION

Microstructural analysis showed that the material in as-received state exhibits a fine-grained microstructure. In the transverse section, equiaxed grains with an average size of 67.2 nm are observed, while in the longitudinal section the grains appear elongated. The average grain size in the longitudinal direction is 147.6 nm. Changes in microstructure were observed after annealing at 450 °C, with local recovery and recrystallization of the grains, leading to coarsening. In the transverse section, a region with strongly recrystallized grains was observed, while in the longitudinal direction, locally equiaxed recrystallized grains were formed. Compared to the original condition, the grain size increased almost threefold. This change influenced the microhardness values, where there was a decrease in the transverse section from 340.5 $HV_{0.5}$ to 326.9 $HV_{0.5}$ and in the longitudinal direction from 315.5 $HV_{0.5}$ to 292.5 $HV_{0.5}$. However, the microstructure was dominated by areas where the original material structure was retained.

ACKNOWLEDGEMENT

The work was created with contribution of Student grant competition project "SP2023/049 The influence of production parameters and operating conditions on the microstructure and utility properties of metallic materials" and supported from the project no. 00424/2022/RRC funded by the Moravian–Silesian Region "Support for gifted students of doctoral studies at VŠB-TUO".

REFERENCES

[1] BRUNETTE, Donald Maxwell, et al. *Titanium in medicine: material science, surface science, engineering, biological responses and medical applications*. New York: Springer, 2001. ISBN 3540669361.

[2] VALIEV, Ruslan Z., Terence G., LANGDON. Principles of equal-channel angular pressing as a processing tool for grain refinement. *Progress in materials science*. 2006, **51**, 881-981.

[3] MAHMOODIAN, Reza, et al. Severe plastic deformation of commercial pure titanium (CP-Ti) for biomedical applications: a brief review. *JOM*. 2019, **71**, 256-263.

[4] DYAKONOV, Gleb S., et al. Annealing behavior of severely-deformed titanium Grade 4. *Materials Science and Engineering: A*, 2019, **742**, 89-101.

[5] HOSEINI, Majid, et al. Thermal stability and annealing behavior of ultrafine grained commercially pure titanium. *Materials Science and Engineering: A*. 2012, **532**, 58-63.

MEASUREMENT OF STRAIN OF TH 3D PRINTED SPACE FRAME OF AUTOMOTIVE HEADLAMP BY DIGITAL IMAGE CORRELATION METHOD

Author(s): Ing. Filip HUVAR, Marek BESEDA, Pavel KLAUS, Filip HAVLÍČEK

Supervisor: doc. Ing. Petra VÁŇOVÁ, Ph.D.

Department: Department of materials and technologies for vehicles, Faculty of Materials Science and Technology, VSB – Technical University of Ostrava

Abstract

This paper discusses and introduces a non-contact method for measuring the deformation of a 3D printed spatial structure by DIC (digital image correlation). A prototype of automotive headlight frame was chosen as the 3D printed structure. The chosen material for 3D printing was EOS MaragingSteel MS1/400W metallic powder. Another part of the work was to design the loading of the headlamp support structure under limit states in operation. The limit state in this case means crossing the transverse threshold at a given speed. These data were measured during experimental runs with the measuring device. Then the work focuses on the design of the measuring device and the measurement of the deformation under static loading. In this case, the design of the measuring stand with the support of the non-contact deformation measurement method DIC was considered. For the purpose of non-contact measurement, the stand and the 3D printed structure were provided with the necessary injection moulding that was required to capture the deformation occurring under load. The results from the non-contact measurement were compared with the control results from the FEM analysis. Simplified 3D models were used for the FEM analysis. The load on the 3D printed structure was measured using a force gauge. The last part of the paper deals with the evaluation and validity of the measured data with the assumptions from the FEM analysis. The aim of the thesis is to evaluate the measured results with a view to designing an optimization of the 3D printed structure so that it still meets the strength requirements that are placed on the headlight of a car.

Key words:

DIC (digital image correlation), deformation measurement, FEM analysis, 3D printed spatial structure.

1. INTRODUCTION

This article deals with the digital image correlation (DIC) method [1], [2]. This method of measurement is now widely used in all industries. Particular applications can be found, for example, in the construction industry for the inspection of bridges, in laboratories and testing institutes for monitoring the stress progression during blast tests, or as a supporting method for checking the strength of machined parts.

In general, the automotive industry today is pushing for weight reduction on almost all parts. Conventional methods of manufacturing parts using technologies such as machining, forging or casting may not always guarantee the lowest weight. New progressive production methods are thus coming on the scene. One of these may be 3D metal printing [3].

This paper discusses the loading method and the actual measurement of deformations on the support structure of this particular headlamp. This part was manufactured using 3D metal printing technology.

The aim of the work is to evaluate the validity of the measured data and compare it with the assumption from the FEM analysis. Then evaluate these results and propose an optimization of the 3D printed headlamp structure [1], [4].

2. MATERIALS

The EOS MaragingSteel MS1/400W system was chosen for 3D printing from metal powder. This is a high strength structural high alloy steel. For this reason, the frame walls could be designed thin, saving weight and material needed for printing. The chemical composition of the material can be seen in Table 1. The mechanical properties of the material can be seen in Table 2.

Table 1 Chemical composition of the material EOS MaragingSteel MS1/400W [wt%].

Element	Fe	Ni	Co	Mo	Ti	Al	Cr, Cu	C	Mn, Si	P, S
Min	Balance	17	8.5	4.5	0.6	0.05	<0.5	<0.03	<0.1	<0.01
Max		19	9.5	5.2	0.8	0.15				

Table 2 The mechanical properties of the material EOS MaragingSteel MS1/400W.

Tensile strenght	
In horizontal direction (XY)	1200 ± 100 MPa
In vertical direction (Z)	1100 ± 150 MPa
Yield ($Rp_{-0.2}$)	
In horizontal direction (XY)	1100 ± 100 MPa
In vertical direction (Z)	930 ± 150 MPa
Modulus of elasticity	
In horizontal direction (XY)	150 ± 25 GPa
In vertical direction (Z)	140 ± 25 GPa

3. DESIGN OF THE LOAD-BEARING STRUCTURE OF AN AUTOMOTIVE HEADLAMP

An experimental fixture was constructed to load the frame to simulate the load in real operation. The design was first constructed in a 3D Solidworks environment.

The final version of the designed fixture uses the support of a welding table to guarantee the rigidity of the system. To fix the frame in the space, a stand made of aluminium profiles was created (See Figure 1). These were to guarantee strength, accuracy and ease of manufacture.

The design is simple and uses a single threaded rod to load the system. The single threaded rod solution was used for reasons of simplicity, space saving and the associated ability to scan the frame from multiple angles and centralise the force to one location (the centre of gravity of the centre headlight).

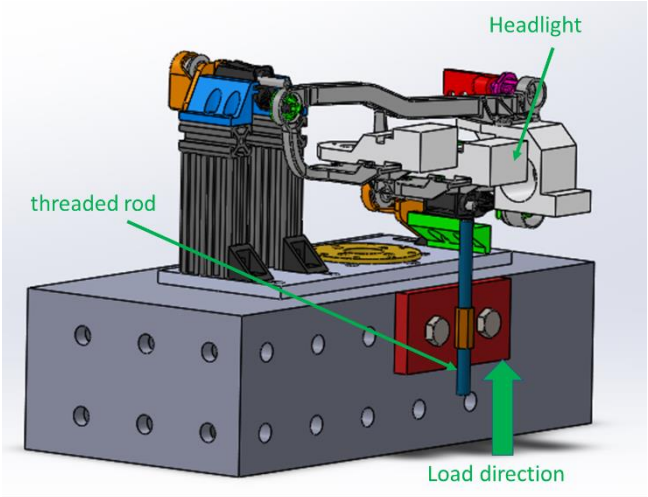

Figure 1 Structure of the product

4. MEASUREMENT OF DEFORMATIONS UNDER STATIC LOADING USING FEM

The geometry of the headlamp bezel has been simplified for this calculation. All curves have been removed. This step helped the formation of the ideal mesh and for the speed of the calculation.

The mesh formation was optimized to an element size of 4 mm. The mesh was refined in the contact area.

This was followed by replacing the headlight lamps with material points. The two headlamps had a mass of 174 g and the headlamp mounted on top of the frame had a mass of 137 g. A mass point was inserted in the centre of gravity of each headlamp.

The joints holding the bezel to the car body were replaced with ties that best matched real-world conditions. The links prevented displacement in all directions and allowed rotation in all three axes.

The acceleration a = 14 715 mm·s^{-2} was chosen as the frame load, This is the value of the acceleration applied to the frame when crossing the transverse threshold at 20 km/h. The force applied to the centre of gravity of the centre headlamp was calculated to be 12.2 N. The resulting force used for the FEM was determined to be 24.4 N. The force was chosen because displacements at a load of 12.2 N might not be detectable on a DIC scan. Thus, we assume a linear increase in force when crossing the threshold at 40 km/h.

The maximum value of the stress in the frame was 3.9 MPa under load. This value is negligible due to the strength of the material.

To compare the FEM and DIC methods, 18 points were placed on the frame at which the displacement was measured (See Figure 2). A comparison was then made with the DIC method.

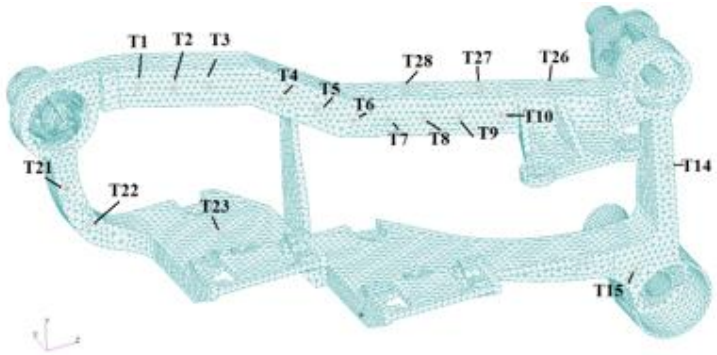

Figure 2 Point distribution for the FEM method

5. MEASUREMENT OF DEFORMATIONS UNDER STATIC LOADING USING DIC

Before the actual DIC measurement, the scanner had to be put in the correct position and calibrated. It was also necessary to coat the frame with a special coating of pattern for correct recognition of the displacements by the camera.

As with the previous FEM method, the force applied to the frame was set at 24.2 N. The force was applied to the frame by a threaded rod on the headlamp. The magnitude of the force was measured using a calibrated force gauge.

During the DIC measurements, 18 points were again placed on the frame at the same locations as during the FEM (See Figure 3). The displacement was measured at these points. In this way, the results of the FEM analysis and the whole model can be validated.

Figure 3 Point distribution for the DIC method

6. EVALUATION OF MEASURED DATA

From the resulting displacement plots for the DIC method, it can be seen that the differences in displacement at individual points are in a significant range from 0.75 mm to 2 mm (See Table 3). These differences can be attributed to the different positions of the points relative to the loading force. The trend that can be seen from the measured data is an increase in values from the left side of the frame to the right side.

The FEM results for the displacement of the points range from a value of 0.93 mm to a value of 2.33 mm. Again, the trend of increasing displacement from left to right is confirmed here.

Table 3 Comparison of DIC and FEM methods

FEM		DIC	
Point	Displacement	Point	Displacement
T1	0.93	T1	0.97
T2	0.96	T2	1.04
T3	1.10	T3	1.13
T4	1.29	T4	1.22
T5	1.37	T5	1.33
T6	1.45	T6	1.4
T7	1.60	T7	1.52
T8	1.75	T8	1.60
T9	1.91	T9	1.69
T10	2.01	T10	1.78
T14	2.20	T14	2.14
T15	2.09	T15	2.13
T21	1.05	T21	0.80
T22	1.40	T22	0.85
T23	1.37	T23	1.20
T26	2.33	T26	1.91
T27	2.02	T27	1.72
T28	1.71	T28	1.56

7. CONCLUSION

The aim of the study was to evaluate the validity of the measured data using the DIC method. The validity of the measured data was verified by FEM calculation. The measured data from this method agreed in almost all observed aspects with the DIC method measurements. The variations in the measurements may be due to the articulation of the components. Specifically, the linkages between the frame and the stand. The measured data can be assessed as valid after describing these reasons for the deviations.

Overall measurements show that the frame structure is significantly oversized. The maximum achieved stress of 3.9 MPa with a material strength of 300 MPa is negligible. Therefore, I would suggest changing the frame geometry to reduce weight and strength, or changing the frame material while maintaining the 3D printing technology. As an option, I would suggest printing from plastic filament containing metal particles. This would address the heat dissipation needed while reducing the overall weight.

ACKNOWLEDGEMENT

Thanks are due to the department 632 for carrying out this work.

REFERENCES

[1] SABIK, A., M. RUCKA, A. ANDRZEJEWSKA a E. WOJTCZAK. Tensile failure study of 3D printed PLA using DIC technique and FEM analysis. : Mechanics of materials [online]. 2022, 2022, 2022(175), 12 [cit. 2023-04-29]. Dostupné z: https://www.sciencedirect.com/science/article/pii/S0167663622002708

[2] EL-AWADY, Khalid A., Steven LAVENSTEIN a Jaafar A. EL-AWADY. Three-dimensional surface displacement tracking for in-situ experiments: An alternative to digital image correlation (DIC). Scripta materialia [online]. 2023, 2023, 2023(224), 6 [cit. 2023-04-29]. Dostupné z: https://www.sciencedirect.com/science/article/pii/

[3] KANYILMAZ, Alper, Ali Gökhan DEMIR a Martina CHIERICI. Role of metal 3D printing to increase quality and resource-efficiency in the construction sector. Additive manufacturing2022 [online]. 2022, 2022(50), 17 [cit. 2023-04-29]. Dostupné z: https://www.sciencedirect.com/science/article/pii/S2214860421006886

[4] SHLYANNIKOV, V, D FEDOTOVA a R KHAMIDULLIN. Couple analysis of DIC and FEM to quantify strain fields and crack-flank displacements in structural materials under cyclic mixed-mode I/II fracture: Dostupné z: https://www.sciencedirect.com/science/article/pii/S2452321622006473. *Procedia Structural Integrity*. 2022, **2022**(42), 8.

COMPARISON OF PROPERTIES OF SLM MADE AND HOT ROLLED PLATE USING SPT METHOD

Author(s): [1,2]Jan KANDER, [1,2]Petr JONŠTA, [2]Šárka HERMANOVÁ, [2]Zdeněk KUBOŇ [2]Jana KOSŇOVSKÁ, [2]Gabriela ROŽNOVSKÁ, [2]Ondřej DORAZIL, [2]Petr ČÍŽEK

Supervisor: doc. Ing. Petr JONŠTA, Ph.D.

Department: [1]Faculty of Materials Science and Technology, VSB - Technical University of Ostrava

[2]MATERIAL AND METALLURGICAL RESEARCH Ltd., Pohraniční 693/31, Ostrava

Abstract

Additive manufacturing (3D printing) of metallic materials is relatively new technology with quickly increasing use. Although it is in interest of many researchers, there are still areas, which are not fully explored. One of those areas is behavior of large components processed by 3D printing. This work is focused on the study of material properties of additive manufactured large block made of AISI 316L steel in two heat treatment conditions (as-printed and solution annealed) and their comparison with properties of hot rolled plate. Mechanical tests were complemented by microstructural investigation and fractographic analysis of fracture surfaces. We found out that mechanical and long-term properties of 3D printed large block of this steel are excellent and well comparable with other published results.

Key words:

Additive manufacturing, steel AISI 316L, mechanical properties, small punch test.

1. INTRODUCTION

3D printing of metallic materials is one of the promising ways how to increase the competitiveness of companies in the engineering industry, especially in production of shape complicated parts. However, before companies include these innovative technologies in their product portfolio, designers in particular must know the properties of the parts produced this way and guarantee their conformity with standards. There are many types of additive manufacturing processes. One of them is metal powder bed fusion technology, as the International Committee ASTM F42 classified it and is included in the ISO/ASTM 52900:2015 [1] standard. Selective laser melting (SLM) as a part of the powder bed fusion was used to produce experimental material used in this work.

Selective laser melting is a technique, which uses a high-power density laser to melt and fuse metallic powders together [2]. This technology can be used for special production in aerospace or automotive components especially in cases where it is difficult to manufacture them by conventional techniques, it means at situations where it is economical and where the material properties are satisfactory.

As the principal advantage of SLM technology lies in producing small and complex products where the material properties cannot be tested by standardized test specimens it would be convenient to have another possibility to study mechanical properties either in the as-received state or even under operating conditions.

One way to test small size components is to use small punch test (SPT) method [3]. SPT is a progressive testing method of miniature test samples and is very often used for instance in nuclear and fossil fuel power plants for determining residual lifetime of the key pressurized parts. It is applied to determine the mechanism of failure and damage of the equipment too [4, 5]. There are many literature references and extensive and long-term experience with this method exploited in practice for wrought steels, but to the author's knowledge, there is only limited information about the use of this method for additive manufactured (3D printed) materials [6, 7, 8].

2. MATERIALS AND TESTING METHODS

The experimental material (3D printed steel) was a block printed out of austenitic stainless steel AISI 316L with dimension of printing base 15 mm x 280 mm and height 170 mm. The block of 3D printed steel was cut into two halves, the first stayed in as-printed condition (marked as 3D), the second half was solution annealed (marked as 3DS). Solution annealing was performed in a laboratory electric furnace at 1050 °C with 15 min soaking time followed by cooling in water. The comparative test material was hot rolled plate of AISI 316L steel with similar dimensions as 3D printed block and solution annealed at producer at 1050 °C and cooled in water. Chemical composition of printing powder, printed block and hot rolled plate can be seen in Table 1.

Table 1 Chemical composition of experimental material (wt.%). Source: (own)

Product	C	Mn	Si	P	S	Cu
Powder	≤ 0.03	≤ 2.00	≤ 1.00	≤ 0.045	≤ 0.030	-
3D	0.025	0.490	0.660	0.0160	0.0050	0.110
Plate	0.019	1.851	0.265	0.0372	0.0014	0.305

Table 1 – continued. Source: (own)

Product	Ni	Cr	Mo	V	O	N
Powder	10-14	16-18	2-3	-	≤ 0.10	≤ 0.10
3D	12.700	16.600	2.360	0.039	0.001	< 0.001
Plate	10.001	16.986	2.022	-	-	0.0298

Tensile tests were performed on MTS 500 kN test rig (speed 0.6 mm/min) at laboratory temperature and the tensile testing was carried out and evaluated in accordance with the standard EN ISO 6892-1. Sample were taken in both longitudinal (L) and transverse (T) direction to the printing base in samples 3D and 3DS and to the rolling direction in Plate sample. See Table 2 for results of tensile test on specimens sampled in lateral (L) and transverse (T) directions.

Table 2 Tensile test results. Source: (own)

Sample	Direction	$R_{p0.2}$ [MPa]	R_m [MPa]	A [%]	Z [%]
3D	**L**	557	690	46.5	59.5
	T	473	591	22.0	35.0
3DS	**L**	373	621	46.5	46.5
	T	352	532	22.5	30.5
Plate	**L**	259	644	79.0	80.5
	T	258	643	76.0	81.5

The principle of small punch test is penetration of a punch through the small disc specimen (diameter = 8 mm, thickness = 0.5 mm) that is clamped between the upper and lower die of the specimen holder in the testing device. During the test the values of force and displacement of the punch tip are recorded and a curve is plotted. The following characteristics can be determined from this curve:

- F_e – the elastic-plastic transition force in the small punch test which characterizes the transition from linearity to the stage connected with the development of plastic deformation through the whole thickness of the sample. This value corresponds to the yield strength in the conventional tensile test and it is defined as the point of intersection of two constructed tangents (one of initial stiffening and second of steady-state plastic stretching) (N).
- F_m – the maximum force during the test which corresponds to the load at the tensile strength in the conventional tensile test (N);
- u_m – the displacement of punch tip which corresponds to the maximum force Fm (mm).

This SPT data can then be translated into conventional tensile test data by correlating results of SPT and standard tensile test – see Eqs. (1) and (2) below [3]. All of the samples were taken from surface to better simulate real SPT sampling on working component. Results of small punch test are summarized in Table 3.

Relation between tensile test and SPT properties:

$$R_{p0.2} = \alpha \cdot \frac{F_e}{{h_0}^2} \quad \text{(MPa)} \tag{1}$$

$$R_m = \beta \cdot \frac{F_m}{h_0 \cdot u_m} \quad \text{(MPa)} \tag{2}$$

where:
$R_{p0.2}$ – proof stress (MPa)
R_m – ultimate strength (MPa)
F_e – elastic-plastic transition force (N)
h_0 – thickness of small disc specimen (mm)
u_m – displacement of punch tip (mm)
α, β – correlation coefficient

Table 3 SPT results. Source: (own)

Sample	$R_{p0.2}$ [MPa]	R_m [MPa]
3D	530	667
3DS	383	604
Plate	249	532

Figure 1 compares SEM micrographs of SPT specimens after the test procedure. It can be seen that the crack in hot rolled plate sample is circumferential, Fig. 1a, which is the usual behavior for most metallic materials. Whereas the SLM printed sample, Fig. 1b, has several branched cracks and point defects in several places. Figure 2 compares microstructure of the hot rolled plate (Fig. 2a) with the SLM printed sample (Fig. 2b). Microstructure of the plate is austenitic, while the SLM printed sample has multilayered structure with visible boundaries of individual passes and is more similar to a weld rather than to conventionally produced steel.

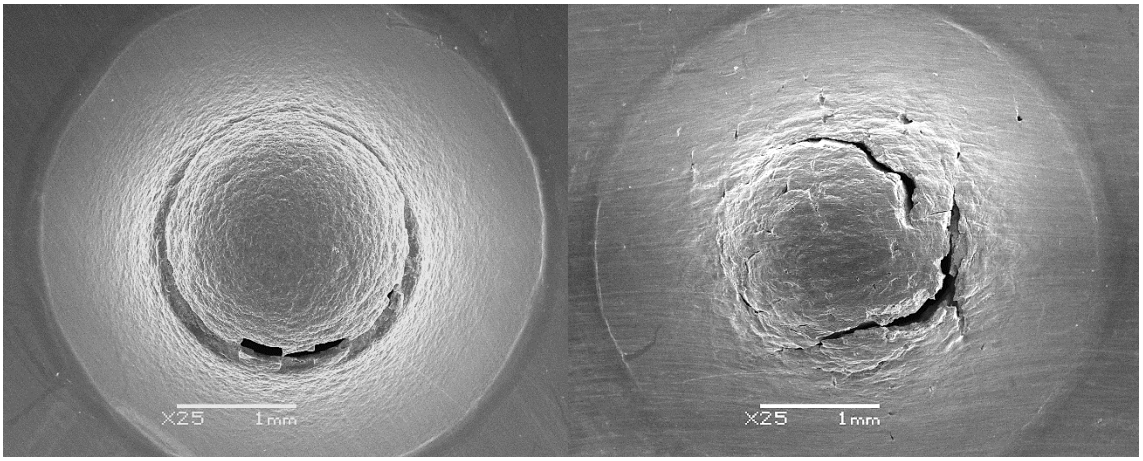

1a **1b**

Figure 1 Macroscopic crack morphology of plate (1a) and SLM printed sample (1b). Source: (own)

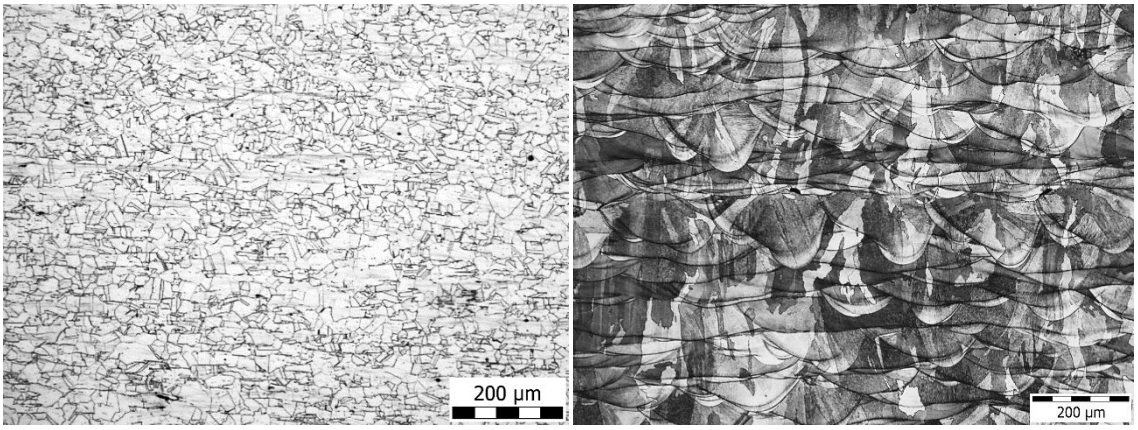

2a **2b**

Figure 2 Microstructure of plate (2a) and SLM printed sample (2b). Source: (own)

3. CONCLUSION

This paper summarizes results of the influence of additive manufacturing (SLM) on material properties of AISI 316L steel. The results are than compared to the plate of same size and steel grade made by conventional methods. The following conclusions can be made:

- The results of tensile testing at room temperature confirmed much higher yield stress of 3D printed material compared to hot rolled plate probably because of the much finer structure of the SLM sample, while the tensile strength remained more or less the same.
- Rapid cooling during of the sample during the SLM causes more residual stress (similar to welding), which leads to hardening that is accompanied by drop in elongation.
- Solution annealing in SLM sample led to decrease in yield stress, but was not followed by raise in ductility as expected.
- SPT confirmed the results gained from tensile test, which means such method can be used for evaluation of properties of additively manufactured parts

ACKNOWLEDGEMENT

This paper was created in the frame of the Institutional support for long-term and conceptual development of a research organization in 2023, provided by the Ministry of Industry and Trade of the Czech Republic.

REFERENCES

[1] ISO/ASTM 52900 Additive manufacturing - General principles – Terminology, 2017, ISO technical committees, Geneva, Switzerland.

[2] CHOO, H.; SHAMA, K.-L.; BOHLING, J.; NGOA, A.; XIAO, X.; RENB, Y.; DEPOND, F. D.; MATTHEWS, J. M.; GARLEA, E. *Effect of laser power on defect, texture, and microstructure of a laser powder bed fusion processed 316L stainless steel*, Materials and Design, 2019, Volume 164*,* pp. 107534.

[3] EN 10371 Metallic materials – Small punch test method, 2021, European Committee for Standardization, Brussels.

[4] LUCON, E.; BENZIG, J.; HRABE, N. *Testing of Small-Sized Specimens*. Comprehensive Materials Processing, 2014, Volume 1, pp. 135-163.

[5] KUBOŇ, Z.; STEJSKALOVÁ, Š.; KANDER, L. *Effect of Sigma Phase on Fracture Behavior of Steels and Weld Joints of Components in Power Industry Working at Supercritical Conditions*. In *Austenitic Stainless Steels - New Aspects*, 2017**;** Borek, W.; Tanski, T.; Brytan, Z. (Eds.); InTech: Rieka, Croatia, 2017, pp. 63-92, ISBN 978-953-51-3701-6.

[6] YU, J. M.; DAO, V. H.; YOON, K. B. *Investigation of creep behavior of 316L stainless steel produced by selective laser melting with various processing parameters*, Journal of Mechanical Science and Technology, 2020, Volume 34 (8), pp. 3249~3259.

[7] TORRES, J.; GORDON, A. Mechanics of the small punch test: a review and qualification of additive manufacturing materials, *Journal of Materials Science,* 2021**,** pp. 56. 1-38.

[8] CUESTA, I.I.; MARTÍNEZ-PAÑEDA E.; DÍAZ A.; ALEGRE J.M. *Cold Isostatic Pressing to Improve the Mechanical Performance of Additively Manufactured Metallic Components*, Materials, 2019, Volume 12, No.15, p.2495

THE EFFECT OF THE HEAT TREATMENT ON THE MICROSTRUCTURE AND FRACTURE SURFACES OF NITI ALLOY

Author(s): Michal KOPELENT

Supervisor: doc. Dr. Ing. Monika LOSERTOVÁ

Department: Department of Materials Engineering and Recycling, Faculty of Materials Science and Technology, VSB – Technical University of Ostrava

Abstract

The study was aimed at investigating how thermal treatment affects the microstructure, fracture characteristics and phase composition of a NiTi alloy containing 56.31 % Ni and 43.69 % Ti (wt. %). The samples were cut of 2 mm thick NiTi sheets and submitted to different thermal treatment that consisted of solution annealing at 850 °C for 1 hour followed by aging at 450 °C for 1 hour, or aging only at the same temperature and time for the as-received material condition, all steps being finished by water quenching. The material in four states, namely as-received, solution treated, solution treated and aged, and aged only, were tensile tested at a strain rate of $6.67 \cdot 10^{-5}$ s^{-1}. The microstructure of the specimens was studied using a transmission electron microscope. The fracture surfaces were evaluated by means of a scanning electron microscope. XRD analysis was used to estimate the phase composition.

Key words:

NiTi alloy, TEM, heat treatment, fracture surfaces, tensile test.

1. INTRODUCTION

The NiTi alloy is a material that can exist in three different states, each of which has a different set of characteristics and behaviors. The most important variable in this alloy is the temperature, which influences the presence of these states: martensite, superelastic austenite and stable austenite. Other alloy properties such as Young's modulus, specific heat capacity and electrical resistivity are also highly temperature dependent [1].

The main types of heat treatment of NiTi alloys include solution treatment and aging. Solution annealing homogenizes the structure and dissolves the precipitates, while aging may form lenticular Ni_4Ti_3 particles [2]. However, the Ni_4Ti_3 precipitates would begin to decompose into needle-shaped Ni_3Ti_2 and granular Ni_3Ti if aging was carried out at high temperatures (slightly below the solution treatment temperature) or for a long period of time, affecting the mechanical properties [3]. However, the formation of these precipitates has an adverse effect on the nickel content of the matrix, which leads to increasing of transformation temperatures. With regard to aging, it has been found that the volume fraction of precipitates is determined by the aging temperature, whereas their size is related to the duration of aging [4].

The fracture mechanisms of NiTi alloys have been the subject of several studies [5-6], providing information on fracture surface characteristics under different conditions. It has been concluded that in the absence of any macroscopic plastic deformation, the fracture surfaces of NiTi alloys have a quasi-cleavage character. In the case of superelastic austenite, there is a further increase in deformation due to the transformation of stress-induced martensite. This causes the fracture surface to have a quasi-cleavage rather than a pure cleavage character [7].

2. EXPERIMENT

The investigated material in this work was NiTi alloy in the form of 2 mm thick sheets with a chemical composition of 56.31 Ni and 43.69 Ti (wt. %) purchased from EdgeTech Industries LLC, USA. The sheets were cut into 250 mm x 10 mm strips by water jet cutting. The strips were then sampled for further testing. Selected samples were tested in the as-received condition, while others were subjected to heat treatment in a Linn HT1800 furnace in an argon atmosphere. The heat treatment consisted of

solution annealing at 850 °C for 1 h followed by aging at 450 °C for 1 h or aging only under the same conditions. Water quenching completed all heat treatments.

Cylinders with a diameter of 3 mm and a height of 2 mm were cut by electroerosion machining from the prepared strips in the as-received condition, but also after each heat treatment. The cylinders were then cut using a WS-25 high precision wire saw with a Siemens LOGO TDE electronic control unit and an abrasive suspension (SiC particles and glycerin) to produce thin specimens of approximately 0.4 mm thickness. Manual grinding of the samples using SiC paper with P1200 grid was used to achieve the required thickness of 0.1 mm. The samples prepared in this way were then electrolytically thinned to a thickness suitable for TEM observation. A Struers TenuPol-5 with an electrolyte consisting of 10% $HClO_4$ and 90% CH_3OH was used for sample thinning. The electropolishing parameters were chosen according to the literature [8]. They were subsequently adjusted as necessary to obtain the best surface quality. The following conditions were used for polishing 10 V, - 30 °C, and 30 mA. In order to avoid further etching, the polished samples were carefully immersed in distilled water. A STEM 1200X electron microscope at 120 kV was used to examine the samples prepared in this way.

The phases present in the structure have been determined by means of XRD analysis. Samples of 10mm x 10mm were prepared and ground with P1200 SiC paper to remove oxides from the surface for this analysis. The analysis of the samples was carried out using a Bruker D8 Advanced diffractometer equipped with a CuKα cathode. Experiments were performed with the following parameters: angle 30-110°, step size 0.025°, scan speed 3s/step in 2Θ.

A JEOL JSM-6490LV scanning electron microscope with an Oxford Inca X-act probe was used to examine the fracture surfaces.

3. RESULTS AND DISCUSSION

TEM ANALYSIS

Bright field TEM images of the NiTi sheet microstructure after different thermal treatments are shown in Figure 1. For the as-received samples, the dislocation structure associated with the rolling process was observed (Figure 1a). There was a very small amount of Ni_4Ti_3 particles with the size of about 1 μm. Unlike for the as-received state, the samples after solution treatment showed Ni_4Ti_3 precipitates of markedly smaller size. The assumption that these precipitates would dissolve during solution annealing under the given condition, has not been confirmed. As their size was probably too large to dissolve completely, a higher temperature or longer time of heat treatment would be required to completely dissolve the Ni_4Ti_3 precipitates.

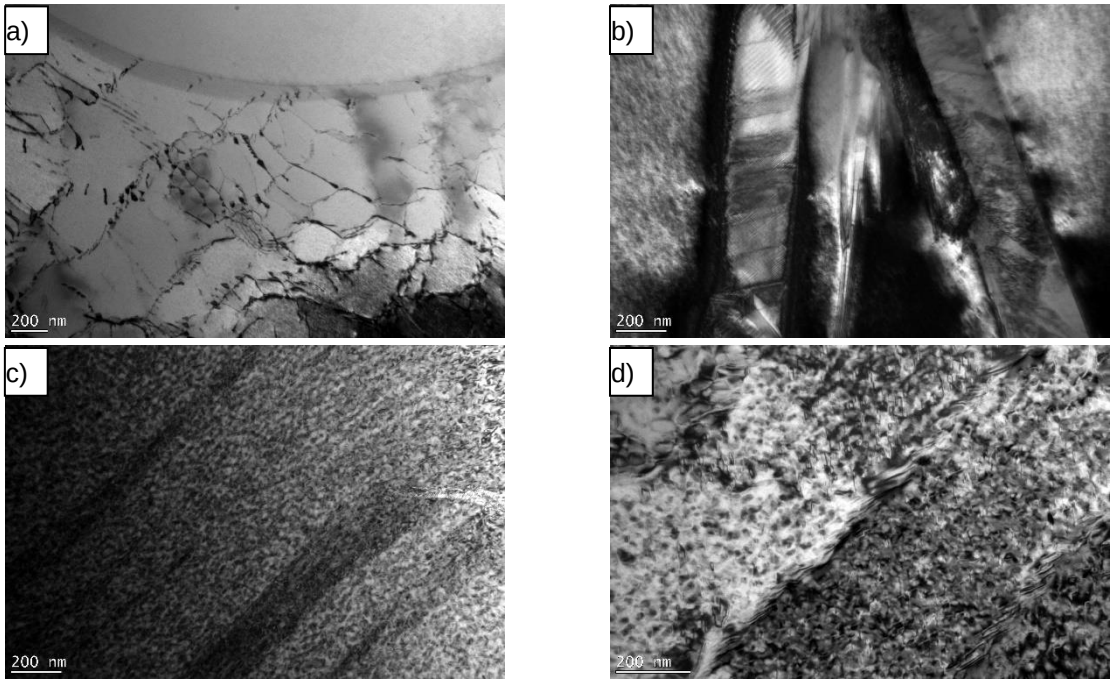

Figure 17 TEM images (bright field images) of microstructure of NiTi sheets after various thermal treatments, a) as-received, b) solution treated, c) solution treated and aged, d) aged.
Source: (own)

Martensitic needles observed in the structure were internally twinned, as can be seen in Figure 1b). On the other hand, Figure 1c) shows the microstructure of the solution treated and aged samples, which shows large amounts of Ni_4Ti_3 precipitates of nanoscale size. It is possible that the precipitates that were already detected in the as-received condition were partially dissolved during the solution treatment and were coarsened during the subsequent aging process. It has also been confirmed that aging of samples under certain conditions results in the formation of these precipitates [9]. As shown in Figure 1d), the structure of the aged samples contained a large amount of nanosized Ni_4Ti_3 precipitates. At the same time, a very small amount of the same precipitates with a much larger size were also observed. It is likely that as a result of the heat treatment the larger precipitates, which were also found in the as-received samples, have continued to grow. Therefore, aging promotes the growth of pre-existing precipitates while encouraging the formation of new precipitates that are homogeneously distributed throughout the sample structure.

FRACTURE SURFACES

The fracture surface of the specimen in the as-received condition consisted of a quasi-cleavage fracture with ductile dimples, brittle facets and local cracks. The fracture surface of the solution treated and aged specimen was characterized by reduced ductility and strength despite elasticity in the plateau region. The fracture surface corresponds to the phase composition of the sample. It consists of the R phase or martensite and $NiTi_2$ or Ni_4Ti_3 particles. The crack propagates easily and the fracture surface is rather flat with cleavage characteristics. Fracture facets reach lengths of up to 200 µm by widths of 50 µm with a river character and are largely oriented in a same direction. Sharp-edged structures were also present, probably associated with $NiTi_2$ particles or NiTi oxides. The fracture surface of the aged specimen is associated with the best super-elastic behavior of all the specimens tested in the tensile test. The surface has a rough surface, but cleavage with elongated quasi-cleavage facets. Sharp-edged structures have also been observed, which may be due to the presence of secondary phase particles. Ductile micro-dimples around the observed precipitates can also be seen among the quasi-cleavage facets.

XRD ANALYSIS

The presence of an austenitic matrix with a cubic lattice was revealed by the XRD spectrum for the sample in the as-received condition. The $NiTi_2$ and Ni_4Ti_3 precipitates were also evaluated. This is in agreement with the TEM analysis where these precipitates were detected.

An austenitic matrix with a cubic lattice, as in the as-received samples, was determined by XRD analysis of the samples after solution treatment. In a similar way, $NiTi_2$ precipitates were also detected here. The spectrum showed peaks for Ni_4Ti_3 precipitates. Only a small amount of these precipitates was seen in the structure by transmission electron microscopy. The hexagonal NiTi phase observed in the analysis may represent some variant of the martensite or R phase.

Similarly, XRD analysis revealed the same phases in the structure of the solution-treated and aged samples as in the solution-treated samples. There was an austenitic matrix with a cubic lattice, $NiTi_2$ precipitates and a hexagonal NiTi phase. Consistent with the TEM analysis, Ni_4Ti_3 precipitates were also detected.

The same phases as in the solution treated and aged samples were seen in the spectrum for the aged samples. In particular, it is an austenitic matrix with a cubic lattice, with $NiTi_2$ and Ni_4Ti_3 precipitates, and with a hexagonal phase. Hexagonal phase can be R-phase or a martensite variation [10].

4. CONCLUSIONS

The dislocation structure and small amount of Ni_4Ti_3 precipitates were detected in the as-received samples by TEM analysis. Ni_4Ti_3 precipitates were also detected in the solution treated samples. However, their size was smaller than in the as-received state due to the solution treatment process. After solution treatment and aging or only aging, a large amount of nanosized Ni_4Ti_3 precipitates was observed in the structure.

The quasi-cleavage character of the surfaces with facets, micro-dimples and local cracks was revealed by the fractographic study of all samples. The largest cleavage facets were observed in the solution treated and aged samples. This was consistent with brittle behavior in tensile tests. Sharp-edged structures observed can possibly be due secondary phase particles cracking. It can therefore be concluded that the solution treatment and aging process resulted in increased brittleness and a quasi-cleavage character of the fracture with large facets, as opposed to the more ductile aged samples.

The XRD analysis of the as-received samples revealed only the presence of the austenitic matrix, $NiTi_2$ and Ni_4Ti_3 precipitates, whereas the hexagonal phases were also detected in the solution treated samples, the solution treated and aged samples or the only aged samples.

ACKNOWLEDGEMENTS

This work has been realized in the framework of the following projects: FV40306 "Development of new implants for correction of angular pediatric deformities in sterile design", NU23-08-0043 "Additive manufacturing of NiTi alloys for applications in orthopedics and traumatology" and SGS SP2023/022 „Development of alternate ways for preparation of progressive materials and their processing".

REFERENCES

[1] WADOOD, Abdul. Brief Overview on Nitinol as Biomaterial. *Advances in Materials Science and Engineering* [online]. 2016, **2016**, 1-9 [cit. 2023-04-24]. ISSN 1687-8434. Available from: doi:10.1155/2016/4173138

[2] NAJI, Hojjat, Jafar KHALIL-ALLAFI and Vida KHALILI. Microstructural characterization and quantitative phase analysis of Ni-rich NiTi after stress assisted aging for long times using the Rietveld method. *Materials Chemistry and Physics* [online]. 2020, **241** [cit. 2023-04-24]. ISSN 02540584. Available from: doi:10.1016/j.matchemphys.2019.122317

[3] KAYA, I., H.E. KARACA, M. NAGASAKO and R. KAINUMA. Effects of aging temperature and aging time on the mechanism of martensitic transformation in nickel-rich NiTi shape memory alloys. *Materials Characterization* [online]. 2020, **159** [cit. 2023-04-24]. ISSN 10445803. Available from: doi:10.1016/j.matchar.2019.110034

[4] FAN, Q.C., Y.H. ZHANG, Y.Y. WANG, M.Y. SUN, Y.T. MENG, S.K. HUANG and Y.H. WEN. Influences of transformation behavior and precipitates on the deformation behavior of Ni-rich NiTi alloys. *Materials Science and Engineering: A* [online]. 2017, **700**, 269-280 [cit. 2023-04-24]. ISSN 09215093. Available from: doi:10.1016/j.msea.2017.05.107

[5] DI COCCO, V., F. IACOVIELLO, C. MALETTA and S. NATALI. Cyclic microstructural transitions and fracture micromechanisms in a near equiatomic NiTi alloy. *International Journal of Fatigue* [online]. 2014, **58**, 136-143 [cit. 2023-04-24]. ISSN 01421123. Available from: doi:10.1016/j.ijfatigue.2013.03.009

[6] MCKELVEY, A. L. and R. O. RITCHIE. Fatigue-crack growth behavior in the superelastic and shape-memory alloy nitinol. *Metallurgical and Materials Transactions A* [online]. 2001, **32**(13), 731-743 [cit. 2023-04-24]. ISSN 1073-5623. Available from: doi:10.1007/s11661-001-1008-7

[7] CHEN, J. H., G. Z. WANG and W. SUN. Investigation on the fracture behavior of shape memory alloy NiTi. *Metallurgical and Materials Transactions A* [online]. 2005, **36**(4), 941-955 [cit. 2023-04-24]. ISSN 1073-5623. Available from: doi:10.1007/s11661-005-0288-8

[8] SIBIREV, A., E. UBYIVOVK, S. BELYAEV and N. RESNINA. In situ transmission electron microscopy study of martensite boundaries movement on cooling and heating of the NiTi shape memory alloy. *Materials Letters* [online]. 2022, **319** [cit. 2023-03-11]. ISSN 0167577X. Available from: doi:10.1016/j.matlet.2022.132267

[9] YU, Hao, Ying QIU and Marcus L. YOUNG. Influence of Ni4Ti3 precipitate on pseudoelasticity of austenitic NiTi shape memory alloys deformed at high strain rate. *Materials Science and Engineering: A* [online]. 2021, **804** [cit. 2023-03-08]. ISSN 09215093. Available from: doi:10.1016/j.msea.2021.140753

[10] URBINA, C., S. DE LA FLOR, F. GISPERT-GUIRADO and F. FERRANDO. Quantitative XRD analysis of the evolution of the TiNi phase transformation behaviour in relation to thermal treatments. *Intermetallics* [online]. 2010, **18**(8), 1632-1641 [cit. 2023-05-14]. ISSN 09669795. Available from: doi:10.1016/j.intermet.2010.04.020

EXPERIMENTAL ASSESSMENT OF WELD RESIDUAL STRESSES IN DISSIMILAR METAL WELD OF REACTOR PRESSURE VESSEL NOZZLE

Author(s): Vratislav MAREŠ[1], Lukáš HORSÁK[1], Pierre DULIEU[2]

Supervisor: prof. Ing. Bohumír STRNADEL, DrSc.

Department: Center of advanced Innovation technologies, Faculty of Materials Science and Technology, VSB – Technical University of Ostrava[1]

Tractebel (ENGIE), B-1000 Brusels, Belgium[2]

Abstract

In the Pressurized Water Reactors, the Reactor Pressure Vessel (RPV) nozzle-to-safe-end Dissimilar Metal Welds (DMW) are made of nickel-base alloy 182. This material is known to be susceptible to Primary Water Stress Corrosion Cracking (PWSCC) if the stress level is high enough. In that frame, it is of utmost importance to precisely assess the residual welding stress field. For that purpose, residual stress measurements on a DMW from the cancelled nuclear power plant are performed with the hole-drilling strain gage method according to ASTM E837. The nozzle-to-safe-end specimen is successively sectioned (machined) from the outside to deduce the residual stress profile through the weld thickness. These plant specific residual stress profiles will be useful to assess the acceptability of flaws that could possibly be detected during In-Service Inspection campaigns and to define reasonable inspection intervals. Residual stress data can be used to plan and verify the residual life of power plant welds. Residual stress is not a single quantity that affects the service life, but it plays a significant role.

Key words:

Residual stress, dissimilar metal weld, hole drilling method, Reactor pressure vessel.

1. INTRODUCTION

Nuclear power plants (Westinghouse design), the reactor pressure vessel (RPV) nozzle-to safe-safe end Dissimilar Metal Welds (DMW) are made of nickel-based 182. This material is known to bee susceptible to the degradation processes. One of the most important degradation mechanisms is called Primary Water Stress Corrosion Cracking (PWSCC) when it is in contact with PWR primary water, if stress level in material is high enough. Although the risk of PWSCC initiation in these welds may be quite low, quantification of risk based on the literature data and manufacturing files of the concerned units remains difficult. Moreover, it is known that this degradation phenomenon is characterized by relatively long incubation periods [1].

Given that the Weld Residual Stresses (WRS) are known to have a major impact on the severity of PWSCC, their quantification is key to properly assess the propagation rate of a potential crack induced by PWSCC. In that frame, the work of Broussard [2] led to the definition of standardized through-wall distributions of dissimilar metal WRS, recently introduced in the ASME Code Case N-899 [2, 3].

The objective is to calculate plant-specific (and even nozzle-specific) WRS profiles that will feed damage tolerance analyses used to assess crack propagation rate and determine appropriate inspection intervals.

The paper presents research / experimental measurement of residual stress profiles in dissimilar weld joint. Based on the obtained results, a welding simulation can be performed, which can solve the impact of the properties on the weld. Subsequently, the thus obtained data from real results and simulation can be used to optimize welding methods, or improvement of the post-weld condition by subsequent post-weld heat treatments.

2. RESIDUAL STRESS

Residual stresses are "locked-in" stresses that exist in materials and structures, independent of the presence of any external loads. The stresses are self-equilibrating, that is, local areas of tensile and compressive stresses sum to create zero force and moment resultants within the whole volume of the material or structure [4].

Knowledge of the magnitude of the residual stresses arises from the need of optimization and design of components. Residual stress together with the operating load significantly affect the overall stress of the component and thus the service life and operational reliability of the entire component. Residual stress analysis has an unforgettable role in diagnostics and the same importance as other methods of determining the physical properties of the material.

Residual stress can be categorized into 3 types according to affecting its volume: I macroscopic (interaction of the whole volume of the component), II microscopic (interaction of grains), III submicroscopic (interaction of dislocations) [4].

3. DISSIMILAR METAL WELD RESIDUAL STRESS MEASUREMENT

Two methods were chosen to measure of the residual stress. The first of these methods was the cutting method, which was selected as an additional analyzing the residual stress of type I.

As the second method for measuring the residual stress, a hole drilling method was chosen that allows the measurement of stresses of type II, which cause small macroscopic changes.

As mentioned above, the hole drilling method [5] was chosen as the main method for the analysis of residual stresses in the weld metal. The hole drilling method for determining residual stresses is one of the mechanical, semi-destructive methods. Residual deformations are released when the integrity is disturbed by drilling a small hole in the surface of the part. These deformations are measured by a strain gauge rosette, which is installed on the surface of the structure. The rosette consists of three resistance strain gauges and a hole is drilled at the intersection of their axes. Drilling is performed step by step and at the end of each step the measured deformations are measured. In this way, a distribution of residual deformations at a given depth to a certain depth below the surface of the part is obtained. These obtained deformations are then evaluated according to various theories, based on which the distribution of residual stresses at a given location is determined [5].

Specimen preparation

Prior to the realization of residual stress measurement, was the weld extracted from NPP which has never been operated (not irradiated). The initial block (top left of Figure 1) was cut circumferentially from both sides to isolate segment with the concerned weld (bottom left of Figure 1). Then, four axial cuts were performed to end up with four specimens of a quarter circumference. For residual stress measurement by hole drilling were used only two specimens with quarter circumference. As shown at the right side of Figure 1, strain gauges have been used to assess the circumferential stress release due to axial cutting (I type, macroscopic circumferential residual stress). This release was only notable after the first axial cut but remained negligible compared to the actual residual stresses measured through the thickness in the next steps.

Figure 1 Specimen machining form reactor nozzle. Source: (own)

Hole drilling method

The hole-drilling strain gage method was used. It involves attaching a strain rosette to the surface drilling a hole at the geometric center of the rosette and measuring the resulting relieved strain. This operation is repeated several times after machining the component layer by layer to obtain the distribution through the thickness.

The integral method proposed by G.S. Schajer [4] allows the residual stresses through the thickness of a workpiece to be calculated selecting the number and the distribution of the depth increments, whereas these parameters are defined and fixed in the ASTM E837-13a standard [5, 6] for

non-uniform stress fields. This method provides a separate residual stress analysis at every hole drilling depth increment. It has been selected as residual stresses are expected to vary significantly with depth. Measurement was carried out by the automatic system for hole drilling MTS 3000 – Restan. Evaluation was carried out by the software for measuring residual stress by the hole drilling method EVAL from SINT Technology and using Matlab software [7].

Integral method provides a separate residual stress analysis at every hole drilling depth increment. The integral method should be chosen when residual stresses are expected to vary significantly with depth; however, it also has the highest sensitivity to test errors. This problem quickly gets worse when you try to raise the spatial resolution increasing the depth increments. This method is often described in technical literature. It is applied for determination of residual stresses in the depth of the hole, especially in locations where the stress along hole depth varies due to different specimen thickness [6]. Due to the limited scope and relatively high complexity of the calculations, the calculation equations are not presented here. Source: [8, 9, 10]

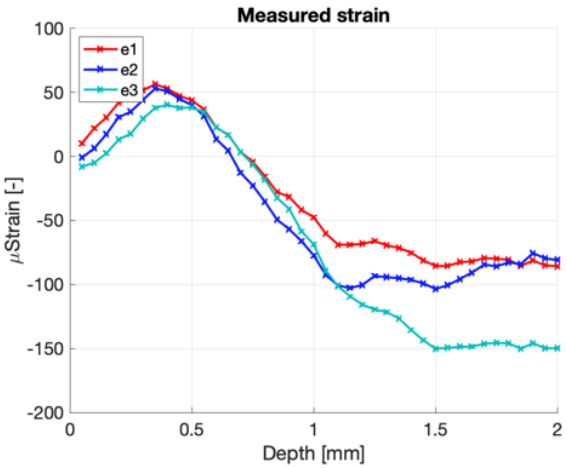

Figure 2 Measured strain at level 1. Source: (own)

Experimental results

The measurements were performed in two circumferential locations (two specimen) and along two profiles through the thickness (path A&B), yielding four profiles for axial stress and four for circumferential stresses. Measurements are first performed at the OD (level 1) and at the ID (level 8). Specimen is then sectioned (machined) from the outside over 10.7mm deep to reach next level of measurement. Before placement of strain gauge rose was surface etched for best focus. Figure 3 shows the two profiles A and B and the eight locations through the thickness where the measurement was performed. Some levels of the machining are also illustrated.

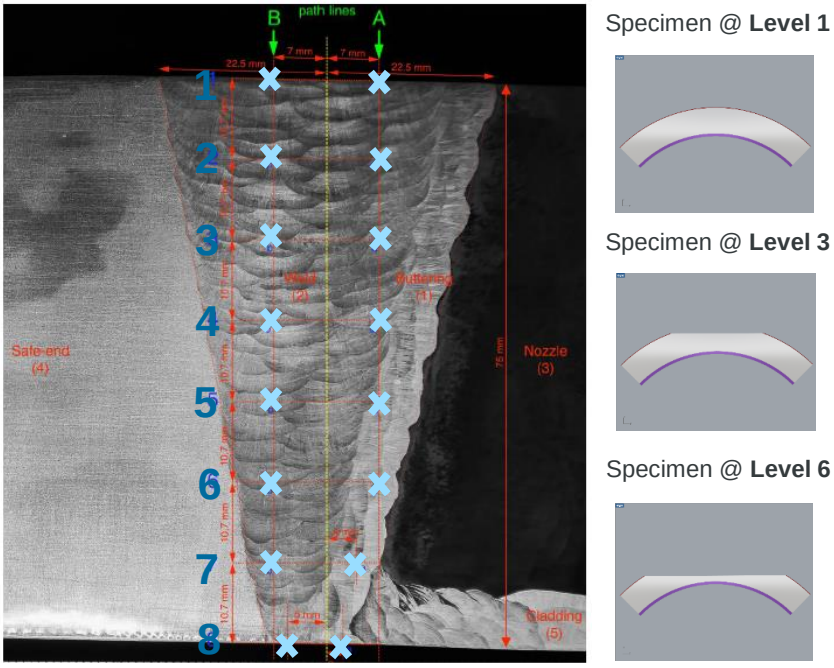

Figure 3 Position of WRS measurement. Source: (own)

4. CONCLUSION

The residual stresses (principal stress or axial/hoop stress) are then derived from the measured strains by the integral method, assuming an isotropic linear elastic material. The processed measured results are shown in Figure 3, which shows the axial and circumferential (hoop) stress curves.

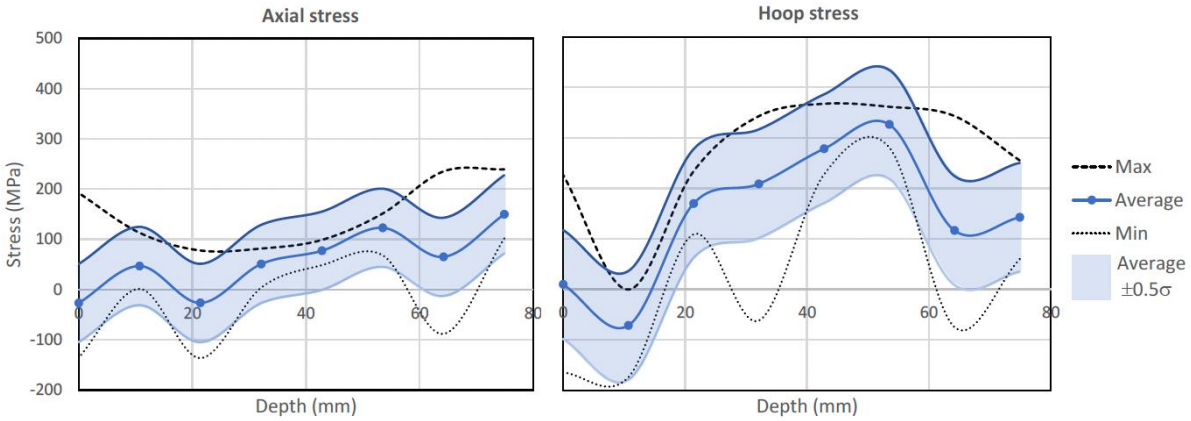

Figure 3 Weld residual stresses measured by drilling method. Source: [6]

The maximum and minimum stress measured at each depth are given in Figure 3 [6], reflecting a significant variability between the results along the profiles. This variability is illustrated by the average value (of the two paths A and B for the two specimen) with related uncertainty area derived from overall standard deviation σ. As it is generally the case for weld residual stresses, the level of hoop stresses is found to be higher than axial stresses. There is a small part of the thickness in compression at the inside surface, for axial as well as for hoop stresses. Given that these measurements include the potential effect of the successive cutting/machining operations on the weld residual stresses, these profiles are not to be used as such for flaw analyses. Residual stress data can be used to plan and verify the residual life of power plant welds. Residual stress is not a single quantity that affects the service life, but it plays a significant role. It would be interesting to compare the measured results with the simulations.

ACKNOWLEDGEMENT

This paper was elaborated as part of the project No. CZ.02.1.01/0.0/0.0/17_048/0007373 "Damage Prediction of Structural Materials" within the Research, Development and Education Operational Programme financed by the European Union and from the state budget of the Czech Republic.

REFERENCES

[1] Hickling, J., "*Materials Reliability Program: Resistance to Primary Water Stress Corrosion Cracking of Alloy 690 in Pressurized Water Reactors* (MRP-258)", EPRI, 2009.
[2] Broussard, J., *"Standardized Through-Wall Distributions of Dissimilar Metal Weld Residual Stress*," Proceedings of the ASME 2015 Pressure Vessels & Piping Conference, Paper PVP2015-45950.
[3] ASME Case N-899, *Weld Residual Stress Distributions for Piping and Vessel Nozzle Butt Welds Fabricated With UNS N06082, UNSW86182, UNS N06052, or UNS W86152 Weld Filler Material*, Section XI, Division 1.
[4] Schajer, G.S., "*Measurement of Non-Uniform Residual Stresses Using the Hole-Drilling Method*. *Part II. Practical Application of the Integral Method*", ASME Journal of Engineering Materials and Technology, Vol. 110, No. 4, pp. 344-349, 1988.
[5] W. Jiang, Y. Luo, J. H. Li, W. Woo, "*Residual Stress Distribution in a Dissimilar Weld Joint by Experimental and Simulation Study*", Journal of Pressure Vessel Technology, Feb 2017, Vol. 139 / 011402-1X.
[6] Dulieu P., Lacroix, Mareš, V, et al., *Experimental and numerical assement of weld residual stress in dissimilar metal weld of reactor pressure vessel nozzles*, Proceeedings of the ASME 2022, Presure Vesels & Piping Conference PVP 2022, July 17-22, 2022, Las Vegas, Nevada, USA
[7] ASTM E837-13a, *Standard Test Method for Determining Residual Stresses by the Hole-Drilling Strain-Gage Method*.
[8] EVAL software for measuring residual stress by the hole drilling method (EVAL back calculation software manual) MTS3000- Restan, SINT Technology.
[9] Hoffmann K., *An Introduction to Measurements using Strain Gages*, Hottinger Baldwin Messtechnik GmbH, 1989, Alsbach, Federal Republic of Germany.
[10] G. Totten, M. Howes, T. *Inoue, Handbook of Residual Stress and Deformation of Steel*, ASM International, 2002, Pages: 499, ISBN: 978-0-87170-729-1

MICROSTRUCTURAL EVOLUTION AND PRECIPITATION BEHAVIOR IN HR3C AUSTENITIC HEAT-RESISTANT STEEL AT 650 °C

Author(s): Renáta PALUPČÍKOVÁ

Supervisor: prof. Ing. Vlastimil VODÁREK, CSc.

Department: Department of Material Engineering and Recycling, Faculty of Materials Science and Technology, VSB – Technical University of Ostrava

Abstract

This study investigates the microstructural evolution and precipitation behaviour of HR3C austenitic refractory steel used in ultra-supercritical boilers. Prolonged exposure to high temperatures leads to significant microstructural changes and precipitate formation. At grain boundaries, weakening occurs due to precipitation of intergranular carbides, while within the grains precipitation initially increases the resistance to high-temperature creep. However, as the precipitates coarsen, their effectiveness decreases. Coherent twin substructures gradually disappear, while incoherent twins persist and contribute to the propagation of intergranular cracks during creep. The presence of various minority phases, including σ-phase, $M_{23}C_6$, NbN and modified Z-phase, is confirmed by microscopic techniques. The modified Z-phase particles, containing a small amount of vanadium, show a plate-like morphology. Thermodynamic modelling predicts a solvus temperature of approximately 1200 °C for the modified Z-phase. This study provides insights into the microstructural characteristics and precipitation behaviour of HR3C steel at long-term exposure to 650 °C.

Key words:

Austenitic steel, high temperature, precipitation, long-term annealing, Z-phase.

1. Introduction

Modern thermal power plants demand increased efficiency while also meeting rising environmental standards for emission reduction. The utilization of supercritical steam parameters allows for achieving power unit efficiencies above 45%. In recent years, high-strength austenitic heat-resistant steels like HR3C have been extensively employed in the construction of ultra-supercritical (USC) boilers, serving as superheater and reheater tubes for new power stations [1].

HR3C, an austenitic heat-resistant steel, was developed by incorporating nitrogen and niobium into the 310-type stainless steel, specifically for these applications. After long-term creep or service exposure, the microstructure undergoes significant changes, accompanied by the subsequent appearance of various types of precipitates [2;3]. Austenitic steels are known to contain multiple types of precipitates, such as $M_{23}C_6$, MX, Z-Phase, σ phase, and Cu-rich phase, which form during final long-term thermal exposure, heat treatment, or extended exposure to creep conditions. The formation of specific precipitates depends on the composition of the austenite, processing methods, and the history of high-temperature exposure [1].

The $M_{23}C_6$ carbide, which is a metastable phase, tends to precipitate preferentially at the grain boundaries during the early stages of service exposure [2]. Zhang et al. discovered that the growth and coarsening of $M_{23}C_6$ at the grain boundaries increase the probability of intergranular cracking [3]. The presence of the Fe-Cr type σ-face significantly reduces the plasticity, toughness, and corrosion resistance of heat-resistant steel after prolonged service. The precipitation of the σ-phase typically occurs at grain boundaries, as reported by [2]. However, there has been limited research addressing the nucleation and growth mechanism of phases within the grain, especially the conditions for Z-phase (secondary NbCrN) formation. According to several previous studies, researchers reported that the Z-phase forms from MX precipitates, while Robinson and Jack [4] suggested Z-phase formation from a solid solution [2].

This study focuses on the precipitation behaviour during long-term annealing at 650 °C. Observations were performed using optical microscopy, SEM, and TEM analysis. Attention was also given to the influence of vanadium on the solvus temperature of the Z-phase, for which thermodynamic modeling using the Thermo-Calc software (TCFE8 database) was used.

2. Experimental Material and Methods

The chemical composition of industrial heat of HR3C steel is presented in Table 1, revealing the presence of a small amount of vanadium. To investigate the impact of thermal exposure on the characteristics of the Z-phase, a solution annealing process was conducted on a tube with dimensions ϕ42.8 × 6 mm at a temperature of 1250 °C for a duration of 2 minutes. The subsequent analysis focused on a sample that underwent annealing at 650 °C for a duration of 8600 hours, examining the effect of elevated temperature on precipitation.

For the identification of minor phases in the austenitic steels under study, scanning electron microscopy (SEM) and transmission electron microscopy (TEM) was used. Extraction carbon replicates were used for electron microscopy examination, which was performed with a JEOL JEM 2100 microscope equipped with an INCA EDX system.

Table 4 Chemical composition of austenitic steel HR3C [wt. %]. Source: (own)

C	S	Mn	Si	P	Cu	Cr	Ni	Mo	Nb	V	N
0.05	0.003	1.18	0.37	0.013	0.06	25.27	20.17	0.17	0.45	0.032	0.256

Thermocalc software was used for prediction of equilibrium minor phases in the steel investigated. Attention was paid to the effect of vanadium in the modified Z-phase on the solvus temperature of this phase in austenite.

3. Results

As is well known, a critical aspect of microstructural stability in the precipitation strengthened steels for heat-resistant applications is the formation of secondary phases in the steel during long term high temperature service [3]. Figure 1 shows a comparison of the microstructure of the sample at as-received state and after long-term exposure, from this comparison, there was a significant increase in the etchability of the grain boundaries. There was significant precipitation along the austenitic grain boundaries. Chains within the grains were identified as primary Z-phase particles. Figure 1c documents a detail of the microstructure of the sample after long-term exposure obtained using a scanning electron microscope. In this image, there is evidence of significant σ-phase precipitation along grain boundaries, which formed a nearly continuous layer, and at the same time there is significant precipitation within the grain and near the grain boundaries. The intra-grain precipitates were identified as Cr-rich $M_{23}C_6$ precipitates, later confirmed by TEM analysis.

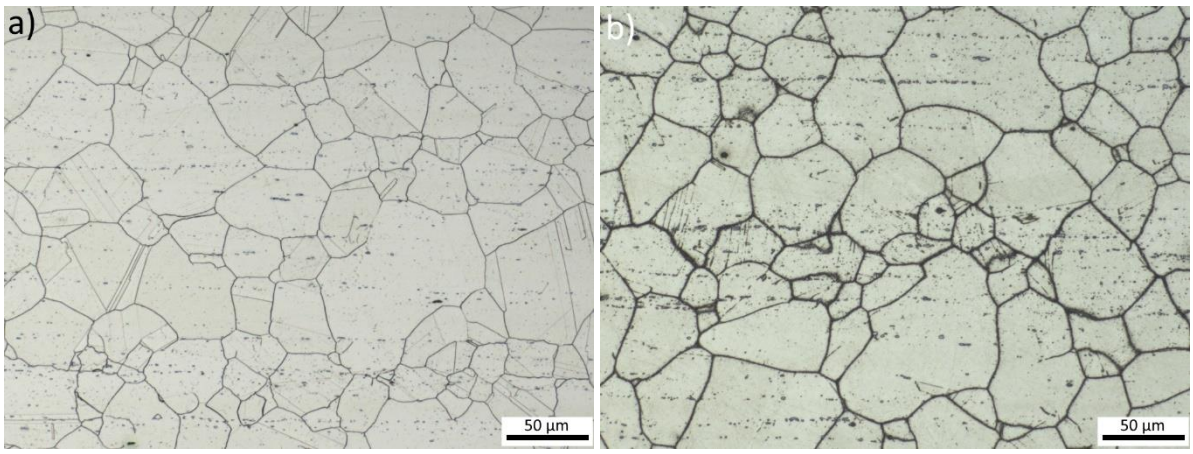

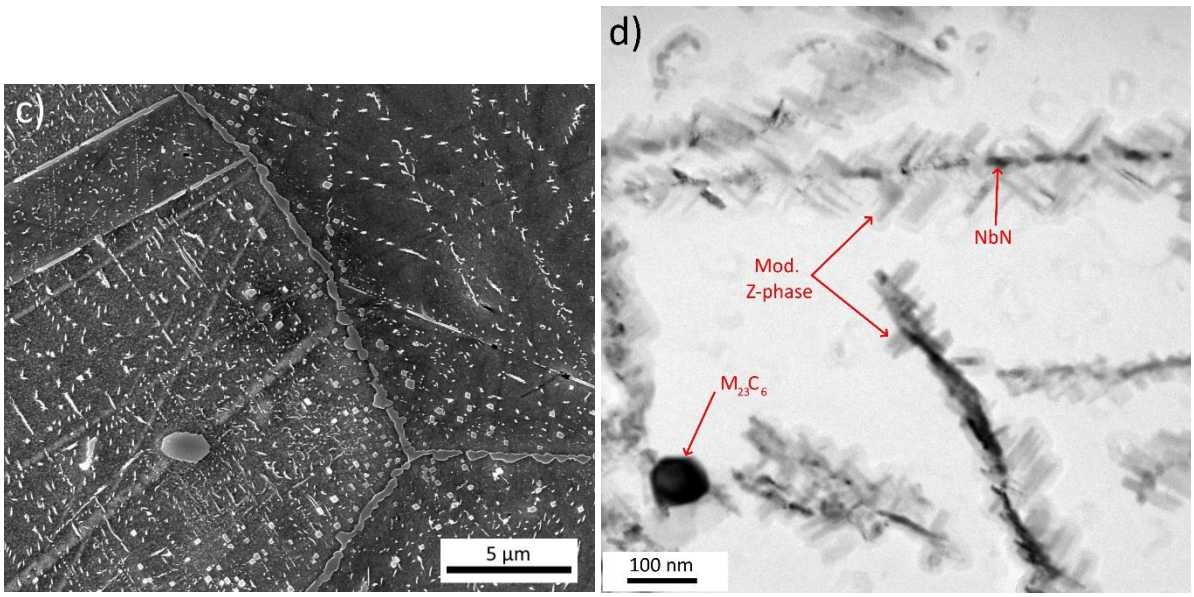

Figure 18 Micrographs of HR3C a) at as-received state, optical microscope; [own] b) after 8600 hours at 650 °C, optical microscope; [own] c) detail of grain boundary with layer of σ-phase, SEM, secondary electrons [own]; d) precipitation of modified Z- phase on NbN particles; TEM: Source: (own)

The precipitation strengthening depends on the number and size of precipitates in the matrix. In order to explore detailed characteristics of the precipitates in the matrix, carbon replicas were observed by TEM. Figure 1d shows TEM micrographs of the sample. It demonstrates very fine and dispersive precipitates in the matrix.

TEM investigations revealed several minor phases in the HR3C steel, including the σ-phase, $M_{23}C_6$, NbN, and the modified Z-phase. Notably, Figure 1d illustrates the presence of modified Z-phase particles in the form of thin plates, which originated from nucleation on NbN particles along dislocations. Li et al. [5] previously reported this mechanism for Z-phase formation in a 25Cr-20Ni-Nb-N austenitic stainless steel. The gradual dissolution of NbN particles provides the necessary niobium and nitrogen for the growth of NbCrN particles, facilitating the relatively rapid development of modified Z-phase particles. In Figure 1d, the typical length of Z-phase particles ranged from 50 to 100 nm. The distribution of modified Z-phase particles within the austenitic grains exhibited significant heterogeneity, forming clusters of thin plates arranged side by side along dislocations. Z-phase is a typical precipitate with a tetragonal structure with a = 0.3073 nm and b = 0.7391 nm, which has a strong hardening effect on the performance of the HR3C steel [2]. The fine dispersion of the Z-phase can pin dislocations and increase the strength [6].

EDX investigations confirmed that due to a small amount of vanadium in the HR3C steel, particles of the Z-phase contained some vanadium. As evident from Table 2, the average content of vanadium in the modified Z-phase was approximately 3 at.%.

Table 5 . Results of semiquantitative EDX analyses of the modified Z-phase in the HR3C steel (at.%). Source: (own)

V	Cr	Fe	Nb	Mo
3.2 ± 1.3	51.0 ± 1.2	2.9 ± 0.9	38.6 ± 4.3	4.3 ± 2.7

Results of the thermodynamic modelling of the solvus temperature of the modified Z-phase ((Nb,V)CrN) in the HR3C steel are shown in Figure 2a. The solvus temperature is approximately 1200 °C. The MX (NbN) phase is predicted as a stable nitride above 1050 °C. For comparison, here is also the result of thermodynamic modelling of the solvus temperature of the Z-phase (NbCrN), Fig. 2b. From this comparison it can be seen that the Z-phase without vanadium addition has a slightly lower solvus temperature of approximately 1180 °C. For the MX phase, the temperature was also reduced to 1015 °C. Nevertheless, it is a very stable phase. From TEM observations, it is evident that the modified Z-

phase particles nucleated on NbN (MX) particles, the gradual dissolution of which supplied the necessary niobium and nitrogen for its growth.

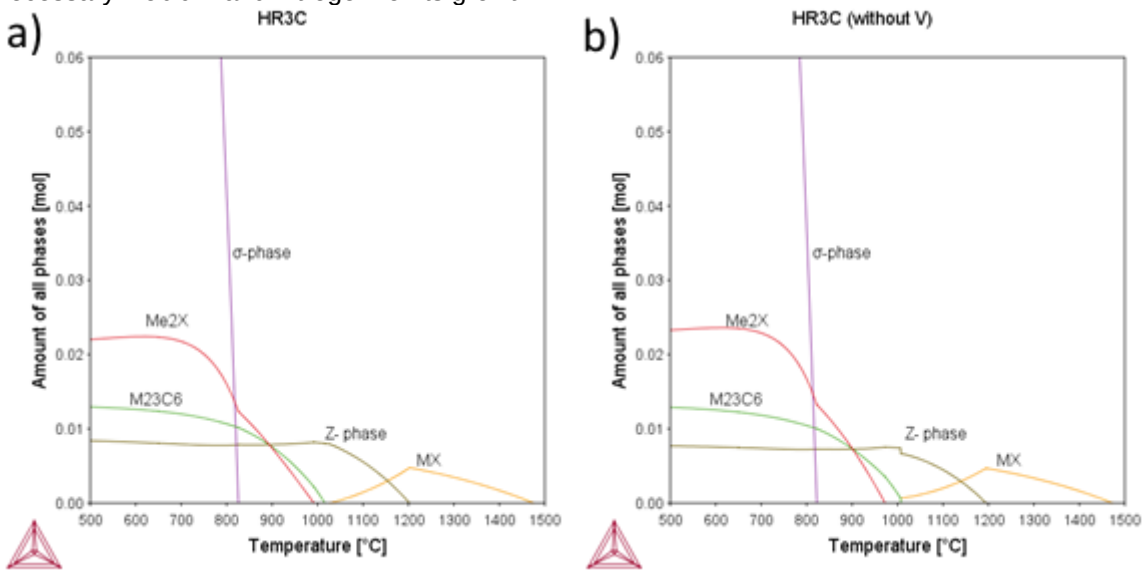

Figure 19 Thermo-Calc simulation of the amount of equilibrium phases on temperature for HR3C steel a) with 0.03 wt. % of vanadium; [own] b) without vanadium. Source: (own)

4. CONCLUSION

The study on HR3C austenitic heat-resistant steel has provided valuable insights into the microstructural changes and precipitation behaviour under long-term high-temperature exposure. The formation of various types of precipitates, including $M_{23}C_6$, NbN, Z-Phase, and σ-phase has been observed. Particles of modified Z-phase nucleated on NbN particles. The Z-phase particles nucleated on NbN particles. The NbN particles, by their gradual dissolution, provided the niobium and nitrogen required for Z-phase growth. The presence of a small residual vanadium content (0.03 at.%) in HR3C steel played a significant role in the precipitation of the modified Z-phase. The particles of modified Z-phase were determined to contain approximately 3 at.% vanadium. Thermo-Calc simulation showed that the solvus temperature of the Z-phase in HR3C steel was estimated to be approximately 1200 °C, while the solvus temperature without vanadium content was predicted to be 1180 °C.

ACKNOWLEDGEMENT

This article was created with the contribution of the Student grant competition project "SP2023/049 The influence of production parameters and operating conditions on the microstructure and utility properties of metallic materials" and with financial support from the project no. 00424/2022/RRC funded by the Moravian–Silesian Region "Support for gifted students of doctoral studies at VŠB-TUO".

REFERENCES

[1] HU, Zheng-Fei, Zhen ZHANG. Investigation the effect of precipitating characteristics on the creep behavior of HR3C austenitic steel at 650 ℃. Materials Science and Engineering: A. 2019, **742**, 451–463. ISSN 0921-5093. DOI: 10.1016/j.msea.2018.10.124

[2] XU, Liming et al. Precipitation Evolution in the Austenitic Heat-Resistant Steel HR3C upon Creep at 700 °C and 750 °C. Materials. Multidisciplinary Digital Publishing Institute, 2022, **15** (13), 4704. ISSN 1996-1944. DOI: 10.3390/ma15134704

[3] ZHANG, Zhen et al. Microstructure evolution in HR3C austenitic steel during long-term creep at 650°C. Materials Science and Engineering: A. 2017, **681**, 74–84. ISSN 0921-5093. DOI: 10.1016/j.msea.2016.10.077

[4] P.W. Robinson, D.H. Jack, Proc. New Developments in Stainless Steel Technology, in: R. Lula (Ed.), ASM, Material Park, OH, 1985, pp. 71–76.

[5] YANNO, Li; Yongchang, Liu; Chenxi, Liu; Chong, Li; Huijun, Li. Mechanism for the formation of the of Z-phase in 25Cr-20Ni-Nb-N austenitic stainless steel. *Mater. Lett.* 2018, ***233***, 16–19.

[6] GOLAŃSKI, Grzegorz et al. The Effect of Service on Microstructure and Mechanical Properties of HR3C Heat-Resistant Austenitic Stainless Steel. *Materials*. Multidisciplinary Digital Publishing Institute, 2020, **13** (6), 1297. ISSN 1996-1944. DOI: 10.3390/ma13061297

RESEARCH ON A JOINT COMBINING ADHESIVE AND SELF-PIERCING RIVET

Author(s): Petr SEHNOUTKA, Marek BESEDA, Filip HAVLÍČEK

Supervisor: doc. Ing. Kateřina SKOTNICOVÁ, Ph.D.

Department: Department of Materials and Technologies for Vehicles, Faculty of Materials Science and Technology, VSB – Technical University of Ostrava

Abstract

The paper focuses on the research of the effect of the combination of riveting and bonding together on the strength of a shear-loaded joint. The joint was prepared from aluminium alloy sheets EN AW 5083 bonded with a 5.3x80 semi-hollow rivet and 3M DP 460 NS adhesive. The prepared specimens were subjected to shear testing. The results were compared with the values of the bonding and riveting alone. Tensile loading showed stiff behaviour of the bonded joint and rather plastic behaviour of the riveted joint. The synergistic effect of both types of joints was not achieved and the overall strength of the joint copied the values of the individual components.

Key words:

Adhesive, Bonding, Semi-hollow rivet, Sheet metal joints.

1. INTRODUCTION

Joining thin materials is a long-standing problem. Joining by welding can be unsuitable as it creates heat-affected areas [1]. Riveting or bonding methods are gaining in popularity. These are effective methods of joining structures, particularly suitable for joining materials with different chemical compositions. These methods are mainly used in aerospace construction or advanced automotive design, where many applications of aluminium alloys and composites are used. Riveting [2] is also used in fully automated plants where various types of special rivets find their application. Bonding is then widespread in aluminium alloy and composite structures, although it is more time-consuming, it provides high strength at low weight and does not damage the material by additional holes. Technological times in curing the adhesive tend to be a significant complication in production, especially for more complicated assemblies. The bonded assembly must be fixed for a period of time before the adhesive reaches full strength. The use of a combination of adhesive and form-fit joints can save time in production, where the rivets joint the assembly together and can be worked on while the adhesive has not yet reached full strength. The adhesive will not fully cure until the assembly is complete and fixed in the fixture.

2. EXPERIMENT

Realization of samples

Three sets of samples were made for the experiment. The first set (A) was to test the strength of the adhesive alone, the second set (B) was to test the strength of the riveted joint and the last set (C) was a combination of both. The material to be bonded was a 3mm thick sheet of EN AW 5083 aluminium alloy with a size of 100×25 mm, of which an area of 25×25 mm is intended as an overlap for bonding (see Figure 1). This area is larger than the standard bonded lap joint tests, due to the addition of a rivet. The surface to be bonded was chemically cleaned and then bonded. In the case of the combination joint, riveting was done before the adhesive was fully cured.

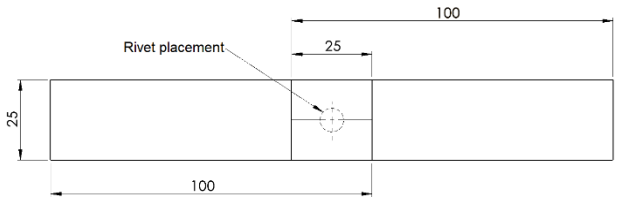

Figure 1 Dimensions of the specimen. Source: (own)

The 3mm aluminium alloy sheet EN AW 5083 was waterjet cut, the edges blunted and cleaned by immersion in organic solvent, then dried with paper towel. Thus, the surface of the rolled sheet was bonded cleanly without roughness treatment. The modification of surface roughness for bonding and its effect on the joint is reported in other studies [3][4].

Bonding

The bonded samples were coated with 3M DP 460 NS two-component epoxy adhesive, which is mixed directly after extrusion from the tube at a volume ratio of 2:1. The samples are then cured in the fixture for 48 hours.

Riveting

A special self-piercing rivet technology was used to rivet the sheets, where the material to be joined is reshaped to form a shape lock between the layers. This technology is designed for the mass production of bodywork. The rivet and its forming die are designed for a given combination of sheets and require a certain ductility of the materials to be joined. For joining 2×3mm sheets, a rivet size SPR 5.30×8.00 was selected, from the equipment manufacturer's recommended press parameters:

Pressing force: 55 kN; Clamping force: 2155 N, Pressing speed: 120mm/s.

Manufacturer's declared joint strength: 9200N in shear, 3600N in tension.

(Data is based on communication with the supplier TOX® PRESSOTECHNIK [5])

The hybrid joint samples were riveted shortly after the adhesive was applied, before it could cure. Figure 2 shows a section of the hybrid joint with both adhesive and rivet. It can be observed that the gap for the adhesive around the rivet is reduced to a minimum, the adhesive has probably been pushed into the surrounding area.

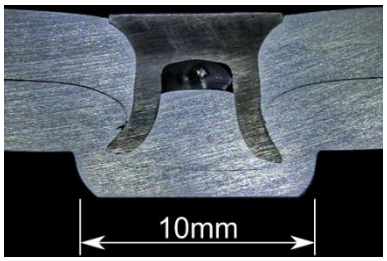

Figure 2 Semi-hollow rivet cross-cut. Source: (own)

Measurement procedure

The tensile loading of the specimens was carried out on an LFV 100 kN tearing machine from Walter+bai ag. The clamping is hydraulic and the specimens were supported at the ends to make the load coaxial. The loading was carried out at a speed of 5mm.min^{-1}.

3. RESULTS AND DISCUSSION

Figure 3 shows the first set (A) of bonded specimens tested. The characteristic below 7kN is identical and nearly linear for all specimens. The significantly different shear strength values can be attributed to the non-constant amount of adhesive in the joint and the lack of surface treatment before adhesive was applied. The failure in adhesion to the base material was evident in the specimens.

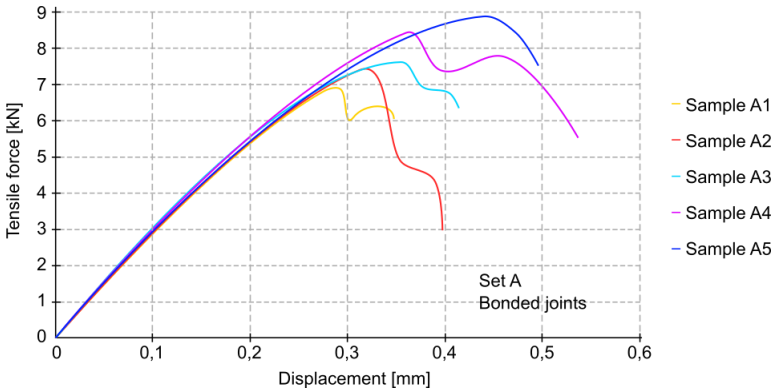

Figure 3 Shear stress on the bonded joint. Source: (own)

The second set tested was a purely riveted joint, the elongation characteristic under shear stress corresponds to the plastic properties of the aluminium alloy (see Figure 4). The riveted joint exerts a local load on the material to be joined and plastically reshapes it. However, even after considerable loading, the joint retains some residual strength and does not loosen. A curve of the bonded joint is also added to the graph for comparison.

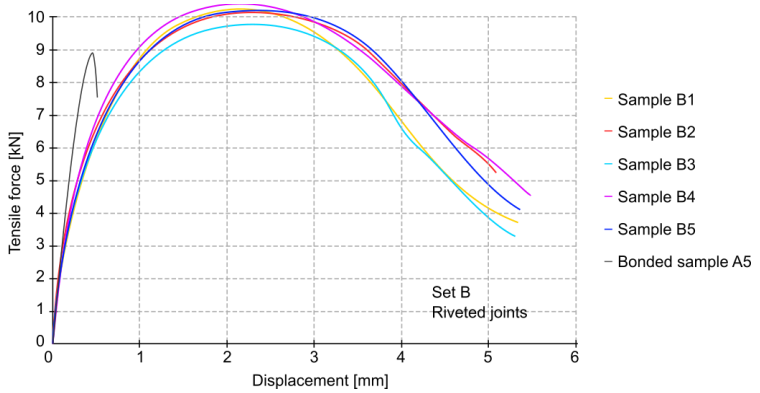

Figure 4 Shear stress on the riveted joint. Source: (own)

Tests of the hybrid adhesive-rivet joint demonstrate the lack of synergistic effect of both technologies. The joint primarily behaves as a bonded joint. When the adhesive bond strength is exceeded, adhesive failure occurs, then joint behaves as a riveted joint. The test record is shown in Figure 5. Two curves of the bonded and riveted joint are also added to the graph for comparison.

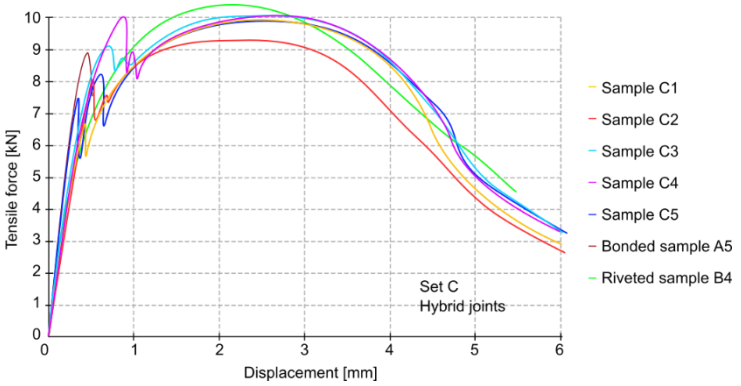

Figure 5 Shear stress on the hybrid – bonded + riveted joint. Source: (own)

A graph (see Figure 6) comparing the results of the individual measurements is provided for reference. The results of the hybrid joint show a slight improvement over the glued-only joint. The graph only partially shows the plastic deformation character of the riveted joint, determining a representative value is up for discussion.

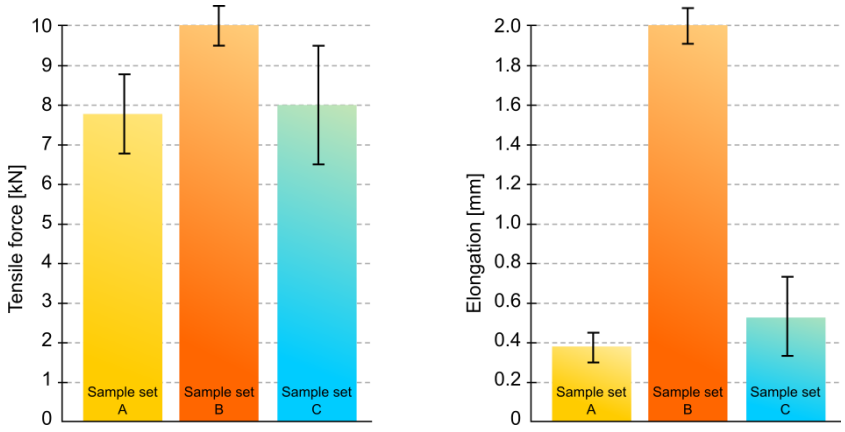

Figure 6 Comparison of maximum shear force and elongation results. Source: (own)

4. CONCLUSION

The test was aimed at investigating the effect of the combination of glued and riveted joints. Such joints can be designed into a real structure and it is therefore advisable to investigate their character in the laboratory. The bonded surfaces were simply chemically degreased without further surface treatment. They represented the surface of a standard aluminium alloy sheet commonly used in structural applications. The formed specimens were subjected to shear stress in the tested joint and the overall specimen to tensile stress. The measurements performed clearly showed the connection between the characteristics of the hybrid joint and the individual components. It can be said that the synergistic effect of both types of joints was not achieved and the overall strength of the joint copied the values of the individual components. As a future course of action, it is advisable to focus the development towards increasing the strength of the bonded joint, which sets the primary strength when combined with the rivet. Riveted joints in combination with adhesive can be considered technological, with a safety function.

ACKNOWLEDGEMENT

This paper was created thanks to the support by the project no. SV6323321/2101 Single-seat electric vehicle design for micro-mobility in urban environments and university campuses.

REFERENCES

[1] KULHÁNEK, Jiří, Petr TOMČÍK, Radim TROJAN, Martin JURÁNEK a Pavel KLAUS. Experimental modeling of weld thermal cycle of the heat affected zone (HAZ). Metalurgija [online]. 2016, 55(4), 733-736 [cit. 2023-05-24]. ISSN 1334-2576. Dostupné z: http://hdl.handle.net/10084/111797

[2] KARATHANASOPOULOS, N., Kedar S. PANDYA a Dirk MOHR. Self-piercing riveting process: Prediction of joint characteristics through finite element and neural network modeling. Journal of Advanced Joining Processes [online]. 2021, 3 [cit. 2023-05-24]. ISSN 26663309. Dostupné z: doi:10.1016/j.jajp.2020.100040

[3] ZHENG, Rui, Jianping LIN, Pei-Chung WANG, Chuanmin ZHU a Yongrong WU. Effect of adhesive characteristics on static strength of adhesive-bonded aluminum alloys. International Journal of Adhesion and Adhesives [online]. 2015, 57, 85-94 [cit. 2023-05-24]. ISSN 01437496. Dostupné z: doi:10.1016/j.ijadhadh.2014.10.007

[4] WU, Yongrong, Jianping LIN, Blair E. CARLSON, Peng LU, Michael P. BALOGH, Nicholas P. IRISH a Yu MEI. Effect of laser ablation surface treatment on performance of adhesive-bonded aluminum alloys. Surface and Coatings Technology [online]. 2016, 304, 340-347 [cit. 2023-05-24]. ISSN 02578972. Dostupné z: doi:10.1016/j.surfcoat.2016.04.051

[5] TOX® PRESSOTECHNIK: Self-Piercing Rivet Solutions. Tox-pressotechnik.com [online]. TOX® PRESSOTECHNIK [cit. 2023-05-24]. Dostupné z: https://uk.tox-pressotechnik.com/applications/riveting-joining/semi-hollow-rivets/

FRACTURE TOUGHNESS EVALUATION OF S355J2G3 STEEL

Author(s): Radek TOMÁŠEK

Supervisor: prof. Ing. Bohumír STRNADEL, DrSc.

Department: Centre for Advanced Innovation Technologies, Faculty of Materials Science and Technology, VSB – Technical University of Ostrava

Abstract

This paper investigates the fracture toughness of the S355J2G3 steel by testing according to the ASTM E1820 standard. The purpose of a fracture toughness is to measure the resistance of a material to the presence of a flaw in terms of the load required to cause a brittle or ductile fracture. The result is expressed in terms of toughness parameters such as K, CTOD and J-integral. Knowledge of the values of mechanical properties is necessary; yield and ultimate tensile strength were obtained from tensile tests. Experiments were performed on servo hydraulic machine on single edge notch bend specimens equipped with clip gage and values of K_{IC}, CTOD (δ) and J_C were calculated using standardized equations at room temperature. S355J2G3 steel was shown to be a highly plastic material with a high level of fracture toughness properties.

Key words:

Fracture mechanics, fracture toughness, stress intensity factor, CTOD, J-integral.

1. INTRODUCTION

Components made from ferritic steel are commonly used in a large number of structures and mechanism parts. Fracture of these steels has been an issue since the industrial revolution. Fracture mechanics is the branch of solid mechanics that is focused on the behavior of bodies with cracks under different loading conditions. Fracture toughness is an important mechanical property of steel used in engineering design and failure assessment of steel structures. Linear elastic fracture mechanic (LEFM) is limited in practical use; it is valid only as long as material deformation is confined to a small region surrounding the crack tip. The property K_{IC} determined by this test method characterizes the resistance of a material to fracture in a neutral environment in the presence of a sharp crack under severe tensile constraint, such that the stress state near the crack front approaches plane-strain, and the crack tip plastic region is small compared to both the crack size and thickness [1]. K stands for stress intensity factor, I represent the tensile mode of the crack opening and C means the critical value. In many materials, it is virtually impossible to characterize fracture behavior only with LEFM, and a more advanced fracture mechanics model is required [2]. All metallic materials and alloys commercially used in structural parts manifest plastic deformation in the area of the tip of the crack tip when they are subjected to applied stress. The amount of plastic deformation at the crack tip is directly related to the material fracture toughness and for a given material varies as a function of the thickness of the parts [1, 3]. Therefore, an elastic-plastic fracture mechanics (EPFM) approach is needed.

Nonlinear loading is characterized by the J-integral and CTOD parameters [4]. J-integral was first introduced by Rice in 1968 [3] is defined as the quantity obtained from evaluating a particular line integral around a path enclosing the tip of the crack [5]. The J-integral has plastic and elastic components J_{pl} and J_{el}. CTOD is then defined as the displacement at the point of intersection of the face of the crack with a line drawn from the crack at an angle of 45 °. It was the first method of fracture toughness measurement that was proposed for nonlinear deformation behavior by Wells in 1961 [4, 5]. Further development of these parameters lead to methods for R-curve fracture toughness which puts into relation J or CTOD and Δa crack extension during stable ductile tearing where R stands for resistance [4].

Fracture toughness properties can be determined from testing on several types of standardized test specimens such as compact tension specimen, single edge notched bend, or disc-shaped compact specimens in the American Society for Testing and Materials (ASTM) standard E1820 [1].

2. EXPERIMENTAL PROCEDURE

The material used for the experiments in this paper was S355J2G3+N steel (ASTM A572Gr50), high tensile fine-grained steel, low- alloyed with ferritic-pearlitic microstructure. It is widely a structural steel that is used in general engineering applications, particularly useful because it offers a unique combination of good welding properties with guaranteed strengths. Its chemical composition is given in Table 1 and mechanical properties in Table 2.

Table 1 Chemical composition of steel S355J2G3+N (wt. %). Source: [6]

C	Mn	Si	P	S
0.22	1.6	0.55	0.025	0.0025

Table 2 Mechanical properties of S355J2G3+N steel. Source: (own)

YS [MPa]	UTS [MPa]	A_5 [%]	Z [%]
288	478	26.8	52.2

Three single edge notch bend (SENB) specimens were manufactured based on the geometry, as can be seen in Figure 1. Width of the specimens was 40 mm, thickness 20 mm and length of 200 mm, the span of roller pins was set to 160 mm. The initial depth of the straight through notch was 18 mm with integral knife edges for placement of clip gage. Test specimens were pre-cracked with three-point bending fatigue based on the maximum force P_m, according to the ASTM E1820 standard. The pre-cracking procedure was carried out with cycle asymmetry R=0.1 and compressive force range P_m from 1000 to 11 500 N to achieve a specified fatigue crack extension 2 mm from the machined notch and total initial crack size a_0 of 20 mm in 10^5 cycles.

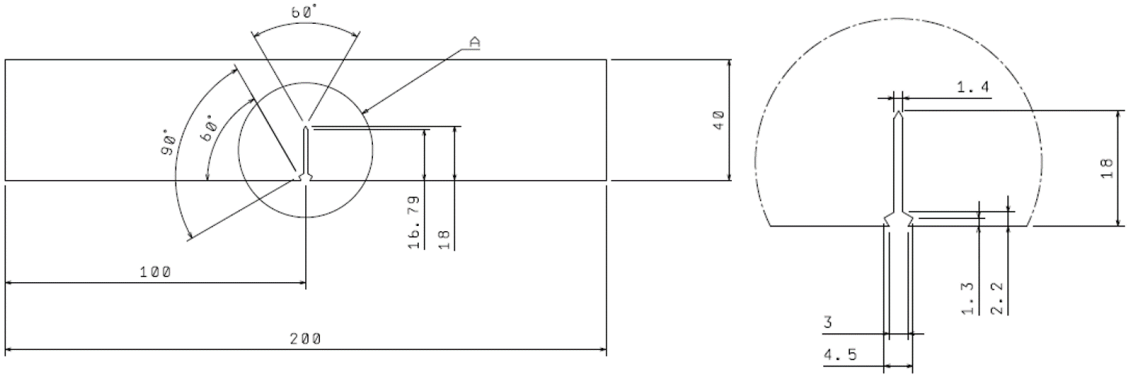

Figure 1 Drawing of the geometry of the SENB specimen. Source: (own)

After the pre-cracking procedure fracture toughness tests on a servo-hydraulic mechanical testing machine at room temperature. All fracture toughness tests also require the measurement of displacement on the specimen, most often a strain-gauged clip gauge is used. After test were measured actual crack lengths in 9 locations on one half of broken specimen. All calculations were performed in MATLAB R2022a software Load-crack opening displacement (COD) plot of this test is shown in Figure 1 for specimen SENB 1 as well as the black tangent line to the initial loading slope and required 0,95 secant line for determination of P_Q. P_{max} is represented by a green asterisk. Test specimens underwent large amount of plastic deformation without sudden failure. Data were collected until COD was so large that clip gage dropped out from the knife edges.

Provisional K_Q values were calculated. Expressions for calculating K_Q are given in the ASTM E1820 standard for each specified specimen geometry. There are 2 conditions in order for K_Q to be qualified as K_{IC}. First, the ratio of P_{max}/P_Q must be below 1.10 and second, the value $2.5(K_Q/\sigma_{YS})^2$, where σ_{YS} is the 0.2 % offset yield strength in tension shall be calculated. If this quantity is less than the size of the specimen ligament b_0, (W–a) then K_Q is equal to K_{IC}. Otherwise, the test is not a valid K_{IC} test. But all of the measurements did not fulfill the condition of plane deformation. Therefore, the results must be specified as K_Q. If the test result fails to meet the standards' requirements, it will be necessary to use a larger specimen to determine the K_{IC}, generally at least 1.5 times larger. The results of the K_{IC} test procedure are summarized in Table 3

Table 3 Results of the K_{IC} test procedure. Source: (own)

Specimen	K_Q [MPa·m$^{1/2}$]	K_{IC} condition	K_Q mean [MPa·m$^{1/2}$]
SENB 1	33.27	NO	33.78
SENB 2	35.95	NO	
SENB 3	32.12	NO	

Because plane strain conditions for K_Q to be qualified as K_{IC} were not met, material was tested further. Nonlinear loading in the presence of plastic deformation is characterized by the parameters J-integral and CTOD [4]. Crack-tip opening displacement (CTOD) parameter measures a displacement near the crack tip and provides a direct characterization of the crack-tip stresses in the presence of plasticity. Results, presented in Table 4, are useful when the thickness of the material to be characterized is not sufficient to determine a valid K_{IC} value[4]. It is intrinsic specimen property with more of the physical meaning.

Table 4 Results of the CTOD test procedure. Source: (own)

Specimen	CTOD δ [mm]	Mean CTOD δ [mm]
SENB 1	0.925	0.893
SENB 2	0.854	
SENB 3	0.901	

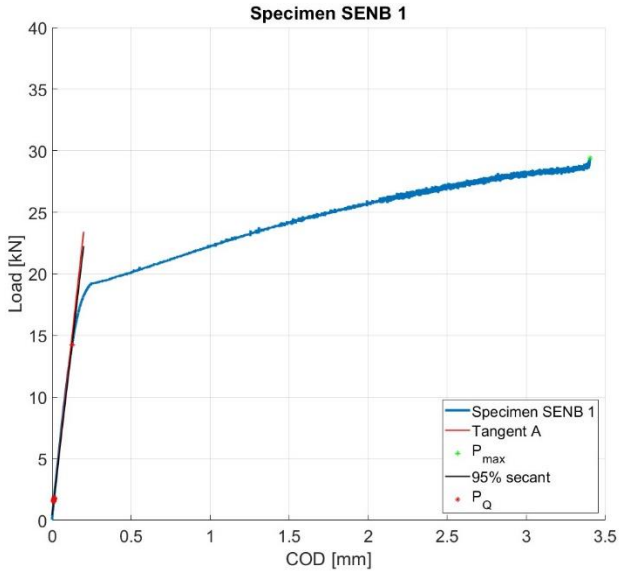

Figure 1 Force-COD plot of specimen SENB 1, calculation of K_{IC}. Source:(own)

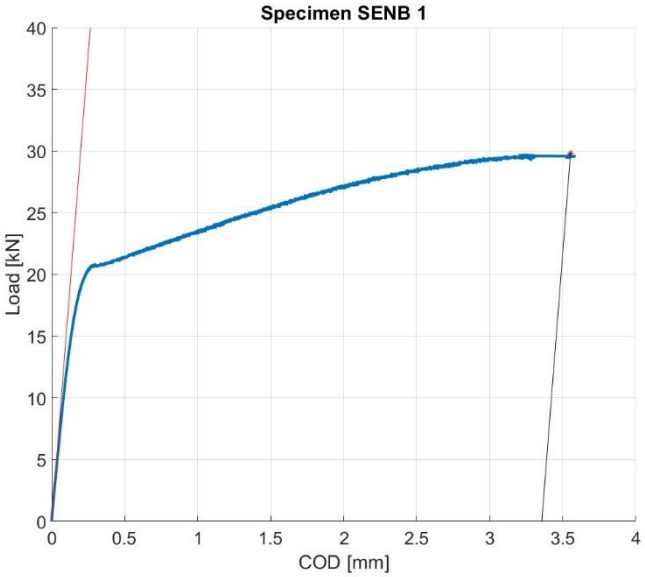

Figure 2 Force-COD plot of specimen SENB 1, calculation of J-integral. Source: (own)

Material characterization by J-integral is in the way very similar to CTOD and both parameters can be related by the equation[4]. J is an energy-based parameter, in the force-displacement diagram is represented by the area between the loading curve and a straight line which is parallel to the initial linear-elastic slope and goes through the point of the maximum loading curve to be evaluated, as can be seen in Figure 2. This point is labeled J_{Qc}, a provisional J_c value. This single point value represents a fracture toughness are instability when fracture occurs before stable tearing, without stable crack extension and independent of in-plane dimensions. There are two conditions for the provisional calculated J_{QC} value to qualified as J_{IC}. Critical J values can be converted to critical values of size-independent K_{JIC} for use in structural assessment [4].Results are summarized in Table 5

Table 5 Results of the J-integral test procedure. Source: (own)

Specimen	J_{pl} [N·mm^{-1}]	$J_{el.}$ [N·mm^{-1}]	J_Q [N·mm^{-1}]	J_C condition	Mean J_Q [N·mm^{-1}]	K_{JIC} [MPa·m$^{1/2}$]
SENB 1	71.28	0.0046	71.29	NO	75.43	122.35
SENB 2	75.79	0.0054	75.98	NO		126.31
SENB 3	79.02	0.0043	79.02	NO		128.82

3. CONCLUSION

In the presented paper were investigated mechanical properties and fracture toughness of the construction steel S355J2G3. Static fracture toughness tests on servo-hydraulic machines were carried out on SENB specimens and K_{IC} (K_Q), CTOD and J-integral values were calculated at the room temperature. Mean value of K_Q was determined to be 33.78 MPa·m$^{1/2}$, mean value of CTOD (δ) was 0.893 mm and lastly, the value of J-integral showed average value of 75.43 N·mm^{-1}. Based on the observed behavior of the steel from Force-COD plots, it can be said that it is able to sustain large plastic deformation before break. Obtained values were in the good agreement with the values in the literature [7, 8]. Knowledge of mechanical and fracture properties of S355J2G3 steel will help in the more precise analysis of its durability and prevent failures in use. In case of this high-plasticity steel, resistance to fracture should be determined by J_{IC}, therefore further research will be devoted to the determination of resistance (J-R) curves.

ACKNOWLEDGEMENT

This paper was created by the project No. CZ.02.1.01/0.0/0.0/17_048/0007373 "Damage Prediction of Structural Materials" within the Research, Development and Education Operational Programme financed by the European Union and from the state budget of the Czech Republic.

REFERENCES

[1] ASTM STANDARD E1820. Standard Test Method for Measurement of Fracture Toughness. *ASTM Book of Standards*. 2013. Vol. i, no. January, p. 1–54. DOI 10.1520/E1820-13.Copyright.

[2] ANDERSON, T. L. *Fracture Mechanics: Fundamentals and Applications, Second Edition*. . 1995. ISBN 9780849342608.

[3] FARAHMAND, Bahram. Elastic-Plastic Fracture Mechanics (EPFM) and Applications. *Fracture Mechanics of Metals, Composites, Welds, and Bolted Joints*. 2001. P. 180–236. DOI 10.1007/978-1-4615-1585-2_4.

[4] SCHWALBE, K.-H, LANDES, J.D. and HEERENS, J. Classical Fracture Mechanics Methods*. In : *Comprehensive Structural Integrity*. Online. Elsevier, 2007. p. 3–42. ISBN 0080437494.

[5] DOWLING, Norman E. *Mechanical Behavior of Materials eBook:International Edition*. . 4. Pearson Education, 2013. ISBN 9781498752695.

[6] ČSN EN 10025-2 Hot rolled products of structural steels – Part 2: Technical delivery conditions for non-alloy structural steels. .

[7] BOZKURT, Fatih and SCHMIDOVÁ, Eva. Fracture toughness evaluation of S355 steel using circumferentially notched round bars. *Periodica Polytechnica Transportation Engineering*. 2019. Vol. 47, no. 2, p. 91–95. DOI 10.3311/PPtr.11560.

[8] DZIOBA, Ihor and LIPIEC, Sebastian. Fracture mechanisms of S355 steel-experimental research, FEM simulation and SEM observation. *Materials*. 2019. Vol. 12, no. 23. DOI 10.3390/ma122333959.

Management of Industrial Systems

ANALYSIS OF STRUCTURAL CHANGES IN THE LABOUR MARKET THAT AFFECT STRATEGIC MANAGEMENT

Author(s): Ondřej BALEK

Supervisor: doc. Ing. Adam PAWLICZEK, Ph.D.

Department: Department of Industrial systems management, Faculty of Materials Science and Technology, VSB – Technical University of Ostrava

Abstract

This thesis analyses structural changes in the labour market and how they affect strategic management. The world labour market is undergoing significant transformations caused by the COVID-19 pandemic, innovations in automation, robotization and the development of artificial intelligence. These changes have a high impact on the economic situation and management control. Technological advances are changing employment and requiring workforce adaptability. The COVID-19 pandemic has caused unemployment and job insecurity, which adds to social inequality, and structural changes in the flexibility of companies and individuals. Future research should focus on the impact of technological progress on employment, addressing labour market inequalities and support measures for the unemployed.

Keywords

Unemployment, Labour market, Pandemic COVID-19, Structural changes in the labour market, Digitalization.

1. INTRODUCTION

The labour market is an economic term that focuses on the interaction between the supply and demand for labour. It represents a space where people look for employment (workers) and employers look for labour meet. Workers contribute their knowledge, expertise, and labour to the job market. On the other side, companies provide employment opportunities and payment. The supply of labour is represented by people who are able and have a will to work, while the demand for labour represents the needs of the employer [1]. It is important to recognize that labour markets differ from ordinary product markets in many ways. There are a few special features that set them apart. For example, although several jobs may be available in the market, job searchers do not have the freedom to choose the position they wish. However, consumers can choose which brand of product to buy in a store without any restrictions [2]. The market currently has to respond to the changes caused by the COVID-19 pandemic, the growth of digitalization, robotization and significant innovations in the field of artificial intelligence in recent years. A significant change can also be observed in the labour market in the relative amount of wages of university graduates, which is indirectly related to their level of education. These findings point to the importance of the demand for skilled labour. Cyclical conditions in the labour market are also significant, as retraining serves as a short-term adaptation mechanism to which the company must constantly respond [3].

2. UNEMPLOYMENT

Unemployment is defined as a condition where individuals who are willing to work and actively look for employment are unable to find suitable work. This situation has a significant impact on the labour market and the social structure of society [4]. Starting a new job is often fraught with uncertainty and potential stress because new employees struggle to learn their job tasks, recognise their roles and meet expectations [5]. However, rising unemployment and precarious work have become a major source of disruption and social division. In many regions, sustained stable jobs lead to emigration, organizational and social displacement, disruption, and division, including the degradation of communities [6]. This environment, which is reinforced by job insecurity, usually brings a greater burden on workers who are left without help to resolve the resulting insecurity [7]. Many unemployed people spend a long time looking for new jobs, but the effectiveness of their efforts is limited by the lack of job opportunities during the recession. Losing a job is a sacrifice and a harsh reality for individuals,

but it can also reduce opportunity costs that could otherwise be devoted to entrepreneurial activities [8]. Studies show that start-up subsidies for the unemployed can activate individuals to engage in economic activity [9]. However, the positive correlation between unemployment and entrepreneurship appears to be more pronounced in wealthier regions than in other areas. The results suggest that only in performing regions with higher unemployment to increase the rate of business creation, while in lower performing regions it actually reduces the net growth of the entrepreneurial population [10].

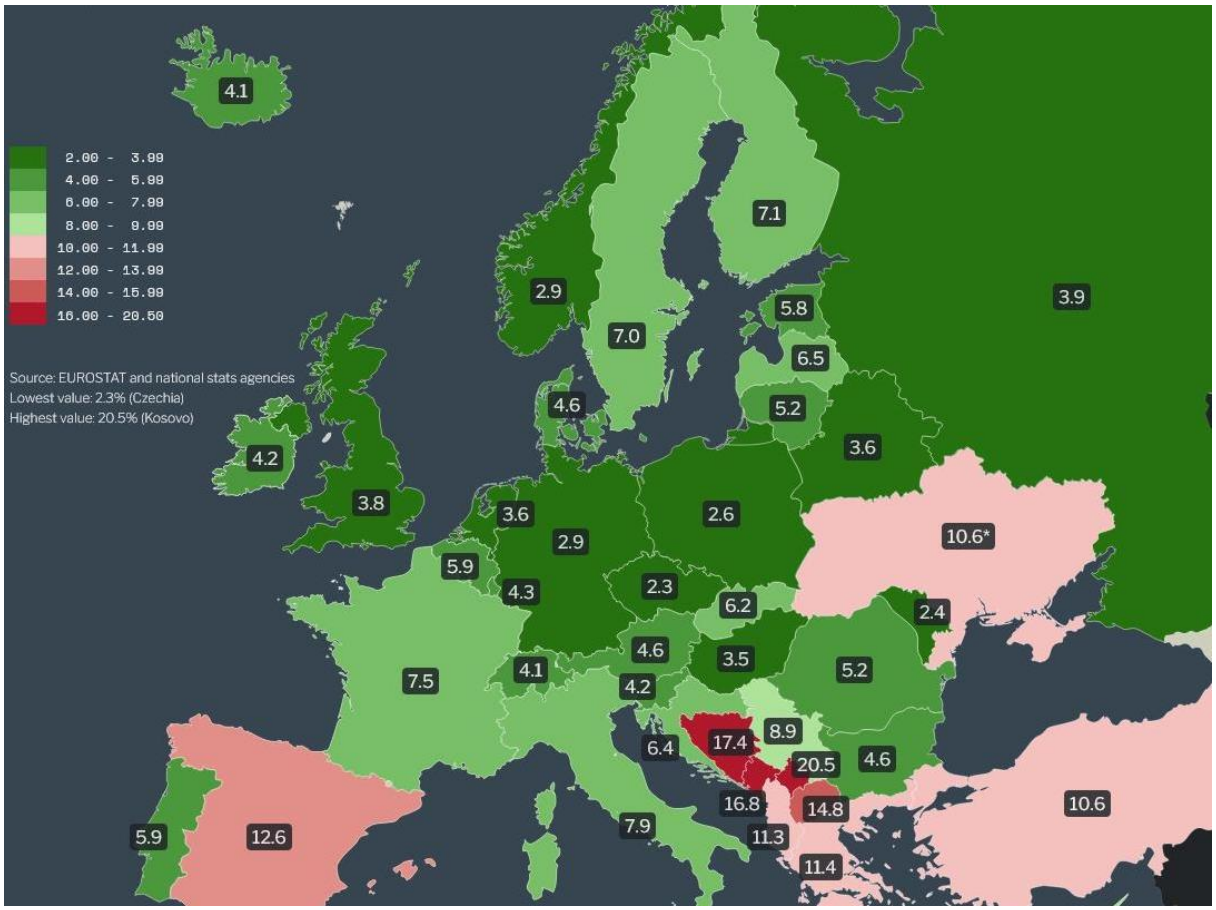

Figure 1 Unemployment in Europe in %, 07/2022. Source: [11]

This figure (see Figure 1) shows significant differences in unemployment rates between European countries. The Czech Republic shows the lowest unemployment rate of just 2.3 %, which is the lowest compared to all other European countries. Germany, Malta, and Norway follow with an unemployment rate of 2.9 %, while Poland has a rate of 2.6 %. These examples represent European Union countries that achieve an unemployment rate of less than 3 %. At the opposite side of the scale in the European Union is Spain, with a highest unemployment rate of 12.6 %. Along with Greece, Spain is the only EU member with an unemployment rate higher than 10 %. Greece has an unemployment rate of 11.4 % [11].

3. IMPACT OF TECHNOLOGY

Technological progress significantly affects the labour market and changes employment dynamics. One consequence is automation, which brings more stable employment to established companies. This trend is driven by workers adapting to new tasks in their original professions. Interestingly, some measures suggest that these new jobs are of higher quality than the previous ones. At the same time, the adaptation of young people to technological development is manifested in the field of education. They adapt to the new environment by adjusting their educational choices towards higher schools and universities. In this way, they try to acquire the necessary knowledge and skills that meet modern technological trends. Within the work environment, industrial robots bring benefits to professionals in various fields. For example, managers and technical scientists can use these robots to complete additional tasks. This frees up their time and allows them to focus on the strategic and creative

aspects of their work [12]. The development of artificial intelligence is also an important factor influencing the labour market. In 2010-2019 showed a dramatic increase in the demand for AI skills in the US economy. This demand is most significant in IT professions, with architecture, engineering, science, and management occupations following close behind. Large companies with larger market capitalizations, higher cash and R&D investments show high demand for AI skills. Managerial occupations then receive the highest wage bonus for these skills. Companies that require more AI skills also offer higher salaries for jobs that aren't directly related to the field. At the same time, digitalization is spreading within society through business education and affects almost all aspects of life. This process contributes to increasing the economic efficiency and productivity of work and at the same time changes the structure of employment [13]. Digitalization enables more efficient data processing, process automatization and the use of modern technologies in business. This leads to the emergence of new job roles and the need for professionals with specialized knowledge in the field of digital transformation. Thus, the demand for experts in IT, digital marketing, data analysis, cyber security and other fields related to the digital sphere is increasing. This technological progress and digitalization also affect the structure of employment. Some manual and routine jobs that are susceptible to automation are gradually disappearing and being replaced by automated systems and robots. On the contrary, there is a growing demand for workers with creative and analytical skills, the ability to solve complex problems and adapt to new technologies. The consequence of these changes is the need for constant adaptation to new technologies and trends on the part of workers. Achieving quality education and developing skills in areas that are in demand on the labour market is becoming a key factor for success and maintaining competitiveness [14].

4. IMPACT OF PANDEMIC

The Covid-19 pandemic has caused unprecedented disruption to labour markets around the world, including job losses and declining incomes. This global crisis has had far-reaching consequences for people's lives, employment, and family life, while fundamentally changing the economic environment. The labour market did not escape the impact of the pandemic and had to adapt to the new conditions [15]. The significant effects of the Covid-19 pandemic were manifested in the labour market itself, which has undergone significant changes. Some industries, such as tourism, gastronomical businnes, or retail, suffered a significant drop in demand and were forced to lay off workers. At the same time, however, new job opportunities have appeared, especially in the field of the digital economy and online services. The pandemic has also opened up space for a more significant implementation of the Industry 4.0 concept, which uses modern technology and automatization in the industrial sector. This trend can increase the competitiveness of companies and bring new job opportunities. Employers are trying to use technology more effectively and digitize their business, which can lead to changes in the requirements for workers and their skills [16]. Government responses to the Covid-19 pandemic differed in various countries, both in terms of the extent of measures and the form of support for the economy and the labour market. Some countries have focused on providing wage subsidies and financial support to minimize the impact on employment and citizens' incomes. These measures were able to temporarily moderate labour market fluctuations. However, in most countries the Covid-19 pandemic has brought a deepening of inequalities in the labour market. Some groups of workers especially those with lower incomes, were more affected and their economic situation worsened [17].

5. CONCLUSION

Structural changes in the labour market have a significant impact on the strategic management of companies. Technological advances and digitalization are changing employment dynamics and require workers to constantly adapt to new technologies and trends. Automatization and the development of artificial intelligence are affecting the employment structure and increasing the demand for experts in digital fields. The Covid-19 pandemic has significantly changed the labour market and created the need to adapt to new conditions. Unemployment and job insecurity cause social inequalities and divide communities. Unemployed people try to find new jobs, but the lack of job opportunities limits their success. However, job loss can also stimulate entrepreneurial activity. Business subsidies for the unemployed can encourage people to start their own businesses. The correlation between unemployment and entrepreneurship is more significant in wealthier regions. Overall, it can be concluded that structural changes in the labour market require flexibility and adaptability on the part of both companies and individuals. Blind spots that may receive attention in the future include further research on the impact of technological progress on employment, addressing labour market inequality and developing support measures for people affected by unemployment.

REFERENCES

[1] HOLMAN, Robert*. Ekonomie: The Rise of Polarized and Precarious Employment Systems in the United States, 1970s to 2000s.* 6. vydání. Praha: C.H. Beck, 2016. Beckovy ekonomické učebnice. ISBN 978-80-7400-278-6.

[2] AZAR, José, Ioana MARINESCU, Marshall STEINBAUM a Nicole WOESSNER. *Labor Market Concentration: How Do Supported Self-employed Individuals Perform?.* Journal of Human Resources. 2022, 57(S), S167-S199. ISSN 0022-166X. Dostupné z: doi: 10.3368/jhr.monopsony.1218-9914R1

[3] CROCE, Giuseppe, Emanuela GHIGNONI, Krzysztof FIRLEJ, Ivan SOUKAL, Martina HEDVIČÁKOVÁ a Zuzana KOZUBÍKOVÁ. *Demand and Supply of Skilled Labour and Overeducation in Europe: A Country-level Analysis.* Comparative Economic Studies. 2012, 2021-3-27, 54(2), 413-439. ISSN 0888-7233. Dostupné z: doi:10.1057/ces.2012.12

[4] VLČEK, Josef. *Ekonomie a ekonomika: The Rise of Polarized and Precarious Employment Systems in the United States,* 1970s to 2000s. 5., aktualizované vydání. Praha: Wolters Kluwer, 2016. Beckovy ekonomické učebnice. ISBN 978-80-7552-190-3.

[5] PLOYHART, Robert E., William J. SHEPHERD a Sam D. STRIZVER. *The COVID-19 pandemic and new hire engagement: Relationships with unemployment rates, state restrictions, and organizational tenure.* Journal of Applied Psychology. 2021, 106(4), 518-529. ISSN 1939-1854. Dostupné z: doi:10.1037/apl0000917

[6] GARCIA-LORENZO, Lucia, Lucia SELL-TRUJILLO a Paul DONNELLY*. Responding to stigmatization: How to resist and overcome the stigma of unemployment*. Organization Studies. 2022, 43(10), 1629-1650. ISSN 0170-8406. Dostupné z: doi:10.1177/01708406211053217

[7] L. KALLEBERG, Arne L. Kalleberg. *Good Jobs, Bad Jobs: The Rise of Polarized and Precarious Employment Systems in the United States, 1970s to 2000s.* New York: Russell Sage Foundation: American Sociological Association Rose Series in Sociology, 2011. ISBN 978-0-87154-480-3.

[8] TOOHEY, Desmond. *Job rationing in recessions: Evidence from work-search requirements.* Unpublished manuscript, 2014.

[9] DVOULETÝ, Ondřej, Lucia SELL-TRUJILLO a Paul DONNELLY. *Starting Business Out of Unemployment: How Do Supported Self-employed Individuals Perform?.* Entrepreneurship Research Journal. 2022, 12(1), 1-23. ISSN 2157-5665. Dostupné z: doi:10.1515/erj-2019-0327

[10] O'LEARY, Daragh, Lucia SELL-TRUJILLO a Paul DONNELLY. *Unemployment and entrepreneurship across high-, middle- and low-performing European regions: How Do Supported Self-employed Individuals Perform?.* Regional Studies, Regional Science. 2022, 9(1), 571-580. ISSN 2168-1376. Dostupné z: doi:10.1080/21681376.2022.2118072

[11] *Unemployment rates in Europe, by country, latest data for 2022* [online]. VIBOR CIPAN, 2022 [cit. 2023-05-26]. Dostupné z: https://viborc.com/unemployment-rates-in-europe-per-country-latest-data-for-2022/

[12] DAUTH, Wolfgang, Sebastian FINDEISEN, Jens SUEDEKUM a Nicole WOESSNER. *The Adjustment of Labor Markets to Robots: How Do Supported Self-employed Individuals Perform?*. Journal of the European Economic Association. 2021, 19(6), 3104-3153. ISSN 1542-4766. Dostupné z: doi:10.1093/jeea/jvab012

[13] ALEKSEEVA, Liudmila, José AZAR, Mireia GINÉ, Sampsa SAMILA, Bledi TASKA a Zuzana KOZUBÍKOVÁ. *The demand for AI skills in the labor market: Who endures, who doesn't and what are the implications for inequality Labour Economics*. 2021, 2021-3-27, 71(1), 5-28. ISSN 09275371. Dostupné z: doi:10.1016/j.labeco.2021.102002

[14] KUZNETSOVA, Alfiya, Amit BASOLE, Surbhi KESAR a Nicole WOESSNER. *Trends of Labor Market Change in the Countries of the European Union and Russia under Conditions of Digitalization of the Economy: How Do Supported Self-employed Individuals Perform?*. Montenegrin Journal of Economics. 2021, 17(1), 175-183. ISSN 1800-5845. Dostupné z: doi:10.14254/1800-5845/2021.17-1.13

[15] ABRAHAM, Rosa, Amit BASOLE, Surbhi KESAR a Nicole WOESSNER. *Down and out? The gendered impact of the Covid-19 pandemic on India's labour market: How Do Supported Self-employed Individuals Perform?.* Economia Politica. 2022, 39(1), 101-128. ISSN 1120-2890. Dostupné z: doi:10.1007/s40888-021-00234-8

[16] MACI, Jan, Petra MARESOVA, Krzysztof FIRLEJ, Ivan SOUKAL, Martina HEDVIČÁKOVÁ a Zuzana KOZUBÍKOVÁ*. Impacts of COVID-19 on the labour market - evidence from the Czech Republic: How Do Supported Self-employed Individuals Perform?.* Montenegrin Journal of Economics. 2021, 2021-3-27, 17(1), 232-241. ISSN 1800-5845. Dostupné z: doi:10.36689/uhk/hed/2021-01-023

[17] SOARES, Sergei, Janine BERG, Krzysztof FIRLEJ, Ivan SOUKAL, Martina HEDVIČÁKOVÁ a Zuzana KOZUBÍKOVÁ. *The labour market fallout of COVID-19: Who endures, who doesn't and what are the implications for inequality.* International Labour Review. 2022, 2021-3-27, 161(1), 5-28. ISSN 0020-7780. Dostupné z: doi:10.1111/ilr.12214

USAGE OF CAMERA SYSTEMS IN INDUSTRIAL ENVIRONMENT

Author(s): Miloslav BEČKA

Supervisor: doc. Ing Robert FRISCHER, Ph.D.

Department: Department of Industrial Systems Management, Faculty of Materials Science and Technology, VSB – Technical University of Ostrava

Abstract

Camera systems have revolutionized industrial operations, playing a pivotal role in improving efficiency, productivity, and safety. This article explores the diverse applications of camera systems in industry, highlighting their integration with advanced technologies, real-world case studies, considerations for data security, and emerging trends. By leveraging camera systems, industries can create a safer and more efficient work environment, leading to enhanced operational performance and productivity.

Key words:

Camera systems, vision, industrial operations, automation.

1. INTRODUCTION

Camera systems employ sophisticated imaging devices, such as thermal imaging cameras, surveillance cameras and vision systems to capture visual data that is crucial for decision-making and analysis. These cameras work in cooperation with various supporting technologies to transform raw visual information into actionable insights. Let's delve into the functioning of each camera system type:

Thermal imaging cameras operate by capturing the infrared radiation emitted by objects and converting it into a visual representation of temperature variations. These cameras are particularly useful for monitoring heat signatures and identifying anomalies that may indicate equipment malfunctions, overheating, or energy inefficiencies. By providing valuable insights into thermal patterns, they enable proactive maintenance and troubleshooting [1, 2].

Surveillance cameras are designed to monitor specific areas or premises in real-time. They employ optical sensors to capture video footage, which can be viewed live or recorded for later analysis. Some advanced surveillance cameras are equipped with features like motion detection, facial recognition, and pan-tilt-zoom capabilities, allowing for enhanced monitoring and control [1, 2].

Vision systems utilize cameras and image processing algorithms to perform automated inspection, quality control, and measurement tasks. These systems capture high-resolution images of products or components, which are then analyzed using specialized software. By comparing captured images to predefined standards or performing image recognition, vision systems can detect defects, measure dimensions, and ensure compliance with quality standards.

The integration of camera systems with advanced technologies such as artificial intelligence (AI), machine learning (ML), and computer vision (CV) further augments their capabilities. AI algorithms can analyze visual data in real-time, enabling automated anomaly detection, predictive maintenance, and intelligent decision-making [2].

By employing camera systems, businesses gain access to a wealth of data that can be leveraged for operational optimization. Real-time monitoring allows for timely identification of bottlenecks, process inefficiencies, and potential safety hazards. The visual data captured by camera systems enables data-driven decision-making, empowering businesses to make informed choices regarding process improvements, resource allocation, and risk mitigation strategies [2, 3].

2. GENERAL TASKS FOR CAMERA SYSTEM

This section will concentrate on real tasks that can occur in an industrial environment and how to solve them using camera.

Camera used for the solution is Keyence CV-X series which stands for a range of machine vision systems developed by Keyence Corporation, a leading provider of industrial automation solutions. The CV-X series offers powerful and versatile vision inspection capabilities, allowing for high-precision quality control and process optimization in industrial environments [5, 6].

The CV-X series features advanced image processing algorithms and a user-friendly interface, making it accessible to both beginners and experienced users. With its robust hardware and software, the CV-X system can handle a wide range of inspection tasks, including defect detection, measurement, alignment, and barcode reading [5, 6].

Key features of the Keyence CV-X series include:

High-Speed and High-Resolution Imaging: The CV-X system is equipped with high-resolution cameras and high-speed image processing capabilities, enabling the capture and analysis of detailed images at high speeds. This makes it suitable for applications that require fast-paced production lines or intricate inspection requirements.

Flexible Connectivity: The CV-X series offers various connectivity options, allowing seamless integration with other factory automation systems, such as programmable logic controllers (PLCs) or robotics. This enables real-time data exchange and synchronization, enhancing overall system efficiency and control.

Intuitive User Interface: The CV-X software provides a user-friendly interface that simplifies the setup and configuration of vision inspections. Users can define inspection parameters, create custom algorithms, and monitor inspection results in real-time. The software also offers powerful tools for image processing, pattern matching, and measurement, allowing for precise and reliable inspections.

Versatile Inspection Tools: The CV-X series offers a wide range of inspection tools to address different application requirements. These include edge detection, blob analysis, color inspection, OCR (Optical Character Recognition), and more. These tools can be combined and customized to create complex inspection algorithms tailored to specific quality control needs.

Data Logging and Traceability: The CV-X system provides comprehensive data logging and traceability features, allowing users to store and analyze inspection results over time. This facilitates process optimization, quality trend analysis, and identification of potential issues for continuous improvement.

The Keyence CV-X series is widely used in industries such as automotive, electronics, pharmaceuticals, and food and beverage, where precision inspection and quality control are critical. Its versatility, high performance, and ease of use make it a popular choice for companies seeking reliable machine vision solutions to enhance their manufacturing processes [5, 6].

First task cluster counting is a common task performed using the Keyence CV-X series machine vision system. Cluster count refers to the process of detecting and quantifying groups or clusters of objects within an image. This task is particularly useful in applications where identifying the number and distribution of objects in a given area is important for quality control, sorting, or process optimization. In the **Figures 1,2** the check of the vitamin plate can be seen and the camera evaluates if all capsules are present during production.

Next task is widely used and searched for it is Optical Character Recognition (OCR). OCR involves the recognition and extraction of text from images or visual data, enabling automated interpretation and processing of textual information. The CV-X series offers robust OCR capabilities, allowing businesses to extract and analyze text from various sources within industrial applications. In the **Figures 2,4** can be seen the yoghurt lid on which the expiry date is checked, if the date is not the same as the entered value the piece will NG.

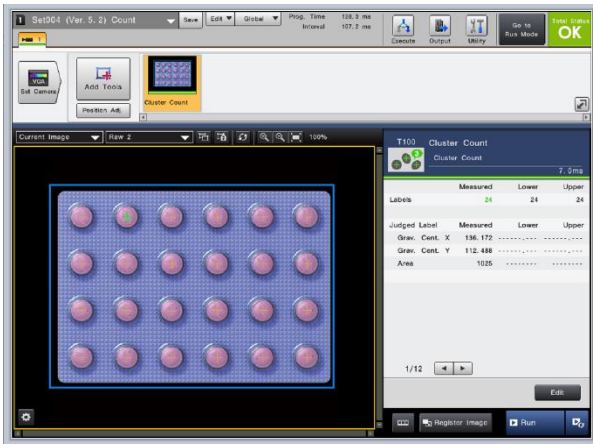

Figure 1 OK part. Source: (own)

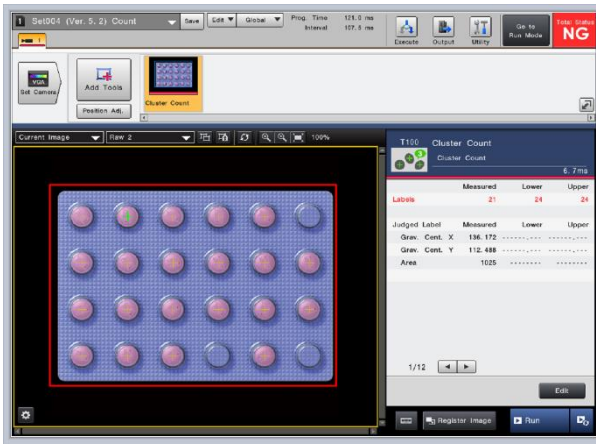

Figure 2 NG part. Source: (own)

Figure 3 OK part. Source: (own)

Figure 4 NG part. Source: (own)

Third task uses flaw detection on curves that can be accomplished using the Keyence CV-X series machine vision system. This task involves inspecting curved surfaces or objects for flaws or defects, such as scratches, cracks, dents, or surface irregularities. The CV-X series offers robust capabilities for flaw detection, enabling businesses to enhance quality control processes and ensure the integrity of curved components. **Figures 5,6** shows the use of this tool on a detergent cap, if the cap is somehow damaged the camera will recognize this and immediately report NG.

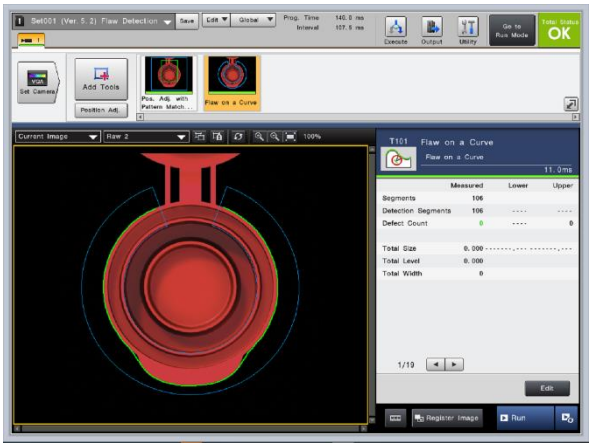

Figure 5 OK part. Source: (own)

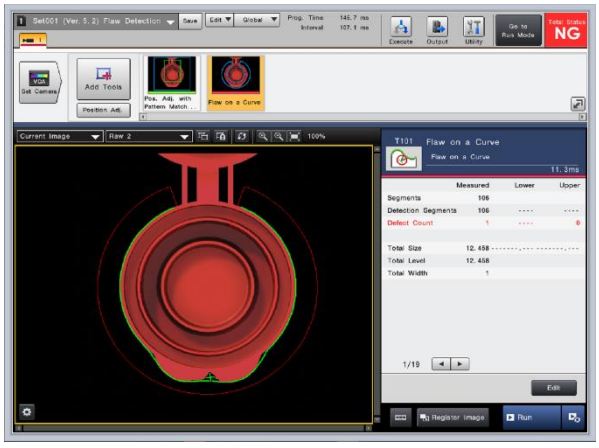

Figure 6 NG part. Source: (own)

Fourth task is involves circle distance measurements. This task involves accurately measuring the distances between circles or circular features within an image. The CV-X series provides powerful image processing algorithms and tools to facilitate precise circle distance measurements, enabling applications such as part alignment, gauging, or dimensional verification. **Figure 7,8** describes the measurement of the concentricity of the circles of an aluminium casting as the inner circle is machined, it is necessary to check this specific object.

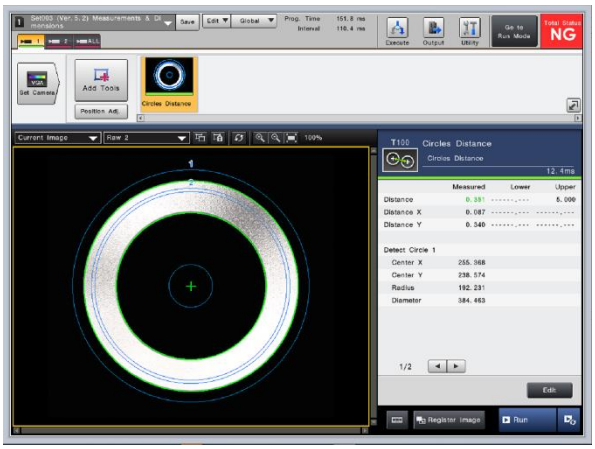

Figure 7 OK part. Source: (own)

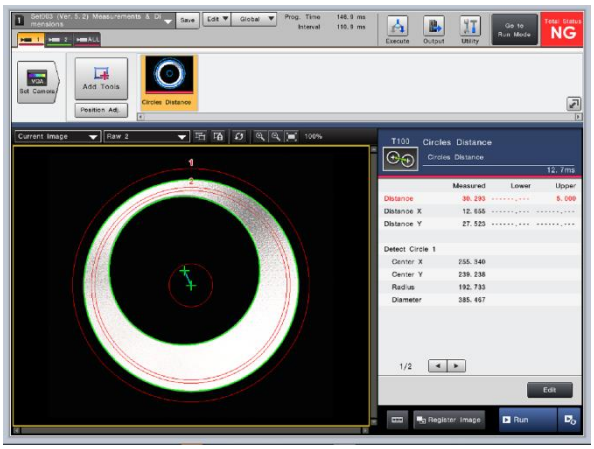

Figure 8 OK part. Source: (own)

3. CONCLUSION

Tasks such as cluster counting, OCR, flaw detection on curves, and circle distance measurements are common applications of camera systems in industrial environments. These tasks contribute to improved quality control, sorting, and process optimization. The ability of camera systems to detect and quantify clusters, recognize text, inspect curved surfaces, and measure distances facilitates efficient operations and ensures the integrity of components.

In summary, camera systems play a crucial role in the industrial environment by providing actionable insights, enhancing quality control, and optimizing processes. They empower businesses to make informed decisions, improve productivity, and achieve operational excellence.

ACKNOWLEDGEMENT

The work was supported by the specific university research of Ministry of Education, Youth and Sports of the Czech Republic No. SP2023/043

REFERENCES

[1] KEBO, Vladimír a Oldřich KODYM. *Virtuální realita a řízení procesů*. Ostrava: VŠB-TU Ostrava ve vydavatelství Montanex, 2011. ISBN 978-80-7225-361-6.FIALA, Jaroslav, Václav MENTL, Pavol ŠUTTA. *Struktura a vlastnosti materiálů*. Praha: Academia, 2003. ISBN 80-200-1223-0.

[2] ŠONKA, Milan a Václav HLAVÁČ. *Počítačové vidění*. V Praze: Grada, 1992. Nestůjte za dveřmi. ISBN 80-85424-67-3.

[3] DAVID, Jiří. *Automatizace v metalurgii*. Ostrava: Vysoká škola báňská - Technická univerzita Ostrava, Fakulta metalurgie a materiálového inženýrství, katedra automatizace a počítačové, 2011. ISBN 978-80-248-2535-9.

[4] *Keyence* [online]. Keyence, 2023 [cit. 30.5.2023]. Available from: https://www.keyence.eu/about-us/

[5] *Keyence CV-X* [online]. Keyence CV-X, 2023 [cit. 30.5.2023]. Available from: https://www.keyence.eu/products/vision/vision-sys/cv-x100/?search_sl=1

AUTOMATION OF PRODUCTION AUDITING

Author(s): Jan DOSTÁL

Supervisor: doc. Ing. Jiří DAVID, Ph.D.

Department: Department of Industrial Systems Management, Faculty of Materials Science and Technology, VSB – Technical University of Ostrava

Abstract

The article describes the audit process in manufacturing companies. It discusses the benefits of auditing and the consequences of neglecting the process. A strategy for selecting supplier manufacturing companies based on various metrics is presented. Weaknesses in the supplier selection process and in the auditing process are described. Unsystematic data collection leading to non-targeting of suitable suppliers is cited as a typical error. Another error may be the tracking of inappropriate performance indicators.

The text contrasts the current era with the upcoming era. It considers the technical opportunities that are opening up with Industry 4.0 and Quality 4.0. The possibility of automating auditing to bring time savings and, more importantly, accuracy and consistency during the process is presented. Using a database of audit questions and elaborated typical answers, an expert system is developed to guide the auditor and point out bottlenecks. Thus, audits will be performed using an application that will be used by auditors throughout the entire coprocess, reducing the variability between audit quality depending on the auditor.

The direction that the quality industry is likely to take, hand in hand with automation, is outlined. Current technological trends, which are only now beginning to meet, are taken into account and offer a wide range of new technical solutions. There will be a move away from enterprise ERP systems such as SAP to complex, self-managed systems that completely handle the running of the business. The idea is set that even these autonomous management systems will be able to audit themselves and certifications like ISO, IATF will disappear and be replaced by IT companies that will certify the autonomy and correctness of the management systems.

Key words:

Audit, Automation, Quality 4.0., Industry 4.0.

1. SUPPLIER AUDITS

In the manufacturing sector, careful planning of processes, operations and orders is crucial. Each production unit has a production plan that determines what will be produced when. This production plan takes into account:

- the similarity of different orders
- the time spent setting up machines for a different order (SMED)
- urgencies from key customers
- potential penalties for late delivery
- availability of input material
- and many other factors

The purpose of a production plan is to process orders in such a sequence that the business generates long-term profit. There are several factors that can immediately sabotage the entire production plan and trigger the process of rescheduling orders, which is associated with:

- contacting customers at will to push back deadlines
- paying penalties for late delivery
- weakening of credibility, which can lead to fewer future orders ('You're not getting what you've got, so you're not getting more')

An approach where the same product is sourced from two suppliers and these two suppliers are kept in constant competition with each other for orders is also common in the automotive environment. The orders are split such that Supplier A receives 70% of the order volume while Supplier B receives only 30% of the volume.

The moment a supplier makes a mistake and delivers, for example, 3 consecutive orders two days late, the volume is automatically re-set to: supplier A 30%, supplier B 70%.

To prevent all the inconveniences mentioned above, there is a supplier quality department. This department monitors suppliers and tries to avert the coming earthquake, and if this is not possible, it tries to at least inform in advance "that there will be a problem here".

One of the quality engineer's powerful tools is auditing. There are a number of standards and norms by which to audit (IATF, VDA, 9001, 45001, others). The purpose is to verify that the audited company is in compliance.

2. SUPPLY CHAIN AUDITING STRATEGY

In Chapter 1, I described how easy it is to sabotage an entire production program and lose current and future orders and possibly customers. In Chapter 2, I describe how to properly plan audits to have a chance of averting the risk of collapse.

Consider a company that manufactures lifting equipment (hall cranes, gantry cranes for ports). It is a multinational enterprise with manufacturing plants all over the world. In Central and Eastern Europe (CEE region). It has 5 production sites.

The total number of suppliers for the CEE region is 2500. The company is lean oriented so that only one auditor takes care of the entire region from an auditing perspective. Therefore it is not possible to go around and audit all 2500 companies every year. So a strategy had to be developed, a key to audit only the companies with the highest risk.

In order to arrive at the key, it is necessary to centralise the data from all production sites. It is only after we have put together the jigsaw of information from each plant and each department that we can select the 100 suppliers we will look at.

And that brings us to enterprise information systems (for example, SAP, QI, Qlickwiev, Power BI) and the selection of appropriate KPIs (key performance indicators).

Monitored supplier metrics:

OTD (On Time Delivery) - On Time Delivery.

OTDr (On time Delivery Requested) - Confirmation of the requested time when the order is created.

OTDc (On Time Delivery Committed) - Actual achievement of the requested deadline

PPM (Parts per Million) - we track the poor quality per product line

Product complexity - do we have other suppliers that can make this product?

Spent - How much business does the supplier do for us (10 million Euros per year or 10 thousand Euros per year?)

Financial indicators (building a new hall, merger of two companies, change of ownership, change of production orientation, relocation to another location). Typically, an external consultancy firm is used (for example, Allianz Trade Euler Hermes), which sends a monthly report of our suppliers with a certain scoring

3. QUALITY 4.0 „THE CALM BEFORE THE STORM“

Over the last 5 years, Quality 4.0 has become a term that has been increasingly bandied about. But what is it? Has anyone defined quality 3.0? The problem is, they haven't. We can, however, consider Lean methods, Six Sigma, ISO standards (VDA, IATF, 9001, etc.), quality tools as the imaginary quality 3.0. It is therefore necessary to realize an extremely important thing, there is no smooth transition between quality 3.0 and 4.0. It is not an evolution, but a revolution.

A whole range of technical disciplines have made huge leaps forward in the last 30 years. However, this evolution has not progressed linearly over time, but exponentially. Thus, the deeper the technological knowledge we achieve, the faster we will achieve more. Today, we have fields dealing with new sensors - so we have very accurate and very cheap sensors. The whole IT industry has enabled us to link the different ERP systems in companies to create one comprehensive management system. We have cloud storage, which allows us to store large amounts of data and everyone can access it in real time.

Now it is necessary to predict where future developments will go. Many representatives of the American Society for Quality believe that Quality 4.0 will go the way of dynamic mathematical and physical models. These models will, for example, be linked to the stock exchange and will themselves order inputs into the plant at calculated prices according to world events - so the whole process of strategic buyers looking for 3-5% annual savings on inputs will disappear. The mills will no longer take advantage of variable energy prices to sell inventory for the biggest profits, thus of course rocking the entire supply chain.

The RnD department will also be transformed according to the same principle. It will no longer be engineers doing a thousand experiments on different designs to find the most optimal one in terms of function and cost. In the new concept, this search for the optimal design will be done by automatically running millions of simulations, from which the most optimal one will be selected by AI.

We are currently in a transition period. Quality management with automation elements is working well, it is efficient, the company is generating profit. However, in the new era there will be a hunt for savings, leadtime, reliability through not doing unnecessary operations with highly skilled workers.

The entire quality community is becoming obsolete and it is necessary to initiate their training and reorientation to new technologies. Indeed, we are facing a more dramatic leap than the introduction of the Internet and computers into businesses.

4. AUDITS ON THE ROAD TO QUALITY 4.0

Consider the contrast between current audits now in 2023 and future Audits 4.0 in 2030, for example.

Current supplier audits are conducted by having one or more auditors physically arrive at a supplier, perhaps thousands of miles away. They spend 1-3 days in the company, talk to people across the business, review the management system, track down evidence, assess relevant risks for the business and leave with a good idea of how the business is performing and how stable it is.

The pitfall of these audits is that we are only sampling the business over time. We are able to say that the business looks good at this point in time, and according to the records and the previous quarter, it was operating well. The problem, however, is that we have no idea what the business will look like a month from now. And it's impossible to go to all the suppliers every month. In addition, there are often long distances to cover, transportation costs, hotels, per diems. If the company employs an auditor, where the total cost of employees can be around 100 thousand crowns, at least another 50 thousand crowns will be spent on travel and hotels. It is not enough for a company to have only one auditor to keep the deliveries under control, but maybe 5. Then we are talking about high employee costs.

The audits of the future will be done differently. Every manufacturing company will have interconnected information systems with a digital network of individual machines, parts, work in progress. It won't be a lengthy and clumsy SAP, but it will be a quick connection of physical objects that will be displayed in an enterprise application. Due to the new sensors, the technical condition of machines, the location of work in progress and more will be continuously monitored. The audit itself will then take place only in the form of a self-test, where the company's information system will send various signals to its various corners and evaluate the answers it receives. In this way it will look for its weak points. The ISO 9001, IATF certificates will be replaced by IT companies that will certify the management system of the enterprise.

Now that we have described the state of today's audits and the state of future audits, we can define where I stand with my work today. My goal is to bridge this state, but we must reflect the current state of digitalisation. Businesses are strengthening automation, but no one is pushing them to go digital yet.

The automation of production audits in my work has the following milestones:

1. Unification of auditors' methodology within one corporation.
   - Consider a corporation that has manufacturing plants on different continents and has a total of 10 supplier auditors sitting in a total of 5 different countries.

2. Unify the methodology for evaluating audit results.
   - Each auditor audits differently and is "planted" on a particular matter. Someone "drills" in maintenance, someone in non-conforming part management, someone in workplace safety.

3. Reduce the time commitment for auditing.
   - After the first hundred or so companies audited, one finds that one gets about five possible answers to the same questions. Even if each manager wraps the lack of communication in a flashy speech so black and white the auditor finds that we are still talking about a few possible answers.

Step 1: Unify the auditors' methodology within a single corporation

An application will be created that will have a database of auditor questions. Every auditor will have this application. This application will also be intelligent and will guide the auditor which next question to ask if the previous question has a certain answer.

This will prevent auditors from 'skimming' on certain unimportant areas and instead dealing with the complexity of the business.

This will be a windows form/java application.

Step 2: Unify the methodology for evaluating the audit results.

The database of questions from the application of step 1 will also have a database of answers attached to each question. Thus, the auditor will circle the answer already predefined in the database, or the one that is closest to it, according to the answers. Each of these questions will be linked to a specific rating. We will thus achieve a fair evaluation, which will increase the trust of the audited company, because we will be transparent.

Step 3: Reduce the time required for auditing.

Before the auditor physically arrives at the business and starts the audit the first step must happen. Self-audit of the business. The auditor will send the enterprise a pre-window application where the management will perform a self-assessment, a self-audit. This will take the form of a window application where the manager of the business has to click through questions and provide basic information about the business. The objective of being an auditor is that the auditor does not have to be in the business for so long and the time commitment is reduced.

ACKNOWLEDGEMENT

I would like to thank Doc. Ing. Jiří David, Ph.D. for pointing out an interesting direction of study, which is very complementary to my profession and will be a contribution to both science and practice.

REFERENCES

[1] David A. Garvin, *"What Does Product Quality Really Mean?" Sloane Management Review*, Vol. 26, No. 1, 1984, pp. 25-43

[2] Watson, Gregory. *Analysis of lean process capability* [online]. Qualityprogress.com, 2020. Available from: https://gregoryhwatson.eu/wp-content/uploads/2021/04/1-QP-Analysis-of-Lean-Process-Capability-54-2-2021-Turunen-and-Watson.pdf

[3] Watson, Gregory. *Constant evolution toward Quality 4.0* [online]. Qualityprogress.com, 2020]. Available from: https://gregoryhwatson.eu/wp-content/uploads/2021/04/2-QP-Constant-Evolution-toward-Quality-4.0-53-8-2020-Watson.pdf

An analysis of the finance performance of BYD and Tesla

Author(s): Jingjing DUAN

Supervisor: prof. Ing. Kamila JANOVSKÁ, Ph.D.

Department: Department of Economic and Management, Faculty of Materials Science and Technology, VSB-TUO

Abstract

The paper focuses on the world's famous new energy automobile enterprise Tesla and China's new energy automobile industry leader BYD and .It discusses the differences between two companies from three dimensions: product matrix, target market and entry mode, and makes a deeper comparison of Finance Performance from four aspects: scale, operating capacity, operating capacity and debt paying capacity. The entropy weight method is used to compare the of the Finance Performance two enterprises, and the corresponding conclusion is drawn.

Key words: New Energy Automobile; Finance Performance; Entropy Weight Method

1. INTRODUCTION

BYD is currently the company with the best development momentum and scale among China's new energy vehicle companies. The new power of car making represented by Tesla is taking advantage of its first-mover advantage and internet gene to seize the market share of traditional car enterprises. Its passenger car sales surpassed BYD in 2019 and ranked the first place [1]. Therefore, this paper will compare Tesla and BYD, two major new energy vehicle companies, to understand the development characteristics and advantages of their respective companies, in the hope of learning from each other and making progress together.

2. A COMPARISON OF TESLA AND BYD ON INTERNATIONALIZATION

Tesla and BYD are now two leading companies on New Energy Automobile, so comparisons on product, target market and enter mode are made as the following table:

Table1 Comparison of internationalization

Company	Product matrix	Target market	Enter mode
Tesla	Using Passenger Vehicle to enter the market, high -end car layout.	Local, Chinese and European markets	Franchise and investment in building factory
BYD	Using Commercial Vehicle to enter the market, low -end car layout.	Developed countries first, then developing countries	Direct exports, investment in factories and strategic alliances

Source: Company official website data collation

3. A COMPARATIVE ANANLYSIS OF FINANCE PERFORMANCE

3.1 Build an indicator system

After consulting relevant materials, this paper selects four capability indicators related to the evaluation of finance performance. They are scale capacity, operation capacity, profitability and solvency [2]. Under the first-level index system, 17 second-level indexes are selected specifically.

Table2 Index System

First level index	Second level index	Unit	Symbol
Scale	Total Asset	One hundred million yuan	X1
	Total revenue	One hundred million yuan	X2
	Debt Asset ratio	%	X3
	R&D expenditure	One hundred million yuan	X4
	Number of employees	People	X5
Operating capacity.	Inventory turnover	%	X6

	Current Assets Turnover	%	X7
	Fixed Assets Turnover	%	X8
	Total Assets Turnover	%	X9
Profitability	Return on equity	%	X10
	Total assets profit ratio	%	X11
	Net profit ratio	%	X12
	Gross profit ratio	%	X13
Solvency capacity	Current ratio	%	X14
	Quick ratio	%	X15
	Cash flow ratio	%	X16
	Equity ratio	%	X17

Source: own

3.2 Data processing

This report takes BYD and Tesla as empirical samples for research, and collects data of BYD and Tesla from 2017 to 2021 from 17 dimensions ranging from level 1 to Level 4 indicators.

Table 3 Tesla Business performance evaluation system

First level index	Second level index	2021	2020	2019	2018	2017
Scale	X1	396.13	340.26	239.35	204.11	187.24
	X2	343.15	205.77	171.46	147.29	76.83
	X3	49.17	54.49	76.36	78.77	80.34
	X4	25.91	14.91	13.43	14.6	13.78
	X5	99290	70757	48016	48817	37543
Operating capacity.	X6	8.16	6.51	6.15	6.48	4.4
	X7	2	1.62	2.41	2.89	1.83
	X8	2.11	1.55	1.27	1.07	0.66
	X9	0.94	0.73	0.77	0.74	0.46
Profitability	X10	21.04	4.99	-14.94	-21.31	-43.63
	X11	9.66	1.67	-2.69	-3.34	-7.64
	X12	10.49	2.73	-3.15	-4.95	-19.05
	X13	25.28	21.02	16.56	18.83	18.9
Solvency capacity	X14	1.38	1.88	1.13	0.83	0.86
	X15	1.08	1.59	0.8	0.52	0.56
	X16	0.58	0.42	0.23	0.21	-0.01
	X17	0.97	1.2	3.23	3.71	4.09

Source：financial report

Table 4 BYD Business performance evaluation system

First level index	Second level index	2021	2020	2019	2018	2017
Scale	X1	2957.8	2010.17	1956.42	1945.71	1780.99
	X2	2161.42	1565.98	1277.38	1300.55	1059.15
	X3	64.76	67.94	68	68.81	66.33
	X4	106.26	85.55	84.21	85.36	62.66

	X5	288186	224300	229145	220152	200949
Operating capacity.	X6	5.03	4.43	4.12	4.71	4.61
	X7	1.56	1.43	1.15	1.19	1.17
	X8	3.73	3.01	2.74	2.99	2.62
	X9	0.87	0.79	0.65	0.7	0.66
Profitability	X10	4.01	7.45	2.88	5.05	7.65
	X11	1.6	3.03	1.09	1.91	3.04
	X12	1.84	3.84	1.66	2.73	4.64
	X13	13.02	19.38	16.29	16.4	19.01
Solvency capacity	X14	0.97	1.05	0.99	0.99	0.98
	X15	0.72	0.75	0.75	0.76	0.79
	X16	0.38	0.43	0.14	0.11	0.06
	X17	1.84	2.12	2.13	2.21	1.97

Source：financial report

After using entropy method to calculate, Table5 shows the final results:

Table 5 Entropy and weight

Second level index	Entropy	Difference coefficient	weight
X1	0.64883333	0.35116667	0.07653561
X2	0.75237499	0.24762501	0.05396905
X3	0.67319180	0.32680820	0.07122676
X4	0.62658785	0.37341215	0.08138394
X5	0.71828248	0.28171752	0.06139940
X6	0.82467367	0.17532633	0.03821179
X7	0.66637794	0.33362206	0.07271182
X8	0.74848858	0.25151142	0.05481608
X9	0.74705109	0.25294891	0.05512937
X10	0.79470371	0.20529629	0.04474364
X11	0.77172117	0.22827883	0.04975261
X12	0.76629618	0.23370382	0.05093497
X13	0.79748417	0.20251583	0.04413765
X14	0.65966497	0.34033503	0.07417489
X15	0.73479202	0.26520798	0.05780120
X16	0.75460170	0.24539830	0.05348374
X17	0.72659595	0.27340405	0.05958750

Source: own

3.3 Comprehensive evaluation of business performance

According to the company data of BYD and Tesla from 2017 to 2021, the entropy weight method is used to calculate the results in the following table:

Table 6 2017-2021 Comprehensive Rating score

	2021	2020	2019	2018	2017
Tesla	0.872538349	0.603618107	0.311483346	0.2744559	0.030312606
BYD	0.595430834	0.480209233	0.154515239	0.265908831	0.290004868

Source: own

According to the comprehensive score, it can be seen that BYD's score fluctuates greatly, but Tesla's score shows a steady upward trend. BYD's comprehensive score in 2018 is higher than Tesla's, but Tesla's comprehensive score develops rapidly and exceeds BYD's in 2019. Therefore, the study of

Tesla's business countermeasures has certain reference significance for the development of new energy vehicle enterprises [3].

Table 7 2017-2021 Scale capability score

	2021	2020	2019	2018	2017
Tesla	0.34260067	0.185593364	0.05806122	0.043020055	0.002316854
BYD	0.288658339	0.102210704	0.085266211	0.078454048	0.009425327

Source: own

The overall evaluation of BYD's scale capability increased steadily from 2017 to 2021, while Tesla increased drastically in 2020. Tesla surpassed BYD in scale from 2020. Both companies have seen one or more significant increases in revenue, headcount and R&D spending starting in 2020.

Table 8 2017-2021 Operating capacity score

	2021	2020	2019	2018	2017
Tesla	0.169935619	0.086121408	0.121701958	0.14153086	0.012045301
BYD	0.220891144	0.117038172	0.005948149	0.062692028	0.026650464

Source: own

On the whole, Tesla's operating capacity showed a fluctuating rising trend from 2017 to 2021, and decreased after 2018, but rose to a new height in 2021. The operating capacity of BYD rise steadily, and surpass Tesla in 2020 and 2021.

Table 9 2017-2021 Profitability score

	2021	2020	2019	2018	2017
Tesla	0.18958783	0.120561982	0.061520373	0.063630077	0.011863235
BYD	0.026707434	0.173782828	0.022712372	0.083041174	0.187020074

Source: own

The profitability of BYD fluctuates greatly, reaching the peak in 2020, but falling sharply in 2021. Tesla has shown a steady upward trend, especially after the completion of the Shanghai Gigafactory in 2020, its profitability has been greatly improved.

Table 10 2017-2021 Solvency capacity score

	2021	2020	2019	2018	2017
Tesla	0.17041423	0.211341353	0.070199795	0.026274907	0.004087217
BYD	0.059173917	0.087177529	0.040588507	0.041721581	0.066909004

Source: own

At first，the solvency and volatility of BYD is higher than Tesla, and the gap between them is always small. Moreover, Tesla gradually surpass BYD in 2019.

4. CONCLUSION

An overall analysis of Tesla and BYD new energy vehicles shows that new energy vehicles can serve as a powerful starting point for the transformation and development of the traditional automobile industry, which faces a very broad market both at home and abroad [4].

REFERENCES

[1] Jiateng Li. Prediction of the Future of Electric Vehicle in the US Market based on Tesla Inc.'s Case.Wuhan Zhicheng Times Cultural Development Co., Ltd..Proceedings of 2020 International Conference on Economic Development and Innovation (EDI 2020).Wuhan Zhicheng Times Cultural Development Co., Ltd.

[2] Dong Xiaojing. A comparative study on the internationalization path of new energy vehicles BYD and Tesla.Jiangxi University of Finance and Economy,2020.

[3] Marcello Contestabile, Mohammed Alajaji, Bader Almubarak. Will current electric vehicle policy lead to cost-effective electrification of passenger car transport? Energy Policy,2017(110):20-30.

[4] Taeseok Yong, Chankook Park. A qualitative comparative analysis on factors affecting the deployment of electric vehicles. Energy Procedia, 2017(129):497-503.

ANALYSIS OF MULTITHREAD IMAGE PROCESING WORKLOADS ON THE ARM SERVER SYSTEMS

Author(s): Petr HAVLÍČEK

Supervisor: doc. Ing. Miroslav MAHDAL, Ph.D.

Department: Department of Industrial Systems Management. Faculty of Materials Science and Technology. VSB – Technical University of Ostrava

Abstract

This study investigates the multithread scalability of the OpenCV framework ARM servers. The performance of various image processing functions, including Canny edge detection, segmentation using Watershed transformation, binarization using adaptive thresholding algorithm, image resizing, and image filtering using Gaussian filter, was compared on both x86 and ARM servers. The results demonstrate the impact of thread count on processing time and highlight the differences between x86 and ARM architectures in terms of performance and scalability.

Key words:

Image processing, arm, multithread, scalability, performance.

1. INTRODUCTION

Image processing tasks are generally considered well-suited for parallel processing, which can result in significant performance enhancements on systems with multiple CPU cores [1]. Many real-world situations can benefit from using simpler capture devices that send data to a centralized processing server. The primary advantages of this approach are cost-effectiveness and easier system management.

When sizing a server, it is essential to consider the amount of data it needs to process and, more importantly, the complexity of the processing itself. In terms of CPU processing, the main factors for calculating delivered power are core count and frequency [1]. The most widely used CPU core architecture today is x86, a complex CISC architecture that supports a wide range of applications. In the past decade, ARM, a more straightforward RISC-based architecture, has emerged as a significant competitor [2]. ARM is usually delivered as a System-on-Chip (SoC) with many other modules packaged in one case.

Initially, ARM was targeted primarily at battery-powered appliances such as cell phones and tablets. In recent years, however, it has also made inroads into the server segment. ARM cores are much more power-efficient than x86 cores, which means that server systems can accommodate a higher number of ARM cores. This can be particularly beneficial for applications with excellent multithread scaling capabilities [2].

This article tests the multithread scalability of the OpenCV framework on multicore x86 and ARM servers. These servers are not specifically designed for image processing. It is evident that more specialized hardware would deliver better performance than the tested systems. However, this study aims to compare the CPU architectures rather than achieve the best possible performance.

2. BECHMARKING

For the test, two physical servers with hardware configurations shown in Table 1 were selected. Both servers run the same operating system, GNU/Linux. The benchmark application was created specifically for this article in Python (version 3.9.2) and used precompiled OpenCV (version 4.7.0).

Table 1 Hardware configuration of testing servers. Source: (own)

	HPE ProLiant RL300 Gen11	DELL PowerEdge R740
CPU Type	Ampere Noverse N1	2x Intel Silver 4215
Cores	80 physical	8 physical (16 logical)
Frequency	3 GHz	2,5 GHz
Memory	512 GB	512 GB

For measurement on each image run set of tests. The processing time is measured after loading image to OpenCV frame and refer only for time of running specific built-in function. The list of tested function is here:

- Canny edge detection [3],
- segmentation using Watershed transformation[4],
- binarization using adaptive thresholding algorithm,
- image resizing,
- image filtering using Gaussian filter.

These functions accept setNumThreads() argument for defining the number of threads that will be used during processing itself. This sets the number of threads for a specific function, not the number of parallel functions or parallel processing, as in the case of multithread implementation in Python itself.

The dataset is a subset from the Open Google Image dataset for machine learning neural networks for image classification. The measurements are based on 10,000 images from the dataset [5], and for comparison, the 5,000 largest images were used because there is a more significant part of CPU processing instead of other overhead with loading images.

Measurements were conducted multiple times with different thread counts, and Figure 1 shows different plots of median time for processing one image.

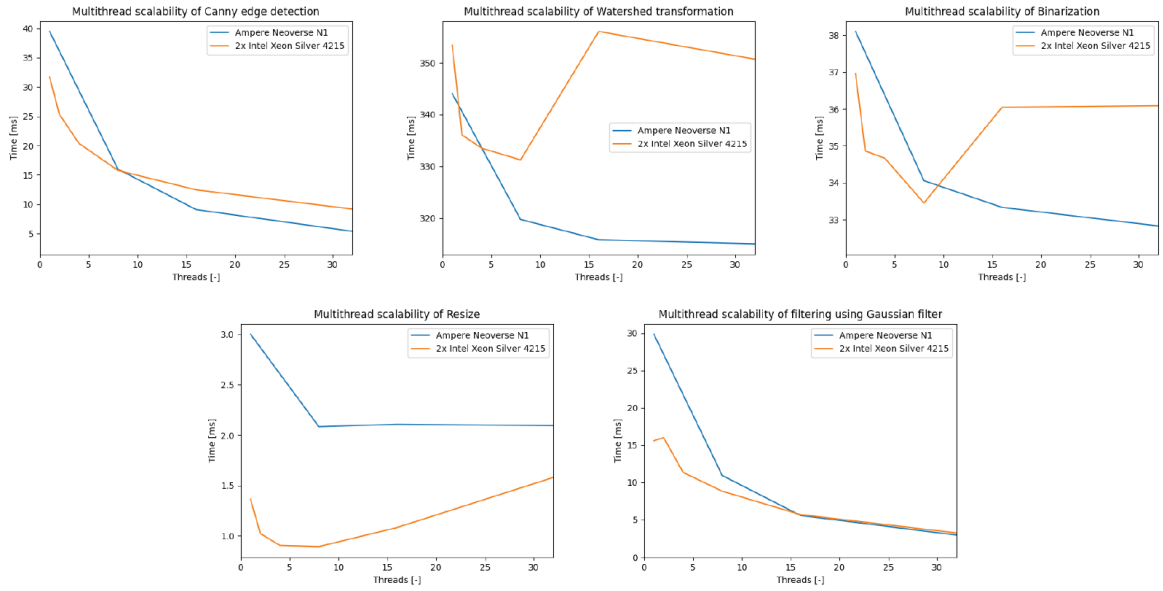

Figure 1 Charts of multithread scalability. Source: (own)

From the plots, it is visible that not all used functions benefit from multithread processing. During the first observation, the idea arose that it could be caused by some other system tasks, so the test on the x86 system was run several times. The results were almost identical in each iteration.

The precise numbers are shown in Table 2, where data up to 80 cores from ARM systems are presented. The 4 threads values are missing for the ARM system because the servers were borrowed for testing and were the first system and showed in direct proportion. There was no need for adding more samples at low core counts. During measurements at x86, it sometimes showed up as an indirect

proportion, so more samples were inserted. However, between the tests, the ARM system was returned, and additional samples could not be obtained.

Table 2 Measured times of individual tests. Source: (own)

	Canny [ms]		Watershed [ms]		Binarization [ms]		Resize [ms]		Gaussian [ms]	
	x86	ARM	x86	ARM	x86	ARM	x86	ARM	x86	ARM
1 Thread	31.7016	39.4881	353.4086	344.0597	36.9637	38.1019	1.3647	3.0017	15.5783	29.8617
4 Threads	20.3938		333.5388		34.6653		0.9050		11.3468	
8 Threads	15.7676	15.9893	331.2583	319.7701	33.4530	34.0593	0.8934	2.0835	8.8329	10.9422
16 Threads	12.4626	9.0897	356.0534	315.8505	36.0470	33.3347	1.0834	2.1083	5.7056	5.5904
32 Threads	9.1746	5.3768	350.6877	315.0511	36.0909	32.8312	1.5805	2.0943	3.2473	2.9533
64 Threads		3.5703		317.0550		32.3455		2.0928		1.6341
80 Threads		3.2382		322.1967		32.5069		2.0885		1.4086

3. THE RESULTS

It is expected that with a higher thread count, the processing time decreases. This trend can clearly be observed in the data, as expected, at least on the ARM system. Canny edge detection and Gaussian filtration benefit the most from multi-thread processing.

Initially, the x86 system was added just for outlining performance differences between systems. First, let's look at single-core tests, where the older x86 CPU usually performs better than a single core on ARM. It is not new that ARM cores are a little slower. The new information is that in binarization, the results are almost the same (the difference in speed is just 3%).

The x86 system has a slightly different architecture due to the two-socket setup. There are non-uniform memory access (NUMA) [6] nodes allocating memory banks to each CPU. In higher core tests, both CPUs must be engaged, and inter-CPU communication occurs. These CPUs are also equipped with hyperthreading (HT) [7] support, which provides hardware acceleration for switching context in CPU registry and some other tasks, and in some circumstances, this can add as much power as a new physical core.

There wasn't a clear way to decide if the 8-core test ran on a single CPU with HT or just physical cores on both processors. This complex optimization probably caused some unclear measured data, where with a higher thread count, it performed slower than with fewer cores.

4. CONCLUSION

During the process of designing a system for image processing and validation, it is crucial to select a system with sufficient power to complete the processing of one image before another arrives. Parallelism can be achieved in processing a single image, but multiple images cannot be processed simultaneously. The only system that benefits from both levels of parallelism is the one where multiple image sources send data to a single server for processing. In such a system, each image source can be processed in parallel.

The results indicate that the OpenCV framework has good built-in multithread support. An increase in performance can be expected with the addition of more cores to the system. The tests clearly demonstrate that multicore scaling in ARM systems is effectively implemented. Further research could involve validating these findings by testing other ARM server systems, as there are ARM processors with 256 cores and even more cores may become available in the future.

The measurements provide greater visibility into the scaling itself. At high thread counts, the benefits are not as significant as expected. Beyond a certain point, there is only a small percentage gain in power with double the core count. With more data sources, it makes much more sense to sacrifice these few percentage points and run another data stream on the second half of the cores.

The great news is that the performance of the ARM processors is getting close to mainstream x86 ones, and it is possible rune more parallel task than on x86 severs. The interesting topic for next measurement is also power consummation of this ARM servers.

This article shows that ARM systems are relevant during methodology of designing image processing systems with parallel data sources for industrial application like quality control during manufacturing.

ACKNOWLEDGEMENT

The work was supported by the project Development of Integrated Management of Industrial Processes through Linking The Principles of Smart Production and Quality Management founded by the of the Ministry of Education, Youth and Sports of the Czech Republic No. SP2023/043.

Thank you the HPE company for borrow the newest ARM system in their portfolio for create this comparative measurement.

REFERENCE

[1] H. WANG, J. ZHAO, H. LI, and J. WANG, "Parallel Clustering Algorithms for Image Processing on Multi-core CPUs," in *2008 International Conference on Computer Science and Software Engineering,* 2008, vol. 3, pp. 450-453. doi: 10.1109/CSSE.2008.1018

[2] S.V. BHARADWAJ and C.K. VUDADHA, "Evaluation of x86 and ARM architectures using compute-intensive workloads," in *2022 IEEE International Symposium on Smart Electronic Systems (iSES)*, 2022, pp. 586-589. doi: 10.1109/iSES54909.2022.00128.

[3] KIM, Y.W., J, I.R. & KRISHNA, A.V. A Study on the Effect of Canny Edge Detection on Downscaled Images. *Pattern Recognit. Image Anal*. **30**, 372–381 (2020). https://doi.org/10.1134/S1054661820030116

[4] A.S. KORNILOV and I.V. SAFONOV, "An Overview of Watershed Algorithm Implementations in Open Source Libraries," *Journal of Imaging*, vol. **4**, no. 10, article no. 123, 2018. ISSN: 2313-433X. doi: 10.3390/jimaging4100123. Available at: https://www.mdpi.com/2313-433X/4/10/123.

[5] Google. Open Images V7 [online]. [Accessed 2023-02-01]. Available from: https://storage.googleapis.com/openimages/web/index.html

[6] C. HOLLOWELL, C. CARAMARCU, W. STRECKER-KELLOGG, A. WONG, and A. ZAYTSEV, "The Effect of NUMA Tunings on CPU Performance," *Journal of Physics: Conference Series*, vol. 664, no. 9, pp. 092010, Dec. 2015. doi: 10.1088/1742-6596/664/9/092010.

[7] MARR, Deborah T., Frank BINNS, David L. HILL, Glenn HINTON, David A. KOUFATY, J. Alan MILLER a Michael UPTON. Hyper-Threading Technology Architecture and Microarchitecture. *Intel Technology Journal* [online]. 2002, 6(1), 1-12 [cit. 2023-05-30]. ISSN 1535864X. Dostupné z: https://search.ebscohost.com/login.aspx?direct=true&db=bsu&an=6769155&scope=site

WILL OPTIMIZING THE DOING BUSINESS BOOST CONSUMPTION? EMPIRICAL ANALYSIS BASED ON WUHAN

Author(s): Weixue HAN

Supervisor: prof. Ing. Kamila JANOVSKÁ, Ph.D.

Department: Department of Economic and Management in industry, Faculty of Materials Science and Technology, VSB-TUO

Abstract

Will improving the Doing Business boost or discourage residential consumption? This study uses the entropy value method to evaluate the Doing Business in Wuhan from 2012-2021.The study found that Wuhan's Doing Business score has shown positive growth over the past decade. Further analysis of the chain growth rate shows that the growth of Wuhan's Doing Business is dynamically fluctuating, and the growth rate has been decreasing year on year for the past three years. A least squares regression model was constructed to explore the relationship between the Doing Business and consumption levels in Wuhan. The study found that Wuhan's Doing Business has a positive and significant impact on residents' consumption.

Key words:
Doing Business; consumption; Wuhan.

1. INTRODUCTION

The coronation epidemic caused a brief break in the global value chain. To prevent and control disease outbreaks, while also protecting local industries. World value chains are trending toward localization and regionalization. As a result of the dramatic external changes, China has also made a major strategic shift from foreign investment to domestic demand to drive economic growth and quality economic development.

Since the COVID-19 in 2020, China's domestic consumer demand has been out of balance with international consumer demand. It grows negatively by -3.6% in 2020 and resumes a very small positive growth in 2021. China's total retail sales of consumer goods exceeded RMB 40 trillion in 2021, an increase of 12.5% over the previous year. The contribution of domestic demand to economic growth will be close to 80%, 4.4% higher than the previous year. Consumption takes another sharp turn in 2022 due to the massive rebound of the epidemic. Total retail sales of consumer goods in China decline by 0.2% year-on-year in 2022. In particular, consumption fell by 1.8% year-on-year in December and by 3.7% in real terms net of prices. The consumer market shows a steady recovery in 2023 with the gradual liberalization of epidemic control in China. According to the National Bureau of Statistics, China's total retail sales of consumer goods were RMB 7.8 trillion, up 3.5% year-on-year.

The Doing Business, as one of the important factors for local economic development, has also received much attention in China in recent years. Improving the quality of the Doing Business is of great importance to the economic development, business investment, employment opportunities and the living standards of residents in all regions.

At present, there is one important issue for further deepening of the Doing Business: will improving the Doing Business boost consumer consumption? How strong is the boost or disincentive?

Based on existing research, the most commonly used consumption expenditure per capita is used as the explanatory variable in this paper. Wuhan was selected as the sample city and the Doing Business of Wuhan over the years was rated through the above index system as the explanatory variable. The urban registered unemployment rate, consumer price index, per capita disposable income of urban residents and gross national product were selected as control variables. In this way, the relationship between the Doing Business and consumption is further explored.

2. Model construction, selection of indicators and data sources

2.1 Model construction

Keynes' theory of absolute consumption states that the relationship between consumption expenditure and income is not simply linear. Rather, there is a certain non-linear relationship. When income is low, consumption expenditure increases rapidly as income rises; when income is high, the rate of increase in consumption expenditure gradually slows down. Therefore, increasing the income

level of residents can promote the growth of consumption. But increasing income does not necessarily increase the growth rate of consumption directly.

Based on the core research theme of this study, with reference to the research results of Liu Hong[7], Yu Yang[8] and Wang Chen[9] et al. The Doing Business was selected as the core explanatory variable and measured by the Doing Business index score calculated by the entropy method. Consumption level was chosen as the explanatory variable and measured by per capita consumption expenditure. The urban registered unemployment rate, consumer price index, urban disposable income per capita and gross national product were chosen as control variables.

According to existing studies, unemployment leads to a reduction in work-related consumption. The consumer price index reflects the trend of commodity price changes. Therefore, the relationship between these two and consumption is considered to be inversely correlated. According to Keynes' absolute income hypothesis, in the short run, income and consumption are correlated, and they show a positive relationship. GDP is an important indicator of economic development. Its development leads to an increase in the income of the population which in turn affects the consumption of the population.

Based on this , this paper aims to explore the impact of Wuhan's Doing Business on residents' consumption. The data involved in the variables are obtained from the Wuhan City Statistical Bulletin. This can be seen in Table 1 below.

Table 1 Variable description. Source: (own)

Characters of variables	Variable names	Variable notation	Data sources
Explained variables	per capita consumption expenditure	PE	Wuhan City Statistical Bulletin
Explanatory variables	Doing Business Index	BEI	Calculated from the indicator system
	Urban registered unemployment rate	URUR	Wuhan City Statistical Bulletin
	Consumer Price Index	CPI	Wuhan City Statistical Bulletin
Control variables	Disposable income per urban resident	UPDI	Wuhan City Statistical Bulletin
	Gross Domestic Product	GDP	Wuhan City Statistical Bulletin

According to Keynes' absolute consumption theory, a regression model of the impact of Doing Business on residents' consumption in Wuhan can be constructed as follows：

$$PE=B+\beta_1 \ln BEI+\beta_2 \ln URUR+\beta_3 \ln CPI+\beta_4 \ln UPDI+\beta_5 \ln GDP+\varepsilon \quad (1)$$

In the above equation, B denotes the constant term; β1, β2, β3, β4 and β5 are the OLS regression model impact coefficients and ε denotes the error term of the regression model.

To attenuate heteroskedasticity in the model data, logarithms were taken for all data in the model.

2.2 Selection and Construction of a Doing Business Evaluation Index System

With reference to the research results of Li Yan [1], Qiu Kangquan [2], Tu Zhengge [3] and others. Based on the connotation of the concept of Doing Business as well as following the principles of scientific, systematic, operable and dynamic construction of a comprehensive index system. A comprehensive evaluation index system of Doing Business is constructed from four latitudes: business cost, factor market, macro environment and ecological environment. There are four criteria level indicators, twelve factor level indicators and twenty-five indicator level indicators in this index system.

2.3 Data sources

The data on the variables involved in this study were obtained from the Wuhan Statistical Yearbook and the Wuhan Statistical Bulletin. The missing data were mainly interpolated by the mean interpolation method and linear interpolation method.

3. Empirical research

3.1 Analysis of the evaluation results of Wuhan's Doing Business

Based on the index system, the indicator data obtained from the Wuhan Statistical Yearbook and Wuhan Statistical Bulletin were integrated. The weights of the indicators of the indicator layer in the comprehensive evaluation index system of the Doing Business in Wuhan were calculated. The Doing Business Index score for Wuhan from 2012-2021 can be calculated. The year-on-year growth rate can also be calculated with the help of the score results at each time point, as shown in Table 2 below.

Table 2 Results of Doing Business Evaluation Index Scores for Wuhan from 2012 to 2021.
Source: (own)

year	2012	2013	2014	2015	2016	2017	2018	2019	2020	2021
score	0.16	0.20	0.24	0.34	0.37	0.51	0.60	0.67	0.70	0.81
rank	10	9	8	7	6	5	4	3	2	1
YOY		25%	20%	41.7%	8.8%	37.8%	17.6%	11.7%	4.5%	15.7%
rank		3	4	1	8	2	5	7	9	6

Firstly, Wuhan's Doing Business Index score has shown a year-on-year increase from 2012 to 2021. This indicates that Wuhan's Doing Business has been continuously improved and enhanced over the past decade. From a score of 0.16 in 2012 to 0.81 in 2021, the overall score has increased by nearly five times, which proves that Wuhan has made significant progress in terms of its Doing Business.

Secondly, the growth rate of the Doing Business Index over the last ten years shows a dynamic fluctuation. The fastest growth rate was recorded in 2015, when the year-on-year growth rate ranked first, reaching 41.7%. This indicates that Wuhan's Doing Business was highly effective in that year. The slowest growth rate was recorded in 2020, when the year-on-year growth rate was at the bottom of the list, at 4.5%. This indicates a relatively low level of improvement in Wuhan's Doing Business in that year, mainly due to the impact of the COVID-19.

Thirdly, the year-on-year growth rate of Wuhan's Doing Business index has gradually slowed down over the past three years. This reflects the fact that the current momentum of Doing Business development in Wuhan is still insufficient. The growth rates over the last three years have been 11.7%, 4.5% and 15.7% respectively, a decline relative to the previous growth rates. There is a need to find further power points to stimulate and promote the development of the Doing Business in order to drive its further optimisation and development.

3.2 An empirical study of the impact of the Doing Business on consumption levels in Wuhan

3.2.1 Descriptive analysis

A descriptive statistical analysis of the variables involved in the impact of Wuhan residents' consumption level on the Doing Business was conducted using Stata 17.0 software. This can be seen in Table 3 below.

Table 3 Descriptive statistics results Source: (own)

Variable	N	Mean	Std. Dev.	Min	Max
PE	10	2.29	0.03	2.24	2.33
BEI	10	-0.91	0.57	-1.83	-0.21
URUR	10	1.10	0.15	0.76	1.34
CPI	10	4.63	0.01	4.61	4.64
UPDI	10	10.57	0.32	10	10.92
GDP	10	9.66	0.61	9.11	11.29

3.2.2 Correlation analysis

Correlation analysis was conducted on the variables involved in this study. The core explanatory variable BEI was found to be positively correlated with the explanatory variable PE, with a correlation coefficient of 0.946 by the 5% significance test. It can therefore be concluded that there is a strong positive correlation between the core explanatory variables and the explanatory variables in this study, and further causal inferences can be made between the explanatory variables and the explanatory variables.

3.2.3 Regression analysis

The regression analysis was carried out for model (1) and the specific influence relationship can be seen in Tables 4 below. It can be found that Doing Business (BEI) has a positive influence on consumption (PE) with a coefficient of influence of 0.084 by 5% significance test. The R2 is 0.965, which is a good explanation rate.

The model was further tested for covariance, F-test, heteroskedasticity and autocorrelation and it was found that the model passed all these tests and therefore the estimation results of model (1) could be considered valid. The regression analysis leads to the following conclusions.

Firstly, the optimisation of Doing Business has boosted consumption in Wuhan. For every unit of improvement in the Doing Business, Wuhan's consumption level will increase by 0.084 units.

Secondly, the control variables show that the disposable income of urban residents passes the 5% significance test. For every unit increase in its level, the consumption level will decrease by 0.007 units, the sign is not as expected. This may be related to various business restrictions and people's

fears, with consumers' desire to spend being greatly curbed. Consumers are more inclined to save rather than spend when they have some surplus after the epidemic. Which is used to satisfy an inner sense of security.

Table 4 Results of regression analysis souce. Source: (own)

PE	Coef.	Std. Err.	t	P>|t|
BEI	.0838258	.0183454	4.57	0.010***
URUR	-.0039671	.0232297	-0.17	0.873
CPI	.1598723	.4741962	0.34	0.753
UPDI	-.0695491	.0230046	-3.02	0.039**
GDP	.0003562	.0020203	0.18	0.869
R-squared 0.965				

Note: significance level:***=p<0.01; **=p<0.05; *=p<0.1

A unit root test on the seven core variables of this study revealed that the variables GDP was found to be significantly stable at the 5% level of zero order; PE, BEI, URUR and UPDI were found to be significantly stable at the 5% level of lagged first order; CPI was found to be significantly stable at the 5% level of lagged second order. Therefore, all the variables involved in this study are considered to be stable.

By using the replacement variable method, the explanatory variable was replaced from consumption expenditure per capita to total retail sales of consumer goods as a share of GDP. Regression analysis was again conducted. The effect of Doing Business on consumption levels in Wuhan was found to remain significant after replacement, with a p-value of 0.051, and for every 1% improvement in Doing Business, consumption levels would increase by 0.345%. The impact of business environment on consumption level is considered to be robust.

4. Conclusions and recommendations for countermeasures

The main conclusion from the above empirical study is that Doing Business can significantly affect the level of consumption. For every unit increase in the Doing Business, the consumption level in Wuhan will increase by 0.084 units. Based on this, this study proposes a strategy to promote the improvement of residents' consumption level with the business environment as the core from four aspects. These are to create an open and inclusive market environment, to build an efficient and convenient governmental environment, to strengthen the security capacity of resource factors, and to actively create a livable and business-friendly ecological environment. The details are as follows:

Creating an open and inclusive market environment. The Wuhan government should promote market-oriented reforms, lower market entry barriers, strengthen market regulation, protect the legitimate rights and interests of consumers, enhance market dynamics, and explore and cultivate new consumption models. This will raise residents' incomes, protect their confidence in consumption as well as meet their diverse consumption needs and raise consumption levels.

Building an efficient and convenient governmental environment. To achieve standardisation, informatisation and intelligence in government services. The government creates a favourable atmosphere for innovation and entrepreneurship through measures such as improving the efficiency of approval and reducing transaction costs for enterprises.

Strengthening the ability to secure resource elements. Increase investment in infrastructure such as transportation, water conservancy and energy, improve public services, strengthen investment in education, science and technology, and improve the quality of talent training.

Actively create a livable and business-friendly ecological environment. Promote the development of clean energy and green industries to improve the quality of the city's ecological environment. Strengthen urban planning and management, and promote the coordinated development of urban ecology and construction in order to enhance the attractiveness and competitiveness of the city.

ACKNOWLEDGEMENT

This paper was created Results were achieved thanks to the financial by the project no. P2023/082Single-seat electric vehicle design for micro-mobility in urban environments and university campuses.

REFERENCES

[1] LI Yan, Zhi ZHANG. Business environment, entrepreneurship and economic growth quality: empirical evidence from Chinese cities [J]. *Macro Quality Research*, 2021, **9**(04), 48-63.

[2] QIU Kangquan, Jing CHEN, Yanqin LV. The measurement, regional differences and dynamic evolution of the comprehensive development level of China's business environment [J]. *Quantitative, economic and technical economic research*, 2022, **39**(02),121-143.

[3] TU Zhengge, Long CHENG, Mu ZHANG. A study of regional differences and spatial and temporal evolution of business environment in China [J]. *Research in Quantitative Economics and Technology Economics*, 2022, **39**(07),3-25.
[4] BEATA Milewska. The Impact of Instability in the Business Environment on the Competitiveness of Enterprises Using the Example of the Apparel Industry [J]. *Sustainability*, 2022, **14**(22),14673

ALTERNATIVE FUELS IN PUBLIC TRANSPORT

Author: Lucie HOFRICHTEROVÁ

Supervisor: prof. Ing. Kamila JANOVSKÁ, Ph.D.

Department: Department of Industrial Systems Management, Faculty of Materials Science and Technology, VSB – Technical University of Ostrava

Abstract

Cities around the world are looking for ways to reduce their carbon footprint, and in the Czech Republic Ostrava is leading the way with its commitment [1] to hydrogen-powered public transport. This article looks at alternative fuel solutions, including innovative hydrogen fuel cell technology and its benefits for the environment and public transport passengers. In addition to being emission-free, hydrogen-powered vehicles provide a quieter and smoother ride, making passengers more comfortable. Given the town of Ostrava's growing emphasis on ecology and sustainability, hydrogen-powered public transport is a key part of Ostrava's vision of a cleaner and more liveable urban environment.

Keywords:

Urban Public Transport, Infrastructure, Environmental, Electric Vehicles, Hydrogen.

1. INTRODUCTION

The energy crisis, the increasing number of vehicles and the related accumulation of negative impacts have made the development of low-emission and high-fuel-efficient vehicles a major research goal for many researchers and companies [2]. The requirements for sustainable development and emission reduction in the transport sector have substantially contributed to the increased use of alternative fuels. This phenomenon is also evident in urban public transport, where urban transport companies are trying to gradually replace diesel powered vehicles with vehicles that are powered by alternative fuels. However, the use of new fuels with minimal environmental impact and the requirements for individual delivery and improved customer service often conflict with the cost of transport. The provision of transport in cities has therefore been a long-standing concern in optimising the transport system in relation to environmental and cost sustainability [3].

In the Czech Republic, it has been Ostrava, the third largest city, that appears to be the pioneer in alternative fuel powered public transportation. The article deals with 3 types of alternative fuels to diesel, which are currently being or planned to be operated in Ostrava, namely electricity, natural compressed gas, and hydrogen powered public transport.

2. OSTRAVA AND ITS ALTERNATIVE FUEL SOLUTIONS

Ostrava is a town located in the northeastern region of the Czech Republic and has a rich industrial history. According to [4], Ostrava ranks among the most polluted cities in Europe, with high levels of particulate matter and nitrogen dioxide. Despite major efforts in tackling air pollution and environmental degradation, more action is needed to address the effects of industrialization to ensure that Ostrava's environment is sustainable for generations to come. The City Council of Ostrava and Ostrava public transport are teaming up to make Ostrava more eco-friendly by using alternative fuel vehicles in public transportation and improving its quality to encourage more people to use it. One of the major projects in the city's strategic development plan [5] is to replace public transport vehicles with low-emission and low-floor models.

Ostrava public transport plans [1] to incorporate at least 60 % of emission-free vehicles and at least 35 % of low-emission EURO 5, EURO 6 vehicles into public transport by 2025. Overall, 95 % of emission-free or low-emission vehicles (electric, hydrogen, CNG) should be used. As of 2021 [1] diesel-

powered buses are being phased out of regular routes and replaced by electric or CNG vehicles. Diesel buses will continue to be kept in service as a back-up in case of breakdowns or emergencies.

Electric drive and natural compressed gas drive

Electric drive has overall environmental benefits due to its energy efficiency. Electric buses consume about 40 % less energy than diesel cars [1]. However, more significant is its local environmental benefit because electric transport does not emit any emissions such as particulate matter and nitrogen oxides. Another advantage is the elimination of bus engine noise.

The use of public transport buses powered by compressed natural gas (CNG) represents an important contribution to the improvement of the environment in Ostrava and at the same time enables cost savings in the operation of these buses. Ostrava public transport has replaced a significant part of its fleet [1] with these CNG-powered low-floor buses. This investment also included the construction of CNG filling stations in Ostrava-Martinov and Hranečník, and resulted in a reduction of approximately 980 tonnes of carbon dioxide emissions per year.

In recent years, the price of gas has been fluctuating in multi-year cycles [6]. The peaks of each cycle are constantly decreasing and the average price is also lower in each cycle so far (see Figure 1). Unfortunately, taxes (VAT and excise tax) and the international situation have the greatest influence on the price development. However, this fuel still appears to be very economical.

Figure 1 Natural gas price per 1MWh / $. Source: [6]

In terms of a long-term fleet development strategy, Janovská et al. [7] conducted research on transport optimisation in Ostrava. As part of this research, the cost of operating CNG and electric buses was also assessed. Three means of transport were included in the evaluation for each category. The aim was to obtain detailed information on the costs of operating both types of equipment, which can be one of the basis for developing a long-term strategy in this area. All vehicles were used on the same routes to allow comparisons to be made on the same route profile. Direct operating costs, indirect costs, revenues and performance were evaluated for all transport means.

Based on the processed data, the evaluation [7] shows that it is more cost-effective to use CNG powered vehicles. A number of studies also report that the lifetime of CNG vehicles is slightly longer than that of electric buses. However, this was not analysed in the research. A limiting factor for the use of electric propulsion not only in the field of mass transit is the performance of the batteries currently in use. Especially in terms of range, but also the possible effects of the external environment, especially air temperature, which can fundamentally affect the range (battery capacity). Current developments in the field of batteries, however, may minimize these disadvantages in the near future. Another aspect that can affect cost is the route profile. For the sake of comparison, vehicles were operated on the same transport line. The character of the whole line profile is rather flat, which is, however, true for most of the territory of the town of Ostrava. However, it can be assumed that in the case of operation of the means of transport in mountainous terrain, it would be possible to detect more significant differences in the average cost per kilometre of travel. Ostrava public transport currently uses predominantly CNG fuels. The big advantage, apart from low emissions, is the price and availability of the fuel**.**

In the case of diesel-powered vehicles still in use, research has shown that their replacement by CNG buses as well as partially electric buses, for example in a 70:30 ratio, can be recommended. Further support for CNG motorisation is also in the context of the infrastructure built. Currently, Ostrava public transport operates two CNG filling stations and is completing the construction of a third. The operation of CNG vehicles is more cost-effective, as research has shown. However, electric drive burdens the environment in a minimum way, and with the expected improvement of this technology, partial diversification of the vehicle fleet can be recommended [7].

Hydrogen drive

For the above reasons, based on Hydrogen Strategy of the CR, it is proving advantageous to start deploying hydrogen in the transport sector (see Figure 2). Fossil fuels are burdened by excise tax and are depletable. Hydrogen technologies may also provide a suitable stimulus for the transformation of the Czech automotive industry.

If we consider the economic criterion, the area where hydrogen can be most effectively deployed is transport [8]. For economic viability, a hydrogen price of around 4 EUR/kg (2021 prices) is necessary. In terms of planning and achieving large-scale consumption, it is advisable to start with road freight transport and urban bus transport [8].

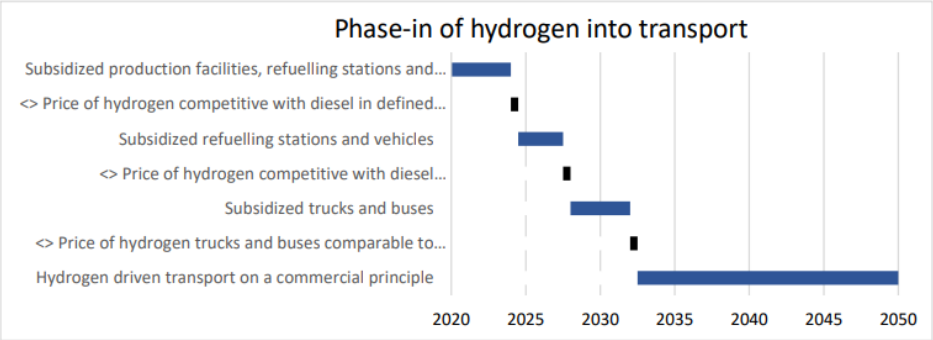

Figure 2 Phase-in of hydrogen into transport. Source: [8]

A basic prerequisite is the construction of filling station infrastructure. The use of hydrogen in transport has some advantages over electric vehicles. Among the main advantages (see Table 1) of hydrogen technology in transport are zero emissions, inexhaustibility of the source for its production, possible savings in operating costs in the future in public transport and for other vehicles operating in one locality.

Table 1: Use of hydrogen in urban bus transport SWOT analysis Source: [8]

STRENGTHS		**WEAKNESSES**
• Emission-free operation • A government bill on the promotion of low-carbon vehicles through public procurement and public passenger transport services • Existing experience and successful projects • Cooperation with foreign entities is possible • Priority to reduce emissions in cities • Replacing diesel with hydrogen is more economically viable than replacing other fossil fuels • Shorter filling times		• Heating in winter – high energy consumption and the need to adequately size the vehicle energy system • Higher acquisition, operating and servicing costs compared to diesel vehicles • A lack of filling station infrastructure • A limited selection of buses • No serial solution for high-capacity vehicle versions (e. g. articulated bus) has been developed yet • The price of hydrogen (transport and compression costs)
OPPORTUNITIES		**THREATS**
• Municipalities and regions themselves have ambitions to reduce emissions		• Reduction in diesel prices • Problems with supplying the network of filling stations when hydrogen production is restricted

The disadvantages are the very high purchase price of hydrogen vehicles, but also the lack of sufficient hydrogen production, the insufficient number of refuelling stations and the difficult transport of hydrogen, which is carried out in a liquefied state at a temperature of 253 °C below zero. Although there are no emissions and only water dripping from the exhaust, the hydrogen must first be produced. Currently, the most common method is water decomposition. The whole process is ecological, but it requires a significant amount of energy [9]. Thus, hydrogen propulsion is only as clean as the energy used to produce it.

Hydrogen infrastructure for transport in Ostrava

The goal for the next decade in the Moravian-Silesian Region is minimum emissions from public transport. Therefore, the introduction of hydrogen buses and trains is absolutely crucial. By 2025, thirty hydrogen-powered buses should be on the roads in the region [9].

Ostrava public transport in cooperation with the town of Ostrava, is preparing the construction of a public refueling station and initiating the project preparation for the introduction and operation of a pilot program involving emission-free hydrogen buses, long-distance transportation, and the development of emission-free passenger transport with hydrogen propulsion in the Ostrava area and its surroundings [10].

It represents a significant opportunity for emission-free road transport solutions. It is a logical continuation of the long-term strategy to make Ostrava the most environmentally friendly public transport in the country. It is important to emphasize that this is a technology that is only in its early stages of development in transport, and the market for vehicles, fuels, refuellers or even legislation is still improving.

3. CONCLUSION

Hydrogen transport could be a great solution for the town of Ostrava when it comes to reducing emissions, improving air quality, but sufficient funding support is needed. Currently, the city of Ostrava is very polluted and needs to take steps to protect its environment. Hydrogen transport could help to combat air pollution, significantly reduce emissions, and contribute to the sustainable development of the city.

However, it is important to note that hydrogen transport is still a relatively new technology and that its deployment could be costly. It is therefore necessary to consider whether the benefits of hydrogen transport are sufficient to justify its deployment.

ACKNOWLEDGEMENT

I would like to thank for the support during the investigation from the institution and my supervisor. This result was supported by project by Ministry of Education, Youth and Sports of the Czech Republic No. SP2023/082 and SP2023/071.

REFERENCES

[1] *Plán dopravní oslužnosti území statutárního města Ostravy na období 2021 – 2025*. Magistrát města Ostravy [online]. 2023 [cit. 2023-10-05]. Available at: https://www.ostrava.cz/cs/urad/magistrat/odbory-magistratu/odbor-dopravy/oddeleni-silnicni-a-drazni-dopravy/odkazy/plan-dopravni-obsluznosti-uzemi-statutarniho-mesta-ostravy

[2] ASLAM, M. U., H. H. MASJUKI, M. A. KALAM, H. ABDESSELAM, T. M. I. MAHLIA and M. A. AMALINA, (2006). *An experimental investigation of CNG as an alternative fuel for a retrofitted gasoline vehicle, Fuel, 85,* 717–724.

[3] MARTINS V. W. B., R. ANHOLON, O. L. G. QUELHAS. (2019). *Sustainable Transportation Methods.* Encyclopedia of Sustainability in Higher Education. Springer, Cham. doi.org/10.1007/978-3-319-63951-2_192-1

[4] VOJTĚCH, J., et al. (2019). *Spatial distribution of ambient particulate matter concentrations in the Czech Republic: Evaluation of health and economic impacts*. Science of The Total Environment, 685, 1064-1076. DOI: 10.1016/j.scitotenv.2019.06.120.

[5] *Strategický plán rozvoje statutárního města Ostravy 2017 – 2023.* FajnOva [online]. 2017 [cit. 2023-10-05]. Available at: https://fajnova.cz/wp-content/uploads/2020/07/Strategicky_plan_rozvoje_statutarniho_mesta_Ostravy_2017-2023_FINAL.pdf

[6] *Cena zemního plynu za 1MWh.* Finex [online]. 2023 [cit. 2023-10-05]. Available at: https://finex.cz/komodita/zemni-plyn/

[7] JANOVSKÁ K., BESTA P., Šafránek M., Vozňáková I. (2021*) Ecological and economic multicriteria optimization of operating alternative propulsion vehicles within the city of Ostrava in the Czech Republic*. Equilibrium 16(4): 907-943 DOI: 10.24136/eq.2021.034

[8] *Vodíková strategie ČR – základní informace*. MPO [online] 2021 [cit. 2021-27-07]. Available at: https://www.mpo.cz/assets/cz/prumysl/strategicke-projekty/2021/8/Vodikova-strategie_CZ_G_2021-26-07.pdf
[9] *Moravskoslezský kraj vsází na vodíkovou dopravu měla by přinést čistší vzuch*. ČT24 [online] 2019 [cit. 2023-10-05]. Available at: https://ct24.ceskatelevize.cz/veda/2773742-moravskoslezsky-kraj-vsazi-na-vodikovou-dopravu-mela-prinest-cistsi-vzduch
[10] *Veřejné zakázky*. PROEBIZ s.r.o. [online] 2023 [cit. 2023-10-05]. Available at: https://profily.proebiz.com/verejne-zakazky/1966

EVALUATION OF THE READINESS OF LOGISTICS PROCESSES IN AN INDUSTRIAL ENTERPRISE

Author(s): Matěj HROUDA

Supervisor: doc. Ing. Šárka VILAMOVÁ, Ph.D., doc. Dr. Ing. Oldřich KODYM

Department: Department of Management of Industrial Systems, Faculty of Materials Science and Technology, VSB – Technical University of Ostrava

Abstract

The subject of my research is logistics systems within an industrial enterprise in Automotive. The aim is to develop a readiness methodology for all logistics processes that are interrelated and interdependent. Also to determine the selection of an appropriate concept for the enterprise, their implementation and management method. The methodology will also include the preparation points before the audit. Finally, in order to make the orientation as simple as possible, a description of the existing systems and their possible simplification will be given.

Key words:

Logistics processes, risk management, control, procedures, audit. Multi-criteria decision making.

1. INTRODUCTION

Nowadays, automotive suppliers are going through several major challenges, whether it's a shortage of input components, labour shortages, soaring energy prices or, last but not least, the imbalance of orders from customers.

All of these challenges put tremendous pressure on all suppliers or subcontractors of components. The automotive segment in which I work is undergoing a huge transformation, with entire plants either closing down or partially relocating to other countries where the operating conditions are more favourable.

In this period it is very difficult to get oriented quickly and to provide everything needed from a logistics point of view. An example of this is the already mentioned problem of input parts, which already complicates normal operations considerably. In the case of a planned closure of an entire production plant and the associated transfer of production lines, the overall planning for such a transfer is considerably more difficult. Related to this issue is the selection and overall logistics systems for the company where the production is to be transferred.

The topic of my dissertation is "Evaluation of the readiness of logistics processes in an industrial enterprise".

I have chosen this topic because of my professional side as well as because of the challenges I am facing during the complete closure and relocation of an entire plant from Germany to the Czech Republic. The issue of this thesis seems very topical nowadays, in the course of my practice there have been several times when a particular step has been underestimated or omitted, which has either slowed down the whole process or completely invalidated it. One mistake or omission of a single input material can completely disable production, with immediate effect on the entire process involved.

As an outcome of my work I would like to construct a methodology that can be used for any logistics operation, whether associated with a complete transfer of production, the establishment of a new manufacturing company, or as a control plan prior to a logistics audit.

Main text:

The issue of the chosen topic can be grasped in several ways, the example we will stick to is the relocation of the entire production due to plant closures. In this case, from a logistical point of view, it is necessary to think about the following steps:

- **Ensuring sufficient input parts for production:** In order to achieve the desired value of manufactured parts per stock, communication in the triangle: input component suppliers - manufacturer - final customer is important. In this line of communication, there must be a clear production plan as well as the value of parts in stock to draw from during the relocation of production lines. For this value, the input material that will deteriorate during production or transport must be added + 10%

- **Sufficient protective packaging for the final part:** ensuring sufficient protective packaging, ideally original, already contractually selected and used between the supplier and the customer. In the absence of original packaging, a suitable alternative must be selected. This must first be approved by the internal quality department of the plant and then presented to the customer as a temporary solution, ready for approval or comment by the customer.

- **Storage area:** Calculation of the required area for internal logistics, whether the required number of materials in packaging is sufficient for the free capacity of the warehouse or whether external storage is necessary. Every company tries to eliminate this storage option, as it is a very financial and time consuming operation with several points that must be met before this step can occur. We are not only talking about finished pieces, but also spaces for input parts, empty packaging and finished production.

- **Transportation:** providing transportation, an important link in the entire logistics process. It is preceded by a calculation of the volume of material to be transported. This results in the arrival of the appropriate type of transport at the required time, at the required place. [2]

Multi-criteria decision making is the ideal tool for making important and risky decisions for society. In this regard, I will be rely heavily on the use of CCM or CPM. Which we will briefly introduce:

CPM method

CPM (Critical Path Method) is one of the methods project management method that views projects as deterministic models that are specific by fixed elements and fixed links between them. This

method was developed in the 1960s was developed by DuPont to manage shutdowns at its chemical plants, to implement maintenance and restarting them.

The advantages of the CPM method include:

Provides a graphical representation of the project
predicts the time required to complete the project
shows the activities critical to meeting the planned project duration.

CCM method

This method can be used as a tool in particular for estimating the duration of a project. It is used as an alternative to the CPM method. The CCM method is mainly used in project management, logistics and transport. [2]

2. CONCLUSION

Managing a large project such as the transfer of an entire manufacturing company requires carefully thought out steps, from the smallest to the largest.

The dissertation will present real calculations using multicriteria analysis. Due to the complexity and the pressure for the entire project to be flawless from the company management, examples from crisis management and examples that led to partial decisions will also be given.

The methods that are used for project management are generally transferable to everyday activities. The resulting methodology will be much more comprehensive with clear descriptions for its use in practice, whether for control or audit preparation.

ACKNOWLEDGEMENT

I would like to thank especially my supervisors, namely Mrs. doc. Ing. Šárka Vilamová, Ph.D. and Mr. doc. Dr. Ing. Oldřich Kodym.

REFERENCES

[1] Metody plánování projektů. [online]. [cit. 02.03.2020]. Dostupné z: http://promis.econ.muni.cz/lecture/2/2/3/
[2] Operační výzkum. JABLONSKY, Josef. Operační výzkum: kvantitativní modely pro ekonomické rozhodovaní. Třetí vydaní. Mikulova 1572, 149 00 Praha 4: Professional Publishing, 2007, 191 - 198. ISBN 978-80-86946-44-3.

IMPLEMENTATION OF INDUSTRY 4.0 AND LEAN MANUFACTURING IN CZECH ENTERPRISES – EVALUATION SCHEME AND SURVEY INITIAL EXECUTION

Author(s): Mikuláš HURTA

Supervisor: prof. Ing. Darja NOSKIEVIČOVÁ, CSc.

Department: Department of Quality Management, Faculty of Materials Science and Technology, VSB – Technical University of Ostrava

Abstract

This paper develops and validates an evaluation scheme for Industry 4.0 and Lean Manufacturing implementation in Czech enterprises with an objective to assess a readiness for further Industry 4.0 implementation. The research initiates by outlining the construct of the survey, followed by the design of the evaluation model and future utilization. Initial validation and first execution of the survey is described and suggests a moderate embrace of Industry 4.0 and Lean Manufacturing.

Key words:

Readiness for Industry 4.0, evaluation scheme, initial survey, Lean Manufacturing, Industry 4.0.

1. INTRODUCTION

The adoption of the fourth industrial revolution, Industry 4.0, within businesses is becoming a defining feature of the current industrial epoch. The transformative potential of this paradigm has been well recognized, however, the readiness and degree of implementation among enterprises is a subject of ongoing research [1]. This paper follows results of research done by the author of this paper in area of a relation between Industry 4.0 and Lean Manufacturing, main factors influencing corporate readiness for Industry 4.0 implementation and literature review of Industry 4.0 readiness evaluation models [2]. The implementation of Lean Manufacturing was found as a crucial aspect for a readiness to Industry 4.0 implementation.

The case of Czech enterprises forms an intriguing area of investigation. Despite the region's strong industrial heritage, there appears to be variance in the implementation of Industry 4.0 and Lean Manufacturing, which suggests potential for increased efficiency and competitiveness [3]. This research contributes to the current discourse by developing and validating an evaluation scheme to assess the readiness of Czech enterprises for further implementation of Industry 4.0. The evaluation scheme is designed to explore the constructs of Industry 4.0 and Lean Manufacturing, thus facilitating an understanding of the nuances of implementation and readiness.

This first chapter begins by contextualizing the current state of Industry 4.0 and Lean Manufacturing implementation. The literature underscores the transformative potential of these paradigms, as well as the challenges inherent in their application [4]. In response to these challenges, the research presents the concrete construct of the survey and the design of its evaluation model, following the path set by recent studies on industrial readiness [5].

The initial validation and first execution of the survey, as described in this paper, suggest a moderate embrace of Industry 4.0 and Lean Manufacturing within Czech enterprises. This finding underpins the study's ultimate goal of creation of a complex Industry 4.0 readiness evaluation model defining the most suitable Industry 4.0 implementation strategies based on an achieved evaluation score.

The subsequent discussion regarding the future utilization of the survey methodology and the interpretation of results reasserts the applicability of this research to both academics and practitioners. The research aligns with the pragmatic calls of Schwab (2016) for action in response to the Fourth Industrial Revolution, encouraging the full realization of its potential.

This paper aspires to make a meaningful contribution to the existing body of research on Industry 4.0 and Lean Manufacturing, while also providing practical insights and a robust tool for enterprises both in the Czech Republic and beyond.

2. EVALUATION SURVEY OF READINESS FOR INDUSTRY 4.0 IMPLEMENTATION

A literature research of main factors influencing readiness for Industry 4.0 implementation had been done before a creation of the evaluation survey [2]. The author of this paper divides these factors in two groups – organizational and operational characteristics. Concretely, the organizational characteristics influencing the readiness are:

- a company size,
- financial performance,
- a sector,
- an economic and political environment.

Besides the organizational characteristics, there are following operational characteristics influencing the readiness:

- maturity level of Lean Manufacturing implementation,
- default technological state,
- use of agile approach,
- IT security,
- level of enterprise communication,
- human resources,
- enterprise strategy,
- education and sustainability.

The survey contains 5 questions in the area of organizational characteristics (an economic and political environment is not included as the survey is done within Czech companies only, so the environment is identical) and 23 questions focused on the operational characteristics. It was created in Czech language to make it friendly for respondents which are Czech companies. Excel software was used for the initial version of the survey which was used in the validation phase. Then, the final version was created in Google Forms. The survey is accessible via https://forms.gle/unEZemvXJMfp5F9h7. The first questions focused on organizational characteristics are:

- Company Name – open box for answer.
- Number of Employees – 0-9, 10-49, 50-249, 250+.
- 2021 Loss/Profit Results – up to 1 million CZK, 1 million - 10 million CZK, 11 million - 100 million CZK, 101 million - 1 billion CZK, 1 billion CZK +, Loss.
- Annual Development Activities Budget – We don't have such a budget, 0-499,000 CZK, 500,000-1 million CZK, 1 million - 10 million CZK, 11 million - 100 million CZK, 100 million CZK +
- What sector do you operate in – dropdown list of official Czech economy sectors.

23 questions for the operational characteristics area are accessible in English here: https://drive.google.com/file/d/1HUhd8j1_j1nI_FtW3Viu9V1VOV7cxg0O/view?usp=sharing.

Final version of the questions construction is a result of survey validation phase. The validation phase had 4 revision rounds. Firstly, a literature review was done to map the latest approaches to Industry 4.0 readiness evaluation. Based on that, the survey was structured and questions constructed. The first revision round was done by the author of this paper by filling trial and identification of bottlenecks – e.g. there was found that number of employees is doubled in 2 answers (originally i) 0-10 and ii) 10-49, after revision i) 0-9, ii) 10-49). The second revision was done by the supervisor of the author of this paper through a consultation. As a part of this revision, potential improvements were identified – e.g. answers of question n. 9 were reformulated to reflect concrete percentage of automatization. The third revision was done via extending the performed literature review by snowball research method. Based on that, questions from education and sustainability area were added. The last revision was done by practical filling the survey by top managers from 3 Czech enterprises and personal interviews with them. It resulted into following improvements:

- Annual turnover was removed from questions and loss/profit 2021 result was kept only – there was big risk of misunderstanding how to fill the right value of annual turnover as there are more options

how to count it. Also the influence of annual turnover on the preparedness to Industry 4.0 implementation is not such significant like loss/profit result.

- Form of filling a sector of the company was changes from open box to dropdown list to avoid uncertainty of answers.
- Names of Lean Manufacturing and Industry 4.0 tools as well as other terminology were not known for respondents, therefore a legenda was added to explain the questions and their meaning.
- Question n. 20 was extended by answer “No, we do not create strategic plans.” as one of the respondents answered they do not make strategic documents at all.
- Grammar mistakes were cleared.

3. METHODOLOGY OF SURVEY EVALUATION MODEL

Survey results are going to be evaluated via multiple-criteria decision analysis methods, concretely weighted sum models. 23 questions focused on operational characteristics are divided into 8 groups according to concrete operational characteristic they are related to. The questions number 1, 2, 5 and 8 belongs to the group of maturity level of Lean Manufacturing implementation, the questions number 3, 4, 6, 7 and 9 define the default technological state, use of agile approach is monitored via the questions number 10, 11 and 12. The question number 13 is related to IT security characteristic, level of enterprise communication is evaluated via the questions number 14, 15 and 16, the questions number 17 and 18 belongs to the group of human resources characteristic, characteristic of enterprise strategy is related to the questions number 19 and 20, and last three questions number 21, 22 and 23 belongs to the group of education and sustainability characteristic.

Operational characteristics are weighted sum model criteria C1-C8. Organizational characteristics are going to influence weighting of the criteria. E.g. an importance of the level of enterprise communication is lower in smaller companies, therefore the weighting of this criterion is going to be lower for small companies. Concrete values are going to be an object of further research to create a complex evaluation model widely usable across companies without any limitation in their size, financial performance or a sector they operates in. The medium values of weighting of C1 (maturity level of Lean Manufacturing implementation) is set up on 0.2, 0.2 for C2 (default technological state), 0.05 for C3 (use of agile approach), 0.05 for IT security, 0.15 for level of enterprise communication, 0.15 for human resources, 0.1 for enterprise strategy and 0.1 for education and sustainability. The weightings were built on discussion with process management experts and can be further revaluated before the final research evaluation.

The model parameters can achieve a value 1, 2, 3, 4 or 5 according to evaluation score achieved in each criterion. Parameter 1 is defined for achieved coefficient 0-0.19, parameter 2 for 0.2-0.39, parameter 3 for 0.4-0.59, parameter 4 for 0.6-0.79 and parameter 5 for 0.8-1. The coefficients are counted as a percentage coefficient to maximal achievable score in each criterion.

Every question is evaluated on ordinal scale according to achieved answer. The questions number 1, 3, 5, 7, 8, 9, 10, 11, 12, 15, 17, 18, 20 can achieve 1-4 score according to selected answers. The questions number 2, 4, 14, 16, 21, 22 and 23 can achieve 0-2 score. The question number 13 can achieve 0-4 score. The questions number 6 and 19 are excluded from the scoring model, they have a supporting role only. Then, the scores are counted within particular criteria and the criteria are evaluated via the model parameters. E.g. maximum achievable score of C1 is 14 points. If there are 6 points achieved, the criteria coefficient is 0.43 which means the parameter 3 for this criterion. In this way, all the criteria parameters are counted, weighted and all the points are sum up.

Based on the final score, the companies are divided into 4 categories: excellent readiness, moderate readiness, basic readiness and insufficient readiness. Concrete score scales for each category needs to be set up after first numeric validation of the model to ensure its proper functionality. As a part of further research, an Industry 4.0 implementation strategy recommendation will be created for each category.

4. INITIAL SURVEY EXECUTION AND FIRST RESULTS

Before the survey distribution, a list of 100 Czech enterprises were created in a way to contain different size companies from all national sectors in corresponding ratio. A cover letter was created and the survey was distributed to the companies management representatives. There is 9 answers so far

from 11.1% micro size, 22.2% small size, 33.3% medium size, 33.3% large size companies representing different financial performance and development budgets and 4 economic sectors. The main initial results are:

1. Majority of the companies use process management methods.
2. The most used Lean Manufacturing tools are 5S, Kanban, Root Cause Analysis and Standard Work Instructions
3. 66,6% of the companies is engaged in implementation of Industry 4.0 tools, mainly in cloud systems and AI technologies.

An objective of further research is to collect statistically sufficient amount of answers, apply the evaluation model on them and advise the respondents about their results and recommended strategy for Industry 4.0 implementation.

5. CONCLUSION

This paper introduced the topic of a readiness for Industry 4.0 implementation and its factors including Lean Manufacturing implementation. The evaluation survey containing 5 questions focused on organizational characteristics and 23 questions from operational characteristics area was constructed and its numerical evaluation model was presented. The model stands on multiple-criteria decision analysis methods, concretely weighted sum models. The survey validation and first execution was described.

The first results showed moderate embrace of Industry 4.0 and Lean Manufacturing in Czech enterprises which could be a positive sign for their readiness for complex Industry 4.0 implementation in future. Further research will continue with the survey distribution and will validate the survey evaluation model, especially the final scoring model and relation between organizational characteristics and weighting values. As a final phase of the research, Industry 4.0 implementation strategies will be created according to achieved readiness score.

ACKNOWLEDGEMENT

This work was supported by the Ministry of Education, Youth and Sports, Czech Republic under specific Grant SP2023/043, which has been solved at the Faculty of Materials Science and Technology, VŠB-TU Ostrava.

REFERENCES

[1] KAGERMANN, Henning, Wolfgang WAHLSTER, Johannes HELBIG. *Recommendations for implementing the strategic initiative INDUSTRIE 4.0: Final report of the Industrie 4.0 Working Group*. Forschungsunion, 2013.
[2] HURTA, Mikuláš. Evaluation of Enterprise Readiness for Industry 4.0 Implementation. In: *Den doktorandů 2021*. Ostrava: Vysoká škola báňská – Technická univerzita Ostrava, 2021. ISBN 978-80-248-4583-8.
[3] VRCHOTA, Jaroslav a Martin PECH. Readiness of Enterprises in Czech Republic to Implement Industry 4.0: Index of Industry 4.0. *Applied Sciences* [online]. 2019, 9(24) [cit. 2023-05-29]. ISSN 2076-3417. Dostupné z: doi:10.3390/app9245405
[4] SCHWAB, Klaus. *The Fourth Industrial Revolution.* New York: Crown Business, 2016. ISBN 9781524758868.
[5] LU, Yang. Industry 4.0: A survey on technologies, applications and open research issues. *Journal of Industrial Information Integration* [online]. 2017, 6, 1-10 [cit. 2023-05-29]. ISSN 2452414X. Dostupné z: doi:10.1016/j.jii.2017.04.005

SMART MOBILITY STRATEGY

Author(s): Natálie KAWULOKOVÁ

Supervisor: doc. Ing. Šárka VILAMOVÁ, Ph.D.

Department: Department of industrial systems management, Faculty of Materials Science and Technology, VSB – Technical University of Ostrava

Abstract

The aim of this paper is to present a Smart mobility strategy, which was created by European commission in 2021. In this paper are presented some of the main points and ways, how the European commissions wants to achieve this. Also in this paper is showed comparison of progress, that is made since this strategy was released.

Key words:

Smart, sustainable, resilient.

1. INTRODUCTION

Although mobility has many advantages for its consumers, it has drawbacks for our society as well. Our health and wellbeing are impacted by harmful factors including greenhouse gas emissions, air and water pollution, but also accidents and traffic jams, traffic congestion, noise pollution, and biodiversity loss. The European Commission presented its 'Sustainable and Smart Mobility Strategy' together with an Action Plan of 82 initiatives that will guide our work for the next four years. This Sustainable and Smart Mobility Strategy is structured around three key objectives: making the European transport system sustainable, smart and resilient.

2. SMART MOBILITY STRATEGY

This plan establishes the groundwork for the EU transportation system's transition to a greener, more technologically advanced, and crisis-resistant state. By 2050, emissions will have decreased by 90%, as stated in the European Green Deal. The European transportation system's progress towards a smart and sustainable future will be guided by specific benchmarks:

By 2030:
• at least 30 million zero-emission cars will be in operation on European roads
• 100 European cities will be climate neutral.
• high-speed rail traffic will double across Europe
• scheduled collective travel for journeys under 500 km should be carbon neutral
• automated mobility will be deployed at large scale
• zero-emission marine vessels will be market-ready

By 2035:
• zero-emission large aircraft will be market-ready

By 2050:
• nearly all cars, vans, buses as well as new heavy-duty vehicles will be zero-emission.
• rail freight traffic will double.
• a fully operational, multimodal Trans-European Transport Network (TEN-T) for sustainable and smart transport with high speed connectivity.

3. SUSTAINABLE MOBILITY

Boosting the uptake of zero-emission vehicles, renewable & low-carbon fuels and related infrastructure.

In road transport, zero-emission solutions are already being implemented. Manufacturers are becoming very interested in battery electric vehicles and they are currently investing a lots of money into this. Market engaging in is already growing, especially for cars, vans and buses used in cities, while trucks and buses are emerging. The increased use and use of renewable and low-carbon fuels must be combined with the creation of a comprehensive network of charging and refueling infrastructure to fully enable the widespread use of low and zero-emission vehicles in all modes of transport. "Recharge and refuel" is a European flagship under the Recovery and Resilience Facility. By 2025, the goal is to build half of the 3,000 hydrogen stations and one million of the 3 million public recharge points required by 2030. The ultimate goal is to ensure a dense, widespread network to ensure easy access for all customers, including heavy-duty vehicle operators. A comparison of the number of public recharging stations in 2021, 2023 and 2030 can be seen in figure 1 and comparison of the number of the hydrogen stations in 2021, 2023 and 2030 can be seen in figure 2.

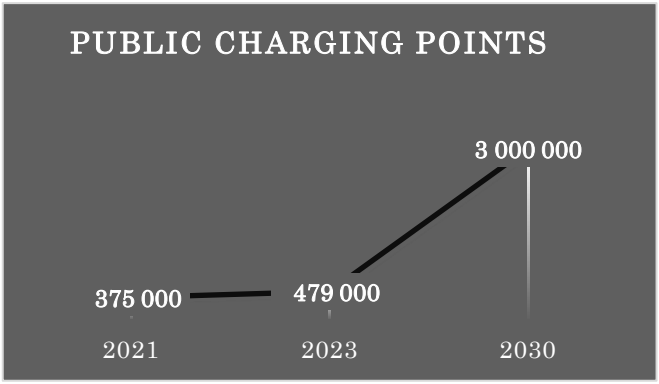

Figure 1 Public charging points. Source: (own)

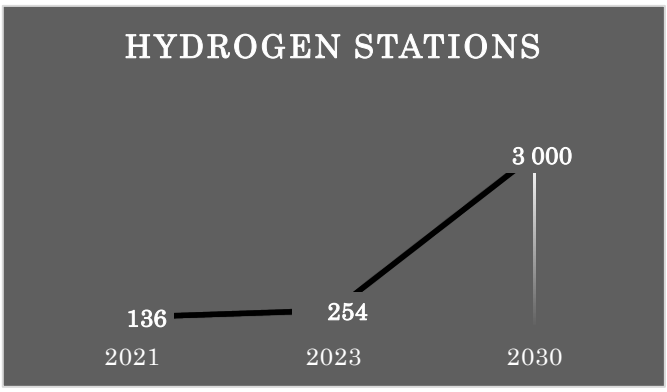

Figure 2 Hydrogen stations. Source: (own)

Creating zero-emission airports and ports

Aircraft manufacturers are investing significant amount of money in new fuel and propulsion technologies, but they will also expect airports to be ready to deliver these fuels.

Research on supplying energy to aircrafts is moving in two different ways. The first possibility is sustainable aviation fuels produced from renewable feedstocks such as biomass, instead of petroleum. The second is energy supply for new aircraft that will be powered by technologies including batteries and hydrogen.

Making interurban and urban mobility healthy and sustainable

To achieve this Europe want to double high-speed rail traffic in 2030. Europe’s high-speed rail network total length is currently of 11,990 km, with another 3,062 km under construction. There are plans for to construct of over 9,200 km, of which over 5,900 km are in the planning stage and over 3,300 km are part of long-term projects.

Another part of this plan is to make key connections between cities faster by better-managed capacity, coordinated timetabling, pools for rolling stock and targeted infrastructure improvements to boost new train services including at night.

Greening freight transport

According to the European Green Deal, a significant part of the 75% of inland freight currently transported by road should be switched to rail and inland waterways. The greening of freight transportation in Europe can also be aided by short-sea shipping and effective zero-emission vehicles. Given the slow progress made thus far, immediate action is required. As an illustration, the modal share of rail in inland freight decreased from 18.3% in 2011 to 17.9% by 2018.

Within and outside of metropolitan regions, multimodal logistics must be a part of this shift. Consumption habits have changed dramatically as a result of the expansion of e-commerce, but it is important to take into account the external costs of millions of deliveries, such as the decrease in empty and pointless runs. Hence, sustainable urban mobility planning should also include the freight dimension through dedicated sustainable urban logistics plans. These plans will accelerate the deployment of zero-emission solutions already available, including cargo bikes, automated deliveries and drones (unmanned aircraft) and better use of inland waterways into cities.

Pricing carbon and providing better incentives for users

Fossil-fuel subsidies should end. The Commission's goal in updating the Energy Taxation Directive is to bring electricity and energy product taxes into line with EU energy and climate policy. The taxation of energy content for various fuels should be better straighten, and the uptake of sustainable transport fuels better incentivised.

4. SMART MOBILITY

Making connected and automated multimodal mobility a reality

The opportunities offered by connected, cooperative, and automated mobility (CCAM) must be taken advantage of by Europe. CCAM can provide access to mobility for everyone, recover crucial time, and increase traffic safety. The Commission will lead research and innovation, perhaps through a new CCAM-focused European collaboration under Horizon Europe and other digital technology-focused partnerships.

Boosting innovation and the use of data and artificial intelligence (AI) for smarter mobility

The Commission fully supports the deployment of drones and unmanned aircraft and will continue to develop the relevant rules, including in U-Space, in order to make it suitable for promoting safe and sustainable mobility. The Commission will also adopt a “Drone Strategy 2.0”, which will provide possible ways to guide the further development of this technology and its regulatory and commercial environment.

5. RESILIENT MOBILITY

Reinforce the Single Market

The Commision wants to reinforce efforts and investments to complete the Trans-European Transport Network (TEN-T) by 2030. They also wants to support the industry in improving its ability to build back better through increased investments, both public and private, in the modernisation of fleets in all modes.

Make mobility fair and just for all

The shift towards sustainable, smart and resilient mobility must be just, otherwise it will not take place. Consequently, the Commission will ensure that the possibilities under the just transitional mechanism are fully explored to make its new mobility affordable and accessible in all regions and to all passengers, including those with disabilities and reduced mobility. The Commission will also continue to contribute by supporting the Cohesion Fund and the EFRD in the less developed Member States and regions.

Step up transport safety and security across all modes

In the maritime sector, the Commission is planning to initiate a major review of existing legislation responsibilities, port state control and accident investigation, together with the continued strengthening of EU rules on recognised organisations.

6. CONCLUSION

In order to ensure seamless, safe, and secure connectivity to all European people, the sustainable European transport system that the EU aspires to must be smart, flexible, and adaptable to ever-changing transport patterns and needs. The transportation sector should serve as a showcase for European intellect and tenacity, leading the way in research, innovation, and entrepreneurship and guiding the twin transitions. The Commission is putting forward a comprehensive set of measures listed in this strategy's action plan such as to double high-speed rail traffic in 2030 or provide access to mobility for everyone, recover crucial time, and increase traffic safety. Another crucial point is to build 3 million public recharge points and 3000 thousands hydrogen stations by 2030. Currently there are 479 000 public recharge points and 254 hydrogen stations. Europe is definitely making a progress in moblity. The main questions still is, if this progress is fast enough.

REFERENCES

[1] EUROPEAN COMMISSION: Mobility and transport. European commision [online]. Brussels, 21 July 2021 [cit. 2023-05-21]. Dostupné z: https://transport.ec.europa.eu/transport-themes/mobility-strategy_en

[2] EUROPEAN COMMISSION: mobility-strategy-and-action-plan. European commision [online]. Brussels, 21 July 2021 [cit. 2023-05-21]. Dostupné z: https://transport.ec.europa.eu/system/files/2021-04/2021-mobility-strategy-and-action-plan.pdf

[3] EUROPEAN COMMISSION: European Commission - Questions and answers. European commision [online]. Brussels, 21 July 2021 [cit. 2023-05-21]. Dostupné z: https://transport.ec.europa.eu/system/files/2020-12/mobility-strategy-memo-qa.pdf

[4] EUROPEAN COMMISSION: Mobility strategy. European commision [online]. Brussels, 21 July 2021 [cit. 2023-05-21]. Dostupné z: https://transport.ec.europa.eu/transport-themes/mobility-strategy_en

[5] AIZARANI, Jessica. Number of hydrogen refueling stations in the European Union from 2015 to 2021. STATISTA [online]. January 31 2023 [cit. 2023-05-21]. Dostupné z: https://www.statista.com/statistics/859095/eu-hydrogen-number-of-fueling-stations/

[6] Another record addition of European hydrogen refuelling stations in 2022. H2STATIONS [online]. February 1 2023 [cit. 2023-05-21]. Dostupné z: https://www.h2stations.org/press-release-2023-another-record-addition-of-european-hydrogen-refuelling-stations-in-2022/

[7] HIEL, Adrian. The EU's Smart and Sustainable Mobility Strategy. ENERGY CITIES [online]. January 18 2021 [cit. 2023-05-21]. Dostupné z: https://energy-cities.eu/the-eus-smart-and-sustainable-mobility-strategy/

[8] CONZADE, Julian, Florian NÄGELE, Swarna RAMANATHAN a Patrick SCHAUFUSS. Europe's EV opportunity—and the charging infrastructure needed to meet it. McKinsey and Company [online]. November 4 2022 [cit. 2023-05-21]. Dostupné z: https://www.mckinsey.com/industries/automotive-and-assembly/our-insights/europes-ev-opportunity-and-the-charging-infrastructure-needed-to-meet-it

[9] The Three Seas ambitious HSR plan. RAILWAY PRO [online]. February 2 2023 [cit. 2023-05-21]. Dostupné z: https://www.railwaypro.com/wp/the-three-seas-ambitious-hsr-plan/

[10] Record 45 New Hydrogen Filling Stations Open in Europe in 2022 – Ryze Hydrogen. Hydrogen central [online]. February 9 2023 [cit. 2023-05-21]. Dostupné z: https://hydrogen-central.com/record-45-new-hydrogen-filling-stations-open-in-europe-2022-ryze-hydrogen/

[11] AIZARANI, Jessica. Number of hydrogen refueling stations in the European Union from 2015 to 2021. STATISTA [online]. January 31 2023 [cit. 2023-05-21]. Dostupné z: https://www.statista.com/statistics/859095/eu-hydrogen-number-of-fueling-stations/

RECOVERY OF WASTE HEAT FROM SOLAR COLLECTORS USING A STIRLING ENGINE

Author: Jan KRÁTKÝ

Supervisor: doc. Ing. Milan HEGER, CSc.

Department: Department of Industrial Systems Management, Faculty of Materials Science and Technology, VSB – Technical University of Ostrava

Abstract

This thesis deals with the structural design and control of a power generator that uses waste heat from solar collectors. This waste heat will be used as a heat source for a Stirling engine that will convert the waste heat into electrical energy. A microcontroller will be used to automatically control the whole process. The efficiency of the process will be improved by optimally controlling the fluid flow in the primary and secondary hydraulic circuits. This control will be achieved by means of sensing elements and regulators. As sensing elements we will use resistance temperature sensors and inductance flow meters. The main flow control devices will be throttling valves and speed control of the circulators. As this is a power plant, it is necessary to take into account the safety of both people and machines, so safety features will need to be implemented in the device. These safety features will be, for example, a shear pin used as a coupling between the shafts to prevent damage to valuable parts of the machine. Other safety features will be covers for rotating parts to prevent foreign objects from getting entangled. The electricity generated by the generator that powers the Stirling engine could be used to reduce household running costs and to air-condition living spaces.

Key words:

Stirling engine, generator, waste heat, regulation, solar collector.

1. INTRODUCTION

The impact of rising energy prices is increasingly placing emphasis on reducing energy consumption of companies and households. This cost reduction is achieved through the use of renewable sources such as photovoltaic panels, which allow the use of solar energy from the sun. The electricity generated from photovoltaic panels can be used to run households and, if there is a surplus, fed into the electricity grid. The disadvantage of this method is the dependence on the intensity of sunlight and the problem of recycling the panels. A second way of reducing energy costs can be wind power, using wind turbines to convert airflow into rotational energy, which is then used as a source for a generator. This method of saving energy is dependent on the intensity of the wind flow around the generator. A third way to save energy in homes and businesses is to use geothermal energy through the use of heat pumps. A heat pump is a heat machine that works by transferring heat from a cooler place to a warmer place. The whole process works on the principle of a cooling cycle that makes the whole process possible. The disadvantage of heat pumps is the high purchase price and the need for regular maintenance. Significant energy savings can be made by energy efficient home construction Well insulated walls, low heat loss windows and proper ventilation can significantly reduce energy consumption and dependence on external energy sources. The next step is to optimise energy consumption in the home. The use of energy efficient appliances, effective energy management, and the use of natural lighting can reduce overall energy consumption and contribute to self-sufficiency. A final way to reduce household consumption is through a solar collector, which is a device designed to capture and use the sun's radiation to heat water or air. Its main purpose is to convert solar energy into heat energy, which is then used for various purposes.

There are several types of solar collectors, but the most common type is the so-called hot water solar collector. This type of collector consists of a glass plate or layer of transparent plastic Figure 1 that serves as a cover, and behind it is an absorbent material Figure 1 that absorbs the sun's radiation and converts it into heat. This heat is then transferred to the water or cool air that passes through the collector Figure 1. Solar collectors are often used for domestic hot water or for heating buildings. They can also be part of solar thermal systems that include thermal storage, pumps and controllers for efficient use

and storage of thermal energy. Solar collectors have several advantages. They are environmentally friendly because they use a renewable energy source, in this case solar radiation. They can reduce energy costs because solar energy is free. In addition, they can reduce dependence on fossil fuels and contribute to environmental protection. It is important to note, however, that solar collectors are particularly effective in sunny weather, and they also need to be properly positioned and oriented to maximize their performance.

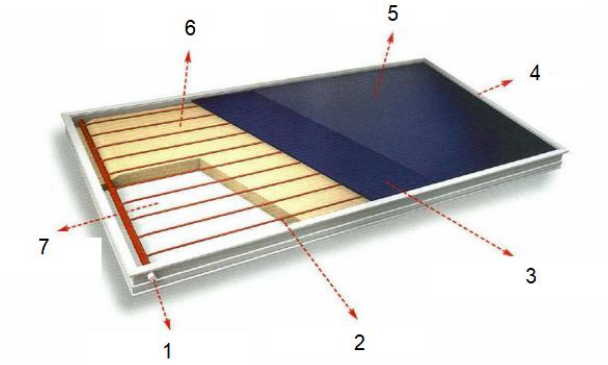

1. Distribution pipe
2. Absorber pipe
3. Whole absorber pipe
4. frame
5. glazing
6. thermal insulation
7. back over

Figure 1 main parts of the solar collector. Source: [7]

In some cases, inefficient use of solar energy may occur when all the water in the hydraulic system is heated to its maximum value. In this case, the circulation system is closed and unused heat is generated which then escapes back into the environment. This waste heat could be used as an energy source for the Stirling engine, which would use a significant part of this energy to generate electricity. [2]

A Stirling engine is a heat engine that uses a cyclic process to convert heat energy into mechanical energy. The Stirling engine works on the principle of alternating compression and expansion of the working gas (usually air) due to temperature changes. The basic components of a Stirling engine include a hot cylinder Figure 2, a cold cylinder Figure 2, and a working gas that cycles between the cylinders due to thermal expansion. These two cylinders are connected by a supercharging channel and sealed crank pistons transfer the rectilinear motion to the rotary. The Stirling engine is considered energy efficient and environmentally friendly because it operates on thermal differential and has no exhaust gases. It can be powered by various heat sources such as biomass combustion, solar heat or waste heat from industrial processes. Stirling engines have many applications, including use in power plants, small power systems, refrigeration, power generation for space missions, and other industrial and domestic applications [1,3,4,5].

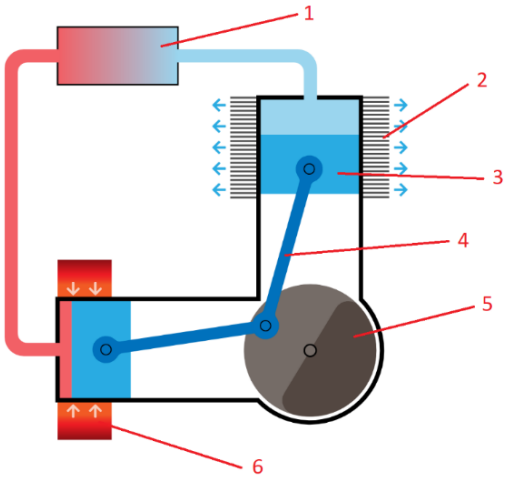

1. Regenerator
2. Cold roller
3. Piston
4. Piston rod
5. Crankshaft
6. Warm roller

Figure 2 Schematic of the Stirling function.
Source: [6]

2. TECHNICAL SOLUTION

In case the heating process reaches a stage where the heating cycle has to be closed, the waste heat could be used as an energy source for the Stirling engine. In this case, only the flow of the heating medium would be redirected to the Stirling hot cylinder Figure 3. This reversal of flow direction would be accomplished using a three-way valve Figure 3. At the same time, the cooling circuit circulator would be switched on to achieve the greatest temperature difference in the Stirling engine cylinders. The motor output shaft will be connected by a shear pin safety coupling to the generator which will convert this rotational energy into electrical energy. The microprocessor will sense and record the temperature of the water in the heat exchanger, should the system overheat it will send a signal to the valves and they will change the direction of flow to the Stirling engine. It will also sense the flow in the pipework to be able to regulate the flow in the pipework to improve convection between the collector and the motor.

During the winter months, an external source such as a solid fuel boiler could be used as a power source to increase the efficiency of power generation. In order to avoid damage to the valves and circulators of the cooling and heating system, a certain insensitivity band would need to be set to avoid the constant opening and closing of the three-way valves and the re-engagement of the circulators resulting in damage to these components. There shall be a mechanically operated coupling between the drive shaft of the Stirling engine and the generator so that the generator can be disconnected from the Stirling engine while running. A variator could be installed between these parts to improve the speed control of the generator as the Stirling engine is difficult to regulate. These moving parts would need to be covered with covers to prevent any foreign objects from getting entangled.

The operation of this generator will be quiet as the Stirling engine is known for its quiet operation. Maintenance requirements will not be difficult as no complex equipment or hazardous substances are used. The cost of acquisition will not be high, as the Stirling engine is a simple machine in design therefore the total purchase price of the generator will not be in the high figures. The interchangeability of components will be simple because of the use of cheap materials and simple components.

The energy produced in this way will then be stored in batteries and can be used to run household appliances, to light the home. Excess electricity could be agitated and fed into the electricity grid to further save household costs.

This solution could be used in modern homes as a cost saving for running the home and as a cost saving for air conditioning. It could also be used as a power source for some devices in industrial plants that do not depend on plant technology such as air sensors or as a source for lighting.

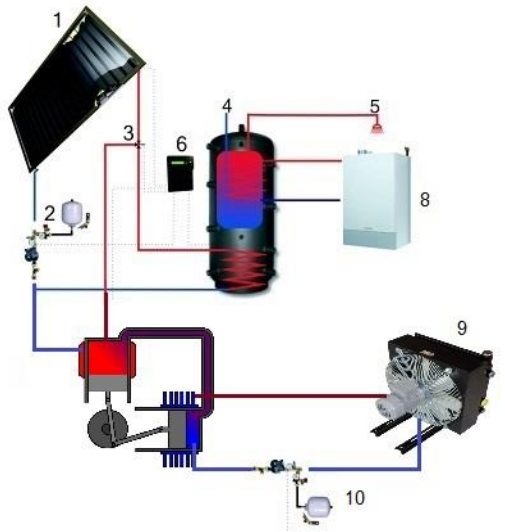

1. Solar collector
2. Circulation pump
3. Controlled three-way valve
4. Water tank
5. Water inlet
6. Control unit
7. Stirling engine
8. External heat supply
9. Cooler
10. Cooling circuit circulator

Figure 3 hydraulic wiring diagram. Source: [8]

3. CONCLUSION

This work deals with the use of waste heat from solar collectors, which is used by a Stirling engine that converts this waste heat into rotational energy. A generator is connected to the drive shaft to generate electricity. It also deals with flow control, which is taken care of by sensors and a microcontroller. It also deals with the reliability and design of the safety features of the generator. Great emphasis is placed on the usability of the energy obtained in this way and the consequent reduction of the costs of running households and industrial plants.

REFERENCES

[1] KAOUTAR L, Noureddine B, Development of a new technique of waste heat recovery in cement plants based on Stirling engine technology, 2022, vol. 210, pp. 118316.
[2] GARZINOVA, R., ŠVEC, P., FRISCHER, R. Operative control with structured data processes in steel operations environment. METAL 2014: 23RD INTERNATIONAL CONFERENCE ON METALLURGY AND MATERIALS. Brno: Tanger Ltd., 2014, pp. 1647-1653.
[3] KRÁTKÝ J, Controlling a power plant with a microcontroller, 2020.
[4] JONGHYEON Y, Inkyum K, Daewon K, Hybrid energy harvesting system based on Stirling engine towards next-generation heat recovery system in industrial fields, 2021, vol. 90, pp. 106508.
[5] SHUNMIN Z, Guoyao Y, Kun L, Wei D, Ercang L, A review of Stirling-engine-based combined heat and power technology, 2021, vol. 294, pp. 116965.
[6] Schéma Stirlingova motoru. In: *Wikipedia: the free encyclopedia* [online]. San Francisco (CA): Wikimedia Foundation, 2008- [cit. 2023-06-01]. Dostupné z: https://cs.wikipedia.org/wiki/Stirling%C5%AFv_motor
[7] PETRUŠKA, BOHUMIL. SOLÁRNÍ KOLEKTORY S VAKUOVÝMI TRUBICEMI. BRNO, 2010. BAKALÁŘSKÁ PRÁCE. VYSOKÉ UČENÍ TECHNICKÉ V BRNĚ. Vedoucí práce Doc. Ing. MICHAL JAROŠ, Dr.
[8] Hydraulické zapojení. VITA SOLAR [online]. [cit. 2023-06-01]. Dostupné z: http://www.vitasolar.cz/solarni-panely-sluzby.html

APPLICATION OF MODERN HIGH-TECH ANALYTICAL AND MATHEMATICAL MODELS IN THE PROCESS OF COMMERCIALIZATION OF INNOVATIONS IN THE CHEMICAL AND METALLURGICAL FIELDS

Author(s): Ivan KUZIN

Supervisor: prof. Ing. Kamila JANOVSKÁ, Ph.D.

Department: Department of Economics and Management in Industry, Faculty of Materials Science and Technology, VSB – Technical University of Ostrava

Abstract

The article presents the main modern and traditional analytical and mathematical models used in the process of commercialization of innovative projects. The analysis of the application of these models in the implementation of innovative projects in the chemical and metallurgical spheres was carried out. The indicators and factors of implementation are presented. The purpose of the article is to study and present modern approaches to the implementation of projects in the chemical and metallurgical sphere, to study the effectiveness of the use of high-tech models, to analyze the interest of the potential market in the implementation of activities in the process of commercialization of chemical and metallurgical projects, to form approaches for further implementation and application in large projects with possible solutions for changing variables e.g. in the conditions of the economic crisis.

Key words:

Analysis of analytical and mathematical models, introducing innovations, technology commercialization analysis, commercialization in the chemical and metallurgical field, innovative aktivity.

1. INTRODUCTION

In the modern world, we use and use the results of research activities of scientists in various fields everywhere. Their research developments were able to find practical application. Innovative developments have become a part of our life and the strongest incentive for competition in the market, with the subsequent formation of the economic growth of the industry. Patent research helps to identify potentially the most successful results of intellectual activity that could be implemented in the future. The chemical and metallurgical industry occupies a significant part of the economy of almost every country. Industrial enterprises are struggling within the framework of market relations and are trying to develop and increase their capitalization in extremely turbulent times.

In the conditions of an increasingly emerging crisis, the analysis of the profitability and effectiveness of the introduction of research and development in industry is an important part of scientific and technological progress in crisis situations and the creation and reform of high-tech production, which forms the prerequisites for stabilizing the country's economy and in the future leads to an increase in its efficiency. A correct and stable strategy is able to overcome all crisis situations and strengthen its structure. The presented theoretical approaches, which are subsequently applied in practice in real projects, are very relevant and significant studies for practical tasks of introducing innovations and research developments at real industrial facilities.

The relevance of the topic is determined by the acute economic need for modern solutions and approaches in confronting crisis situations that are increasingly emerging in the economy. In the chemical and metallurgical industries, there are many issues on the agenda to study and reduce risks in the work and prospects of industry enterprises. The profitability of the implementation projects in crisis situations and in the current state of economic development is becoming a very topical issue. Not only the creation of a new product, but also the profitability of bringing the product to the consumer.

To date, there are many types of innovative infrastructure facilities: technoparks, business incubators, special economic zones, technopolises, etc. The meaning of their existence can be summarized as follows: the activities of such infrastructure facilities should contribute to the speedy

promotion of the results of scientific research and development in the field of material production, commercialization of the results. [1]. The relevance of scientific and technical development is determined by the industry specifics, which have an impact on obtaining an economic effect, the possibility of putting into practice the results of research with economic efficiency [2]. The stagnation of the relationship between the production and scientific sectors of the economy, the low level of mastering the results of fundamental and applied research of industrial enterprises, the lack of stimulating factors in the use of scientific achievements, the inconsistency of innovative ideas with market needs are the reasons for the low efficiency of the development of innovative processes in the economy [1].

2. PRACTICAL PART

In modern financial activity, such a promising and dynamic direction as project financing has received active development. This type of financial support for innovation is especially relevant for countries and regions that are in particular need of support and modernization, renewal and improvement of capital-intensive industries. From the total mass of research and development work, it is advisable to single out both long-term priority national projects that use various forms of state support, and priority short-term projects financed by a mixed public-private principle. The commercialization of scientific developments and technologies is directly associated with innovation and the innovation process, as a result of which the resulting development or research result is realized with commercial profit. There are 3 alternative financing mechanisms that have received the greatest stimulation at the moment:

1. The Pan-European Venture Capital Fund Program, better known as VentureEU, which provides projects with new sources of financing from various funds and the opportunity to grow into leading global firms in the future.
2. The implementation of the Horizon 2020 program is the entry of a small and medium-sized enterprise that has received grant support from the EU into an IPO.
3. Crowdfunding platforms that act as intermediaries between investors and enterprises, allowing the former to more easily identify and support projects in which they are interested, and for projects attract relatively small amounts of money, but from a larger number of investors [3].

Project financing clearly reflects three main provisions on the organization and financing of this innovative activity [4].

First, the example of industrialized countries shows us that the bulk of innovation processes can be implemented by private investment of companies. Innovative processes in this case act not as an end in itself, but as a means of achieving entrepreneurial success. Innovation business in various organizational frameworks becomes an intermediary between academic "pure science" and the interests of private capital, since the innovation process is seen as profitable.

Secondly, the state innovation policy can manifest itself not only in a direct impact on the innovation process, but also in the creation of a favorable economic climate for innovation along with all sorts of financial, legislative, tax, social and other methods of indirect state support for innovation. The state in the current state of the Russian economy cannot take on the main burden of innovation policy, but can provide a full range of activities that support the development of innovative business [5].

Thirdly, the flexibility, multivariance and alternativeness of innovative activity is the best way to promote the emergence of numerous forms of cooperation between public and private entrepreneurship, private and foreign investors. A wider practice of project financing and the development of innovative activities can find their rightful place if the state acts as a guarantor of political, macroeconomic and environmental risks.

In modern conditions, even an experienced leader is not always able to detect and objectively compare the advantages and disadvantages of various solutions, so management using models can reduce their harmful effects. Solving problems on models is cheaper. Low simulation costs allow simulating "economic storms"

Economic and mathematical methods should be understood as a tool, and economic and mathematical models - as a product of the process of economic and mathematical modeling. This method of modeling - as a way of theoretical analysis and practical action - is aimed at the development and use of models, it is based on the principle of analogy, the possibility of studying a real object not directly, but through consideration of a similar and more accessible object, its model. A model is an image, a substitute for a real object or process, presented in a material or ideal form, described by

symbolic means and reflecting the essential properties of the object or process being modeled and replacing it in the course of the study.

Currently, there is a powerful toolkit for assessing the potential for technology commercialization at an early stage. There are many different methods, consider the most popular. Technology marketing analyzes all activities aimed at achieving the goal of technology commercialization. The goals of technology marketing are the selection and purposeful positioning of the activities of a research institution in the field of technology development and promotion.

The next method for evaluating the commercialization of innovative projects is GAP-analysis, which consists in finding the difference that exists between the current development trend of a research institution or an innovative company and the potentially possible way of their development when implementing a technology commercialization project. Based on the GAP analysis, four possible strategies are built, and then the optimal direction of activity for the commercialization of the proposed technologies is selected from them. The essence of constructing such a graph is to project the current trend in the development of a research organization or an innovative enterprise into the future, as well as to find ways to optimize this trend. It is also worth mentioning the most basic and common analysis method – SWOT (strengths, weaknesses, opportunities, and threats) analysis is a method for identifying and analyzing internal strengths and weaknesses and external opportunities and threats that shape current and future operations and help develop strategic goals.

The latest methods of conducting expert examinations of technology commercialization projects are applied. Among them is the LIFT (Linking Innovation, Finance and Technology) methodology, which was developed as part of the Fifth Framework Program of the European Commission with the participation of INBIS Corporation (UK) to determine the degree of commercialization of innovative technologies. This technique combines the conduct of technology audit and business planning. Essentially, it is a method for selecting technology commercialization projects for funding. A LIFT technology audit is typically conducted by a team of three experts who are experts in technology commercialization, intellectual property, and the economics of innovation. The technology audit procedure consists of three stages: filling out a technology commercialization project questionnaire; interviews of experts with developers; issuance of an opinion by the experts who conducted the audit. The methodology is built on a modular basis and consists of sections that allow you to characterize the various aspects of an innovative project. This technique does not pretend to be a complete answer to the questions that arise during a technology audit, but it gives a certain snapshot of the state of the project for the commercialization of a particular innovative technology [6].

Another striking example of the latest foreign experience in evaluating intellectual property objects and their commercial potential is the TAME™ System, which was developed by Lambic Innovation Ltd to provide a clearly structured approach to technology and market evaluation for its commercialization. It is usually enough to outline the market prospects for the new technology, assess the opportunities and provide a cost forecast, so that potential investors decide whether they will work with the proposed technology or not.

The TAME™ system is based on five main evaluation criteria:

1. Strengths and breadth of market applications provided by the intellectual property.
2. The essence of the new technology.
3. Problems of technology commercialization.
4. Problems of facilitating the technology commercialization process.
5. Commercial matters.

To assess each of these sections, questionnaires with ranked responses have been developed. The main task of the system as a whole is a systematic approach to the prospects of commercialization. This is due to the fact that the evaluation of different technologies according to different criteria can be ambiguous.

Dynamics of innovation distribution by has a diffusion nature (diffusion of innovation). Essence of diffusion innovation consists in dissemination in the environment consumption of innovative products due to unsaturation of the given environment with them, as it occurs with the spread, for example, of molecules of one gas in a volume with a lower concentration, up to the equalization of concentrations. Volume of diffusing products per time dt (diffusion processes) is described expression.

$$dV = rV(1 - V/Vm)dt \quad (1)$$

where:
V – is the current volume of used innovations in the environment;
V_m – level of maximum volumes diffusion of innovation in the environment (when it is saturated with an innovative product);
r – is the innovation diffusion rate indicator (innovation diffusion coefficient).

Thus, all of the listed methods for assessing the potential commercialization of technologies in the early stages is united by one thing - the goal their implementation. The main focus of technology commercialization projects should be it becomes a question of potential buyers who are ready to buy innovative goods or services at a price that will bring the greatest economic effect.

All the most common methods are well applicable in the framework of chemical and metallurgical projects. As with projects in other areas, the feasibility of an innovation primarily depends on the ability to scale and the interest of the market.

While working on the study of various methods and materials within the framework of the topic, a huge number of classical and author's methods, models that can work effectively under certain conditions with different variables, have been identified. More complex mathematical models are able to take into account a larger number of variables and thus allow for more accurate calculations. Unites all these models and methods - the scope of their application and effectiveness, there is no universal one that would be better everywhere and always, taking into account all the variables. It is worth selecting and applying the methodology and models exclusively for the specific tasks of the project or work, at certain stages, which will help to commercialize the innovation more effectively to varying degrees.

3. CONCLUSION

Thus, all of the listed methods for assessing the potential commercialization of technologies in the early stages is united by one thing - the goal their implementation. The main focus of technology commercialization projects should be it becomes a question of potential buyers who are ready to buy innovative goods or services at a price that will bring the greatest economic effect.

All the most common methods are well applicable in the framework of chemical and metallurgical projects. As with projects in other areas, the feasibility of an innovation primarily depends on the ability to scale and the interest of the market.

While working on the study of various methods and materials within the framework of the topic, a huge number of classical and author's methods, models that can work effectively under certain conditions with different variables, have been identified. More complex mathematical models are able to take into account a larger number of variables and thus allow for more accurate calculations. Unites all these models and methods - the scope of their application and effectiveness, there is no universal one that would be better everywhere and always, taking into account all the variables. It is worth selecting and applying the methodology and models exclusively for the specific tasks of the project or work, at certain stages, which will help to commercialize the innovation more effectively to varying degrees.

REFERENCES

[1] E.S.ANDREEVA. Analysis of problems and conditions of effective operation of innovation infrastructure facilities. *Journal of Economics and Business*. 2021, 3-1 (73), 6-8.
[2] A.A. ARSKY. Evaluation of the economic efficiency of scientific research. *Bulletin of the MFUA*, 2022, 1, 83-86.
[3] N.A. SENZHOVA. Alternative mechanisms for financing scientific research in the European Union. *Actual problems of Russian law*. 2020, 15-8 (117), 203-208.
[4] L.N. OGOLEVA. Innovation management: textbook. allowance - Moscow: Infra-M, 2003. - 238 p.
[5] V.V. MENSHIKOV, V.A. KOLESNIKOV. Commercialization of innovative technologies: textbook. allowance – Moscow: LLC "*Publishing house" LKM-press* ", 2009. - 84 p.
[6] DURAND, Thomas, Conelius HERSTATT, Arie NAGEL, David PROBERT. Bringing technology and innovation into the boardroom: strategy, innovation, and competences for business value. T. Durand (Ed.). Palgrave Macmillan London, 2004. ISBN: 978-0-230-51277-1.

COMPARATIVE ANALYSIS OF TIME ALLOCATION FOR CALCULATION USING THE AURENDI WEB APPLICATION AND CONVENTIONAL APPROACH

Author(s): Dalibor LABOUNEK

Supervisor: prof. Ing. Kamila JANOVSKÁ, Ph.D.

Department: Department of Economics and Management in Industry, Faculty of Materials Science and Technology, VSB – Technical University of Ostrava

Abstract

The article compares the time allocation for the calculation of tender calculations of metal sheet parts using the conventional approach and using the Aurendi application, at the same time it describes the methodology of the conventional approach and the functions of the automated tool. At the beginning of the research, the input conditions of the experiment are defined, including the default settings of the application, as well as the examined sample. The comparison of the time required for the calculation is made on 50 parts and distinguishes separately the time devoted to automated operations and work operations in which a qualified estimate is required. The output of the article is specific time savings arising from the use of the web application with comments and analysis of individual/most striking differences.

Key words:

Comparative Analysis, offer calculations, metal sheet processing, efficient calculations.

1. INTRODUCTION

Market trends are gradually leading to digitization, the use of technology and the transformation of businesses in the era we call Industry 4.0. The most important aspect of any company's success is a satisfied customer. The business environment is changing year by year and marketing and business practices are witnessing an ever-increasing tendency to focus on the customer and their needs [1,2]. Due to the growing importance of costs for companies in the global market, the term "Cost Engineering" is also being promoted. Cost engineering mainly covers cost estimation and control of products throughout their life cycle [3]. Calculation is an activity and at the same time the result of this activity (e.g. calculation of a specific product). Calculations are used both to determine the task (preliminary calculations) and to determine the achieved fact (resulting calculations) [4]. By calculation we mean the calculation of costs, margin, profit, price or other value quantity for a product, work or service or for an activity or operation that needs to be carried out. It is the fact that costing displays in relation to each other both in kind and value-expressed performance unit, that makes it the most important tool of economic management [5]. The price is expressed as the monetary value of the goods, but at the same time, in no case is the price equal to the value of the goods. The price can be divided into balance and market. The equilibrium price means the price at which it trades when supply and demand are equal. The market price arises from the current relationship between supply and demand [6]. In terms of time, costing is divided into preliminary: the estimated costs per costing unit are listed here, it is compiled before the start of production (or at the beginning of a certain period) and final: compiled after the execution of the work to contain the actual costs per costing unit (the data is drawn from accounting; its purpose is to compare actual costs with predetermined ones) [7]. The main tools for cost management include the costing system. Different types of calculations are divided in this system. Individual types of calculations are influenced by the type of business, the size of the business and other factors [8]. The cost breakdown can be divided into two categories: direct costs, which are directly related to a specific type of performance, and indirect costs, which are not tied to one type of performance and ensure the course of the company's business process in broader contexts [9].

2. MATERIALS AND METHODS

In order to perform a comparative analysis with reliable results, it is necessary to set the appropriate input conditions of the experiment. The key element before starting the experiment is setting the parameters of the Aurendi web application. The application settings must be modeled according to the economic parameters of a specific production enterprise; hourly rates of workers at different centers, hourly rates of machines and variable settings depending on the technical parameters of the laser and the press brake. At the same time, a uniform procedure for determining trade margins must be set. The application must contain the same input data as those with which a specific company usually calculates. An integral part of the experiment is the necessity of a qualified worker who is able to adequately evaluate the complexity of the parts with regard to their manufacturability and a qualified estimate of the production cost price related to the given topic. At the same time, it is important to select suitable samples on which the experiment will be performed, taking into account the similar complexity of production using the same technologies. It follows from this condition that the samples should be of the same type of material with a maximum sheet thickness of 5 mm, which is suitable for the selected type of material cutting and bending. At the same time, it is advisable to build the experiment on simpler parts that do not require many work operations that are too difficult to estimate, for example, complex welded structures and assemblies. The last point in the preparation of the experiment is a sufficient selection sample of the contracting documentation, which must be prepared in .pdf format in the case of drawing documentation and at the same time a 3D model in .stp format due to the use of automated functions of the web application. 50 different production drawings of parts were selected for this experiment.

The methodology of the experiment consists in the initial setting of the application according to the economic values of the selected enterprise in which the experiment will be carried out. Although the resulting price is not an evaluated indicator in this experiment, the correctness of the methodology must be observed so that the resulting calculations can be considered correct. Based on the correct settings of the application, it is possible to access the time estimation for comparison. As a part of the calculation of costs through the Aurendi web application, the results will be divided into two parts. The first one is the time required to import the .stp file into the application. This is an automated process, which, however, significantly affects the overall time allocation for the calculation of individual parts. In the second step, the time measure of the calculation will be made (start when the file is already uploaded to the application). The time required for the calculation step itself in the application is limited by the beginning of the calculation, i.e. the input file is already uploaded to the user environment and the end of the calculation process, which is characterized by filling in all required values within the calculation methodology and ending the calculation by pressing the "Finish" button in the application interface. Measurements will be made in the same way for 50 selected samples. The basis for the calculation is the tender documentation in electronic form in .pdf file format.

The conventional way of carrying out costing is the way of calculating by qualified worker using basic office supplies. As part of the calculation, there is no uniform methodical procedure, however, the given calculation should always include the following steps: Calculation of the material price and cutouts, cutting process and bending process; time estimation of further workshop operations, handling and packaging; determination of margin. These points has to be recorded in spread sheet.

The time measurment is made after the preparation of the workplace and all office supplies for calculation, including the contracting documentation in electronic form. The measure begins with the display of the documentation and ends with the entry of the sales price into the prepared spreadsheet. All calculations are carried out without breaks within partial calculations, but with breaks between individual calculations. The resulting values of the measurements are listed in Table 1.

Table 1 Output data from time measure Source: (own)

Part No.	Time of calculation using Aurendi App			Time of calculation using conventional approach
	Time of file import [h:mm:ss]	Time of calculation [h:mm:ss]	Total time of calculation [h:mm:ss]	Total time of calculation [h:mm:ss]
LTA_01	0:00:42	0:01:15	0:01:57	0:05:23
LTA_02	0:00:16	0:00:52	0:01:08	0:06:10
LTA_03	0:00:12	0:00:48	0:01:00	0:05:32
LTA_04	0:00:13	0:00:51	0:01:04	0:04:15

LTA_05	0:00:10	0:00:47	0:00:57	0:05:46
LTA_06	0:00:12	0:00:48	0:01:00	0:06:02
LTA_07	0:00:13	0:00:49	0:01:02	0:09:32
LTA_08	0:00:16	0:00:51	0:01:07	0:11:39
LTA_09	0:00:17	0:00:46	0:01:03	0:09:44
LTA_10	0:00:15	0:00:48	0:01:03	0:07:01
LTA_11	0:00:24	0:00:49	0:01:13	0:06:47
LTA_12	0:00:23	0:00:50	0:01:13	0:05:29
LTA_13	0:00:27	0:00:52	0:01:19	0:11:42
LTA_14	0:00:13	0:00:47	0:01:00	0:05:07
LTA_15	0:00:15	0:00:45	0:01:00	0:05:22
LTA_16	0:00:12	0:00:47	0:00:59	0:04:39
LTA_17	0:00:29	0:00:49	0:01:18	0:04:58
LTA_18	0:00:19	0:00:46	0:01:05	0:06:43
LTA_19	0:00:12	0:00:53	0:01:05	0:04:55
LTA_20	0:00:12	0:00:51	0:01:03	0:06:14
LTA_21	0:00:13	0:00:49	0:01:02	0:05:19
LTA_22	0:00:11	0:00:48	0:00:59	0:09:37
LTA_23	0:00:12	0:00:44	0:00:56	0:08:29
LTA_24	0:00:13	0:00:47	0:01:00	0:07:32
LTA_25	0:00:13	0:00:46	0:00:59	0:08:07
LTA_26	0:00:23	0:00:48	0:01:11	0:07:16
LTA_27	0:00:13	0:00:51	0:01:04	0:06:51
LTA_28	0:00:14	0:00:50	0:01:04	0:07:44
LTA_29	0:00:19	0:00:52	0:01:11	0:06:19
LTA_30	0:00:14	0:00:48	0:01:02	0:07:26
LTA_31	0:00:14	0:00:44	0:00:58	0:08:29
LTA_32	0:00:17	0:00:44	0:01:01	0:07:53
LTA_33	0:00:14	0:00:44	0:00:58	0:04:31
LTA_34	0:00:17	0:00:43	0:01:00	0:05:42
LTA_35	0:00:13	0:00:45	0:00:58	0:06:28
LTA_36	0:00:18	0:00:45	0:01:03	0:04:36
LTA_37	0:00:20	0:00:46	0:01:06	0:05:29
LTA_38	0:00:20	0:00:47	0:01:07	0:06:46
LTA_39	0:00:14	0:00:46	0:01:00	0:05:39
LTA_40	0:00:12	0:00:47	0:00:59	0:07:12
LTA_41	0:00:11	0:00:45	0:00:56	0:08:48
LTA_42	0:00:12	0:00:44	0:00:56	0:09:23
LTA_43	0:00:13	0:00:44	0:00:57	0:05:16
LTA_44	0:00:12	0:00:45	0:00:57	0:07:17
LTA_45	0:00:11	0:00:45	0:00:56	0:06:45
LTA_46	0:00:14	0:00:46	0:01:00	0:08:11
LTA_47	0:00:29	0:00:47	0:01:16	0:05:47
LTA_48	0:00:17	0:00:45	0:01:02	0:06:25
LTA_49	0:00:14	0:00:44	0:00:58	0:05:14
LTA_50	0:00:11	0:00:46	0:00:57	0:09:32

The table shows a significant difference between the total time allocation for calculation using the application and the total time allocation needed to calculate the same calculation using the conventional method. By calculating the weighted average of the set of values of both approaches, it is possible to obtain average values that can be compared within the research. The average resulting time to calculate the costing using the automated application Aurendi is 1 minute and 4 seconds. The average calculation time result for the conventional calculation method is 6 minutes and 52 seconds.

3. CONCLUSION

As part of the research, the methodology of the experiment was determined. Based on the methodology, the measurements of both compared approaches were made. The achieved data were entered into the table. Average values were subtracted from the resulting values and compared. With the conventional costing calculation approach, an average result of 6 minutes and 52 seconds was achieved. At the same time, a high dispersion of values can be observed depending on the complexity of individual parts. In the absence of automation, more demanding parts are more time-consuming to calculate, especially in the area of cost estimation for material cutouts and cutting. Here it is necessary to point out the fact that it was only a calculation of one piece from each specified part. If the task would be to calculate parts in several quantitative levels, it is possible to note a further increase in the time required for the calculation. This is a topic for further research based on this paper. The average calculation time using the application was 1 minute and 4 seconds. The calculation method with automation was more than 6 times faster than the conventional approach due to the use of automation and methodology in the calculation. Since the application is also ready for calculations in multiple quantitative levels, it is possible to declare that the calculation time would remain the same, since the data is automatically processed in the application. The main factor in addition to automation is the establishment of a uniform methodology, where the user's work could be even faster thanks to the ever-repeating processes. A value that cannot be influenced by the user is the time required to import the file into the application. Further research could be devoted to the ergonomics of the user interface of the application to achieve further time savings.

ACKNOWLEDGEMENT

This paper was created Results were achieved thanks to the financial by the project no. P2023/082Single-seat electric vehicle design for micro-mobility in urban environments and university campuses.

REFERENCES

[1] ERKMEN, Ezgi. (2018). Managing Your Brand for Employees: Understanding the Role of Organizational Processes in Cultivating Employee Brand Equity. Administrative Sciences. 8. 52. 10.3390/admsci8030052.
[2] BARRETO, Tatyana Belém de Oliveira, Plácido Rogério Pinheiro, and Carolina Ferreira Gomes Silva. 2018. The Multicriteria Model Support to Decision in the Evaluation of Service Quality in Customer Service. In Software Engineering and Algorithms in In-telligent Systems. Edited by Silhavy Radek. Cham: Springer International Publishing, pp. 158–67. ISBN 978-3-319-91186-1.
[3] XU Y., Elgh F., Erkoyuncu J.A., Bankole O., Goh Y., Cheung W.M., Roy R. Cost Engineering for manufacturing: Current and future research International Journal of Computer Integrated Manufacturing, 25 (4-5) (2012), pp. 300-314
[4] KUTÁČ, Josef, Kamila JANOVSKÁ. *Podnikový controlling*. Vysoká škola báňská – Technická univerzita Ostrava, 2012. ISBN 978-80-248-2593-9
[5] FIBÍROVÁ, Jana, Libuše ŠOLJÁKOVÁ, Jaroslav WAGNER. *Manažerské účetnictví: Nástroje a metody*. Praha: Wolters Kluwer, 2019. ISBN 978-80-7598-486-9
[6] SOUKUPOVÁ Věra, Dana Strachová. *Podniková ekonomika*. Vysoká škola chemickotechnologická v Praze, 2016.
[7] HANSEN, Don R., Maryanne MOWEN. *Cornerstones of Cost Management*. Boston: Cengage Learning, 2017. ISBN 13: 978-1-305-97066-3
[8] PNG, Ivan, Dale E. LEHMAN. *Managerial economics*. 3rd ed. Malden: Blackwell, 2007. ISBN 978-1-4051-6047-6.
[9] POPESKO, Boris, Šárka PAPADAKI. *Moderní metody řízení nákladů*. Praha: Grada, 2016 ISBN 978-80-247-5773-5

MODULE FOR OPTIMISED ENERGY FLOW CONTROL

Author(s): Jan MINARČÍK

Supervisor: doc. Ing. Robert FRISCHER, Ph.D.

Department: Department of Industrial Systems Management, Faculty of Materials Science and Technology, VSB – Technical University of Ostrava

Abstract

This paper presents a module that is capable of managing the sale and purchase of electricity on the spot market. This module then further optimizes the flow of energy to storage devices, from generation along with the purchase/sale of energy. The module will be based on real data from the daily OTE market. The main objective is to motivate more people to acquire their own power generation plant that uses a renewable source (solar), mainly due to better return on investment. This could lead to an alleviation of the energy crisis, for the people who will use this module, and it also leads to a better environmental situation.

Key words:

Photovoltaic, spot market, energy.

1. INTRODUCTION

In today's world, especially in the European Union, of which our country is a part, renewable energy sources are increasingly welcomed. Recently, photovoltaic power plants (PV), which can be installed both on a building and on a plot of land, have gained great popularity. The situation in the east of the country, which is one of the main reasons for the increase in electricity prices, is also contributing to this popularity [1].

One of the main problems of current PV system is the lack of smart energy flow control. Most PV plants operate in such a way that the energy produced is either consumed immediately or stored in batteries. When the capacity of the batteries is filled and the consumption of the building is covered, the surplus energy is sold to the electricity distribution system, without any strategy and at the current spot market price, which may not be economically viable and may even be negative. Thus, it is even realistically possible that the owner of the PV system would even have to pay for each kW of energy delivered to the grid [1, 2].

The idea and overall development of the module was inspired by the real shortcomings of the current PV system and the requirements of users who have the system installed. Also, the emphasis is on the design of the module, especially the fact that it can be easily added to the electrical distribution box on the DIN rail.

2. OTE-ČR

Without daily spot market data, the module could not work. This data is always known at least 12 hours in advance and then uploaded to the module. The module works with a database of electricity price movements two years back. The price is always given here on an hourly basis, for a better idea, Figure 1 shows the price movement on the spot market. This figure is directly from the official website of OTE CR.

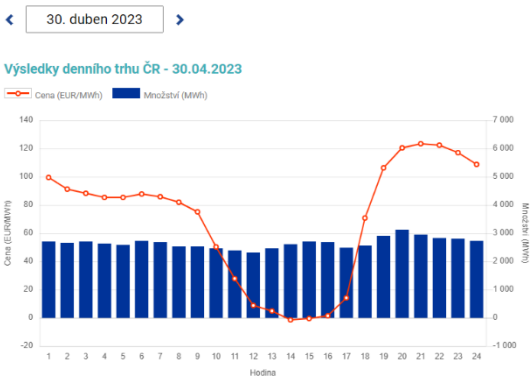

Index	EUR/MWh	Změna (%)	Celkové množství ČR (MWh)
BASE LOAD	68,88	31,57	63 781,6
PEAK LOAD	39,72	56,62	31 244,9
OFFPEAK LOAD	98,04	10,66	32 536,7

Hodina	Cena (EUR/MWh)	Množství (MWh)	Saldo DT (MWh)	Export (MWh)	Import (MWh)
1	99,28	2 697,8	1 691,3	1 722,3	-31,0
2	91,09	2 661,8	1 653,2	1 688,9	-35,7
3	88,38	2 696,3	1 691,4	1 820,7	-129,3

Figure 20 Data for the day on the OTE market. Source:[3]

3. WORKING WITH DATA

With the data obtained from the OTE market, the MATLAB software program will be used to perform the numerical calculations and the control algorithm that will control the energy flow. The module will contain 3 control variants so that the user will have full control over the management of the overall process. Using mathematical equations, the module will calculate approximately a day ahead the time when it is economically profitable to take energy from the grid and when to sell it, thus looking for the optimal difference between the maximum and minimum price at the optimal time. The module is able to buy energy and then sell it up to 5 times a day, but the market situation is not expected to allow this many times a day. The 3 modes mentioned will be described in the next chapter: "CONTROL MODES".

4. MODULE DESIGN

In the development of the module, emphasis is also placed on the design so that the installation of the module in the switchboard is as simple as possible and the overall interconnection of the module with the PV system does not have to be too complicated. The design of the back of the module is constructed in such a way that the module can be mounted on a DIN rail. On the front of the module there will be a data display for better clarity. The module will of course have to be connected to the network, using an RJ-45 connector. Since the design is not yet fully completed, Figure 2 at least shows the design of another module. These designs tend to be identical since the DIN rail has the specified dimensions and shape.

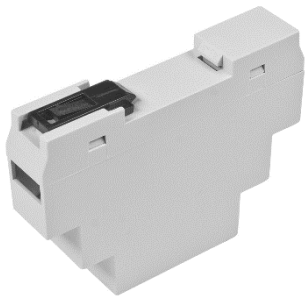

Figure 21 Possible future design of the module. Source [4]

5. CONTROL MODES

For the most efficient control of the energy flow, there are 3 control modes. These modes keep in mind both profit maximization and optimization as well as the user's own needs.

- Profit maximization mode. This mode mainly follows the OTE market data, and is not that interested in PV panel production. The mode looks to maximize the price difference in hourly intervals where it could buy energy at lower (sometimes negative prices) and store it in batteries, and then sell it at higher prices. Since the actual consumption parameter is not even important for this scheme, it can be used mainly when people are not present in the premises, e.g. weekends in office spaces, etc.
- Mode for optimal control of energy flows. This mode also monitors the OTE market data, but is much more interested in the actual PV panel production than the previous mode. It tries to manage energy as efficiently as possible so that the total energy in the battery storage is not sold, so that consumption has to be supplied by purchased energy from the grid. This scheme tries to seek an optimum between meeting consumption and then trading off the price differences in the market.
- The last mode is user mode. Here the user chooses the degree of maximisation and optimal control he wants, so he can combine the principles in the previous two modes in any proportion. However, it should be kept in mind that e.g. a 10 kWh battery, which is the most used, cannot be fully charged and discharged in a few tens of minutes.

A sample calculation of the expected profit due to the module is shown in Table 1, the last column "Yield from the production of PV with module" shows the values that are added to the penultimate column under the heading "Yield from the production of conventional PV".

Table 1 Yield model example. Source: (own)

Period	Estimated PV production per year	Price per 1 kWh of energy	Yield from the production of conventional PV	Yield from the production of PV with module
1	20 976 kWh	7,5 Kč	157 320 Kč	+ 33 025 Kč
2	20 871 kWh	6,5 Kč	135 662 Kč	+ 32 365 Kč
3	20 767 kWh	5,5 Kč	114 217 Kč	+ 31 714 Kč
4	20 663 kWh	5,5 Kč	113 646 Kč	+ 31 079 Kč
5	20 559 kWh	5,5 Kč	113 077 Kč	+ 30 459 Kč
6	20 457 kWh	5,5 Kč	112 511 Kč	+ 29 850 Kč
7	20 354 kWh	5,5 Kč	111 950 Kč	+ 29 250 Kč
8	20 253 kWh	5,5 Kč	111 390 Kč	+ 28 666 Kč
9	20 151 kWh	5,5 Kč	110 833 Kč	+ 28 092 Kč
10	20 051 kWh	5,5 Kč	110 278 Kč	+ 27 533 Kč

A fictitious power plant with an output of 15.8 kWp was used for the sample calculation. The expected return on investment due to the module should be reduced to 3.3 years instead of 4.1 years. For larger systems this difference will be even greater.

6. CONCLUSION

Photovoltaic power plants have a great future, both in terms of partial energy independence and in terms of ecology, as it is a renewable energy source. However, most photovoltaic plants are not as efficient as they could be. This module is compatible with most inverter and battery brands in use, so it should be possible to install it on new power plants as well as on existing ones. Which is also a huge advantage, as there is no need to build only new power plants, but existing power plants can only be enriched with this module. The other advantages of this module are, first of all, in the earlier payback,

which can affect very many thinking citizens, and also large companies, for which payback is also a very important aspect. The advantage of this module is also the visibility of the energy flow and the possibility of controlling the control. 3 control modes are sufficient to meet the needs of each user. It is expected that this module could be improved in the future with weather forecasting and thus could further optimize profitability, as it would have data on forecasted production as well.

PV systems generally have a long lifetime so the module can serve for decades, improving the energy crisis for citizens and businesses. According to the available data from already installed PV systems, the panels over a period of 25 years, have only lost their efficiency in the order of percentages. Also for these reasons, the module could be very helpful, as the overall installation is predicted to be here for more than ten years.

In the future, the module could manage wallboxes, as it is currently a challenge to effectively manage multiple wallboxes. Thus, the module could be placed, for example, in some parking lot that will contain wallboxes, and could effectively manage the wallboxes and also monitor the consumption of each wallbox independently.

ACKNOWLEDGEMENT

The work was supported by specific university research of the Ministry of Education, Youth and Sports of the Czech Republic No. SP2023/043.

REFERENCES

[1] IRENA – International Renewable Energy Agency. IRENA – International Renewable Energy Agency [online]. Copyright © 2011 [cit. 21.05.2023]. Dostupné z: https://www.irena.org/
[2] [online]. Dostupné z: https://www.greenpeace.org/czech/
[3] Denní trh — Čeština. [online]. Copyright © OTE, a.s., 2018 [cit. 23.05.2023]. Dostupné z: https://www.ote-cr.cz/cs/kratkodobe-trhy/elektrina/denni-trh?date=2023-04-30
[4] Plastová krabička BKDIN175 V/605 - www.krabicky-pro-elektroniku.cz. Krabičky-pro-elektroniku.cz - nejširší nabídka v ČR [online]. Dostupné z: https://www.krabicky-pro-elektroniku.cz/plastova-krabicka-bkdin175-v-605/

UTILIZING ARTIFICIAL INTELLIGENCE FOR THE OPTIMIZATION OF PROCESS AUTOMATION

Author(s): Andrei LAPTEV, Cristian PETRACHI, Ondrej KOZINSKI

Supervisor: doc. Ing. Jiří DAVID, Ph.D.

Department: Department of Industrial Systems Management, Faculty of Materials Science and Technology, VSB – Technical University of Ostrava

Abstract

The modern metallurgical industry is characterized by increased demands for quality, cost-effectiveness, and efficiency of technological processes. Automation based on a systematic approach to problem-solving is focused on improving technical means, increasing work productivity, and improving product quality. The ultimate goal is to create automatic systems that function without human intervention. This article describes the current state of heavy profiled rail and proposes the automation of its individual components. The main objective of the article is to demonstrate the use of a camera system and artificial intelligence in the automation of heavy industry processes. Machine vision using a laser camera system with digital image processing will be used to automate the rolling process on heavy profiled rail, specifically the movement of the rolled block (slab) between individual stands and between rolling calibers within a rolling stand. The intended automation operation follows the trend of Industry 4.0, which is beginning to inspire these heavy operations. The concept of an automation system based on artificial intelligence and machine vision is highly sought after and rapid development in these scientific areas can be expected.

Key words:

Heavy profiled rail, rolling stand, camera system, automation.

1. INTRODUCTION

The goal of the article was to observe and document the current state of the heavy profile track (TPT) and to propose an automation design for controlling the rolling stock and propulsion on the TPT using a camera system. The heavy profile track was put into operation in 1914 and has since undergone several major modernizations. The new modifications should enable the control of all functions, currently performed from 4 cabins directly on the cars, from a single central workstation in the K3 roller cabin. The expected benefit is a reduction in operating costs and an increase in the safety of TPT operations. The actual rolling mill consists of 4 reversible duo stands. There are a total of 4 handling cars, also called rolling transfer cars, used for the transverse movement of the rolls between the stands. The basic technical equipment of the profile rolling mill includes a Step-type entry table, Pusher, Entry table, Reheating furnace, Rolling transfer cars, Reversible rolling stands, Hot saw, and Cooling bed. The image (Figure 1) provides an overall overview of the layout of the rolling process technology and control cabins.

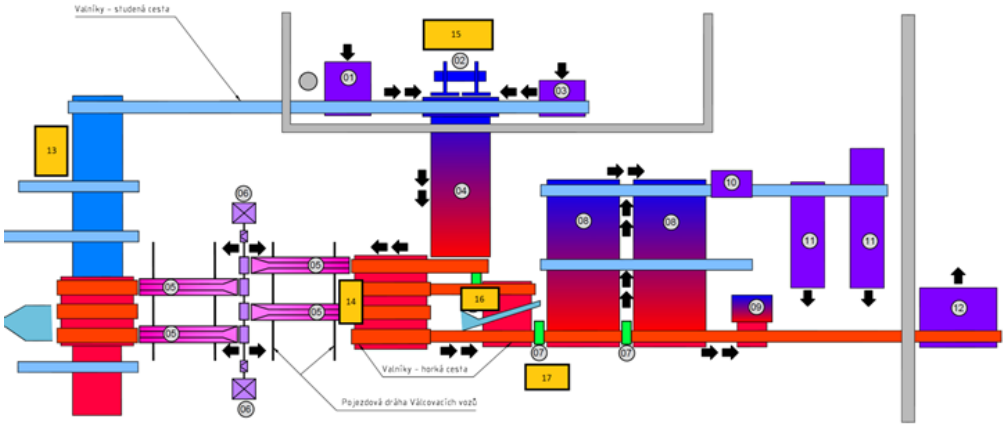

Figure 1 The layout of the TPT device. Source: (own)

2. DESCRIPTION OF THE PRODUCTION PROCESS

The main production program of TPT consists primarily of brush rails, but other types of profiles can also be rolled here. Brush rails are rolled from a prescribed length and rectangular cross-section of a basic block. The basic blocks intended for rolling brush rails are gradually inserted into the Ramming Furnace "04" through the Step Sizing Grate "01", Sizing Grate "03", and Pusher "02". Since the "TPT" operation is equipped with a Ramming Furnace for heating the blocks, it is necessary to insert so-called "partitions" between the individual blocks to prevent two blocks from sticking together. Partitions are not intended for rolling - they usually have a square cross-section for easy recognition from blocks intended for rolling.

The basic working "takt time" of the Ramming Furnace is 6 minutes. The working "takt time" is not fixed by the control system, but all activities of the Ramming Furnace are controlled by the furnace operator based on the completion of the previous rolling process. The equipment is operated from a cabin in front of the furnace. After the hot block falls out of the Ramming Furnace onto the roller conveyor behind the furnace, the hot block is transported to the turner. The main task of the turner is to turn the hot block intended for rolling by 90°. Blocks unsuitable for rolling (bent and otherwise damaged) are turned by 180° and "partitions" are not turned at all. At the same time, a significant removal of block scale occurs at this point. The roller conveyor behind the furnace is operated from cabins K3 and K4, while the turner is operated from cabin K4.

A block designated for rolling, turned 90 degrees, is transported via a roller between the Turner and Rolling Carriage No. 2 onto the rolling carriage No. 2. This carriage can be controlled from cabins K3 and K4. Blocks unsuitable for rolling and "barriers" are also moved from the Turner to the rolling carriage No. 2.

The "TPT" operation is equipped with a total of 4 rolling stock "05", numbered 1 to 4. The basic production and technological equipment of the "TPT" operation consists of 4 rolling tables "06", numbered 1 to 4, driven by two asynchronous motors through a gearbox. Two rolling stock are located on a common railway track in front of the rolling tables (No. 1 and 3), and two other stock on a common railway track behind the rolling tables (No. 2 and 4). Each rolling stock is operated by one operator directly from the cabin of the rolling stock, where there are two control panels. Each rolling stock is able to serve 3 rolling tables if another stock on the common railway track is located at the end of the railway track.

The rolling process always starts with car No. 2, which is capable of serving rolling tables No. 1, 2 and 3. On the other hand, car No. 1 assists it behind rolling tables No. 1, 2 and 3. The rolling stock performs all manipulations with the hot block and then with the product according to the rolling instructions, i. e. car No. 2 inserts the block into the appropriate calibrator of the appropriate rolling table according to the instructions, car No. 1 on the opposite side "catches" this block, car No. 1 stands opposite car No. 2, i. e. opposite the appropriate calibrator of the appropriate rolling table according to the rolling instructions. During the rolling process, the rolling stock's own rollers are activated, which rotate in the direction of movement (insertion) of the block into the rolling table. When the block passes completely through the calibrator of the rolling table, the product stops on the roller of car No. 1 and the function is reversed. After performing the necessary production and technological operations, such as "edging" or "angling" and setting the main rolling rollers on the table according to the rolling instructions, car No. 1 will insert the product into the appropriate calibrator of the appropriate rolling table and car No. 2 will "catch" the product. Both stock must move transversely together if the rolling process according to the rolling instructions requires the product to pass through another calibrator of the rolling rollers or to transition to another rolling table.

Rolling wagons No. 3 and 4 complete the rolling process in the same way. The cross movement of wagons No. 3 and 4 along the track is enabled at rolling stands No. 4, 3, and 2, where production and technological operations with the billet are carried out according to the rolling instructions. The rolling process is completed by rolling wagon No. 4, which then transports the finished product, the rail, to the trucks for division saws. The total length of the finished rail reaches approximately 80 meters. During the process of dividing the rolled rail into expedition lengths, the rail extends to the truck of rolling wagon No. 4 with its length. The rolling stands are driven by two DC motors, which are controlled by the rollers from cabin K3. The rolling process always proceeds according to the rolling instructions, which all operators are familiar with and carry out production and technological activities in accordance with these instructions. During the rolling of rolls, the introduction of the block into the gauge is blocked. The current system relies only on light signaling using a semaphore at stands No. 2 and No. 4 or on the knowledge of operators of rolling wagons No. 2 and No. 1 in the case of rolling stand No. 1.

3. LASER CAMERA SYSTEM

When the block is being rolled, the cross movement of the rolling stock, which "catches" the slab, must be blocked until it is clear that the slab has left the guide of the corresponding calibre and that the whole slab is already on the trailer of the rolling stock. During the so-called "catching" of the slab, only manual correction of the car allowing for correct guidance of the slab from the calibre of the rolling mill to the trailer of the rolling stock or to the trailer behind the rolling stock must be allowed. Blocking the trailer on each rolling stock when the rolling cylinders are being set on the rolling mill. Blocking the cross movement of rolling stock No. 4 during the division of the finished beam into final shipping lengths.

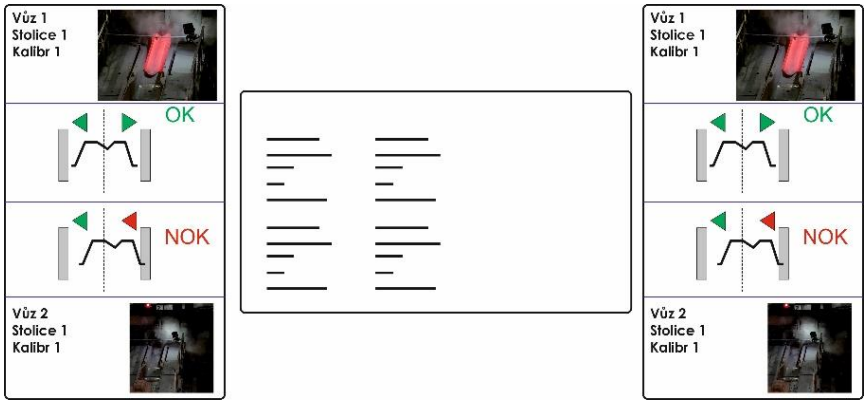

Figure 2 Laser camera system. Source: (own)

4. PROPOSAL FOR AUTOMATION OF ROLLING STOCKS

From the observation of the process, it has emerged that full automation of the movement of the rolling stock during rolling is not possible. The following can be automated: • Transitions of the rolling stock to the assumed axis of the rolling positions of the profile • Transitions of the rolling stock to the basic position and transfer position • Transitions of the rolling stock to the safety position, etc.

The movements of the rolling stock can be initiated automatically, automatically with confirmation, or manually. It is assumed that the rolling stock will automatically stop in the same end positions with a defined tolerance - a stop offset. However, when introducing the section into the profile, its actual position on the rolling stock, its curvature, etc. must be taken into account. Based on visual monitoring by a camera system, manual correction of the rolling stock stop must be possible. The whole system should be set up to minimize the number of manual interventions by the operator. Similarly, the movement of the section on the discharge side must be visually monitored and its direction corrected by the movement of the rolling stock, the tilting table, etc. Controlled (corrected) movements do not occur simultaneously, they are connected sequentially. The introduction into the profile and subsequent rolling follow immediately after each other. Control by a single operator should be an advantage. A condition for this is the perfect information of the operator about the status on the track through the camera system and the visualization of the position of the section on the rolling stock.

The position of the rolling stock with respect to the rolling stands will be ensured by the optical analysis of the image from the installed cameras. A system of digital cameras with high resolution and auxiliary laser emitters will be used, which will ensure precise calibration of the positional system. The operator will have a comprehensive view of the rolling stands from individual rolling stock on a large-screen display. Advanced image analysis will take place on a specialized server, which will determine the mutual position of the pre-section and the rolling stand. Analytical information will be projected into the actual image from the cameras for better orientation for the operator. The system will record image data for the purpose of verifying operating conditions and other information for future use.

The principle of determining the position of a rolled gate before entering the roller table is derived from determining the object's profile using a laser line. A linear laser is projected onto the object from above perpendicular to the ground. The reflected beam visible on the object copies its surface structure - the profile. The image is periodically captured using an industrial camera and sent via Ethernet for further processing. Image processing can be done analytically or using an artificial neural network. However, even for an artificial neural network, the input image needs to be modified in

some way. In this case, only the part corresponding to the red component was used from the image. A classic image consists of three color components defined by pixels and their brightness. In this case, the red component was chosen because the laser used was red, and therefore the highest intensity of pixel brightness is likely to be in the red component of the image. For example, the laser would not be visible at all in the blue component of the image, making detection impossible. This natural filtering ability is highly desirable. The image is then binarized in the next step (Fig. 4). For illustration purposes, only a portion of the image is binarized, and the rest is in shades of gray, or only the red component of the image is displayed. A binarized image is an image whose pixel brightness component takes only two values, 0 and 255. Such an image is suitable for further processing, whether analytical or using neural networks. The threshold is important for binarization, defining which pixel will be dark and which bright in the result. A system of such profiles placed close together will create the final profile (Fig. 6) of the object, and its position can be precisely determined relative to the starting position.

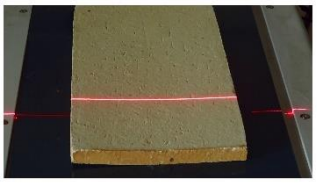

Figure 3 Original image. Source: (own)

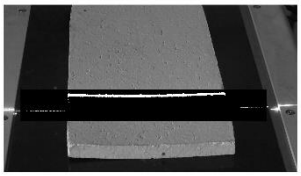

Figure 4 Binary image. Source: (own)

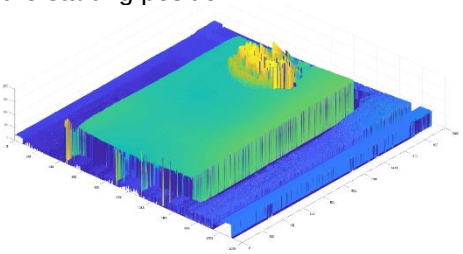

Figure 6 Composite profile of the object. Source: (own)

5. CONCLUSION

The use of a camera system and artificial intelligence in the future can facilitate and optimize the production process and quality control of technological processes. With the help of a camera system and image processing developed and tested in collaboration with the Department of Automation and Computer Technology in Industry, it will be easy to evaluate the positioning of the rolling stock. The support of the camera system will be based on strict edge detection using proprietary algorithms that guarantee accurate and fast determination of the position of the front of the rolled profile before entering the rolling mill. Standard camera systems fail in this case, mainly due to the presence of steam and variable lighting in the detection scene. We have been working on evaluation algorithms for more than a year. The developed algorithms are of a robust type with auto-calibration that monitors the intensity of ambient lighting. The lasers used are of the line type in the red and green color spectrum. With this method, we are able to precisely and efficiently detect the profile of the pre-roller and its position relative to the inlet. As part of the feasibility study, it was found that the main advantage of automating operations will be reducing the impact of the human factor in production processes. Other benefits will include speeding up the production process and its recording for use in potential claims. It also limits the difficult work in hazardous areas.

ACKNOWLEDGEMENT

The work was supported by the specific university research of Ministry of Education, Youth and Sports of the Czech Republic No. SP2023/043

REFERENCES

[1] ROBERTS, WILLIAM L. Hot Rolling of Steel. New York: Marcel Dekker, Inc. 1983.
[2] LUNEV V. A. Tváření kovů. Leningrad, 1975.
[3] KOLMOGOROV V. L. Mechanika tváření kovů. Staryj Oskol: TNT, 2017
[4] GONZALEZ R., WOODS R. Digitální zpracování obrazu. Moskva: Technosphera, 2012.
[5] GREGOR, Michal. Detektory objektů v obraze a jejich realizace. Brno, 2008. Bakalářská práce. Vysoké učení technické v Brně. Vedoucí práce Ing. František Kyselý.
[6] PANJKOVIC V. Friction and the Hot Rolling of Steel. Boca Raton: CRC Press, 2014.

ALTERNATIVE FUELS IN EUROPE: TECHNOLOGY READINESS LEVEL

Author(s): Kristýna PUSTĚJOVSKÁ

Supervisor: prof. Ing. Kamila JANOVSKÁ, Ph. D.

Department: Department of Industrial Systems Management, Faculty of Materials Science and Technology, VSB-TUO

Abstract

One of the much-discussed topics is alternative fuels, not only because of lower emissions but also because of the depletion of fossil resources and possible instability in supply. However, the research, preparation, and innovation of new technologies for low-emission fuels is often complicated and lengthy. An important indicator of the development of technology is its degree of readiness, called the technology readiness level (TRL), which describes the stage at which the development is located. This article provides an up-to-date overview of the production of alternative fuels in the EU, together with their degree of readiness, from various sources.

Key words:

Alternative fuels, technology readiness level.

1. INTRODUCTION

In broad terms, the objective of conducting technology readiness assessments in a timely and accurate manner is to supply management with information and aid critical decision-making during the implementation of advanced technology system development projects. Technology readiness levels (TRLs) have been developed to establish a shared measurement framework that facilitates the communication of knowledge about the maturity of new technologies between programme executives, system developers, technology researchers, and individuals from various organisations. Importantly, TRLs are not limited to a specific technical field. Furthermore, the utilisation of TRLs can establish a necessary basis for the development and communication of an understanding of the risks associated with the advancement of a new system and its constituent technology components [1].

2. TRL IN THE CONTEXT OF ALTERNATIVE FUELS

In 1969, NASA was preparing plans for a space station following the Apollo programme. To evaluate whether the technology was ready to start such a programme, a review of technology readiness was suggested. This system then simply rolled over to other areas. The first predecessor of the NASA TRL system was developed as early as 1974. It contained seven levels, then in 1990 it was modified to a nine-level system, which was then codified in a white paper in 1995, where it stated its terms, concepts, and arguments explained rigorously, but explaining a proposal [1–3].

Technology readiness levels (TRLs) are a set of managerial indicators that help assess the maturity of a specific technology, enabling consistent comparisons between different types of technologies within the context of a particular system, application, and operational environment. The TRL framework was later refined into the TRIMIS system, which condensed the original nine readiness levels into four development phases. This adjustment acknowledges the inherent uncertainty associated with attempting to overly specify a technology's TRL, considering the limited information typically available about the status of technologies under research in a project. The first phase of TRIMIS development is Research (corresponding to TRL 1 and 2), then Validation (TRL 3 and 4), the third phase is Demonstration/prototyping/pilot production (TRL 5, 6 and 7) and the last phase Implementation (TRL 8 and 9). A short description of individual TLR levels and corresponding levels for Market Readiness Level (MRL) and Commercial Readiness Level (CRL) can be seen in Table 1. For a more detailed orientation in TRL, Figure 1 presents the thought process for the technology maturity assessment (TMA) thought process, including TRL 10, which according to some studies is missing from the scale [1, 3–6].

Table 1 Description of TRL with the corresponding MRL and CRL. Source:[5]

Description TRL	TRL	MRL	CRL
Basic principles observed	1	–	–
Technology concept formulated	2	–	–
Experimental proof of concept	3	–	–
Technology validated in lab	4	1	–
Technology validated in relevant environment (industrially relevant environment in the case of key enabling technologies)	5	2	–
Technology demonstrated in relevant environment (industrially relevant environment in the case of key enabling technologies)	6	3	–
System prototype demonstration in operational environment	7	4	1
System complete and qualified	8	5	2
Actual system proven in operational environment (competitive manufacturing in the case of key enabling technologies; or in space)	9	6	3
Multiple commercial applications becoming evident locally although still subsidised. Verifiable data on technical and financial performance in the public domain driving interest from variety of debt and equity sources however still requiring government support. Regulatory challenges being addressed in multiple jurisdictions.	–	–	4
Market competition driving widespread deployment in context of long-term policy settings. Competition emerging across all areas of supply chain with commoditisation of key components and financial products occurring.	–	–	5
'Bankable' grade asset class driven by same criteria as other mature energy technologies. Considered as a 'bankable' grade asset class with known standards and performance expectations. Market and technology risks not driving investment decisions. Proponent capability, pricing and other typical market forces driving uptake.	–	–	6

Figure 1 Technology maturity assessment (TMA). Source: [3]

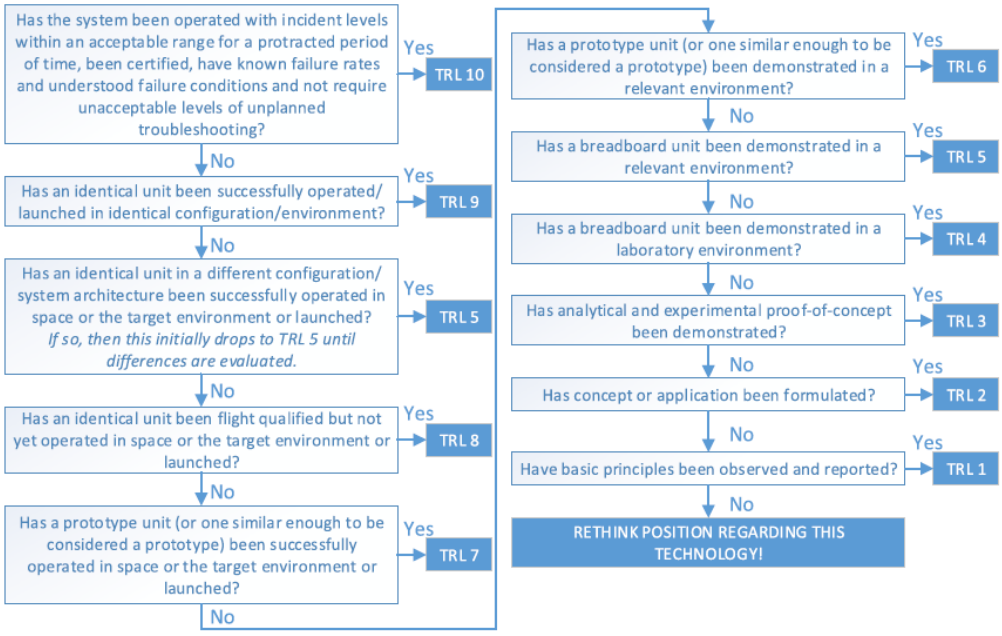

The current environmental context, driven by political interventions such as the Green Deal, Sustainable Development Goals, and Renewable Energy Directive II, places a strong emphasis on the imperative need to decarbonize the transportation sector. Advanced biofuels present themselves as one of the viable options for achieving decarbonisation in the short to medium term, particularly for aviation, marine, and heavy-duty vehicles, such as trucks and buses (HDVs), which currently lack immediate alternatives in comparison to light-duty vehicles, such as cars and vans (LDV). Although the adoption of alternative fuels can effectively reduce emissions and generate employment opportunities, particularly in biomass-related sectors, it should be noted that their production costs are higher compared to fossil fuels. Furthermore, significant innovation, technological advancements, and scaling-up are still

necessary for their widespread implementation. In order to meet the targets set for 2030, it is crucial to accelerate the market deployment of advanced biofuels.

Between 2004 and 2018, there was a notable increase in the average proportion of renewable energy sources (including liquid biofuels, hydrogen, biomethane, and green electricity) used in the transportation sector. Specifically, the share of renewables in terms of energy consumption rose from 1.5% in 2004 to 8.3% in 2018. When considering the energy content, biodiesel represented the majority at 82.0%, followed by bioethanol at 17.1%, and biomethane fuel at 0.9%.

Most biofuels are produced in the form of fatty acid methyl ester (FAME) from waste fats and oils, with a smaller percentage sourced from agricultural and forest by-products such as Used Cooking Oil (UCO), tall oil, and cellulosic feedstock oils. Advanced biofuels represent the most readily available solution for meeting the 2030 objectives of reducing greenhouse gas emissions in the transportation sector. Although electricity and hydrogen show promise, they are still in the early stages of development and will not be fully established by that timeframe.

Table 2 provides an overview of advanced biofuel options and their current level of technology readiness.

Table 2 Overview of the advanced biofuel options with their current TRL. Source:[7]

Raw material	Conversion pathway	Biofuel type	Status TRL	Fuel	Market
Waste oils and fats, Used cooking Oil (UCO), Veg Oil, liquid waste streams and effluents	Esterification of transesterification	Traditional biodiesel- Fatty Acid Methyl Ester (FAME)	Commercial	Blends with fossil diesel, B7 (drop-in), B10, B30, or neat FAME	LDV, HDV
	Hydrotreatment	Hydrotreated Vegetable Oil (HVO) / Renewable Diesel		Drop-in blends with road diesel (i.e. H30) or neat HVO, Sustainable Aviation Fuels	Aviation, LDV, HDV
MSW, sewage sludge, animal manure, agricultural residues, energy crops	Biogas or landfill production & removal of CO_2	Biomethane		bioCNG; bio-LNG in heavy duty road, LBG in marine, and CBG in light duty road transport, captive fleets or injected in the gas grid	Marine, LDV, HDV
Lignocellulosic, MSW, solid industrial waste streams/ residues	Enzymatic hydrolysis & fermentation	Ethanol	TRL 8-9	Gasoline blends such as E5, E10 (drop-in), E20 (minor engine modifications), E85 flexi-fuel engines), ethanol with ignition improvers for diesel engines (ED95), or ethanol/butanol	LDV, Aviation HDV
		Other alcohols (methanol, butanol)	TRL 6-7		
	Gasification + Fermentation	Ethanol	TRL 6-7	Upgraded to biokerosene (ATJ)	

Lignocellulosic, MSW, *liquid* industrial waste streams & effluents or intermediate energy carriers	Gasification + catalytic synthesis	Synthetic fuel	TRL 6-7	Drop-in blends with diesel, gasoline, sustainable aviation fuels, bunker fuel or as pure biofuel e.g. bio-SNG, DME, methanol	Aviation, Marine, LDV, HDV
Pyrolysis oils or biocrudes from lignocellulosic, MSW, and waste streams	Pyrolysis or liquefaction (i.e. HTL) + Hydrotreatment	Hydrotreated bio-oil/ biocrude	TRL 4-5	Neat or drop-in diesel, bunker fuel, gasoline, Sustainable Aviation Fuels	Aviation, Marine, LDV, HDV
	Co-processing in existing petroleum refineries	Co-processed bio-oil/ biocrude	TRL 7-8	Neat or drop-in diesel, bunker fuel, gasoline, Sustainable Aviation Fuels	Aviation, Marine, LDV, HDV
CO_2 from RES systems	Reaction with RES H_2	Synthetic	TRL 6-7	Depends on fuel type, i.e. bio-SNG, methanol or DME, ATJ	Aviation, Marine, LDV, HDV

3. CONCLUSION

The research and development of alternative fuels is a complicated matter. Progress and current status can be better approached by the TRL. A simple principle, however, is irreplaceable and helps us navigate the sometimes complex results of research and their readiness for use.

REFERENCES

[1] *ECSS-E-HB-11A – Technology readiness level (TRL) guidelines (1 March 2017)* | *European Cooperation for Space Standardization* [online]. Available at: https://ecss.nl/home/ecss-e-hb-11a-technology-readiness-level-trl-guidelines-1-march-2017/

[2] HÉDER, Mihály. From NASA to EU: the evolution of the TRL scale in Public Sector Innovation. *The Innovation Journal* [online]. 2017. Available at: https://www.semanticscholar.org/paper/From-NASA-to-EU%3A-the-evolution-of-the-TRL-scale-in-H%C3%A9der/7d72b6a1dd7f1920934464d0075ea6aac8a848a3

[3] STRAUB, Jeremy. In search of technology readiness level (TRL) 10. *Aerospace Science and Technology* [online]. 2015, **46**, 312–320. ISSN 12709638. Available at: doi:10.1016/j.ast.2015.07.007

[4] GKOUMAS, Konstantinos, Mitchell VAN BALEN, Anastasios TSAKALIDIS a Ferenc PEKAR. Evaluating the development of transport technologies in European research and innovation projects between 2007 and 2020. *Research in Transportation Economics* [online]. 2022, **92**, 101113. ISSN 07398859. Available at: doi:10.1016/j.retrec.2021.101113

[5] *Advanced alternative fuels technology market report*. Luxembourg: Publications Office of the European Union, 2019. ISBN 978-92-76-12602-7.

[6] GKOUMAS, Konstantinos, Fabio Luis MARQUES DOS SANTOS, Marcin STEPNIAK a Ferenc PEKÁR. Research and Innovation Supporting the European Sustainable and Smart Mobility Strategy: A Technology Perspective from Recent European Union Projects. *Applied Sciences* [online]. 2021, **11**(24), 11981. ISSN 2076-3417. Available at: doi:10.3390/app112411981

[7] PANOUTSOU, Calliope, Sonja GERMER, Paraskevi KARKA, Stavros PAPADOKOSTANTAKIS, Yuri KROYAN, Michal WOJCIESZYK, Kyriakos MANIATIS, Philippe MARCHAND a Ingvar LANDALV. Advanced biofuels to decarbonise European transport by 2030: Markets, challenges, and policies that impact their successful market uptake. *Energy Strategy Reviews* [online]. 2021, **34**, 100633. ISSN 2211467X. Available at: doi:10.1016/j.esr.2021.100633

BENCHMARK COMPUTING PLATFORMS FOR EDGE DETECTION

Author(s): Lukáš RASZKA

Supervisor: doc. Ing. Robert FRISCHER, Ph.D.

Department: Department of industrial systems management, Faculty of Materials Science and Technology, VSB – Technical University of Ostrava

Abstract

The course of edge detection is platform dependent. Devices that are able to provide more computing power are expected to detect faster. Recently, single-board computers, which are much smaller than a conventional computer, have become very popular, but their computational power is lower in proportion to the computers. In order to compare and apply edge detection on different types of devices, an algorithm performing edge detection has been constructed using Sobel, Laplacian and Canny operators. The result of the performance benchmark is a confirmation of the dominant role of computers, but also the great potential of the application of single-board computers in relation to their purchase price, size and computational power.

Key words:

Canny edge detector, Canny, Sobel, Laplacian, Benchmark.

1. INTRODUCTION

One of the possibilities of digital image processing is edge detection. This detection detects transition points where there is a large change in the luminance function. There are a large number of edge detectors operating on different mathematical principles. They are mainly divided into three categories [2, 6, 9]. The first one is the search for the maxima of the first derivatives, the next one focuses on the search for the transitions of the maxima of the second derivatives and the last one uses the local approximation of the image function by a parametric model. A widely used method is the first category of finding the maxima of the first derivatives which includes the Roberts, Sobel, Prewitt, Canny, etc. detectors and also the search for the passages of the second derivatives through zero which is represented for example by Laplacian [3, 6, 7, 8].

Different detectors have different computing power requirements for edge detection, which significantly affects the detection rate. Due to the deployment, it is not always an ideal option to use very powerful equipment, which often has the disadvantages of high cost and space. An interesting alternative can be single-board computers which are usually more cost-effective, smaller in size, but also weaker in performance. A benchmark was conducted to see how much of a difference there is in the detection rate for these categories of devices [11].

2. CANNY EDGE DETECTOR

Very popular edge detectors are based on the principle of finding first derivatives, namely Sobel and Canny, as well as finding the passages of second derivatives through zero (Laplacian) [4, 1].

The Sobel operator works on the principle of computing the intensity function of an image, namely the gradient approximation. At each point in the image, the output is the gradient vector or the norm of this vector. The Sobel operator is depicted by Equation 1. In general, the Sobel operator needs less computational power compared to the Laplacian and Canny [4, 1].

$$\begin{pmatrix} -1 & -2 & -1 \\ 0 & 0 & 0 \\ 1 & 2 & 1 \end{pmatrix} \tag{1}$$

The great advantage of Laplacian is its invariance to rotation. The popularity of this approach is mainly due to the fact that detecting the zero crossing is much easier than finding the extremum of the functions, but the second derivatives are more sensitive to noise. The Laplacian is represented using equation 2. [1]

$$\nabla^2 f(x,y) = \frac{\partial y^2}{\partial^2 x} + \frac{\partial^2 f(x,y)}{\partial^2 y} \quad (2)$$

The Canny detector can be seen as the culmination of the search for the best edge detector. At present it is the most widely used solution. The principle is based on finding the approximate directions of the gradients, 1D derivatives for these directions at each pixel using a mask and then finding the local maximum. The edge points are obtained by thresholding with hysteresis. Sometimes, edge fusion is also performed for edges obtained for different smoothing values [5].

For benchmarking purposes, an algorithm used for edge detection was constructed using Sobel, Laplacian and Canny approaches [10]. The algorithm ran thanks to the Python programming language and mainly used the digital image processing oriented library OpenCV. Figure 1 was used as input data.

Figure 22 Image for edge detection. Source: [12]

For the Sobel operator, the gradient of both x and y was used, as well as their mutual blending. The resulting detection is shown in Figures 2 (Left, Middle and Right).

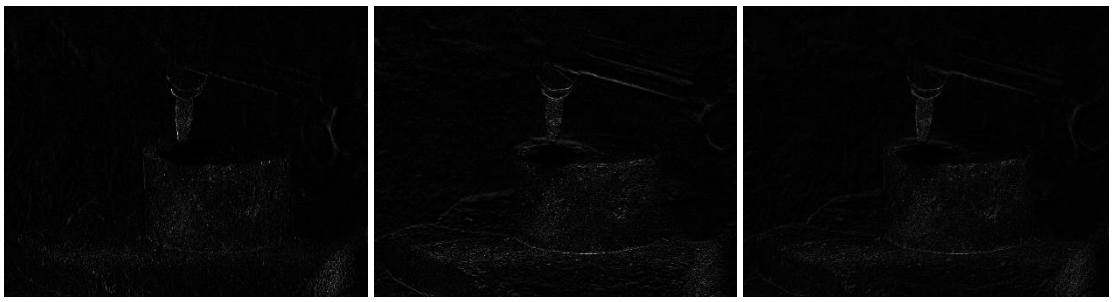

Figure 23 Left – Sobel x, **Middle – Sobel y**, **Right – Sobel xy.** Source: (own)

This was followed by edge detection using Laplacian shown in Figure 3 (Left) and also Canny which can be seen in Figure 3 (Right). The edge detection performed by Laplacian came out worst for these input data.

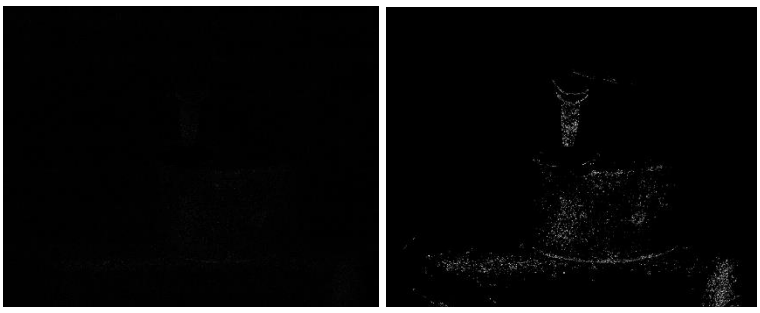

Figure 3 Left – Laplacian, Right – Canny. Source: (own)

The primary purpose of this research was not to compare the resulting quality of edge detection, but the time it takes to complete the detection. For this purpose, 6 different devices were selected. The desktop category was represented by the ThinkCentre M75s Gen2 and the Omen by HP 45L Gaming. For the laptop, the HP EliteBook 840 G2 was used. Single-board computers were represented by twin devices from the manufacturer Khadas, namely the Khadas Edge2 and the Khadas VIM4. The widely popular Raspberry Pi 4 Model B was not spared from comparison. Detection on a per-access basis was performed thousands of times. The individual times were then averaged. These results are shown in Table 1.

Table 6 Comparison of different edge detection approaches. Source: (own)

Device	Sobel x (ms)	Sobel y (ms)	Sobel xy (ms)	Laplacian (ms)	Canny (ms)
HP EliteBook 840 G2	12.819	11.486	7.316	12.194	29.546
ThinkCentre M75s Gen2	6.105	5.803	4.667	6.872	18.657
Omen by HP 45L Gaming	4.354	3.937	2.899	5.578	9.796
Khadas Edge2	16.317	15.392	9.191	20.054	18.362
Khadas VIM4	31.397	29.844	12.397	34.388	19.939
Raspberry Pi 4 Model B	38.269	34.998	16.204	41.898	46.943

Unsurprisingly, detection was fastest on the Omen by HP 45L Gaming, which has the highest computing power of the devices mentioned above. However, a significant drawback is that this is redeemed by the high purchase price of the device and also by the fact that this device is the largest of all mentioned. The second desktop computer also achieved decent results. In this case, due to the relatively fast detection times and the significantly lower purchase price, we can talk about a good price/performance combination. A significant disadvantage is still the relatively large size, which may complicate the deployment in industry. The category represented by single-board computers achieved surprisingly good results. Specifically, the Khadas Edge2 saw comparable results to the HP EliteBook 840 G2 laptop for most detectors, which, given the purchase cost and size, gives the Khadas Edge2 very interesting application possibilities. The Khadas VIM4 and Raspberry Pi 4 Model B also achieved decent results, but here the ills of cheaper single-board computers have already asserted themselves and this can also be seen in the results.

3. CONCLUSION

The research focused on benchmarking the duration of edge detections for the methods of finding maxima of first derivatives (Sobel and Canny) and finding passages of second derivatives through zero (Laplacian). The desktop computers subjected to this benchmarking were ThinkCentre M75s Gen2 and Omen by HP 45L Gaming. In addition, the HP EliteBook 840 G2 laptop was tested. The single-board computer category was represented by the Khadas Edge2, Khadas VIM4 and Raspberry Pi 4 Model B. The Omen by HP 45L Gaming desktop computer came out best in the benchmarking with the highest computing power. A positive surprise was the Khadas Edge2 single-board computer, which achieved very positive results due to its small size and reasonable price. Another interesting extension of the research could be to focus on image binarization (segmentation) and subsequent benchmarking with edge detection methods.

ACKNOWLEDGEMENT

The work was supported by the specific university research of the Ministry of Education, Youth and Sports of the Czech Republic No. SP2023/043.

REFERENCES

[1] XIN WANG. Laplacian Operator-Based Edge Detectors. *IEEE Transactions on Pattern Analysis and Machine Intelligence*. 2007, **29**(5), 886-890. ISSN 0162-8828. Dostupné z: doi:10.1109/TPAMI.2007.1027

[2] PELLEGRINO, F.A., W. VANZELLA a V. TORRE. Edge Detection Revisited. *IEEE Transactions on Systems, Man and Cybernetics, Part B (Cybernetics)*. 2004, **34**(3), 1500-1518. ISSN 1083-4419. Dostupné z: doi:10.1109/TSMCB.2004.824147

[3] SUN, Weixuan, Shaodi YOU, Janine WALKER, Kunming LI a Nick BARNES. Structural Edge Detection: A Dataset and Benchmark. *2018 Digital Image Computing: Techniques and Applications (DICTA), Digital Image Computing* [online]. 2018, 1-8 [cit. 2023-05-31]. ISBN 9781538666029. ISSN edseee.IEEEConferenc. Dostupné z: doi:10.1109/DICTA.2018.8615801

[4] GAO, Wenshuo, Xiaoguang ZHANG, Lei YANG a Huizhong LIU. An improved Sobel edge detection. *2010 3rd International Conference on Computer Science and Information Technology, Computer Science and Information Technology (ICCSIT), 2010 3rd IEEE International Conference on* [online]. 2010, **5**, 67-71 [cit. 2023-05-31]. ISBN 9781424455379. ISSN edseee.IEEEConferenc. Dostupné z: doi:10.1109/ICCSIT.2010.5563693

[5] DING, Lijun a Ardeshir GOSHTASBY. On the Canny edge detector. *Pattern Recognition*. 2001, **34**(3), 721-725. ISSN 00313203. Dostupné z: doi:10.1016/S0031-3203(00)00023-6

[6] CHENG, H.D., X.H. JIANG, Y. SUN a Jingli WANG. Color image segmentation: advances and prospects. *Pattern Recognition*. 2001, **34**(12), 2259-2281. ISSN 00313203. Dostupné z: doi:10.1016/S0031-3203(00)00149-7

[7] KONISHI, S., A.L. YUILLE, J.M. COUGHLAN a SONG CHUN ZHU. Statistical edge detection: learning and evaluating edge cues. *IEEE Transactions on Pattern Analysis and Machine Intelligence*. 2003, **25**(1), 57-74. ISSN 0162-8828. Dostupné z: doi:10.1109/TPAMI.2003.1159946

[8] HEATH, Mike, Sudeep SARKAR, Thomas SANOCKI a Kevin BOWYER. Comparison of Edge Detectors. *Computer Vision and Image Understanding*. 1998, **69**(1), 38-54. ISSN 10773142. Dostupné z: doi:10.1006/cviu.1997.0587

[9] YITZHAKY, Y. a E. PELI. A method for objective edge detection evaluation and detector parameter selection. *IEEE Transactions on Pattern Analysis and Machine Intelligence*. 2003, **25**(8), 1027-1033. ISSN 0162-8828. Dostupné z: doi:10.1109/TPAMI.2003.1217608

[10] LUAN, Guangyu a Rensheng CHE. A Simple and Efficient Edge Detection Algorithm. *2008 International Symposium on Computer Science and Computational Technology*. IEEE, 2008, 2008, 40-44. ISBN 978-0-7695-3498-5. Dostupné z: doi:10.1109/ISCSCT.2008.328

[11] BUICHARI, Syed Usama Khalid, Remus BRAD a Constantin BALA-ZANIFIRESCU. Fast Edge Detection Algorithm for Embedded Systems. *STUDIES IN INFORMATICS AND CONTROL* [online]. 2014, **23**(2), 163-169 [cit. 2023-05-31]. ISSN 12201766. Dostupné z: https://search.ebscohost.com/login.aspx?direct=true&db=edswsc&an=000338689200004&scope=site

[12] Image for edge detection. In: *Pixabay* [online]. Germany: Pixabay, 2016 [cit. 2023-05-31]. Dostupné z: https://pixabay.com/photos/acetylene-aluminium-aluminum-bars-1239325/

APPROACHES TO PROCESS CAPABILITY ANALYSIS IN CASE OF NON-NORMALLY DISTRIBUTED DATA

Author(s): Monika SEKANINOVÁ

Supervisor: prof. Ing. Jiří PLURA, CSc.

Department: Department of Quality Management, Faculty of Materials Science and Technology, VSB – Technical University of Ostrava

Abstract

Process capability analysis is an important part of product quality planning and management and can be defined as the long-term ability to meet customer requirements. Capability indices are used to assess process capability. In case of measurable quality characteristics, the process in control and normality of the data are basic assumptions. This paper focuses on the interpretation of knowledge about current approaches to process capability analysis, with a focus on the situation when the data normality assumption is not met.

Key words:

Process capability indices (PCI), process capability analysis, non-normal data.

1. INTRODUCTION

Capability assessment of manufacturing processes is an integral part of product quality planning and management. The IATF 16 949, a standard used in the automotive industry, requires organizations to manage special characteristics [1]. In a process capability analysis, the production process is verified to ensure that it is capable of meeting the specified quality criteria in the long term. Performing this analysis also makes it possible to estimate the probability of non-conforming products, to optimise the planning of production activities or to initiate improvement activities. Process capability indices (PCI) are used to evaluate process capability analysis [2]. Estimates of these indices are often not correctly interpreted, nor are the underlying assumptions made about the data always verified. Exploratory data analysis is primarily aimed at detecting statistical peculiarities of the data associated with shape peculiarities of the data distribution, the presence of suspicious values and the comparison of the data distribution with typical distributions. When assessing process capability for measurable quality characteristics, process in control and normality of the data are basic assumptions [3]. Failure to meet normality is often encountered in practice, since for many measurable characteristics the normal distribution is not a natural distribution. In the case of non-normally distributed data, it is therfore necessary to apply appropriate procedures to ensure an objective evaluation of the process capability.

2. PROCESS CAPABILITY ANALYSIS

Process capability is defined as a statistical measure of the inherent variability of a process for a given characteristic and is often related to the proportion of the output that is found in the product specification. Since the process should be in control and described by a predictable probability distribution, the proportion of outputs or out-of-specification products can be estimated. The following procedure is recommended for assessing process capability – selection of the monitored quality characteristic, measurement system analysis, collection of data on the monitored quality characteristic, assessment of statistical control of the process, verification of the normality of the monitored quality characteristic, calculation of capability indices. [4]

Process capability is most often evaluated using capability indices *Cp* and *Cpk*. If the process is not in a state of statistical control, the process performance is evaluated using performance indices *Pp* a *Ppk* instead of process capability. The *Cp* a *Pp* indices are based on the standard deviation properties of the normal distribution. This is the proportion between the range of the upper tolerance limit (USL) and the lower tolerance limit (LSL) and the width of the natural variability band of the characteristic under study, which covers 99.73 %. This band is referred to by ISO 22514-4 as the reference interval [5], which in the case of a normal data distribution corresponds to six times the standard deviation, i. e. 6σ. In the case of the *Cpk* or *Ppk* indice, it is the proportion of the distance of

the mean to the closest tolerance to half the width of the natural variability band (3σ). An overview of those and other performance and capability indices and their characteristics is presented in the literature [2,3]. Normal distribution is a probability model that describes a large number of random occurrences. It is a suitable statistical model when a large number of subtle and mutually independent occurrences affect the variation of a random variable.

3. NON-NORMAL DISTRIBUTED DATA

For non-normally distributed data, the mean and standard deviation are not sufficient to express the characteristics of the process under study. The magnitude of the errors may vary depending on the unknown parameters of the distribution [6]. The standard deviation here lacks the property that the reference interval (μ-3σ, μ+3σ) covers the values of a normally distributed random variable with probability 0.9973. The 6σ interval must therefore be replaced by a quantile range. The approach consists of estimating the parameters of the distribution and using them to determine the relevant quantiles. Figure 1 presents the shape of the non-normally distributed data, where parameter *a* represents the reference interval and the values of *Y1* and *Y2* are estimated using the methods presented in the following section.

In the case of a non-normal distribution, the calculation of capability/performance indices by the conventional method would lead to erroneous and confusing results. A number of experts have supported this claim with studies focusing on the interpretation of erroneous results due to incorrect application of the standard method to non-normal data [7, 8, 9].

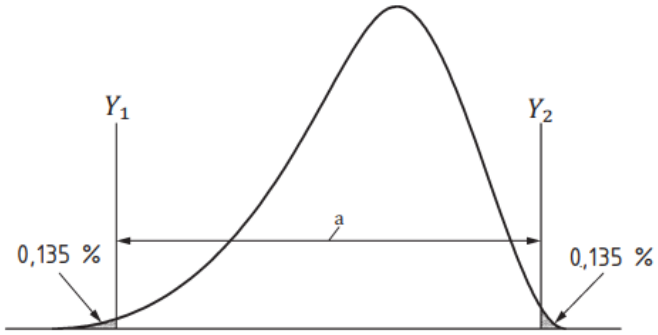

Figure 1 Non-normally distributed data. Source: [5]

4. CURRENT APPROACHES

The estimation of PCI for non-normally distributed data has been the subject of much research. There are two basic approaches. The first is to estimate PCI using a quantile method that allows one to work with distributions of arbitrary shape. The second approach is based on transformation techniques, using which the data are converted to data originating from a normal distribution and then estimating the PCI using standard formulas.

The quantile method or Clements percentile method is the most commonly used technique. Data on the quality characteristic of interest can often be described by a different probability distribution, and it is always necessary to validate the appropriate theoretical model of the distribution of the monitored characteristic using goodness-of-fit tests. Once a suitable distribution has been found, the necessary quantiles corresponding to the theoretical model are determined [10]. Modified symbols are used for the capability indices *Cp* and *Cpk*, which are then calculated according to the relations (1) and (2). Other techniques based on quantile calculations are the Burr quantile method, the Pearson curve method, the empirical percentile method and the probability paper method [3, 5]. The approaches consists of estimating the parameters of the distribution and using them to derive the corresponding quantiles.

$$C'_p = \frac{USL - LSL}{x_{0.99865} - x_{0.00135}} \tag{1}$$

where:

$C´p$ – estimation of the capability indice,
USL – upper tolerance limit,
LSL – lower tolerance limit,
$x0.99865$ – 99.865% quantile of the corresponding distribution,
$x0.00135$ – 0.135% quantile of the corresponding distribution.

$$C´_{p_k} = \min\left(\frac{USL - x_{0.5}}{x_{0.99865} - x_{0.5}}; \frac{x_{0.5} - LSL}{x_{0.5} - x_{0.00135}} \right) \tag{2}$$

where:
$C´pk$ – estimation of the capability indice,
$x0.5$ – median of the corresponding distribution.

The data transformation method consists of converting the original data into new data, including the transformation of tolerance limits. A suitably chosen transformation leads to stabilization of the variance, better symmetry of the data and often to normality of the distribution of the data set. It is desirable to use statistical software to find the optimal parameters of the transformation function. The procedure using the transformation function can be summarised as follows - calculation of the transformed variable, verification of normality of the transformed variable, recalculation of tolerance limits using the transformation function, calculation of capability indices according to standard relations. [11] Among the most widely used transformation techniques is the Box-Cox power transformation, which is used to ensure that the sampling distribution approximates the normal distribution with respect to skewness and kurtosis. It uses the parameter λ, which is chosen to minimize the standard deviation. The maximum likelihood method can be used to estimate the parameter λ. In the selected interval, the function ln L = f(λ) can be plotted, and at the point where the likelihood function curve reaches its maximum, the x-coordinate corresponds to the estimate of λ [12]. Another technique is the Johnson transformation system based on the moment function, converting the data to a normalized normal distribution with parameters (0,1) [13]. Techniques such as the quadratic transformation [14] and root transformation have also been presented [15].

Most international standards work with the assumption that the process is in control and the data comes from a normal distribution. However, the behaviour of real production processes shows that this state is rather rare. For this reason, the International Organization for Standardization (ISO) has put forward the ISO 22514-2 [16] providing a framework for estimating process performance and capability for different cases of time-dependent changes in the distribution of the observed quality characteristic. These situations are categorised on the basis of the stability of the mean ad the stability of the variance in case of their constancy, systematic changes or completely random changes. The standard works with eight model situations, where the behaviour of the characteristic under study can be described by probability distribution, shape, variance and location, whose parameters are generally time-dependent functions. The standard also provides calculations of PCI and makes recommendations for the addition of the calculation of confidence intervals [16].

The actual estimation of PCI for non-normally distributed data has been the subject of many studies and many proposals have been made to address this situation – for Poisson distribution [17], gamma distribution [18], Weibull distribution [19], log-normal distribution [20], etc. Similarly, proposals for entirely new [21, 22, 23] or modified PCI [24] have been put forward in recent years. Also, the effectiveness of standard methodologies has been compared with each other – comparing the Clemens, Box-Cox and Johnson methods for Weibull distribution [25], comparing Clemens, Box-Cox and Burr methods for non-normal data [26] or comparing the Box-Cox transformation with the root transformation on simulated data coming from the gamma, beta and Weibull [27] distributions. One can also find studies modifying standardly used methods, such as the Box-Cox transformation technique [28].

5. CONCLUSION

Process capability analysis is an important area of research. This is particularly the case when one of the basic assumptions of a standard analysis procedure, which is data normality, is not met. For the purpose of further research, an analysis of suitable solutions for selected quality characteristics is proposed and the focusing on those characteristics where suitable solutions do not yet exist.

ACKNOWLEDGEMENT

The work was supported by the specific university research of the Ministry of Education, Youth and Sports of the Czech Republic No. SP2023/043

REFERENCES

[1] IATF 16 949:2016. *Norma pro systémy managementu kvality v automobilovém průmyslu.* Praha: ČSJ, 2016.
[2] KOTZ, S., LOVELANCE, C. R. *in Theory and Practice.* London: Arnold, 1998.
[3] KOTZ, S., PEARN, W. L. *Encyklopedia and Handbook of Process Capability Indices: A comprehension Exposition of Quality Control Measures.* Singapore: World Scientific Publishing Co. Pt. Ltd., 2006.
[4] PLURA, J. *Plánování a neustálé zlepšování jakosti.* Praha: Computer Press, 2001.
[5] ISO 22514-4. *Statistical methods in process management – Capability and performance. Part 4: Process capability estimates and performance measures.* ISO, 2016.
[6] SENVAR, O., KAHRAMAN, C. Type-2 fuzzy process capability indices for nonnormal processes. *Journal of* Intelligent and Fuzzy Systems, 27(2), 769-781, 2014. DOI: 10.3233/IFS-131035
[7] SARKAR, A., PAL., S. Estimation of process capability index for concentricity. *Quality Engineering*, 9(4), 665-671, 1997.DOI: 10.1080/08982119708919088
[8] CHOU, Y. M., POLANSKY, A. M., MASON, R. L. Transforming non-normal data do normality in statistical process control. *Journal of Quality Technology*, 30, 133-141, 1998. DOI: 10.1080/00224065.1998.11979832
[9] SOMERVILLE, S. E., MONTGOMERY, D. C. Process capability indices and non-normal distributions. *Quality Engineering,* 9(2), 305-316, 1996. DOI: 10.1080/08982119608919047
[10] CLEMENTS, J. A. Process capability calculations for nonnormal distributions. *Qual Prog,* 22, 95-100, 1989.
[11] PLURA, J. *Analýza způsobilosti procesů. Studijní opory.* Ostrava: Vysoká škola báňská – Technická univerzita Ostrava, 2015.
[12] MELOUN, M., MILITKÝ, J. *Kompendium statistického zpracování dat*. Praha: Academia, 2006.
[13] JOHNSON, N. L. Systems of frequency curves generated by methods of translation. *Biometrika*, 36:149–176, 1949.
[14] SOMERVILLE, S. E., MONTGORMERY, D. C. Process capability indices and non-normal distributions. *Quality Engineering*, 9(2), 305-316, 1996. DOI: 10.1080/08982119608919047
[15] NIAKI, S. T. A., ABBASI, B. Skewness reduction approach in multi-attribute process monitoring. *Commun Stat Theory Methods*, 36(12):2313–2325, 2007. DOI: 10.1080/03610920701215456
[16] ISO 22514-2. *Statistical methods in process management – Capability and performance. Part 2: Process capability and performance of time-dependent process models.* ISO, 2017.
[17] Alevizakos, V.,Koukouvinos, Ch., Castagliola, P. Process capability index for Poisson regression profile based on the Spmk index, *Quality Engineering*, 31(3), 430-438, 2019. DOI: 10.1080/08982112.2018.1523426
[18] Alevizakos, V., Koukouvinos, Ch. Evaluation of process capability in gamma regression profiles. *Communications in Statistics - Simulation and Computation*, 51(9), 5174-5189, DOI: 10.1080/03610918.2020.1758941
[19] THAVORN, E., SUDASNA, P. The Effects of Weibull Distribution on Supplier Comparison using Lower Process Capability Index: A Case Study. *Trends in Sciences,* 19(3), 2158, 2022. DOI: 10.48048/tis.2022.2158
[20] WU, CH-CH., WU, S-F. Analysis of the estimation of process capability index of non-normal proces data using the lognormal distributions. *ICIC Express Letters,* 14(2), 197-202, 2020.DOI: 10.24507/icicel.14.02.197
[21] RAO, G. S., Albassam, M., Aslam, M. Evaluation of Bootstrap Confidence Intervals Using a New Non-Normal Process Capability Index. *Symmetry,* 11 (4), 484, 2019. DOI: https://doi.org/10.3390/sym11040484
[22] Erfanian, M., Gildeh, B. S. A new capability index for non-normal distributions based on linex loss function. *Quality Engineering*, 33(1), 76-84, 2021. DOI: 10.1080/08982112.2020.1761026
[23] SAHA, M., DEY, S. Estimation and Confidence Intervals of Modified Process Capability Index Using Robust Measure of Variability. *Stochastics and Quality Control*, 37(2), 153-164, 2022. DOI: 10.1515/eqc-2022-0014
[24] LIAO, M-Y., PEARN, W. L. Modified weighted standard deviation index for adequately interpreting a supplier´s lognormal process capability. *Journal of Engineering Manufacture,* 233(3), 999-1008, 2019. DOI: 10.1177/0954405418755820
[25] SENVAR, O., SENNAROGLU, B. Comparing performances of clements, Box-Cox, Johnson methods with Weibull distributions for assessing process capability. *Journal of Industrial Engineering and Management,* 9(3), 634-656, 2016. DOI: http://dx.doi.org/10.3926/jiem.1703
[26] WOOLURU, Y., SWAMY, D. R., NAGESH, P. Process capability estimation for non-normally distributed data using robust methods – A comparative study. *International Journal for Quality Research,* 10(2), 407-420, 2016. DOI: 10.18421/IJQR10.02-11
[27] HOSSEINIFARD, S. Z., ABBASI, B., AHMAD, S., ABDOLLAHIAN, M. A transformation technique to estimated the process capability index for non-normal process. *International Journal of Advanced Manufacturing Technology,* 40(5), 521-517, 2009. DOI: 10.1007/s00170-008-1376-x
[28] YANG, Y., ZHU, H. A study of non-normal process capability analysis based on box-cox transformation. *Proceedings – 3rd Internationl Conference on Computational Intelligence and Applications, ICCIA 2018,* 240-243. DOI: 10.1109/ICCIA.2018.00053

USING 3D SENSOR FOR VISION SYSTEM

Author(s): Tomáš SIRNÍK

Supervisor: doc. Ing. Robert FRISCHER, Ph.D.

Department: Department of Industrial Systems Management, Faculty of Materials Science and Technology, VSB – Technical University of Ostrava

Abstract

The trend these days is to automate everything. In the process, all modern production and storage halls contain smart readers, sensors, cameras and other equipment related to the vision system. Machine vision systems operating automatically and reliably detect defective products and thereby increase quality. This article Deals with the area of image processing and analysis and its subsequent industrial use. Explains some examples of using sensors for specific sensing areas. Project realization it uses an application from IFM sensor 0D302 as the main tool, which can then be used for signals to the control system mostly PLC.

Key words:

Machine vision, smart sensor, smart reader, image, box.

1. INTRODUCTION

We already encounter machine vision very often in production and storage halls. The issue of storing stocks and handling them is a very current topic. A good choice of the right storage and transport system can save the company financial resources. Previously used conventional warehouses, which used e.g. forklift trucks for handling materials, are now being replaced by automated warehouses with automatic transport and storage of material, such as carousel systems, which automatically transport the required unit from the stored position to the delivery point after entering a request into the control system place, or vice versa to the designated place in the shelf. In this case, smart readers of either DMC, QR or barcodes are deployed, where this code carries information about the product. The use of an automatic system entails significant advantages such as: speed, efficiency and accuracy of storage/unloading. The main advantage is the reduction of human error when handling the material. The system can control the total amount of stock [1].

Machine vision systems rely on digital sensors protected inside industrial cameras with specialized optics to acquire images, so that computer hardware and software can process, analyze, and measure various characteristics for a variety of different types of detection. Smart sensors generate and receive data and the information. They enable substantial increases in efficiency, are more flexibility, and better planning security for predictive plant maintenance. The difference is that the smart sensor no longer needs additional HW to send the results. According to the settings, it can automatically send and receive data further to the control system (good and bad piece). It performs predefined and programmed functions on a specific type of collected data, then transmits the data through a network connection. The features of the smart sensor are; self-identification, digital sensor data, smart calibration and compensation, multi-sensing capacity, sensor communication for configuration of remote and remote monitoring, etc. Smart sensor is the product of the combination of sensor integration and microprocessor. A raw base sensor is used to provide the sensing capability, it is designed to measure a physical quantity and produce an analog signal. This analog signal must be processed by the microprocessor. See the figure 1 the main component of a smart sensor [2, 3, 4].

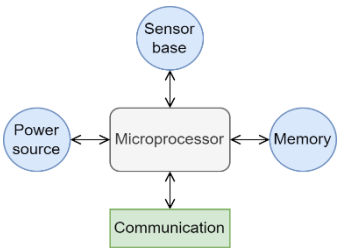

Figure 1 Main component of smart sensor. Source: [4]

2. DETECTING OF BOX

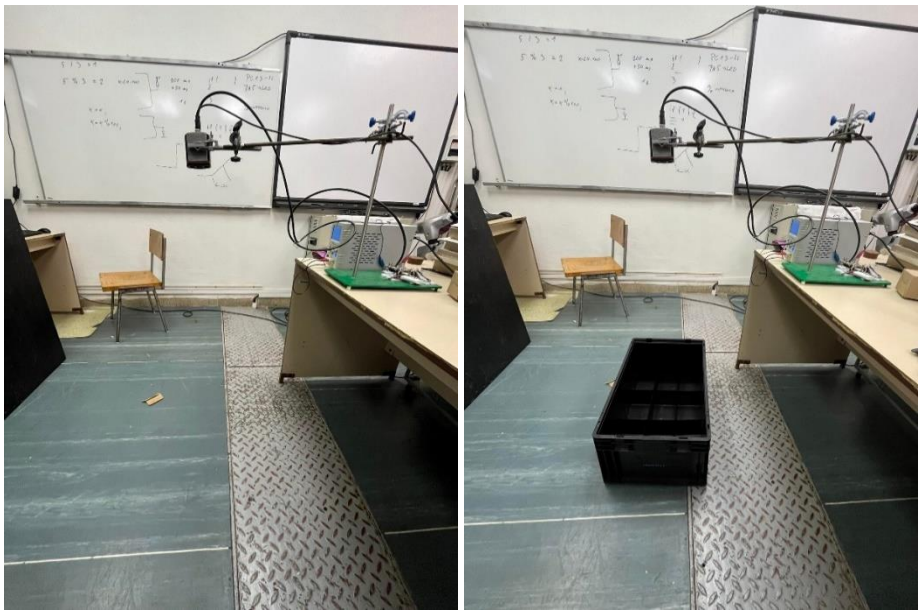

Figure 2 Reference plane with box. Source: (own)

Finding a box in terms of its length, width and height. The scanner did not come with a bracket. In the research, an additional 3D model of the holder was devised and then it was printed on a 3D printer for better manipulation of the settings. The sensor was perpendicular to the crate. On the left side we can see the area without the box on the right side is with the box see figure 2. The sensor that was used for this kind of application is from IFM type 03D302. 3D sensor is reliable measurement of height, width and length to calculate strap length and volume. Reliable detection of size, orientation and position of the objects for automated storage space planning. Reliable volume determination for storage and conveyor technology. In order to use the 3D dimension search mechanism, you must first create a base plane, or coordinate system, from which to determine the reference of the smart sensor. Must be created reference plane. The reference plane is the surface on which the rectangular object is to be measured. Must be clean and all object was removed from the field of view. Then was used region of interest (ROI) to define and teach the new reference plane. If that the scanner works well and the lens can focus. It is necessary to have a smart sensor at a working distance see table 1. For testing, the scanner was approximately 1 m away from the reference surface. According to table see 1, a maximum of 0.75 x 1 m can be seen [4, 5].

Table 1 Field of view size with lens distortion correction. Source: [5]

range (m)	lenght	width
0,5	0,37	0,5
1	0,75	1
2	1,5	2

3	2,25	3
4	3	4
5	3,75	5

Communication is by industry standard 4 pin ethernet with an M12 connector that is converted to an RJ45 connector for easier connection to a computer to communicate with the device. The power is using the M12-8 pin connector (24 V), where there is also access for signals from the control unit. [5].

In general, every company that manufactures smart sensors, readers and cameras has its own software for setting up the program. In this case, IFM Vision Assistant was used for research. A function from the dimension application was used to recognize the box. As you can see on figure 3 the image around the box is blue, which means that it is possible to detect objects in this whole area. ROI again marked area of future detection. In this section, the sensor surface (calibration) is taught. The box is in the given area under the sensor and the sensor detects it, the protrusion is data like (height, width, length), the required dimensions can be set so that the sensor finds the right box. More detailed information about the output from the sensor (width, height, length and coordinates of the crate). It is also possible to see the rotation of the box, where the output value is an angle. Different colors can be noticed in the picture. This color indicates the distance from the sensor. E.g. blue will represent the greatest possible distance (reference surface). On the contrary, a redder color shows a smaller distance from the sensor. In this case, we can see in figure 3 that a rectangle has appeared from the red pixels. We can detect this box well or whatever. It is necessary to know its exact dimensions. Subsequently, parameters can be set into the program: width, length and height. The box has dimensions of 40x60x28 cm. Or or and conditions can be set into the program. Based on research, it was determined that the width must be greater than 35x55x26 cm. According to the parameterization, the scanner recorded this black box and sent an OK result to the counter. If a box other than the specified dimensions passed through, NOK sent the result to the counter.

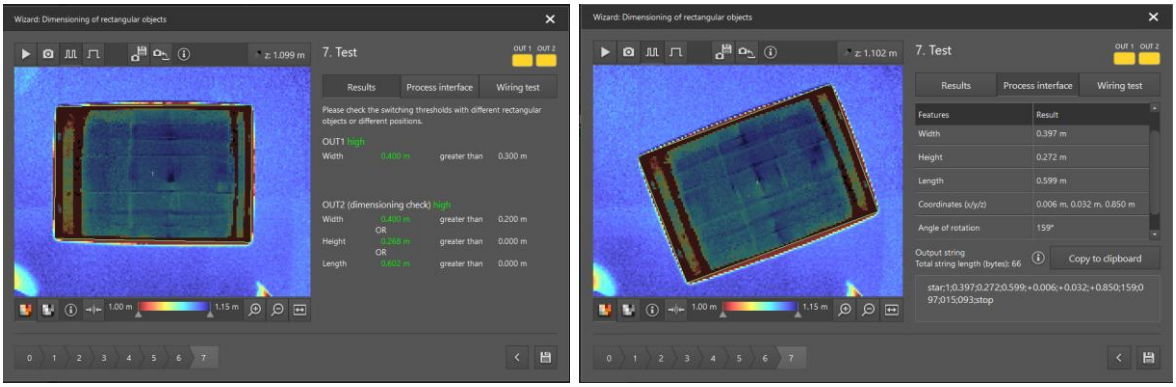

Figure 3 Detecting of box. Source: (own)

The detection of bottles in the transporter was also a subject of research. The subject was whether the sensor detects an empty space in the container or a different one (smaller bottle). It has been proven in testing that after a successful and correct setting, it is possible to detect an empty place as well as a smaller or larger bottle that does not belong in the place. This detection can be seen in figure 4. On the left are all the bottles in the crate and on the right 2 are missing. This test is again based on the height difference compared to the reference plane, but we add a larger number of regions of interest to detect missing bottles.

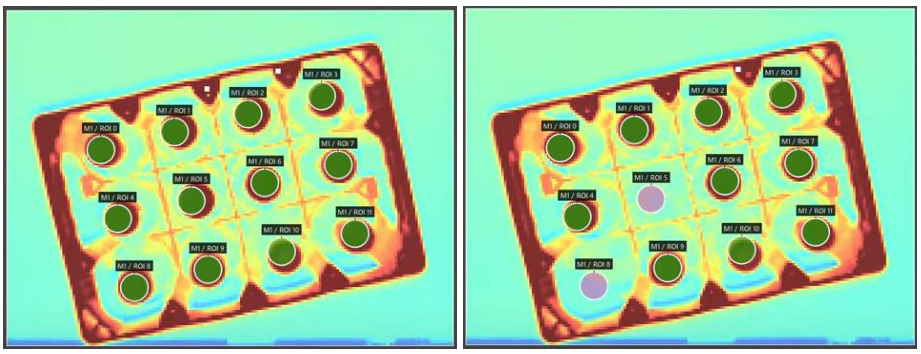

Figure 4 Missing bottle. Source: (own)

3. CONCLUSION

More and more new production and storage halls are being built both in the Czech Republic and abroad. In order to increase efficiency and reduce costs, automated storage and production lines are increasingly being used. Where human power is not even needed in some cases. New storage and automated technologies are still being developed in this direction, and new smart sensors and cameras are introduced to the market every year. A great future can be seen in this direction.

The project tested a smart sensor from the IFM company, which can be applied primarily for automated storage halls. It has been proven that the crate can be detected and its width, length and height can also be measured in real time. Based on the specification, a test sequence was devised to sort the box, whether they have this dimension according to the specification and discard the bad box. All inputs and outputs from the smart sensors are digital. Furthermore, these signals can be processed into a control system, usually a PLC.

In the next task, it was possible to find out whether there is the correct number of bottles in the crate. By adding another condition, it was possible to find that the bottle can be there, but it must be a certain size from according to the given specification. This sensor proved that the detection was very reliable in both cases. It must be noted that these were static conditions. The sensor was not tested in dynamic mode. It is currently not possible to test a treadmill with multiple boxes. In the future, it is possible to test this sensor in dynamic mode with multiple crates and send them one after the other at a certain interval.

ACKNOWLEDGEMENT

The work was supported by the specific university research of Ministry of Education, Youth and Sports of the Czech Republic No. SP2023/043

REFERENCES

[1] FREJLACHOV Katerina. Steel Cities: The Architecture of Logistics in Central and Eastern Europe. First edition. Curych, Switzerland: Park Books, 2020. ISBN 978-80-270-7038-1.
[2] *Fierceelectronics* [online]. Fierceelectronics, 2021 [cit. 28.5.2023]. Available from: https://www.fierceelectronics.com/electronics/what-are-smart-sensors
[3] *Fourfaith* [online]. Fourfaith, 2022 [cit. 28.5.2023]. Available from: https://www.fourfaith.com/industry-news/smart-sensor.html
[4] *Instrumentationtools* [online]. Instrumentationtools, 2023 [cit. 29.5.2023]. Available from: https://instrumentationtools.com/smart-sensors-in-industry/
[5] *Ifm* [online]. Ifm, 2023 [cit. 30.5.2023]. Available from: https://www.ifm.com/de/en/product/O3D302

POSSIBILITIES OF DEVELOPING APPROACHES TO QUALITY PLANNING FOR INDUSTRY 4.0 CONDITIONS

Author: Iveta SLANCOVÁ

Supervisor: prof. Ing. Jiří PLURA, CSc.

Department: Department of Quality Management, Faculty of Materials Science and Technology, VSB – Technical University of Ostrava

Abstract

The article analyses the possibilities of developing approaches to quality planning for Industry 4.0 conditions. The work presents the current state of knowledge of product quality planning and its sub-processes, the concept of Industry 4.0 with a focus on the possibilities of digitizing data needed for quality planning and software support for quality planning. The aim is to improve the course of quality planning processes and other quality management processes. The main goal is to outline the areas on which it is appropriate to focus research activities.

Key words:

Quality planning, Quality planning sub-processes, digitizing of quality planning, use of quality planning outputs, Industry 4.0.

1. INTRODUCTION

The current pressure for digitalization of businesses creates more favourable conditions for ensuring that customers' growing demands for products and services are met. Organizations must be able to react to these requirements as promptly as possible. This brings increased attention to quality planning processes and increased interest in the benefits resulting from the implementation of Industry 4.0 in companies in order to maintain competitiveness. The basic building block for the production of quality products is quality data in quality planning process. This data is also important for other phases of the life cycle and directly affects the quality of the final product. This is confirmed by the modern approaches of companies, which move from quality assurance in the production phase to quality planning in the pre-production phases, thereby ensuring the prevention of nonconformities occurrence in the production phase. It is necessary to increase emphasis on product quality planning processes to ensure smooth product life cycle which effectiveness can be significantly increased by optimizing information flows. The current trend linked with digitization and automation of production brings new opportunities to make quality planning process more efficient and to better use their outputs in other quality management processes.

2. Analysis of the current state

Literature review analysis was conducted, in which 63 publications were collected and reviewed, of which 14 were current Czech and foreign standards. The selected publications were analysed and divided into three areas 1) product quality planning and its sub-processes 2) the concept of Industry 4.0 with focus on the possibilities of digitizing data needed for quality planning 3) software support for quality planning. The possibilities of developing approaches to quality planning for the Industry 4.0 conditions were identified based on the extraction of knowledge from the literature review.

Product quality planning and its sub-processes

Quality planning is defined as the process of forming quality objectives and developing the means to meet these objectives [1]. Quality planning includes many sub-processes. Sub-processes of quality planning overlap to other stages of the product life cycle helping to minimize risks during production and ensure customer satisfaction. The division of quality planning process into individual sub-processes can be viewed from the perspective of the APQP [2] and VDA-MLA [3] methodics, quality planning methods [4][5] (eg: QFD methods and FMEA methods) or the product life cycle concept.

The product life cycle concept includes quality planning. Juran's quality spiral, APQP and VDA-MLA, are the most well-known approaches to quality planning with a direct relationship to the product

life cycle. The aim of the APQP and VDA-MLA methodics is to achieve and continuously improve the quality of new products. Both methodics are used in the early phase of the project management and apply elements of simultaneous engineering. The differences are in the defined project milestones. The analysed quality planning methods are QFD (Quality Function Deployment), FMEA (Failure Mode and Effects Analysis), FTA (Fault Tree Analysis), Process Capability Analysis and MSA (Measurement Systems Analysis). These methods are used to effectively implement quality planning processes. Applications of some of these methods are required, for example, by suppliers to the automotive industry.

The quality planning process was divided into 10 basic sub-processes based on the analysis conducted:

- **Identification of product requirements:** identification of product requirements is a basic building block of quality planning. It is important to accurately identify product requirements. In addition to customer requirements, process inputs are for example legislative requirements, results of benchmarking or information about the state of science and technology in a given area.
- **Transformation of product requirements into product quality characteristics:** this process is very important for satisfying requirements. Requirements, which are mostly formulated in the customer language, are converted into technical specifications.
- **Product design and development**: a product that should meet the target values of the quality characteristics set in the previous step, is developed in this sub-process.
- **Optimization of product design in terms of risks of possible failures:** an important part of product design and development should be its optimization in terms of risks of possible failures. The FMEA method is used as a standard for this optimization.
- **Product design review:** is a comprehensive, systematic and objective assessment of the design conducted by a team of independent experts from various fields. Its main aim is to assess the ability of the proposal to meet the requirements, identify potential problems and propose a way to solve them.
- **Process design and development:** this sub-process aims to fulfil the requirements according to which the process is designed and developed. The proposed process should be mainly able to produce the proposed product in the required quality in the long term.
- **Optimizing the process design in terms of possible failures:** the process is based on previous step; the aim is to minimize the risk of creation of non-identical products or other failures of designed process.
- **Process design review:** the process design optimization is followed by its review. Its result is an assessment of the process from different points of view and possible proposals for process changes.
- **Test production and demonstration of process capability:** a significant production batch is produced as part of test production after which the process capability is evaluated. This phase is crucial in terms of transferring data to other follow-up processes.
- **Production preparation:** in this sub-process, it is necessary to ensure the necessary technical and organizational conditions for successful course of real production process.

Quality control during production and quality improvement are the most important processes that follow quality planning and that communicate with each. The mentioned sub-processes of quality planning have their inputs and outputs and their analysis, including the analysis of their flows, is a proposal for the next area of research. The course of sub-processes of quality planning can be made significantly more efficient by using appropriate quality planning methods. The methods use and simultaneously produce a large amount of data that needs to be further managed.

Industry 4.0 concept with focus on the possibilities of digitizing data needed for quality planning

Quality 4.0 was brought by trends in the field of digital transformation. Quality 4.0 is a new concept that responds to the principles of Industry 4.0 and adapts quality management activities to them. Interesting publications in this area are the work of: Dias et al. [6] and the work of Hu-Chen LIU at al. [7]. The work of Dias et al. [6] conducts a bibliometric analysis and descriptive review of the literature dealing with the process of digital transformation related to Quality 4.0. The work of Hu-Chen LIU et al. [7] comprehensively reviewed previous studies related to Quality 4.0 from Scopus database from 2017-2022.

Quality 4.0 elaborates on the principles of Industry 4.0, which are interoperability, virtualization, decentralization, real-time capacity, service orientation and modularity in the field of quality management. A typical Quality 4.0 feature is digitalization, feedback from machines etc. Quality 4.0

together with Industry 4.0 represents ‘daws of digital transformation’[8] and uses artificial intelligence (AI- artificial intelligence), machine learning, broadened reality, the internet of things, robotics and other technologies leading to improve communication between people, data and devices. Quality 4.0 brings a shift away from paper-based and manual systems, reduces the number of errors caused by human factor, removes obstacles to mutual cooperation across the supply chain and solves problems with traceability.

Individual approaches to quality planning in the form of methodics, methods and tools contain a lot of necessary data. There are a number of methods and tools in quality planning, thanks to which it is possible to obtain extensive data about a product in the pre-production phase, but only a small part of them is used or further processed by companies. Based on the analysis of selected publications, the low level of their digitization was identified as a limiting factor for the use of data from sub-processes of quality planning.

Software support of quality planning

Software support for quality planning was another area of current state research. Based on the analysis of the selected software for the support of quality planning, it shows that there are software working with data related to some sub-processes of quality planning. Thanks to quality planning software, data can be available from the perspective of quality planning methods and tools, from the perspective of project management, or from the perspective of document and data flow. The fact that the analysed software deals with the issue does not mean that it deals with it sufficiently. The outputs of quality planning processes are not sufficiently used in other processes, especially in the production process, where the elements of Industry 4.0 are fulfilled the most. This may be because they are not in digitized form or are difficult to access as they are stored in different software environments. In further research, it would be appropriate to focus on the analysis of the availability of individual inputs and outputs of quality planning processes in companies and the extent of their use in subsequent life cycle processes.

The low level of attention paid to the management of quality planning processes in the conditions of Industry 4.0 is the main incentive for solving the given issue. Although the principles of Industry 4.0 are increasingly being used in medium and large companies, they focus more on the production process. The development of digitization, which creates new opportunities for improving quality planning processes, is the main reason for developing a proposal to improve the availability of inputs and outputs of quality planning and their use in other processes.

2. CONCLUSION

A number of publications have been devoted to quality planning processes for a long time. However, the concept of Industry 4.0 is a new area of research. Based on a literature review, it was found that although these two areas are satisfactorily explored, the development of approaches to quality planning in the conditions of Industry 4.0 has not been paid much attention so far. The main cause identified are mainly:

- Inputs and outputs from sub-processes of quality planning are mostly not digitized which limits their use in the conditions of Industry 4.0
- Some quality planning methods are rarely used in companies which leads to little or no innovation of these methods.
- Available software support for quality planning targets the application of selected quality planning methods: FMEA, MSA and process capability assessment. Since the software focuses on narrow part of quality planning, the use of outputs of sub-process of quality planning in subsequent processes of the product life cycle is limited.
- Available published studies of Industry 4.0 concept mainly focus on the main production processes. Therefore, increased attention is also paid to quality control processes during production, but the necessary attention is not paid to quality planning processes.
- The Quality 4.0 concept is a new area that is developing and with it also the digital transformation in quality management.

These identified causes show that quality planning methods and tools that are applied in paper form, or their output is not stored in an accessible storage, bring blind spots to the digitization of quality planning processes. Smart products carry data that is further unable to communicate with a quality management system (QMS) because it is not digitized. For further development, quality management

processes should be managed in accordance with the Industry 4.0 concept. On the basis of further research, the subject of which will be the improvement of the conditions for the development of approaches to quality planning in the conditions of Industry 4.0, one can expect to achieve scientific and practical benefits. Benefits in the field of improving the availability of quality planning inputs and outputs and their use in other quality management processes can be achieved if the following conditions are met:

- The issue of quality planning in the Industry 4.0 conditions must be looked at from the overall perspective of the product life cycle concept.
- Possible ways of implementing sub-processes of quality planning should correspond to the actual situation in companies, which should enable a use of results across sectors.
- Inputs and outputs of sub-processes of quality planning should reflect existing mehodics, requirements and methods of quality planning.
- The proposal for improving the availability of inputs and outputs of quality planning should be set on the basis of research into real conditions in companies.
- The proposal should correspond utmost to the Industry 4.0 concept.

ACKNOWLEDGEMENT

The work was supported by the specific university research of the Ministry of Education, Youth and Sports of the Czech Republic No. SP2023/043

REFERENCES

[1] DEFEO A. Joseph. *Juran's quality handbook: the complete guide to performance excellence*. Edition 7 th. New York: Kindle Edition, 2016. ISBN: 978-1259643613.

[2] ČESKÁ SPOLEČNOST PRO JAKOST. *Moderní plánování kvality produktu (APQP) a plán kontroly a řízení*. Praha: Česká společnost pro jakost, 2009. ISBN: 978-80-02-02142-1.

[3] VDA QMC. *Product Development – Maturity Level Assurance for New Parts*. Berlin: German Association of the Automotive Industry, 2022.

[4] PLURA, Jiří. *Plánování a neustálé zlepšování jakosti.* Praha: Computer Press, 2001. ISBN: 80-7226-543-1.

[5] NENADÁL, Jaroslav et al*. Management kvality pro 21. století.* Praha: Management Press, 2018. ISBN 978-80-726-1561-2.

[6] LIU, Hue-CHen, LIU, Ran, GU, Xiuzhu, YANG, Miying. From total quality management to Quality 4.0: A systematic literature review and future research agenda. *Frontiers of Engineering Management*. 2023. ISSN: 2095-7513, 2096-0255. DOI: 10.1007/s42524-022-0243-z.

[7] DIAS, Ana Margarida., CARVALHO, André M., SAMPAIO, Paulo. Quality 4.0: literature review analysis, definition and impacts of the digital transformation process on quality. *International Journal of Quality & Reliability Management*. 2022, Vol. 39 Issue 6, p1312-1335.

[8] REEDY, Scott. *Koncept Kvalita 4.0 přetváří způsob vývoje produktů* [online]. Vše o průmyslu – portál pro bezporuchovou výrobu, 2020 [cit. 7.4.2023]. Available from: www.vseoprumyslu.cz: https://www.vseoprumyslu.cz/udrzba-a-diagnostika/asset-management/koncept-kvalita-4-0-pretvari-zpusob-vyvoje-produktu.html

INNOVATIVE DEVELOPMENT IN POWDER METALLURGY

Author(s): Daria STRAPOLOVA

Supervisor: doc. Ing. Kateřina SKOTNICOVÁ, Ph.D.

Department: Department of Materials and Technologies for Vehicles, Faculty of Materials Science and Technology, VSB – Technical University of Ostrava

Abstract

The main purpose of the publication is to describe the need to create a database in the powder metallurgy industry, as well as to consider external and internal factors affecting the development of a plan for innovative projects at powder metallurgy enterprises. As well as creating an idea of which project today can be considered as an innovative project in the field of powder metallurgy. The publication presents the problems of modern resource turnover in powder metallurgy and the ideas of solutions through simplified selection and sale of products. Giving an example of the possibility of recycling titanium alloy waste.

Key words:

Innovations, powder metallurgy, optimization, technology marketing.

1. INTRODUCTION

Currently, the development of technologies and technological processes affects almost all spheres of human life, therefore, enterprises that produce products are obliged to closely monitor the latest trends and innovations in order to maintain their level of competitiveness and not work at a loss. Technological marketing in powder metallurgy includes the use of innovative methods of production and promotion of goods on the market. It is aimed at improving the quality of products, reducing the time of its production, increasing the competitiveness of enterprises and increasing revenues. All competitive manufacturing organizations invest in the introduction of various scientific and technological achievements, such as new products, production processes and techniques, business processes, business ideas. From the above, it follows that innovations are divided into product (introduction of new or improved products) and process (development of new forms and methods of production organization) [1].

Technological marketing includes the development and introduction of new materials that have high technical characteristics, reliability and lower cost. New developments in the field of composite materials allow to create products with improved characteristics, which allow to meet new consumer requirements, increase competitiveness in the market. In powder metallurgy, in the last two decades, this industry has lagged behind many companies of the metallurgical complex, which were able to launch an improved product in accordance with increased and modified demand. Therefore, before drawing up the financial plan of the project, it is necessary to build a sufficiently long logical chain, answering a number of consecutive questions. The first question should be considered "What is the situation on the market at the moment and what products are in demand?"

Interest in the achievements of the powder metallurgy industry has increased dramatically despite the fact that previously they were used only in certain narrow niches due to the high cost of blanks and, consequently, the lack of mass application of them. Now we live in a time when there is a revolution in materials science, as a result of which projects are being implemented using the following latest technologies:

- *Hot isostatic pressing* is a process that consolidates material and closes pores within parts through the application of high temperature of several hundreds to 2000 °C and isostatic pressure of several tens to 200 MPa at the same time. This process enables to increase the component's density, ductility, fatigue resistance and other material properties.
- *Metal injection moulding* is an advanced metal forming technique that uses injection moulding equipment for manufacturing both simple and complex metal parts to tight tolerances. This technology can replace other metal forming techniques such as investment casting and

machining. It is mainly used for the production of small components weighing less than 100 grams.

- *Additive manufacturing*, mainly powder bed fusion technology (e.g., selective laser melting) requires spherical particles of metal powder prepared by gas or centrifugal atomization. The quality of powder plays a key role concerning process performance and end part properties. The spheroidized powder is well applied as a working layer, compactly fits into a given volume and facilitates the work of the laser in consolidating the particles.

Technological marketing includes the use of new technologies to improve production by reducing production costs. Automatic control, management and monitoring technologies make it possible to improve the quality of products and rationally use the resources of the enterprise. Based on information about existing innovations obtained from external or internal sources, the company has the opportunity to decide what products it wants and can produce, having made minimal investments, but having received the maximum result expressed in the amount of profit. Relying on its existing production facilities, material, and human resources. An organization often faces a dilemma whether to carry out radical, combinatorial, or modifying innovations [2]. In addition, the company must choose the right strategy for implementing innovations: an intensive development strategy (with gradual capacity building through better use of its internal forces and capabilities provided by the external environment), an integration development strategy (integration with suppliers, supply structures, developing and manufacturing organizations), a strategy of diversification development (aimed at the production of structurally new products using the existing capabilities and strengths of the enterprise) or a reduction strategy (with the identification and reduction of inappropriate costs in the implementation of innovative measures) [3].

2. THE MAIN PART

When implementing innovative projects, the company's management should remember about the constant transformation of business processes and that it may suffer great losses due to the lack of a clear technical and economic flexible planning structure. Including the ability to respond quickly and accurately. We are talking about the optimization of existing enterprises for which development in the market is necessary by raising the status and increasing competitiveness in the market in the outgrowth and / or enterprises that want to enter a niche.

We can talk about the urgent need to create such a project that can carry out a quick selection of material or equipment with a minimum resource request. Now, everyone involved in the industry may have difficulties buying raw materials or selling finished products. The problem is relevant due to the oversaturation of the market by firms that face a complex process in the purchase or sale of products and waste and the lack of healthy competition.

Speaking about the production based on working with titanium allow powder, the simplified scheme will look like this:

Figure 1 Simplified scheme of operation of metal (titanium) powder. Source: (own)

In the diagram, you can see that resources are needed to obtain the powder. In this case, we are talking about blanks of various configurations, such as ingots for centrifugal or metal of various shapes for gas and so on. In the center is the position of powder the very receipt of the by all methods known at this stage of development .And finally, at the exit, we see the use of powder. Titanium alloy powder can be used both in additive manufacturing, baking in molds, and sale and/or recycling. One of the methods of processing titanium alloy powders is the combustion of metal powders in an aerodisperse burner [4]. A method for the synthesis of nanoscale oxide particles for the manufacture of semiconductor, ceramic, and catalytic materials. Studies report that aluminium, magnesium, titanium, beryllium, and zirconium can be used as energy components of solid fuels, explosives, and pyrotechnic compositions. We can say that an unrealized product, a product coated with an oxide film, can be realized as a resource for further production.

Production planning is a separate segment that is implemented at all levels of management.

When implementing an innovative project, there are certain difficulties associated with a high level of identifiable and unidentifiable risks and huge efforts to remove risks, as well as the presence or absence of certain resources (financial, human) to bring a new or improved product to the market and promote it.

There are external and internal factors that can have an impact on production.

External factors may include the following:

- political situation (sanctions, relations with various states, unfavorable socio-political changes);
- increase of excise taxes on fuel and lubricants, taxes on mining;
- conducting military operations in certain regions;
- natural and climatic conditions and man-made disasters;
- development of the scientific industry, making previous innovations irrelevant;
- depletion of natural resources;
- changes in economic legislation and the current economic situation.

These factors influence management's decision to purchase innovative equipment or a business process; for example, management is likely to hesitate to purchase equipment from a state that imposes sanctions on this type of product, or from a State in whose territory military operations are taking place. A change in the external political or economic situation may have an impact on the implementation of an innovation project, which implies adequate management of all changes in this project. For example, the appearance of the same improved product at another enterprise may have a negative impact on the amount of profit received. Or if the company has always previously purchased from a certain country, a change of political leader will entail a change in legislation in the field of mining, as a result of which the purchase of this raw material will no longer be so profitable, the company can either leave this country as its supplier, thereby forcing adjustments to the financial plan for the project or look for another supplier.

Internal factors influencing the implementation of an innovative project are related to the circumstances and situations that may arise at the enterprise itself and that must be taken into account when choosing the purchased product:

- product cost;
- trust in the manufacturer;
- country of manufacture;
- technical specifications;
- availability of technical support;
- availability of spare parts for equipment;
- possibility of delivery;
- compliance of the new equipment with the energy and resource standards of the enterprise;
- availability of personnel with appropriate qualifications.

The solution of the problem is an innovative project that will contain an accessible database with a simplified system for selecting and marketing products. Its use will allow you to declare yourself on the market and provide your product within the framework of a change in a particular factor more quickly.

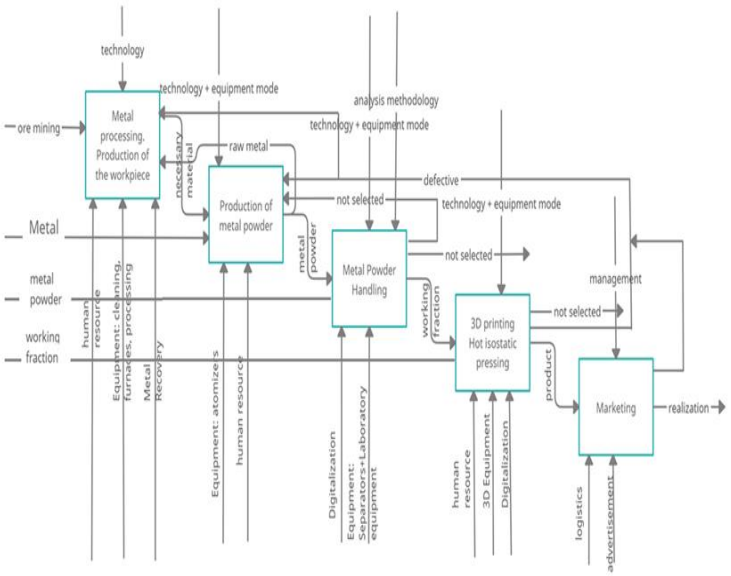

Figure 1 The scheme of interaction in the industry. Source: (own)

From this diagram it can be seen that for each option there is not only an input, but also an output. It follows from this that it is necessary to consider in detail all the possibilities of each cell, taking into account all the modern possibilities of working with metallic powder. One example is the use of titanium alloy. the resulting material [5[can be used as a powder for tri-d, as a powder for pressing, as a sale in the form of raw materials for combustion, as ingots for melting. Each stage should be viewed as a separate enterprise that can work both independently and in the system as a whole.

3. CONCLUSION

In the modern world of powder metallurgy, the actual problems of the sale and purchase of products for production. This problem is solved by a modern innovative project that includes the creation of a single repository of information about products from different suppliers and buyers, followed by simplified interaction through a simple system for selecting the resource of interest. It is worth noting that this particular project will optimize production.

ACKNOWLEDGEMENT

The work was supported by the specific university research of the Ministry of Education, Youth and Sports of the Czech Republic No. SP2023/082.

REFERENCES

[1] SEMENOV, Michail. *Enterprise economics.* St. Petersburg: Peter, 2015
[2] KRASNOVA, L. N., M. Y. Ginzburg, R. R. Sadykova. *Enterprise economics.* INFRA-M: Moskow, 2016. ISBN: 978-5-16-010700-4.
[3] STRELKOVA, L. V. Economics and organization of innovations.UNITY-DANA: Moscow*, 2015.* ISBN 978-5-238-02451-6.
[4] ZOLOTKO A. N., VOVCHUK Ya. I., POLETAEV N. I. Synthesis of nanooxides in two-phase laminar flames. Physics of gorenje i explosion.1996, 15, 24-33.
[5] SUN, Z., XIAO, Y., AGTERHUIS, H., SIETSMA, J., & YANG, Y. *Recycling of metals from urban mines – a strategic evaluation*. Journal of Cleaner Production, 2016. 112, 2977–2987. doi:10.1016/j.jclepro.2015.10.116 10.1016/j.jclepro.2015.10.116/

ADVANCED IMAGE THRESHOLDING METHODS IN DUST PARTICLE DETECTION TASKS

Author(s): Nikita STRATINSKIY, Jan PSZCZOLKA

Supervisor: doc. Ing. Milan HEGER, CSc.

Department: Department of Industrial Systems Management, Faculty of Materials Science and Technology, VSB – Technical University of Ostrava

Abstract

Image thresholding is a fundamental technique used in image processing to separate objects or regions of interest from the background. This article serves as an introduction to the fundamental concepts of image thresholding and aims to evaluate the effectiveness of different image thresholding methods specifically in the context of dust particle detection. The presence of dust particles in various industries, such as manufacturing and cleanrooms, can have adverse effects on product quality and human health. Therefore, accurate and efficient dust particle detection is of utmost importance.

Key words:

Digital Image Processing, Image Thresholding, Dust Particle Detection.

1. INTRODUCTION

The growing need for accurate and efficient dust particle detection methods is evident in various industries and applications. For instance, in environmental monitoring, the precise detection and characterization of dust particles in air are crucial for assessing air quality, identifying pollution sources, and mitigating environmental impacts. In industrial processes, dust particles can adversely affect product quality, damage equipment, and pose health risks to workers. As a result, effective dust particle detection methods are essential for ensuring product quality, maintaining equipment performance, and protecting human health and safety.

Measuring the size and distribution of dust particles is essential for understanding the nature of dust and designing equipment for handling and managing it. One method for measuring the size of particulate material is machine vision. Computer vision and machine vision systems are interdisciplinary fields that focus on developing algorithms and techniques to enable computers to interpret visual information from digital images or videos. They are widely used in various applications, ranging from autonomous vehicles, robotics, healthcare, surveillance, and industrial automation. There are numerous studies available on the use of machine vision in various fields, including robotic weed control, detecting defects in fruits and vegetables, grading, inspection, classification, analyzing different agricultural and food products, as well as fish eggs counting [1], [2], [3], [4].

2. IMAGE THRESHOLDING

To conduct size and size distribution analysis in computer vision using digital images, two essential requirements are needed: an input image and an image processing algorithm. Devices that can acquire these images include digital cameras, charge-coupled device cameras, or flatbed scanners. Achieving clear contrast between particles and the background is crucial for optimal results in image preprocessing. Additionally, the arrangement of particles in relation to one another is also critical [5].

One fundamental algorithm that can be applied in a field of dust particle detection is an image thresholding, which involves converting a grayscale or color image into a binary image by segmenting the image into regions of interest (ROI) based on pixel intensity values. It is a simple and effective technique for image segmentation and object extraction, where the goal is to separate the pixels or regions of interest from the background based on a certain intensity threshold. The basic idea of thresholding is to compare the intensity values of each pixel in the image with a predefined threshold value. If the intensity value of a pixel is above the threshold, the pixel is assigned to one class (e.g., foreground or object), and if it is below the threshold, the pixel is assigned to another class (e.g.,

background). This process results in a binary image with only two intensity levels, typically represented as black and white pixels, where black represents the pixels below the threshold and white represents the pixels above the threshold [6].

If $g(x,y)$ is a thresholded version of $f(x,y)$ at some global threshold T,

$$g(x,y) = \begin{cases} 1, & if\ f(x,y) > T \\ 0, & if\ f(x,y) \leq T \end{cases} \quad (1)$$

Thresholding can be used for various image processing tasks, such as image segmentation, object detection, image enhancement, and feature extraction. Thresholding can be implemented using various programming languages, libraries and software's, such as OpenCV, MATLAB, Python, ImageJ. Some common thresholding techniques include:

Global Thresholding: A single threshold value, T, is applied to the entire image, and pixels with intensity values above or below the threshold are classified as foreground or background, respectively. This method is simple and computationally efficient but may not be suitable for images with varying lighting conditions or complex backgrounds. The global simplest thresholding method is called binary thresholding. It creates a binary image from a grayscale image based on the threshold value, T.

Adaptive Thresholding: Different threshold values, T, are applied to different regions of the image based on local characteristics, such as local mean or median intensity values. This approach is more robust to varying lighting conditions and background complexities, since it adapts to the local characteristics of each region. The local characteristics can be determined using various methods. However, since this method requires calculations to be performed on each local region of the image, it may be computationally more intensive than other thresholding methods.

Otsu's method: This is a widely used thresholding technique for automatically determining the optimal threshold value, T, based on the histogram of intensity values in the image. This method uses the histogram of intensity values in the image to maximize the inter-class variance between foreground and background regions, resulting in an optimal threshold value that separates the two regions. The inter-class variance is a measure of the separability of the foreground and background regions, and Otsu's method maximizes it to find the optimal threshold value. This method is particularly suitable for images with uneven lighting conditions or complex backgrounds, where other thresholding methods may not perform as well.

The whole computation equation of Otsu's method can be described as:

$$\sigma_w^2(t) = w_0(t)\sigma_0^2(t) + w_1(t)\sigma_1^2(t) \quad (2)$$

where:

w_0, w_1 — probabilities of the two classes divided by a threshold t,

σ_0^2, σ_1^2 — variances of these two classes [7], [8].

Gradual brightness gradient of image pixels in the longitudinal axis method: This is a method of image cleaning to remove unimportant background noise and leave only anomalies suitable for further processing. The essence of the method is therefore to perform the following steps:

a) a digital image is created of the area of interest with a possible surface defect, anomaly,
b) the digital image is converted into a matrix form,
c) the image resolution is reduced by averaging the pixels in a user-defined square window according to a formula:

$$Px(red)_{x,y} = \frac{1}{h^2}\sum_{i=1}^{h}\sum_{j=1}^{h} Px(orig)_{i,j} \quad (3)$$

where:

$Px(red)_{x,y}$ is the new pixel of the reduced image in the x, y coordinate,

h is the size of the square window,

$Px(orig)_{i,j}$ represents a pixel of the original image at coordinate i, j.

d) in the reduced image, a derivation of the pixel brightness values is then performed in the X or Y axis direction and a new binarized image is created using thresholding, and,
e) in the derived image, the orphan pixels are searched for and removed from the image [9].

3. EXPERIMENTAL PART

In order to conduct an analysis and comparison of various threshold techniques for the detection of dust particles, the MATLAB environment was utilized. This powerful software providing the necessary tools and functionalities to carry out the experiments effectively. Was obtained an image containing dust particles by the digital camera equipped with a specialized optical lens and an industrial laser. The source image is shown in Figure 1. The processed images with various image thresholding techniques are shown in Figures 2-5.

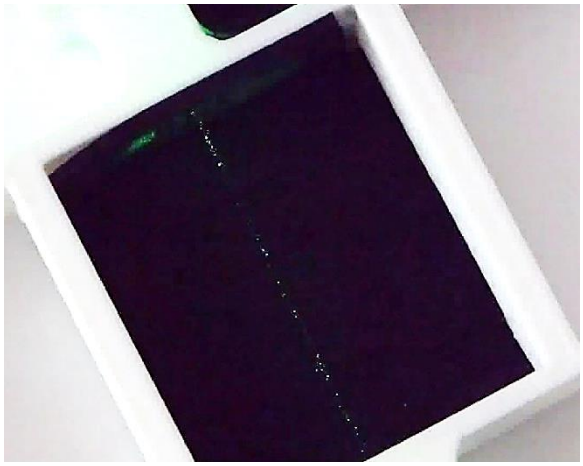

Figure 1 Source image. Source: (own)

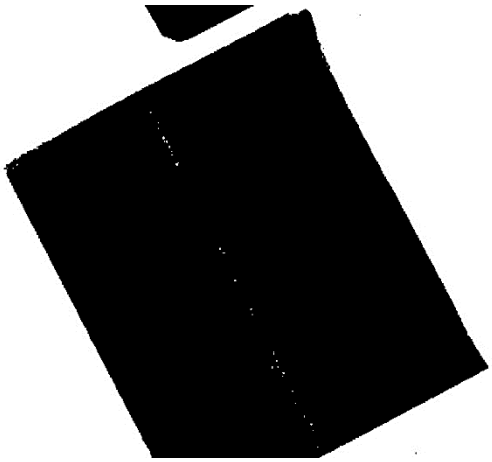

Figure 2 Global Thresholding. Source: (own)

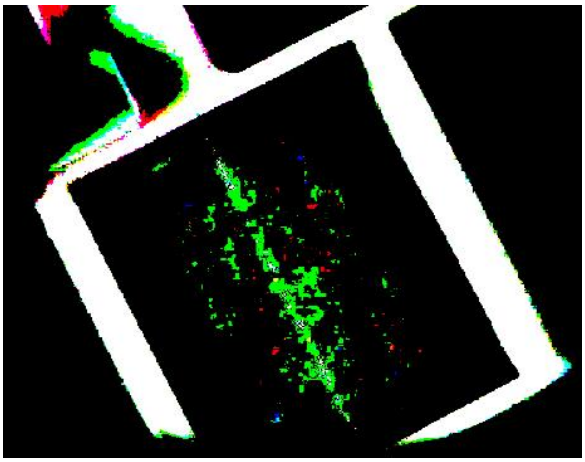

Figure 3 Adaptive Thresholding. Source: (own)

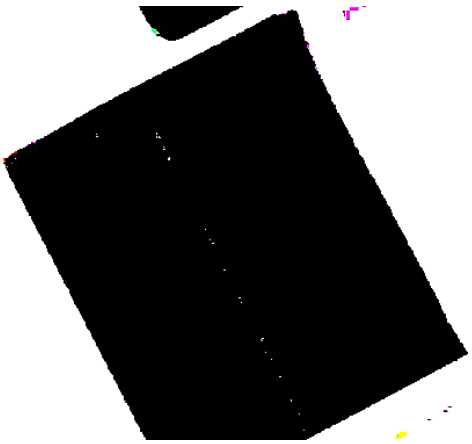

Figure 4 Otsu's Thresholding. Source: (own)

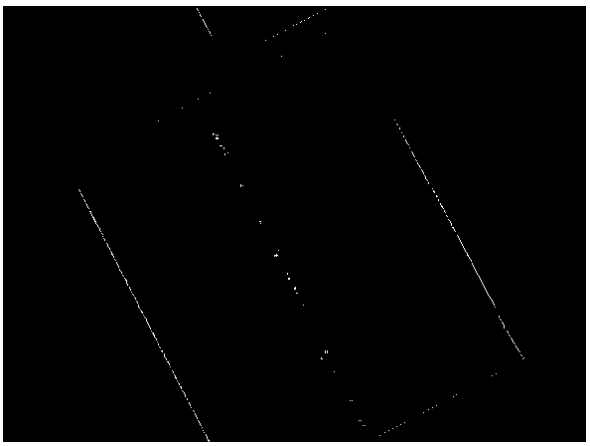

Figure 5 Patent method. Source: (own)

4. CONCLUSION

The Global Thresholding shown in Figure 2 is not suitable because of the uneven illumination of the scene by the laser beam. The Adaptive Thresholding shown in Figure 3 in this case behaves too sensitive to noise and challenging image conditions, which is not suitable for the purpose. The Otsu Thresholding shown in Figure 4 is suitable for lower contrast images where the dust particles relative to the background have high contrast, the method ignores some small particles. The method disclosed in patent 308 988 shown in Figure 5 appears to be the most suitable for the purpose of image binarization for dust particle detection. However, a comprehensive evaluation would require a more detailed analysis of the images and their characteristics. The research on dust particle detection will continue. Other image processing methods for this field will be tested to create a better solution.

ACKNOWLEDGEMENT

The work was supported by specific university research of the Ministry of Education, Youth and Sports of the Czech Republic No. SP2023/043.

REFERENCES

[1] SLAUGHTER, David, GILES, D. Ken, DOWNEY, Daniel. Autonomous robotic weed control systems: A review. *Computers and Electronics in Agriculture*. 2008, 1. 63-78. ISSN: 01681699

[2] FIROUZ, Mahmoud Soltani, SARDARI, Hamed. Defect Detection in Fruit and Vegetables by Using Machine Vision Systems and Image Processing. *Food Engineering Reviews*. 2022. 353-379. ISSN: 1866-7910

[3] BROSNAN, Tadhg SUN, Da-Wen. Inspection and grading of agricultural and food products by computer vision systems - A review. *Computers and Electronics in Agriculture*. 2002, 2-3. 193-213. ISSN: 01681699

[4] AMA-ABASI, Daniel E. FRIEDLAND, Kevin D. Automated egg counting and sizing from scanned images: Rapid sample processing and large data volumes for fecundity estimates. *Journal of Sea Research*. 2005, 4. 307-316. ISSN: 13851101.

[5] CANNAYEN, Igathinathane, PORDESIMO Lester O. Sieveless particle size distribution analysis of particulate materials through computer vision. *Computers and Electronics in Agriculture*. 2009, 2. 147-158. ISSN: 01681699.

[6] GONZALEZ Rafael, WOODS Richard. *Digital Image Processing, Global Edition*. London: Pearson Education, 2018. ISBN-13: 978-1-292-22304-9.

[7] OpenCV. *OpenCV: Image Thresholding* [online]. [cit. 26.04.2023]. Available from: https://docs.opencv.org/4.x/d7/d4d/tutorial_py_thresholding.html

[8] OTSU, Nobuyuki. Threshold selection method from gray-level histograms. *IEEE Transactions on Systems, Man, and Cybernetics*. 1979, 1. 62-66. ISSN: 00189472.

[9] University of Hradec Kralove. A method of image processing by a method of gradual gradient of brightness of image pixels in the longitudinal axis and a device for performing this method. Czech Republic. PATENT FILE 308 988. 20.03.2019.

ELECTROMAGNETIC INTERFERENCE CAUSED BY SEMICONDUCTOR CONTROLLING CIRCUIT

Author(s): Jonáš STÝSKALA

Supervisor: doc. Ing. Robert FRISCHER, Ph.D.

Department: Department of Industrial Systems Management, Faculty of Materials Science and Technology, VSB – Technical University of Ostrava

Abstract

Semiconductor controlling is crucial for industries, enabling efficient process control, productivity enhancement, quality assurance, energy efficiency improvement, safety enhancement, and adaptability. Compliance with EMC regulatory standards ensures proper operation, prevents interference, and ensures regulatory compliance, promoting reliability and competitiveness in the industrial sector. A triac control circuit is presented to demonstrate compatibility with EMC standard, providing an example of a change of circuit design and its impact to EMC results.

Key words:

Semiconductor, controlling, triac, EMC, PCB.

1. INTRODUCTION

Industrial processes often involve complex and dynamic systems with inherent uncertainties. Variations in input parameters, environmental conditions, or material properties can make it challenging to achieve precise and consistent control. Uncertainty can lead to deviations from desired set-points, making it difficult to maintain optimal conditions.

EMC stands for Electromagnetic Compatibility. It is the ability of electronic devices, equipment, and systems to function properly and coexist in their intended electromagnetic environment without causing or experiencing unacceptable electromagnetic interference (EMI). EMC encompasses the design, implementation, and testing of electronic devices to ensure that they can operate effectively and reliably in the presence of electromagnetic disturbances while minimizing interference with other devices or systems. The EMC covers two main domains which are emission control and emission immunity.

Emission control involves limiting the amount of electromagnetic energy radiated or conducted by a device or system. Emission control ensures that the device doesn't generate excessive electromagnetic noise that can interfere with the operation of other devices or communication systems. Emission immunity or susceptibility refers to the ability of a device or system to resist and operate properly in the presence of electromagnetic disturbances. Immunity measures ensure that the device can tolerate external electromagnetic fields or noise without malfunctioning or degrading its performance.

Various standards and regulations govern EMC requirements for different industries and applications. These standards define limits for emissions and immunity, specify test methods, and outline mitigation techniques. EMC considerations include proper circuit and PCB layout, shielding and grounding techniques, effective filtering and decoupling, appropriate selection of components, and compliance testing.

The general principle of triac controlling involves using a solid-state electronic device called a triac to regulate the power delivered to a load. A triac is a bidirectional semiconductor switch that can control the flow of current (AC) by modulating the conduction angle of the AC waveform. Due to the fast switching of the triac and the inductive or capacitive nature of loads, snubber circuits are often employed to suppress voltage transients and reduce electromagnetic interference (EMI). Snubber circuits typically consist of resistors, capacitors, and/or snubber diodes to provide protection and improve the performance and reliability of the triac and the overall system.

2. ARTICLE

A control circuit was developed and manufactured for the purpose of measuring and demonstrating the triac control mechanism. The main components of the circuit are a triac, labeled as Q1 in Figure 24, and a triac driver marked as U1, equipped with heat feedback. The circuit was manufactured in the form of a Printed Circuit Board (PCB), and the basic characteristics were measured using an oscilloscope at various test points (TPx) specified in the schematic.

The principle of heat feedback is based on measuring temperature and converting it into an electrical signal. This is achieved by using an external NTC device connected to connector J3. The NTC transforms temperature into electrical resistance, which is then converted into a voltage level within the operating range of the triac driver integrated circuit (U1) using a voltage divider in the circuit. The driver can then decide whether to open the triac and allow electrical current to flow into the load or close the triac to stop the current. When the triac is opened, the current flows into the load, generating heat. This heat is measured by the NTC, and the information is fed back to the driver, closing the feedback loop. This approach is known as closed-loop control.

To achieve precise temperature control, the circuit requires the selection of the desired temperature. This is accomplished using a voltage divider composed of the NTC, R2, Rs1, and Rdef1 resistors. The resistance configuration is mentioned in Figure 24 for each resistor device. The NTC has is marked as TH1. The values align with the specifications provided in the driver's datasheet. The circuit is designed to maintain a target temperature of 30 degrees Celsius.

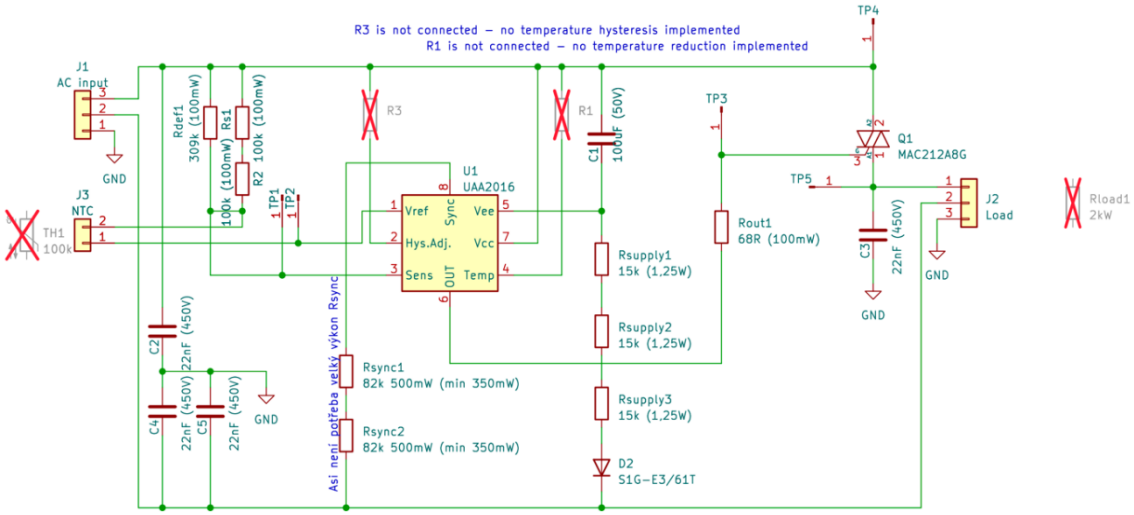

Figure 24 Schematic of triac controlling circuit. Source: (own)

The measurement of voltage characteristics in Figure 25 illustrates two graphs. The yellow graph represents the DC voltage of the load, measured using AC coupling. The blue graph shows the input source voltage of the circuit. The three distinct peaks on the graphs indicate the moments when the triac opens, allowing the load voltage to rise to its nominal value and then gradually return to zero volts. This behavior is expected for the connected load, which, in this case, was LED lamp for growth purpose with a diode bridge. Additionally, the input voltage waveform from the grid exhibits noticeable distortions during the triac's open events. These fluctuations, consisting of drops and peaks, are generated by the switching action of the triac and propagate through the AC grid, causing electromagnetic interference (EMI). The deformations occur during the transition from the negative half-wave to the positive half-wave and vice versa, resulting from the non-linear characteristics of the triac at zero-crossing points.

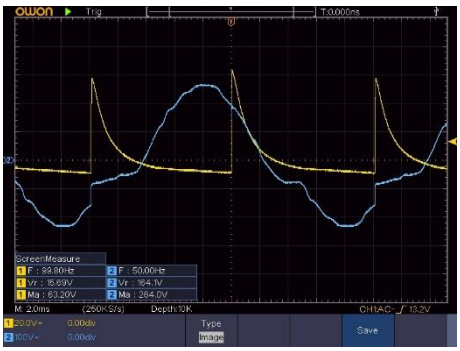

Figure 25 Load voltage (yellow, AC coupling) and AC input voltage (blue). Source: (own)

The graphs in Figure 26 depict the DC voltage of the load in yellow, serving as a reference, along with the output waveform of the AC voltage at the triac's output. The output waveform corresponds to the voltage measured at TP5 in Figure 24. It is evident that the blue waveform is distorted. Two types of deformations are noticeable: the first is a flattened waveform caused by the load characteristics, and the second is observed during the triac's open events. During these events, a drop in voltage followed by a rapid rise in voltage can be observed. These rapid voltage changes are the source of electromagnetic interference (EMI). The triac's open events provide evidence that even partial waveform switching can be effective, enabling precise control of the output power.

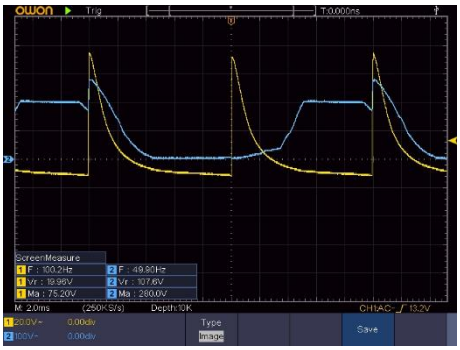

Figure 26 Load voltage (yellow, AC coupling) and AC output of triac (blue). Source: (own)

EMI characteristics were measured and are displayed below in pictures Figure 27 Figure 28. The blue curve represents the ESN6100 Quasipeak mixture measurement method, while the red curve represents the ESN6100 average measurement method. These curves represent the thresholds that define acceptable levels of EMI. The measurement graphs are provided for both the Quasipeak method (in purple) and the average method (in green). From the first figure, it is evident that the measurement graphs exceed their limits for both the Quasipeak and average methods. Such results are non-compliant with regulatory standards, and a device with these results cannot be used on the Czech electrical grid.

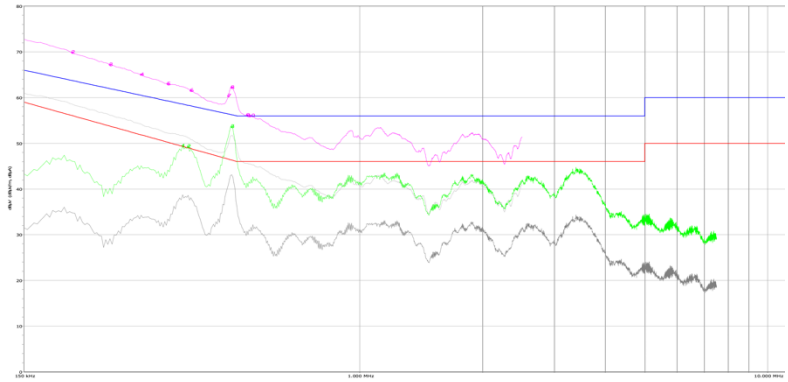

Figure 27 Measurement of EMI without filtering. Source: (own)

EMI characteristics were re-measured after implementing EMI reduction measures in the circuit. The reduction was achieved by adding capacitors at the grid input (C2 and C4 in Figure 24) and at the load output (C3 and C5 in Figure 24) for filtering purposes. As a result, the EMI reduction has brought the circuit into compliance with ESN6100 standards. The measurement results can be observed in Figure 28, where all the measured graphs are positioned below their respective threshold levels.

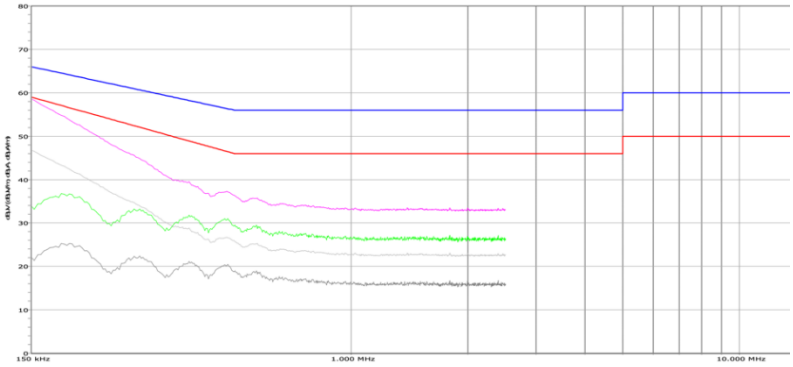

Figure 28 Measurement of EMI with filtering. Source: (own)

The gray graphs in Figure 27 and Figure 28 represent the actual measured data, while their images with applied offsets are shown in green and purple. The offset is applied as a correction based on the difference between the certified testing laboratory and the non-certified testing laboratory, primarily to save costs. Since the measurement process is time-consuming, only limited frequency results are provided instead of the full range (150 kHz - 30 MHz). Based on previous measurements, it is evident that the lower frequencies are the ones that reach the threshold levels and are therefore more significant for demonstrating the measurement results.

3. CONCLUSION

An electronic circuit designed for heat control applications was introduced, utilizing a modern approach with semiconductor switches. The circuit was fabricated as a PCB (printed circuit board), and its fundamental functionality was validated by measuring voltage graphs using an oscilloscope. Subsequently, the circuit underwent EMI testing to demonstrate the generation of electromagnetic pollution exceeding the compliance threshold of regulatory standards. To mitigate this, a filtering method was implemented to showcase its effectiveness in reducing interference to an acceptable level. This highlights the significance of both schematic and PCB design in achieving regulatory compliance.

ACKNOWLEDGEMENT

The work was supported by the specific university research of the Ministry of Education, Youth and Sports of the Czech Republic No. SP2023/043.

REFERENCES

[1] KHERA, Neeraj. *Development of Microcontroller Based Digital AC Dimmer for Light Intensity Control* [online]. IEE 2018 [cit. 14.3.2023]. Available from: https://ieeexplore.ieee.org/document/8665457
[2] KIRAWANICH, Phumin. *An emission management framework for implementing a large railway system with interface complexity* [online]. IEEE 2018 [cit. 1.5.2023]. Available from: https://ieeexplore.ieee.org/document/8410662
[3] NAGRIAL, M.H. *EMI/EMC issues in switch mode power supplies (SMPS)* [online]. IEEE 1999 [cit. 20.1.2023]. Available from: https://ieeexplore.ieee.org/document/791115
[4] OTT, Henry W. *Electromagnetic compatibility engineering*. New Jersey: John Wiley & Sons, Inc. 2009. ISBN 978-047018930-6
[5] SIVARO, Ugo. *EMC and earthing concept of the ITER EC-system* [online]. Fusion Engineering and Design 2023 [cit. 24.2.2023]. Available from: https://www.sciencedirect.com/science/article/pii/S0920379623003022?via%3Dihub
[6] SIRAVO, Ugo. *EMC improvement of an ECH power supplies system at TCV* [online]. Fusion Engineering and Design 2017 [cit. 2.2.2023]. Available from: https://www.sciencedirect.com/science/article/pii/S0920379617303022

MODERN MEANS OF TECHNICAL DIAGNOSTICS

Author(s): Stanislav SZKANDERA

Supervisor: doc. Ing. Milan HEGER, CSc.

Department: Department of Materials Engineering, Faculty of Materials Science and Technology, VSB – Technical University of Ostrava

Abstract

The presented work deals the technical elements of the tire of the circuity for measuring the profile what contacts with the road. This describes his to design, including video data collection and schematics in live drive. To scan deformation parameters it can be projected emitted laser line inside the tire which is recorded by camcorder for later data process. To diagnose collected data is used developed application in UNIX like tools and Java. The aim of the work is to develop hardware and software solution.*

Key words:

Diagnostics, tire, deformation.

1. INTRODUCTION

Development of motor vehicles, increasing traffic speed requirements for safe operation and passenger comfort, forcing engineers to continually improve tire performance. Without high-quality tires by road transport barely reached the current level. Tire is one of the most important parts of the vehicle, as it represents a single element, which connects it to the ground. Tires can not be replaced by another mechanism or device, which could be achieved by springing similar properties. Characteristics of the tire determines whether the transportation is convenient, fast and safe. Structurally, the tire is a complex system with high parameters [1].

In point of contact with the ground, the tire deforms partly on the sides and in the tread. Turning the wheels to the whole circumference of the tire gradually deforms and returns to its original shape. In point of contact with the ground to tread adapts to the road surface and the sidewall is flexed; stress thus transferred to the tire bead [2].

In a moving vehicle is at the point of contact with the ground due to many factors to deflection cord and its deformation. If wanted to diagnose deformation parameters can be projected inside the tire laser line and visually analyze it. It requires installed inside the shell document camera with additional lighting, which will record the deflections with later data collection. The entire sensing technology should fit in rotating tires [3] and [4].

2. THEORETICAL BACKGROUND

Implementation of laser optical sensor camera requires the use of specific properties. Modern cameras have a built-in miniature A/D converters are equipped with flash memory, which stores the video already in digital form, often with audio component which able to store audio track too, some compressed lossy codec. Type of the codec used to influence the size of the data stream. Consequently, there is record length per unit of time.

Total size of uncompressed video file can be calculated by formula 1

Formula 1 Size of recorded video

$$B = W * H * 1/8 * C * F \quad (1)$$

where:

- B – bytes per second
- W – pixels on width
- H – pixels on height

- C – color depth
- F – frames per second

If it is used color depth eight bits per color channel, then C will equal 24.

Recorded video details can provide tool 'ls' or 'file'. Detailed list about used codecs, bitrate and many more properties can provide tool 'ffmpeg'. For example recorded video can dispose resolution 720 x 480 pixels, bitrate 4690 Kilobytes per second. In case it is used memory card with capacity 32 gigabytes, this one can store at least six and half hours of video streaming.

As less is the camcorder lens as less is quality of video. These micro camcorder purpose is not for professional using, but for basic diagnostics it is enough.

Transferring the data between microcamera and personal computer is realised by universal serial bus (USB). Connecting the microcamera to personal computer it is showed as 'Mass storage'. It is independent on any operating system or, and dependencies on proprietary software by third party. Using UNIX/LINUX like operating systems can be collecting these videos using scrips, i. e. automatic collecting data or updated new videos.

3. EXPERIMENTAL TECHNIQUE

To measure the profile of the tire is required to place the laser light source and microcamera inside wheel. The outgoing laser beam is deflected sideways sweep creates a light beam that is in terms of transmitters appear light line (see Figure 2). However, the impact of the surface inner the tire out of view from a different angle creates a curve replicating curvature shell. The properties of this curve will be subject to analyzes the behavior of the tire in contact with the ground. The design and dimensions of the rim edges of the tire in contact with the rim, limiting the use of the components as regards their external dimensions. The figure 1 shows the locations of the microcamera and laser.

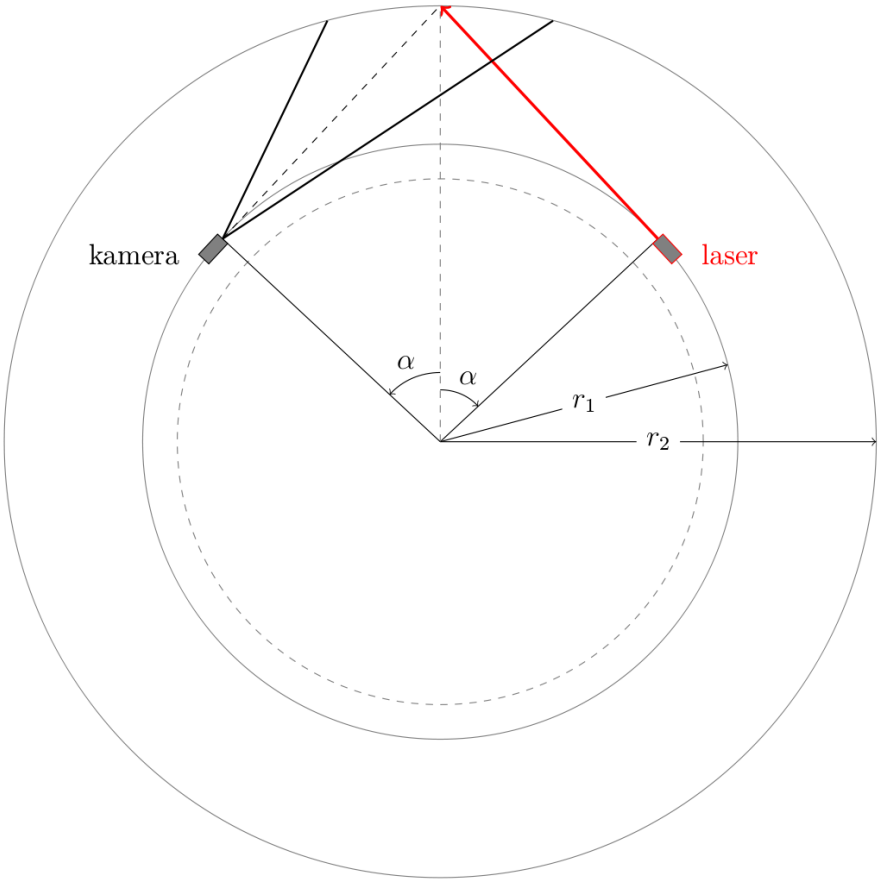

Figure 1 Placement of microcamera and laser emitor.
Source: (own)

where:

- r1 – radius of the wheel
- r2 – radius of the tire

- α – angle location
- – the microcamera relative to the center scanned image
- – laser to the axis of the transmitted image

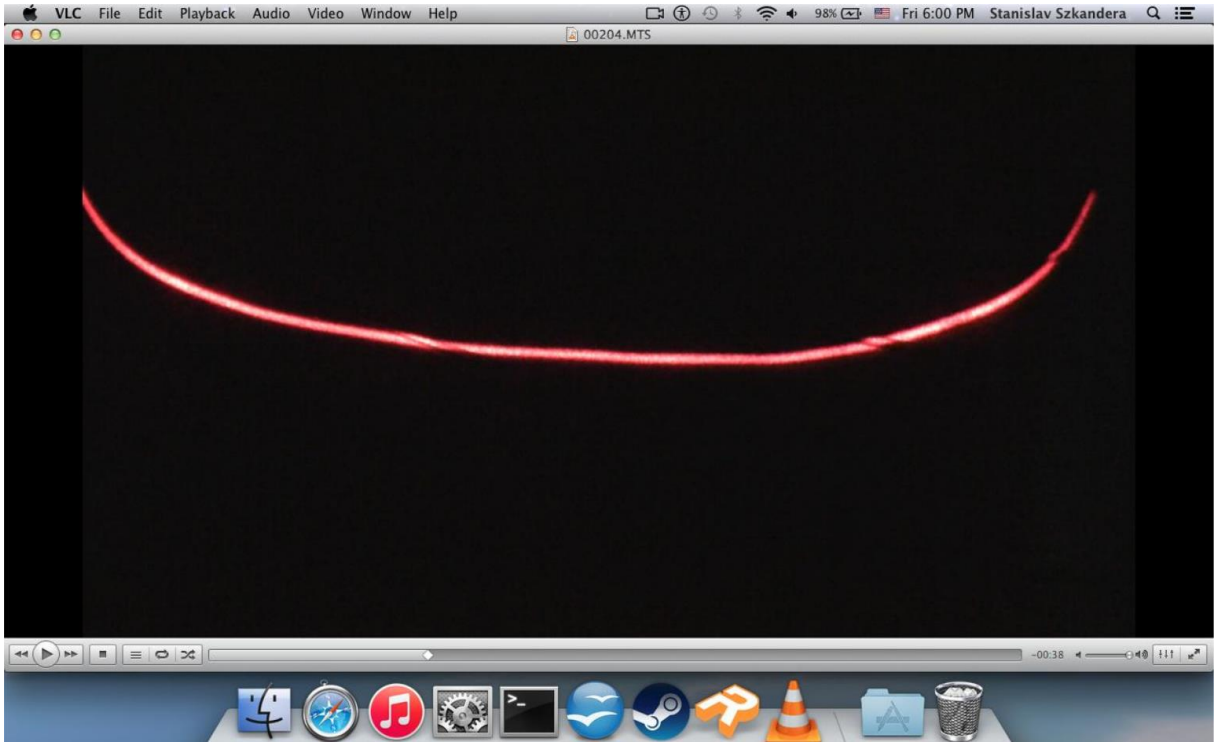

Figure 2 The red line projected by a laser emitor. Source: (own)

To process recorded video it needed to convert it into frames. For this purpose suitable tool 'ffmpeg'. Next operation is atomize each frame to its picture file for later analysis. For this purpose's the best way is used shell script. Its output is plain text file as the easiest way. Next analysis consists on scattering frames to columns and then pixels. These data can be later analysis using diagnostic tools [5] using application written in Java.

4. CONCLUSION

From presented approaches it is possible to measure the deformation of the tires.

As it is seen the microcamera can record laser line as both microcamera and laser emitor were mounted in the tire.

The validity of the theoretical model was tested experimentally. Tire profile measurement system has been tested in real traffic, proved fully functional and can be used for future measurements.

All experimental data were processed to comfirm previously mentioned.

REFERENCES

[1] CHELI, F., BRAGHIN, F., BRUSAROSCO, M., MANCOSU, F. & SABBIONI, E., *Design and testing of an innovative measurement device for tyre-road contact forces*, Mechanical systems and signal processing, vol. 25, Aug 2011

[2] ERDOGAN, G., Alexander, L. & Rajamani, R., Estimation of Tire-Road Friction Coefficient Using a Novel Wireless Piezoelectric Tire Sensor, IEEE sensors journal, vol. 11, Feb 2011.

[3] NI, T., ZHAO, DX., & ZHANG, HY., *Realistic Vehicle Driving Simulator with Dynamic Terrain Deformation*, 2009 IEEE international conference on mechatronics and automation, vols. 1-7, 2009.
[4] YI, JG. & TSENG, EH., *A "Smart tire" system for tire/road friction estimation*, Proceedings of the ASME dynamic systems and control conference 2008, pts A and B, 2009.
[5] VROŽINA M, *Základy spolehlivosti – Učební texty pro kombinované studium*, Ostrava

THEORETICAL DEFINITION OF CIRCULAR ECONOMY OND ITS PRINCIPLES

Author(s): Marcela ŠČEPKOVÁ

Supervisor: prof. Ing. Kamila JANOVSKÁ, Ph.D.

Department: Department of industrial systems management, Faculty of Materials Science and Technology, VSB – Technical University of Ostrava

Abstract

The concept of a circular economy is based on extending the life cycle of a product and minimizing product-related waste. It strives for efficient and environmentally friendly utilization of all resources. Resources and raw materials from products that can no longer be used should be used in such a way as to create additional value for the economy.

The circular economy has been developing rapidly in recent years. Society and companies are very interested in innovating their processes in such a way that usable resources are saved. The use of the circular economy will lead to an improvement of the environmental, social and economic situation. The purpose of this arcticle is to review and analyze promising areas of the circular economy.

Key words:

Circular economy, linear economy, principe, economy model.

1. INTRODUCTION

The circular economy is currently a widespread topic. This is the best solution that can face the environmental problem, as there is a growing need to reduce the impact of human activity on the planet [1; 2]. The circular economy aims to create an environment that is stable and sustainable. Mainly in industry, when it would solve the issue of lack of original material (from usable sources). This change must occur in the value chain from production to consumption [3], we are talking about the so-called closed-loop economy, which was first mentioned in the academic literature by Stahel [5]. According to Awan et al. [3], “The circular economy is an industrial system that can be considered a system that integrates economics with ecological aspects of design and proposes a completely different way of using resources” (p. 12). In simple terms, we can say that the common goal is to maximize the value of the resources used and thereby reduce emissions, energy consumption and waste disposal. The circular economy is a method of such optimization that saves especially material flows and thereby protects nature and minimizes the extensive use of energy for the transformation of primary materials [6].

If we focus on businesses that will start using or are already using the circular economy, they can draw on the benefits that CE offers. Companies applying circular economy principles not only improve economic, environmental and social aspects, but can also draw on some potential benefits. These benefits include reducing risk costs, increasing competitiveness, minimizing environmental impacts, improving the efficiency of workplace resources, and developing the skills and knowledge of workers [7].

2. DISTRIBUTION OF TYPES OF ECONOMIES

As can be seen in Figure 1, the economy can be divided into three categories: Linear, recycling and circular.

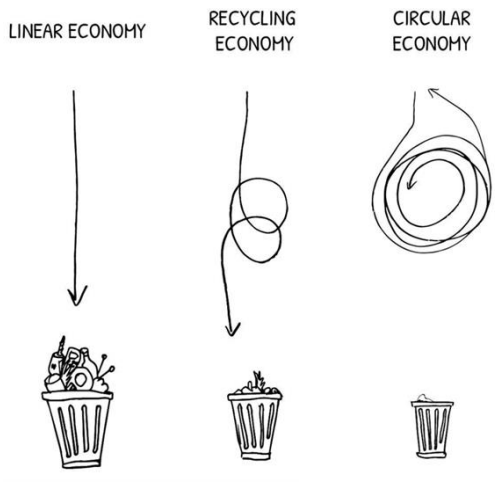

Figure 1 The Circular Economy by Circular Flanders. Source: [18]

The linear economy model, also referred to as "take-make-waste" can be characterized as a one-way system (see Fig. 2), where it starts from the extraction of raw materials to the end of the product's life. At the end of their life, these products end up as waste and are thrown away. The principle of the linear economy is one of the main causes of the great depletion of natural resources [8].

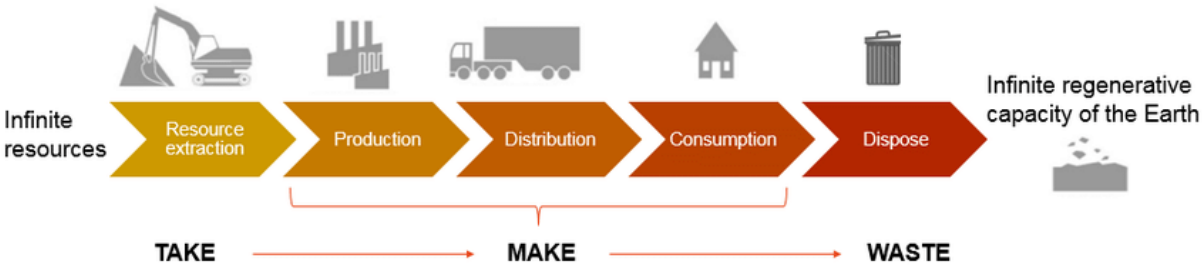

Figure 2 The linear economy – The „také, make and waste“ approach od production. Source [19].

The recycling economy is very close to the concept of the circular economy, but the circular economy includes an even more complex system, when it already takes into account its entire life cycle during the development and design of the product. The life cycle in the circular economy of products should be: as waste-free as possible, as long as possible and closed.

3. PRINCIPE OF CIRCULAR ECONOMY

The circular economy combines many principles that make it possible to use a minimum of natural resources and at the same time produce a minimum amount of waste. Currently, it is generally based on three principles, the so-called 3R concept [12]:

- Reducing (waste and pollution),
- reuse (keeping products and materials in service),
- Recycle.

According to Suarez-Eiro et al. (2019) [14] who analyzed the circular economy and defined seven operational principles for the sustainability of the circular economy. He thus combined theoretical goals with practical actions. The operating principles are based on the connection between the theoretical objectives of the circular economy and some practical strategies for implementation. The model designed by Suarez-Eiroa et al. (2019) [14] overcame the limitations of the following models for CE presented by the:

- European Commission (2018) [14] - model versus that of Suarez-Eiroa et al. (2019) (14) does not consider desing as a basic concept and does not include inputs and outputs either.
- Ellen MacArthur Foundation (2015c) [15] - this model is only usable on a macro scale.

The proposed model (Fig. 3) defines nine elements that need to be monitored:

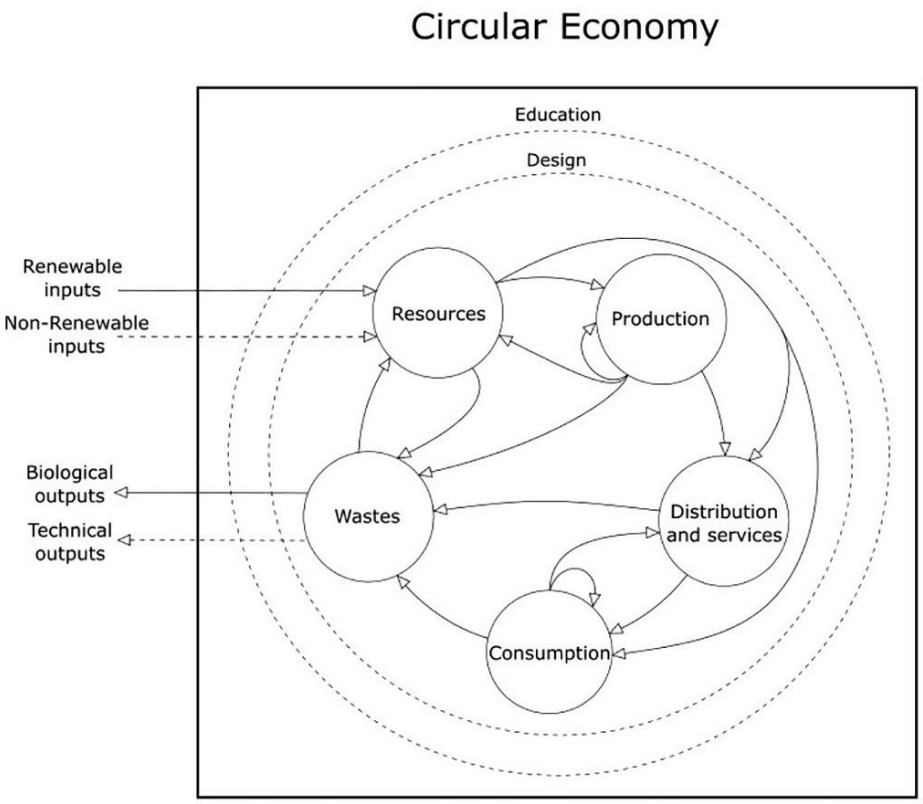

1. Inputs
2. Outputs
3. Resources
4. Production
5. Distribution and services
6. Consumption
7. Waste management
8. Design
9. education

Figure 3 Model according to Suarez-Eiro et al. (2019). Source [14].

The circular economy is defined according to Geissdoerfer et al. (2017) [13] as “a regenerative system in which resource inputs and energy waste, emissions and leakages are minimized by slowing, closing and narrowing material and energy loops. This can be achieved through sustainable design, maintenance, repair, reuse, refurbishing, renovation and recycling.”

4. CONCLUSION

It is important to include the circular economy in the everyday life of companies and society. However, it is not easy to find such principles for the correct and sustainable implementation of this economy. The principles are quite different in developed and developing countries. Principles that may work in developed countries may not fully work in the rest of the world [17].

The circular economy is currently very much supported by the European Union and other countries around the world. In order for the circular economy to be usable for every business and society, it is necessary to formulate and define goals that can be implemented in every society. For now, these principles are very diverse.

REFERENCES

[1] BRESSANELLI, Gianmarco, Marco PERONA a Nicola SACCANI. Challenges in supply chain redesign for the Circular Economy: a literature review and a multiple case study. *International Journal of Production Research* [online]. 2019, **57**(23), 7395-7422 [cit. 2023-05-26]. ISSN 0020-7543. Dostupné z: doi:10.1080/00207543.2018.1542176

[2] Nevím

[3] KIRCHHERR, Julian, REIKE, Denise and HEKKERT, Marko, 2017. Conceptualizing the circular economy: An analysis of 114 definitions [en ligne]. December 2017. Elsevier BV. Disponible à l'adresse : http://dx.doi.org/10.1016/j.resconrec.2017.09.005

[4] AWAN, Usama, KANWAL, Narmeen and BHUTTA, Mohammed Khurrum S., 2020. A Literature Analysis of Definitions for a Circular Economy [en ligne]. 2020. Springer Berlin Heidelberg. Disponible à l'adresse : http://dx.doi.org/10.1007/978-3-642-33857-1_2

[5] Jobs for tomorrow : the potential for substituting manpower for energy in SearchWorks catalog. *SearchWorks catalog : Stanford Libraries* [online]. Copyright © [cit. 26.05.2023]. Dostupné z: https://searchworks.stanford.edu/view/9965259

[6] CALISTO FRIANT, Martin, VERMEULEN, Walter J.V. and SALOMONE, Roberta, 2020. A typology of circular economy discourses: Navigating the diverse visions of a contested paradigm [en ligne]. October 2020. Elsevier BV. Disponible à l'adresse : http://dx.doi.org/10.1016/j.resconrec.2020.104917

[7] ROSA, Paolo, SASSANELLI, Claudio and TERZI, Sergio, 2019. Circular Business Models versus circular benefits: An assessment in the waste from Electrical and Electronic Equipments sector [en ligne]. September 2019. Elsevier BV. Disponible à l'adresse : http://dx.doi.org/10.1016/j.jclepro.2019.05.310

[8] MICHELINI, Gustavo, MORAES, Renato N., CUNHA, Renata N., COSTA, Janaina M.H. and OMETTO, Aldo R., 2017. From Linear to Circular Economy: PSS Conducting the Transition [en ligne]. 2017. Elsevier BV. Disponible à l'adresse : http://dx.doi.org/10.1016/j.procir.2017.03.012

[9] News European Partliament. Circular economy: definition, importance and benefits [cit. 20.05.2023]. Dostupné z: https://www.europarl.europa.eu/news/en/headlines/economy/20151201STO05603/circular-economy-definition-importance-and-benefits

[10] GEISSDOERFER, Martin and MORIOKA, Sandra and MONTERIO de Carvalho, Marly and EVANS, Steve, Business Models and Supply Chains for the Circular Economy (July 2018). Journal of Cleaner Production, Volume 190, 20 July 2018, Pages 712-721, Available at SSRN: https://ssrn.com/abstract=3189380

[11] RAGOSSNIG, Arne M and SCHNEIDER, Daniel R, 2019. Circular economy, recycling and end-of-waste [en ligne]. February 2019. SAGE Publications. Disponible à l'adresse : http://dx.doi.org/10.1177/0734242X19826776

[12] SAKTHIVELMURUGAN, E., SENTHILKUMAR, G. and KARTHICK, K.N., 2022. Analysis of the impact of circular economy over linear economy in the paper processing industry [en ligne]. 2022. Elsevier BV. Disponible à l'adresse : http://dx.doi.org/10.1016/j.matpr.2022.05.449

[13] GEISSDOERFER, Martin, SAVAGET, Paulo, BOCKEN, Nancy M.P. and HULTINK, Erik Jan, 2017. The Circular Economy – A new sustainability paradigm? [en ligne]. February 2017. Elsevier BV. Disponible à l'adresse : http://dx.doi.org/10.1016/j.jclepro.2016.12.048

[14] SUÁREZ-EIROA, Brais, FERNÁNDEZ, Emilio, MÉNDEZ-MARTÍNEZ, Gonzalo and SOTO-OÑATE, David, 2019. Operational principles of circular economy for sustainable development: Linking theory and practice [en ligne]. March 2019. Elsevier BV. Disponible à l'adresse : http://dx.doi.org/10.1016/J.JCLEPRO.2018.12.271

[15] EUROPEAN COMMISSION, 2018, EU-report on critical raw materials and the circular economy. SWD 2018. Dostupné z: https://ec.europa.eu/docsroom/documents/27327

[16] HORVATH, Balint, MALLINGUH, Edmund and FOGARASSY, Csaba, 2018. Designing Business Solutions for Plastic Waste Management to Enhance Circular Transitions in Kenya [en ligne]. 21 May 2018. MDPI AG. Disponible à l'adresse : http://dx.doi.org/10.3390/su10051664

[17] DIDENKO, Nikolay, KLOCHKOV, Yuri and SKRIPNUK, Djamilia, 2018. Ecological Criteria for Comparing Linear and Circular Economies [en ligne]. 8 August 2018. MDPI AG. Disponible à l'adresse : http://dx.doi.org/10.3390/resources7030048

[18] REPLATNTED. Dostupné z: https://www.replated.co/learn/what-is-the-circular-economy

[19] RESEARCHGATE.dostupné z: https://www.researchgate.net/figure/The-linear-economy-The-take-make-and-waste-approach-of-production_fig2_323809440

MODEL LEVEL CONTROL OF CONTINUOUS FURNACES

Author: Dagmar ŠPIČKOVÁ

Supervisor: doc. Ing. Milan HEGER, CSc.

Department: Department of Industrial Systems Management, Faculty of Materials Science and Technology, VSB – Technical University of Ostrava

Abstract

The basic idea of reducing the energy consumption of heating in industrial furnaces is based on the adjustment of the furnace environment temperatures depending on the temperature conditions modelled in the heated material, taking into account the material quality, size, technological heating regulations and the residence time of the material in the furnace temperature field. However, it is not unusual for furnace aggregates operating in complex production conditions, characterised by frequent changes in product range and variable production rates, to achieve even more substantial energy savings [1].

Key words:

Heating furnaces, temperature model, model level control.

1. INTRODUCTION

Heating material in industrial furnaces is a very energy-intensive process. Any reduction in energy consumption, or increase in efficiency of the furnace unit, results in not insignificant savings, both in fuel and metal [2].

The whole furnace control problem can be divided into levels:

- The basic stabilisation level of the furnace control, whose task is to maintain the required parameters of the furnace aggregate, in particular the stabilisation of the temperature of the furnace environment.
- The higher control level, which is responsible for reacting to changed requirements and, based on these requirements, setting selected setpoints for the lower control level so that the heating process runs optimally according to the selected criteria. The selection of the optimum values is based on the continuously evaluated temperature field of the material to be heated.

Optimisation of heating control, while maintaining the minimum possible energy consumption, can be modified to control compliance with various technological heating conditions.

2. CONTROL SYSTEM STRUCTURE

In terms of a comprehensive solution to the heating control problem, it is appropriate to develop several interacting models that always solve a specific and closed problem [3].

As we have already mentioned, the heating control in continuous furnaces can be understood as a hierarchical structure of the following systems:

- proprietary heating furnace technology,
- temperature stabilisation control,
- model level,
- connections to the technological surroundings of the furnace, input and output of material.

The actual technology of the continuous heating furnace must be equipped so that the stabilisation control level is able to ensure the basic conditions after heating of the material.

The input to the stabilisation level of furnace control, at least in terms of material heating, is the desired temperature in the individual furnace zones. These inputs can be provided by

- furnace operator,
- model level of management.

The model control level must react to the changed external conditions of the furnace (change of heating rate, downtime, start and emptying of the furnace) similarly to the operator and assign the actual

required temperatures in the furnace zones to the changed operating conditions. It is also necessary to ensure the heating boundary conditions (limitation of the temperature gradient in the furnace zones, minimum and maximum temperatures). The model can be designed in two variants, differing in the approach to the solution, as:

- static control model
- dynamic management model.

2.1 Static control model

The static part of the control model forms an intermediate layer between the basic control level of the stabilising type, the process coordination level (material inputs and their classification, material flow monitoring) and the core of the dynamic furnace control model. The static control model is suitable under steady and little changing operating conditions. Its task is to allocate temperatures to zones depending on the material class membership in relation to the DTP.

2.2 Dynamic model of thermal management of furnaces

The task of the model is to determine the desired temperatures in the furnace zones so that the material is at the furnace output at the desired time and in the desired condition. This can be achieved by meeting the following conditions:

- Knowledge of the real temperature of each ingot in the furnace, which is determined by the heating operating model.
- Knowledge of the final condition at the furnace output, determination of the furnace temperature profile and remaining heating time for each log in the furnace. These data are derived from a simulation model of the heating for a given heating group from the corresponding heating curve.
- The near-optimal heating control is achieved by setting the desired temperatures in the furnace zones with a certain time advance, which is determined by the dynamic behaviour of the controlled temperature stabilisation system of the individual furnace zones.

2.3 Malfunctions during heating

The interruption of the continuous heating process can be planned or unplanned. The heating control system can react to planned downtime (furnace interruption) by adjusting the expected residence time of ingots in the furnace accordingly. Unscheduled downtime will be understood as failures, namely those that are not directly related to the furnace heating system but are usually caused by causes outside the furnace, usually in the following technology. The duration of these unplanned downtimes is usually unknown. In the context of furnace DTO, the failures during furnace operation can be divided into two basic groups:

- disorders of short duration,
- long-term disorders.

Short-term failures are those failures whose duration is small and do not significantly interfere with the heating process of the material. The duration of these faults is less than 20 to 30 minutes.

Malfunctions longer than 30 minutes will be considered as furnace stagnation and for these cases the furnace must be operated in a special mode.

3. IMPLEMENTATION OF THE MODEL LEVEL OF THE CONTINUOUS FURNACE IN TŘINECKÉ ŽELEZÁRNY A. S.

The design of the application is based on the original version of the visualisation for the old step furnace model (from 1995). It was taken into account that operators are familiar with the old environment and major changes could lead to slower reactions and incorrect interventions [3].

The main part of the visualisation is a panel with six tabs: Chart, Heating Strategies, Overview, Piece Info, History and Service.

3.1 Chart

In this tab there is a panel with seven curve charts and one point chart. In the legend there is a description of each graph. In the legend, it is also possible to hide the graph in the panel by checking/unchecking it.

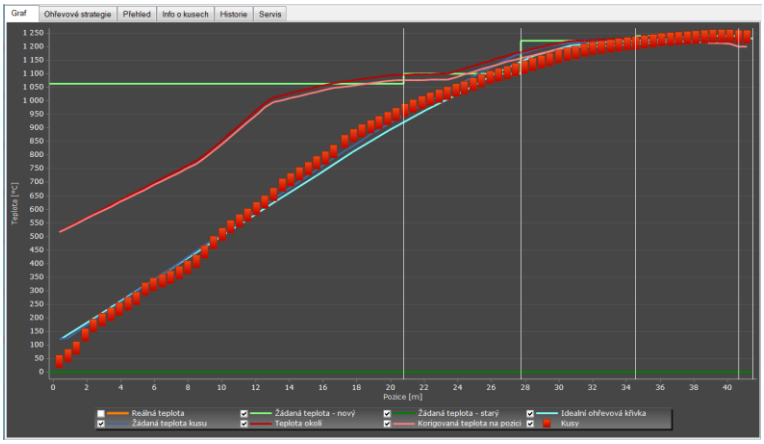

The point chart "Pieces" shows the individual pieces in the furnace. By clicking on the individual "pieces" you can go to the "Piece Info" page, where information about the piece is displayed. (See Fig. 1.)

Fig. 1 Chart Source: (own)

3.2 Heating strategies

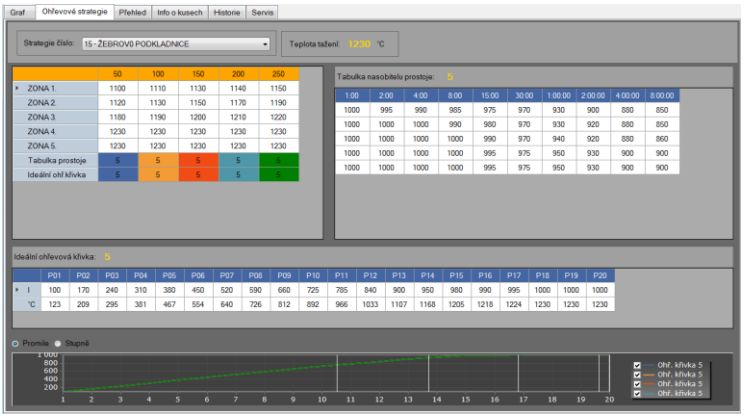

4. Tab heating strategies serves as an overview of the heating strategies registered in the system. (see Fig. 2).

Fig. 2 Heating Strategies Source: (own)

3.3 Overview

Heating strategies give the basic overview for step furnace operators. The graph (see Fig. 3) shows the deviation of the mean temperature from the desired temperature of each piece in the oven. Each bar represents one piece. Click on a column to go to the "Piece Info" page to display information about the piece.

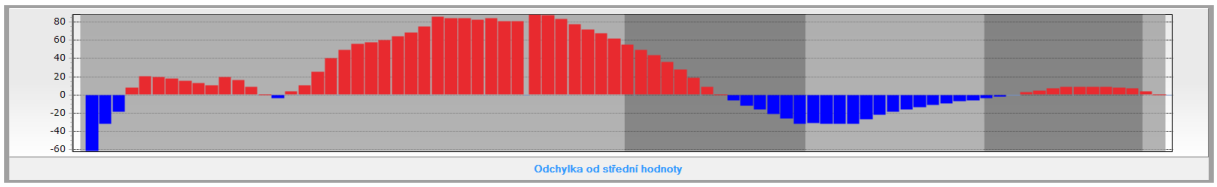

Fig. 3 Graph Deviation from the Mean Value Source: (own)

3.4 Info about pieces

This tab contains information about individual pieces in the furnace / optionally about historical pieces. The left table shows the pieces in the furnace (by checking "Pieces per furnace" you can browse

through the historical pieces). Clicking on the desired piece in the list the information about that piece will display.

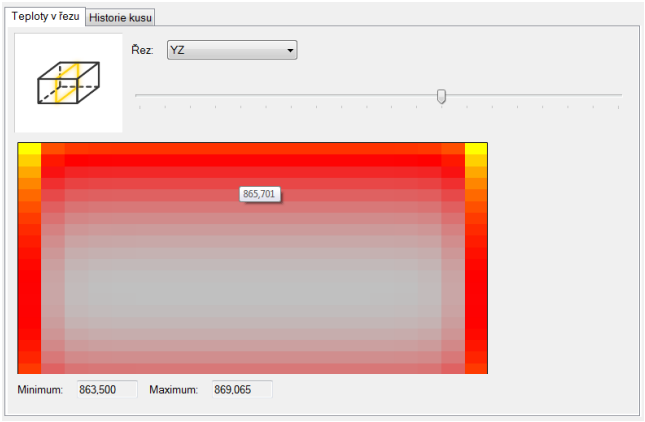

The tab Section temperatures shows the temperature field calculated by the model (see Fig. 4). The "cut" list can be used to switch the plane of the slice and the slider below the list can be used to move the slice in that plane. By moving the mouse cursor over any point in the section the temperature will display. The display of these values is not automatically updated. The current values can be retrieved by clicking the "Refresh" button in the "Information" tab.

Fig. 4 Section temperatures Source: (own)

5. CONCLUSION

The design of the model level of continuous furnace control was successfully implemented in Třinecké železárny a.s. The proposed structure proved to be fully functional and corresponded to the requirements of the operation. The use of theoretical knowledge and its transfer into practice has been proved as beneficial both for the research itself as well as for the operational practice.

ACKNOWLEDGEMENT

The work was supported by the specific university research of the Ministry of Education, Youth and Sports of the Czech Republic No. SP2023/043.

REFERENCES

[1] SPICKA, Ivo, Milan HEGER, Ondrej ZIMNY and Maria STRANAVOVA. BACKGROUND OF REDUCTION OF OPERATING COSTS OF CONTINUOUS REHEATING FURNACES. In: *21ST INTERNATIONAL CONFERENCE ON METALLURGY AND MATERIALS (METAL 2012)*. KELTICKOVA 62, SLEZSKA, OSTRAVA 710 00, CZECH REPUBLIC: TANGER LTD, 2012, pp. 1739-1745. ISBN 978-80-87294-31-4.

[2] TYKVA, Tomas, Ivo SPICKA, Milan HEGER and Ondrej ZIMNY. THE STRUCTURE OF HEATING FURNACE. In: *METAL 2016: 25TH ANNIVERSARY INTERNATIONAL CONFERENCE ON METALLURGY AND MATERIALS*. B.m.: TANGER Ltd; Tech Univ Ostrava; pp. 1659-1664. ISBN 978-80-87294-67-3.

[3] ŠPIČKA, Ivo., Jiří DAVID, Milan HEGER and Romana OVČAČÍKOVÁ. Solution of Optimal Heating Process Control for Continuous Industrial Furnaces. In. *International Scientific Conference "FORMING 2005*". B.m.: VŠB - TU Ostrava, 2005, pp. 261-265

COMPARISON OF MULTIVARIATE CONTROL CHARTS IN PRACTICAL APPLICATION IN THE AUTOMOTIVE INDUSTRY

Author(s): Eva TYLEČKOVÁ

Supervisor: prof. Ing. Darja NOSKIEVIČOVÁ, CSc.

Department: Department of Quality Management, Faculty of Materials Science and Technology, VSB – Technical University of Ostrava

Abstract

The aim of the paper is to compare the possibilities of detecting the changes in process or shifts of process parameters by multivariate control charts. The comparison is made using real data from automotive industry, where multiple quality characteristics are measured.

Key words:

Multivariate Control Charts, Hotelling chart, MCUSUM, MEWMA.

1. INTRODUCTION

Industry 4.0 characterized by digitization of industrial processes, the deployment of cyber-physical systems and interconnectivity between elements brings new opportunities for better understanding processes and improving their quality. Moreover Industry 4.0 brings new challenges, in the area of data analysis, these challenges can be seen mainly in unstructured data of large volumes, high dimensionality of data and the acquisition of data from multiple locations on product, in which case individual quality characteristics may be dependent.

In the field of statistical process control, various control charts are offered to face these new opportunities. Due to changes in production processes caused by digitalization and new data collection possibilities, it can be expected that the multivariate control charts will play a major role.

A multivariate control chart represents a single diagram in which each represented point carries information about several observed quality characteristics. It simplify large volumes of data and help uncover relationships between them.

The multivariate control charts are based on Hotelling's T^2 statistic. The principle of the Hotelling statistic is based on the conversion of multivariate observations arranged in vector form into distance values from a vector of mean values. With this conversion, the values can be plotted in a similar way to univariate control charts. The aim of multivariate control charts is to highlight the specific causes of variability in terms of individual observed characteristics, but also in terms of the combination of their values [1].

Compared to classical Shewhart control charts, the construction of multivariate control charts is more complicated and requires the use of statistical software. A clear advantage of multivariate control charts is detection of not only changes in the process due to the effect of assignable causes of variability on individual quality characteristic, but also changes due to the combination of values of correlated quality characteristics.

2. PRACTICAL APPLICATION

The data for a practical application of multivariate control charts comes from the automotive industry. Specifically, the data represents results of weld seam quality assessment, during which the following quality characteristics are monitored:

- length of weld seam,
- weld penetration into base material,

- weld penetration into additional material,
- length of residual material.

The process from which the data originates, provides satisfactory results and a very small percentage of nonconforming weld seams. Nevertheless, there is no long-term monitoring of this process, so there was a need to find a suitable way of monitoring the process in order to detect any deviations, changes in the process or changes in the process parameters.

Statistical process control was proposed as a suitable tool for monitoring changes in this process. To select a suitable control charts, an exploratory data analysis and normality test was first performed for all 4 quality characteristics. The Box-Whisker plots showed that the data contained outliers (4 in total), which were removed from data set for further analysis. According to the Shapiro-Wilk test, the null hypothesis that the data set is normally distributed could not be rejected for any of 4 quality characteristics (with an alpha level of 0.05). The independence of the data was verified by a correlogram. The correlations were identified between some of the quality characteristics. Specifically, correlation of r = -0.26 was identified between the length of weld seam and the weld penetration into base material and correlation of r = -0.30 between the weld penetration into base material and weld penetration into additional material. Both correlations found are statistically significant at the alpha level of 0.05.

As a result of the correlation between quality characteristics, the use of individual control charts for statistical process control could cause incorrect conclusions about the statistical stability of the process. Therefore, instead of classical Shewhart control chart for each quality characteristic, the Hotelling control chart was constructed (see Figure 1).

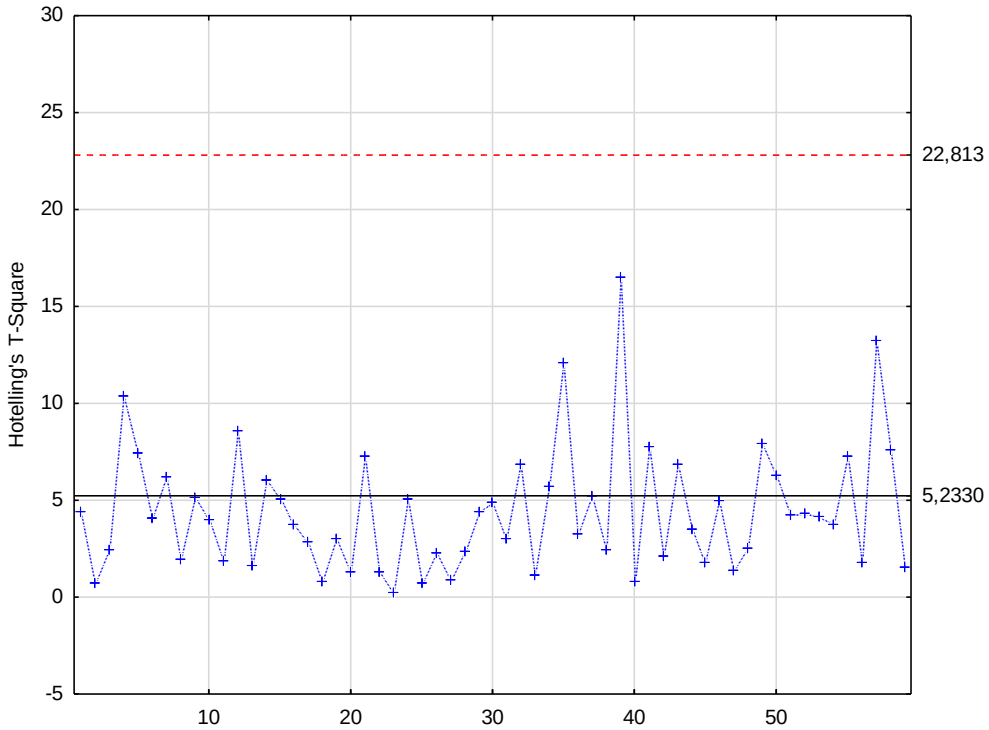

Figure 1 Hotelling chart. Source: (own)

Hotelling chart in figure 1 does not detect any point lying outside the upper control limit and thereby any influence of assignable causes of variability. The points in the chart are situated around the central line and they are not close to the upper control limit. Thus it could be concluded that the process is statistically stable.

In addition to the Hotelling diagram, an MCUSUM (multivariate cumulative sum) chart was also created for the same data set (see Figure 2).

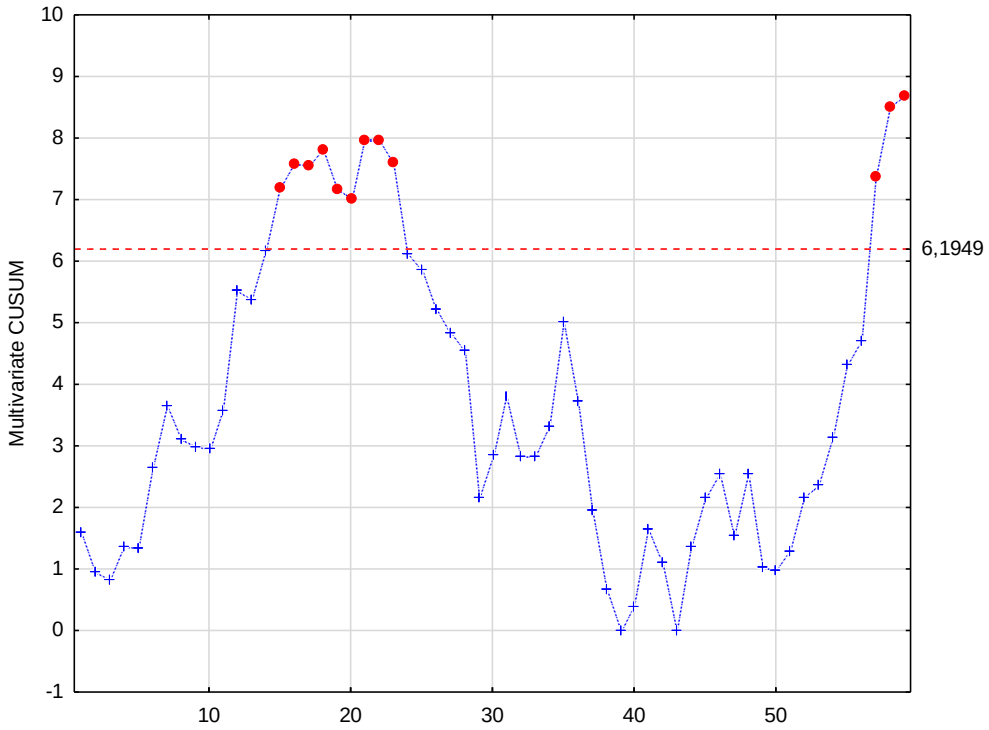

Figure 2 MCUSUM chart. Source: (own)

In contrast to the Hotelling chart, in MCUSUM chart in figure 2 is a clear progression of values towards the control limit until it is exceeded by 9 values in row. This is followed by a noticeable downward trend, but the last values show an increase and control limit is exceeded again by 3 values.

The last multivariate control chart constructed was MEWMA (multivariate exponentially weighted moving average) (see Figure 3). The smoothing parametr λ = 0.2 was chosen according to recomendations in [2].

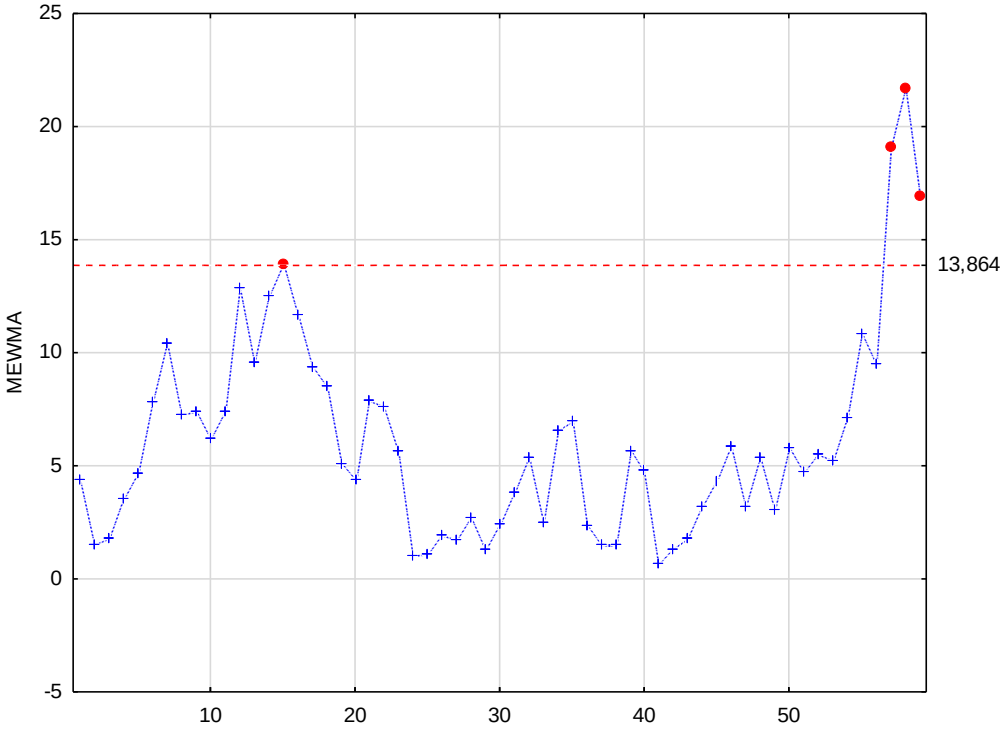

Figure 3 MEWMA chart. Source: (own)

Like MCUSUM, MEWMA chart in figure 3 shows points above the control limit. Compared to the CUSUM, however, there are only 4 points exceeding control limit. It can be concluded that the course of values in MEWMA chart is similar to the course in MCUSUM chart.

3. CONCLUSION

The multivariate control charts are a suitable tool for simultaneous monitoring of multiple quality characteristics on the product. In practical application in this paper the Hotelling chart, MEWMA chart and MCUSUM chart were constructed on the same data set of weld seam quality characteristics.

While the Hotelling chart did not detect any effects of assignable causes of variability, MCUSUM and MEWMA charts showed a few changes in process course. Practical application of the multivariate control charts has confirmed, that MCUSUM and MEWMA charts are generally more sensitive to smaller changes in the mean vector, compared to Hotelling chart. The MCUSUM and MEWMA charts are useful tools for detecting changes in capable processes, where several quality characteristics are assessed.

ACKNOWLEDGEMENT

The work was supported by the specific university research of the Ministry of Education, Youth and Sports of the Czech Republic No. SP2023/043.

REFERENCES

[1] JAROŠOVÁ, Eva a Darja NOSKIEVIČOVÁ. *Pokročilejší metody statistické regulace procesu*. Praha: Grada Publishing, 2015. Expert (Grada). ISBN 978-80-247-5355-3.
[2] MONTGOMERY, Douglas C. *Introduction to statistical quality control*. 8th Edition. Hoboken, NJ: John Wiley & Sons, 2020. ISBN 978-1-118-98915-9.

THE COMPARISON OF TRADITIONAL AND MODERN COSTING METHODS IN THE METALLURGICAL INDUSTRY

Author: Martina ZÁVRBSKÁ

Supervisor: prof. Ing. Petr BESTA, Ph.D.

Department: Department of Industrial Systems Management, Faculty of Materials Science and Technology, VSB – Technical University of Ostrava

Abstract

The article deals with problems related to cost management and calculation methods in foundry production. Through a case study in a selected industrial enterprise, the paper aims to compare a traditional Absorbing cost calculation method with a modern Activity-Based Costing calculation method in foundry production. Furthermore, this work seeks to demonstrate the important role of management costs, not only from the point of view of company management but also from the position of competitive strength and company viability.

Key words:

Activity-Based costing, absorbing costing, cost management, calculation methods, metallurgy.

1. INTRODUCTION

The foundry industry can be characterized as a high capital-intensity field that allocates a significant amount of funds to technology, technical equipment, and environmental safety processes. Therefore, systematically building a competitive advantage in cost management areas is necessary. A company that wants to maintain its position in the market should actively work to preserve and increase its competitiveness. Currently, industrial foundry companies are looking for the most efficient solutions for cost management. This approach requires a cost management process with effective use of modern methods. The paper aims to compare a traditional and modern costing method in foundry production through a case study in a selected industrial enterprise.

2. METHODOLOGICAL BACKGROUND

Foundry Production

Casting is a method of manufacturing parts or articles. First, the molten metal is poured into a mould. This mould has the shape and size of the future product. The product created by the solidification of liquid metal in the mould is called a casting. The casting can sometimes be a finished product or part, or it can be machined even further [1].

We can cast the casting into a foundry mould. This form can be either permanent or non-permanent. A model device (model and cores) is required to make the mould. The device aids us in achieving the desired casting shapes. Castings are often cast in non-permanent, disposable moulds (made from sandstone or a ceramic mixture) or permanent moulds (metal moulds). The inner cavities of the casting are formed by cores, which must be made in special core boxes [1].

Non-permanent moulds are made of moulding material and destroyed after casting. Moulding materials usually contain three components: slags, binders, and additives. The slag forms the basic skeleton of the moulding material and consists of grains larger than 0.02 mm. It determines the basic properties of the mixture, especially compaction, breathability, and chemical and thermal resistance to molten metal. The material most frequently used as slag is Quartz (silica – SiO_2). A binder is a substance that forms the binder system of a moulding mixture and binds them together. Both organic and inorganic binders can be used, but physical principles such as magnetism, vacuum, or freezing can also bond the mixture. Additives improve specific properties of moulding materials. For example, carbonaceous substances may improve the mixture's plasticity properties. Filling of the mould cavity is provided by the inlet system, which consists of the following parts: inlet (casting) hole, inlet channel (pole), impact hole, slag remover, notches. Finally, molten metal is poured into the inlet well [2].

Costing

Calculations are an instrument for the determination of costs and sales prices. Therefore, it follows their strategic importance for managing cost performance. The calculation assigns a cost to the appropriate object (cost unit). The allocation object can be performances, units, or a managerial decision. Cost allocation provides information about relevant costs for decisions [3]. In the traditional concept of cost, calculations provide information on the total cost of a particular object. This information is the basis for profit generation. However, the current market economy brings about new aspects that must be included in cost calculations. It shows that the traditional calculation concept currently providing information on a single cost level needs improvement. Now, cost structures that provide information for various purposes are being used [4].

Absorbing Costing

Absorbing costing is the most widespread calculation method in practice. The advantage of this method is its wide availability and simplicity. The assigning overhead cost to cost object is performed based on the allocation base. The allocation bases can be divided into natural and monetary bases [5]. In the cause monetary bases, the indirect cost rate is calculated in percentages as a proportion of indirect overheads to the chosen monetary base. On the other hand, the indirect cost rate in the cause natural base is determined as a proportion of indirect overhead costs and the natural base selected [6].

Method Activity-Based Costing (ABC)

The calculation principle is allocating overhead costs to individually defined activities. The ABC method was first developed in the 1980s in the United States and is associated with the names Kaplan, Cooper, and Johnson [7].

The essence of the ABC calculation is allocating indirect costs to individual activities through which they are assigned to cost objects based on the causal relationship between the financial source and the cost object. From a methodological point of view, this is a total cost calculation (the so-called absorption method), which can be combined with the non-absorption approach. The implementation of the method was divided into three primary phases. In the first phase, the reasons for implementation are defined, and the structure of the ABC model is then determined. In the next step, an analysis of the implementation costs is performed, and the expected outputs of the system are defined. The second phase is creating the model, which includes implementing the individual steps of creating the ABC system. Finally, the system is operated in the third phase, and automated data acquisition and processing are addressed to ensure its complexity [8,9].

3. THE COMPARISON OF TRADITIONAL AND MODERN COSTING METHODS IN METALLURGY

The case study aimed to compare traditional and modern costing methods in foundry production. The study was performed at a foundry company, which is among the "small enterprises “, based on the criteria for assessing the size of a company (according to Recommendation 2003/361/EC). The foundry’s production programme is focused on the piece and small series production of steel castings (unalloyed, low-alloyed), flake graphite cast iron (FG, Grey Iron), spheroidal graphite cast iron (SG Iron) and non-ferrous metals (aluminium and copper alloys). In addition, products are manufactured based on demand.

Traditional Costing Methods

The costing model applied in the foundry company was the standard type costing model. It is the full cost calculation, so-called absorption costing. The first step of costing is quantifying the liquid metal value of the product. It represents the cost of the primary raw material and energy. The second step is the allocation of labor costs to the prime. The next is the sum of the prime material, the prime labor, and the other prime costs. The result is the prime cost of performance. The third phase is assigning overhead costs according to the traditional calculation method known as absorbing costing. Assigning overhead costs is performed based on the monetary allocation base. The indirect cost rate is calculated in percentages as a proportion of indirect overhead to the direct labor cost. In the result, the full cost of performance is calculated [10].

A comparison between actual and calculated costs was made to obtain basic information on the accuracy of the existing calculations. The analysis demonstrated that calculated costs are compared to the actual cost relatively undervalued. The growing differences in calculations are caused by increasing overhead costs not implemented in the costing.

Based on the analysis result, the implementation of the modern calculation method Activity-Based Costing was proposed.

Modern Costing Methods

Based on the analysis results, the modern calculation method Activity-Based Costing was implemented. The implementation of the ABC method was divided into several primary stages.

The first implementation phase defined the company's activities and cost objects. 14 primary activities were identified to map the basic production operations and human resources (e.g., core production, moulding, extrusion of castings, finishing of castings, blasting, grinding, etc.). Finally, a cost object was identified, namely a casting.

In the second stage, spent economic resources (indirect costs) were assigned to individual activities based on a relational cost variable called the Resource Cost Driver. Total company costs were divided into direct, wage, variable, and fixed. Wages and variable costs were assigned to individual primary activities, and fixed costs were to support activities. The aim was to quantify the total costs of individual activities.

The relationship quantities were determined for the primary and secondary activities in the third step. For this purpose, the activity's relational quantity, called Activity Cost Drivers, was used. It represents certain causal factors that cause a change in the cost of the activity.

Furthermore, the relationship quantities consumed by individual activities were quantified. Then, the unit cost of the activities, the Activity Primary Rate (APR), was calculated. The APR presents the number of expenses per unit of activity. We determine the APR as a proportion of the total expenses and the relationship quantities.

The final stage was assigning the costs of activities to the cost object (for instance, one casting). The assignment of activity costs is performed based on the multiplication of the number of activity units consumed and the unit cost of the activity. Based on the ABC method, a new structure of the calculation sheet was created [10].

4. RESULTS AND DISCUSSION

To evaluate the results of implementing the modern ABC calculation method, a comparison was performed between the traditional absorbing calculation method and the modern ABC calculation method. For comparison, the calculation of grey iron castings for the period 2021 and 2022 was used. In the study framework, direct costs are assumed to include the prime material, the prime labor, and the other prime costs. Furthermore, it is assumed that indirect costs are equal to overhead costs.

In the first step of the analysis, the total calculated costs and the grey iron castings' actual costs were compared (see Table 1). This calculation was performed according to the traditional absorbing calculation method.

Table 1 Comparison of grey iron castings calculation according to the absorbing costing for 2021 (in CZK thousands). Source: (own)

	Calculated costs (CC)	Actual costs	Variance (CC)	Variance (CC) in %
Direct costs	**9 525**	**11 240**	**1 715**	**18.0**
Indirect costs	**20 452**	**28 676**	**8 224**	**40.2**

The second step was comparing the total calculated costs and the actual costs of the grey iron castings calculated according to the ABC calculation (see Table 2).

Table 2 Comparison of grey iron castings calculation according to the ABC calculation for 2022 (in CZK thousands). Source: (own)

	Calculated costs (CC)	Actual costs	Variance (CC)	Variance (CC) in %
Direct costs	**6 125**	**6 702**	**577**	**9.4**
Indirect costs	**16 250**	**18 254**	**2 004**	**12.3**

The analysis has shown that when using absorption costing, the direct cost variance is 18.0 %, and the indirect cost variance is 40.2 %. Based on the ABC method, the direct cost variance is 9.4 %, and the indirect cost variance is 12.3 %. The comparison demonstrates that the ABC calculation method gives a more precise assignment of overhead costs to cost objects than the absorbing cost

calculation. The individual calculation models allocate overhead costs according to dissimilar concepts as follows:

- The principle of ABC calculation is the allocation of overhead costs to individual defined activities, through which they are assigned to cost objects on the basis of a causal relationship between the economic resource and the cost object.
- The traditional absorbing costing method is based on the relationship between cost and volume.

The assessment seems to show that the ABC method concept is more suitable for the constantly changing business environment of the metallurgical industry than the traditional cost concept.

5. CONCLUSION

The current business environment is characterized by customers constantly changing needs and wishes, technological progress, and growing competition. A company that wants to maintain its position in the market must actively work to maintain and increase its competitiveness. The development of the business environment has led to changes in the structure of production processes in accordance with the difference in costs. The decrease in direct labour costs and the increase in overhead costs have shown that traditional costing methods must provide better allocation costs. Traditional cost concepts were based on the relationship between cost and volume. According to Popesko and Petrik, this problem was solved by the Activity-Based Costing method [8,9]. The calculation principle is allocating overhead costs to individually defined activities.

The paper aimed to compare a traditional costing method in foundry production with a modern costing method through a case study in a selected industrial enterprise. The comparison indicates that the ABC calculation method has higher accuracy in assigning overhead costs to cost objects than the absorbing cost calculation. Compared with the traditional absorbing costing, the ABC method is more appropriate for constantly changing the business environment in the metallurgical industry. Method Activity-Based Costing may enable foundry companies to respond more quickly to business environment changes and thus be competitive.

ACKNOWLEDGEMENT

The work was supported by the specific university research of the Ministry of Education, Youth, and Sports of the Czech Republic No. SP2022/27.

REFERENCES

[1] ELBEL, Tomáš. *Základy slévárenské technologie*. Ostrava: Vysoká škola báňská – Technická univerzita Ostrava, 2006.
[2] IŽDINSKÁ, Zita. *Metal casting*. Bratislava: Slovenská technická univerzita, 2007. ISBN 978-80-227-2660-3.
[3] DRURY, Colin. *Management and cost accounting*. 2nd ed. London: Chapman & Hall, 1988. ISBN 0-412-34110-7.
[4] DEAKIN, Edward B., Michael W. MAHER. *Cost accounting*. 2nd ed. Homewood: Irwin, 1987. ISBN 0-256-03572-5.
[5] WILSON, Richard Malcolm Sano, Wai Fong CHUA. *Managerial accounting: method and meaning*. London: VNR International, 1988. ISBN 0-278-00021-5.
[6] LUCEY, Terence. *Costin*g. 3rd ed. London: DP Publications, 1991. ISBN 1870941349.
[7] DOYLE, David. *Cost Control*. London: CIMA Publishing, 2002. ISBN 1 85971 517 6.
[8] POPESKO, Boris. *Moderní metody řízení nákladů*. Praha: Grada Publishing, 2016.ISBN 978-80-271-9050-8.
[9] PETŘÍK, Tomáš. *Procesní a hodnotové řízení firem a organizací - nákladová technika a komplexní manažerská metoda: ABC/ABM (Activity-based Costing/Activity-based Management).* Praha: Linde, 2007. ISBN 978-80-7201-648-8.
[10] *Závěrečná zpráva 2018-2022*.Foundry company, 2022.

Author	PhD students of Faculty of Materials Science and Technology
Faculty	Faculty of Materials Science and Technology
Title	PhD students´day FMST 2023
Place, year of issue	Ostrava, 2023, 1. issue
Number of pages	349
Publisher	VSB – Technical University of Ostrava not for sale
ISBN	978-80-248-4697-2 (on-line)
DOI	10.31490/9788024846972

Faculty of Materials Science and Technology
VSB – Technical University of Ostrava
17. listopadu 2172/15 708 00 Ostrava-Poruba
+420 597 325 374
dekanat.fmt@vsb.cz
fmt.vsb.cz/en